Journal of
Marine Science and Engineering

Special Issue Reprint

Coastal Disaster Assessment and Response

Edited by
Deniz Velioglu Sogut

mdpi.com/journal/jmse

MDPI

Coastal Disaster Assessment and Response

Coastal Disaster Assessment and Response

Guest Editor

Deniz Velioglu Sogut

Basel • Beijing • Wuhan • Barcelona • Belgrade • Novi Sad • Cluj • Manchester

Guest Editor
Deniz Velioglu Sogut
Ocean Engineering and
Marine Sciences
Florida Institute of
Technology
Melbourne, FL
USA

Editorial Office
MDPI AG
Grosspeteranlage 5
4052 Basel, Switzerland

This is a reprint of the Special Issue, published open access by the journal *Journal of Marine Science and Engineering* (ISSN 2077-1312), freely accessible at: https://www.mdpi.com/journal/jmse/special_issues/41096WM1M6.

For citation purposes, cite each article independently as indicated on the article page online and as indicated below:

Lastname, A.A.; Lastname, B.B. Article Title. *Journal Name* **Year**, *Volume Number*, Page Range.

ISBN 978-3-7258-4133-2 (Hbk)
ISBN 978-3-7258-4134-9 (PDF)
https://doi.org/10.3390/books978-3-7258-4134-9

Contents

About the Editor

Deniz Velioglu Sogut

Deniz Velioglu Sogut earned her B.Sc. in Civil Engineering, M.Sc. in Hydromechanics, and Ph.D. in Ocean Engineering from Middle East Technical University in Ankara, Turkiye. After completing her Ph.D., she joined the State University of New York at Stony Brook as a postdoctoral researcher. She is currently an Assistant Professor in the Department of Ocean Engineering and Marine Sciences at Florida Institute of Technology. Her research integrates physical modeling, numerical simulations, and machine learning techniques to enhance the resilience of coastal communities to natural hazards such as storms and tsunamis. She has authored over 40 peer-reviewed publications and received multiple honors in recognition of her scholarly contributions. She currently serves as a reviewer and editorial board member for several high-ranking, peer-reviewed journals in the fields of coastal and ocean engineering and has chaired sessions at major national conferences. Her work has been featured in the media, and she frequently gives invited talks at national and international institutions. She also serves as the faculty advisor for the Students & New Professionals chapter of the American Shore and Beach Preservation Association (ASBPA), supporting the next generation of coastal scientists and engineers. She teaches both undergraduate- and graduate-level courses in coastal engineering and actively mentors M.Sc. and Ph.D. students.

Journal of
Marine Science and Engineering

MDPI

Editorial

Coastal Disaster Assessment and Response

Deniz Velioglu Sogut

Ocean Engineering and Marine Sciences, Florida Institute of Technology, 150 W University Blvd, Melbourne, FL 32901, USA; dvelioglusogut@fit.edu

Coastal communities have become increasingly susceptible to natural hazards over the past few decades, largely due to the effects of climate change [1,2]. The rising frequency and intensity of storms place immense pressure on coastal populations, particularly in low-lying areas, and in regions where economic and logistical challenges often hinder evacuation and recovery efforts [3,4]. Similarly, tsunamis pose a severe threat to coastal communities, especially those near tectonic subduction zones [5]. Communities lacking adequate tsunami early warning systems or evacuation plans face heightened vulnerability, underscoring the urgent need for enhanced disaster preparedness and adaptive resilience strategies.

Traditional Disaster Risk Reduction (DRR) efforts have primarily focused on response and recovery. However, integrating DRR with climate adaptation strategies offers a more proactive approach, enabling local communities to effectively respond to coastal hazards [6]. A key element of building resilience is the implementation of nature-based solutions, which act as natural barriers to mitigate these risks [7–9]. Nature-based approaches can not only protect coastal populations but also enhance biodiversity and ecosystems. Likewise, advances in Geographic Information Systems (GISs) and climate modeling could improve hazard prediction and risk mapping, facilitating improved planning and response measures [10–13]. At the same time, empowering local communities through participatory decision-making and knowledge sharing could ensure that adaptation strategies align with their specific needs. Considering these factors, this Special Issue brings together innovative research on risk assessment and enhancing community resilience in response to coastal hazards.

The article by Yoo and Kwon (contribution 1) explores the liquefaction and reliquefaction behavior of coastal embankments subjected to repeated seismic loading. Through a shaking table experiment, they investigate how different ground conditions influence soil response under cyclic loading with a particular focus on the effects of groundwater fluctuations. Their findings indicate that when an upper non-liquefiable layer is present, liquefaction may not occur initially but can develop after multiple seismic excitations. As repeated earthquakes cause the groundwater level to rise, liquefaction is eventually triggered, even in cases where the main seismic event does not cause immediate failure. Significantly, the study highlights that aftershocks can contribute to liquefaction due to the cumulative effect of groundwater migration. These insights challenge current seismic design codes, which typically assess liquefaction risk only for soil layers below the groundwater table. To enhance the earthquake resilience of coastal infrastructure, the authors stress the importance of incorporating aftershock-induced liquefaction risk and groundwater level variations into hazard assessment frameworks.

Recognizing the growing risks associated with storm-induced coastal processes, Chalmoukis (contribution 2) assesses vulnerability levels through morphodynamic simulations using the Storm-induced BEAch CHange (SBEACH) model. These simulations are combined with inundation estimates derived from two empirical equations for comparative

Received: 26 March 2025
Accepted: 31 March 2025
Published: 14 April 2025

Citation: Velioglu Sogut, D. Coastal Disaster Assessment and Response. *J. Mar. Sci. Eng.* **2025**, *13*, 780. https://doi.org/10.3390/jmse13040780

analysis. By correlating both hazards with return period-based assessments, high-risk coastal areas are identified, offering crucial insights for hazard mitigation planning. A key takeaway from Chalmoukis's research is the importance of accurate hazard modeling to ensure reliable vulnerability mapping. The study highlights the limitations of existing predictive models, many of which assume smooth coastal profiles and uniform seabed conditions—assumptions that may not hold for irregular terrains with submerged rocks and varying sediment grain sizes. Chalmoukis provides an initial large-scale vulnerability assessment, which serves as a valuable guide for optimizing disaster preparedness strategies for coastal regions.

In their study, Nezhad et al. (contribution 3) explore the potential of ENNs to enhance the accuracy, reliability, and robustness of storm surge predictions compared to single-model approaches, highlighting the increasing importance of accurate flood prediction in coastal disaster management. A key focus of Nezhad et al.'s study is the techniques used to aggregate predictions from multiple neural network models, demonstrating how the integration of diverse models can lead to more reliable flood forecasts. The study reveals that there is no universal approach to constructing an optimal ENN model for storm surge forecasting. Instead, it is necessary to assess different ensemble configurations to strike a balance between bias and variance, ensuring a trade-off between accuracy, diversity, stability, generalization, and computational efficiency. Nezhad et al.'s findings are particularly relevant for coastal researchers, engineers, and planners, emphasizing the growing role of ENNs in storm surge forecasting, supporting better preparedness and response strategies for coastal hazards. The authors were awarded the Editor's Choice Article Award in recognition of their work.

Li et al. (contribution 4) assess the applicability of the Global Synthetic Tropical Cyclone Hazard (GSTCH) dataset for tropical cyclone hazards. To evaluate its reliability, the authors compare it with the Tropical Cyclone Best Track (TCBT) dataset, an authoritative dataset developed by the China Meteorological Administration. The findings indicate that key cyclone characteristics, such as landfall wind speed, central pressure at landfall, and annual cyclone frequency, show no statistically significant differences between the two datasets at a 95% confidence level. Additionally, the cumulative distributions of the central maximum wind speed and central minimum pressure along cyclone tracks pass the Kolmogorov–Smirnov test, confirming that the GSTCH dataset aligns with the TCBT dataset at the provincial and regional scales. They conclude that the GSTCH dataset is a reliable and applicable data source for tropical cyclone hazard assessments, demonstrating strong agreement with the widely accepted TCBT dataset. These findings reinforce the credibility of the GSTCH dataset as a valuable tool for long-term cyclone hazard studies and risk assessments.

In their study, Hwang et al. (contribution 5) examine the morphological changes in coastal areas following the Super Typhoon Hinnamnor (2022), emphasizing the need for accurate observation and modeling to support coastal management. They employ the XBeach model to simulate pre- and post-storm subaerial data. To enhance model accuracy, Hwang et al. place particular emphasis on waveform parameters, including wave skewness and asymmetry, assessing whether these factors should be treated independently or integrated to improve the representation of sediment deposition from overwash events. They evaluate the model's performance and sensitivity by analyzing volume changes, revealing that waveform parameters significantly impact deposition patterns. Their findings provide valuable insights into optimizing parameter selection and calibration for models simulating coastal sediment transport, improving predictive accuracy in coastal morphological modeling.

Velioglu Sogut et al. (contribution 6) investigate the performance of two numerical approaches in estimating non-equilibrium foundation scour patterns around a non-slender square structure subjected to a transient wave. They compare numerical results with experimental data to evaluate the accuracy and effectiveness of these approaches. The first numerical approach models sediment particles as a separate continuum phase, directly solving continuity and momentum equations for both sediment and fluid phases. The second approach predicts sediment transport using the quadratic law of bottom shear stress, achieving accurate bed evolution estimates through careful calibration and validation. Their findings underscore notable differences in the predictive capabilities of both methods, particularly in modeling non-equilibrium scour evolution at low Keulegan–Carpenter numbers. Their work provides valuable insights into the strengths and limitations of these numerical approaches, contributing to advancing scour prediction techniques in coastal engineering applications.

In their study, Ma et al. (contribution 7) examine the impact of vegetation on wave attenuation and dune erosion, using the XBeach surfbeat model (XBSB) to simulate conditions at Mexico Beach during Hurricane Michael (2018). They investigate how different vegetation drag coefficients influence wave energy reduction and dune stability. Their findings highlight the significant role of dune vegetation in wave attenuation and erosion control. Ma et al. emphasize that as vegetation drag coefficients increase, wave energy dissipation improves, resulting in less dune erosion. Additionally, higher vegetation density enhances wave height reduction and flow velocity damping within vegetated areas. However, the findings suggest that beyond a certain density, the rate of improvement in wave attenuation diminishes, providing negligible additional benefits. Ma et al.'s results emphasize the vital role of coastal vegetation in enhancing resilience against storm-induced impacts, offering valuable insights for coastal management strategies and disaster mitigation planning.

In their work, Corkran et al. (contribution 8) analyze the spatiotemporal trends of tropical cyclones (TCs) affecting the state of Georgia, recognizing that research on Georgia-specific TCs remains limited due to the state's small coastline and the infrequency of direct landfalls. Using data from the North Atlantic Basin hurricane database, they quantify both direct and indirect TC landfalls in Georgia from 1851 to 2021. Applying a multi-method approach by combining statistical analysis and mapping, the authors examine 113 tropical cyclones that affected Georgia, identifying September as the month with the highest percentage of TC-induced rainfall, followed by October and August, which aligns with peak TC activity. Their findings highlight the heightened risk posed by TCs during the peak season, emphasizing the need for increased preparedness, strategic resource allocation, and disaster planning to protect Georgia's communities, historical landmarks, and natural environments from the long-term impacts of TC activity.

In their research, Santos and Mileu (contribution 9) evaluate the tsunami inundation risk in Caxias, Portugal. They generate a Digital Elevation Model (DEM) using newly obtained LiDAR data and integrate it into the TUNAMI-N model to improve the precision of inundation predictions. Additionally, the authors highlight the coastal characteristics and existing protective structures in the region, which are identified through a field survey conducted at various locations. The findings reveal that low-lying areas in the study region would be flooded if a tsunami comparable to the 1755 Lisbon event occurred. To mitigate these risks, the authors recommend constructing seawalls and installing a pedestrian bridge over the Barcarena Stream, which would act as a barrier against incoming tsunami waves. This study underscores the importance of integrating these coastal protection measures into long-term resilience planning to minimize the impacts of tsunamis and winter storm surges, not only in Caxias but also in other vulnerable coastal regions in Portugal.

Hu et al. (contribution 10) examine the 2018 Sulawesi tsunami, utilizing simple and accessible remote sensing techniques to assess the extent of destruction and indirectly evaluate the region's vulnerability to such disasters. The authors employ Sentinel-2 and

Maxar WorldView-3 satellite imagery to analyze the affected areas in Palu, Indonesia, by quantifying changes in vegetation, soil moisture, and water bodies, effectively mapping the tsunami's impact on land cover. The resulting inundation map reveals that the most heavily affected zones are concentrated in urban centers, low-lying areas, and coastal regions. Unlike high-resolution remote sensing methods that depend on specialized or proprietary tools, Hu et al. emphasize a more accessible and cost-effective approach that is particularly beneficial for resource-limited regions and rapid disaster response efforts. Additionally, the research tackles the challenge of distinguishing tsunami-related damage from other geological phenomena such as liquefaction, utilizing index-based thresholds to enhance classification accuracy. The proposed framework is highly adaptable and can be applied to other vulnerable coastal areas, offering a practical, efficient, and low-cost solution for post-tsunami damage assessment.

The concluding study in this Special Issue, conducted by Mayorga et al. (contribution 11), analyzes the structural response of single-story timber houses to the 2010 Chile tsunami in San Juan Bautista, an island town in the Pacific Ocean. The ASCE 7–22 energy grade line analysis (EGLA) is used to calculate flow depths and velocities, incorporating topographic data and recorded runup measurements. The structural evaluation follows Load and Resistance Factor Design (LRFD) principles, accounting for both dead and live loads. The findings reveal that houses near the shoreline undergo significant displacement and collapse, caused by hydrodynamic forces, drag, and buoyancy effects, which weaken foundation anchorage. In contrast, structures further inland experience lower flow velocities, leading to reduced displacement, lower structural demand, and an increased tendency to float. To verify the approach, Mayorga et al. perform a nonlinear analysis on structures exposed to tsunami forces at varying distances from the coast. Although lightweight timber houses demonstrate strong seismic performance, the authors find them unsuitable for tsunami-prone areas due to their vulnerability to hydrodynamic loads. The research emphasizes the importance of using heavier, more rigid materials in flood-prone areas and relocating lightweight structures to safer zones to improve tsunami resilience in coastal communities.

Acknowledgments: As the Guest Editor of the Special Issue, *Coastal Disaster Assessment and Response*, I wholeheartedly acknowledge the efforts of all the authors. Their contributions have played a vital role in making this Special Issue a success.

Conflicts of Interest: The authors declare no conflicts of interest.

List of Contributions

1. Yoo, M.; Kwon, S.Y. Evaluation of Reliquefaction Behavior of Coastal Embankment Due to Successive Earthquakes Based on Shaking Table Tests. *J. Mar. Sci. Eng.* **2023**, *11*, 1002. https://doi.org/10.3390/jmse11051002.
2. Chalmoukis, I.A. Assessing Coastal Vulnerability to Storms: A Case Study on the Coast of Thrace, Greece. *J. Mar. Sci. Eng.* **2023**, *11*, 1490. https://doi.org/10.3390/jmse11081490.
3. Nezhad, S.K.; Barooni, M.; Velioglu Sogut, D.; Weaver, R.J. Ensemble Neural Networks for the Development of Storm Surge Flood Modeling: A Comprehensive Review. *J. Mar. Sci. Eng.* **2023**, *11*, 2154. https://doi.org/10.3390/jmse11112154.
4. Li, X.; Hou, Q.; Zhang, J.; Zhang, S.; Du, X.; Zhao, T. Applicability Evaluation of the Global Synthetic Tropical Cyclone Hazard Dataset in Coastal China. *J. Mar. Sci. Eng.* **2024**, *12*, 73. https://doi.org/10.3390/jmse12010073.
5. Hwang, B.; Do, K.; Chang, S. Morphological Changes in Storm Hinnamnor and the Numerical Modeling of Overwash. *J. Mar. Sci. Eng.* **2024**, *12*, 196. https://doi.org/10.3390/jmse12010196.
6. Velioglu Sogut, D.; Sogut, E.; Farhadzadeh, A.; Hsu, T.-J. Non-Equilibrium Scour Evolution around an Emerged Structure Exposed to a Transient Wave. *J. Mar. Sci. Eng.* **2024**, *12*, 946. https://doi.org/10.3390/jmse12060946.

7. Ma, M.; Huang, W.; Jung, S.; Oslon, C.; Yin, K.; Xu, S. Evaluating Vegetation Effects on Wave Attenuation and Dune Erosion during Hurricane. *J. Mar. Sci. Eng.* **2024**, *12*, 1326. https://doi.org/10.3390/jmse12081326.
8. Corkran, R.; Trepanier, J.; Brown, V. Spatiotemporal Climatology of Georgia Tropical Cyclones and Associated Rainfall. *J. Mar. Sci. Eng.* **2024**, *12*, 1693. https://doi.org/10.3390/jmse12101693.
9. Santos, A.; Mileu, N. Coastal Protection for Tsunamis. *J. Mar. Sci. Eng.* **2024**, *12*, 2349. https://doi.org/10.3390/jmse12122349.
10. Hu, Y.; Barberopoulou, A.; Koch, M. Tracing the 2018 Sulawesi Earthquake and Tsunami's Impact on Palu, Indonesia: A Remote Sensing Analysis. *J. Mar. Sci. Eng.* **2025**, *13*, 178. https://doi.org/10.3390/jmse13010178.
11. Mayorga, D.O.; Vielma, J.C.; Winckler, P. Structural Failure Modes of Single-Story Timber Houses Under Tsunami Loads Using ASCE 7'S Energy Grade Line Analysis. *J. Mar. Sci. Eng.* **2025**, *13*, 484. https://doi.org/10.3390/jmse13030484.

References

1. U.S. Global Change Research Program. *Climate Science Special Report: Fourth National Climate Assessment, Volume I.*; U.S. Global Change Research Program: Washington, DC, USA, 2017. [CrossRef]
2. Michel, V.; Eghdami, S.; Shafiee-Jood, M.; Louis, G. Addressing social equity in coastal climate adaptation planning: A case study of Norfolk, Virginia. *PLoS Clim.* **2024**, *3*, e0000516. [CrossRef]
3. Logan, T.M.; Guikema, S.D.; Bricker, J.D. Hard-adaptive measures can increase vulnerability to storm surge and tsunami hazards over time. *Nat. Sustain.* **2018**, *1*, 526–530. [CrossRef]
4. Velotti, L. Natural Hazards: Tsunamis. In *Encyclopedia of Security and Emergency Management*; Springer International Publishing: Cham, Switzerland, 2021; pp. 693–696.
5. Velioglu, D. Advanced Two-and Three-Dimensional Tsunami Models: Benchmarking and Validation. Ph.D. Thesis, Middle East Technical University, Ankara, Turkey, 2017. Available online: https://www.tandfonline.com/doi/full/10.1080/13549839.2025.2462556 (accessed on 20 March 2025).
6. Dinh, N.C.; Tan, N.Q.; Ty, P.H.; Phuong, T.T.; Linh NH, K. Bridging climate vulnerability and household poverty: Perspectives from coastal fishery communities in Vietnam. *Local Environ.* **2025**, 1–18. [CrossRef]
7. Seddon, N. Harnessing the potential of nature-based solutions for mitigating and adapting to climate change. *Science* **2022**, *376*, 1410–1416. [CrossRef] [PubMed]
8. Torabbeigi, M.; Akbari, H.; Adibzade, M.; Abolfathi, S. Modeling wave dynamics with coastal vegetation using a smoothed particle hydrodynamics porous flow model. *Ocean Eng.* **2024**, *311*, 118756. [CrossRef]
9. Emery, K.; Baxter, T.; Callahan, M.; Cavanaugh, K.; Dugan, J.; Engeman, L.; Hubbard, D.; Johnston, K.; Walker, I.; Wisniewski, J. Evaluating the response of a pilot dune restoration project on an urban beach to an extreme wave surge event. *Shore Beach* **2024**, *92*, 28–33. [CrossRef]
10. Darwish, K. Integrated coastal zone management (ICZM) using satellite remote sensing and GIS technology. In *New Advancements in Geomorphological Research: Issues and Challenges in Quantitative Spatial Science*; Springer Nature: Cham, Switzerland, 2024; pp. 355–381.
11. Prem Kooniyara, V. Predicting Urban Greening Potentials with Artificial Intelligence Model: A GIS-based Machine Learning Approach for Local Assessment. Master's Thesis, Technical University of Munich, Munich, Germany, 2025.
12. Eldardiry, H.; Sun, N.; Yan, H.; Reed, P.; Thurber, T.; Rice, J. Characterizing how meteorological forcing selection and parameter uncertainty influence Community Land Model version 5 hydrological applications in the United States. *J. Adv. Model. Earth Syst.* **2025**, *17*, e2024MS004222. [CrossRef]
13. Ekeh, A.H.; Apeh, C.E.; Odionu, C.S.; Austin-Gabriel, B. Leveraging machine learning for environmental policy innovation: Advances in Data Analytics to address urban and ecological challenges. *Gulf J. Adv. Bus. Res.* **2025**, *3*, 456–482. [CrossRef]

Journal of
Marine Science and Engineering

Article

Evaluation of Reliquefaction Behavior of Coastal Embankment Due to Successive Earthquakes Based on Shaking Table Tests

Mintaek Yoo [1] and Sun Yong Kwon [2,*]

[1] Department of Civil & Environmental Eng., Gachon University, 1342 Seongnam-daero, Seongnam-si 13120, Republic of Korea; mintaekyoo@gachon.ac.kr
[2] Environmental Assessment Group, Korea Environment Institute, 370 Sicheong-daero, Sejong-si 30147, Republic of Korea
* Correspondence: sykwon@kei.re.kr

Abstract: Liquefaction caused by long-term cyclic loads in loose saturated soil can lead to ground subsidence and superstructure failures. To address this issue, this study aimed to emulate the liquefaction phenomenon based on a shaking table test while especially focusing on the soil behavior mechanism due to the reliquefaction effect. Liquefaction and reliquefaction behaviors were analyzed by ground conditions where an embankment was located on the coastal ground. Silica sand was used for the experiment for various thickness and liquefiable conditions, and the embankment model was constructed above the model ground. For seismic waves, sine wave excitation was applied, and a total of five excitations (cases) were conducted. When the upper ground layer consisted of a non-liquefiable layer, liquefaction did not occur due to the first excitations but occurred by the third excitation. The results indicated that as the earthquake was applied, the water level in the liquefiable layer increased to the height of the non-liquefiable layer and liquefaction could occur. It was identified that even if liquefaction did not occur for the main earthquake, liquefaction could occur due to aftershocks caused by a rise in the groundwater level due to a series of earthquakes. In a general seismic design code, liquefaction assessment is performed only for soil layers below the groundwater level; however, when successive earthquakes occur, unexpected liquefaction damage could occur. Therefore, to mitigate the earthquake risk of liquefaction for coastal embankments, it is necessary to evaluate the liquefaction by aftershocks even when the groundwater level of the ground layer under an embankment is low.

Keywords: reliquefaction; liquefaction; coastal embankment; excess pore pressure; aftershock

Citation: Yoo, M.; Kwon, S.Y. Evaluation of Reliquefaction Behavior of Coastal Embankment Due to Successive Earthquakes Based on Shaking Table Tests. *J. Mar. Sci. Eng.* **2023**, *11*, 1002. https://doi.org/10.3390/jmse11051002

Academic Editor: Deniz Velioglu Sogut

Received: 7 April 2023
Revised: 4 May 2023
Accepted: 5 May 2023
Published: 8 May 2023

1. Introduction

In recent years, the coast has been reclaimed in several areas of the world for the development of industrial complexes, wind power generation, tourism complexes, etc., and coastal areas with high liquefaction concerns are increasing. In particular, with the increasing number of cases of constructing a coastal embankment after reclamation and using the embankment as a foundation for a wind power generation facility or using it as a walking trail or bicycle road for tourism effects, concerns over liquefaction damage to coastal embankments are growing. Liquefaction is a phenomenon in which soil loses its resistance and behaves in a manner similar to a liquid due to a gradual increase in excess pore water pressure caused by long-term cyclic loads in loose saturated soil. When liquefaction occurs, the soil loses its strength and ability to support superstructures such as buildings and bridges, which can lead to ground subsidence and superstructure failures.

On the other hand, soil densification due to rearrangement and reconsolidation of particles after liquefaction increases the resistance in future earthquakes, and this theoretical mechanism is widely applied to ground improvement construction such as compaction to prevent liquefaction. However, some cases suggest that this intuitive theory is not necessarily applicable in all cases. After the first liquefaction, severe cases of reliquefaction due to aftershocks have been continuously reported [1–6], and the results of related lab experiments also support these cases [7–11]. To understand and prepare for the dynamic behavior of the ground that is different from the widely known general theory, in-depth research on aftershock and reliquefaction mechanisms is required, but related research is still lacking. Moreover, the recent Türkiye–Syria earthquake resulted in more serious damage due to aftershocks than due to the main earthquake, reminding us of the need for research on aftershocks, which have been relatively understudied.

Based on the 1983 Nihonkai–Chubu earthquake, Ohara et al. found that liquefaction occurs in the soil at lower peak ground acceleration and shear stress ratio values than those at the initial states, and reliquefaction can occur during earthquakes with magnitudes smaller than those of earthquakes that occurred previously [12]. Oda et al. investigated the reliquefaction behavior of saturated granular soils through lab tests [13]. They identified that liquefaction resistance was significantly lost if large excess pore pressure was generated in the first cycle. Furthermore, they investigated the influence of several soil parameters such as the void ratio, relative density, inherent isotropy, and void shape on reliquefaction behavior. Zhao and Ye performed a series of 3D DEM simulations of undrained cyclic triaxial tests, and the entire process of main shock-induced liquefaction, reconsolidation with various degrees, and aftershock-induced reliquefaction was reproduced [14]. They identified that the reliquefaction resistance of a completely reconsolidated soil may be higher or lower than its initial liquefaction resistance, which is mainly affected by the residual anisotropy caused by the first liquefaction. They also identified that reliquefaction resistance is significantly affected by the reconsolidation degree. By employing a shaking table test, Ha et al. created soils based on five types of sand tests with a high likelihood of liquefaction and analyzed the effects of the sand gradation characteristics on changes in the reliquefaction resistance during reliquefaction [15]. They observed that as D_{10}/C_u increased, the reduction rate of the reliquefaction resistance decreased linearly, and that as D_{10}/C_u exceeded 0.15 mm, the reduction rate of resistance during reliquefaction was constant at approximately 20%. Moreover, based on the number of loading cycles and excess pore water pressure over time, it was confirmed that the probability of liquefaction decreased as the excess pore water pressure decreased when the fourth and fifth shaking loads were applied. In a recent study on reliquefaction, Nepal et al. measured the excess pore water pressure and acceleration response based on reliquefaction experiments [16]. As observed, (a) the liquefaction resistance of sand was lower in the second liquefaction than that in the first, (b) the liquefaction resistance varied with depth, and (c) the probability of liquefaction of the soil layer near the surface was high. In addition, several researchers confirmed that seismic shear wave damping in a liquefiable soil layer had different characteristics from that of a general soil layer. In contrast, several studies recently investigated liquefaction behavior while considering biaxial effects using experimental and numerical approaches [17–21]. They studied the relationship between detailed properties of the soil and the liquefaction pattern according to the occurrence of excess pore water pressure and found important results such as the effects of load non-proportionality and a direct function of the phase angle of the induced shear stresses on pore water pressure buildup.

The results of the studies described above are meaningful in helping us understand the reliquefaction behavior following the occurrence of aftershocks and recent advances on soil liquefaction. However, considering that the greatest damage in the event of liquefaction and reliquefaction is mainly due to settlement or collapse of superstructures, there is a limitation because these studies treated the behavior of the soil itself and not of the soil with structures such as an embankment. Several previous studies employed a numerical approach to investigate the seismic behavior for the liquefiable soil condition of offshore structures such as breakwaters and pipelines [22,23]. Other studies performed numerical or experimental studies on earthquake behavior of embankments and identified that the widespread damage to such piles and embankments occurred mainly due to the liquefaction of foundation soil, resulting in excessive settlements, lateral spreading, and slope instability [24–31]. However, the key to the above studies was to investigate the seismic behavior of the embankments or other coastal structures, which was far from the reliquefaction behavior of embankment structures, which play an important role in securing the stability of major infrastructure. Therefore, it is necessary to investigate reliquefaction in scenarios involving structures such as embankments.

In this study, the reliquefaction behavior characteristics of coastal embankment structures, which have location characteristics with great concerns regarding liquefaction and reliquefaction occurrences and may cause great damage, were investigated. As demonstrated in this study based on a shaking table that could simulate liquefaction, the thicknesses of the liquefiable and non-liquefiable layers in the ground on which an embankment was installed to obtain shaking load data for each ground layer when reliquefaction occurred were used to confirm the natural frequency and time history graphs of the response data. Additionally, the excess pore water pressure ratios were calculated from the first to fifth liquefaction cycles using a pore water pressure transducer, and a comparative analysis was conducted on the correlation between the acceleration and excess pore water pressure ratio during reliquefaction.

2. Liquefaction and Reliquefaction Mechanisms

Liquefaction can be classified into flow liquefaction and cyclic mobility. Flow liquefaction can occur when the static shear stress exceeds the steady-state strength. This phenomenon occurs primarily on slopes and causes flow failure, which is the most dangerous form of liquefaction-related damage. Cyclic mobility occurs when the static shear stress is less than the shear strength of the liquefiable ground. It mainly occurs in coastal areas with gentle slopes and when shaking occurs in uncompacted sandy soil with a short sedimentation age, such as saturated sand [32].

A characteristic of soil reliquefaction behavior is that the liquefaction resistance can decrease rapidly although the soil density increases as induced by drainage after liquefaction. Oda et al. reported that when liquefaction occurs in the soil, the grain structure of the soil is rendered unstable due to shear deformation [13]. Accordingly, excess pore water pressure increases abruptly, thereby allowing for liquefaction to occur more readily even due to small earthquakes. Ha compared the number of loading cycles with the change in excess pore water pressure during reliquefaction and confirmed that fewer load repetitions were required to trigger reliquefaction when compared with the initial liquefaction [33].

3. Materials and Methods

3.1. Ground Properties and Embankment Specifications

Silica sand No. 7 was used for the ground composition of the shaking table test. Figure 1 presents the grain size distribution of silica sand No. 7, which is included in the liquefaction hazard range (grain size range: 0.01–1.0 mm) suggested by the Applied Technology Council [34]. Table 1 lists the physical properties of the silica sand. The specific gravity (Gs) of the silica sand No. 7 used in this test was 2.65, the maximum dry unit weight was 18.17 kN/m^3, and the minimum unit dry weight was 13.47 kN/m^3. The dimensions of the model embankment were determined virtually based on the coastal embankment located in the S-Project in South Korea. Three types of similitude law were suggested by Iai [35]. Given that liquefaction closely resembles the strain-softening behavior, the third form of the similitude law was applied, and the ratio of the similitude was 40. Table 2 lists the properties of the embankment models.

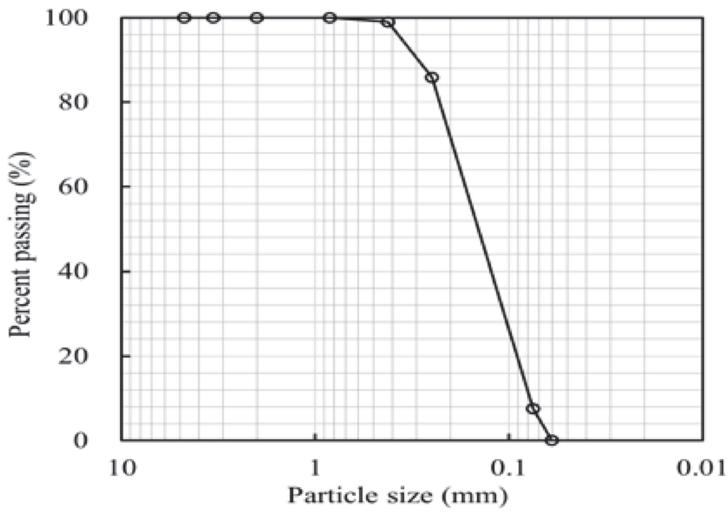

Figure 1. Particle size distribution curve for model soil.

Table 1. Soil properties of the model soil.

Parameter	Value
Specific gravity, G_s	2.65
Maximum void ratio, e_{max}	0.93
Minimum void ratio, e_{min}	0.43
Relative density, D_r(%)	50
Residual friction angle, $\varnothing$(°)	30.5
Mean particle size, D_{50}(mm)	0.11
Uniformity coefficient, C_u	2.89
Coefficient of curvature, C_c	1.07
Permeability, k (m/s)	2.51×10^{-4}

Table 2. Mechanical properties of the embankment model.

Parameter	Prototype	Model	Similitude Relationship
Top (mm)	14,000	350	λ
Bottom (mm)	28,400	710	λ
Height (mm)	4000	100	λ
Length (mm)	20,000	500	λ
Volume (cm^3)	1.696×10^9	26,500	λ^3
Density (kg/m^3)	2000	2000	1
Load (kg)	3,392,000	53	λ^3
Stress (kgf/m^2)	5971.83	149.30	λ

3.2. Seismic Waves

Figure 2 presents the input base motion profile, which was measured on a shaking table. In the shaking table test, a sinusoidal wave of 5 Hz was determined as the input motion, which corresponded to a sinusoidal wave of 0.8 Hz at the prototype scale while applying Iai's type 3 similitude relationship. Each sine wave excitation had a duration of 8 s; namely, 1.5 s for the increasing section, 5.0 s for the constant section, and 1.5 s for the decreasing section with an input acceleration of 0.2 g, which is the return period of a 2400-year earthquake in the Korean seismic design code. A total of five vibrations were excited to analyze the reliquefaction behavior due to successive earthquakes. The excitation interval was set to 1800 s so that the excess pore water pressure could be sufficiently dissipated. As a result of observing the dissipation of the excess pore water pressure through the measured pore water pressure with the pore water pressure transducer, it was confirmed that the excess pore water pressure converged to zero at around 600 s.

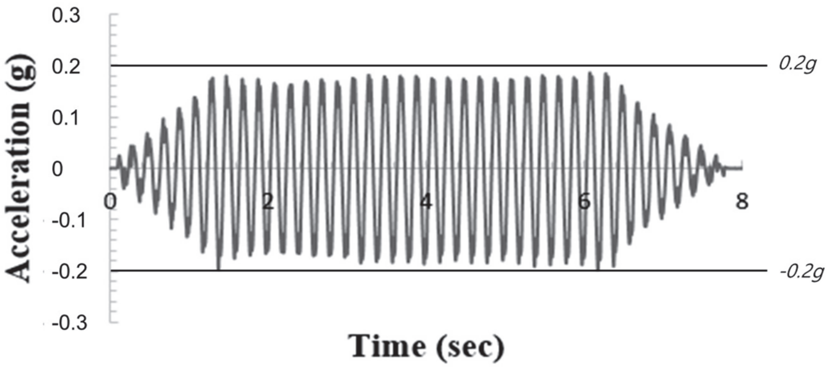

Figure 2. Base motion at 0.2 g and 5 Hz.

3.3. Experimental Method

To analyze the behavior of the coastal embankment with respect to the thickness of the non-liquefiable layer, the soil compositions were divided into two cases as follows. In Case 1, the soil layer comprised only a 50 cm liquefiable layer, and in Case 2, there were two layers; i.e., a 32.5 cm lower liquefiable layer and a 17.5 cm upper non-liquefiable layer. For each experiment, a reliquefaction test was conducted with five sine wave excitations using a shaking table. Gravel with a size ranging from 1 to 2 cm and a unit weight of 2.0 kN/m^3 was used for the embankment, which had a height of 10 cm and a fixed slope ratio of 1:1.8. The model simulated an actual embankment at a scale of 1:40. Given that an embankment is a fill structure on a road surface, an overload of 53 kg was applied while considering the actual weight of the section. To form the ground of the liquefiable layer, a sieve was installed on the soil box. Next, the soil particles were separated as evenly as possible; they were slowly dropped into the water to create a composition similar to the formation principle of the sedimentary layer, and the silica sand was saturated in water for 72 h. The model ground was formed at a relative density of 50%. The relative density was measured during a preliminary test. A sample could be placed every 10 cm from the bottom of the soil box when preparing the model ground. The ground composition was stopped; the sample was removed; and the weight, volume, and water content were measured to calculate the unit weight and relative density when the ground composition was completed. Afterwards, the model ground was formed in the same way, and the target relative density was constructed by making the weight of soil used in ground composition the same as that in the preliminary test. The non-liquefiable layer formed a total liquefiable ground, and then a hose was installed and dewatered after excavating so that the location did not interfere with the installation of the embankment and instrumentation to create the non-liquefiable layer. Figure 3 illustrates the procedure employed for the experimental setup. The test was conducted using a soil chamber with a length, width, and height of 200 cm, 50 cm, and 70 cm, respectively. To reduce the boundary effect of waves due to the stiffness of the soil chamber during shaking, a 5 cm thick sponge was installed on both walls of the soil chamber. Figures 4 and 5 present the cross sections in the experiment, including the measuring instrument. To analyze the ground behavior during reliquefaction and the occurrence of liquefaction with respect to depth, piezometers were installed at the end of the embankment, at the center of the embankment, and in the free field at depths of approximately 10 cm, 20 cm, 30 cm, 40 cm, and 45 cm from the ground surface. The piezometers were fixed using aluminum rods to maintain a constant height in the liquefiable soil. Accelerometers were installed at depths of 0, 10, 20, 30, 40, and 50 cm from the ground surface and fixed to a square acrylic plate to ensure soil-like behavior when liquefaction occurred. Linear variable differential transformers (LVDTs) were installed at the center of the embankment and free field to measure the amount of settlement in the embankment and free field. The test programs are summarized in Table 3.

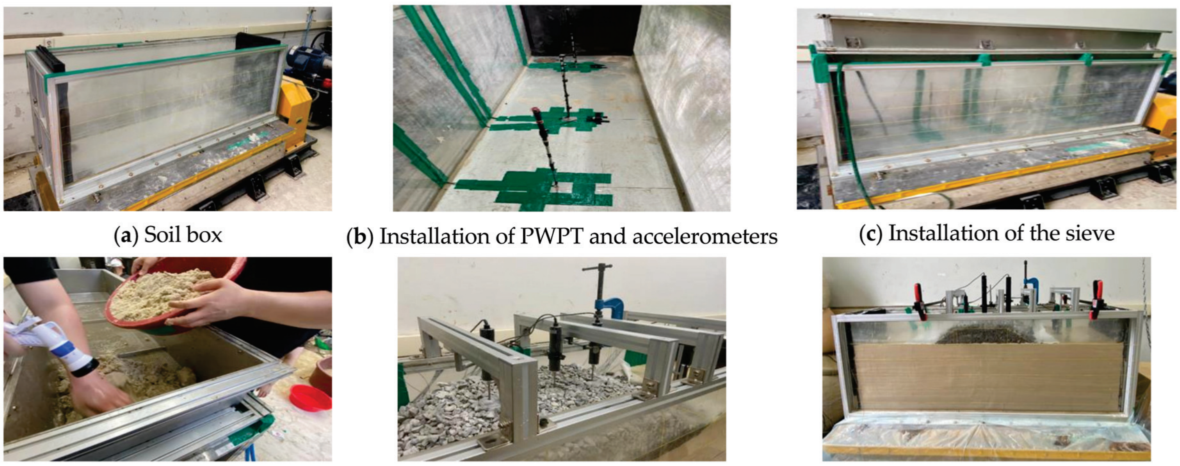

(**a**) Soil box (**b**) Installation of PWPT and accelerometers (**c**) Installation of the sieve

(**d**) Construction of ground layer (**e**) Construction of embankment (**f**) Completion of model ground

Figure 3. Test setup.

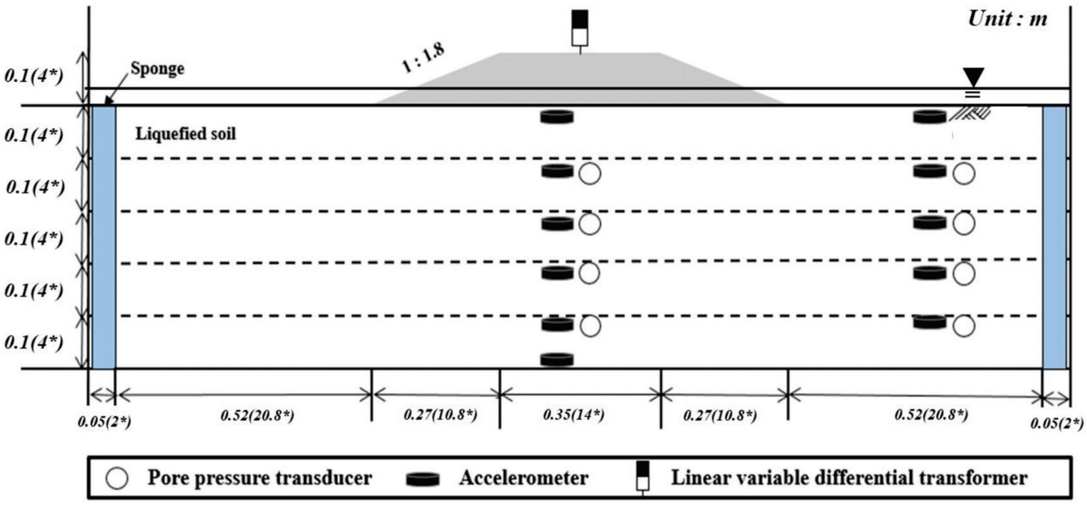

Figure 4. Schematic drawing of test section of liquefiable ground for model scale of Case 1 (* prototype scale).

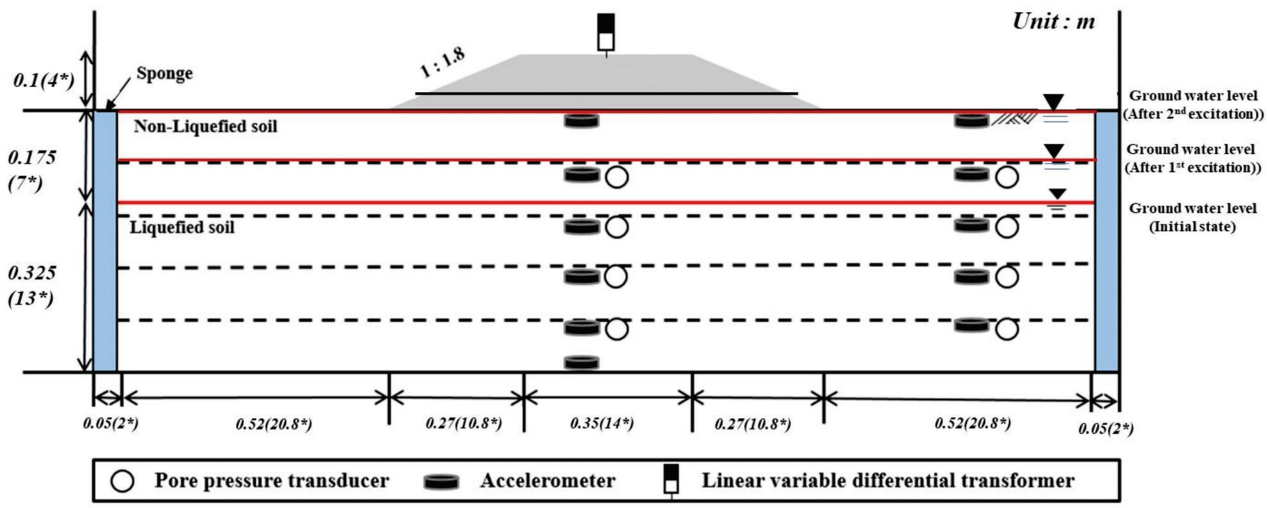

Figure 5. Schematic drawing of test section of non-liquefiable and liquefiable ground for model scale of Case 2 (* prototype scale).

Table 3. Test program.

Case	Composition of Facilities	Thickness of the Lower Liquefiable Layer (m)	Thickness of the Upper Non-Liquefiable Layer (m)	Note
Case 1	Embankment (h = 0.1 m, slope: 1:1.8 fixed)	0.500 (20) *	0	Performance with 1–5 vibrations to confirm reliquefaction behavior
Case 2		0.325 (12.5) *	0.175 (7.5) *	

* Prototype properties.

4. Results and Discussion

Based on the shaking table tests, the accelerometers, piezometers, and LVDTs installed in each layer were used to calculate the acceleration–time history, excess pore water pressure ratio, embankment settlement amount, and relative density. The results presented in the subsequent sections were based on a scaled embankment model (1:40) experiment scaled to the prototype size using the third form of the Iai similitude.

4.1. Liquefiable Ground Case (Case 1)

All test results were described at the prototype scale by applying a similitude ratio. To obtain data on the shaking load for each ground layer and check the state of liquefaction, 11 accelerometers and 8 pore water pressure transducers were installed for the experiment as shown in Figure 4. Figure 6 presents the acceleration–time history measured during the first excitation using accelerometers installed on the ground surface and at a depth of 16 m in the free field. The acceleration–time history also indicates the occurrence of liquefaction. Figure 6a reveals that the acceleration decreased rapidly due to the occurrence of liquefaction at the ground surface below the embankment. Given that the ground behaved similarly to a liquid when liquefaction occurred, the ground reaction did not occur and the amplitude decreased [36]. In contrast, liquefaction did not occur at a depth of 16 m; therefore, the acceleration value did not decrease significantly. It was also confirmed by the excess pore water pressure ratio and acceleration that during the first excitation, liquefaction occurred from the ground surface to a depth of 8 m and not more than a depth of 12 m from the ground surface (Figure 7).

The excess pore water pressure ratio was calculated by dividing the excess pore water pressure generated over time by the effective stress. The effective stress below the embankment was calculated by applying an additional surcharge of the embankment body. Based on previous research, the occurrence of liquefaction is determined when the excess pore water pressure exceeds 1.0 [37–39]. The liquefied ground was determined when the excess pore water pressure increased to a value larger than 1.0. Figures 7–9 present a representative graph of the excess pore water pressure ratio with a depth below the center of the embankment and the free field due to successive excitations; in addition, the maximum values of the excess pore water pressures in all cases are described in Tables 4 and 5. The porewater pressure transducer installed at a 8 m depth in the free field did not work because of technical issues; therefore, measurements could not be performed. Below the center of the embankment (as shown in Figure 7), the excess pore water pressure ratios at depths of 4 m and 8 m exceeded unity, indicating that liquefaction occurred. The excess pore water pressure ratios at depths of 12 m and 16 m were less than 1 as listed in Figure 7a and Table 5. These findings indicated that liquefaction did not occur. However, according to the piezometers located in the free field (Figure 7b), liquefaction occurred at all depths during the first excitation. This indicated that due to the overload pressure caused by embankment subsidence, the ground-confining pressure increased more than that in the free field, leading to different trends from those obtained at a depth of more than 12 m.

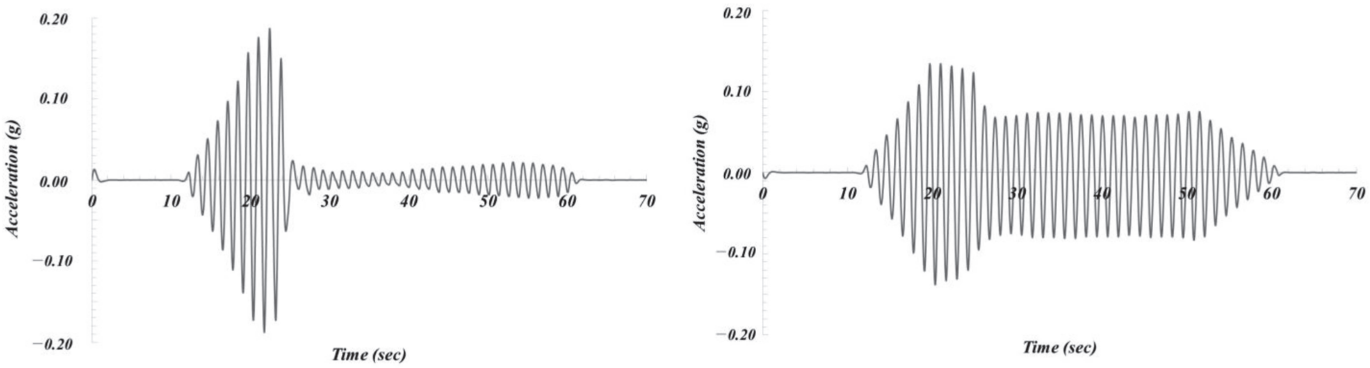

(**a**) **Ground surface**

(**b**) **Depth of 16 m**

Figure 6. Measured acceleration–time history for first shaking event in Case 1.

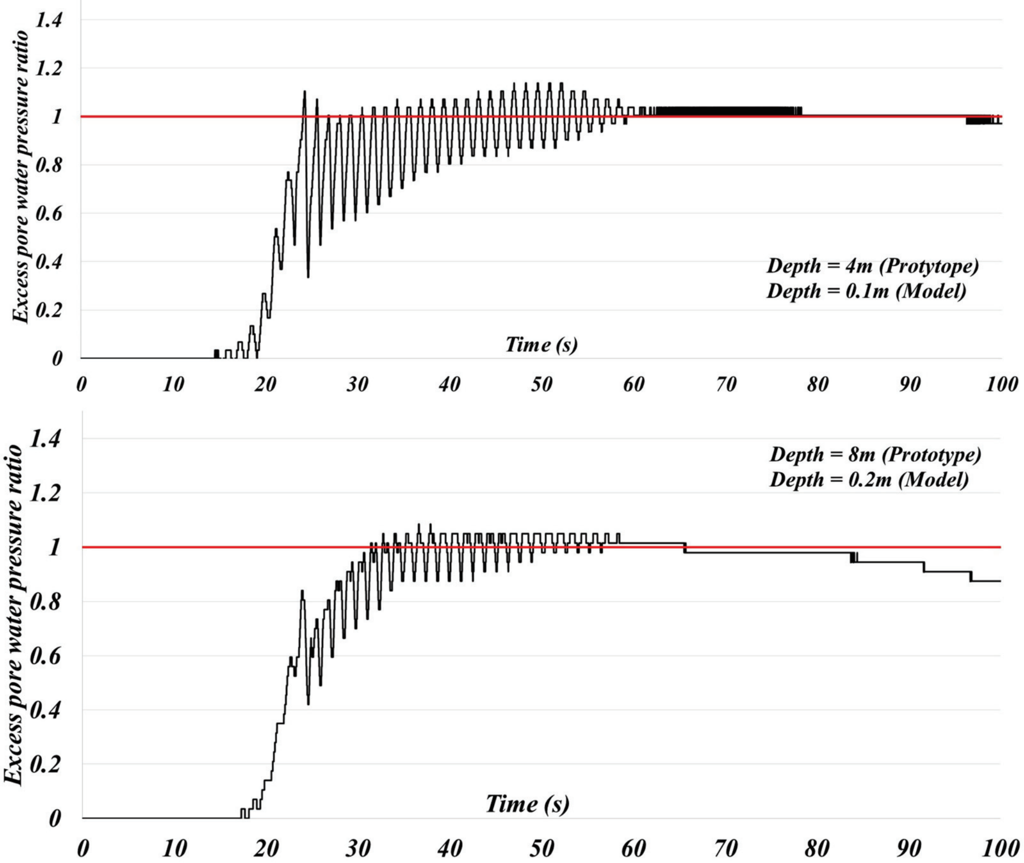

Figure 7. *Cont.*

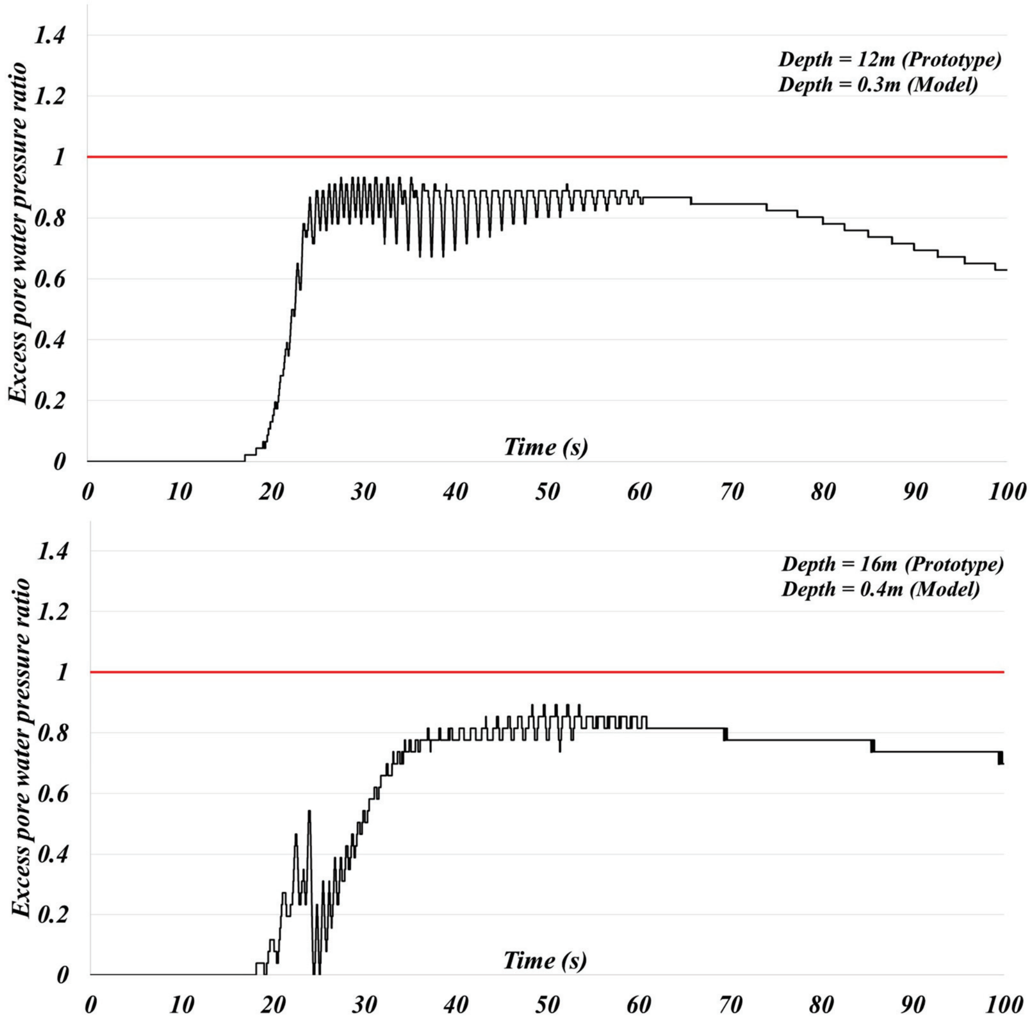

(**a**) Excess pore water pressure ratio below the center of embankment

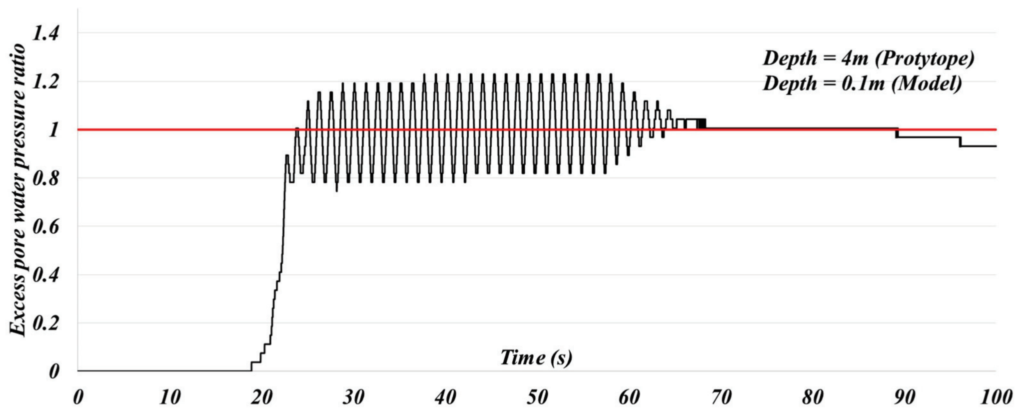

Figure 7. *Cont.*

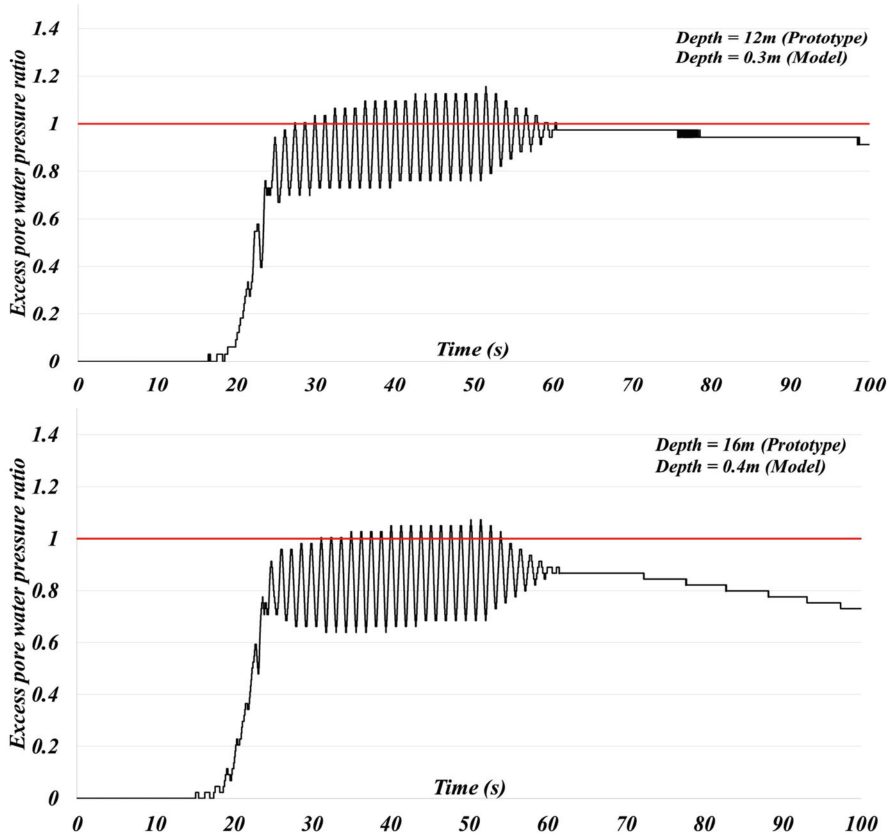

(**b**) Excess pore water pressure ratio in free field

Figure 7. Excess pore water pressure ratio for first shaking event (Case 1).

Table 4. Excess pore water pressure ratio at the center of the embankment (Case 1).

Event Number	Excess Pore Water Pressure Ratio (Depth: 4 m)	Excess Pore Water Pressure Ratio (Depth: 8 m)	Excess Pore Water Pressure Ratio (Depth: 12 m)	Excess Pore Water Pressure Ratio (Depth: 16 m)
First	1.14	1.09	0.93	0.85
Second	1.01	0.85	0.87	0.80
Third	0.84	0.73	0.71	0.70
Fourth	0.70	0.65	0.62	0.62
Fifth	0.54	0.60	0.57	0.57

Table 5. Excess pore water pressure ratio in the free field (Case 1).

Event Number	Excess Pore Water Pressure Ratio (Depth: 4 m)	Excess Pore Water Pressure Ratio (Depth: 8 m)	Excess Pore Water Pressure Ratio (Depth: 12 m)	Excess Pore Water Pressure Ratio (Depth: 16 m)
First	1.22	N/A	1.15	1.07
Second	1.15		1.05	0.92
Third	1.02		0.87	0.84
Fourth	0.92		0.85	0.73
Fifth	0.82		0.72	0.68

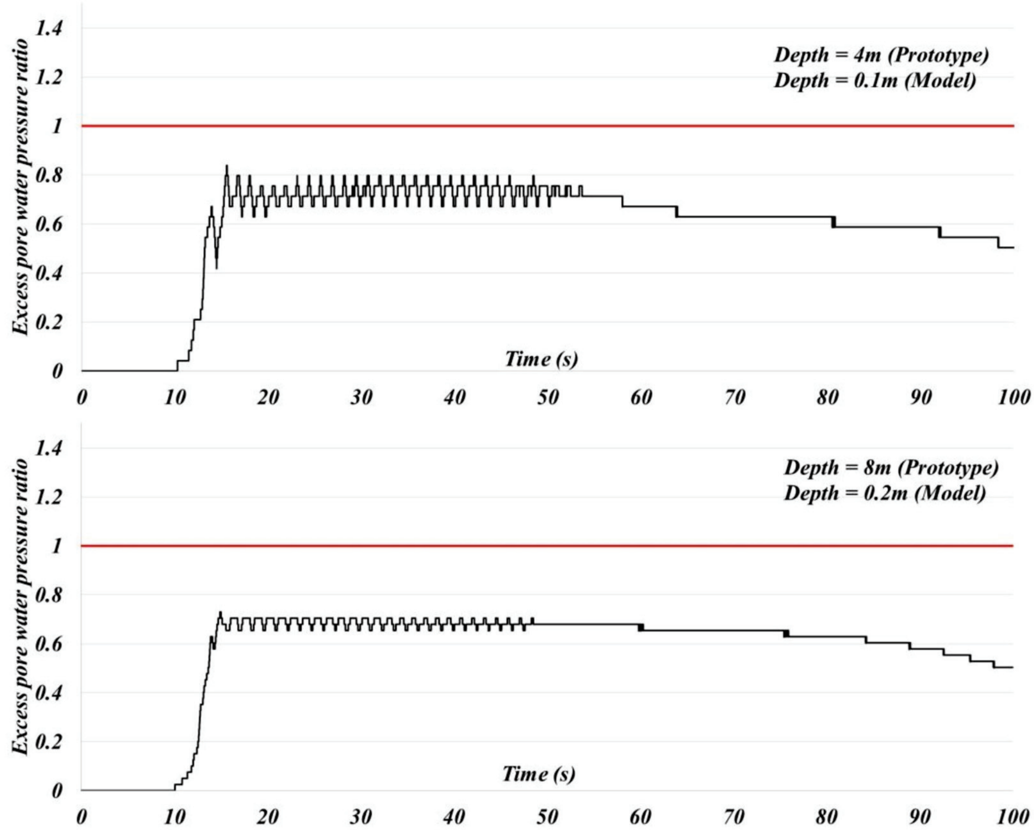

(**a**) Excess pore water pressure ratio below the center of embankment

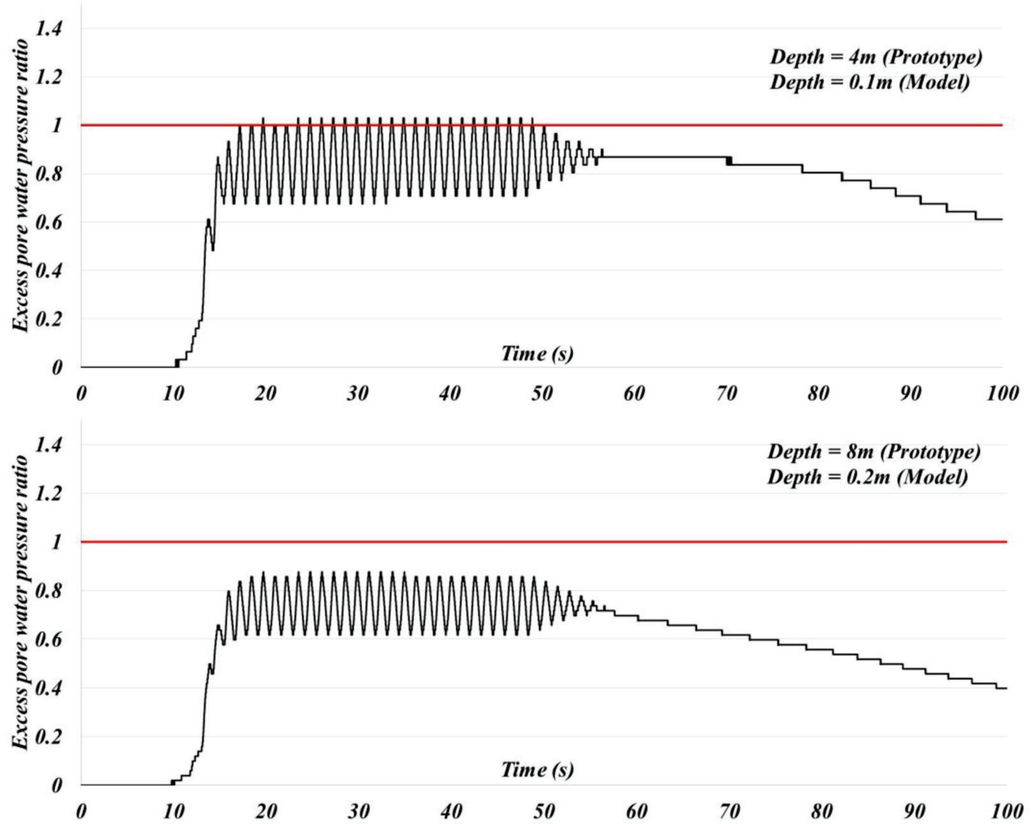

(**b**) Excess pore water pressure ratio at free field

Figure 8. Excess pore water pressure ratio for the third shaking event (Case 1).

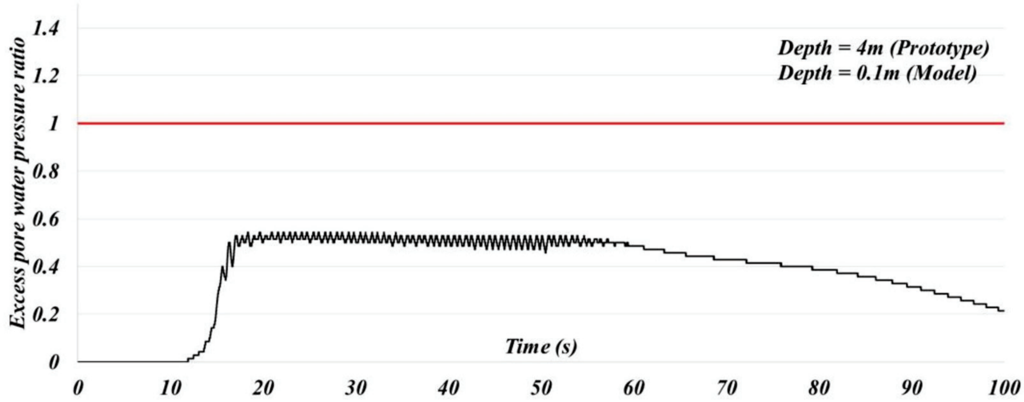

(**a**) Excess pore water pressure ratio below the center of embankment

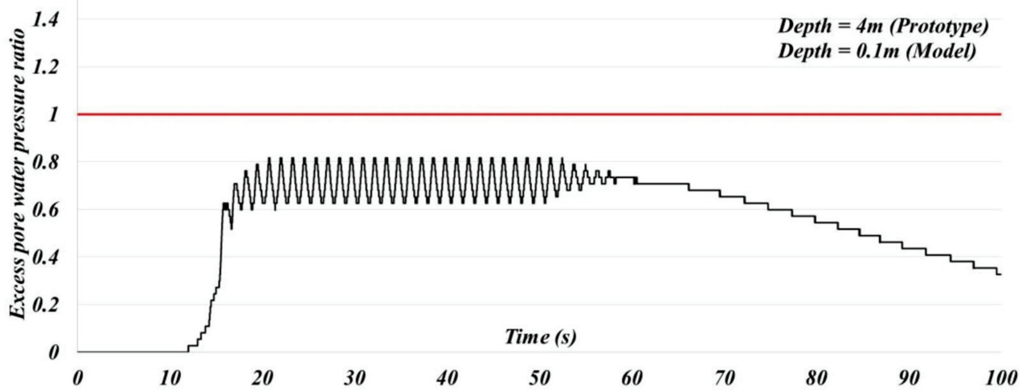

(**b**) Excess pore water pressure ratio in the free field

Figure 9. Excess pore water pressure ratio for the fifth shaking event (Case 1).

Figure 8 shows the pore water pressure ratio for the third shaking event. As shown in Figure 8a, liquefaction did not occur at the center of the embankment during the third shaking excitation due to densification of the ground and confining pressure of the embankment structure. As shown in Figure 8b, liquefaction only occurred at a depth of 4 m in the free field.

During the fifth excitation, the excess pore water pressure ratios below the center of the embankment and free field were less than unity at all depths, indicating that liquefaction did not occur (Figure 9, Tables 4 and 5) because of densification of the ground during successive earthquakes. These findings suggested that liquefaction did not occur because the relative density increased due to ground subsidence caused by the overload pressure from the embankment and repeated shaking. In addition, as shown in Table 5, the maximum excess pore water pressure at a depth of 8 m was lower than that at a depth of 4 m below the center of embankment by the fifth earthquake. This meant that the increase in the confining pressure and the densification of the ground occurred more in the shallow ground due to the settlement of the embankment structure due to repeated earthquakes.

As shown in Figure 10, settlement (as measured using the LVDTs) rapidly occurred during the first excitation and substantially decreased from the first to fifth excitations. The settlement increased while the excitation continued, and after excitation ended, little additional settlement occurred even though the excess pore water pressure still remained. This result was consistent with that of a previous study [40]. Table 6 presents the data for the settlement amount and relative density according to the number of excitations. The relative density was calculated using the value obtained by dividing the total volume and mass of the ground while considering the settlement. Although the relative density should be presented with respect to each ground depth and excitation step, due to experimental limitations, this paper presents the relative density for the entire ground. These findings suggested that the relative density increased to 67.7% during the fifth excitation; that as the number of excitations increased, the settlement amount decreased; and that liquefaction did not occur in the lower ground in the free field. In addition, when the relative density reached 60%, the excess pore water pressure ratio did not exceed unity except at a depth of 4 m; therefore, further liquefaction did not occur below the embankment under an excitation level of 0.2 g.

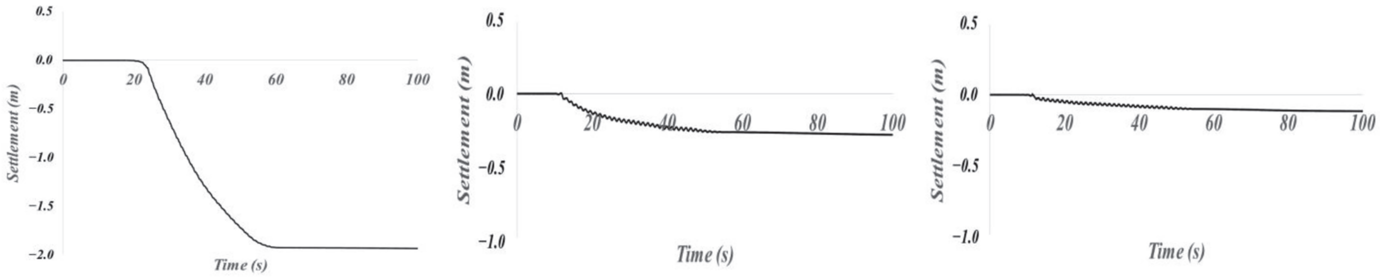

(**a**) First shaking event (**b**) Third shaking event (**c**) Fifth shaking event

Figure 10. LVDT at the center of the embankment (Case 1).

Table 6. Relative density and ground settlement at the center of the embankment (Case 1).

Event Number	Shake 1	Shake 2	Shake 3	Shake 4	Shake 5
Settlement (prototype) (Accumulated settlement), m	1.96 (1.96)	0.78 (2.74)	0.29 (3.03)	0.15 (3.18)	0.12 (3.3)
Settlement (model) (Accumulated settlement), m	0.049 (0.049)	0.019 (0.068)	0.007 (0.075)	0.004 (0.079)	0.003 (0.082)
Relative density, %	59.4	63.1	64.5	65.3	65.8

Figure 11 presents the correlation between the excess pore water pressure ratio and the relative density at different depths below the center of the embankment for comparison. The relative density gradually increased as the number of excitations increased, and liquefaction occurred in the first excitation at depths of 4 m and 8 m as the excess pore water pressure ratio exceeded 1. However, liquefaction did not occur at depths of 12 m and 16 m when the excess pore water pressure ratio was less than 1. In addition to the non-occurrence of liquefaction, the increasing trend of relative density declined. When the relative density exceeded approximately 65–66%, the excess pore water pressure ratio decreased to values less than 1 at all depths. These findings suggested that as the number of excitations increased and the relative density reached a certain value, the ground density increased; thus, the excess pore water pressure ratio did not exceed 1, and liquefaction did not occur.

4.2. Liquefiable and Non-Liquefiable Ground Case (Case 2)

When there was an upper non-liquefiable layer in the ground as shown in Figure 12, liquefaction did not occur in any of the ground layers during the first excitations. Figure 13 presents a representative graph of the excess pore water pressure ratio with a depth below the center of the embankment caused by successive excitation; in addition, the maximum values of the excess pore water pressure in all cases are described in Tables 7 and 8. In Case 2, the excess pore water pressure ratio was calculated by considering the change of effective stress due to the groundwater level rise.

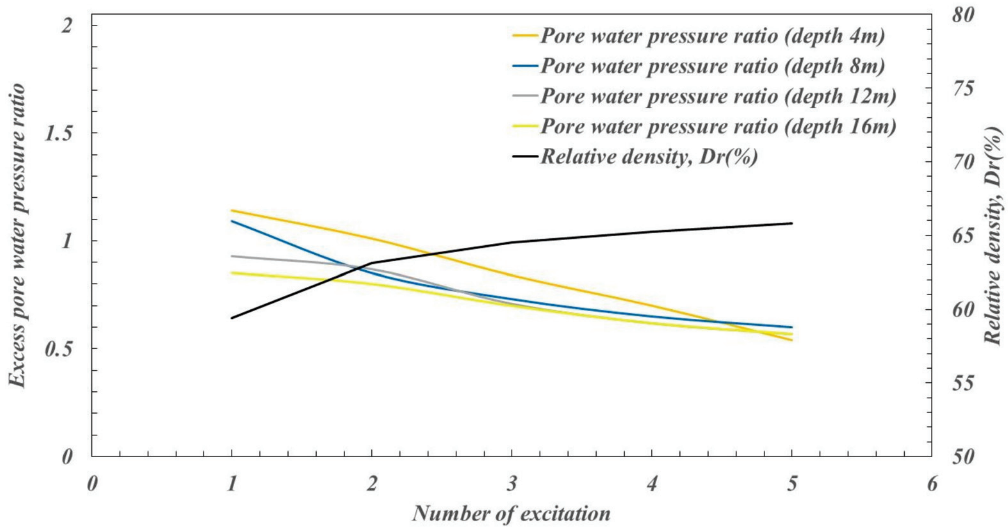

Figure 11. Excess pore water pressure ratio and relative density (center of the embankment, Case 1).

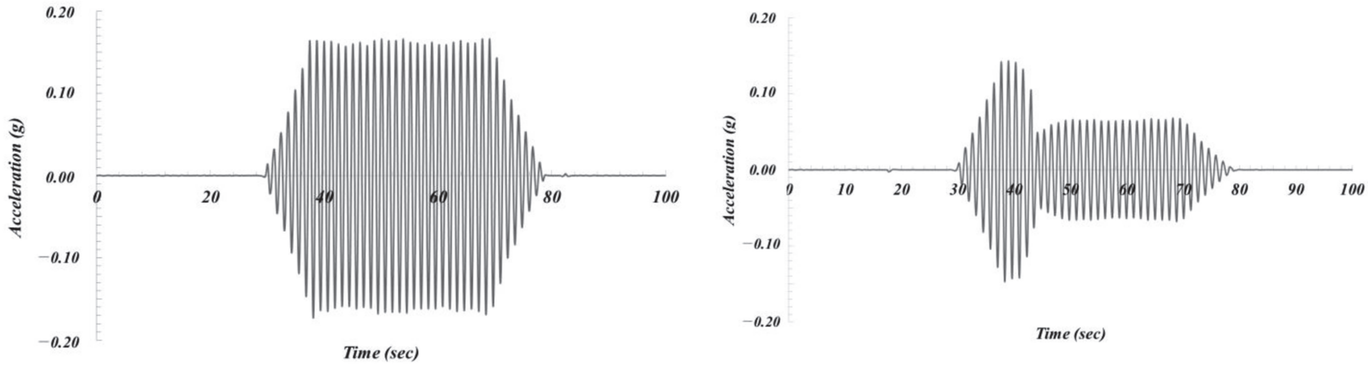

(**a**) Ground surface

(**b**) Depth of 16 m

Figure 12. Measured acceleration time history for first shaking event in Case 2.

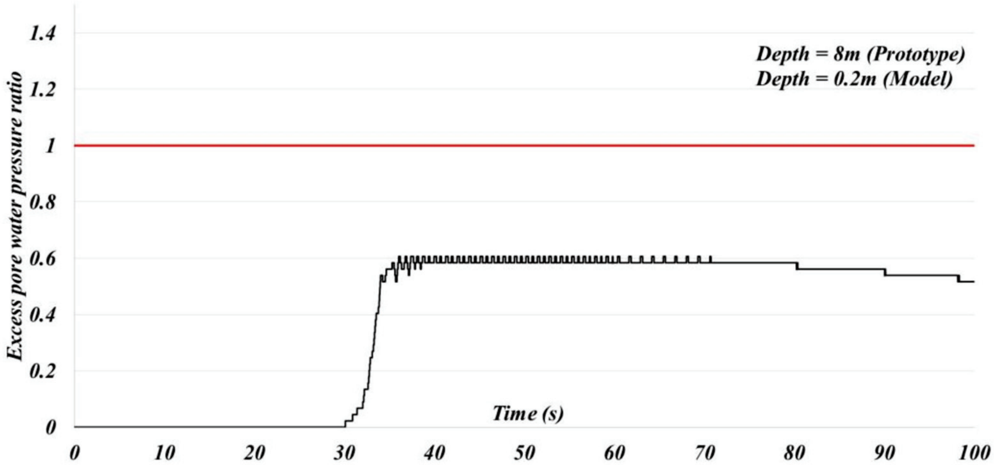

Figure 13. *Cont*.

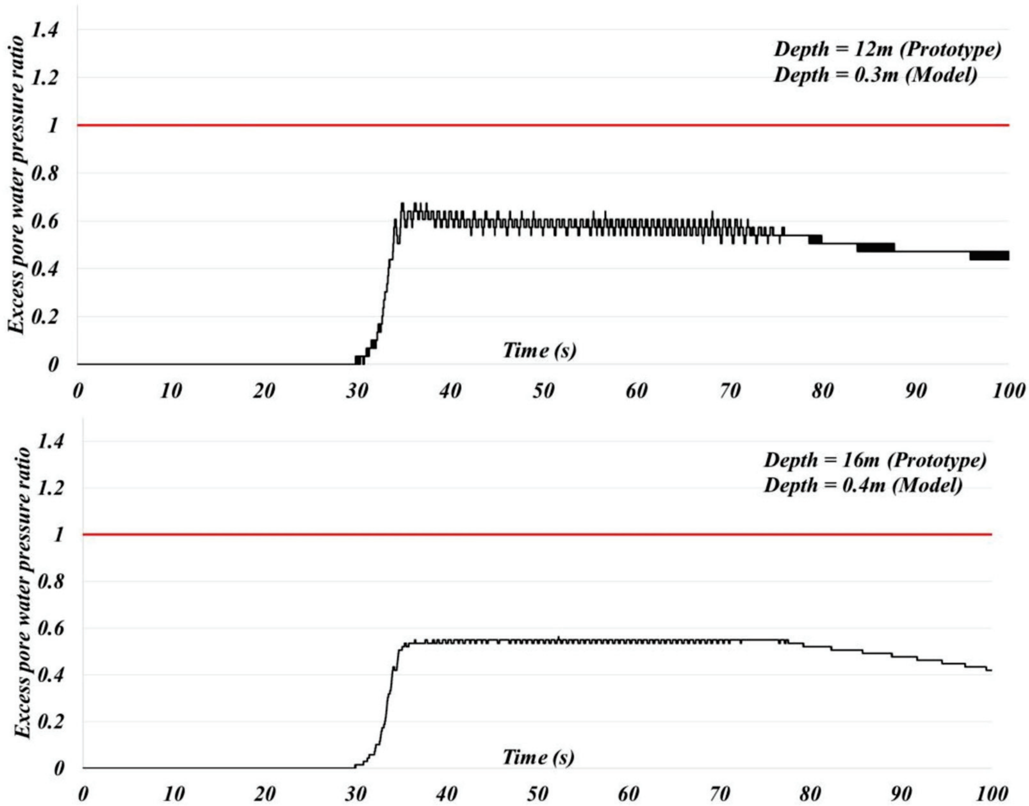

(**a**) Excess pore water pressure ratio for first shaking event

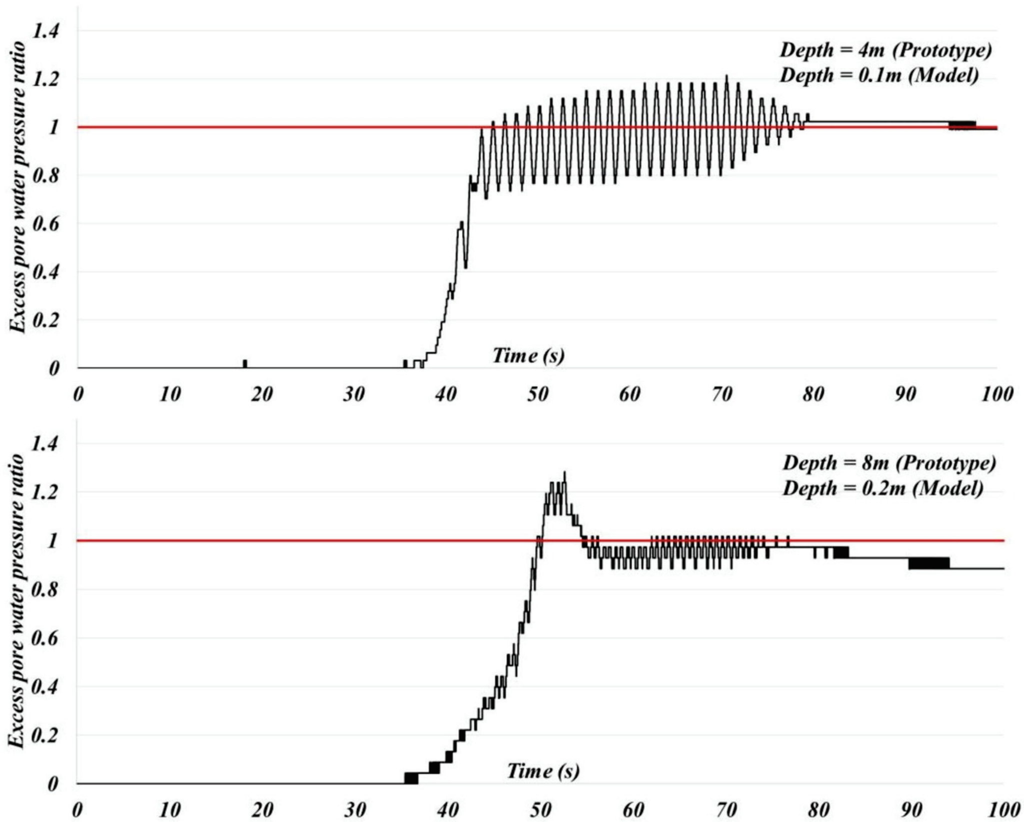

Figure 13. *Cont*.

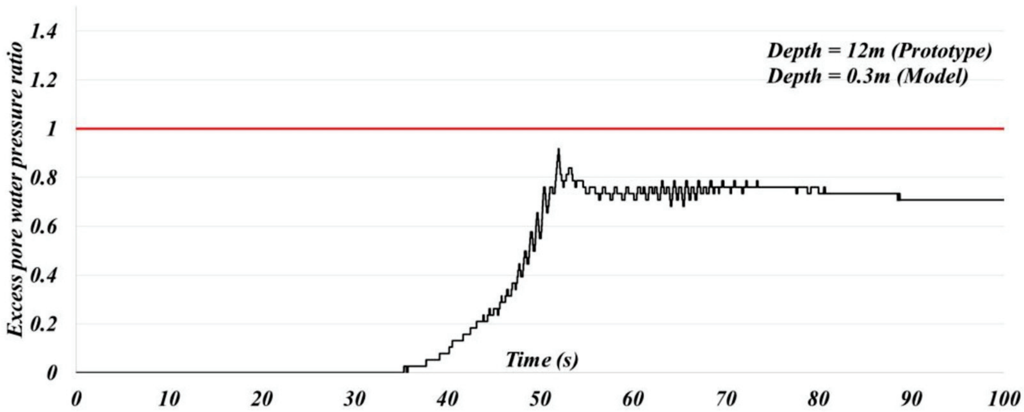

(**b**) Excess pore water pressure ratio for third shaking event

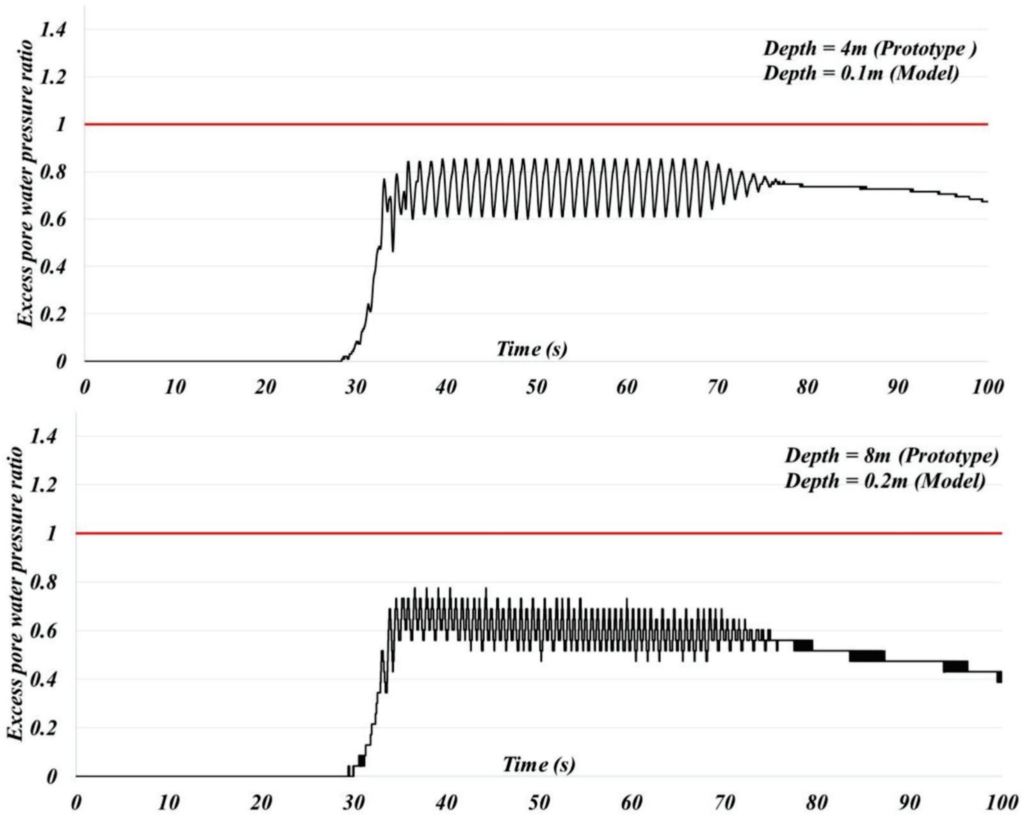

(**c**) Excess pore water pressure ratio for fifth shaking event

Figure 13. Excess pore water pressure ratio for successive shaking events below the center of the embankment (Case 2).

Table 7. Excess pore water pressure ratio at the center of the embankment (Case 2).

Event Number	Excess Pore Water Pressure Ratio (Depth: 4 m)	Excess Pore Water Pressure Ratio (Depth: 8 m)	Excess Pore Water Pressure Ratio (Depth: 12 m)	Excess Pore Water Pressure Ratio (Depth: 16 m)
First	0.00	0.60	0.67	0.56
Second	0.42	0.70	0.73	0.63
Third	1.21	1.28	0.92	0.81
Fourth	1.01	0.92	0.83	0.76
Fifth	0.85	0.78	0.76	0.68

Table 8. Excess pore water pressure ratio in the free field (Case 2).

Event Number	Excess Pore Water Pressure Ratio (Depth: 4 m)	Excess Pore Water Pressure Ratio (Depth: 8 m)	Excess Pore Water Pressure Ratio (Depth: 12 m)	Excess Pore Water Pressure Ratio (Depth: 16 m)
First	0.00		0.83	0.63
Second	0.53		0.91	0.78
Third	1.18	N/A	1.02	0.87
Fourth	1.07		0.93	0.82
Fifth	0.91		0.81	0.75

As shown in figure, liquefaction did not occur in the first excitation, whereas it occurred in the third excitation. The groundwater level rose to 4 m below the ground surface in the first earthquake and up to the ground surface in the second earthquake (Figure 5). These findings suggested that as the seismic load was applied, the groundwater level in the liquefiable layer increased to the height of the non-liquefiable layer, the entire ground was submerged in groundwater, and liquefaction occurred in the third excitation onward. To confirm the effects of reliquefaction, a total of five excitations were performed. According to Table 7, the excess pore water pressure ratio exceeded 1.0 above the layer of 8 m in the third and above the layer of 4 m in the fourth excitation, indicating that liquefaction occurred. In addition, even in the layer where liquefaction did not occur, excess pore water pressure values were observed in the fourth and fifth excitation that were larger than those after the first earthquake because the effect of the confining pressure was reduced due to an increase in the groundwater level. As shown in Table 8, when there was a non-liquefiable layer, liquefaction occurred above 12 m in the third excitations and above 4 m in the fourth excitation in the free field and not in the fifth excitations. The difference in the occurrence of liquefaction between the free field and below the center of the embankment mirrored the observations from Case 1. In particular, liquefaction did not occur in the third excitation at a depth of 12 m when there was an embankment; this was due to the overload confining pressure, which was in contrast to the ground case without an embankment.

Figure 14 presents a graph of the amount of embankment settlement based on the LVDT installed at the center of the embankment. Table 9 presents the data for the settlement amount and relative density according to the number of excitations. The change in relative density was not significant in the first and second excitations because liquefaction did not occur in the saturated ground due to the relatively high confining pressure caused by non-liquefiable ground. In addition, the groundwater level increased, and the entire ground was submerged in groundwater; it was judged that the upward pressure of groundwater level led to a relatively low settlement. The relative density remained similar; therefore, liquefaction occurred from the third excitation. Subsequently, the relative density increased, and the amount of settlement in each excitation decreased in subsequent excitations.

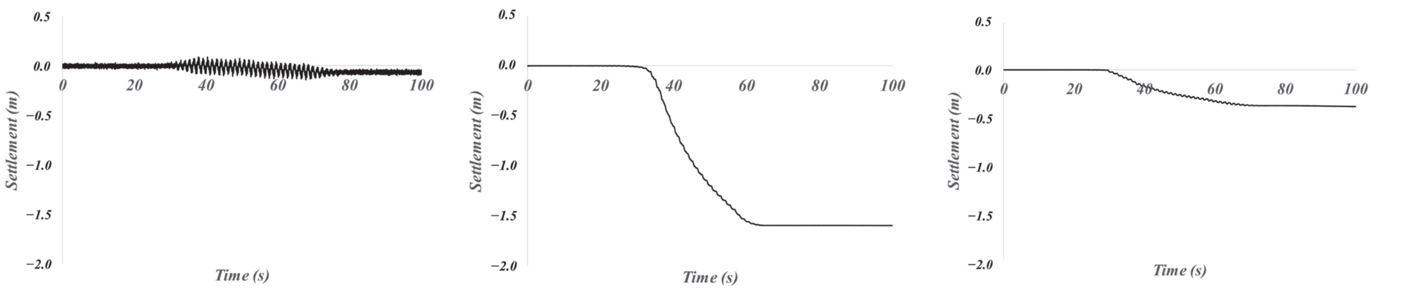

(**a**) First shaking event (**b**) Third shaking event (**c**) Fifth shaking event

Figure 14. LVDT at the center of the embankment (Case 1).

Table 9. Relative density and ground settlement at the center of the embankment (Case 2).

Event Number	Shake 1	Shake 2	Shake 3	Shake 4	Shake 5
Settlement (prototype) (Accumulated settlement), m	0.13 (0.13)	0.25 (0.38)	1.59 (1.97)	0.51 (2.48)	0.40 (2.88)
Settlement (model) (Accumulated settlement), m	0.003 (0.003)	0.007 (0.010)	0.040 (0.050)	0.013 (0.063)	0.010 (0.073)
Relative density, %	50.6	51.9	59.5	61.9	63.9

Figure 15 presents a graph of the correlation between the excess pore water pressure ratio and the relative density at different depths below the center of the embankment when there was an upper non-liquefiable layer in the ground. Liquefaction did not occur until the third excitation when there was a non-liquefiable layer. Thus, no significant changes were observed in the relative density or excess pore water pressure ratio. However, liquefaction occurred during the third excitation, and the excess pore water pressure ratio exceeded 1.0, demonstrating an increasing trend similar to that of the relative density. Furthermore, after the relative density reached 60% or greater, the excess pore water pressure ratio did not exceed unity, indicating that further liquefaction did not occur under an excitation level of 0.2 g. It was determined that this phenomenon could occur when the thickness of the non-liquefaction layer was relatively low and the thickness of the liquefiable layer was more than twice the thickness of the non-liquefaction layer.

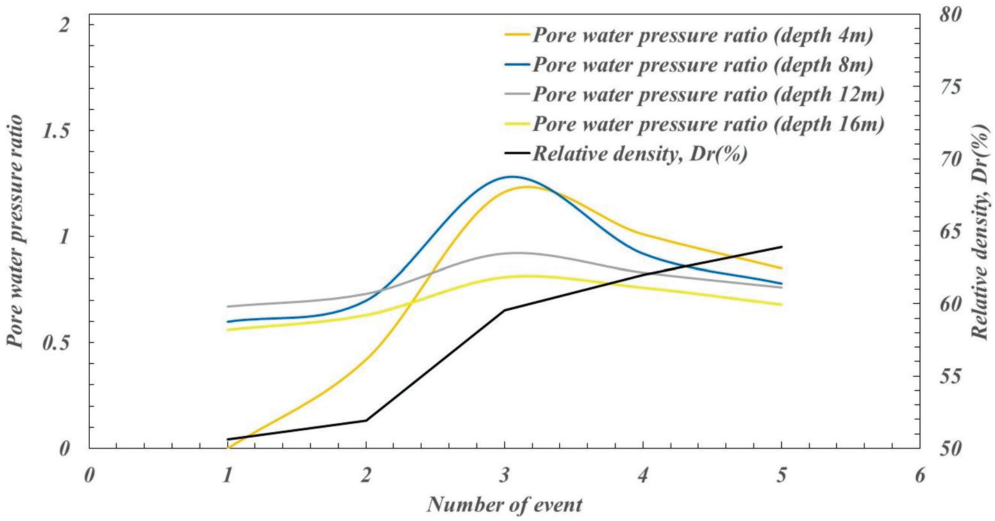

Figure 15. Excess pore water pressure ratio and relative density (center of the embankment, Case 2).

Based on a series of results, it was confirmed that the risk of liquefaction due to aftershocks is greater than that of the main earthquake in the case of a coastal embankment where the groundwater level is low (especially when the relative density of the ground is lower than 60%). In the case of general seismic design criteria, liquefaction risk assessment is not performed for soil layers higher than the groundwater level; however, if repeated aftershocks occur, unexpected liquefaction damage may occur due to an increment in the groundwater level. Therefore, to mitigate the earthquake risk of liquefaction for coastal embankments, it is necessary to evaluate liquefaction by aftershocks even when the groundwater level of the ground layer under an embankment is low. However, since this study summarized the results of experiments performed for limited experimental cases, additional experimental and numerical analysis studies on various liquefaction layer thicknesses are needed.

5. Conclusions

In this study, a series of shaking table tests were conducted while considering the thicknesses of liquefiable and non-liquefiable layers in saturated sand upon which an embankment was installed. Accelerometers, piezometers, and LVDTs were used to analyze the occurrence of liquefaction and ground behavior with respect to the depth during reliquefaction. The findings of this study can be summarized as follows:

(1) In Case 1, the liquefaction occurred above 12 m in the first and the second excitations in the free field and only occurred at the depth of 4 m in the third excitation. At the center of the embankment, the excess pore water pressure ratio exceeded unity above 8 m in the first excitation and only reached unity at the depth of 4 m in the second excitation. In this regard, the difference in the confining pressure caused by the overload pressure from the embankment most probably influenced the occurrence of liquefaction.

(2) When the upper ground layer consisted of a non-liquefiable layer (Case 2), liquefaction did not occur in the first excitation and occurred in the third excitation. These results indicated that as the shaking load was applied, the water level in the liquefiable layer increased to the height of the non-liquefiable layer, and liquefaction occurred. This suggested that when there is a liquefiable layer under a non-liquefiable layer, liquefaction may occur due to aftershocks. In the case of general seismic design criteria, liquefaction risk assessment is not performed for soil layers higher than the groundwater level; however, if repeated aftershocks occur, unexpected liquefaction damage may occur due to an increment in the groundwater level.

(3) In Case 1, the excess pore water pressure ratio decreased below unity after a relative density of 65% at a depth of 4 m. Additionally, in ground with a non-liquefiable layer, the excess pore water pressure ratio decreased after a relative density of approximately 63%. In both cases, liquefaction did not occur when the relative density was approximately 65% or higher, which can serve as a basis for gauging the likelihood of liquefaction when the relative density reaches a certain value.

(4) In this study, it was confirmed that even if liquefaction does not occur at the main earthquake, liquefaction occurs due to aftershocks caused by a rise in the groundwater level. In a general seismic design criterion, liquefaction assessment is performed only for soil layers below the groundwater level; however, if aftershocks occur, unexpected liquefaction damage may occur to coastal embankments. Therefore, to mitigate the earthquake risk of liquefaction for coastal embankments, it is necessary to evaluate liquefaction due to aftershocks even when the groundwater level of the ground layer under an embankment is low.

For the results of this study to be applied quantitatively, additional research on groundwater level rise due to earthquakes and the evaluation of liquefaction of subsequent aftershocks should be conducted via dynamic centrifuge tests and numerical analysis. In addition, further studies on various soil types also should be conducted in order to derive effective results that can be applied to various field conditions.

Author Contributions: M.Y. organized the paperwork, produced the analysis plan, and performed the shaking table test and data analysis; S.Y.K. supported the test result analysis and paperwork organization. Both authors contributed to the writing of the paper. All authors have read and agreed to the published version of the manuscript.

Funding: This research was supported by a grant from the Korea Institute of Energy Technology Evaluation and Planning (KETEP) funded by the Korean government (MOTIE) (20203020020040, Development of environmental monitoring and information disclosure system for onshore wind farms for data-based environmental evaluation and enhancement of acceptance, 2023-011(R)), which was conducted by the Korea Environment Institute (KEI); and a grant (RS-2023-00238458, Development and Verification of Integrated Management System for High-Risk Disaster Response in Deep Railway Facilities) from the Development of a Disaster Response Complex Training Center for Deep Tunnels (GTX, etc.) Program funded by the Ministry of Land, Infrastructure, and Transport of the Korean government. We greatly appreciate the support.

Institutional Review Board Statement: Not applicable.

Informed Consent Statement: Not applicable.

Data Availability Statement: Not applicable.

Conflicts of Interest: The authors declare no conflict of interest.

References

1. Yasuda, S.; Tohno, I. Sites of reliquefaction caused by the 1983 Nihonkai-Chubu earthquake. *Soils Found.* **1988**, *28*, 61–72. [CrossRef] [PubMed]
2. Sims, J.D.; Garvin, C.D. Recurrent liquefaction induced by the 1989 Loma Prieta earthquake and 1990 and 1991 aftershocks: Implications for paleoseismicity studies. *Bull. Sies. Soc. Am.* **1995**, *85*, 51–65.
3. Yasuda, S.; Harada, K.; Ishikawa, K.; Kanemaru, Y. Characteristics of liquefaction in Tokyo Bay area by the 2011 Great East Japan earthquake. *Soils Found.* **2021**, *52*, 793–810. [CrossRef]
4. Cubrinovski, M.; Henderson, D.; Bradley, B. *Liquefaction Impacts in Residential Areas in the 2010–2011 Christchurch Earthquakes*; University of Canterbury: Christchurch, New Zealand, 2012.
5. Quigley, M.C.; Bastin, S.; Bradley, B.A. Recurrent liquefaction in Christchurch, New Zealand, during the Canterbury earthquake sequence. *Geology* **2013**, *41*, 419–422. [CrossRef]
6. Lees, J.J.; Ballagh, R.H.; Orense, R.P.; Van Ballegooy, S. CPT-based analysis of liquefaction and re-liquefaction following the Canterbury earthquake sequence. *Soil Dyn. Earthq. Eng.* **2015**, *79*, 304–314. [CrossRef]
7. Bouferra, R.; Benseddiq, N.; Shahrour, I. Saturation and preloading effects on the cyclic behavior of sand. *Int. J. Geomech.* **2007**, *7*, 396–401. [CrossRef]
8. El-Sekelly, W.; Abdoun, T.; Dobry, R. PRESHAKE: A database for centrifuge modeling of the effect of seismic preshaking history on the liquefaction resistance of sands. *Earthq. Spectra* **2016**, *32*, 1925–1940. [CrossRef]
9. Toyota, H.; Takada, S. Variation of liquefaction strength induced by monotonic and cyclic loading histories. *J. Geotech. Geoenviron. Eng.* **2017**, *143*, 04016120. [CrossRef]
10. Teparaksa, J.; Koseki, J. Effect of past history on liquefaction resistance of level ground in shaking table test. *Géotechnique Lett.* **2018**, *8*, 256–261. [CrossRef]
11. Ye, B.; Zhang, L.; Wang, H.; Zhang, X.; Lu, P.; Ren, F. Centrifuge model testing on reliquefaction characteristics of sand. *Bull. Earthq. Eng.* **2019**, *17*, 141–157. [CrossRef]
12. Ohara, S.; Yamamoto, T.; Yurino, H. Experimental study on reliquefaction potential of saturated sand deposit. In Proceedings of the 10th WCEE, Madrid, Spain, 23 July 1992; Volume 3, pp. 1425–1430.
13. Oda, M.; Kawamoto, K.; Suzuki, K.; Fujimori, H.; Sato, M. Microstructural interpretation on reliquefaction of saturated granular soils under cyclic loading. *J. Geotech. Geoenviron. Eng.* **2001**, *127*, 416–423. [CrossRef]
14. Zhao, T.; Ye, J. 3D DEM Simulation on the Reliquefaction Behavior of Sand Considering the Effect of Reconsolidation Degree. *J. Earthq. Eng.* **2022**, *12*, 1–23. [CrossRef]
15. Ha, I.S.; Olson, S.M.; Seo, M.W.; Kim, M.M. Evaluation of reliquefaction resistance using shaking table tests. *Soil Dyn. Earthq. Eng.* **2011**, *31*, 682–691. [CrossRef]
16. Nepal, D.B.; Deng, J.; Chen, J.; Maakoe, T. Re-liquefaction of sand in shaking table. *Mater. Sci. Eng.* **2020**, *758*, 012050. [CrossRef]
17. El-Shafee, O.; Abdoun, T.; Zeghal, M. Centrifuge modeling and analysis of site liquefaction subjected to biaxial dynamic excitations. *Geotechnique* **2016**, *67*, 260–271. [CrossRef]
18. El-Shafee, O.; Abdoun, T.; Zeghal, M. Physical modeling and analysis of site lique-faction subjected to biaxial dynamic excitations. *Innov. Infrastruct. Sol.* **2018**, *3*, 173–185.
19. Reyes, A.; Adinata, J.; Taiebat, M. Impact of bidirectional seismic shearing on the volumetric response of sand deposits. *J. Soil Dyn. Earthq. Eng.* **2019**, *125*, 105665. [CrossRef]
20. Reyes, A.; Adinata, J.; Taiebat, M. Liquefaction hazard evaluation under bidirectional seismic shearing: Optimal ground motion intensity measures. In Proceedings of the VII ICEGE 7th International Conference on Earthquake Geotechnical Engineering, Rome, Italy, 17–20 June 2019.
21. Zeghal, M.; El-Shafee, O.; Abdoun, T. Analysis of soil liquefaction using centrifuge tests of a site subjected to biaxial shaking. *J. Soil Dyn. Eqrthq. Eng.* **2018**, *114*, 229–241. [CrossRef]
22. Ye, J.; Lu, Q. Seismic dynamics of a pipeline shallowly buried in loosely deposited seabed foundation. *Ocean. Eng.* **2022**, *243*, 110194. [CrossRef]
23. Ye, J.; Wang, G. Seismic dynamics of offshore breakwater on liquefiable seabed foundation. *Soil Dyn. Earthq. Eng.* **2015**, *76*, 86–99. [CrossRef]
24. Aydingun, O.; Adalier, K. Numerical analysis of seismically induced liquefaction in earth embankment foundations. Part I. Benchmark model. *Can. Geotech. J.* **2003**, *40*, 753–765. [CrossRef]
25. Ishikawa, H.; Saito, K.; Nakagawa, K.; Uzuoka, R. Liquefaction analysis of a damaged river levee during the 2011 Tohoku earthquake. In Proceedings of the 14th International Conference of the International Association for Computer Methods and Advances in Geomechanics, Kyoto, Japan, 22–25 September 2014.

26. Kwon, S.Y.; Yoo, M. Numerical Analysis Method for Liquefaction-induced Damage Evaluation to Railway Structure. *KSCE J. Civil Eng.* **2022**, *26*, 3752–3763. [CrossRef]
27. Lopez-Caballero, F.; Modaressi, A.; Stamatopoulos, C. Numerical evaluation of earthquake settlements of road embankments and mitigation by preloading. *Int. J. Geomech.* **2016**, *16*, C4015006. [CrossRef]
28. Maharjan, M.; Takahashi, A. Liquefaction-induced deformation of earthen embankments on non-homogeneous soil deposits under sequential ground motions. *Soil Dyn. Earthq. Eng.* **2014**, *66*, 113–124. [CrossRef]
29. Oka, F.; Tsai, P.; Kimoto, S.; Kato, R. Damage patterns of river embankments due to the 2011 off the Pacific Coast of Tohoku Earthquake and a numerical modeling of the deformation of river embankments with a clayey subsoil layer. *Soils Found.* **2012**, *52*, 890–909. [CrossRef]
30. Singh, R.; Roy, D.; Jain, S.K. Analysis of earth dams affected by the 2001 Bhuj Earthquake. *Eng. Geol.* **2005**, *80*, 282–291. [CrossRef]
31. Stamatopoulos, C.; Aneroussis, S. Sliding-block back analyses of liquefaction-induced slides. In Proceedings of the 13th World Conference on Earthquake Engineering, Vancouver, BC, Canada, 1–6 August 2004; p. 3209.
32. Han, J.T. Please explain the definition of liquefaction and how to design the pile foundation in liquefiable soils. *Korean Soc. Civ. Eng. Mag.* **2012**, *60*, 90–93.
33. Ha, I.S.; Kim, M. Evaluation of characteristics of re-liquefaction resistance in saturated sand deposits using 1-g shaking table test. *J. Korean Geotech. Soc.* **2005**, *21*, 65–70.
34. ATC. *Seismic Evaluation and Retrofit of Concrete Building*; Report ATC; Applied Technology Council: Redwood City, CA, USA, 1996; Volume 40.
35. Iai, S. Similitude for shaking table tests on soil-structure-fluid model in 1g gravitational field. *Soils Found.* **1989**, *29*, 105–118. [CrossRef]
36. Byrne, P.M.; Park, S.S.; Beaty, M.; Sharp, M.; Gonzalez, L.; Abdoun, T. Numerical modeling of liquefaction and comparison with centrifuge tests. *Can. Geotech. J.* **2004**, *41*, 193–211. [CrossRef]
37. Hazirbaba, K.; Omarow, M. Strain-based assessment of liquefaction and seismic settlement of saturated sand. *Cogent Eng.* **2019**, *6*, 1537788. [CrossRef]
38. Yoo, M.T.; Han, J.T.; Choi, J.I.; Kwon, S.Y. Development of predicting method for dynamic pile behavior by using centrifuge tests considering the kinematic load effect. *Bull. Earthq. Eng.* **2017**, *15*, 967–989. [CrossRef]
39. Al-Jeznawi, D.; Mohamed Jais, I.B.; Albusoda, B.S.; Alzabeebee, S.; Keawsawasvong, S.; Khalid, N. Numerical Study of the Seismic Response of Closed-Ended Pipe Pile in Cohesionless Soils. *Transp. Infrastuct. Geotechnol.* **2023**, *10*, 1–27. [CrossRef]
40. Sharp, M.K.; Dobry, R.; Abdoun, T. Liquefaction Centrifuge Modeling of Sands of Different Permeability. *J. Geotech. Geoenviron. Eng.* **2003**, *129*, 1083–1091. [CrossRef]

Journal of
Marine Science and Engineering

MDPI

Article

Assessing Coastal Vulnerability to Storms: A Case Study on the Coast of Thrace, Greece

Iason A. Chalmoukis

Department of Civil Engineering, University of Patras, 26500 Patras, Greece; ichalmoukis@upatras.gr

Abstract: Climate change is expected to increase the risks of coastal hazards (erosion and inundation). To effectively cope with these emerging problems, littoral countries are advised to assess their coastal vulnerabilities. In this study, coastal vulnerability is first assessed by considering two basic storm-induced phenomena, i.e., erosion and inundation. First, the erosion is computed using the numerical model for Storm-induced BEAch CHange (SBEACH), whereas the inundation is estimated using two different empirical equations for comparison. Then, the integration of the vulnerabilities of both storm-induced impacts associated with the same return period permits the identification of the most hazardous regions. The methodology is applied to the coast of Thrace (Greece). The majority of the coastline is not vulnerable to erosion, except for some steep and narrow beaches and the coast along the city of Alexandroupolis. Beaches with very low heights are highly vulnerable to inundation. Half of the studied coastline is considered highly or very highly vulnerable, whereas the other half is relatively safe. The above results will help decision-makers choose how to invest their resources for preventing damage.

Keywords: coastal vulnerability; integrated coastal management; erosion; inundation

Citation: Chalmoukis, I.A. Assessing Coastal Vulnerability to Storms: A Case Study on the Coast of Thrace, Greece. *J. Mar. Sci. Eng.* **2023**, *11*, 1490. https://doi.org/10.3390/jmse11081490

Academic Editor: Deniz Velioglu Sogut

Received: 12 June 2023
Revised: 17 July 2023
Accepted: 18 July 2023
Published: 26 July 2023

1. Introduction

Coastal vulnerability is generally defined as the potential of a beach to be damaged by storm-induced phenomena [1]. It is quantified by comparing the magnitude of the impact to the adaptation ability of the coast [2]. The impact is estimated using the intensity of the storm-induced processes, whereas the capacity of the beach to cope with the considered impacts is derived from its geomorphology (i.e., beach slope, width, and height). The most common storm-induced impacts are erosion and inundation [3].

Throughout the last century, pressure on coastal areas has increased due to urbanization and large migration towards them. Approximately, a 70% increase in population has been observed worldwide in low-elevation coastal zones [4]. In particular, the population around the Mediterranean Sea is estimated to reach 572 million by 2030 [5]. Furthermore, climate change is expected to have long-term impacts with frequent and intense extreme storm events and a permanent 1.5 °C increase in global surface temperature by 2050 [6]. Consequently, sea level rise will threaten more coasts, and in combination with storm events and local erosion trends, this can impose severe flood risks. Due to the above, the Mediterranean coastline is identified by the Intergovernmental Panel on Climate Change as a vulnerable zone with a high risk of inundation, coastal erosion, and, in general, land degradation [6]. The increasing erosion and flood phenomena arising in the Mediterranean push public administrations towards a strategic approach for integrated coastal zone management (ICZM) with an emphasis on coastal protection. More than a decade ago, the importance of including hazard assessments in coastal zone policies was highlighted by the Protocol on ICZM in the Mediterranean [7]. It recommends that its littoral countries address the effects of natural disasters along their coastlines by assessing their vulnerability.

Following this recommendation, Mendoza and Jimenez [1] estimated the erosion potential of the Catalonian coast in Spain using the Storm-induced BEAch CHange (SBEACH) numerical model. From the results of the beach retreat, a five-class storm categorization was proposed for the Catalonian coast. Monioudi et al. [8] assessed the erosion risk of the eastern Cretan coastline in Greece under sea level rise. Three analytical equations were used to estimate the long-term beach evolution, whereas short-term erosion was modeled using three numerical response models (XBeach, Leont'yev, SBEACH). They found that the last two models presented similar results. Furthermore, an evaluation of the economic impact of erosion on tourism revenue for Crete Island in Greece was presented by Alexandrakis et al. [9], following a similar approach to that of McLaughlin et al. [10]. In contrast, De Leo et al. [11] studied only the flooding potential of Lalzit Bay in Albania using offshore wave climate (regional) and nearshore wave climate (local). Their analysis concluded that the results vary in the run-up estimation, and thus the coastal vulnerability, due to the different wave climates.

Studies that considered both the erosion and inundation impacts to assess the integrated coastal vulnerability have also been performed [3,12–15]. The advantage of these articles is that the vulnerability to erosion and inundation were evaluated separately, and then the contribution of the forcing (storm properties) and receptor (geomorphology) were quantified for the overall vulnerability. A disadvantage in the work of Jiménez et al. [12] is that they did not provide a method to calculate the return period and thus it was arbitrarily selected. The drawback in the study of Bosom and Jiménez [3] is that an empirical formula specifically derived from numerical simulations of SBEACH along the Catalonian coast [1] was used to predict the erosion. The results showed that beach erosion estimations similar to the predictions of SBEACH can be obtained in a simple manner for Catalonian beaches using the storm characteristics and the proposed erosion classes. However, the empirical formula cannot be used for other coasts without appropriate calibration. Ferreira et al. [15] analyzed several European coasts, with three of them being in the Mediterranean Sea. The numerical model XBeach was used to estimate the erosion, and XBeach coupled with the overland flood model LISFLOOD-FP were used to compute the inundation. The advantage of this approach is that their results are more reliable because the impacts are analyzed in detail. However, its drawback is the increased computational time, since setting up XBeach and LISFLOOD-FP requires more workload.

It should be mentioned that, in addition to the Mediterranean Sea, similar studies have also been performed worldwide (e.g., Brazil [16], Bangladesh [17], Colombia [18], and South Korea [19]). A GIS-based coastal vulnerability assessment of state of Pará, Brazil, was performed by Szlafsztei and Sterr [16]. A new approach implementing fuzzy logic based on geospatial techniques was used to analyze the vulnerability of the coast of Bangladesh [17]. The authors claim that they can analyze the vulnerability at a cell size of 10 m. The drawback of this approach is the reliability and access of several necessary GIS data. The vulnerability of the Caribbean and Pacific coast of Colombia was estimated roughly through a semi-quantitative approximation by applying relative indices to different variables [18]. The advantage of this approach is that they included human aspects in their variables, such as housing density, contamination, etc.

The aim of this article is to present a tool to assess the integrated coastal vulnerability to storm-induced inundation and erosion following a similar probabilistic approach as in the work of Bosom and Jiménez [3] and apply it on the coast of Thrace, Greece (Figure 1). The modification of the present study is the use of SBEACH to compute the beach retreat, instead of an empirical equation. In addition, two different empirical formulas to estimate the wave run-up are used to analyze their differences, and the inundation vulnerability framework includes overtopping to better determine the flooding impact. After calculating the time series of the two hazards, extreme probability functions are fitted to estimate their magnitudes with large return periods. When both probability distributions are known, an accepted risk and a time period of concern are selected to estimate a specific return period. This permits the comparison of vulnerabilities with the same return period and the identification of the most vulnerable areas. Finally, a simple approach to integrate the vulnerabilities of both hazards is presented.

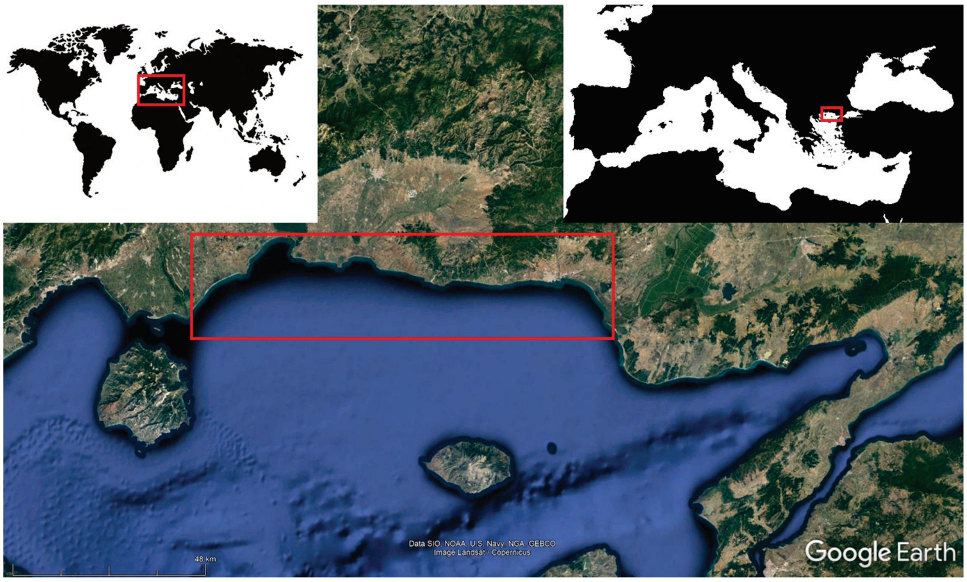

Figure 1. Panoramic view of the globe (**top-left** corner) with indication of the Mediterranean basin. The red rectangle at the Mediterranean map (**top-right** corner) indicates the studied area, coast of Thrace, Greece (Photo courtesy of Google Earth).

2. Study Coast and Data

The studied coastline is in the Mediterranean Sea and, particularly, in the region of Thrace, northeast Aegean Sea of Greece (Figure 1). Its length is about 108 km, and its boundaries are the Nestos and Evros rivers, which are located at the west and east, respectively. Along the river streams, three dams were constructed, resulting in the reduction of the sediment towards the coast [20]. Apart from the two large rivers, it comprises of long straight sandy beaches, cliffs, pocket beaches, deltas, lagoons, salt pits and a lake. The only city on the coastline is Alexandroupolis. The coastal zone of this city is of high economic value due to its port where commercial, transportation and tourist activities occur. In contrast, the lagoons, the lake, and the deltas have low economic value, because any investment will face significant environmental restrictions due to the Ramsar and Natura 2000 protection [21,22]. The socio-economic structure of the rest of the coastline is based on tourism, aquaculture, agriculture and residential developments, and its economic value is characterized as medium.

The coastline experiences mild wave climate, which is typical at the North-Eastern Mediterranean (microtidal and fetch-limited wave conditions) [23]. To characterize the storms, 3 h hindcasts of the WAM model for ten years (January 1995–December 2004) at four stations (Figure 2) were used, provided by the Hellenic Centre of Maritime Research. The wave dataset included the significant wave height, H_s, wave peak period, T_p, wave direction, H_{dir}, wind speed, W_s, and wind direction, W_{dir}. It should be stressed that the Aegean Sea presents short fetches and storms of limited duration, which may lead to model errors in comparison to ocean predictions [24]. However, the hindcasted values are considered representative of the actual wave conditions because they were compared to available measurements from buoys, and no significant differences were observed [25].

Information about the basic beach dimensions (height, width, and slope) was obtained from the Hellenic Military Geographical Service through a digital terrain model with 5 m resolution. The beach slope is mild (~0.002) around the deltas and steep (~0.067) at the center of the coastline. The sediment diameter varies between 0.22 mm and 0.5 mm [20]. The selected beaches for the present vulnerability assessment are shown in Figure 3.

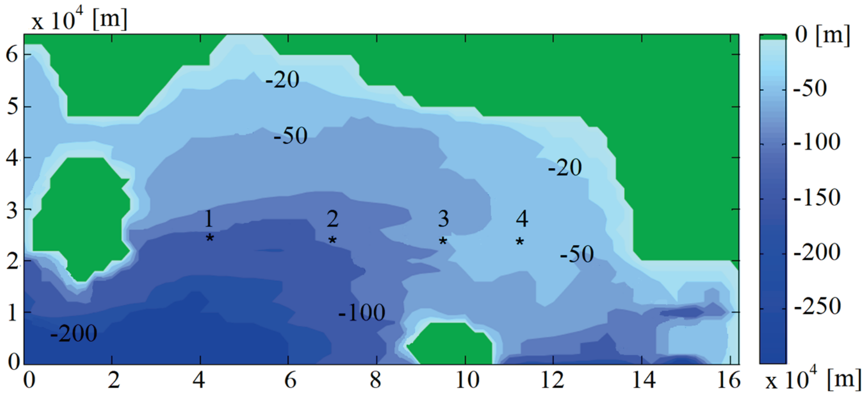

Figure 2. The bathymetry of the studied area with indication of the four stations (1, 2, 3, 4). Thasos and Samothraki islands can be observed at the west and south, respectively.

Figure 3. The studied coastline with the eleven selected beaches.

The first and last beach (1 and 11) are located at the deltas of the two rivers, Nestos and Evros, respectively. Area 3 (Lagoon) is a barrier beach, which is a narrow strip of land with low elevation. It is a crucial buffer that protects the lagoon against storm damage and flooding, but its existence is very fragile. The rest of the studied beaches (2 until 10) are typical sandy ones, whereas beach 10 (City) runs along the city of Alexandroupolis. The characteristics of each beach are presented on Table 1.

Table 1. Characteristics of the studied beaches.

	Length [m]	Width [m]	Height [m]	Slope	Buoys
1 Delta	2000	500	0.9	0.002	1
2	1300	30	0.4	0.013	1
3 Lagoon	700	20	0.3	0.018	1
4	300	20	0.4	0.020	2
5	500	20	0.8	0.040	2
6	1500	15	1	0.067	3
7	1000	30	2	0.067	3
8	1100	30	2	0.067	3
9	6000	25	0.8	0.032	3
10 City	9000	15	0.5	0.033	4
11 Delta	8000	125	1	0.008	4

3. Methodology

The methodological framework to assess integrated coastal vulnerability to storm-induced impacts is schematized in Figure 4. It consists of four main steps: (a) estimation of the storm-induced phenomena, (b) calculation of the probability distribution of the induced hazards, (c), selection of the return period, and (d) integration of the coastal vulnerability.

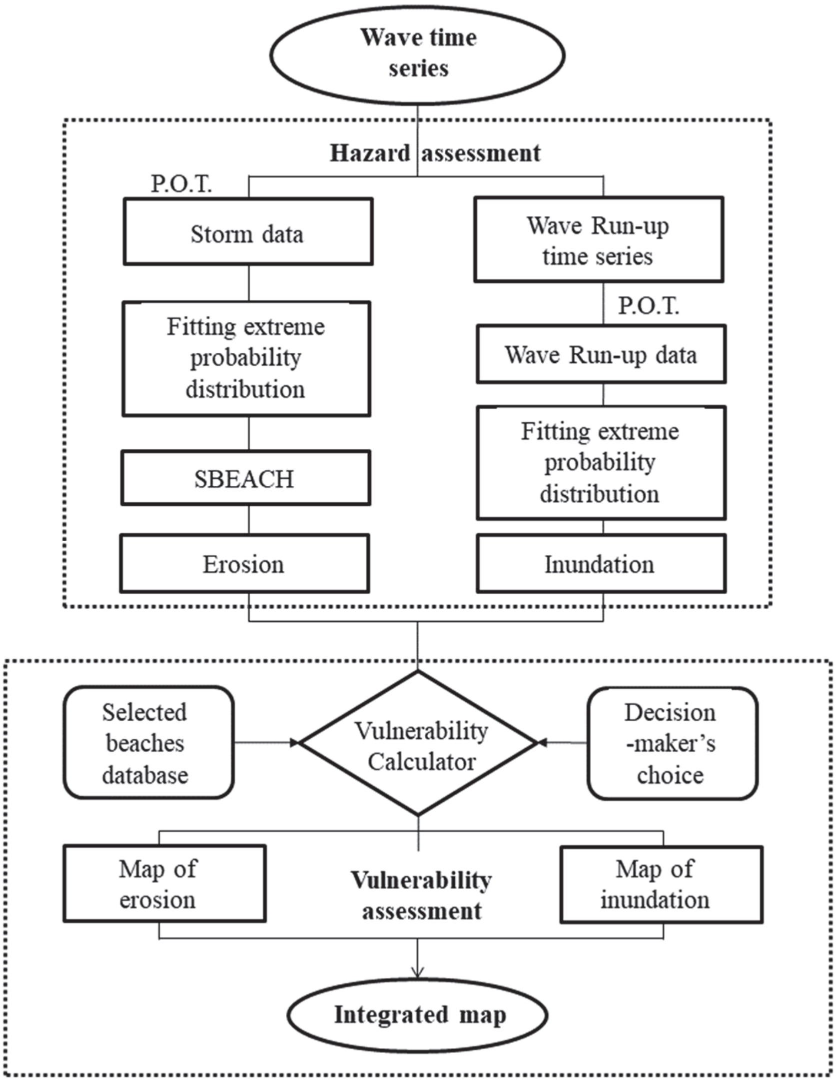

Figure 4. Methodological framework for integrated coastal vulnerability assessment to storms.

The event approach [26] is followed to estimate the erosion, since it is impossible to calculate its time-series, but only the erosion produced by independent storms. Therefore, wave height extreme distributions are first calculated from the storm time-series, then, other related parameters (i.e., wave period and storm duration) are estimated, and finally, the storm-induced erosion for each return period is computed.

On the other hand, the response approach [26] is used to estimate the inundation, because the run-up time-series can be directly calculated from wave data. Afterwards, extreme probability distributions are fitted, and from them, the inundation probability distribution is estimated. This reduces the uncertainty in the present analysis, since it allows the hazard magnitude associated with a given probability of occurrence to be obtained without assuming relationships between the driving variables [15].

Once the erosion and inundation probability distributions are estimated, vulnerability maps are drawn based on a selected return period. Following this methodology, decision-makers (public or private administrators, municipalities, coastal managers, etc.) can select an acceptable return period for each area of the coastline depending on its characteristics (economy, infrastructure, environment, etc.). Selecting spatially varying return periods allows comparisons of vulnerabilities associated with different probabilities.

3.1. Erosion Parameterization

Cross-shore erosion occurs mainly during extreme storms, and unlike long-shore erosion, which is difficult to observe in the short-term, it can transport large sediment volumes over intervals as short as one day. Since storm-induced hazards are considered in this project, only cross-shore erosion will be estimated.

To start with its vulnerability assessment, first step consists of finding the hazards forcing, i.e., identify storms in the study area. Subsequently, in order to do so, a storm data set must be built using the existing wave time-series. In this study, the peak-over-threshold (P.O.T.) method was used, where a storm is defined as an uninterrupted sequence of waves with height exceeding a threshold value and direction towards the under-consideration beaches. The wave height threshold is selected by calculating the 95% quantile of its cumulative distribution function. Then, extreme probability (Gumbel, Generalized Extreme Value, Generalized Pareto, and Weibull) distributions were used to fit the storm wave data. Apart from the extreme wave height, its corresponding period and storm duration are computed using regression analysis to the existing wave data. With these parameters, the erosion of every storm can be predicted. Finally, the numerical model SBEACH is selected to estimate the beach profile response. A detailed description of the model is available in [27,28], whereas its disadvantages were presented by Thieler et al. [29]. The direction and rate of cross-shore sediment transport predicted by SBEACH is based on empirical criteria derived from wave-tank experiments. Its fundamental assumption is that the beach is changed only by cross-shore erosion, resulting in a redistribution of sediment across its profile with no net gain or loss of material (sand conservation). Furthermore, it should not be used to examine profile changes near jetties or similar structures because, in these cases, profile changes might be controlled more by the interruption of long-shore transport than by cross-shore. Therefore, SBEACH should only be applied if long-shore erosion can be neglected, as is in this case. In addition, it is an easy and fast numerical model that produces reliable results [8].

In this study, beach erosion is characterized by the beach retreat, ΔX, that is defined as the shoreward displacement of the initial beach line after a storm (Figure 5). This is a simplification of a real beach response because pre-storm morphology, among other factors, affects the induced erosion [30]. Furthermore, event grouping, when significantly more erosion, which can occur from two consecutive storms [31], is not considered. However, the objective is not to reproduce the exact beach response to storms but to estimate an order of magnitude of the erosion.

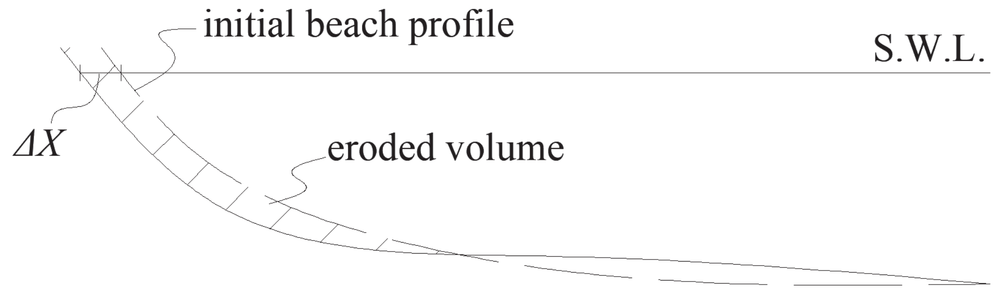

Figure 5. Initial and final beach profile. The eroded volume and beach retreat are marked. S.W.L. is defined as standing water level.

The final step includes the ability of a coast to cope with erosion in order to quantify its vulnerability. The parameter used as a characteristic of the coast resilience is the beach width, W. Wide beaches do not face significant problems even if their short-term erosion is large. Therefore, the lowest vulnerability will occur when beach width is greater or equal to the minimum required beach width, $W_{\min}$, plus the beach retreat, Δx:

$$W \geq W_{\min} + \Delta x \tag{1}$$

The minimum required beach width is a distance to maintain a coast operative and to avoid direct exposure of the hinterland to seawater [3]. In this work, W_{min} = 10 m to let machinery work operate after storm damages. On the other hand, the highest vulnerability is defined when beach width is less or equal to its retreat:

$$W \leq \Delta x \tag{2}$$

This is the case when a beach is fully eroded, and the infrastructure is exposed to waves. The erosion vulnerability is quantified using a linear function between Equation (1), lowest value (safe beach), and Equation (2) highest value (vulnerable beach). It is also divided in four qualitative classes (green: lowest, yellow: low, orange: high, and red: highest).

3.2. Inundation Parameterization

In general, inundation is caused by a combination of high-water levels due to tide and wave run-up. Consequently, joint probability analysis should be performed to estimate the highest water level during a storm. However, the tidal range in the studied coastline is very low [23], and thus, it can be neglected. The wave run-up describes the phenomenon when an incoming wave climbs the beach profile up to a level that can be higher than its crest. The vertical distance between the S.W.L. and the highest point reached by the 2% of the incident waves is called run-up, $R_{2\%}$. For this study, the wave run-up time series is computed using the formula [32]:

$$R_{2\%} = 1.1\left(0.35\tan\beta(H_s L_o)^{0.5} + \frac{[(H_s L_o(0.563\tan\beta^2 + 0.004)]^{0.5}}{2}\right) \tag{3}$$

and the existing wave time series. In Equation (3), L_o (= $1.562 \cdot T_p{}^2$) is the deep-water wavelength associated with the wave peak period, T_p, and tanβ is the beach slope. This equation (henceforth, Stockdon eq.) is selected because it was derived from field measurements on natural sandy beaches [32] and it is widely used [3]. However, it was reported that Stockdon eq. might underpredict the wave run-up [33]. Therefore, the equation presented by Reis et al. [34] (henceforth, Reis eq.) is also used to estimate the wave run-up time series and to compare the two empirical formulas,

$$R_{2\%} = \left(\frac{(0.38 + 1.67\xi)H_s}{1.085}\right) \tag{4}$$

The Irribaren number is defined as $\xi = \tan\beta/(H_s/L_o)^{0.5}$. It should be noted that other formulas [35] to estimate the wave run-up could be used. Nevertheless, to increase the reliability of a vulnerability assessment, it is recommended to verify that the selected equations capture the actual processes. The threshold of the wave run-up time series is selected by finding the 95% quantile of the corresponding cumulative distribution functions. After applying the P.O.T. method to the wave run-up time series, extreme distributions are fitted to the highest run-up values.

The beaches resilience against flooding is a function of their height. Higher beaches will be less inundated. Based on these, the lowest vulnerability is defined when beach height, B, is greater or equal to the run-up:

$$B \geq R_{2\%} \tag{5}$$

On the other hand, the highest vulnerability is defined when the run-up exceeds beach height by a value Z or more:

$$B \leq R_{2\%} - Z \tag{6}$$

The variable Z needs to be adapted based on the specific conditions of the studied area. For the highest vulnerability, it represents overtopping conditions with significant water volumes flowing to the hinterland. It can be defined after comparing the average overtopping discharge of every beach with values allowed in order to have a littoral road, pedestrian sidewalk, etc. without any obstructions [36]. In this study, the overtopping discharge, Q, was calculated by [33]:

$$Q = A\sqrt{gR_{2\%}^3}\left(1 - \frac{B}{R_{2\%}}\right)^C, \ \text{for} R_{2\%} > B \tag{7}$$

where g is the gravitational acceleration, A = 0.033, and C = 10.2 − 0.275/tanβ. Similarly with erosion, four levels of vulnerability exist, and a linear relationship is assumed between Equations (5) and (6).

3.3. Integrating Coastal Vulnerability

After the estimation of the extreme distributions, the last steps of the methodology are to consider an appropriate return period and to integrate the vulnerability against the hazards of inundation and erosion. The return period is estimated by [37]:

$$T_r = \frac{1}{1 - (1 - P)^{\frac{1}{N}}} \tag{8}$$

where P is a probability of occurrence, and N is a time period of concern. In general, these variables should be defined by the decision-makers of each region, and hence, different return periods can be analyzed. This permits to study different safety levels, which are a function of the hinterland importance. The integration of the vulnerability of both hazards is performed following Table 2. This approach is conservative, because a high or very high vulnerability has more weight for the estimation of the integrated vulnerability.

Table 2. Approach to integrate the vulnerability of erosion and inundation. The four different colors classify the vulnerability (green: lowest, yellow: low, orange: high, and red: highest vulnerability).

		Erosion			
		very Low	low	high	very high
Inundation	very low	very low	low	high	high
	low	low	low	high	high
	high	high	high	high	very high
	very high	high	high	very high	very high

4. Results

4.1. Erosion Results

In this study, the threshold value of the wave height to define a storm was found to be 1.5 m. After applying the P.O.T. method in the wave time series, the storm wave data for beach 10 (City) are shown in Figure 6 (left). Among the extreme probability distributions that were used, the Gumbel distribution was chosen (Figure 6-right) as it presented the best fit. The method that was used to calculate its parameters was the maximum product of spacings with 95% confidence intervals. It should be stressed that only extreme wave heights with return periods of maximum 30 years will be considered reliable, because the extent of a time-series must be at least one-third of the duration to which a variable is being extrapolated [38]. For the present case, thirty years are considered sufficient to produce long-term coastal planning.

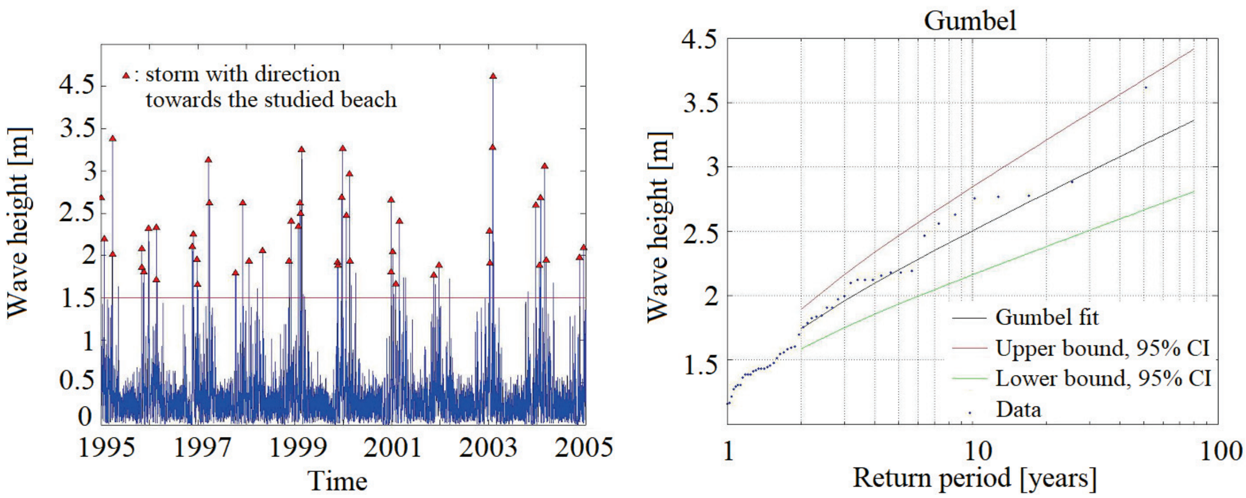

Figure 6. **Left**: Wave time series for area 10 (City). The marked peaks above the red line (threshold = 1.5 m) are the storms with a direction towards the studied beach. **Right**: Wave height Gumbel distribution for area 10 (City). The red and green lines are the 95% confidence intervals.

Using the wave height with a return period of 30 years from Figure 6 (right), the final profile of a representative cross-section at beach 10 (City) can be simulated from SBEACH (Figure 7).

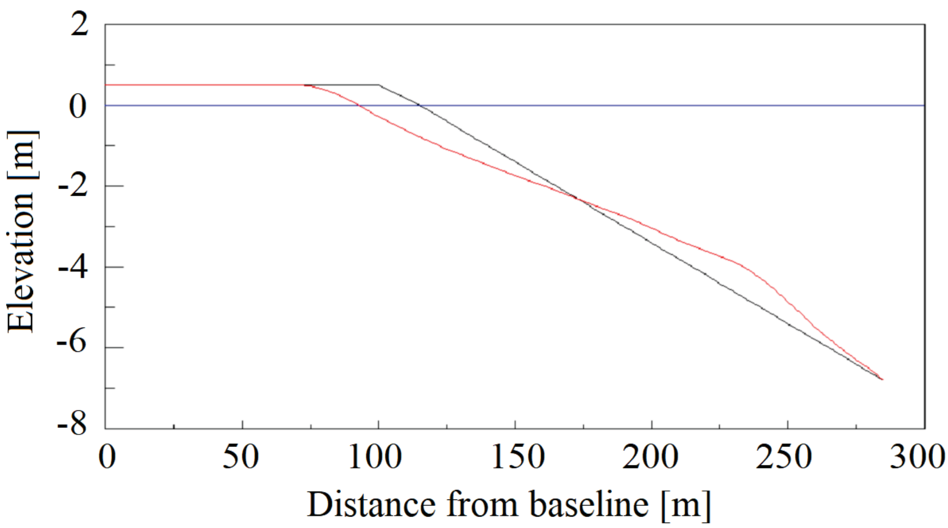

Figure 7. Initial (black line) and post−storm (red line) profile of beach 10 (City) for T_r = 30 years.

After following the above procedure for all beaches, the erosion results for three different return periods are summarized in Table 3. It should be noted that beaches 1–4 and 11 are not eroded (even for storms with T_r = 30 years), whereas the others lose much sediment and width. Another interesting fact is that the eroded beaches are located in the sheltered region of Samothraki Island (Figures 2 and 3), receiving storms with lower energy than the non-eroded beaches that are more exposed. This is explained by the beach slope. The mild slope beaches at the deltas and the lagoon (Table 1) dissipate more wave energy, and thus, they are safer against erosion.

Table 3. Beach retreat and difference between beach width and retreat for all examined areas with three return periods T_r. The four different colors classify the erosion vulnerability (green: lowest, yellow: low, orange: high, and red: highest vulnerability).

	Beach Width [m]	Beach Retreat [m] *Tr* [yrs]			Beach Width–Beach Retreat [m] *Tr* [yrs]		
		5	10	30	5	10	30
1 Delta	500	0.0	0.0	0.0	500.0	500.0	500.0
2	30	0.0	0.0	0.0	30.0	30.0	30.0
3 Lagoon	20	0.0	0.0	0.0	20.0	20.0	20.0
4	20	0.0	0.0	0.0	20.0	20.0	20.0
5	20	13.6	16.2	20.1	6.4	3.8	−0.1
6	15	16.5	18.6	22.2	−1.5	−3.6	−7.2
7	30	15.9	16.1	18.8	14.1	13.9	11.2
8	30	15.9	16.1	18.8	14.1	13.9	11.2
9	25	6.4	7.9	9.3	18.6	17.1	15.7
10 City	15	12.2	14.4	18.1	2.8	0.6	−3.1
11 Delta	125	0.0	0.0	0.0	0.0	0.0	0.0

The vulnerability map to erosion of the coastline is presented in Figure 8 for the return period of 30 years. Narrow beaches (5, 6 and 10) are those that have erosion problems, whereas beaches 7 and 8 with 30 m width and large beach retreats (18.8 m for T_r = 30 yrs), are not even characterized with low vulnerability. In conclusion, the majority of the coastline is not vulnerable to erosion, except for the steep and narrow beaches 5 and 6, with 20 m maximum width, and the coast along the city of Alexandroupolis (10).

Figure 8. Coastal vulnerability map to erosion with T_r = 30 years.

4.2. Inundation Results

As it was explained in Section 3.2, the wave run-up time series can be calculated from Equations (3) and (4). In Figure 9, the two different run-up time series due to Equations (3) and (4) are presented for beach 10 (City).

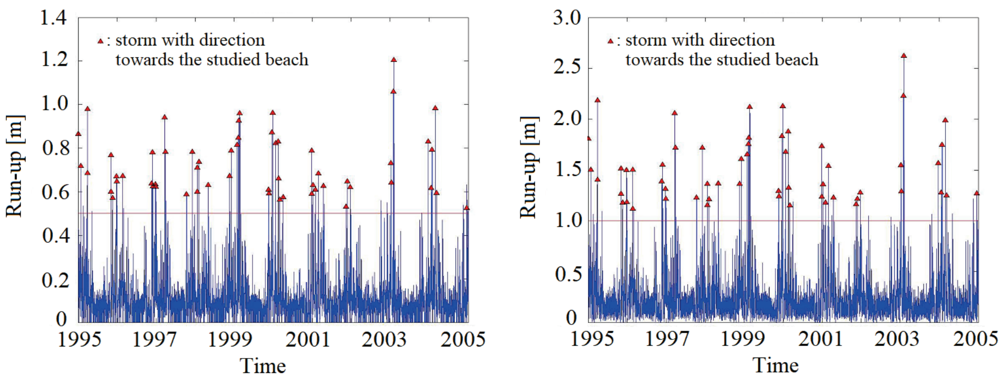

Figure 9. Wave run-up time series (**left**—Stockdon eq., **right**—Reis eq.) for beach 10 (City). The red line is the threshold. The marked peaks are the storms with direction towards the studied coastline.

For both run-up time series, the GUMBEL distribution presented the best fit. Hence, it was selected to estimate the wave run-up values for different return periods (Figure 10).

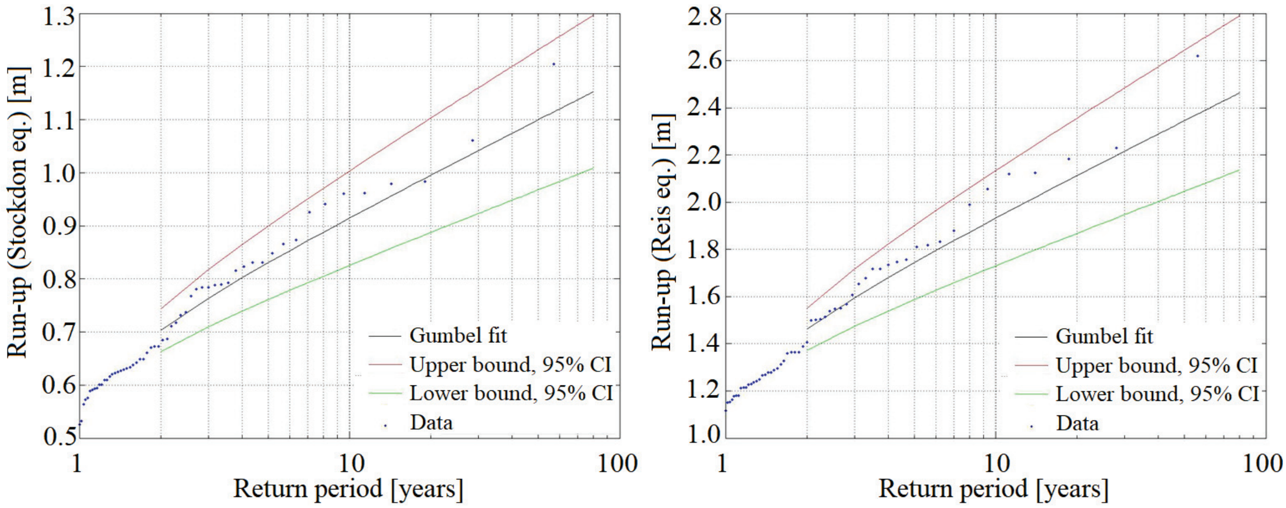

Figure 10. Gumbel distribution of wave run-up for beach 10 (City), calculated with Stockdon (**left**) and Reis (**right**) equation. The red and green lines are the 95% confidence intervals.

The inundation results for all examined beaches are presented in Table 4. The wave run-up values calculated by Stockdon eq. are approximately half from the ones calculated by Reis eq. This stresses that using different equations can lead to highly expensive measures against an overestimated hazard, or, in contrast, can pose danger on the under-consideration coastline if the hazard is underestimated. Therefore, selecting the correct equation to describe a physical phenomenon is of paramount importance.

Table 4. Beach height and wave run-up predicted by Stockdon and Reis equations for all examined areas with three return periods T_r.

	Beach Height [m]	**Stockdon Eq. [m] *Tr* [yrs]**			**Reis Eq. [m] *Tr* [yrs]**		
		5	10	30	5	10	30
1 Delta	0.9	0.73	0.80	0.90	1.50	1.65	1.82
2	0.4	0.80	0.88	1.05	1.75	1.95	2.25
3 Lagoon	0.3	0.77	0.85	0.91	1.80	2.05	2.35
4	0.4	0.82	0.90	1.03	1.80	2.10	2.45
5	0.8	0.90	1.03	1.20	2.05	2.40	2.70
6	1.0	0.85	0.93	1.05	1.80	2.05	2.45
7	2.0	0.85	0.93	1.05	1.80	2.05	2.45
8	2.0	0.85	0.93	1.05	1.80	2.05	2.45
9	0.8	0.71	0.77	0.85	1.55	1.65	1.80
10 City	0.8	0.83	0.91	1.05	1.70	1.90	2.20
11 Delta	1.0	0.74	0.80	0.88	1.45	1.60	1.80

It should be noted that the wave run-up values of the lagoon area (3) and the coast of Alexandroupolis (10) are almost the same (Table 4), even though the lagoon (3) is an exposed beach, and the coast in (10) is semi-protected due to the sheltering effect of the islands. This is explained because the wave characteristics are not the only inputs to estimate the run-up; beach slope is also significant. Milder slopes reduce wave run-up, since $tan\beta$ is proportional to $R_{2\%}$ in Equations (3) and (4). Furthermore, large run-up values do not necessarily imply high vulnerability. For example, Reis eq. yields the same run-up for beach 3 (Lagoon) and beach 7 for T_r = 5 years (Table 4). However, beach 7 does not have any flooding problem, because its beach height = 2.0 m > 1.8 m, whereas beach 3 (Lagoon) is completely inundated (beach height = 0.3 m < 1.8 m).

The results of the overtopping discharge using Reis eq. for a return period of 30 years are presented in Table 5. The Reis eq. and 30 years return period were selected to be on the conservative side. It is reported that an overtopping discharge of more than 150 lt/sec causes damage to structures (buildings, revetments, etc.) and it is dangerous and unsafe for pedestrians and driving on coastal roads [35]. Based on this and the corresponding results, the variable Z was set equal to 2 m in Equation (6), e.g., both beach 3 (Lagoon) and 4 experience an overtopping discharge of approximately 175 lt/sec, while having a wave run-up two meters higher than their height.

Table 5. Beach height, wave run-up based on Reis eq., and overtopping discharge for all examined beaches.

	Beach Height [m]	**Reis Eq. [m] T_r = 30 yrs**	**Q [lt/s] T_r = 30 yrs**
1 Delta	0.9	1.82	10.28
2	0.4	2.25	139.02
3 Lagoon	0.3	2.35	174.49
4	0.4	2.45	171.50
5	0.8	2.70	87.93
6	1.0	2.45	16.38
7	2.0	2.45	0.01
8	2.0	2.45	0.01
9	0.8	1.80	15.76
10 City	0.8	2.20	100.39
11 Delta	1.0	1.80	5.52

Based on the above, the vulnerability maps to inundation are presented in Figures 11 and 12 for Stockdon and Reis equations, respectively. Beaches with very low heights (2, 3, 4, 5 and 10 in Table 4) are highly vulnerable to inundation, whereas beaches 7 and 8, that are two meters high, are not expected to have flooding problems.

Figure 11. Coastal vulnerability map to inundation predicted by Stockdon eq. with T_r = 30 years.

Figure 12. Coastal vulnerability map to inundation predicted by Reis eq. with T_r = 30 years.

4.3. Integrated Coastal Vulnerability Assessment

In this study, the minimum period of concern for coastal protection is set to n = 10 years, following the recommendation of the Greek Ministry of Public Works (GMPW). In addition, for the majority of the studied coastline, failure of a beach will not cause human losses and it will have medium economic impact. This corresponds to an accepted probability, p = 0.3 (GMPW). By substituting this value in Equation (8), the return period equals to thirty years. Based on this, the vulnerability maps to erosion and inundation (Figures 8, 11 and 12) were presented with a return period of 30 years.

For the integrated coastal vulnerability assessment, the results of Reis eq. were used. This was conducted because the hinterland of this coastline is known to be prone to inundation and Reis eq. yields larger wave run-up values that seem to agree with observations. As a result, the integrated coastal vulnerability to inundation and erosion associated with thirty years return period along the coast of Thrace is presented in Figure 13. From the integrated vulnerability map, half of the studied coastline is considered highly or very highly vulnerable, whereas the other half is relatively safe for Tr = 30 years. The barrier beach (3 Lagoon) is characterized by high vulnerability only due to inundation (Figure 12), whereas the coast of Alexandroupolis (10 City) is very highly vulnerable to both inundation and erosion (see also Figures 8 and 12).

Figure 13. Integrated coastal vulnerability map associated with a return period of 30 years.

5. Discussion

An assumption to apply the above methodology is that the beach dimensions were averaged for each studied area. This may underestimate or overestimate the vulnerability in some parts. To improve the present assessment in the future, in situ analytical measurements of beach slope, width and height are required. Another point to be considered is that coastal geomorphology needs to be updated as beach profiles evolve constantly. As it was previously mentioned, the hazard intensity and the beach capacity to cope with it depend on the pre-storm morphology. Hence, if decision-makers want to have a reliable live estimation, the present method needs to be complemented with a coastal monitoring plan.

In addition, the present analysis revealed the importance of correctly estimating a hazard in order to have a reliable vulnerability map. Therefore, the used equations and models should be validated in order to increase the reliability of the coastal vulnerability assessments. Most models assume a smooth profile or straight and parallel seabed contours. This is an assumption that may be completely invalid on coasts that have submerged rocks or boulders. In the real world, there is also substantial regional and local variability in grain size. The above should be taken into consideration for the validity of the results.

All in all, the results based on the above hypotheses may contain a degree of uncertainty for some parts of the under-consideration coastline. However, the aim of the present study is not to replace a detailed beach modeling analysis, but to provide a first approach to the vulnerability assessment of a large coastline. This can help decision-makers choose how to invest their resources for preventing damages.

6. Conclusions

In this article, the probabilistic vulnerability to storms of the coast of Thrace, Greece was assessed. To this end, the methodology presented by Bosom and Jiménez [3] has been applied with three modifications. The introduced modifications were the use of the numerical model SBEACH to estimate the beach retreat, instead of an empirical formula. Furthermore, two different run-up equations, instead of one, were used to compare their different estimations concerning the flooding results. Finally, the vulnerability to inundation was defined after considering the corresponding overtopping discharge.

A large vulnerability variation along the coast of Thrace was found, stressing the importance of waves and beach geomorphology to the integrated hazards assessment. The majority of the coastline is not vulnerable to erosion, except for some steep and narrow beaches, and the coast along the city of Alexandroupolis. Beaches with very low heights are highly vulnerable to inundation, whereas beaches that are two meters high, are not expected to have flooding problems. Half of the studied coastline is considered highly or very highly vulnerable, whereas the other half is relatively safe for $Tr = 30$ years. It was also found that an area that is affected by a high-intensity hazard is not necessarily vulnerable, because coastal vulnerability is defined by the beach capacity to cope with an extreme hazard.

This methodology is simple, and it can be similarly applied to other Mediterranean coasts. For different regions, (e.g., beaches with high tide), or under climate change scenarios (e.g., higher S.W.L.) it can be modified and applied accordingly if the required information is known.

Funding: This research received no external funding.

Institutional Review Board Statement: Not applicable.

Informed Consent Statement: Not applicable.

Data Availability Statement: Data available on request.

Acknowledgments: I would like to thank J.A. Jiménez for introducing me to the coastal vulnerability assessment methodology.

Conflicts of Interest: The author declares no conflict of interest.

References

1. Mendoza, E.T.; Jiménez, J.A. Storm-Induced Beach Erosion Potential on the Catalonian Coast. *J. Coast. Res.* **2006**, 81–88. Available online: http://www.jstor.org/stable/25737386 (accessed on 11 June 2023).
2. Anfuso, G.; Postacchini, M.; Di Luccio, D.; Benassai, G. Coastal Sensitivity/Vulnerability Characterization and Adaptation Strategies: A Review. *J. Mar. Sci. Eng.* **2021**, *9*, 72. [CrossRef]
3. Bosom, E.; Jiménez, J.A. Probabilistic coastal vulnerability assessment to storms at regional scale—Application to Catalan beaches (NW Mediterranean). *Nat. Hazards Earth Syst. Sci.* **2011**, *11*, 475–484. [CrossRef]
4. Neumann, B.; Vafeidis, A.T.; Zimmermann, J.; Nicholls, R.J. Future coastal population growth and exposure to sea-level rise and coastal flooding—A global assessment. *PLoS ONE* **2015**, *10*, 3. [CrossRef] [PubMed]
5. UNEP. United Nations Environment Programme, Mediterranean Action Plan, Barcelona Convention. *Mediterr. Qual. Status Rep.* **2017**. Socioeconomic Characteristics. Available online: https://www.unep.org/unepmap/index.php/resources/quality-status-report-mediterranean-med-qsr-2017 (accessed on 10 August 2022).
6. Masson-Delmotte, V.; Zhai, P.; Pirani, A.; Connors, S.L.; Péan, C.; Berger, S.; Caud, N.; Chen, Y.; Goldfarb, L.; Gomis, M.; et al. IIPCC: Climate Change 2021: The Physical Science Basis. Contribution of Working Group I to the Sixth Assessment Report of the Intergovernmental Panel on Climate Change. *Camb. Univ.* **2021**, *3*, 31. [CrossRef]
7. PAP/RAC. *ICZM Protocol in the Mediterranean, Split*. 2007. Available online: https://www.paprac.org/iczm-protocol (accessed on 1 December 2022).
8. Monioudi, I.N.; Karditsa, A.; Chatzipavlis, A.; Alexandrakis, G.; Andreadis, O.P.; Velegrakis, A.F.; Poulos, S.E.; Ghionis, G.; Petrakis, S.; Sifnioti, D.; et al. Assessment of vulnerability of the eastern Cretan beaches (Greece) to sea level rise. *Reg. Environ. Chang.* **2016**, *16*, 1951–1962. [CrossRef]
9. Alexandrakis, G.; Manasakis, C.; Kampanis, N.A. Valuating the effects of beach erosion to tourism revenue. A management perspective. *Ocean. Coast. Manag.* **2015**, *111*, 1–11. [CrossRef]
10. McLaughlin, S.; McKenna, J.; Cooper, A. Socio-economic data in coastal vulnerability indices: Constraints and opportunities. *J. Coast. Res.* **2002**, *36*, 487–497. [CrossRef]
11. De Leo, F.; Besio, G.; Zolezzi, G.; Bezzi, M. Coastal vulnerability assessment: Through regional to local downscaling of wave characteristics along the Bay of Lalzit (Albania). *Nat. Hazards Earth Syst. Sci.* **2019**, *19*, 287–298. [CrossRef]

12. Jiménez, J.A.; Ciavola, P.; Balouin, Y.; Armaroli, C.; Bosom, E.; Cervais, M. Geomorphic coastal vulnerability to storms n microtidal fetch-limited environments: Application to NW Mediterranean & N Adriatic Seas. *J. Coast. Res.* **2009**, *56*, 1641–1645.
13. Di Paola, G.; Aucelli, P.P.C.; Benassai, G.; Rordiguez, G. Coastal vulnerability to wave storms of Sele littoral plain (southern Italy). *Nat. Hazards* **2014**, *71*, 1795–1819. [CrossRef]
14. Rizzo, A.; Aucelli, P.P.C.; Gracia, F.J.; Anfuso, G. A novelty coastal susceptibility assessment method: Application to Valdelagrana area (SW Spain). *J. Coast. Conserv.* **2018**, *22*, 973–987. [CrossRef]
15. Ferreira, O.; Viavattene, C.; Jimenez, J.A.; Bolle, A.; das Neves, L.; Plomaritis, T.A.; McCall, R.; van Dongeren, A.R. Storm-induced risk assessment: Evaluation of two tools at the regional and hotspot scale. *Coast. Eng.* **2018**, *134*, 241–253. [CrossRef]
16. Szlafsztein, C.; Sterr, H. A GIS-based vulnerability assessment of coastal natural hazards, state of Pará, Brazil. *J. Coast. Conserv.* **2007**, *11*, 53–66. [CrossRef]
17. Mullick, M.R.A.; Tanim, A.H.; Samiul, S.M. Coastal vulnerability analysis of Bangladesh coast using fuzzy logic based geospatial techniques. *Ocean. Coast. Manag.* **2019**, *174*, 154–169. [CrossRef]
18. Coca-Domínguez, O.; Ricaurte-Villota, C. Validation of the Hazard and Vulnerability Analysis of Coastal Erosion in the Caribbean and Pacific Coast of Colombia. *J. Mar. Sci. Eng.* **2019**, *7*, 260. [CrossRef]
19. Kim, T.K.; Lim, C.; Lee, J.L. Vulnerability Analysis of Episodic Beach Erosion by Applying Storm Wave Scenarios to a Shoreline Response Model. *Front. Mar. Sci.* **2021**, *8*, 759067. [CrossRef]
20. Sylaios, G.K.; Anastasiou, S.; Tsihrintzis, V.A. Restoration of a seashore eroded due to dam operation through beach nourishment. *Ecohydrol. Hydrobiol.* **2012**, *12*, 123–135. [CrossRef]
21. Ramsar Organization List. *The List of Wetlands of International Importance*; 1975; Available online: https://www.ramsar.org/country-profile/greece (accessed on 1 May 2023).
22. Natura 2000. Available online: https://natura2000.eea.europa.eu (accessed on 1 May 2023).
23. Stiros, S.C.; Psimoulis, P.A. Identification of Nearshore Wave Characteristics Using Robotic Total Stations. *J. Surv. Eng.* **2010**, *136*, 172–179. [CrossRef]
24. Cavaleri, L.; Bertotti, L. Accuracy of the modelled wind and wave fields in enclosed seas. *Tellus A Dyn. Meteorol. Oceanogr.* **2004**, *56*, 167–175. [CrossRef]
25. Galiatsatou, P.; Prinos, P. Modeling non-stationary extreme waves using a point process approach and wavelets. *Stoch. Environ. Res. Risk Assess.* **2011**, *25*, 165–183. [CrossRef]
26. Garrity, N.J.; Battalio, R.; Hawkes, P.J.; Roupe, D. Evaluation of Event and Response Approaches to Estimate the 100-year Coastal Flood for Pacific Coast Sheltered Waters. In *Coastal Engineering*; World Scientific Publishing Company: Singapore, 2006; pp. 1651–1663. [CrossRef]
27. Larson, M.; Kraus, N.C. *SBEACH: Numerical Model for Simulating Storm-Induced Beach Change, CERC-89-9*; US Army Corps of Engineers: Vicksburg, MS, USA, 1989.
28. Wise, R.S.; Smith, S.J.; Larson, M. *SBEACH: Numerical Model for Simulating Storm-Induced Beach Change, CERC*; US Army Corps of Engineers: Vicksburg, MS, USA, 1996.
29. Thieler, E.R.; Pilkey, O.H.; Young, R.S.; Bush, D.M.; Fei, C. The Use of Mathematical Models to Predict Beach Behavior for U.S. Coastal Engineering: A Critical Review. *J. Coast. Res.* **2000**, *16*, 48–70.
30. Morton, R.A. Factors controlling storm impacts on coastal barriers and beaches: A preliminary basis for near real-time forecasting. *J. Coast. Res.* **2002**, *18*, 486–501.
31. Callaghan, D.P.; Nielsen, P.; Short, A.; Ranasinghe, R. Statistical simulation of wave climate and extreme beach erosion. *Coast. Eng.* **2008**, *55*, 375–390. [CrossRef]
32. Stockdon, H.F.; Holman, R.A.; Howd, P.A.; Sallenger, A.H. Empirical parameterization of setup, swash, and runup. *Coast. Eng.* **2006**, *53*, 573–588. [CrossRef]
33. Laudier, N.A.; Thornton, E.B.; MacMahan, J. Measured and modeled wave overtopping on a natural beach. *Coast. Eng.* **2011**, *58*, 815–825. [CrossRef]
34. Reis, M.T.; Hu, K.; Hedges, T.S.; Mase, H.A. Comparison of empirical, semiempirical and numerical wave overtopping models. *J. Coast. Res.* **2008**, *24*, 250–262. [CrossRef]
35. Park, H.; Cox, D.T. Empirical wave run-up formula for wave, storm surge and berm width. *Coast. Eng.* **2016**, *115*, 67–78. [CrossRef]
36. U.S. Army Corps of Engineers. *Coastal Engineering Manual, Coastal Overwash: Part 1, Overview of Processes*; U.S. Army Corps of Engineers: Washington, DC, USA, 2011; pp. 1–17.
37. Borgman, L. Risk Criteria. *J. Waterw. Port. C.* **1963**, *WW3*, 1–35. [CrossRef]
38. Borgman, L.E.; Resio, D.T. Extremal Prediction in Wave Climatology. In *Proceedings, Ports*; ASCE: New York, NY, USA, 1977; Volume 77, pp. 394–412.

Journal of
Marine Science and Engineering

MDPI

Review

Ensemble Neural Networks for the Development of Storm Surge Flood Modeling: A Comprehensive Review

Saeid Khaksari Nezhad *,†, Mohammad Barooni †, Deniz Velioglu Sogut and Robert J. Weaver

Ocean Engineering and Marine Sciences, Florida Institute of Technology, Melbourne, FL 32901, USA; mbarooni2018@my.fit.edu (M.B.); dvelioglusogut@fit.edu (D.V.S.); rjweaver@fit.edu (R.J.W.)
* Correspondence: skhaksarinez2021@my.fit.edu
† These authors contributed equally to this work.

Abstract: This review paper focuses on the use of ensemble neural networks (ENN) in the development of storm surge flood models. Storm surges are a major concern in coastal regions, and accurate flood modeling is essential for effective disaster management. Neural network (NN) ensembles have shown great potential in improving the accuracy and reliability of such models. This paper presents an overview of the latest research on the application of NNs in storm surge flood modeling and covers the principles and concepts of ENNs, various ensemble architectures, the main challenges associated with NN ensemble algorithms, and their potential benefits in improving flood forecasting accuracy. The main part of this paper pertains to the techniques used to combine a mixed set of predictions from multiple NN models. The combination of these models can lead to improved accuracy, robustness, and generalization performance compared to using a single model. However, generating neural network ensembles also requires careful consideration of the trade-offs between model diversity, model complexity, and computational resources. The ensemble must balance these factors to achieve the best performance. The insights presented in this review paper are particularly relevant for researchers and practitioners working in coastal regions where accurate storm surge flood modeling is critical.

Keywords: deep learning; storm surge prediction; ensemble model; sea level rise

Citation: Nezhad, S.K.; Barooni, M.; Velioglu Sogut, D.; Weaver, R.J. Ensemble Neural Networks for the Development of Storm Surge Flood Modeling: A Comprehensive Review. *J. Mar. Sci. Eng.* **2023**, *11*, 2154. https://doi.org/10.3390/jmse11112154

Academic Editor: Barbara Zanuttigh

Received: 5 October 2023
Revised: 27 October 2023
Accepted: 7 November 2023
Published: 11 November 2023

1. Introduction

Rising sea levels increase the risk of coastal flooding depending on the relative rate of mean sea/land level changes [1–3]. The impacts are linked to concurrent near-term trends as well as gradual escalation of long-term coastal inundation risk over time [4]. Estuaries and coastal areas should adapt to changing climate and implement the necessary mitigation measures. A complex process such as a storm surge is sensitive to abrupt changes in several storm parameters, such as intensity, surface atmospheric pressure at the center of the storm, maximum sustained wind speed, size, and forward speed, in addition to the effects driven by the characteristics of dynamic coastal settings, such as shoreline geography, estuaries, and bay barriers [5]. The interdependency of these different factors make it notoriously hard to predict the timing and intensity of the hydrodynamic response (e.g., water levels and currents) [6–9]. Parametric models conventionally incorporate historical or synthetic hurricanes using storm size, intensity, and track, allowing for the prediction of storm surge heights and overland flooding [10,11].

During a storm surge event (caused by tropical or extratropical cyclones), the potential impacts extend beyond the surge itself and could exacerbate flooding and structural damage. This can be further intensified by the surface gravity waves due to the superimposed storm tide [12]. Wave driven set-ups can contribute up to 30% of the total increase in water level (including both typical fluctuations and any additional rise) along the coast [13]. The combination of elevated water levels along with the destructive power of waves poses a tremendous danger to densely populated areas adjacent to coastal waters. The U.S. Atlantic and Gulf Coasts, for example, are expected to experience a sea level rise of, on average, 0.25–0.30 m in 30 years (2020–2050) [14]. This further increases the vulnerability of coastal regions to compound flooding (CF), where the interaction of rainfall, rivers, and ocean storm surges combine and create a cataclysmic force [15]. To overcome these challenges, physics-based approaches, such as hydrodynamic models, have been used to estimate hydrological processes and flood hazards/the probability of particular events that require land–atmosphere–ocean coupling [16]. Although these models explain the nature of flooding phenomena and show great skill for a wide variety of flood prediction scenarios, they usually deal with the physical dynamics and require various types of datasets, as the occurrence of floods varies with time and space [17,18]. This requires a large amount of computation, which makes short-term predictions very challenging. The reader is kindly referred to [17,19,20] for the comprehensive studies related to the development of physics-based models, their challenges, and capabilities.

Hydrodynamic modeling has also been extensively used to investigate the spatial and temporal variability of storm surges. Hydrodynamic models are widely utilized to describe coastal ocean processes and near-shore circulation and to simulate future scenarios of possible storm surge flooding [21]. These models are well-developed to account for the inherent uncertainties associated with sea level rise and storm surges. They also consider the relative impacts of different meteorological forces in total water levels [22,23]. However, these models are computationally demanding and time consuming. This limits their ability to simulate large complex domains or ensembles of events.

Some parametric models, such as the Bayesian model averaging, autoregressive integrated moving average, and peak over threshold methods, are among the most preferred methods to predict the statistical behavior of storm surge flooding [24,25]. However, these models are, at times, computationally demanding and typically sophisticated. Furthermore, generalizing the potential impacts of a storm surge for a particular geographical area to other areas with different parameters and settings is not a reliable approach [23]. Flood prediction requires constructing a minimum of a decade of non-tidal residual data from measurement by sea-level gauges [26]. In small datasets, i.e., those with a lack of large-sample observational data, even a few outliers will significantly alter the model or affect the correlation among the predicting variables [27].

Low-fidelity numerical storm surge models such as SLOSH (Sea, Lake, and Overland Surges from Hurricane) [28] are used by emergency managers and researchers to assist in forecasting the hydrodynamic response to a predicted hurricane track, size, and intensity. These models have significant uncertainty when used for forecasting [29,30]. Coupling ADCIRC (ADvanced CIRCulation model) [31] with WAM (WAve prediction Model) [32], STWAVE (Steady-State Spectral Wave Model) [33], or SWAN (Simulating WAves Nearshore) [34] is a widely used method for generating high-resolution storm surge models of specific regions [35,36]. Considering their additional wave forcing processes, finer mesh sizes, and smaller time steps, high-fidelity models are computationally more expensive [37]; thus, the accurate and quick assessment of hurricane-induced flooding has always been a challenging task.

Surrogate models are another approach to overcome this huge obstacle by simplifying approximations of more complex, higher-order models [10]. The Surge and Wave Island Modeling Study (SWIMS) [38] in the USACE, for example, developed a fast surrogate model by simulating hundreds of hurricanes to predict peak storm surges and hurricane responses in only a couple of seconds, which is an advantage over high-fidelity coupled simulations. Considering this issue, in a national-scale effort, the U.S. Army Engineer Research and Development Center developed a statistical analysis and probabilistic modeling tool named the StormSim Coastal Hazards Rapid Prediction System (StormSim-CHRPS) [39]. The tool preserves the accuracy of the high-fidelity hydrodynamic numerical simulation methods, such as ADCIRC, while significantly reducing computational demands, making it more convenient for real-time emergency management applications. The intricate input/output relationships inherent in high-fidelity numerical models are approximated using a machine learning method called Gaussian process metamodeling (GPM), enabling the rapid prediction of the peak storm surge and hurricane responses within seconds and for different hurricane scenarios.

Lee et al. [37] sought to enhance coastal resilience by providing a rapid storm surge prediction surrogate model called C1PKNet, a combination of a convolutional neural network model (CNN), principal component analysis, and a k-means clustering method, which was trained efficiently on a dataset of 1031 high-fidelity storm surge simulations. The resulting model is capable of predicting peak storm surges from realistic tropical cyclone track time series. A few studies, such as [40,41], even consider global warming, earth–moon–sun gravitational attractions, and storm surges to estimate the coastal sea level at an hourly temporal scale. The model in [40] was developed using an artificial neural network (ANN) approach called long short-term memory (LSTM) and trained on the ECMWF (European Center for Medium-Range Weather Forecasts) reanalysis dataset, ERA5 (more information on raw input data generation using ERA5 is available in Section 5.1).

To the best of our knowledge, only a limited number of researchers, such as [37,42–44] aimed to assess the concept of ANN ensemble learning for storm surge prediction. Braakmann-Folgmann et al. [43], for example, developed a combined convolutional and recurrent neural network to analyze both the spatial and the temporal evolution of sea level anomalies in the northern and central Pacific Ocean. They show how neural network architectures outperform simple regression to improve predictions for the future sea level. A novel deep learning architecture was implemented by [44] in contrast to a primitive model called the general ocean circulation model ensemble or NEMO (Nucleus for European Modelling of the Ocean). Their aim was to reduce the uncertainty associated with accurate sea level predictions and also to show the importance of sea level and atmospheric inputs for shorter forecast times. In the latter study, the ensemble ANN method for sea level forecasting known as HIDRA (HIgh-performance Deep tidal Residual estimation method using Atmospheric data) implements variants of temporal convolutional networks (TCN) and LSTM to encode temporal features of atmospheric and sea-level data. The dataset was trained on a 10-year (2006–2016) time series of atmospheric surface fields using a single member of the ECMWF atmospheric ensemble.

More recent papers such as [42,43] investigated the capability of different combinations of neural network (NN) models to predict surge levels. The fundamental core of this research revolves around selecting the best NN architecture for an ensemble approach to outperform a simple probabilistic model. Tiggeloven et al. [43], for example, combined a CNN-LSTM (ConvLSTM) model to capture the spatio-temporal dependencies for peak water level observations. This research has important implications for the sensitivity analysis of predictor variables and investigates how uncertainty in the predictions changes with input or architecture complexity. Tropical cyclones can also be parametrically represented via the joint probabilities method (JPM) [45]. However, the parametric description of complex systems, such as large-scale, non-frontal, low-pressure tropical cyclones, is intrinsically difficult to determine. As an alternative approach to these models, data-driven methods such as multiple linear regression [26,46], decision tree, ANN [40,42,43,47–50], and support vector machine [51,52] have been widely used for the prediction of storm surge heights. In most of studies where data-driven surrogate models are trained with physics-based simulations, such as ADCIRC [37,42,52], a major hurdle is the lack of sufficiently long datasets for training, validating and testing the surrogate models. As [53] explains, a long record in a storm surge reconstruction dataset is critical to capture as many storm events as possible; thus low-probability, high-impact, extreme events could be accounted for.

This review paper is structured as follows. Section 2 highlights the general concept of neural network ensembles and introduces several challenges and limitations. A theoretical framework for the geometry of neural networks, transfer learning, and their application to storm surge prediction models and different ensemble generation methods (i.e., how to combine the predictions from multiple models) are presented in Section 3. Section 4 discusses the less-debated topic of ensemble pruning and fine-tuning, the next stage after ensemble generation. Section 5 introduces data preparation considerations on developing an ensemble of neural networks, and different sources of datasets commonly used to predict storm surge levels are presented as well. Section 6 discusses some important factors and parameters regarding the best model selection and how the performance of the selected ensemble is evaluated. Finally, in Section 7, a summary is presented.

2. Neural Network Ensemble

Ensemble learning refers to techniques that involve combining the predictions of several base estimators based on classification or regression problems, aiming at improving predictability. This approach has gained a lot of attention in recent years, and the reported results regarding sea level rise projections have been satisfactory, such as in [7,44,54]. Ensembles have been reported to achieve higher certified robustness than single machine learning algorithms, as discussed in Section 2. Therefore, coastal hydrodynamic modeling techniques have been applied in ensemble with data-driven models such as deep learning techniques, especially neural networks, to develop ocean circulation and flood simulation models. This is due to the popularity and application of the finite element methods in numerical hydrodynamic models and their adequate modeling resolution [55–57]. These numerical models are conventionally applied to probabilistic coastal ocean forecast systems such as Surge Guidance System Forecasts (ASGS) or NOAA P-Surge to accommodate thousands of simulations [58].

Various types of neural networks are helpful to solve regression prediction problems where the aim is to predict the output of a continuous value such as water levels. Multilayer perceptrons (MLPs), a classical type of neural network, can reconstruct and validate atmospheric forcing, such as maximum sustained wind speed [59–61]. Convolutional neural networks (CNNs) have been developed to capture spatial and temporal dependencies for surge-level observations on a grid-based dataset and could potentially identify and predict regional and global patterns in storm and climate datasets [62]. They can also extract water bodies from remote sensing images [63]. Recurrent neural networks (RNNs) could be helpful in modeling storm behavior and time series of water levels in a sequence prediction framework [43], which requires a longer training time (not dependent on a fixed input size) compared to CNNs. Long short-term memory (LSTM), a subtype of RNN, is a successful model and has been used to capture long-term temporal dependencies of meteorological forcing [64,65] and to analyze the rapid intensification and occurrences of cyclones [66]. A diverse set of base learners (individual learners of the ensemble), such as MLPs, CNNs, and RNNs with appropriate training and tuning, is one empirical way to improve model performance by generating more complex models [67].

The focus of this paper is to introduce ensemble methods that can predict storm surge levels using a supervised ANN. Some challenges associated with using ANNs are the inability to capture peak water levels (due to the complex and nonlinear nature of the physical processes) [65,68], long-term processes (which are unavailable due to instrument failures, insufficient data, or sparse observational records), and predictions of storm surges at ungauged sites [43,69]. However, when utilized appropriately, ANN ensemble models have the potential to provide better and faster results than finite element hydrodynamic models. Figure 1 emphasizes the essential need for rapid prediction models, e.g., ENNs, by presenting a benchmark for the Aransas Wildlife Refuge station in Texas during and following Hurricane Harvey in 2017 [39]. This descriptive example compares storm surge predictions from a rapid empirical prediction model against water level observations from NOAA tide gauges and predictions from operational ADCIRC runs performed at the U.S. Army Engineer Research and Development Center's Coastal and Hydraulics Laboratory (ERDC-CHL). Hurricane Harvey started as a modest tropical storm in August. However, after re-forming over the Bay of Campeche, it intensified rapidly into a category 4 hurricane. Harvey made its landfall along the central Texas coast and then stalled for four days, resulting in unprecedented rainfall, exceeding 1520 mm and resulting in a surge reaching 1.4 m across southeastern Texas [70]. Figure 1 also highlights the rate of change and meteorological and oceanographic observations during the hurricane. Forecasts are typically updated at 6 hour intervals. However, for unusual storm scenarios comparable to Hurricane Harvey with rapid approach trajectories or extended durations within flood plains, the expected update intervals can be reduced to 3 h or even shorter.

A thorough and extensive literature review can be found in [1,71], where machine learning models are compared to traditional physically based models.

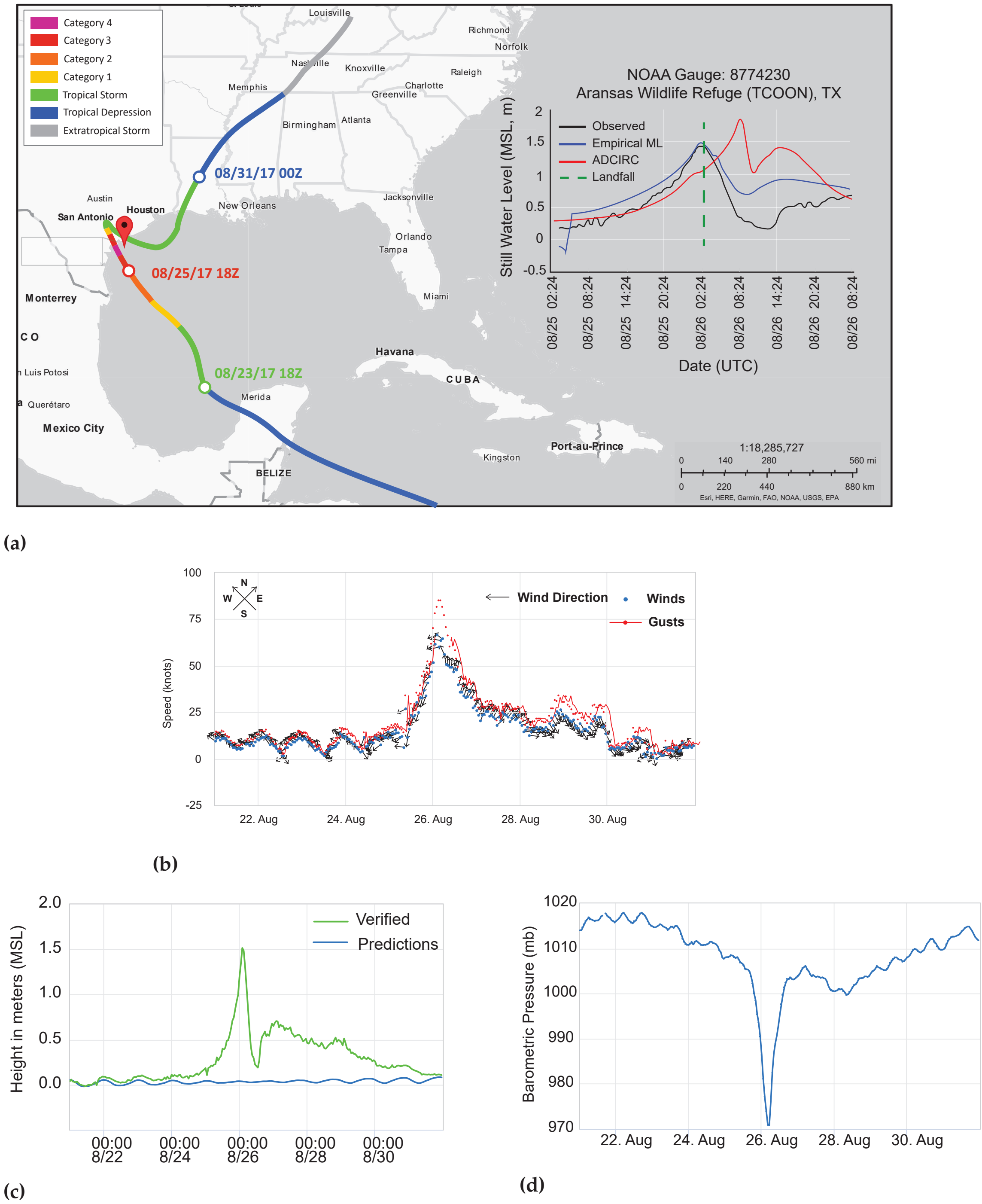

Figure 1. *Cont.*

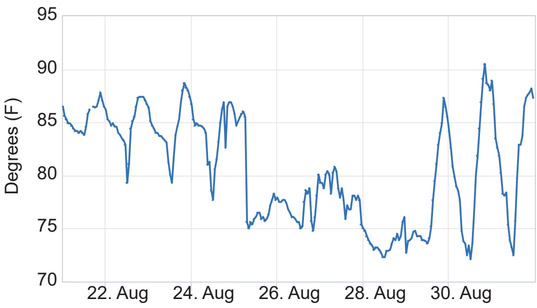

(e)

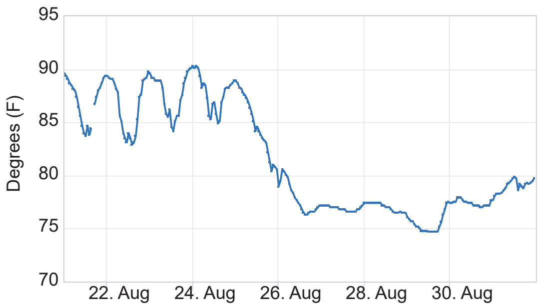

(f)

Figure 1. (**a**) Best track positions and storm surge predictions from the empirical CHRPS model compared to water level observations from select NOAA tide gauge and storm surge predictions from operational ADCIRC simulations performed at CHL [39]. (**b**) Winds. (**c**) Hourly heights. (**d**) Barometric pressure. (**e**) Air temperature. (**f**) Sea surface temperature in Aransas Wildlife Refuge station, TX, for Hurricane Harvey (August 2017).

3. Theoretical Framework

3.1. Neural Network Architectures

The NN architecture consists of individual members called neurons, which are combined to simulate the biological behavior of the brain to solve real-world problems [37,41]. Neural networks are not an exclusive standardized method; instead, they involve learning algorithms and architectures that can be applied to a wide range of supervised flood and storm surge forecasting models. These models use a set of individual independent variables, such as tidal and meteorological data points, and a real value dependent variable that represents the phenomenon, such as storm surge levels [42,43,72]. A general scheme is shown in Figure 2 based on a fully connected MLP representation. In the basic MLP architecture, the input layer is connected to one or multiple hidden layers and finally to the output layer to construct a fully connected system. The information is primarily processed in the forward direction (feed-forward) and is put through a linear transformation using a weights matrix [47,73]. An activation function defines how the weighted sum of the input vector is transformed to the neurons of the next layer [47]. The choice of activation function in both the hidden and output layers significantly influences the performance of the NN model in learning from the training dataset and predicting storm surge events. Empirical testing and cross-validation are essential to determine the most appropriate activation function that can effectively capture non-linear relationships within the data. Table 1 presents some frequently used activation functions specifically tailored for storm surge prediction models, as well as the relationship between each activation function and its corresponding Python library. The elementwise activation function is usually shifted with a bias to adjust the final output matrix. Different model configurations associated with learning processes and choices of the right dimensions of the NN structure, including the number of hidden layers, learning rate, batch size, choice of the activation function and loss function, etc., are referred to as hyperparameters [74–76]. Table 2 presents a summary of the major hyperparameters in NN models. These tuning parameters pertain to the physical components, training/optimization procedures, and regularization effect in a neural network.

In order to train a MLP feed-forward NN model, a backpropagation NN (BPNN) is widely used. This algorithm has been identified as one of the simplest and the most powerful ML prediction tools suitable for flood time series and short-term storm surge predictions [77–80]. In a BPNN algorithm, the gradient of the loss function (the vector of the partial derivatives) is calculated through a method called chain rule to adjust each weight and its contribution to the overall error. Further details of BPNN algorithms can be found in Appendix A.

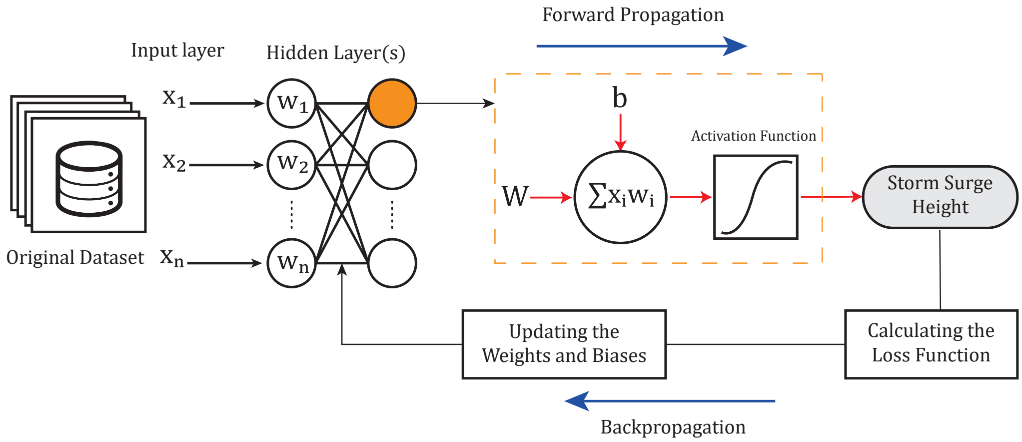

Figure 2. Flow diagram of transfer learning in NN, including the reuse of a pre-trained model on a new problem.

Table 1. Frequently used activation functions in ANN storm surge prediction models.

Activation Function	Equation	Python Library	Applications
ReLU (Rectified Linear Unit)	$f(x) = \max(0, x)$	`tensorflow`, `keras`	MLP, CNN
Sigmoid	$f(x) = \frac{1}{1+e^{-x}}$	`tensorflow`, `keras`	RNN
Tanh (Hyperbolic Tangent)	$f(x) = \frac{e^x - e^{-x}}{e^x + e^{-x}}$	`tensorflow`, `keras`	RNN
Softmax	$f(x_j) = \frac{e^{x_j}}{\sum_{k=1}^{K} e^{x_k}}$	`tensorflow`, `keras`	Classification, normalizing the output
Leaky ReLU	$f(x) = \max(\alpha x, x)$	`tensorflow`, `keras`	MLP, CNN

Table 2. Classification of major hyperparameters in NN models .

Physical Components	Training/Optimization Procedures	Regularization
Number of hidden layers within the network	Defining the optimizer algorithm	Degree of regularization (lambda)
Number of hidden Neurons	Configuring the learning rate	Number of active neurons (dropout rate)
Choice of key activation function	Defining the main type of loss function	
	Choice of evaluation metric for regression problem	
	Number of training samples (mini-batch)	
	Setting the random initialization	
	Number of training cycles (epochs)	

3.2. Transfer Learning

In some scenarios, the NN algorithms use different sources of information such as historical tropical cyclones, topography, meteorological forcing, and other sources to make a complex network. Training an ensemble of NN models on such a massive volume of raw data can be computationally expensive [81]. On the other hand, when datasets are expensive or difficult to collect or data are scarce for a specific problem (such as the short-term analysis of hurricane tracks) [64,82], obtaining a training dataset to discern a meaningful pattern could be problematic. Transfer learning, as shown in Figure 3, is a functional method of tackling these problems through, i.e., building a high performance NN model while reducing training time [83]. This is performed by obtaining a high-accuracy and large pre-trained model from a related source and transferring the knowledge from the trained data to the target domain in a time-saving way [84]. Surge time series data over long time scales are usually subject to seasonal variability known as seasonality [85–87] (which can be simply defined using a Fourier transform and finding the seasonal frequencies). Removing seasonality from the time series data might happen during data preparation (which is further discussed in Section 5). Extractions of sparse time series samples from short-term extreme impacts during dominant seasons could be limited in size, implying that the insufficient training data are unable to represent the target efficiently [85]. Therefore, transferring knowledge from a diverse, large-scale, and pre-trained dataset of a time series of a similar task (with minor adjustments) could be reasonable [88] when a NN model is adapted to forecast a new time series, thus avoiding the need for additional training [83].

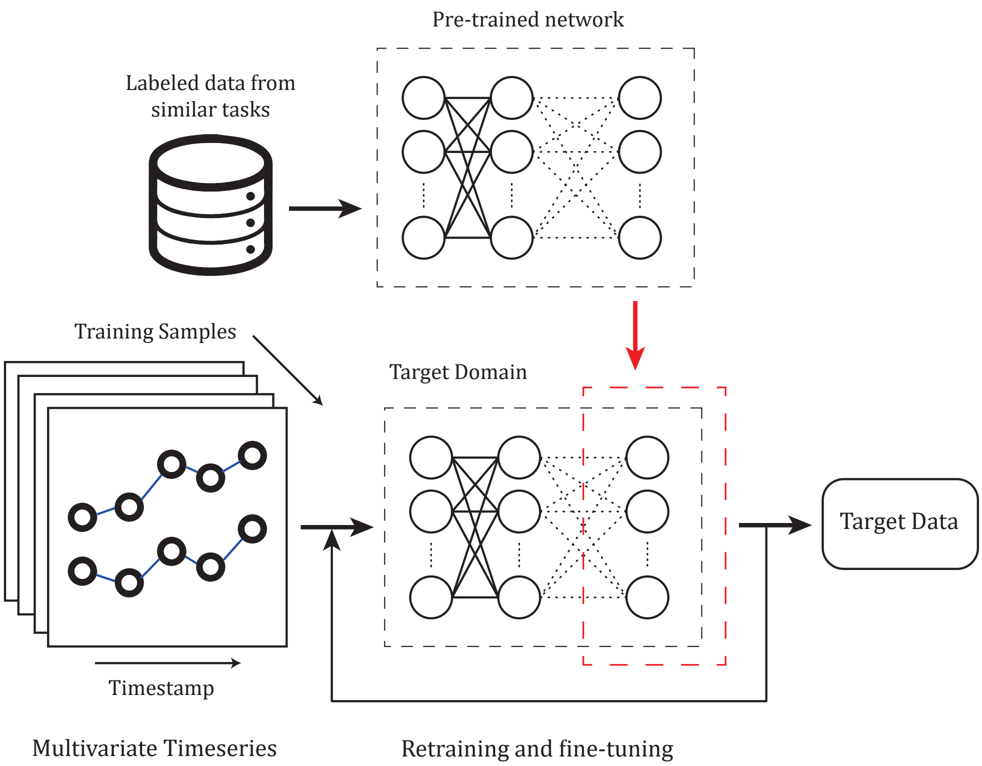

Figure 3. Flow diagram of transfer learning in NN involving the reuse of a pre-trained model on a new problem.

3.3. Ensemble Generation Methods

Ensemble neural networks basically consist of [54]: (1) generating multiple base learners (weak classifiers) and (2) combining the predictions to make a strong learner. The notion is that various classes of neural networks are created as base learners and then combined as a strong learner to predict the storm surge [55]. When ensemble members employ a single-type base learning algorithm but are generated upon a different subset of training data, they are classified as homogeneous [67,89]. Heterogeneous ensembles, on the other hand, consist of classifiers (base learners) of different types, such as MLP, CNN, or LSTM, which are usually trained on the same dataset [67,90]. These ensemble models are designed such that base learners are generated in sequential or parallel format. The basic motivation of the former is to create successive learning algorithms over iterations where predictions of a base learner are corrected and fine-tuned, then provided to the subsequent base learners. In the latter, the base learners are generated in parallel and independent from each other. Predictions of the diverse base learners are then combined using ensemble learning techniques such as bagging and stacking. These methods can potentially reduce the inference time (the amount of time taken for a forward propagation) and increase the overall performance [91].

Generating NN ensembles that predict storm surge heights from historical, synthetic, or predicted hurricanes and/or are able to estimate overland flooding (or surge-induced maximum inundation) requires supervised algorithms to learn how to fit the input labeled data into a continues function [89,91]. This raises the question of how to incorporate predictions from different models. In this regard, three leading algorithms for combining weak learners are recognized.

Bootstrap aggregating (bagging): To ensure diversity among base learners, one notion is to train each learner on a distinct subset of the available training data. An autonomous training process can be conducted in parallel for each learner through a popular subsampling ensemble method known as bootstrap aggregation, more commonly referred to as bagging [91,92]. This method uses randomly generated training sets (extracted from the initial preprocessed dataset) to obtain an ensemble of predictors and subsequently trains an integrated neural network associated with training sets (Figure 4). Bagging can considerably reduce variance and is an efficient solution to overfitting [92–94] (i.e., it helps with the generalization of a NN ensemble model to unseen data). Given a series of extreme flooding events in coastal regions with noisy data obtained from the tide stations, particularly during times when a storm surge coincides with normal high tide, the bootstrap learning approach could effectively combine uncertainties originating from various measurements. In a meteorological forecast of the storm's behavior, for instance, this approach involves random sampling of the initial training dataset through standard bagging resampling with replacement, thus resulting in a low-variance ensemble model [95]. In a regression problem, assuming that the model is trained on the input vector of $A = ([x_1, y_1], [x_2, y_2], \ldots, [x_n, y_n])$, to learn the mapping $y_i = f(x_i), \ \ i = 1, \ldots, n$, bootstrap aggregation takes the average of the predictions y_i from a collection of bootstrap samples $A_j^*, \quad j = 1, \ldots, m$. Each sample is independent and drawn uniformly among $A_1^*, \ldots, \ A_m^*$ with replacement; thus, all the samples are independent and identically distributed (i.i.d) [92]. The aggregated (bagged) prediction for each base learner is expressed by

$$y_{bs} = \frac{\sum_{j=1}^{m} A_j^*(x)}{m} \tag{1}$$

where $A_1^*(x), \ \ldots, \ A_m^*(x)$ are the predictions from the i.i.d samples. This method limits the variance through building different base learners of diverse datasets [96] and helps to create a more stable and robust overall model. This can be particularly useful in situations where the data are noisy or where there is high variability in the predicted outcome, such as in predicting the effects of category 4 and 5 storms. Since ensemble models with low correlations are preferred in these predictions, the sampling with replacement method allows more difference in the training dataset and, in turn, results in greater differences between the predictions of the base learners. It is worth mentioning that the bagging process, depending on its number of iterations or combination with time series, could be computationally demanding to fit, as explained in [97]. Figure 5 shows a pseudo-code for a bagging NN ensemble algorithm; note that this is a simple example, and the actual implementation of bagging in neural networks may vary depending on each specific case and library. Additionally, this example does not cover how to handle the overfitting problem that might occur on these models.

Boosting: This ensemble approach works in a forward stagewise process and learns the predictions from the previous weak learner by adjusting the weighted data and fitting the model to an updated training dataset in a sequential order [98] (Figure 6). In the case of regression, the final output is usually built as the weighted average of a sequence of the fitted base learners [96,99]. A boosting algorithm reduces the bias owing to the progressive refinement of the base learner over time [100]. The AdaBoost algorithm, short for Adaptive Boosting, is one of the most popular boosting algorithms [101]. In this approach, instead of dividing a training dataset, multiple classifiers are iteratively constructed from the entire dataset. Using the neural network ensemble model, the subsequent component highlights the false prediction of the previous step to transform a weak learner into a strong learner. In other words, training data inaccurately predicted by the former NN become more influential in the training of the latter NN [92]. This learning approach could be extended to neural network ensembles aiming at predicting storm surges or generating a mean estimation of residual water levels [102]. Figure 7 shows a pseudo-code based on the AdaBoost algorithm [99]. It is important to note that the actual implementation of boosting in neural networks may vary depending on the case and library that is implemented. Additionally, there are other boosting algorithms, such as Gradient Boosting [103] or XGBoost [104], that have some variations in their pseudo-code.

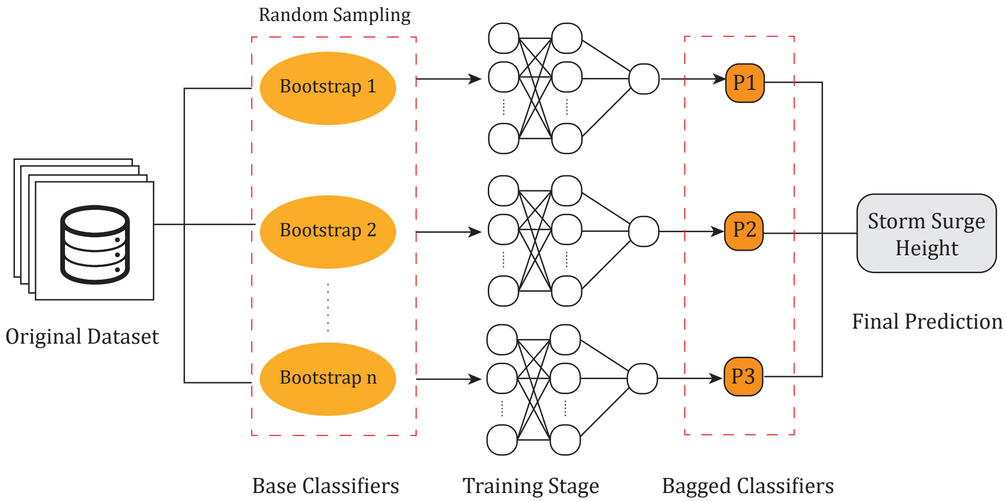

Figure 4. A general scheme of the bagging ensemble approach.

```
Step 1: Initialize the ensemble
        ensemble_models = []
Step 2: Build base ensemble models
        for i in range(num_ensemble_models):
        # Sample dataset with replacement to create a new training set
        sample_data = random.sample(original_data, len(original_data))
        # Train a model on the sampled dataset
        model = train_neural_network(sample_data)
        # Add the trained model to the ensemble
        ensemble_models.append(model)
Step 3: Make predictions
        def ensemble_predict(ensemble_models, input_data):
                predictions = []
                for model in ensemble_models:
                        predictions.append(model.predict(input_data))
                # Average the predictions to get the final ensemble prediction
                ensemble_prediction = np.mean(predictions)
                return ensemble_prediction
```

Figure 5. A simplified pseudo-code of an ensemble learning algorithm for bagging.

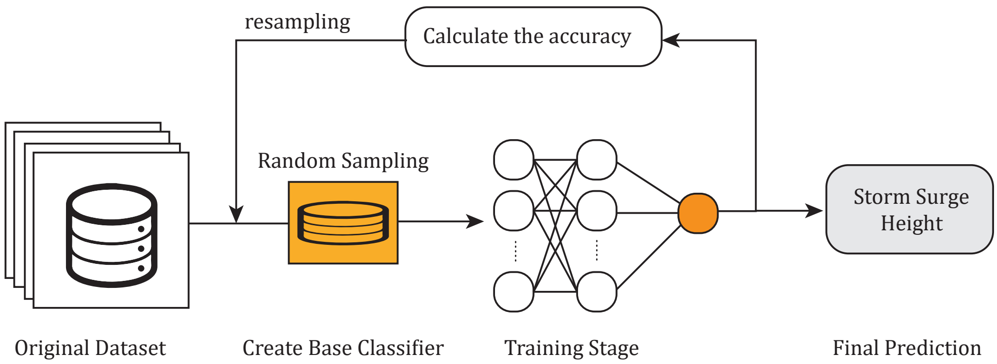

Figure 6. A general schematic of the boosting ensemble approach.

```
Step 1: Initialize the ensemble with a base model
        ensemble_models = [base_model]
Step 2: Expand ensemble
        for i in range(num_iterations):
                # Predictions with current ensemble
                ensemble_predictions = ensemble_predict(ensemble_models, data)
                # Calculate the error of the ensemble predictions
                error = calculate_error(ensemble_predictions, data_labels)
                # Train a new neural network to predict the error
                new_model = train_neural_network(error)
                # Add the new model to the ensemble with a weight
                ensemble_models.append((new_model, weight))
Step 3: Make predictions
        def ensemble_predict(ensemble_models, input_data):
                # Get weighted predictions
                predictions = []
                for model, weight in ensemble_models:
                        prediction = weight * model.predict(input_data)
                        predictions.append(prediction)
                # Sum the predictions to get the final ensemble prediction
                ensemble_prediction = np.sum(predictions)
                return ensemble_prediction
```

Figure 7. A simplified pseudo-code of an ensemble learning algorithm for boosting.

Assuming that each of n base learners make a prediction y_i out of a random sample, the weighted average of the boosted model would be [105]

$$y_{bt} = \frac{\sum_{j=1}^{n} \beta y_i(x)}{n} \quad (2)$$

where β is the shrinkage coefficient that controls the rate at which the boosting algorithm reduces the error. β is similar to the learning rate hyperparameter in NN.

When using synthetic storm data to support the incomplete dataset (or data which cannot capture an event resulting from instrument failures), it is possible that the generated dataset could be more biased and less accurate than real-world data, such as in tide stations [88,106]. Boosting algorithms focus on weak learners to determine which factors are contributing to false outcomes and treat those factors carefully in testing data, decreasing the bias error.

Stacking: Stacked generalization, also known as stacking, is a heterogeneous ensemble strategy proposed by Wolpert [106] to train a set of diverse weak learners in parallel with greater predictive accuracy. Base learners (also called level 0/first-level learners) serve as input to run a combiner or meta-learner (also called the level 1/second-level/super learner) (Figure 8). Both the precision and diversity of base learners are crucial to the performance of a stacking ensemble such that various base learners could construct a well-functioning model with improved results [107].

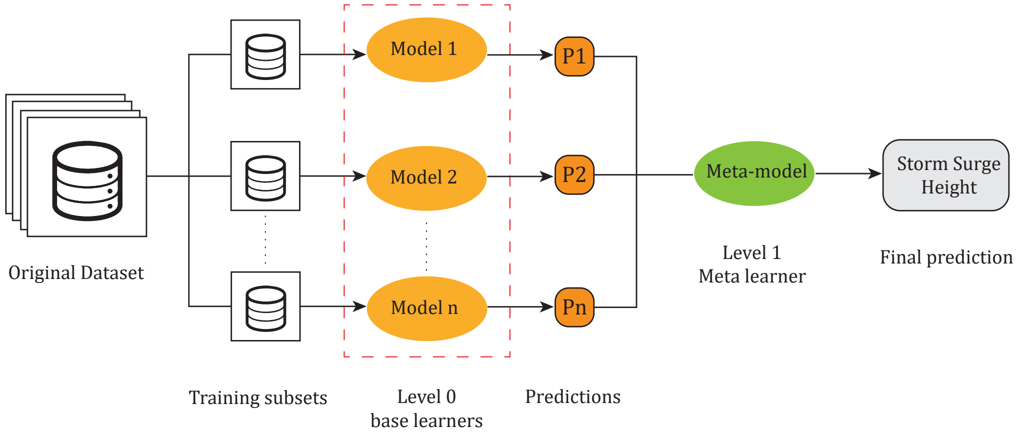

Figure 8. A general scheme of the stacking ensemble approach.

The predictive performance of a stacking ensemble is influenced by the number of individual base learners [107,108]; however, there are only a few NN combinations available (as explained in Section 3.3) to investigate the accuracy of combined predictions associated with different combinations of base learners. Choosing the optimal subset of stacked base learners is explained in [109–111]. Figure 9 shows a pseudo-code for the stacking ensemble algorithm. It is to be noted that the provided snippet code is a basic instance, and the actual implementation of stacking in neural networks might differ according to each specific case and the implemented methods. Other stacking ensemble algorithms include Blending [112] and Super Learner [113], which have some variations in this pseudo-code. Let $y_i^m = f(x_i)$ represent the mapping function applied to the model m with $N = 1, \ldots, i$ observations in the training set N, where predictions from a set of heterogeneous weak learners (sub-models) $m = 1, 2, \ldots, M$ are combined as new training data for the metalearner. The stacking weights are defined as the minimum value of the Euclidean distance between the weighted prediction and the target y_i [114]

$$W_{st} = \arg\min\left(\sum_{i=1}^{N}\left[y_i - \sum_{m=1}^{M} W^{(m)}.\, y_i^{(m)}\right]^2\right) \tag{3}$$

which leads to the final stacked ensemble prediction $y_{st} = \sum_{m=1}^{M}\left(W_{st}\,.\, y^{(m)}\right)$.

Here, the learning method to train the metalearner is based on the most common form of regression analysis, linear regression. High-fidelity ocean circulation models such as ADCIRC predict a skewed distribution of the peak storm surge height at the early stages or with biased subsets of training datasets [42]. Stacking ensembles can help to mitigate the effects of data bias and improve the overall performance of the model since they take into account the strengths and weaknesses of sub-models and make robust predictions to the biases that may be present in any individual subset.

```
Step 1: Initialize the ensemble with base models
        ensemble_models = [base_model_1, base_model_2, ...]
Step 2: Generate meta-features based on base model predictions
        meta_features = []
        for model in ensemble_models:
                predictions = model.predict(original_data)
                meta_features.append(predictions)
        meta_features = np.concatenate(meta_features, axis=1)
Step 3: Train a new neural network on the meta-features
        meta_model = train_neural_network(meta_features, original_data_labels)
Step 4: Add the meta-model to the ensemble
        ensemble_models.append(meta_model)
Step 5: Make predictions
        def ensemble_predict(ensemble_models, input_data):
                base_predictions = []
                for model in ensemble_models[:-1]:
                        base_predictions.append(model.predict(input_data))
                meta_features = np.concatenate(base_predictions, axis=1)
                ensemble_prediction = ensemble_models[-1].predict(meta_features)
                return ensemble_prediction
```

Figure 9. A simplified pseudo-code of ensemble learning algorithm for stacking.

An overview of six different studies is outlined in Table 3, summarizing the utilization of ensemble approaches and evaluation metrics, along with the data collection sources for each study. A comparative analysis is illustrated in Figure 10 based on a qualitative reference value (rv) and a representative skill metric (sm) across the different studies summarized in Table 3.

$$Relative\ Score = \frac{rv - sm}{rv} \tag{4}$$

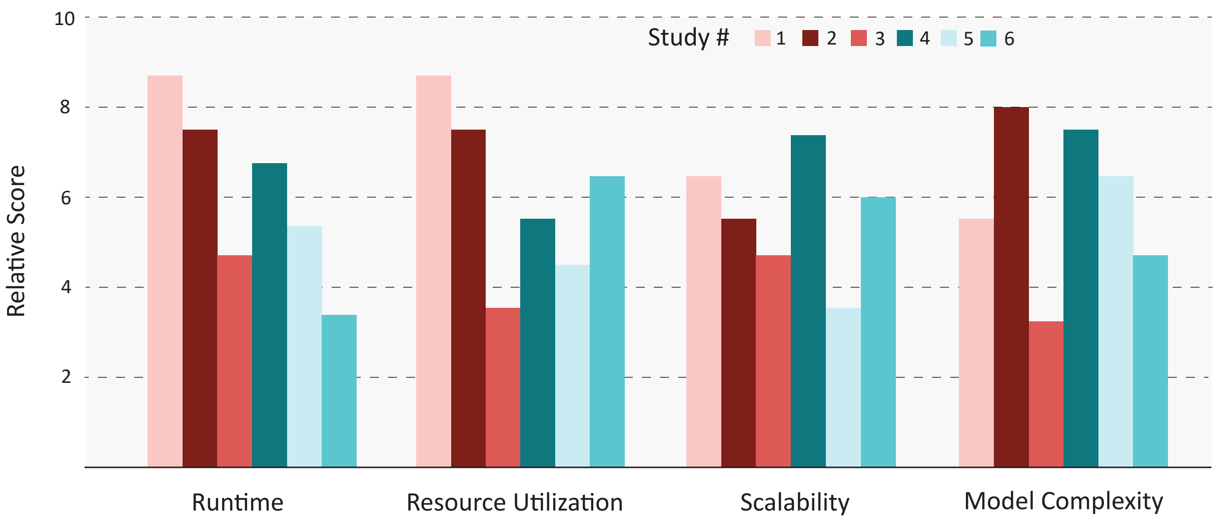

Figure 10. Qualitative assessment of studies numbered 1 to 6 from Table 2.

Table 3. Comparative analysis of ensemble approaches, evaluation metrics, and data collection in different studies (2015–2022).

Study Number	Target Goal	Methodology	Ensemble Approach	Evaluation Metric	Data Collection
1 [42]	Low-probability peak storm surge height due to TCs	ANN and coupled ADCIRC + SWAN simulations	GBDTR and AdaBoost Regressor	RAE, MRAE, and RMSE	Synthetic TCs + Historical typhoon data in the New York metropolitan area
2 [115]	Storm tide and resurgence	Hydrodynamic and Hydrologic Ensemble Forecast	Stacking (super-ensemble) based on RMSE and bias correction	RMSE, PRE, and COU	US mid-Atlantic and Northeast coastline wind and tide data
3 [43]	Hourly surge time series at the global scale	ANN, CNN, LSTM, and ConvLSTM	Bootstrap aggregation	RMSE and CRPS	GESLA Version 2 tide station database
4 [37]	Peak storm surges from TC track time series	C1PKNet (1D CNN, principal component analysis, and k-means clustering)	Average of ten trained C1PKNet model predictions	MSE and CC	NACCS synthetic TC surge database
5 [83]	Real time and accurate storm surge	CNN and LSTM, transfer learning	–	RMSE, MAE, and CC	Storm surge level time series in the southeastern coastal region of China
6 [116]	Rapid prediction of storm surge time series	ANN and CSTORM-MS coupled model	–	RMSE and CC	Synthetic storms in the Gulf of Mexico

GBDTR = Gradient Boosted Decision Tree Regressor; RAE = relative absolute error; MRAE = mean relative absolute error; RMSE = root-mean-square error; MAE = mean absolute error; CC = correlation coefficient; PRE = peak relative error; COU = coverage of observation uncertainties; CRPS = continuous ranked probability score.

4. Ensemble Pruning and Fine-Tuning

An ensemble model is a systematic process of combining individual diverse base predictive learners to produce robust and accurate predictions. The concept of an ensemble model might be potent enough for the default parameters to shine; however, many studies, such as [117–122], acknowledge that the accuracy could be improved further through tuning. An intuitive approach is to alter the network's setup in a process known as pruning. This is followed by fine-tuning the hyperparameters of the diverse base learners through the regular process of developing the networks. Pruning entails reducing trivial (or redundant) parameters from an existing network systematically [123]. In the case that the model has poor performance after pruning, the hyperparameters are fine-tuned, i.e., the parameters of each individual model are adjusted, and then the models are retrained to restore the best possible accuracy [121]. The result is an ensemble of relatively accurate and robust fine-tuned models with a lower correlation between the independent predictions and residuals [119]. A general scheme on pruning and fine-tuning steps in a neural network ensemble is shown in Figure 11.

Pruning: The main idea of pruning networks is to reduce the complexity and energy required to implement large trained networks and make predictions on new input data in real time [124]. This could be a crucial stage in predicting storm surge time series [54,55], such that accurate real-time predictions of storm surge can help emergency management officials issue evacuation orders, take preemptive measures to protect infrastructures, and minimize the economic impact of the storm. Typically, the initial network is large and tends to achieve higher accuracy; generating a smaller network with comparable precision is preferable. This approach has seen a significant amount of growth over the past decade [123]. However, a handful of studies, such as [125–127], addressed the process of ensemble pruning, especially in predicting time series of water surface elevations during or after storms. One major reason is that some ensemble techniques, such as the Adaboost algorithm, inherently mitigate overfitting by independently optimizing input parameters to reach an optimal value. Once the accuracy of individual base learners slightly surpasses random guessing, the final model is proven to reduce generalization error, yielding enhanced performance as a strong learner [123]. Furthermore, NN ensemble pruning can also be interpreted as a special type of stacking technique (as introduced in Section 3) in which a meta-learner is applied to improve the predictive performance of the models [128].

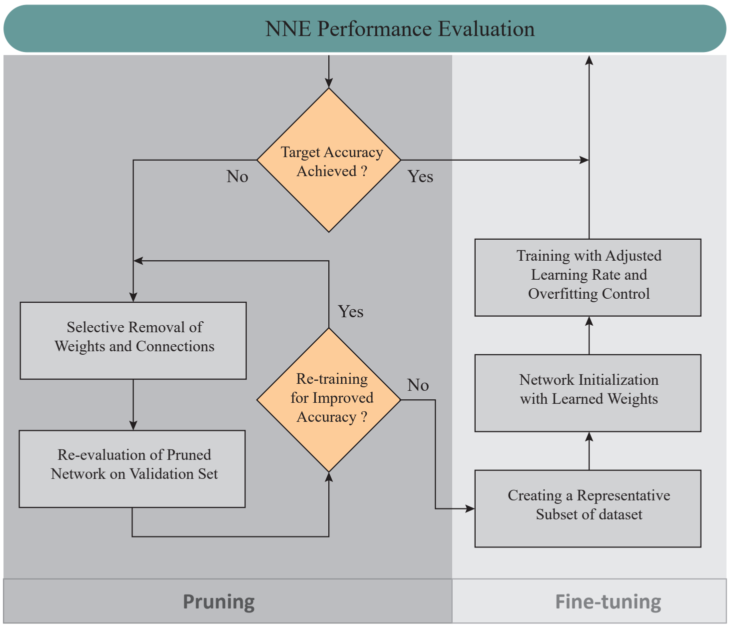

Figure 11. General process of pruning and fine-tuning in a neural network ensemble.

The major pruning techniques that are applicable to NN ensembles are as follows: (1) weight decay [129], which involves adding a regularization term to the loss function that penalizes the complexity of the ensemble; (2) an error-based approach [130], which involves calculating the prediction errors of each network in the ensemble and removing the networks with the highest error rates; and (3) neuron pruning [131], which involves removing the neurons in each network of the ensemble that have the least impact on the network's output.

Fine-tuning: Once a pruned ensemble is created, the next common stage is to perform fine-tuning, where the network is retrained using the pruned architecture, possibly with a smaller learning rate and fewer training epochs. Fine-tuning can help restore some of the accuracy lost during pruning and can lead to better generalization performance [132].

Tuning methods cannot be overlooked since less complex but fine-tuned real-time predictive models could possibly result in accurate predictions of water level and flood extent [118,119]. which are essential for real-time monitoring and timely warnings of potential floods. When constructing predictive models, finding a set of optimal hyperparameters for each individual learner is a challenge. Tuning the base models (learners) individually and tuning all the models in an ensemble simultaneously are the two fundamental methods to determine the optimal parameters [67]. In the former approach, the hyperparameter tuning process for each base model is often carried out as an independent procedure based on unique sets of hyperparameters. To illustrate, different base models in an ensemble may use different types of activation functions, optimization algorithms, regularization techniques, or learning rates. Tuning these hyperparameters separately can help ensure that each model is individually optimized and contributes to the overall performance of the ensemble. This conventional approach is described in [133,134]. It is important to note that the hyperparameter tuning process should also take into account the interactions between the base models in the ensemble [128,133] (the later approach). The weights assigned to each base model have a significant impact on the overall performance of the ensemble, so these weights may also need to be tuned in conjunction with the hyperparameters of each individual model. Such a kind of connection is usually more compatible with probabilistic approaches, such as Bayesian optimization [135]. This method usually involves modeling the objective function (e.g., accuracy) as a Gaussian process [136], which can be more efficient than other fine-tuning methods, such as grid search [137] and random search [138],in some cases, as it leverages previous evaluations of the objective function to better guide the search process [139].

5. Data Preparation

Data preparation in neural network ensembles refers to the process of preprocessing and organizing raw data before training a group of neural networks together as an ensemble [140]. The goal of this crucial step is to ensure that the input data are consistent, relevant, and suitable for use by the ensemble, which can lead to better model performance and more accurate predictions. A dataset in a traditional ANN can be represented as a set of input–output pairs, where the input is a vector of features and the output is a scalar target value [47]. In a regression problem such as water level prediction, a dataset of size N would be stored as follows:

$$\begin{bmatrix} x_{11} & x_{12} & \cdots & x_{1j} \\ x_{21} & x_{22} & \cdots & x_{2j} \\ \vdots & & \ddots & \vdots \\ x_{i1} & \cdots & & x_{ij} \end{bmatrix} \tag{5}$$

Each *i*th row is an observation in the dataset, and each jth column represents an individual component of an observation in the dataset $\left(x_{ij} \in \mathbb{R}\right)$. In contrast to an ANN, the input x_i in convolutional neural networks is a 2D or 3D matrix of pixel values representing an image with dimensions (height, width, and channels), and a set of convolutional filters are applied to detect patterns in the image [141]. However, they can also be applied to time series data by treating the time dimension as a spatial dimension; thus, the input would be a 1D sequence of data points and a set of 1D filters, which are applied to detect patterns in the time series [142]. By structuring the time series as a sequence, a CNN can detect local patterns that correspond to different storm events or meteorological conditions over shorter time intervals [62].

5.1. Raw Input Data

Datasets are an integral part of ensemble models, and major improvements in the final prediction highly depend on the availability of high-quality input and training datasets. There is a diverse assortment of sources and domains that provide data on the oceans and coasts of the United States. These data can be utilized to improve hurricane prediction models and create strategies for coping with the impact of climate change on coastal communities, including rising sea levels [143,144]. With current developments, researchers can generate various independent records of tropical cyclone datasets from the measured tide and oceanographic data (Table 4) or take advantage of hindcasting (a retrospective analysis of past weather conditions) and reanalyzing archives (a more comprehensive and detailed reconstruction of observations combined with numerical models), such as high-resolution temperature, pressure, humidity, and wind datasets from a forecast system (Table 4). Some systems are adept at computing random, short-crested waves in coastal regions using third-generation wave models, such as WAVEWATCH III, WAM, or SWAN, or coupling them with other finite-element-based hydrodynamic models [35,36], such as ADCIRC. Atmospheric and tidal forcing is commonly applied to high-resolution wave models such as ADCIRC or SWAN [37,52] to simulate the behavior of ocean waves under different storm conditions and generate synthetic storm datasets that can be used for assessing flood risk and improving coastal management strategies [11].

Ensemble NN models have high variability in their input data type and are commonly considered heterogeneous. While homogeneity could be a desirable property of the input data (in terms of the features and their scales) for neural networks, a heterogeneous dataset in a regression problem such as storm surge prediction may work better [145] because it includes a variety of features that capture different aspects of the storm and its effects on the surge. This helps the neural network learn more robust and diverse features that can be better generalized to new, unseen data [92,94]. Table 4 presents brief descriptions and features of the ocean datasets that have been extensively used to predict storm surge levels and flood extents. These datasets address a wide range of features, including: (1) storm characteristics, such as storm intensity, wind speed and direction, and track; (2) oceanographic features, such as water temperature, salinity, and currents; (3) meteorological features, such as air pressure, temperature, and humidity; (4) geographical features, such as the shape and slope of the coastline, the depth of the ocean floor, islands, and shoals, and (5) historic storm surge records, including the timing, intensity, and duration of the surge. Common points and major differences between these datasets are outlined in Table 5.

Table 4. Description and main features of the most widely used storm and flood datasets. The symbol ✓ indicates that the feature is included, while the symbol ✗ signifies that the feature is not included.

Dataset	Description	Features	Source
North Atlantic Coast Comprehensive Study (NACCS)	A combined set of 1050 synthetic tropical and 100 synthetic extratropical storms using the coupled ADCIRC/STWAVE models	✓ Consistent across the entire North Atlantic Coast region. ✓ Covers storm surge, sea level rise, and erosion ✓ Easily accessible ✗ Coarse spatial resolution ✗ Limited temporal scope ✗ Relies on certain assumptions and uncertainties	The U.S. Army Corps of Engineers (USACE) [146]
ECMWF Re-Analysis (ERA5)	The latest generation of atmospheric reanalysis of the global climate with detailed information on a wide range of atmospheric variables.	✓ High temporal and spatial resolution ✓ Covers a wide range of atmospheric variables ✓ Publicly available ✗ Complex and may require advanced technical skills ✗ Limited vertical resolution (137 pressure levels)	Copernicus Climate Change Service (C3S), the joint C3S-NOAA project [147,148]
Global Extreme Sea-Level Analysis Version 2 (GESLA-2)	Provides 39148 years of sea level data from 1355 station records, with information on extreme sea levels, including storm surges, tidal cycles, and rise in sea level.	✓ Covers a wide range of extreme sea-level events ✓ Consistent across the entire globe and different geographic locations ✓ Publicly available ✗ Gaps in the data particularly for remote or sparsely populated regions. ✗ Relies on certain assumptions and uncertainties ✗ Limited information on coastal morphology and human activities	University of Hawaii and the National Oceanic and Atmospheric Administration (NOAA) [2]

Table 4. *Cont.*

Dataset	Description	Features	Source
NOAA Global Real Time Ocean Forecasting System (RTOFS global	provides nowcasts (analyses of near-present conditions) and forecast guidance on up to eight days of ocean temperature and salinity, water velocity, sea surface elevation, sea ice coverage, and sea ice thickness.	✓ Provides high-quality and updated oceanographic and meteorological data in real time ✓ Global coverage ✓ High spatial and temporal resolution ✓ Integration with other models for a more comprehensive understanding of storm surge ✗ Limited data availability for a particular area or time period ✗ Relies on certain assumptions and uncertainties ✗ Requires significant computational resources	National Centers for Environmental Prediction (NCEP), NOAA [4]
Coastal Hazards System (CHS)	National coastal storm hazard data resource for probabilistic coastal hazard assessment (PCHA) results and statistics, including measurements of water level, wind speed, and wave height	✓ High-quality data ✓ High spatial resolution with detailed information about storm surge patterns ✓ Provides historical data ✗ Limited to the coastal areas of the United States ✗ Limited temporal resolution for predicting a storm surge during an ongoing event ✗ Needs to be integrated with other models to make accurate predictions	Pacific Coastal and Marine Science Center of the United States Geological Survey (USGS) [149]
The Sea, Lake and Overland Surges from Hurricanes (SLOSH) model	Uses a combination of historical storm data, topographical data, and numerical algorithms to simulate the impact of a hurricane on coastal areas and predict storm surge heights and flooding potential associated with hurricanes.	✓ Specifically designed and tested for storm surge prediction ✓ Can be customized to specific geographic areas ✓ Can be integrated with other models, such as atmospheric and wave models ✗ Resource-intensive ✗ Limited data availability (requires input data, such as atmospheric pressure and wind speed) ✗ Limited spatial resolution ✗ Relies on certain assumptions and uncertainties	National Oceanic and Atmospheric Administration (NOAA) [150]
National Water Level Observation Network (NWLON)	A network of tide gauges that can be used for storm surge prediction.	✓ Specifically designed and tested for storm surge prediction ✓ Provides historical data ✓ Wide geographic coverage throughout the United States ✗ Limited spatial resolution ✗ Lack of a comprehensive model for predicting storm surge (needs to be integrated with other models) ✗ Limited data availability in all coastal regions	National Oceanic and Atmospheric Administration's (NOAA) Center for Operational Oceanographic Products and Services (CO-OPS) [151]

Table 5. General comparison between the datasets in Table 4. The symbol ✓ indicates that the feature is included, while the symbol ✗ signifies that the feature is not included.

	NACCS	ERA5	GESLA2	RTOFS	CHS	SLOSH	NWLON
Spatial resolution	0.25 degrees	0.25 degrees	0.25 degrees	0.08 to 0.25 degrees	0.02 to 0.05 degrees	0.02 to 0.05 degrees	0.08 to 0.33 degrees
Temporal resolution	6 h	Hourly	Monthly	Hourly	Hourly	Hourly	Hourly
Coverage	North Atlantic Coast region	Global	Global	Global	Coastal areas of the United States	Atlantic and Gulf coasts of the United States	Coastal areas of the United States
Availability	Open access	Open access (needs license for real-time products)	Open access	Open access	Limited access	Limited access	Open access
Complexity	Highly complex	Highly complex	Complex	Complex	Fairly complex	Complex	Fairly complex
Possible data gap	Incomplete coverage or missing data for certain time periods	Missing or incomplete weather station data in certain regions or periods	Limited or no data on certain sea levels and time periods	Incomplete coverage or missing data for certain time periods	Incomplete coverage or missing data for certain time periods	Missing or incomplete data for certain hurricanes or regions	Incomplete coverage or missing data for certain time periods
Integration with other models	✓	✗	✓	✓	✓	✓	✓

5.2. Data Preprocessing and Wrangling

Data preprocessing and wrangling are critical steps in any machine learning workflow, and they often take up a significant amount of time and effort [140,152]. The pre-mentioned datasets may contain several types of data issues that need to be addressed and preprocessed before NN algorithms can be applied effectively. Some of the most common issues include missing values, outliers, categorical data (such as storm category, wind direction, tidal phase, landfall location, and storm direction), correlated and irrelevant features, and issues related to scaling and normalization [152,153]. The dataset presented in Table 6 displays a subset of hurricane Harvey's tracking data (Figure 1) derived from the International Best Track Archive for Climate Stewardship (IBTrACS) [154,155], which, although comprehensive, requires careful data processing to be suitable for ENN. Here, the maximum sustained wind speed reported from multiple agencies for the current location needs to be converted to a unified 10 min sustained wind speed. Then, important features must be extracted and interpolated according to desired time steps. Missing values are handled using interpolation or imputation techniques, such as mean imputation or predictive modeling. Another dataset can be found in [156], where both recent and historical standard meteorological and water level information is provided by the National Data Buoy Center (NDBC). The data can be collected from the stations near an area of interest (Port Aransas, Texas) combined with the extracted TC tracks and then fed into the ENN model.

As mentioned in Section 3.3, data-driven models are usually agnostic to physical laws because they rely only on data. However, it is important to note that while data-driven models do not explicitly incorporate physical laws, they can still be used to make predictions about physical phenomena based on empirical data [55,56]. For example, a NN model can be trained on data from a time series of gauge data to predict the uncertainty related to storm surge flooding [55,57], even if the underlying physical laws are not fully understood or modeled. Therefore, the accuracy and reliability of data are heavily influenced by the quality of data preprocessing steps, such as cleaning and filtering the data, handling missing values, normalizing or scaling the data, and feature selection or extraction. Last but foremost, some important issues related to the data preprocessing stage that can impact the performance of NN ensemble are as follows:

Table 6. Sample best-track dataset associated with hurricane Harvey (2017) in the North Atlantic basin [154,155].

SID	ISO_TIME	NATURE	LAT	LON	WMO_WIND	WMO_PRES	DIST2LAND	LANDFALL
			degrees_N	degrees_E	kts	mb	km	km
2017228N14314	8/25/2017 3:00	TS	25.2924	−94.7578			243	204
2017228N14314	8/25/2017 6:00	TS	25.6	−95.1	90	966	204	170
2017228N14314	8/25/2017 9:00	TS	25.935	−95.4651			160	133
2017228N14314	8/25/2017 12:00	TS	26.3	−95.8	95	949	133	123
2017228N14314	8/25/2017 15:00	TS	26.6999	−96.0652			126	108
2017228N14314	8/25/2017 18:00	TS	27.1	−96.3	105	943	108	67
2017228N14314	8/25/2017 21:00	TS	27.4875	−96.5806			67	34
2017228N14314	8/26/2017 0:00	TS	27.8	−96.8	115	941	34	11
2017228N14314	8/26/2017 3:00	TS	28	−96.9	115	937	11	0
2017228N14314	8/26/2017 6:00	TS	28.2	−97.1	105	948	0	0
2017228N14314	8/26/2017 9:00	TS	28.4534	−97.2205			0	0

Data cleaning: Large amounts of data from various sources, such as weather sensors, tide gauges, and satellite imagery, can be prone to errors, missing data, and outliers, which can significantly affect the accuracy of the model's predictions. Therefore, it is essential to perform data cleaning to remove any errors or inconsistencies in the data before feeding it into the neural network ensemble model [157]. This process may involve identifying and removing outliers, handling missing data through imputation, and smoothing noisy signals.

Feature scaling: Neural networks require all features to be on the same scale to ensure that no feature dominates the others, where feature scaling techniques such as normalization, standardization, or range scaling can be applied [37]. Choosing the wrong scaling technique can lead to poor model performance. In storm surge prediction, input features such as sea level, wind speed, and atmospheric pressure can have very different scales and ranges. Therefore, it is important to apply feature scaling to ensure that all features have a similar impact on the model's predictions.

Feature selection: Ensemble models can have a large number of features, which can lead to overfitting and poor generalization. The input features may include various meteorological and oceanographic variables, such as wind speed, air pressure, water temperature, tidal levels, and ocean currents. However, not all of these features may be equally important for predicting storm surges. By removing irrelevant or redundant features, the model can focus on learning the most important patterns in the data, leading to more accurate predictions [83]. There are various techniques for feature selection (including filter methods, wrapper methods, and embedded methods) which can be applied before or during training the NN ensemble model to select the most relevant features.

Data transformation: The goal of data transformation is to convert the input data into a format that is more suitable for analysis and modeling by the neural network ensemble. Transforming data to fit a particular distribution can improve the performance of neural network ensembles and lead to more accurate and robust predictions of storm surges [158]. Some common data transformation techniques include normalization, logarithmic transformation, PCA transformation, and discretization. However, it is important to choose the right transformation technique to avoid introducing noise into the data.

Handling class imbalance: This refers to a situation where the distribution of the target variable is heavily skewed towards one class (base model). In such cases, failing to handle the class imbalance can lead to biased models with inaccurate predictions that perform poorly on the minority classes [54]. Various techniques for handling class imbalances include resampling, synthetic data generation, and cost-sensitive learning.

6. Model Selection and Evaluation

There is no optimal ensemble configuration for predicting peak surge levels under different scenarios. It is essential to carefully evaluate the performance of different ensemble models and select the one that provides the best trade-off between bias and variance, accuracy, diversity, stability, generalization, and computational cost [67,91,92,159]. The final stage would evaluate and validate the performance of the selected ensemble model using appropriate evaluation metrics and statistical tests, such as the mean absolute error (MAE) [21,83,160], root-mean-squared error (RMSE) [106,161], correlation coefficient (CC) [49,83,106,161], and coefficient of determination (R-squared) [42,43,161–163]. The following section covers some of the fundamental concepts that are considered when evaluating a neural network ensemble for storm surge prediction.

6.1. Bias–Variance Tradeoff

The process of designing a NN ensemble, which involves combining multiple models or algorithms, can be optimized by finding the best balance between bias and variance [92,164]. Bias refers to the extent to which a model consistently misses the mark in its predictions, while variance refers to the extent to which a model's predictions are sensitive to small perturbations in the training data. A good ensemble should strike a balance between these two factors in order to minimize the overall prediction error [92]. To achieve this balance, the optimal choice of weights for each base learner in the ensemble needs to be determined. The weights are chosen such that they minimize the prediction error of the ensemble. By doing so, the ensemble becomes more robust to different types of data and can achieve better overall performance [83]. The bias-variance decomposition of the mean squared error (MSE) is actually a method for analyzing the behavior of a stochastic model [92,164,165]. Each individual base learner in the ensemble may have some degree of stochasticity or variability in its predictions due to factors such as the initialization of the weights or the selection of the training data. By decomposing the MSE (between the estimated output variable y and the estimator $f(x)$) into its bias and variance components, it is possible to gain insight into the sources of error in the model [83,165]. For a given sample dataset x, the error made by the estimator $f(x)$ is defined as $\varepsilon = f_{(x)} - y$; hence, the MSE of the estimator is defined as the expected value of the squared error, i.e., $MSE(f_{(x)}) = E[\varepsilon^2]$. For every unseen sample x, the MSE can be decomposed as

$$E[(f_{(x)} - y)^2] = Bias^2(f_{(x)}) + Var(f_{(x)}) + Var(\varepsilon) \tag{6}$$

The last term in Equation (6) contains an irreducible error that is inherent in the relationship between the input and output and cannot be reduced by any model. This error arises from the fact that the input may not contain enough information to perfectly predict the output or that there may be random variations in the data that cannot be modeled [133,166]. Therefore, an ensemble model cannot reduce irreducible error, but it can help improve the overall performance of the model by reducing the bias and variance.

6.2. Ensemble Diversity

Ensemble diversity can be particularly important to ensure that the ensemble is able to accurately capture the complex dynamics of the ocean and the atmosphere that influence storm surge. By using different training data or model architectures, the ensemble can better account for different sources of uncertainty in the data and avoid overfitting to any particular aspect of the data [83,165,166]. As discussed in Section 3.3, there are several techniques that can be used to promote ensemble diversity, including bagging, boosting, and stacking. One commonly used metric to evaluate ensemble diversity is cross-entropy. Cross-entropy measures the difference between the predictions of each individual model and the predictions of the ensemble [164,166,167]. A lower cross-entropy value indicates that the ensemble is more diverse. Another metric to evaluate ensemble diversity is disagreement, which measures the degree of disagreement between the predictions of each individual model [168,169]. A higher disagreement value indicates that the ensemble is more diverse. Correlation is another metric that can be used to evaluate ensemble diversity [83,106]. It measures the degree of similarity between the predictions of each individual model. A lower correlation value indicates that the ensemble is more diverse. When selecting the final model for a neural network ensemble, a good approach is to choose the model that achieves good individual performance while contributing to higher ensemble diversity.

This can be done by evaluating each model's performance on a validation set and then evaluating the ensemble's performance on a separate test set. The final model should be chosen based on a combination of good individual performance and high ensemble diversity, as measured by the chosen diversity metric.

6.3. Probabilistic Performance

The predictive ability of probabilistic models can be assessed by probabilistic performance and skill metrics, which can also be used to select the final model in a neural network ensemble considering ensemble diversity in storm surge prediction [43]. The most commonly used probabilistic performance metrics are mentioned below. These metrics can provide a more comprehensive evaluation of the performance of the models in the ensemble, including their ability to accurately capture the uncertainty in the predictions. Models that have good individual performance and contribute to higher ensemble diversity should be chosen.

The Brier skill score (BSS) measures the skill of a forecast by comparing the predictions with a reference forecast, such as a climatological forecast or a persistence forecast. The BSS ranges from $-\infty$ to 1, with a score of 1 indicating a perfect forecast and a score of 0 indicating no skill beyond the reference forecast. BSS can be used to evaluate the probability of a surge or total water level exceeding a given threshold and thus yields the accuracy of the system's probabilistic forecasts [7,170].

The mean square skill score (MSSS) measures the improvement in the mean squared error (MSE) of the forecast system relative to a reference forecast, such as a climatological forecast or a persistence forecast. The MSSS ranges from $-\infty$ to 1, with a score of 1 indicating perfect skill and a score of 0 indicating no improvement beyond the reference forecast. When the system generates a probability distribution for the water level, the MSSS can measure the improvement in the mean squared error of this distribution over a given time period compared to the reference forecast [171,172]. The MSSS can be a useful metric when the focus is on the mean of the forecast distribution rather than the full distribution itself. However, it does not provide information on the reliability and resolution of the forecast, which are important for assessing the quality of probabilistic forecasts.

The continuous ranked probability score (CRPS) is used to evaluate the accuracy of probabilistic forecasts. It measures the distance between the cumulative distribution function (CDF) of the forecast probability distribution and the CDF of the observed outcomes. The lower the CRPS, the better the forecast. When the system generates a probability distribution for the water level, the CRPS can measure the accuracy of this distribution over a given time period by comparing it to the observed water levels. The CRPS takes into account both the reliability and sharpness of the forecast probability distribution, which makes it a more informative metric than the Brier skill score in some cases [148].

7. Summary

The present paper focuses on various approaches that can predict storm surge levels using ensemble neural networks. The challenges and limitations of accurately predicting peak water levels, which are often caused by complex interactions between ocean currents, winds, and atmospheric pressure systems, are also emphasized. Despite the limitations, supervised neural networks, specifically those utilizing the backpropagation technique, have proven to be a powerful tool for predicting storm surge levels, particularly for short-term forecasting. However, the accuracy of BPNN models can be limited by overfitting, which occurs when the model becomes too complex and fits the training data too closely. To address the limitations of single BPNN models, ensemble methods that combine multiple neural network models to improve accuracy and reduce overfitting are preferred. Ensemble methods involve generating multiple base learners (weak classifiers) and combining their predictions to create a strong learner. There are three leading meta-algorithms for combining weak learners: bootstrap aggregating (bagging), boosting, and sitting. Bagging involves generating multiple training datasets by randomly sampling from the original dataset with replacement, then training each base learner on a different dataset. Boosting involves iteratively training weak classifiers, with each subsequent model focusing on the samples that were misclassified by the previous model. Stacking involves training a meta-learner that combines the predictions of multiple base learners. As the networks grow larger, the importance of pruning and fine-tuning, as well as data preparation and wrangling, become unquestionable. Data preparation involves preprocessing and organizing raw data before training a group of neural networks together as an ensemble. The goal of this crucial step is to ensure that the input data are consistent, relevant, and suitable for use by the ensemble. The paper highlights different sources of input data type for storm surge prediction and the need for careful data preprocessing and wrangling to ensure accurate predictions. However, there is no one-size-fits-all approach for creating an ensemble of neural networks for predicting storm surge levels. Instead, it is essential to carefully evaluate the performance of different ensemble models and select the one that provides the best trade-off between bias and variance, accuracy, diversity, stability, generalization, and computational cost. Overall, the paper provides valuable insights into the use of ensemble methods for storm surge flood modeling, which can contribute to better predictions and preparedness for extreme weather events.

Author Contributions: Conceptualization, S.K.N. and M.B.; methodology, S.K.N. and D.V.S.; investigation, M.B., S.K.N. and D.V.S.; resources, R.J.W.; data curation, S.K.N.; writing—original draft preparation, M.B.; writing—review and editing, D.V.S. and R.J.W.; visualization, S.K.N.; supervision, D.V.S.; funding acquisition, D.V.S. All authors have read and agreed to the published version of the manuscript.

Funding: This research received no external funding

Institutional Review Board Statement: Not applicable

Informed Consent Statement: Not applicable

Data Availability Statement: Not applicable

Conflicts of Interest: The authors declare no conflict of interest.

Appendix A. Implementation of Backward Propagation of Errors

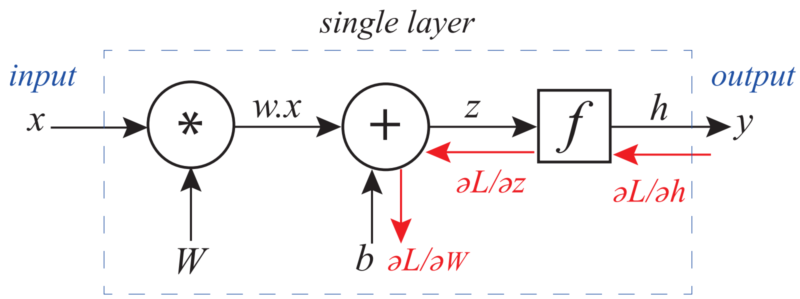

Figure A1. Simplified BP algorithm in a 1-layer NN with 2D input.

- Defining the sigmoid activation function and its derivative

```
def activation(x):
    return 1 / (1 + np.exp(-x))
def activation_derivative(x):
    return activation(x) * (1 - activation(x))
```

- Defining the forward propagation function

```
    def forward_propagation(x, weights, biases):
    a = [x]
    z = []
    for l in range(1, len(weights) + 1):
```

```
        z.append(np.dot(weights[l], a[l-1]) + biases[l])
        a.append(activation(z[l-1]))
    return a, z
```

- Defining the backward propagation function

```
def backward_propagation(x, y, a, z, weights, biases,
    learning_rate):
    L = len(weights)
    delta = [None] * (L + 1)
    gradients = {}
```

- Running the error propagation using the chain rule $\frac{\partial L}{\partial w} = \frac{\partial L}{\partial h}\frac{\partial h}{\partial z}\frac{\partial z}{\partial w}$, $h = f_{(z)}$, and Loss Function $L = \frac{1}{n}\sum_{j=1}^{n}(h_j - y_j)$

```
    # Compute the output layer delta
delta[L] = (a[L] - y) * activation_derivative(z[L-1])
    # Compute deltas for the hidden layers
    for l in range(L-1, 0, -1):
        delta[l] = np.dot(weights[l+1].T, delta[l+1]) *
            activation_derivative(z[l-1])
    # Compute gradients for weights and biases
    for l in range(1, L+1):
        gradients[f'dW{l}'] = np.dot(delta[l], a[l-1].T)
        gradients[f'db{l}'] = delta[l]
```

References

1. Heberger, M.; Cooley, H.; Herrera, P.; Gleick, P.H.; Moore, E. Potential impacts of increased coastal flooding in California due to sea-level rise. *Clim. Chang.* **2011**, *109*, 229–249. [CrossRef]
2. Woodruff, J.D.; Irish, J.L.; Camargo, S.J. Coastal flooding by tropical cyclones and sea-level rise. *Nature* **2013**, *504*, 44–52. [CrossRef] [PubMed]
3. Barooni, M.; Nezhad, S.K.; Ali, N.A.; Ashuri, T.; Sogut, D.V. Numerical study of ice-induced loads and dynamic response analysis for floating offshore wind turbines. *Mar. Struct.* **2022**, *86*, 103300. [CrossRef]
4. Cahoon, D.R.; Hensel, P.F.; Spencer, T.; Reed, D.J.; McKee, K.L.; Saintilan, N. Coastal wetland vulnerability to relative sea-level rise: Wetland elevation trends and process controls. In *Wetlands and Natural Resource Management*; Springer: Berlin/Heidelberg, Germany, 2006, pp. 271–292.
5. Dube, S.; Jain, I.; Rao, A.; Murty, T. Storm surge modelling for the Bay of Bengal and Arabian Sea. *Nat. Hazards* **2009**, *51*, 3–27. [CrossRef]
6. Hashemi, M.R.; Spaulding, M.L.; Shaw, A.; Farhadi, H.; Lewis, M. An efficient artificial intelligence model for prediction of tropical storm surge. *Nat. Hazards* **2016**, *82*, 471–491. [CrossRef]
7. Flowerdew, J.; Horsburgh, K.; Wilson, C.; Mylne, K. Development and evaluation of an ensemble forecasting system for coastal storm surges. *Q. J. R. Meteorol. Soc.* **2010**, *136*, 1444–1456. [CrossRef]
8. Lynett, P.J.; Gately, K.; Wilson, R.; Montoya, L.; Arcas, D.; Aytore, B.; Bai, Y.; Bricker, J.D.; Castro, M.J.; Cheung, K.F.; et al. Inter-model analysis of tsunami-induced coastal currents. *Ocean. Model.* **2017**, *114*, 14–32. [CrossRef]
9. Arabi, M.G.; Sogut, D.V.; Khosronejad, A.; Yalciner, A.C.; Farhadzadeh, A. A numerical and experimental study of local hydrodynamics due to interactions between a solitary wave and an impervious structure. *Coast. Eng.* **2019**, *147*, 43–62. [CrossRef]
10. Al Kajbaf, A.; Bensi, M. Application of surrogate models in estimation of storm surge: A comparative assessment. *Appl. Soft Comput.* **2020**, *91*, 106184. [CrossRef]
11. Qiao, C.; Myers, A.T.; Arwade, S.R. Validation and uncertainty quantification of metocean models for assessing hurricane risk. *Wind. Energy* **2020**, *23*, 220–234. [CrossRef]
12. Arns, A.; Dangendorf, S.; Jensen, J.; Talke, S.; Bender, J.; Pattiaratchi, C. Sea-level rise induced amplification of coastal protection design heights. *Sci. Rep.* **2017**, *7*, 40171. [CrossRef]
13. Weaver, R.J.; Slinn, D.N. Effect of wave forcing on storm surge. In *Coastal Engineering 2004: (In 4 Volumes)*; World Scientific: Singapore, 2005; pp. 1532–1538.
14. Sweet, W.V.; Kopp, R.E.; Weaver, C.P.; Obeysekera, J.; Horton, R.M.; Thieler, E.R.; Zervas, C. In *Global and Regional Sea Level Rise Scenarios for the United States*; Technical Report; National Oceanic and Atmospheric Administration: Washington, DC, USA, 2017.

15. Liu, Z.; Cheng, L.; Hao, Z.; Li, J.; Thorstensen, A.; Gao, H. A framework for exploring joint effects of conditional factors on compound floods. *Water Resour. Res.* **2018**, *54*, 2681–2696. [CrossRef]
16. Xi, D.; Lin, N. Understanding uncertainties in tropical cyclone rainfall hazard modeling using synthetic storms. *J. Hydrometeorol.* **2022**, *23*, 925–946. [CrossRef]
17. Dtissibe, F.Y.; Ari, A.A.A.; Titouna, C.; Thiare, O.; Gueroui, A.M. Flood forecasting based on an artificial neural network scheme. *Nat. Hazards* **2020**, *104*, 1211–1237. [CrossRef]
18. Velioglu, D. Advanced Two-and Three-Dimensional Tsunami Models: Benchmarking and Validation. Doctoral Dissertation, Middle East Technical University, Ankara, Turkey, 2017.
19. Chen, Y.; Li, J.; Xu, H. Improving flood forecasting capability of physically based distributed hydrological models by parameter optimization. *Hydrol. Earth Syst. Sci.* **2016**, *20*, 375–392. [CrossRef]
20. Agudelo-Otálora, L.M.; Moscoso-Barrera, W.D.; Paipa-Galeano, L.A.; Mesa-Sciarrotta, C. Comparación de modelos físicos y de inteligencia artificial para predicción de niveles de inundación. *Tecnol. Cienc. Agua* **2018**, *9*, 209–235. [CrossRef]
21. Zhang, Z.; Liang, J.; Zhou, Y.; Huang, Z.; Jiang, J.; Liu, J.; Yang, L. A multi-strategy-mode waterlogging-prediction framework for urban flood depth. *Nat. Hazards Earth Syst. Sci.* **2022**, *22*, 4139–4165. [CrossRef]
22. Oddo, P.C.; Lee, B.S.; Garner, G.G.; Srikrishnan, V.; Reed, P.M.; Forest, C.E.; Keller, K. Deep uncertainties in sea-level rise and storm surge projections: Implications for coastal flood risk management. *Risk Anal.* **2020**, *40*, 153–168. [CrossRef]
23. Ju, Y.; Lindbergh, S.; He, Y.; Radke, J.D. Climate-related uncertainties in urban exposure to sea level rise and storm surge flooding: A multi-temporal and multi-scenario analysis. *Cities* **2019**, *92*, 230–246. [CrossRef]
24. Makris, C.V.; Tolika, K.; Baltikas, V.N.; Velikou, K.; Krestenitis, Y.N. The impact of climate change on the storm surges of the Mediterranean Sea: Coastal sea level responses to deep depression atmospheric systems. *Ocean. Model.* **2023**, *181*, 102149. [CrossRef]
25. Camargo, S.J.; Barnston, A.G.; Zebiak, S.E. A statistical assessment of tropical cyclone activity in atmospheric general circulation models. *Tellus A Dyn. Meteorol. Oceanogr.* **2005**, *57*, 589–604. [CrossRef]
26. Tadesse, M.; Wahl, T.; Cid, A. Data-driven modeling of global storm surges. *Front. Mar. Sci.* **2020**, *7*, 260. [CrossRef]
27. Bevacqua, E.; Maraun, D.; Vousdoukas, M.; Voukouvalas, E.; Vrac, M.; Mentaschi, L.; Widmann, M. Higher probability of compound flooding from precipitation and storm surge in Europe under anthropogenic climate change. *Sci. Adv.* **2019**, *5*, eaaw5531. [CrossRef]
28. Jelesnianski, C.P. Numerical computations of storm surges without bottom stress. *Mon. Weather. Rev.* **1966**, *94*, 379–394. [CrossRef]
29. Kim, Y.H. Assessment of coastal inundation due to storm surge under future sea-level rise conditions. *J. Coast. Res.* **2020**, *95*, 845–849. [CrossRef]
30. Seo, J.; Ku, H.; Cho, K.; Maeng, J.H.; Lee, H. Application of SLOSH in estimation of Typhoon-induced Storm Surges in the Coastal Region of South Korea. *J. Coast. Res.* **2018**, 551–555. . [CrossRef]
31. Dietrich, J.C.; Tanaka, S.; Westerink, J.J.; Dawson, C.N.; Luettich, R.; Zijlema, M.; Holthuijsen, L.H.; Smith, J.; Westerink, L.; Westerink, H. Performance of the unstructured-mesh, SWAN+ ADCIRC model in computing hurricane waves and surge. *J. Sci. Comput.* **2012**, *52*, 468–497. [CrossRef]
32. De Las Heras, M.; Burgers, G.; Janssen, P. Wave data assimilation in the WAM wave model. *J. Mar. Syst.* **1995**, *6*, 77–85. [CrossRef]
33. Bender, C.; Smith, J.M.; Kennedy, A.; Jensen, R. STWAVE simulation of Hurricane Ike: Model results and comparison to data. *Coast. Eng.* **2013**, *73*, 58–70. [CrossRef]
34. Booij, N.; Holthuijsen, L.; Ris, R. The "SWAN" wave model for shallow water. *Coast. Eng.* **1996**, 668–676. . [CrossRef]
35. Reffitt, M.; Orescanin, M.M.; Massey, C.; Raubenheimer, B.; Jensen, R.E.; Elgar, S. Modeling storm surge in a small tidal two-inlet system. *J. Waterw. Port, Coastal, Ocean. Eng.* **2020**, *146*, 04020043. [CrossRef]
36. Ramos Valle, A.N.; Curchitser, E.N.; Bruyere, C.L.; Fossell, K.R. Simulating storm surge impacts with a coupled atmosphere-inundation model with varying meteorological forcing. *J. Mar. Sci. Eng.* **2018**, *6*, 35. [CrossRef]
37. Lee, J.W.; Irish, J.L.; Bensi, M.T.; Marcy, D.C. Rapid prediction of peak storm surge from tropical cyclone track time series using machine learning. *Coast. Eng.* **2021**, *170*, 104024. [CrossRef]
38. Smith, J.M.; Westerink, J.J.; Kennedy, A.B.; Taflanidis, A.A.; Cheung, K.F.; Smith, T.D. SWIMS Hawaii hurricane wave, surge, and runup inundation fast forecasting tool. In Proceeings of the Solutions to Coastal Disasters Conference, Anchorage, AK, USA, 25–29 June 2011; pp. 89–98.
39. Torres, M.J.; Nadal-Caraballo, N.C.; Ramos-Santiago, E.; Campbell, M.O.; Gonzalez, V.M.; Melby, J.A.; Taflanidis, A.A. StormSim-CHRPS: Coastal Hazards Rapid Prediction System. *J. Coast. Res.* **2020**, *95*, 1320–1325. [CrossRef]
40. Ishida, K.; Tsujimoto, G.; Ercan, A.; Tu, T.; Kiyama, M.; Amagasaki, M. Hourly-scale coastal sea level modeling in a changing climate using long short-term memory neural network. *Sci. Total Environ.* **2020**, *720*, 137613. [CrossRef] [PubMed]
41. Tebaldi, C.; Ranasinghe, R.; Vousdoukas, M.; Rasmussen, D.; Vega-Westhoff, B.; Kirezci, E.; Kopp, R.E.; Sriver, R.; Mentaschi, L. Extreme sea levels at different global warming levels. *Nat. Clim. Chang.* **2021**, *11*, 746–751. [CrossRef]
42. Ayyad, M.; Hajj, M.R.; Marsooli, R. Machine learning-based assessment of storm surge in the New York metropolitan area. *Sci. Rep.* **2022**, *12*, 19215. [CrossRef]
43. Tiggeloven, T.; Couasnon, A.; van Straaten, C.; Muis, S.; Ward, P.J. Exploring deep learning capabilities for surge predictions in coastal areas. *Sci. Rep.* **2021**, *11*, 17224. [CrossRef] [PubMed]

44. Žust, L.; Fettich, A.; Kristan, M.; Ličer, M. HIDRA 1.0: Deep-learning-based ensemble sea level forecasting in the northern Adriatic. *Geosci. Model Dev.* **2021**, *14*, 2057–2074. [CrossRef]
45. Ho, F.P.; Myers, V.A. *Joint probability method of tide frequency analysis applied to Apalachicola Bay and St. George Sound, Florida*; U.S. Department of Commerce, National Oceanic and Atmospheric Administration, National Weather Service, Office of Hydrology: Washington, DC, USA, 1975; Volume 18.
46. Feng, J.; Li, D.; Li, Y.; Liu, Q.; Wang, A. Storm surge variation along the coast of the Bohai Sea. *Sci. Rep.* **2018**, *8*, 11309. [CrossRef]
47. Ramos-Valle, A.N.; Curchitser, E.N.; Bruyère, C.L.; McOwen, S. Implementation of an artificial neural network for storm surge forecasting. *J. Geophys. Res. Atmos.* **2021**, *126*, e2020JD033266. [CrossRef]
48. Igarashi, Y.; Tajima, Y. Application of recurrent neural network for prediction of the time-varying storm surge. *Coast. Eng. J.* **2021**, *63*, 68–82. [CrossRef]
49. Kim, S.W.; Lee, A.; Mun, J. A surrogate modeling for storm surge prediction using an artificial neural network. *J. Coast. Res.* **2018**, pp. 866–870. [CrossRef]
50. Royston, S.; Lawry, J.; Horsburgh, K. A linguistic decision tree approach to predicting storm surge. *Fuzzy Sets Syst.* **2013**, *215*, 90–111. [CrossRef]
51. Bezuglov, A.; Blanton, B.; Santiago, R. Multi-output artificial neural network for storm surge prediction in north carolina. *arXiv* **2016**, arXiv:1609.07378.
52. Bass, B.; Bedient, P. Surrogate modeling of joint flood risk across coastal watersheds. *J. Hydrol.* **2018**, *558*, 159–173. [CrossRef]
53. Tadesse, M.G.; Wahl, T. A database of global storm surge reconstructions. *Sci. Data* **2021**, *8*, 125. [CrossRef]
54. Palmer, M.; Domingues, C.; Slangen, A.; Dias, F.B. An ensemble approach to quantify global mean sea-level rise over the 20th century from tide gauge reconstructions. *Environ. Res. Lett.* **2021**, *16*, 044043. [CrossRef]
55. Bruneau, N.; Polton, J.; Williams, J.; Holt, J. Estimation of global coastal sea level extremes using neural networks. *Environ. Res. Lett.* **2020**, *15*, 074030. [CrossRef]
56. Chen, R.; Zhang, W.; Wang, X. Machine learning in tropical cyclone forecast modeling: A review. *Atmosphere* **2020**, *11*, 676. [CrossRef]
57. De Oliveira, M.M.; Ebecken, N.F.F.; De Oliveira, J.L.F.; de Azevedo Santos, I. Neural network model to predict a storm surge. *J. Appl. Meteorol. Climatol.* **2009**, *48*, 143–155. [CrossRef]
58. Taylor, A.A.; Glahn, B. Probabilistic guidance for hurricane storm surge. In Proceedings of the 19th Conference on Probability and Statistics, New Orleans, LA, USA, 21–24 January 2008; Volume 74.
59. Feng, X.; Ma, G.; Su, S.F.; Huang, C.; Boswell, M.K.; Xue, P. A multi-layer perceptron approach for accelerated wave forecasting in Lake Michigan. *Ocean. Eng.* **2020**, *211*, 107526. [CrossRef]
60. Deo, R.C.; Ghorbani, M.A.; Samadianfard, S.; Maraseni, T.; Bilgili, M.; Biazar, M. Multi-layer perceptron hybrid model integrated with the firefly optimizer algorithm for windspeed prediction of target site using a limited set of neighboring reference station data. *Renew. Energy* **2018**, *116*, 309–323. [CrossRef]
61. Kulkarni, P.A.; Dhoble, A.S.; Padole, P.M. Deep neural network-based wind speed forecasting and fatigue analysis of a large composite wind turbine blade. *Proc. Inst. Mech. Eng. Part C J. Mech. Eng. Sci.* **2019**, *233*, 2794–2812. [CrossRef]
62. Chattopadhyay, A.; Hassanzadeh, P.; Pasha, S. Predicting clustered weather patterns: A test case for applications of convolutional neural networks to spatio-temporal climate data. *Sci. Rep.* **2020**, *10*, 1317. [CrossRef] [PubMed]
63. Luo, Y.; Feng, A.; Li, H.; Li, D.; Wu, X.; Liao, J.; Zhang, C.; Zheng, X.; Pu, H. New deep learning method for efficient extraction of small water from remote sensing images. *PLoS ONE* **2022**, *17*, e0272317. [CrossRef]
64. Hunt, K.M.; Matthews, G.R.; Pappenberger, F.; Prudhomme, C. Using a long short-term memory (LSTM) neural network to boost river streamflow forecasts over the western United States. *Hydrol. Earth Syst. Sci.* **2022**, *26*, 5449–5472. [CrossRef]
65. Zilong, T.; Yubing, S.; Xiaowei, D. Spatial-temporal wave height forecast using deep learning and public reanalysis dataset. *Appl. Energy* **2022**, *326*, 120027. [CrossRef]
66. Varalakshmi, P.; Vasumathi, N.; Venkatesan, R. Tropical Cyclone prediction based on multi-model fusion across Indian coastal region. *Prog. Oceanogr.* **2021**, *193*, 102557. [CrossRef]
67. Sagi, O.; Rokach, L. Ensemble learning: A survey. *Wiley Interdiscip. Rev. Data Min. Knowl. Discov.* **2018**, *8*, e1249. [CrossRef]
68. Young, C.C.; Liu, W.C.; Hsieh, W.L. Predicting the water level fluctuation in an alpine lake using physically based, artificial neural network, and time series forecasting models. *Math. Probl. Eng.* **2015**, *2015*, 708204. [CrossRef]
69. Kim, S.; Matsumi, Y.; Pan, S.; Mase, H. A real-time forecast model using artificial neural network for after-runner storm surges on the Tottori coast, Japan. *Ocean. Eng.* **2016**, *122*, 44–53. [CrossRef]
70. Blake, E.S.; Zelinsky, D.A. National Hurricane Center Tropical Cyclone Report; Hurricane Harvey. National Hurricane Center, National Oceanographic and Atmospheric Association: Miami, FL, USA, 2017.
71. Qin, Y.; Su, C.; Chu, D.; Zhang, J.; Song, J. A Review of Application of Machine Learning in Storm Surge Problems. *J. Mar. Sci. Eng.* **2023**, *11*, 1729. [CrossRef]
72. Yu, Y.; Zhang, H.; Singh, V.P. Forward prediction of runoff data in data-scarce basins with an improved ensemble empirical mode decomposition (EEMD) model. *Water* **2018**, *10*, 388. [CrossRef]
73. Le, X.H.; Ho, H.V.; Lee, G.; Jung, S. Application of long short-term memory (LSTM) neural network for flood forecasting. *Water* **2019**, *11*, 1387. [CrossRef]

74. Liao, L.; Li, H.; Shang, W.; Ma, L. An empirical study of the impact of hyperparameter tuning and model optimization on the performance properties of deep neural networks. *ACM Trans. Softw. Eng. Methodol. (TOSEM)* **2022**, *31*, 1–40. [CrossRef]
75. Victoria, A.H.; Maragatham, G. Automatic tuning of hyperparameters using Bayesian optimization. *Evol. Syst.* **2021**, *12*, 217–223. [CrossRef]
76. Yu, T.; Zhu, H. Hyper-parameter optimization: A review of algorithms and applications. *arXiv* **2020**, arXiv:2003.05689.
77. Hu, C.; Wu, Q.; Li, H.; Jian, S.; Li, N.; Lou, Z. Deep learning with a long short-term memory networks approach for rainfall-runoff simulation. *Water* **2018**, *10*, 1543. [CrossRef]
78. Zhang, X.q.; Jiang, S.q. Study on the application of BP neural network optimized based on various optimization algorithms in storm surge prediction. *Proc. Inst. Mech. Eng. Part M J. Eng. Marit. Environ.* **2022**, *236*, 539–552. [CrossRef]
79. Lee, T.L. Back-propagation neural network for the prediction of the short-term storm surge in Taichung harbor, Taiwan. *Eng. Appl. Artif. Intell.* **2008**, *21*, 63–72. [CrossRef]
80. Tsai, C.; You, C.; Chen, C. Storm-surge prediction at the Tanshui estuary: Development model for maximum storm surges. *Nat. Hazards Earth Syst. Sci* **2013**, *1*, 7333–7356.
81. Alzubaidi, L.; Zhang, J.; Humaidi, A.J.; Al-Dujaili, A.; Duan, Y.; Al-Shamma, O.; Santamaría, J.; Fadhel, M.A.; Al-Amidie, M.; Farhan, L. Review of deep learning: Concepts, CNN architectures, challenges, applications, future directions. *J. Big Data* **2021**, *8*, 1–74. [CrossRef] [PubMed]
82. Giffard-Roisin, S.; Yang, M.; Charpiat, G.; Kumler Bonfanti, C.; Kégl, B.; Monteleoni, C. Tropical cyclone track forecasting using fused deep learning from aligned reanalysis data. *Front. Big Data* **2020**, *3*, 1.. [CrossRef]
83. Wang, T.; Liu, T.; Lu, Y. A hybrid multi-step storm surge forecasting model using multiple feature selection, deep learning neural network and transfer learning. *Soft Comput.* **2023**, *27*, 935–952. [CrossRef]
84. Weiss, K.; Khoshgoftaar, T.M.; Wang, D. A survey of transfer learning. *J. Big Data* **2016**, *3*, 1–40. [CrossRef]
85. Wu, W.; Westra, S.; Leonard, M. A basis function approach for exploring the seasonal and spatial features of storm surge events. *Geophys. Res. Lett.* **2017**, *44*, 7356–7365. [CrossRef]
86. Wolf, J.; Flather, R. Modelling waves and surges during the 1953 storm. *Philos. Trans. R. Soc. A Math. Phys. Eng. Sci.* **2005**, *363*, 1359–1375. [CrossRef] [PubMed]
87. Feng, J.; von Storch, H.; Jiang, W.; Weisse, R. Assessing changes in extreme sea levels along the coast of C hina. *J. Geophys. Res. Ocean.* **2015**, *120*, 8039–8051. [CrossRef]
88. Bloemendaal, N.; Haigh, I.D.; de Moel, H.; Muis, S.; Haarsma, R.J.; Aerts, J.C. Generation of a global synthetic tropical cyclone hazard dataset using STORM. *Sci. Data* **2020**, *7*, 40. [CrossRef]
89. Adhikari, R.; Agrawal, R. A homogeneous ensemble of artificial neural networks for time series forecasting. *arXiv* **2013**, arXiv:1302.6210.
90. Guan, H.; Mokadam, L.K.; Shen, X.; Lim, S.H.; Patton, R. Fleet: Flexible efficient ensemble training for heterogeneous deep neural networks. *Proc. Mach. Learn. Syst.* **2020**, *2*, 247–261.
91. Zhou, Z.H.; Zhou, Z.H. *Ensemble Learning*; Springer: Berlin/Heidelberg, Germany, 2021.
92. Zhou, Z.H.; Wu, J.; Tang, W. Ensembling neural networks: Many could be better than all. *Artif. Intell.* **2002**, *137*, 239–263. [CrossRef]
93. Ghojogh, B.; Crowley, M. The theory behind overfitting, cross validation, regularization, bagging, and boosting: Tutorial. *arXiv* **2019**, arXiv:1905.12787.
94. Brodeur, Z.P.; Herman, J.D.; Steinschneider, S. Bootstrap aggregation and cross-validation methods to reduce overfitting in reservoir control policy search. *Water Resour. Res.* **2020**, *56*, e2020WR027184. [CrossRef]
95. Altman, N.; Krzywinski, M. Ensemble methods: Bagging and random forests. *Nat. Methods* **2017**, *14*, 933–935. [CrossRef]
96. Dietterich, T.G. Ensemble methods in machine learning. In Proceedings of the Multiple Classifier Systems: First International Workshop, MCS 2000, Cagliari, Italy, 21–23 June 2000; pp. 1–15.
97. Cassales, G.; Gomes, H.; Bifet, A.; Pfahringer, B.; Senger, H. Improving the performance of bagging ensembles for data streams through mini-batching. *Inf. Sci.* **2021**, *580*, 260–282. [CrossRef]
98. Maxwell, A.E.; Warner, T.A.; Fang, F. Implementation of machine-learning classification in remote sensing: An applied review. *Int. J. Remote Sens.* **2018**, *39*, 2784–2817. [CrossRef]
99. Zounemat-Kermani, M.; Batelaan, O.; Fadaee, M.; Hinkelmann, R. Ensemble machine learning paradigms in hydrology: A review. *J. Hydrol.* **2021**, *598*, 126266. [CrossRef]
100. Elith, J.; Leathwick, J.R.; Hastie, T. A working guide to boosted regression trees. *J. Anim. Ecol.* **2008**, *77*, 802–813. [CrossRef]
101. Freund, Y.; Schapire, R.E. A decision-theoretic generalization of on-line learning and an application to boosting. *J. Comput. Syst. Sci.* **1997**, *55*, 119–139. [CrossRef]
102. Lawry, J.; He, H. Linguistic decision trees for fusing tidal surge forecasting models. In *Combining Soft Computing and Statistical Methods in Data Analysis*; Springer: Berlin/Heidelberg, Germany, 2010; pp. 403–410.
103. Bentéjac, C.; Csörgő, A.; Martínez-Muñoz, G. A comparative analysis of gradient boosting algorithms. *Artif. Intell. Rev.* **2021**, *54*, 1937–1967. [CrossRef]
104. Chen, T.; Guestrin, C. Xgboost: A scalable tree boosting system. In Proceedings of the 22nd ACM Sigkdd International Conference on Knowledge Discovery and Data Mining, San Francisco, CA, USA, 13–17 August 2016, pp. 785–794.

105. Drucker, H. Improving regressors using boosting techniques. In Proceedings of the Fourteenth International Conference on Machine Learning (ICML 1997), Nashville, TN, USA, 8–12 July 1997; Volume 97, pp. 107–115.
106. Muis, S.; Apecechea, M.I.; Dullaart, J.; de Lima Rego, J.; Madsen, K.S.; Su, J.; Yan, K.; Verlaan, M. A high-resolution global dataset of extreme sea levels, tides, and storm surges, including future projections. *Front. Mar. Sci.* **2020**, *7*, 263. [CrossRef]
107. Sesmero, M.P.; Ledezma, A.I.; Sanchis, A. Generating ensembles of heterogeneous classifiers using stacked generalization. *Wiley Interdiscip. Rev. Data Min. Knowl. Discov.* **2015**, *5*, 21–34. [CrossRef]
108. Barton, M.; Lennox, B. Model stacking to improve prediction and variable importance robustness for soft sensor development. *Digit. Chem. Eng.* **2022**, *3*, 100034. [CrossRef]
109. Džeroski, S.; Ženko, B. Is combining classifiers with stacking better than selecting the best one? *Mach. Learn.* **2004**, *54*, 255–273. [CrossRef]
110. Breiman, L. Stacked regressions. *Mach. Learn.* **1996**, *24*, 49–64. [CrossRef]
111. Zucco, C. Multiple Learners Combination: Stacking. In *Encyclopedia of Bioinformatics and Computational Biology*; Ranganathan, S., Gribskov, M., Nakai, K., Schönbach, C., Eds.; Academic Press: Oxford, UK, 2019; pp. 536–538. [CrossRef]
112. Sill, J.; Takács, G.; Mackey, L.; Lin, D. Feature-weighted linear stacking. *arXiv* **2009**, arXiv:0911.0460.
113. Young, S.; Abdou, T.; Bener, A. Deep super learner: A deep ensemble for classification problems. In Proceedings of the Advances in Artificial Intelligence: 31st Canadian Conference on Artificial Intelligence, Canadian AI 2018, Toronto, ON, Canada, 8–11 May 2018; pp. 84–95.
114. Wolpert, D.H. Stacked generalization. *Neural Netw.* **1992**, *5*, 241–259. [CrossRef]
115. Ayyad, M.; Orton, P.M.; El Safty, H.; Chen, Z.; Hajj, M.R. Ensemble forecast for storm tide and resurgence from Tropical Cyclone Isaias. *Weather. Clim. Extrem.* **2022**, *38*, 100504. [CrossRef]
116. Kim, S.W.; Melby, J.A.; Nadal-Caraballo, N.C.; Ratcliff, J. A time-dependent surrogate model for storm surge prediction based on an artificial neural network using high-fidelity synthetic hurricane modeling. *Nat. Hazards* **2015**, *76*, 565–585. [CrossRef]
117. Guo, T. Hurricane Damage Prediction based on Convolutional Neural Network Models. In Proceedings of the 2021 2nd International Conference on Artificial Intelligence and Computer Engineering (ICAICE), Hangzhou, China, 5–7 November 2021; pp. 298–302.
118. Gebrehiwot, A.; Hashemi-Beni, L.; Thompson, G.; Kordjamshidi, P.; Langan, T.E. Deep convolutional neural network for flood extent mapping using unmanned aerial vehicles data. *Sensors* **2019**, *19*, 1486. [CrossRef]
119. Accarino, G.; Chiarelli, M.; Fiore, S.; Federico, I.; Causio, S.; Coppini, G.; Aloisio, G. A multi-model architecture based on Long Short-Term Memory neural networks for multi-step sea level forecasting. *Future Gener. Comput. Syst.* **2021**, *124*, 1–9. [CrossRef]
120. Kaur, S.; Gupta, S.; Singh, S.; Koundal, D.; Zaguia, A. Convolutional neural network based hurricane damage detection using satellite images. *Soft Comput.* **2022**, *26*, 7831–7845. [CrossRef]
121. Korzh, O.; Joaristi, M.; Serra, E. Convolutional neural network ensemble fine-tuning for extended transfer learning. In Proceedings of the Big Data–BigData 2018: 7th International Congress, Held as Part of the Services Conference Federation, SCF 2018, Seattle, WA, USA, 25–30 June 2018; pp. 110–123.
122. Becherer, N.; Pecarina, J.; Nykl, S.; Hopkinson, K. Improving optimization of convolutional neural networks through parameter fine-tuning. *Neural Comput. Appl.* **2019**, *31*, 3469–3479. [CrossRef]
123. Blalock, D.; Gonzalez Ortiz, J.J.; Frankle, J.; Guttag, J. What is the state of neural network pruning? *Proc. Mach. Learn. Syst.* **2020**, *2*, 129–146.
124. Araghinejad, S.; Azmi, M.; Kholghi, M. Application of artificial neural network ensembles in probabilistic hydrological forecasting. *J. Hydrol.* **2011**, *407*, 94–104. [CrossRef]
125. Chen, W.; Hong, H.; Li, S.; Shahabi, H.; Wang, Y.; Wang, X.; Ahmad, B.B. Flood susceptibility modelling using novel hybrid approach of reduced-error pruning trees with bagging and random subspace ensembles. *J. Hydrol.* **2019**, *575*, 864–873. [CrossRef]
126. Du, L.; Gao, R.; Suganthan, P.N.; Wang, D.Z. Bayesian optimization based dynamic ensemble for time series forecasting. *Inf. Sci.* **2022**, *591*, 155–175. [CrossRef]
127. Pham, B.T.; Jaafari, A.; Nguyen-Thoi, T.; Van Phong, T.; Nguyen, H.D.; Satyam, N.; Masroor, M.; Rehman, S.; Sajjad, H.; Sahana, M.; et al. Ensemble machine learning models based on Reduced Error Pruning Tree for prediction of rainfall-induced landslides. *Int. J. Digit. Earth* **2021**, *14*, 575–596. [CrossRef]
128. Rooney, N.; Patterson, D.; Nugent, C. Reduced ensemble size stacking [ensemble learning]. In Proceedings of the 16th IEEE International Conference on Tools with Artificial Intelligence, Boca Raton, FL, USA, 15–17 November 2004; pp. 266–271.
129. Naftaly, U.; Intrator, N.; Horn, D. Optimal ensemble averaging of neural networks. *Netw. Comput. Neural Syst.* **1997**, *8*, 283. [CrossRef]
130. Huang, W.; Hong, H.; Bian, K.; Zhou, X.; Song, G.; Xie, K. Improving deep neural network ensembles using reconstruction error. In Proceedings of the 2015 International joint conference on neural networks (IJCNN), Killarney, Ireland, 12–17 July 2015, pp. 1–7.
131. Zeng, X.; Yeung, D.S. Hidden neuron pruning of multilayer perceptrons using a quantified sensitivity measure. *Neurocomputing* **2006**, *69*, 825–837. [CrossRef]
132. Smith, C.; Jin, Y. Evolutionary multi-objective generation of recurrent neural network ensembles for time series prediction. *Neurocomputing* **2014**, *143*, 302–311. [CrossRef]
133. Shahhosseini, M.; Hu, G.; Pham, H. Optimizing ensemble weights and hyperparameters of machine learning models for regression problems. *Mach. Learn. Appl.* **2022**, *7*, 100251. [CrossRef]

134. Palaniswamy, S.K.; Venkatesan, R. Hyperparameters tuning of ensemble model for software effort estimation. *J. Ambient. Intell. Humaniz. Comput.* **2021**, *12*, 6579–6589. [CrossRef]
135. Snoek, J.; Larochelle, H.; Adams, R.P. Practical bayesian optimization of machine learning algorithms. *Adv. Neural Inf. Process. Syst.* Curran Associates, Inc.: Red Hook, NY, USA, 2012, Volume 25.
136. Wu, J.; Chen, X.Y.; Zhang, H.; Xiong, L.D.; Lei, H.; Deng, S.H. Hyperparameter optimization for machine learning models based on Bayesian optimization. *J. Electron. Sci. Technol.* **2019**, *17*, 26–40.
137. Priyadarshini, I.; Cotton, C. A novel LSTM–CNN–grid search-based deep neural network for sentiment analysis. *J. Supercomput.* **2021**, *77*, 13911–13932. [CrossRef] [PubMed]
138. Huang, G.B.; Chen, L. Enhanced random search based incremental extreme learning machine. *Neurocomputing* **2008**, *71*, 3460–3468. [CrossRef]
139. Agnihotri, A.; Batra, N. Exploring bayesian optimization. *Distill* **2020**, *5*, e26. [CrossRef]
140. Zhou, J.; Peng, T.; Zhang, C.; Sun, N. Data pre-analysis and ensemble of various artificial neural networks for monthly streamflow forecasting. *Water* **2018**, *10*, 628. [CrossRef]
141. Aloysius, N.; Geetha, M. A review on deep convolutional neural networks. In Proceedings of the 2017 International Conference on Communication and Signal Processing (ICCSP), Melmaruvathur, India, 6–8 April 2017; pp. 0588–0592.
142. Kiranyaz, S.; Avci, O.; Abdeljaber, O.; Ince, T.; Gabbouj, M.; Inman, D.J. 1D convolutional neural networks and applications: A survey. *Mech. Syst. Signal Process.* **2021**, *151*, 107398. [CrossRef]
143. Trice, A.; Robbins, C.; Philip, N.; Rumsey, M. *Challenges and Opportunities for Ocean Data to Advance Conservation and Management*; Ocean Conservancy: Washington, DC, USA, 2021.
144. Velioglu Sogut, D.; Yalciner, A.C. Performance comparison of NAMI DANCE and FLOW-3D® models in tsunami propagation, inundation and currents using NTHMP benchmark problems. *Pure Appl. Geophys.* **2019**, *176*, 3115–3153. [CrossRef]
145. Costa, W.; Idier, D.; Rohmer, J.; Menendez, M.; Camus, P. Statistical prediction of extreme storm surges based on a fully supervised weather-type downscaling model. *J. Mar. Sci. Eng.* **2020**, *8*, 1028. [CrossRef]
146. Cialone, M.A.; Massey, T.C.; Anderson, M.E.; Grzegorzewski, A.S.; Jensen, R.E.; Cialone, A.; Mark, D.J.; Pevey, K.C.; Gunkel, B.L.; McAlpin, T.O.; et al. *North Atlantic Coast Comprehensive Study (NACCS) Coastal Storm Model Simulations: Waves and Water Levels*; US Army Engineer Research and Development Center, Coastal and Hydraulics Laboratory: Vicksburg, MS, USA , 2015.
147. Yang, C.; Leonelli, F.E.; Marullo, S.; Artale, V.; Beggs, H.; Nardelli, B.B.; Chin, T.M.; De Toma, V.; Good, S.; Huang, B.; et al. Sea surface temperature intercomparison in the framework of the Copernicus Climate Change Service (C3S). *J. Clim.* **2021**, *34*, 5257–5283. [CrossRef]
148. Hersbach, H. Decomposition of the continuous ranked probability score for ensemble prediction systems. *Weather. Forecast.* **2000**, *15*, 559–570. [CrossRef]
149. Wallendorf, L.; Cox, D.T. *Coastal Structures and Solutions to Coastal Disasters 2015: Tsunamis*; American Society of Civil Engineers: Reston, VA, USA, 2017.
150. Conver, A.; Sepanik, J.; Louangsaysongkham, B.; Miller, S. *Sea, Lake, and Overland Surges from Hurricanes (SLOSH) Basin Development Handbook v2.0*; NOAA/NWS/Meteorological Development Laboratory: Silver Springs, MD, USA, 2008.
151. Miller, A.; Luscher, A. NOAA's national water level observation network (NWLON). *J. Oper. Oceanogr.* **2019**, *12*, S57–S66. [CrossRef]
152. Raschka, S. *Python Machine Learning*; Packt Publishing Ltd.: Birmingham, UK, 2015.
153. Yang, H. Data preprocessing. In *Data Mining: Concepts and Techniques* ; Pennsylvania State University, CiteSeerX, USA 2018.
154. Knapp, K.R.; Kruk, M.C.; Levinson, D.H.; Diamond, H.J.; Neumann, C.J. The International Best Track Archive for Climate Stewardship (IBTrACS). *Bull. Am. Meteorol. Soc.* **2010**, *91*, 363–376. [CrossRef]
155. Knapp, K.R.; Diamond, H.J.; Kossin, J.P.; Kruk, M.C.; Schreck, C.J. In *International Best Track Archive for Climate Stewardship (IBTrACS) Project*; Version 4; NOAA National Centers for Environmental Information: Asheville, NC, USA, 2018; [CrossRef]
156. NOAA National Data Buoy Center. In *Meteorological and Oceanographic Data Collected from the National Data Buoy Center Coastal-Marine Automated Network (C-MAN) and Moored (Weather) Buoys*; NOAA National Centers for Environmental Information, Dataset: Port Aransas, TX, USA, 1971.
157. Adebisi, N.; Balogun, A.L.; Min, T.H.; Tella, A. Advances in estimating Sea Level Rise: A review of tide gauge, satellite altimetry and spatial data science approaches. *Ocean. Coast. Manag.* **2021**, *208*, 105632. [CrossRef]
158. Kyprioti, A.P.; Taflanidis, A.A.; Plumlee, M.; Asher, T.G.; Spiller, E.; Luettich, R.A.; Blanton, B.; Kijewski-Correa, T.L.; Kennedy, A.; Schmied, L. Improvements in storm surge surrogate modeling for synthetic storm parameterization, node condition classification and implementation to small size databases. *Nat. Hazards* **2021**, *109*, 1349–1386. [CrossRef]
159. Queipo, N.V.; Nava, E. A gradient boosting approach with diversity promoting measures for the ensemble of surrogates in engineering. *Struct. Multidiscip. Optim.* **2019**, *60*, 1289–1311. [CrossRef]
160. Freeman, J.; Velic, M.; Colberg, F.; Greenslade, D.; Divakaran, P.; Kepert, J. Development of a tropical storm surge prediction system for Australia. *J. Mar. Syst.* **2020**, *206*, 103317. [CrossRef]
161. Beuzen, T.; Goldstein, E.B.; Splinter, K.D. Ensemble models from machine learning: An example of wave runup and coastal dune erosion. *Nat. Hazards Earth Syst. Sci.* **2019**, *19*, 2295–2309. [CrossRef]
162. Goodarzi, L.; Banihabib, M.E.; Roozbahani, A. A decision-making model for flood warning system based on ensemble forecasts. *J. Hydrol.* **2019**, *573*, 207–219. [CrossRef]

163. Chang, L.C.; Amin, M.Z.M.; Yang, S.N.; Chang, F.J. Building ANN-based regional multi-step-ahead flood inundation forecast models. *Water* **2018**, *10*, 1283. [CrossRef]
164. Neal, B.; Mittal, S.; Baratin, A.; Tantia, V.; Scicluna, M.; Lacoste-Julien, S.; Mitliagkas, I. A modern take on the bias-variance tradeoff in neural networks. *arXiv* **2018**, arXiv:1810.08591.
165. Ganaie, M.A.; Hu, M.; Malik, A.; Tanveer, M.; Suganthan, P. Ensemble deep learning: A review. *Eng. Appl. Artif. Intell.* **2022**, *115*, 105151. [CrossRef]
166. James, G.; Witten, D.; Hastie, T.; Tibshirani, R. *An Introduction to Statistical Learning*; Springer: Berlin/Heidelberg, Germany, 2013;m Volume 112.
167. Ortega, L.A.; Cabañas, R.; Masegosa, A. Diversity and generalization in neural network ensembles. In Proceedings of the International Conference on Artificial Intelligence and Statistics, Valencia, Spain, 28–30 March 2022; pp. 11720–11743.
168. Tsymbal, A.; Pechenizkiy, M.; Cunningham, P. Diversity in search strategies for ensemble feature selection. *Inf. Fusion* **2005**, *6*, 83–98. [CrossRef]
169. Dutta, H. Measuring Diversity in Regression Ensembles. In Proceedings of the ICAI, Las Vegas, NV, USA, 13–16 July 2009; Volume 9, p. 17.
170. Horsburgh, K.; Flowerdew, J. Real-Time Coastal Flood Forecasting. In *Applied Uncertainty Analysis for Flood Risk Management*; World Scientific Publishing Co. Pte. Ltd.: London, UK, 2014; pp. 538–562.
171. Murphy, A.H. Skill scores based on the mean square error and their relationships to the correlation coefficient. *Mon. Weather. Rev.* **1988**, *116*, 2417–2424. [CrossRef]
172. Tonani, M.; Pinardi, N.; Fratianni, C.; Pistoia, J.; Dobricic, S.; Pensieri, S.; De Alfonso, M.; Nittis, K. Mediterranean Forecasting System: Forecast and analysis assessment through skill scores. *Ocean. Sci.* **2009**, *5*, 649–660. [CrossRef]

Journal of
Marine Science and Engineering

Article

Applicability Evaluation of the Global Synthetic Tropical Cyclone Hazard Dataset in Coastal China

Xiaomin Li [1], Qi Hou [2], Jie Zhang [1,2,*], Suming Zhang [2], Xuexue Du [2,3] and Tangqi Zhao [2]

1 First Institute of Oceanography, Ministry of Natural Resources of China, Qingdao 266061, China; lixiaomin@fio.org.cn
2 College of Oceanography and Space Informatics, China University of Petroleum (East China), Qingdao 266580, China; h17853683859@163.com (Q.H.); sumingzhang@s.upc.edu.cn (S.Z.); zjupcpaper@163.com (X.D.); zhaotangqi0919@163.com (T.Z.)
3 Duyun Power Supply Bureau of Guizhou Power Grid Co., Ltd., Duyun 558000, China
* Correspondence: zhangjie@upc.edu.cn

Abstract: A tropical cyclone dataset is an important data source for tropical cyclone disaster research, and the evaluation of its applicability is a necessary prerequisite. The Global Synthetic Tropical Cyclone Hazard (GSTCH) dataset is a dataset of global tropical cyclone activity for 10,000 years from 2018, and has become accepted as a major data source for the study of global tropical cyclone hazards. On the basis of the authoritative Tropical Cyclone Best Track (TCBT) dataset proposed by the China Meteorological Administration, this study evaluated the applicability of the GSTCH dataset in relation to two regions: the Northwest Pacific and China's coastal provinces. For the Northwest Pacific, the results show no significant differences in the means and standard deviations of landfall wind speed, landfall pressure, and annual occurrence number between the two datasets at the 95% confidence level. They also show the cumulative distributions of central minimum pressure and central maximum wind speed along the track passed the Kolmogorov–Smirnov (K-S) test at the 95% confidence level, thereby verifying that the GSTCH dataset is consistent with the TCBT dataset at sea-area scale. For China's coastal provinces, the results show that the means or standard deviations of tropical cyclone characteristics between the two datasets were not significantly different in provinces other than Guangdong and Hainan, and further analysis revealed that the cumulative distributions of the tropical cyclone characteristics in Guangdong and Hainan provinces passed the K-S test at the 95% confidence level, thereby verifying that the GSTCH dataset is consistent with the TCBT dataset at province scale. The applicability evaluation revealed that no significant differences exist between most of the tropical cyclone characteristics in the TCBT and GSTCH datasets, and that the GSTCH dataset is an available and reliable data source for tropical cyclone hazard studies in China's coastal areas.

Keywords: Global Synthetic Tropical Cyclone Hazard (GSTCH) dataset; Tropical Cyclone Best Track (TCBT) dataset; tropical cyclone; applicability evaluation; coastal China

Citation: Li, X.; Hou, Q.; Zhang, J.; Zhang, S.; Du, X.; Zhao, T. Applicability Evaluation of the Global Synthetic Tropical Cyclone Hazard Dataset in Coastal China. *J. Mar. Sci. Eng.* **2024**, *12*, 73. https://doi.org/10.3390/jmse12010073

Academic Editor: Deniz Velioglu Sogut

Received: 4 November 2023
Revised: 16 December 2023
Accepted: 19 December 2023
Published: 27 December 2023

1. Introduction

Tropical cyclones (TCs), also referred to as typhoons, are one of the most severe types of natural disasters [1], and usually manifest as strong destructive winds and heavy precipitation that can severely impact people, economies and the environment in coastal areas when they make landfall [2,3]. The damage caused by TCs includes wind-induced damage and storm surges risk due to rising water levels [4]. Storm surges, which are the main secondary disaster hazard triggered by TCs, present high disaster intensity [5], and are often the greatest threat to life and property [6,7]. With rising sea levels and rapid economic development in coastal areas, the losses caused by TCs have dramatically increased and will pose an increasing and extreme hazard around the globe [8,9]. It is therefore crucial to study TC hazards for TC risk assessments and corresponding TC risk management.

A reliable TC dataset is of great importance both for TC hazards research and for sustainable development in coastal areas [10–12]. Currently, the most commonly used TC dataset resources include the China Meteorological Administration (CMA) dataset, the Japan Meteorology Agency (JMA) dataset, and the Joint Typhoon Warning Center (JTWC) dataset [13]. According to TC records, approximately 90 ($\pm$10) TCs per year are formed globally [14], of which 16, on average, make landfall with wind speeds greater than 33 m/s [15]. It is thus clear that the amount of TC data available for regional hazard research is limited, and that this problem must be addressed by the establishment of suitable datasets.

To expand the TC data resource, many studies have used historical tropical cyclone data (HTCD) to generate a large amount of synthetic tropical cyclone data (STCD) using various methods. One method is to create STCD through statistical resampling and the modeling of historical TC tracks and intensities of meteorological datasets from climate patterns [16–21]. This method, which has been explored widely, has been used by Bloemendaal et al. to create the Global Synthetic Tropical Cyclone Hazard (GSTCH) dataset [2]. The GSTCH dataset, which includes information on TC track, intensity, and size, is particularly useful for TC risk assessment because it serves as input for storm surge and wave impact modeling and has characteristics that are important for wind damage assessment [22]. At the same time, the dataset length of 10,000 years enables it to perform proper statistical analysis of the return periods of various landfalling TCs.

Before a dataset can be applied to a specific area and a specific research purpose, its availability and reliability must be evaluated. Many previous studies have shown that the mean, standard deviation, frequency distribution and cumulative distribution of the TC features can be used to assess the consistency of STCD with HTCD. Bloemendaal et al. compared the means and standard deviations of TC features, believing that a mean value within the standard deviation verified the consistency of STCD with HTCD [2]. Vickery et al. performed a T-test on the mean and an F-test on the standard deviation of each TC feature to evaluate whether statistically significant differences existed between STCD and HTCD. Then, for those TC features whose mean or standard deviation values did not pass the test, a Chi-squared test was used to examine the frequency distribution [16]. Similarly, Nakajo et al. [23] and Lee et al. [24] also compared the frequency distribution and the cumulative distribution of TC features in STCD and HTCD to evaluate the performance of STCD. Additionally, the degree of consistency between STCD and HTCD was analyzed for specific study areas by applying the path assessment method to the paths of TCs in both datasets [2,13,23,24]. In summary, the mean, standard deviation, frequency distribution, cumulative distribution, and corresponding hypothesis tests have primarily been used to evaluate the degree of consistency between STCD and HTCD.

Because of the global coverage and the large number of TCs, the GSTCH dataset is also a crucial data source for TC hazard assessment and TC risk management in coastal China. The objective of this study is to evaluate the applicability of the GSTCH dataset for further research and application in coastal China. The standard dataset for the evaluation is the Tropical Cyclone Best Track (TCBT) dataset proposed by the CMA [25,26]. The TC characteristics used include the central maximum wind speed along the track, central minimum pressure along the track, landfall wind speed, landfall pressure, annual occurrence number, and annual landfall number. The Northwest Pacific is the sea area with the highest frequency, strongest intensity, and greatest impact on China in terms of global TCs [27,28]. Over one third of global TCs occurred in this area, and approximately nine TCs made landfall in the coastal areas of China per year from 1950 to 2019 [29]. Therefore, the applicability evaluation of the GSTCH dataset in this study is performed in relation to two regions—the Northwest Pacific and the provinces of coastal China.

2. Materials and Methods

2.1. The GSTCH Dataset

The GSTCH dataset on TC characteristics on a global scale was presented by Bloemendaal et al. using a newly developed synthetic resampling algorithm called the Synthetic Tropical cyclOne geneRation Model (STORM). TC characteristics in the GSTCH dataset comprise the time of occurrence (year and month), order of occurrence, longitude, latitude, central minimum pressure, central maximum wind speed, radius of maximum wind speed, whether landfall occurred and distance from land. These characteristics were extracted from the global historical dataset International Best Track Archive for Climate Stewardship (IBTrACS) for the time period 1980–2018 (38 years of data), and were statistically extended to 10,000 years of TC activity under present climate conditions [2,30]. The IBTrACS dataset was developed under the auspices of the World Data Center for Meteorology of the National Oceanic and Atmospheric Administration by collecting and integrating TC datasets from 12 national meteorological offices that included those of China, Japan, the United States, and Australia [31,32]. Bloemendaal et al. validated the performance of the GSTCH dataset by demonstrating that the mean values of various TC characteristics are within one standard deviation from those found in the IBTrACS dataset and showed that this dataset can be used by anyone interested in studying the different aspects of TCs and the wind and storm surge hazards they trigger [2,22].

2.2. The TCBT Dataset

The TCBT dataset is a multi-source, multi-time-scale, multi-spatial-scale, and comprehensive TC database, and includes relevant features of all TCs that passed across the Northwest Pacific during 1949–2021, e.g., the time of occurrence (year, month, day, and hour), central longitude and latitude, central minimum pressure, and central maximum wind speed of each TC [26,29]. The CMA overseen the compilation and release of the TCBT dataset, and it has developed strict procedures and rules to ensure that the dataset incorporates long temporal coverage, wide spatial coverage, various observational elements, and high accuracy [33]. The TCBT dataset has been passed through rigorous quality control and has always been considered to be the most authoritative TC dataset for the coastal areas of China [9]. Therefore, this study selects the TCBT dataset as the benchmark to evaluate the GSTCH dataset's applicability in coastal China.

This study considered a 32 year (1990–2021) TCBT dataset. For comparability, 10 different sets of 32 year periods were selected randomly from the GSTCH dataset, and the statistical averages of the evaluation indicators of those 10 sets were taken as the evaluation indicators of TC characteristics. Finally, for the Northwest Pacific, 7122 TCs were selected from the GSTCH dataset, and 802 TCs were selected from the TCBT dataset. For coastal China provinces, 2230 TCs were selected from the GSTCH dataset, and 234 TCs were selected from the TCBT dataset.

2.3. TC Characteristics for Evaluation

TC intensity (peak intensity and landfall intensity), annual occurrence frequency, and annual landfall frequency are key TC characteristics [23]. The central maximum wind speed along the track and the central minimum pressure along the track represent the peak intensity of a TC. The landfall wind speed and landfall pressure represent the intensity of a TC when it makes landfall. The annual occurrence and landfall numbers represent the annual occurrence frequency and annual landfall frequency, respectively. Therefore, this study considered the central maximum wind speed along the track, central minimum pressure along the track, landfall wind speed, landfall pressure, annual occurrence number, and annual landfall number as typical TC characteristics for evaluation to verify the degree of consistency between the GSTCH and TCBT datasets.

2.4. Indicators for Evaluation

The degree of consistency between the GSTCH and TCBT datasets was evaluated using the mean, standard deviation, frequency distribution, cumulative distribution, and the corresponding T-test, F-test, Chi-squared test, and Kolmogorov–Smirnov (K-S) test. The mean and standard deviation reflect the average level and fluctuation of the TC characteristics of the GSTCH and TCBT datasets. The frequency distribution and the cumulative distribution indicate the overall distribution of the TC characteristics. T-test, F-test, Chi-squared test, and K-S test can determine whether statistically significant differences exist between the mean, standard deviation, frequency distribution, and cumulative distribution of the TC characteristics in the GSTCH and TCBT datasets.

The formulas for the calculation of the mean, standard deviation, T-test statistic, and F-test statistic [16] are as follows:

$$\overline{X_1} = \frac{\sum_{i=1}^{n_1} X_{i1}}{n_1} \tag{1}$$

$$\overline{X_2} = \frac{\sum_{i=1}^{n_2} X_{i2}}{n_2} \tag{2}$$

$$S_1 = \sqrt{\frac{\sum_{i=1}^{n_1} \left(X_{i1} - \overline{X_1}\right)^2}{n_1 - 1}} \tag{3}$$

$$S_2 = \sqrt{\frac{\sum_{i=1}^{n_2} \left(X_{i2} - \overline{X_2}\right)^2}{n_2 - 1}} \tag{4}$$

$$t = \frac{\overline{X_1} - \overline{X_2}}{\sqrt{\frac{(n_1-1)S_1^2+(n_2-1)s_2^2}{n_1+n_2-2}\left(\frac{1}{n_1} + \frac{1}{n_2}\right)}} \tag{5}$$

$$f = \frac{S_1^2}{S_2^2} \tag{6}$$

where $\overline{X_1}$ and $\overline{X_2}$ are the means of the TC characteristics in the TCBT dataset and the GSTCH dataset, respectively; S_1 and S_2 are the standard deviations of the TC characteristics in the TCBT dataset and the GSTCH dataset, respectively; t is the T-test statistic; f is the F-test statistic; X_{i1} and X_{i2} are the values of the TC characteristics in the TCBT dataset and the GSTCH dataset respectively, read directly from the two datasets; and n_1 and n_2 are the numbers of TC characteristics included in the TCBT dataset and the GSTCH dataset, respectively.

The formulas for the calculation of the frequency distribution and the Chi-squared test statistic [34] are as follows:

$$\mathrm{P}_1 = \frac{f_{i1}}{n_1}(i = 1, 2, \ldots\ldots, m) \tag{7}$$

$$\mathrm{P}_2 = \frac{f_{i2}}{n_2}(i = 1, 2, \ldots\ldots, m) \tag{8}$$

$$X_{df}^2 = \sum_{i=1}^{m} \frac{(f_{i1} - f_{i2})^2}{f_{i1}} \tag{9}$$

where P_1 and P_2 are the frequency distributions of the TC characteristics in the TCBT dataset and the GSTCH dataset, respectively; X_{df}^2 is the Chi-squared test statistic; f_{i1} and f_{i2} are the frequencies of the different values of TC characteristics falling into each group i (the groups are incremented according to the index i) in the TCBT dataset and the GSTCH dataset, respectively; and m is the statistical grouping of the values of TC characteristics in the TCBT and GSTCH datasets into m groups. The m value is determined by the group spacings of the frequency distribution histograms and the magnitude of the values of TC characteristics. The group spacings of the frequency distribution histograms of central maximum wind speed along the track and landfall wind speed refer to the notice of the CMA: "About the Implementation of the National Standard of Tropical Cyclone Rating" GB/T 19201-2006 [35], and the group spacings of the frequency distribution histograms of the central minimum pressure along the track and landfall pressure refer to the Saffir–Simpson Hurricane Wind Scale [36]. The maximum and minimum values of the abscissa of the frequency distribution histogram are determined from the maximum and minimum values of the TC characteristics in the TCBT and GSTCH datasets.

The formulas for the calculation of the cumulative distribution and the K-S test statistics [37] are as follows:

$$\mathrm{F}_1(X_{i1}) = \mathrm{P}\{X_{i1} \leq X\}(i = 1, 2, \ldots\ldots, m) \tag{10}$$

$$\mathrm{F}_2(X_{i2}) = \mathrm{P}\{X_{i2} \leq X\}(i = 1, 2, \ldots\ldots, m) \tag{11}$$

$$\mathrm{D} = sup|\mathrm{F}_1(X_{i1}) - \mathrm{F}_2(X_{i2})| \tag{12}$$

where $\mathrm{F}_1(X_{i1})$ and $\mathrm{F}_2(X_{i2})$ are the cumulative distributions of the TC characteristics in the TCBT dataset and the GSTCH dataset, respectively. On the basis of the grouping of the values of the TC characteristics in the TCBT and GSTCH datasets into m groups, the cumulative distribution is the probability that X_{i1} is less than X in the TCBT dataset, and that the X_{i2} is less than X in the GSTCH dataset. The groupings and maximum values of the TC characteristics determine the X. The groupings of the central maximum wind speed along the track and landfall wind speed are referred to in the notice of the CMA: "About the Implementation of the National Standard of Tropical Cyclone Rating" GB/T 19201-2006 [35], and the groupings of the central minimum pressure along the track and landfall pressure refer to the Saffir–Simpson Hurricane Wind Scale [36]. In Equation (12), D is the K-S test statistic, and sup represents the upper-bound function. If set A of real numbers exists such that no number in A exceeds a minimum real number M, then M is the upper bound of set A. According to the definition of the upper bound function, the K-S test statistic in this study took the absolute value of the maximum difference of the cumulative distributions of the TCBT and GSTCH datasets.

The outcomes of the T-test, F-test, Chi-squared test, and K-S test are statistical hypothesis tests. Their original hypotheses are that the means, standard deviations, frequency distributions, and cumulative distributions of the TC characteristics in the GSTCH and TCBT datasets are not statistically significantly different. In this study, the confidence level of the hypothesis test is set at 95% ($\alpha = 1 - 95\% = 0.05$), indicating a 95% probability that the original hypothesis is correct. SPSS software (version: v28.0.1.1) is used to obtain the T-test statistics (and the corresponding p values), F-test statistics (and the corresponding p values), and Chi-squared test statistics (and the corresponding p values). PyCharm software (version: 2022.1.4) is used to obtain the K-S test statistics and the corresponding p values. Comparison of p value and α value can reveal whether the original hypotheses of the T-test, F-test, Chi-squared test, and K-S test are valid. The relationship between the p value and α value is shown in Table 1.

Table 1. Relationship between the p value and α value.

p-Value	Whether the Original Hypothesis Is Established	Statistical Significance
$p > \alpha$	Established	The evaluation indicators of TC characteristics in the TCBT dataset and the GSTCH dataset do not show a significant difference
$p < \alpha$	Not Established	The evaluation indicators of TC characteristics in the TCBT dataset and the GSTCH dataset show a significant difference

2.5. Specific Process for Evaluation

The applicability evaluation of the GSTCH dataset in coastal China focuses on two regions: the Northwest Pacific and China's coastal provinces. The specific steps of the research framework are shown in Figure 1. First, the means and standard deviations of the TC characteristics in the GSTCH and TCBT datasets are calculated for the two study regions. Then, T-tests and F-tests with 95% confidence intervals are performed on the means and standard deviations, respectively. If the means are within the standard deviations of each other, and if the means and standard deviations pass the T-tests and the F-tests, respectively, the consistency between the GSTCH and TCBT datasets is considered verified for the coastal areas of China. If the means of the TC characteristics in the GSTCH and TCBT datasets are not within the standard deviations, and if the means or standard deviations of the TC features are statistically significantly different, further analysis is performed on their frequency and cumulative distributions. If the frequency distributions of the TC characteristics pass the Chi-squared test at the 95% confidence level or if the cumulative distributions pass the K-S test at the 95% confidence level, the consistency between the GSTCH and TCBT datasets is considered verified for the coastal areas of China.

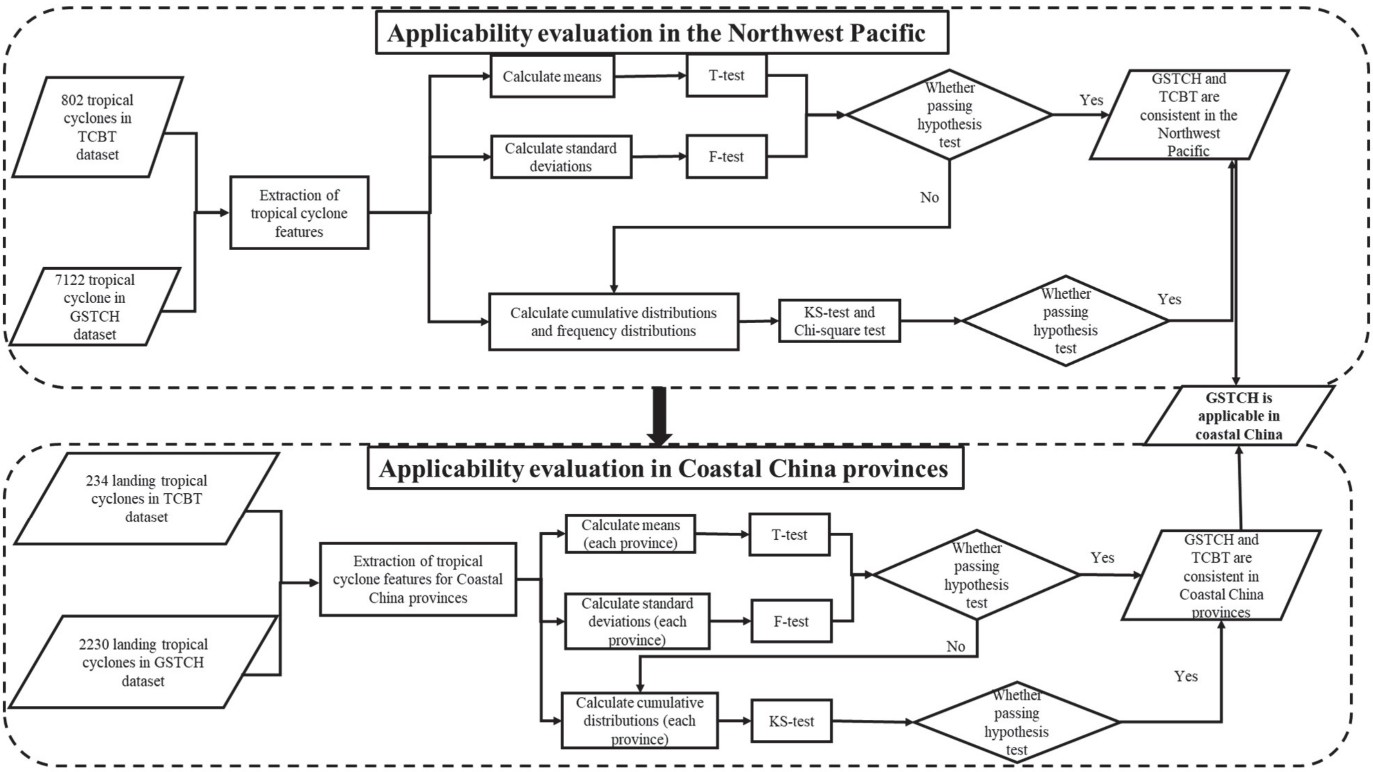

Figure 1. The research framework of this study.

3. Results

3.1. The Northwest Pacific

3.1.1. Means and Standard Deviations

Table 2 and Figure 2 compare the means and standard deviations of the central maximum wind speed along the track, landfall wind speed, central minimum pressure along the track, landfall pressure, annual occurrence number, and annual landfall number of the TCs in the Northwest Pacific in the GSTCH and TCBT datasets. The differences between the means and the standard deviations of the landfall pressure, landfall wind speed, and annual occurrence number are small. The mean of the central minimum pressure along the track in the GSTCH dataset is lower than that in the TCBT dataset, and the mean of the central maximum wind speed along the track in the GSTCH dataset is higher than that in the TCBT dataset. Nevertheless, all of these fall within the standard deviation of each other. Except for the annual landfall number, the means of TC characteristics in the GSTCH and TCBT datasets are within the standard deviations of each other. In summary, the GSTCH dataset successfully reproduces the intensity and annual occurrence frequency of TCs in the Northwest Pacific.

Table 2. Means and standard deviations of TC characteristics in the Northwest Pacific.

TC Characteristics	Dataset	Mean	*t*	P (*t*)	Standard Deviation	*f*	P (*f*)
Central maximum wind speed along the track (m/s)	TCBT GSTCH	37.315 42.805	−0.049	0.961	14.149 13.801	33.329	0
Landfall wind speed (m/s)	TCBT GSTCH	31.232 30.972	0.312	0.755	10.757 9.135	6.732	0.1
Central minimum pressure along the track (hpa)	TCBT GSTCH	964.041 956.491	5.075	0.001	26.363 28.335	0.754	0.385
Landfall pressure (hpa)	TCBT GSTCH	974.518 972.096	1.523	0.128	18.691 19.03	1.545	0.214
Annual occurrence number (item)	TCBT GSTCH	25.063 22.256	1.612	0.112	4.472 4.424	0.256	0.614
Annual landfall number (item)	TCBT GSTCH	7 11.335	−8.317	0	2 3.135	1.89	0.174

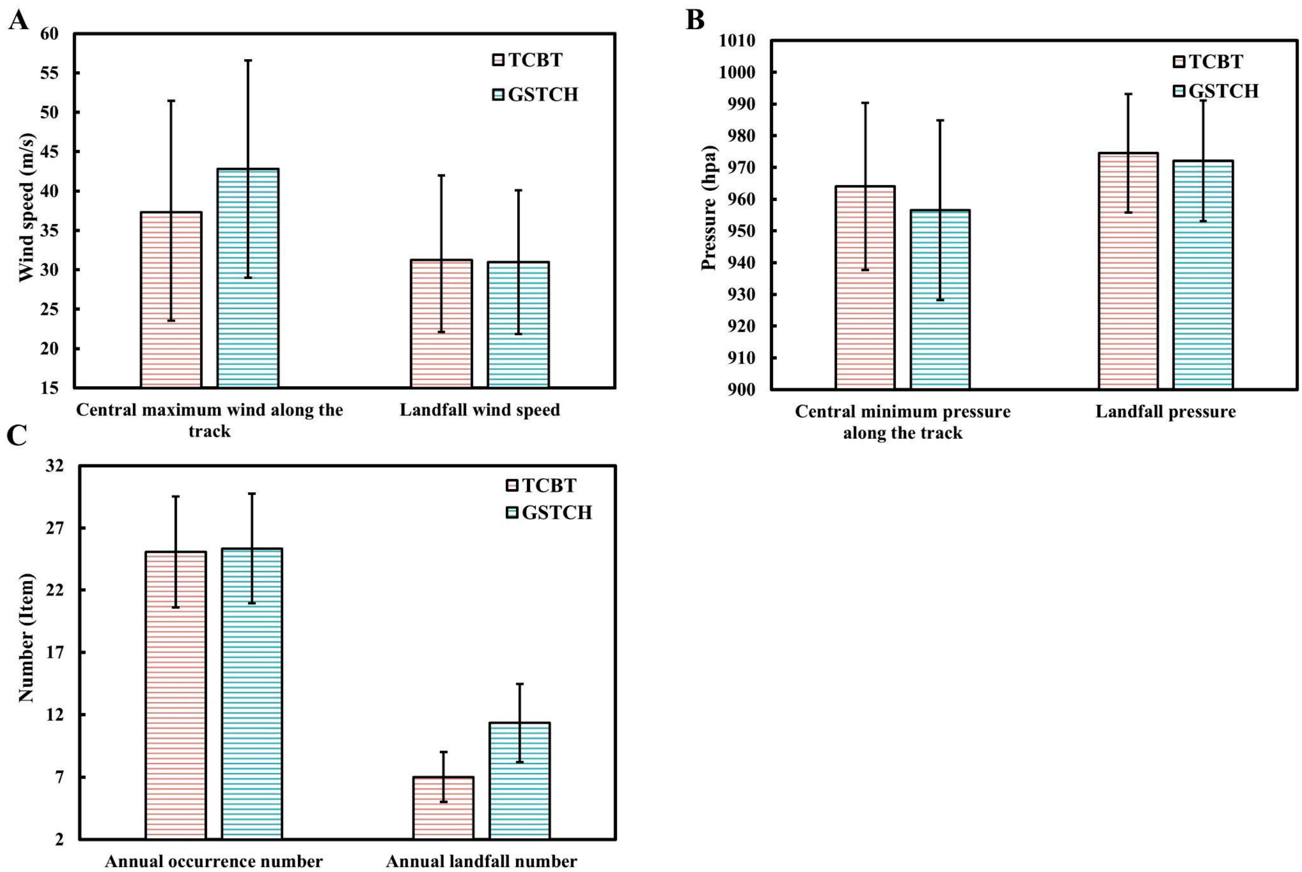

Figure 2. Means and standard deviations of Tropical cyclone (TC) characteristics. (**A**) Central maximum wind speed along the track, and Landfall wind speed. (**B**) Central minimum pressure along the track, and Landfall pressure. (**C**) Annual occurrence number, and Annual landfall number) in the Northwest Pacific.

The T-tests and F-tests were performed to determine whether the means and standard deviations of the TC characteristics in the GSTCH and TCBT datasets are equivalent. As shown in Table 2, the means of the central minimum pressure along the track and the annual landfall number failed the T-test at the 95% confidence level, and the standard deviation of the central maximum wind speed along the track failed the F-test at the 95% confidence level. Therefore, the frequency distributions and cumulative distributions of the central maximum wind speed along the track, central minimum pressure along the track, and annual landfall number of the TCs in the GSTCH and TCBT datasets were further compared and analyzed.

3.1.2. Frequency Distributions and Cumulative Distributions

Figure 3 shows that the frequency distributions of the central maximum wind speed along the track, central minimum pressure along the track, and annual landfall number of the TCs in the GSTCH and TCBT datasets are not in good agreement. Comparison of the cumulative distributions of the TC characteristics is another way to verify the degree of consistency between the GSTCH and TCBT datasets. The cumulative distributions of the central maximum wind speed and the central minimum pressure along the track of the GSTCH and TCBT datasets are in good agreement. However, the cumulative distributions of the annual landfall number are less consistent (Figure 3). The Chi-squared test results on the frequency distributions and the K-S test results on the cumulative distributions are listed in Table 3. The cumulative distributions of the central maximum wind speed along the track and the central minimum pressure along the track in the GSTCH dataset pass the K-S test at the 95% confidence level.

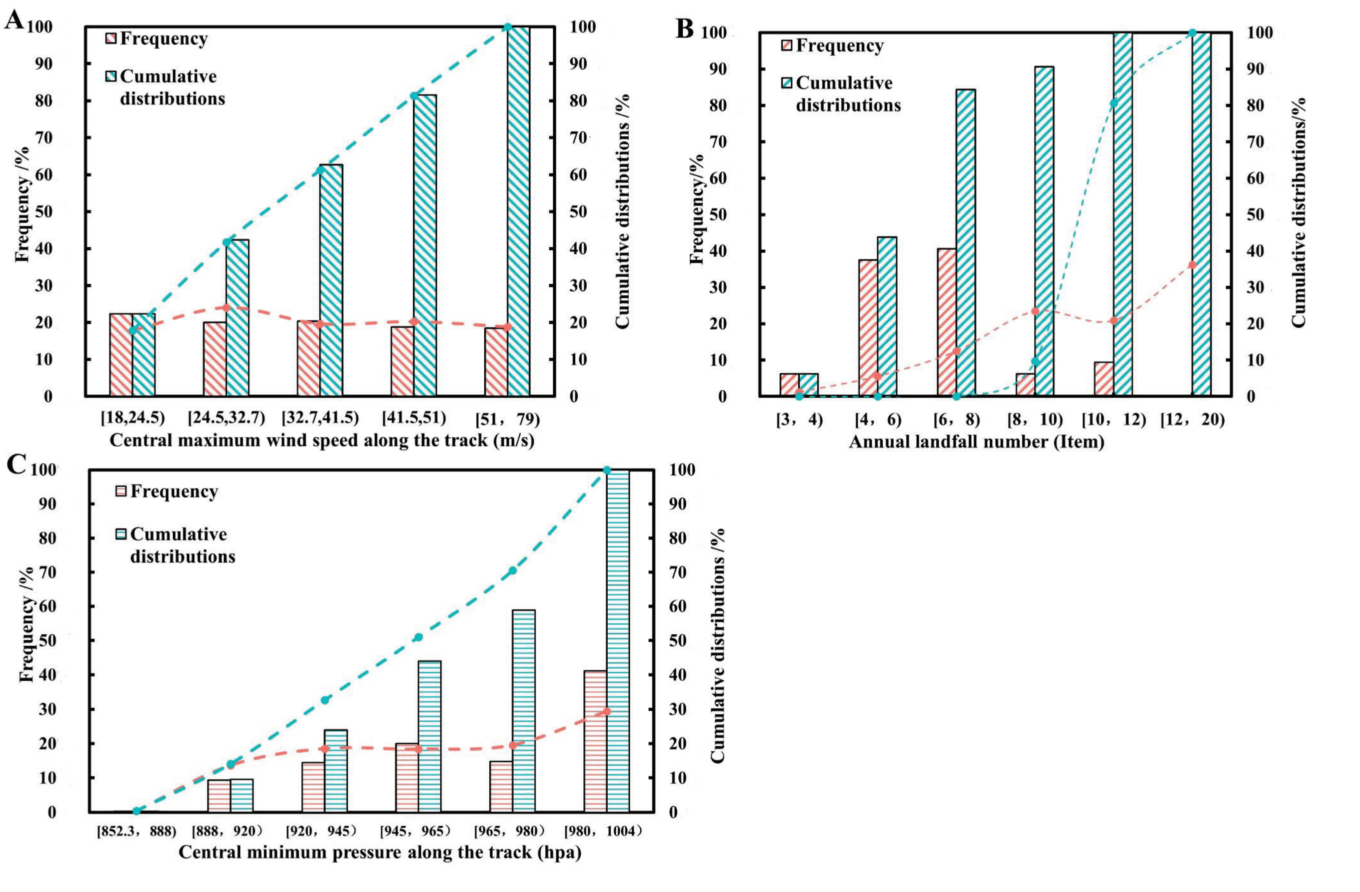

Figure 3. Frequency and cumulative distributions of the central maximum wind speed along the track (**A**), the annual landfall number (**B**), and the central minimum pressure along the track (**C**) in the Northwest Pacific (broken lines represent GSTCH data; bar charts represent TCBT data).

Table 3. Results of the Chi-squared test and Kolmogorov–Smirnov (K-S) test in the Northwest Pacific.

TC Characteristics	X^2_{df}	P (X^2_{df})	D	P (D)
Central maximum wind speed along the track (m/s)	18.41	0.001	0.1254	0.0789
Central minimum pressure along the track (hpa)	57.645	0	0.1237	0.0946
Annual landfall number (item)	51.463	0	0.5625	5.223×10^{-5}

In sum, the applicability evaluation results in the Northwest Pacific reveal that there is no statistically significant difference between the means and standard deviations of the landfall wind speed, landfall pressure, and annual occurrence number of the GSTCH dataset and the TCBT dataset at the 95% confidence level. The cumulative distributions of the central minimum pressure and central maximum wind speed along the track pass the K-S test at the 95% confidence level, verifying that the GSTCH dataset is consistent with the TCBT dataset at the sea-area scale.

3.2. China's Coastal Provinces

3.2.1. Means and Standard Deviations

Figure 4 shows the number of TCs in the TCBT and GSTCH datasets that made landfall in each province. The study period of the TCBT and GSTCH datasets is 32 years, with the former ranging from 1990 to 2021 and the latter being the ensemble average of 10 different sets of 32 year periods which are selected at random from the GSTCH dataset.

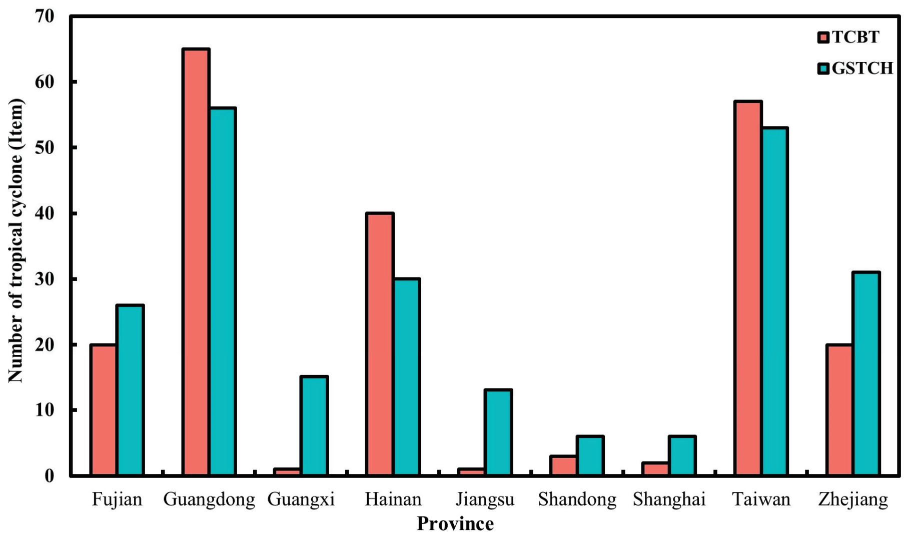

Figure 4. Number of TCs that made landfall in China's coastal provinces (item).

Figure 4 clearly shows that the trend of the number of TCs making landfall in each province in the GSTCH and TCBT datasets is broadly consistent. The landfalling TCs are concentrated mainly in Fujian, Guangdong, Hainan, Taiwan, and Zhejiang provinces, accounting for approximately 97% of the total number of TCs making landfall along the coast of China. In descending order, the provinces with the highest frequency of landfalling TCs are Guangdong, Taiwan, Hainan, Zhejiang, and Fujian. The TCs making landfall in the provinces of Guangdong, Taiwan, and Hainan, that are in the coastal area of southern China, account for 60.4% of the total number of landfalling TCs annually. The TCs making landfall in the provinces of Zhejiang and Fujian, in the coastal area of eastern China, account for 37.5% of the total number of landfalling TCs annually.

Overall, the GSTCH dataset underestimates the number of TCs that make landfall in Guangdong, Hainan and Taiwan provinces, and overestimates the number of TCs that make landfall in Fujian and Zhejiang provinces. The TCBT dataset only includes TC data for a period of 32 years, and some provinces have very few TCs, making it ineffective when comparing the number of TC landfalls within each province (Figure 4). Therefore, further analysis of the annual number of landfalling TCs in the GSTCH and TCBT datasets was performed in the provinces of Fujian, Guangdong, Hainan, Taiwan, and Zhejiang. On the basis of the TCs that made landfall in the above provinces in the GSTCH and TCBT datasets, the means and standard deviations of the TC characteristics relevant to each province are listed in Table 4 and illustrated in Figure 5.

Table 4. Means and standard deviations of TC characteristics in China's coastal provinces.

Province	TC Characteristics	Dataset	Mean	*t*	P (*t*)	Standard Deviation	*f*	P (*f*)
Guangdong	Central maximum wind speed along the track (m/s)	TCBT	35.089	−0.935	0.352	11.785	0.667	0.416
		GSTCH	37.008			9.958		
	Central minimum pressure along the track (hpa)	TCBT	968.089	2.484	0.014	20.886	0.574	0.45
		GSTCH	958.223			22.657		
	Landfall wind speed (m/s)	TCBT	29.494	1.154	0.251	9.808	6.476	0.012
		GSTCH	27.608			7.002		
	Landfall pressure(hpa)	TCBT	977.063	−0.476	0.635	16.337	0.48	0.51
		GSTCH	978.351			11.403		
	Annual landfall number (item)	TCBT	2.469	3.183	0.002	1.502	6.221	0.015
		GSTCH	1.469			0.95		
Hainan	Central maximum wind speed along the track (m/s)	TCBT	32.271	0.653	0.516	14.822	2.64	0.108
		GSTCH	30.277			9.765		
	Central minimum pressure along the track (hpa)	TCBT	971.646	0.292	0.771	26.319	0.65	0.422
		GSTCH	970.007			20.127		
	Landfall wind speed (m/s)	TCBT	26.583	0.991	0.325	9.9	8.646	0.004
		GSTCH	24.643			5.143		
	Landfall pressure(hpa)	TCBT	980.896	−0.129	0.898	16.782	0.64	0.45
		GSTCH	981.327			9.249		
	Annual landfall number (item)	TCBT	1.5	2.143	0.036	1.016	1.117	0.295
		GSTCH	0.967			0.967		
Taiwan	Central maximum wind speed along the track (m/s)	TCBT	42.053	0.468	0.641	14.043	1.913	0.17
		GSTCH	40.901			11.157		
	Central minimum pressure along the track (hpa)	TCBT	955.667	1.629	0.106	25.738	0.572	0.451
		GSTCH	947.48			26.455		
	Landfall wind speed (m/s)	TCBT	34.386	0.703	0.483	11.865	2.773	0.099
		GSTCH	32.95			8.974		
	Landfall pressure(hpa)	TCBT	969.421	0.535	0.593	20.842	0.446	0.506
		GSTCH	967.371			18.713		
	Annual landfall number (item)	TCBT	1.781	0.618	0.539	1.289	0.516	0.475
		GSTCH	1.594			1.132		
Zhejiang	Central maximum wind speed along the track (m/s)	TCBT	45.105	0.538	0.593	10.619	0.07	0.792
		GSTCH	43.498			10.031		
	Central minimum pressure along the track (hpa)	TCBT	951.053	1.169	0.248	4.769	1.692	0.2
		GSTCH	942.868			4.629		
	Landfall wind speed (m/s)	TCBT	38.737	1.825	0.074	8.678	0.155	0.696
		GSTCH	33.778			9.692		
	Landfall pressure(hpa)	TCBT	963.053	−0.604	0.549	14.883	2.034	0.16
		GSTCH	966.542			22.29		
	Annual landfall number (item)	TCBT	0.594	−1.729	0.089	0.615	3.109	0.083
		GSTCH	0.969			1.062		
Fujian	Central maximum wind speed along the track (m/s)	TCBT	39	0.137	0.891	15.023	2.015	0.163
		GSTCH	38.512			9.266		
	Central minimum pressure along the track (hpa)	TCBT	961.55	0.779	0.44	29.552	0.842	0.364
		GSTCH	955.756			21.512		
	Landfall wind speed (m/s)	TCBT	32.25	0.18	0.859	10.109	0.478	0.493
		GSTCH	31.76			8.553		
	Landfall pressure(hpa)	TCBT	974.2	0.034	0.855	16.379	0.439	0.662
		GSTCH	971.937			18.199		
	Annual landfall number (item)	TCBT	0.625	0.852	0.36	1.07	−0.907	0.368
		GSTCH	0.844			0.847		

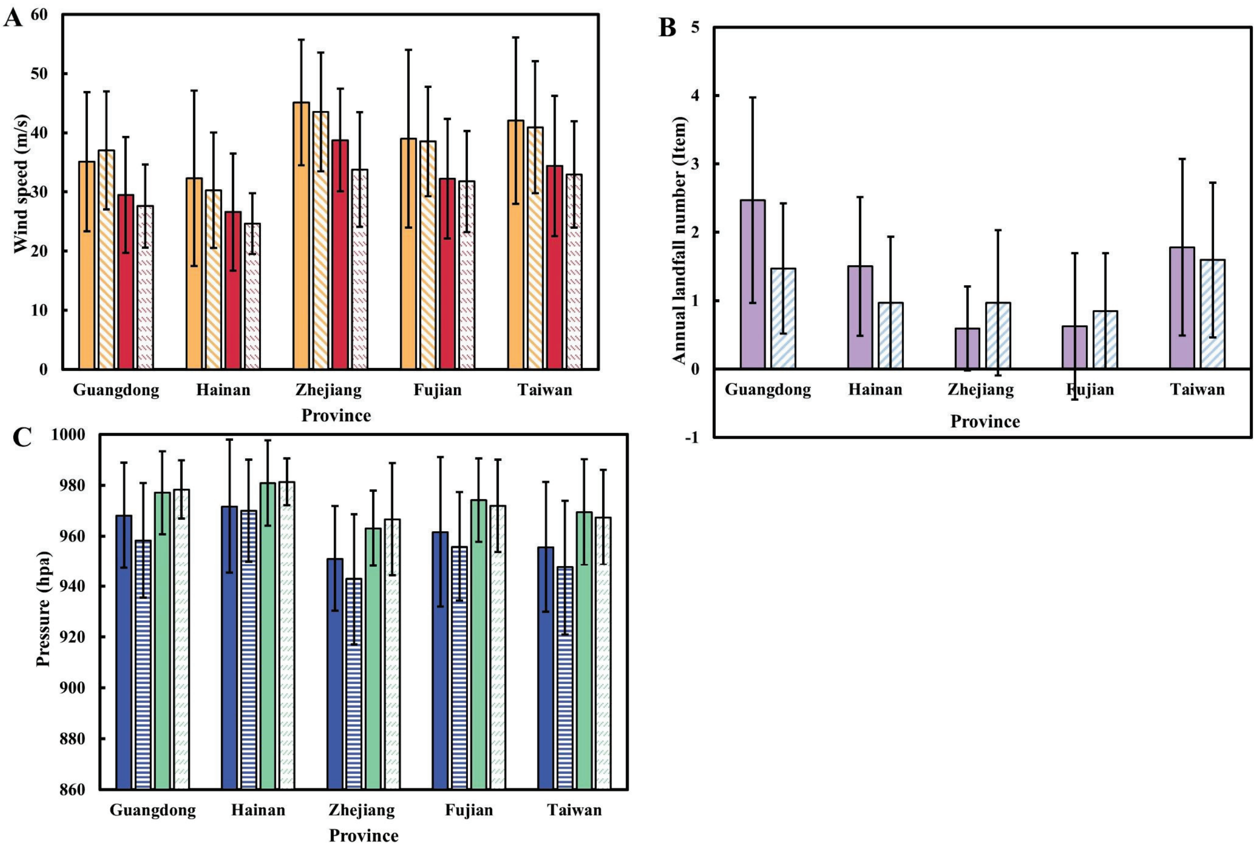

Figure 5. (**A–C**) Means and standard deviations of the TC characteristics in China's coastal provinces (orange color represents the central maximum wind speed along the track; red color represents landfall wind speed; purple color represents annual landfall number; blue color represents central minimum pressure along the track; green color represents landfall pressure. Solid color fills represent TCBT data; pattern fills represent GSTCH data).

The results show that the means of the TC characteristics all fall within the standard deviations of each other within each province in the GSTCH and TCBT datasets. Moreover, the mean deviations of all of the TC characteristics are small, i.e., the largest mean deviation of the central maximum wind speed along the track, central minimum pressure along the track, annual landfall number, landfall wind speed, and landfall pressure is 1.994 m/s, 9.866 hpa, 1 item, 4.959 m/s, and 3.489 hpa, respectively. Thus, the GSTCH dataset successfully reproduces the intensity and annual landfall frequency of those TCs that made landfall in each province.

As shown in Figure 5, the landfall wind speed of the TCs making landfall in Hainan and Guangdong provinces is lower than that of the TCs making landfall in Zhejiang, Taiwan, and Fujian provinces, which is consistent with the fact that TCs with low landfall wind speed that make landfall in Guangdong and Hainan provinces are most numerous. The relatively large standard deviations in the TC characteristics in both the GSTCH and the TCBT datasets indicate that TC intensity has case-by-case differences, and that the annual number of landfalling TCs has interannual variability. Standard statistical tests (i.e., the T-tests and F-tests) were performed to verify that the means and the standard deviations of the TC characteristics between the GSTCH and TCBT datasets are equivalent, as presented in Table 4.

Table 4 clearly shows that TCs with characteristics that failed the T-test or the F-test (i.e., central minimum pressure along the track, landfall wind speed, and annual landfall number) are concentrated in Guangdong and Hainan provinces. The following sections further investigate the cumulative distributions of the landfall wind speed and the annual landfall number of TCs that made landfall in Guangdong and Hainan provinces, as well as the central minimum pressure along the track of TCs that made landfall in Guangdong province.

3.2.2. Landfall Wind Speed

Figure 6A shows the cumulative distributions of the landfall wind speed of the TCs in the GSTCH and TCBT datasets in Guangdong and Hainan provinces. In comparison with the cumulative distribution of the landfall wind speed of the TCs in the TCBT dataset, the cumulative distribution of the landfall wind speed of the TCs in the GSTCH dataset passes the K-S test at the 95% confidence level, as presented in Table 5.

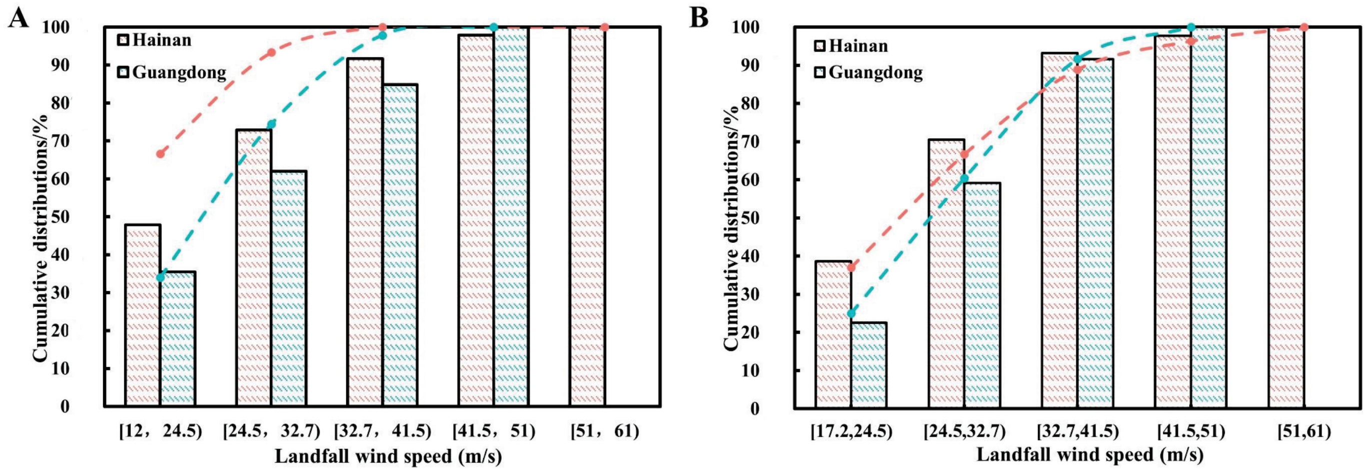

Figure 6. Cumulative distributions of the landfall wind speeds considering (**A**) and ignoring (**B**) tropical depressions in Guangdong and Hainan provinces (broken lines represent GSTCH data; bar charts represent TCBT data).

Table 5. Results of the K-S test of the cumulative distributions of the landfall wind speed and the annual landfall number in Guangdong and Hainan provinces.

TC Characteristics	Province	D	P (D)
Landfall wind speed (considering tropical depression) (m/s)	Guangdong	0.213	0.239
Landfall wind speed (ignoring tropical depression) (m/s)		0.227	0.207
Annual landfall number (item)		0.255	0.093
Landfall wind speed (considering tropical depression) (m/s)	Hainan	0.267	0.239
Landfall wind speed (ignoring tropical depression) (m/s)		0.182	0.465
Annual landfall number (item)		0.313	0.088

Figure 6A indicates that the landfall wind speed of TCs in Guangdong province in the TCBT dataset is mainly within the range of [12, 41.5), i.e., approximately 85%, and that the landfall wind speed probability of TCs in Guangdong province in the GSTCH dataset within this range is approximately 95%. Overall, the landfall wind speed of TCs in Guangdong and Hainan provinces is underestimated in the GSTCH dataset, which might be related to the fact that the TCs in the GSTCH dataset include tropical depressions [2]. A tropical depression is the weakest category of TC, able to cause damage to vegetation and unsecured mobile homes but posing no real threat to other structures [36]. Therefore, verifying whether the landfall wind speeds in the GSTCH and TCBT datasets are reliable without considering tropical depressions is appropriate.

As shown in Figure 6B, the cumulative distributions of the landfall wind speed of TCs in the GSTCH and TCBT datasets are consistent when neglecting tropical depressions. In comparison with the cumulative distribution of the landfall wind speed of TCs in the TCBT dataset, the cumulative distributions of the landfall wind speed of TCs in the GSTCH dataset pass the K-S test at the 95% confidence level, as listed in Table 5.

3.2.3. Annual Landfall Number

Changes in the annual landfall number of TCs directly affect the mean and standard deviation of the annual landfall number. Figure 7 shows the number of TCs that made landfall in Guangdong and Hainan provinces annually during 1990–2021.

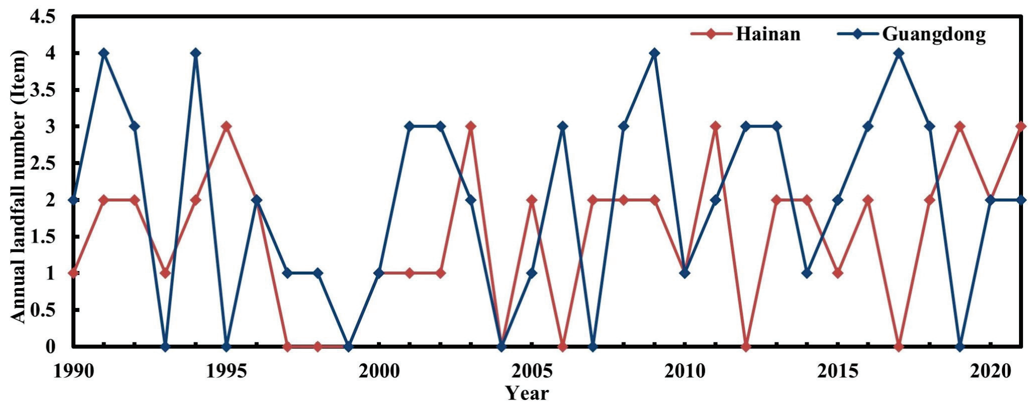

Figure 7. Annual landfall number of TCs in Guangdong and Hainan provinces during 1990–2021.

Figure 7 clearly shows that the annual landfall number reflects long-term change in Guangdong and Hainan provinces, affecting the mean and standard deviation of the annual landfall number. Therefore, in addition to the mean and standard deviation, consideration of the cumulative distribution is important when verifying the degree of consistency between the annual landfall numbers of Guangdong and Hainan provinces in the GSTCH and TCBT datasets. The cumulative distributions of the annual landfall numbers of Guangdong and Hainan provinces in the GSTCH and TCBT datasets are shown in Figure 8.

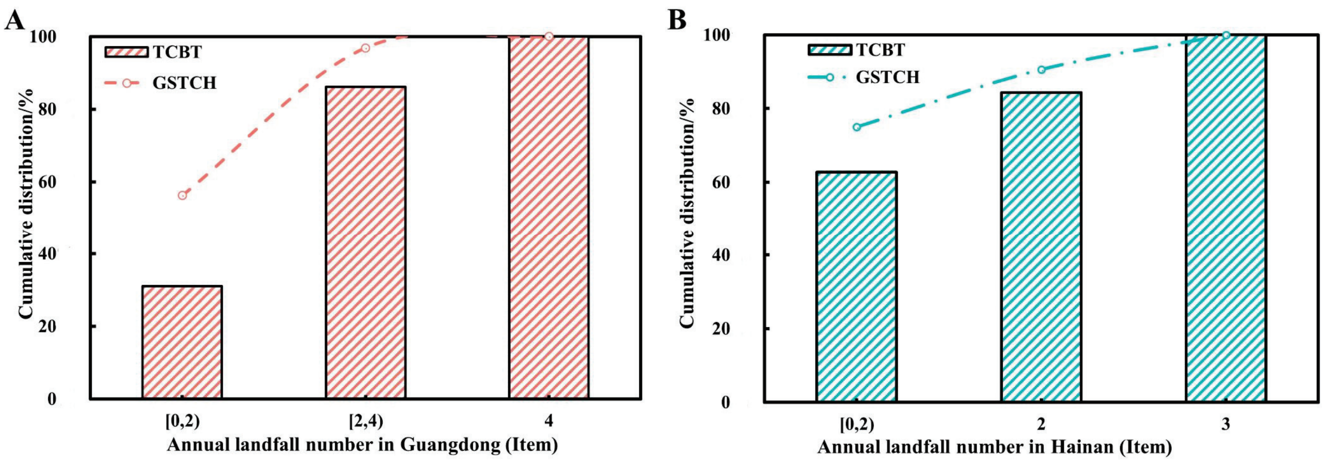

Figure 8. Cumulative distributions of the annual landfall number of TCs in Guangdong (**A**) and Hainan (**B**) provinces.

Figure 8 shows that the annual landfall numbers of Guangdong province is mainly concentrated in the range [0, 3]. In this range, the probability for Guangdong province in the GSTCH dataset is up to 96.88%, while the probability in the TCBT dataset is 86.21%. The annual landfall numbers of Hainan province are mainly concentrated in the range [0, 2], and the probability in the GSTCH dataset is up to 90.63%, while the probability in the TCBT dataset is 84.38%. In comparison with the cumulative distributions of the annual landfall numbers in Guangdong and Hainan provinces in the TCBT dataset, the cumulative distributions of the annual landfall numbers in Guangdong and Hainan provinces in the GSTCH dataset pass the K-S test at the 95% confidence level, as presented in Table 5.

3.2.4. Central Minimum Pressure along the Track

The cumulative distributions of the central minimum pressure along the track of TCs that made landfall in Guangdong province in the TCBT and GSTCH datasets are shown in Figure 9. It can be seen that the GSTCH dataset overestimates the ratio of TCs that made landfall in Guangdong province with the central minimum pressure along the track in the range [905, 980). Moreover, the p value of the K-S test statistic of the cumulative distribution in Guangdong province is 0.002, i.e., much lower than 0.05. Thus, the central minimum pressure of TCs in Guangdong province in the GSTCH dataset does not pass the K-S test at the 95% confidence level, and there is a significant difference between the two datasets.

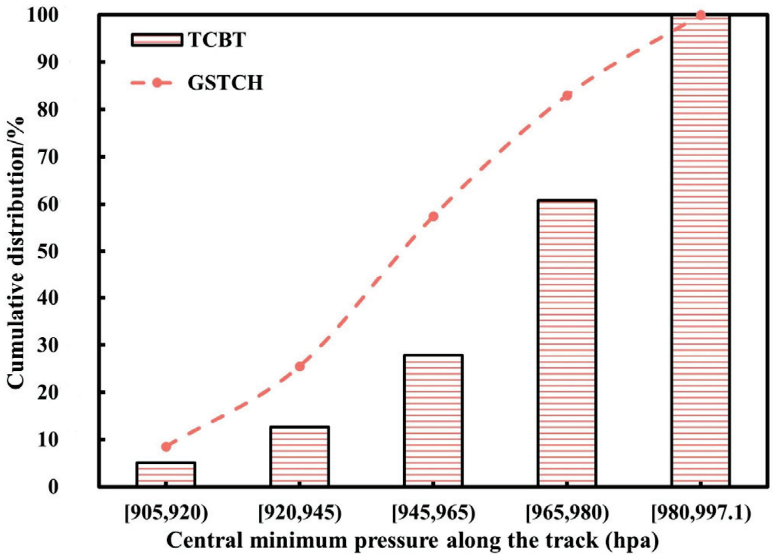

Figure 9. Cumulative distributions of central minimum pressure along the track of TCs in Guangdong province.

Guangdong is the province with the most frequent occurrence of TCs making landfall along the coast of China, and the landfall period is concentrated mainly between June and October. Differences in sea level pressure and sea surface temperature at different times affect the magnitude of the central minimum pressure along the track, and the central minimum pressure along the track in the GSTCH dataset considers environmental conditions (i.e., monthly mean sea level pressure and monthly mean sea surface temperature) [2]. Therefore, this study verifies the degree of consistency between the central minimum pressure along the track of TCs that made landfall in Guangdong province during June–October in the GSTCH and TCBT datasets.

As shown in Figure 10, during June–October, the mean differences in the central minimum pressure along the track of TCs that made landfall in Guangdong province are very small and within the range of standard deviation of each other. The GSTCH dataset overestimates the mean central minimum pressure along the track in September, and the standard deviation of the central minimum pressure along the track in the GSTCH dataset does not pass the F-test at the 95% confidence level (Table 6). The cumulative distributions of the central minimum pressure along the track of TCs that made landfall in Guangdong province in September in the GSTCH and TCBT datasets are shown in Figure 11.

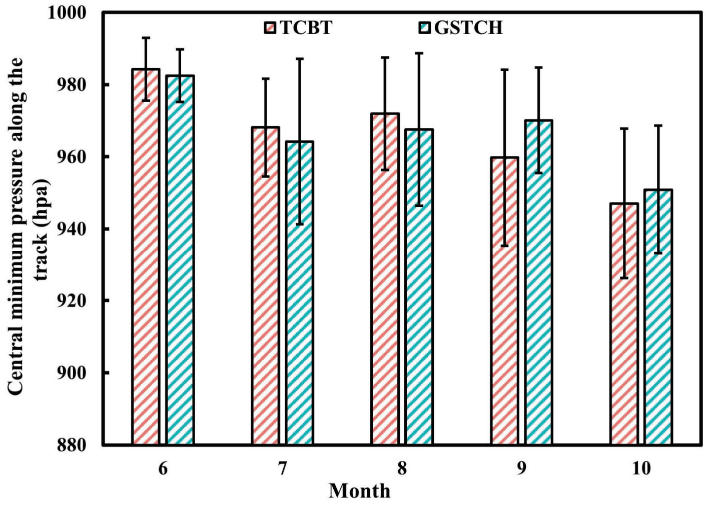

Figure 10. Means and standard deviations of the central minimum pressure along the track of TCs in Guangdong province from June to October.

Table 6. Results of the T-test of means and the F-test of standard deviations of the central minimum pressure along the track of TCs in Guangdong province from June to October.

Month	t	P (t)	f	P (f)
6	0.589	0.561	0.374	0.546
7	0.645	0.523	3.1	0.087
8	0.854	0.397	2.577	0.115
9	−1.581	0.123	7.737	0.009
10	−0.319	0.758	0.169	0.692

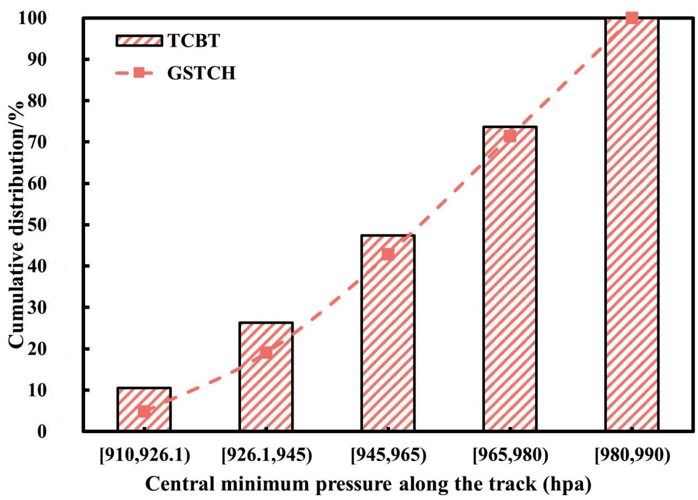

Figure 11. Cumulative distributions of central minimum pressure along the track of TCs in Guangdong province in September.

Figure 11 clearly shows that the cumulative distributions of the central minimum pressure along the track of TCs that made landfall in Guangdong province in September are consistent between the GSTCH and TCBT datasets. The p value of the K-S test statistic of the cumulative probability distribution is 0.68, which is greater than 0.05, indicating that it passes the K-S test at the 95% confidence level. The results reveal no statistically significant difference between the GSTCH and TCBT datasets in terms of the number of TCs within each value range of the central minimum pressure along the track that made landfall in Guangdong province in September.

4. Discussion

4.1. Usage of the GSTCH Dataset in Coastal China

TCs usually induce other hazards, such as strong wind, huge waves, heavy precipitation, and storm surges [38–40]. They can substantially damage housing, infrastructure and ecosystems both in coastal areas and far inland. Research by Bloemendaal et al. [2,22] demonstrates that the GSTCH dataset with 10,000 years of TC activity can be used in studying the different aspects of TC hazards, including TCs and other induced hazards risk analysis over the open ocean and in coastal areas, coastal modeling, food risk assessments, and wind return periods estimation and damage assessments. In particular, the GSTCH dataset is also applicable to global small islands. Because of its global coverage and the large number of TCs, there are also enough TCs to perform the risk assessment in the aforementioned regions.

The long coastline and low-lying terrain of China's mainland coast (the area of land below 5 m above sea level is approximately 143,900 km^2) make it an area prone to frequent TC disasters. Moreover, the extended continental shelf and shallow sea areas of coastal China contribute to the development of storm surges associated with TCs that can cause substantial economic losses and serious casualties. For example, in 2017, the storm surge caused by Typhoon *Hato* caused direct economic losses of 5.154 billion yuan in coastal areas of Guangdong province, with six people reported killed or missing. In 2018, Super Typhoon *Mangkhut* caused total direct economic losses of 2.457 billion yuan in Guangdong, Guangxi, and Fujian provinces. In 2019, owing to the combined influence of the storm surge of Typhoon *Lekima* and nearshore waves, the direct economic losses of the eight coastal provinces stretching from Fujian to Liaoning totaled 10.288 billion yuan. To sum up, the coastal areas of China are frequently affected by TCs and their induced storm surges, and the caused disaster losses are very serious.

Applicability evaluation of this study verifies that the GSTCH dataset provides a critical data source for the relevant research on TCs and their induced hazards in the coastal areas of China. It is hoped that this will contribute to disaster risk assessment, proposal of disaster prevention and reduction actions, and disaster emergency response plan.

4.2. Some Limitations

In previous sections, this study has demonstrated that the GSTCH dataset is well consistent with the TCBT dataset in China's coastal areas. There are, however, some limitations regarding the subsequent usage of this dataset, which are briefly reflected upon here. In this section we shall also give future research directions.

First, the GSTCH dataset is based on average present-day climate conditions (1980–2017) [2], and the TC activities represented by GSTCH may be biased by the phases of multi-decadal variability contained in the 38 year period of record that was used to generate the dataset [22]. Therefore, the GSTCH dataset cannot be used to assess the climate trends over longer timescales.

Second, the TC characteristics in the TCBT dataset selected in this study are derived from satellite observations, high-density ground observations, ground-based radar, weather maps, and satellite cloud pattern recognition [25,26]. They are considered highly accurate. However, the 32 year (1990–2021) TC data in the TCBT dataset represent only a limited temporal range. Future research could extend the temporal scale of the available TC data by e.g., collecting more historical TCs data and conducting data reanalysis. They may then be applied to the accurate evaluation of new synthetic TC datasets and to the study of different aspects of TC hazards. In addition, issues such as changes in observation methods, data homogeneity, and data quality over time should also be addressed, to ensure the reliability of the consistency analysis.

Last, landfall wind speed and landfall pressure in this study refer to the initial landfall wind speed and landfall pressure of a TC, for which the value of the former is usually the largest and the value of the latter is the lowest [25,26]. TCs might make landfall twice or even three times. Nevertheless, after the first landfall, the intensity of a TC diminishes rapidly owing to the combined effects of ground friction and insufficient energy supply. Therefore, the wind speed at the time of the first landfall is a better representation of the TC intensity. For the period 1990–2021, the TCBT dataset includes 56 TCs with twice landfalls and 16 TCs with thrice landfalls, but they have little supporting data. Therefore, the lack of TC data available for the second and third landfalls means that verifying the degree of consistency between the GSTCH and TCBT datasets is impossible in such a case. Future research could extend the TC data for second and third landfalls by statistical resampling or modeling.

5. Conclusions

This study evaluated the applicability of the GSTCH dataset in coastal China in relation to two regions: the Northwest Pacific and China's coastal provinces. The TC characteristics for evaluation include central maximum wind speed along the track, central minimum pressure along the track, landfall wind speed, landfall pressure, annual occurrence number, and annual landfall number. The evaluation indicators are the mean, standard deviation, frequency distribution, and cumulative distribution, together with their corresponding hypothesis tests (T-test, F-test, Chi-squared test, and K-S test).

For the Northwest Pacific, the comparison results showed no significant differences in the means and standard deviations of landfall wind speed, landfall pressure, and annual occurrence number between the GSTCH and TCBT datasets at the 95% confidence level. In addition, the cumulative distributions of central minimum pressure and central maximum wind speed along the track passed the K-S test at the 95% confidence level. These verified that the GSTCH dataset is consistent with the TCBT dataset at the sea-area scale.

For China's coastal provinces, the comparison results show that the means or standard deviations of TC characteristics between the two datasets were not significantly different in provinces other than Guangdong and Hainan. Further analysis revealed that the cumulative distributions of the TC characteristics in Guangdong and Hainan provinces passed the K-S test at the 95% confidence level, verifying that the GSTCH dataset is consistent with the TCBT dataset at the province scale.

In general, the TCBT dataset is considered to be the most authoritative TC dataset for the coastal areas of China, and it can be used as a benchmark for evaluating the applicability of the GSTCH dataset in coastal China. Therefore, the excellent agreement between the GSTCH and TCBT datasets for the Northwest Pacific and China's coastal provinces verifies that the GSTCH dataset is an available and reliable data source for TC hazard studies in China's coastal areas.

Author Contributions: Conceptualization, X.L. and J.Z.; methodology, X.L. and Q.H.; data collection, Q.H., S.Z., X.D. and T.Z.; data curation, Q.H.; writing—original draft, X.L. and Q.H.; writing—review and editing, J.Z. and S.Z.; project administration, X.L. and J.Z.; funding acquisition, J.Z. All authors have read and agreed to the published version of the manuscript.

Funding: This research was funded by the National Key R&D Program of China (2022YFC3105100).

Institutional Review Board Statement: Not applicable.

Informed Consent Statement: Not applicable.

Data Availability Statement: Global Synthetic Tropical Cyclone Hazard dataset was developed in Bloemendaal et al. [2] and is available from the 4TU. Centre for Research Data repository [30]: https://doi.org/10.4121/uuid:82c1dc0d-5485-43d8-901a-ce7f26cda35d (accessed on 25 May 2022). The Tropical Cyclone Best Track dataset is available from the China Meteorological Administration Tropical Cyclone data center [25,26]: https://tcdata.typhoon.org.cn/zjljsjj.html (accessed on 7 June 2022).

Acknowledgments: The Global Synthetic Tropical Cyclone Hazard dataset provided by the 4TU Centre and the Tropical Cyclone Best Track dataset provided by the China Meteorological Administration Tropical Cyclone data center are highly appreciated.

Conflicts of Interest: Xuexue Du was employed by Duyun Power Supply Bureau of Guizhou Power Grid Co., Ltd. The remaining authors declare that the research was conducted in the absence of any commercial or financial relationships that could be construed as a potential conflict of interest.

References

1. Emanuel, K. Tropical cyclones. *Annu. Rev. Earth Planet. Sci.* **2003**, *31*, 75–104. [CrossRef]
2. Bloemendaal, N.; Haigh, I.D.; de Moel, H.; Muis, S.; Haarsma, R.J.; Aerts, J.C.J.H. Generation of a global synthetic tropical cyclone hazard dataset using STORM. *Sci. Data* **2020**, *7*, 40. [CrossRef]
3. Chan, K.T.F.; Chan, J.C.L.; Wong, W.K. Rainfall asymmetries of landfalling tropical cyclones along the South China coast. *Meteorol. Appl.* **2018**, *26*, 213–220. [CrossRef]
4. Zheng, M.L.; Mu, L.; Li, W.J.; Wang, F.; Li, Y. Regime shifts in the damage caused by tropical cyclones in the Guangdong–Hong Kong–Macao Greater Bay area of China. *J. Mar. Sci. Eng.* **2023**, *11*, 1889. [CrossRef]
5. Shi, X.W.; Tan, J.; Guo, Z.X.; Liu, Q.Z. A review of risk assessment of storm surge disaster. *Adv. Earth Sci.* **2013**, *28*, 866–874.
6. Seo, N.S.; Bakkensen, L.A. Is tropical cyclone surge, not intensity, what kills so many people in South Asia. *Weather Clim. Soc.* **2017**, *9*, 71–81. [CrossRef]
7. Zhu, P.J.; Luo, N.X.; Zhao, Q.S. Forecast of maximum water increase in typhoon storm surge based on random forest model. *Bull. Sur. Map.* **2021**, *12*, 71–74+82.
8. Peduzzi, P.; Chatenoux, B.; Dao, H.; De Bono, A.; Herold, C.; Kossin, J.; Mouton, F.; Nordbeck, O. Global trends in tropical cyclone risk. *Nat. Clim. Chang.* **2012**, *2*, 289–294. [CrossRef]
9. Velden, C.; Burton, A.; Kuroiwa, K. The first international workshop on satellite analysis of tropical cyclones: Summary of current operational methods to estimate intensity. *Trop. Cycl. Res. Rev.* **2012**, *1*, 469–481.
10. Yang, G.S. Historical change and future trends of storm surge disaster in China's coastal area. *J. Nat. Dis.* **2000**, *9*, 23–30.
11. Yang, X.X.; Liu, Q. Economic loss assessment of storm-surge disasters based on the KPCA-RBF model. *Mar. Sci.* **2021**, *45*, 32–39.
12. Hao, J.; Liu, Q. Pre-assessment of typhoon storm surge disaster loss based on the SSA-ELM model. *Mar. Sci.* **2022**, *46*, 55–63.
13. Zhong, J.; Zhou, Q.; Gu, S.D.; Wang, L.Q.; Sun, Y.M.; Han, M.M. Analysis of the different characteristics of tropical cyclogenesis among different best track data in the northwest Pacific. *Mar. For.* **2019**, *42*, 114–119.
14. Emanuel, K. The hurricane-climate connection. *Bull. Am. Meteorol. Soc.* **2008**, *5*, ES10–ES20. [CrossRef]
15. Weinkle, J.; Maue, R.; Pielke, R., Jr. Historical global tropical cyclone landfalls. *J. Clim.* **2012**, *25*, 4729–4735. [CrossRef]
16. Vickery, P.J.; Skerlj, P.F.; Twisdale, L.A. Simulation of hurricane risk in the US using empirical track model. *J. Struct. Eng.* **2000**, *126*, 1222–1237. [CrossRef]
17. Emanuel, K.; Ravela, S.; Vivant, E.; Risi, C. A statistical deterministic approach to hurricane risk assessment. *Bull. Am. Meteorol. Soc.* **2006**, *87*, 299–314. [CrossRef]
18. Powell, M.D.; Soukup, G.; Cocke, S.; Gulati, S.; Morisseau-Leroy, N.; Hamid, S.; Dorst, N.; Axe, L. State of Florida hurricane loss projection model: Atmospheric science component. *J. Wind Eng. Ind. Aerod.* **2005**, *93*, 651–674. [CrossRef]
19. Haigh, I.D.; Wijeratne, E.M.S.; MacPherson, L.R.; Pattiaratchi, C.B.; Mason, M.S.; Crompton, R.P.; George, S. Estimating present day extreme water level exceedance probabilities around the coastline of Australia: Tides, extra-tropical storm surges and mean sea level. *Clim. Dyn.* **2014**, *42*, 121–138. [CrossRef]
20. Casson, E.; Coles, S. Simulation and extremal analysis of hurricane events. *J. R. Stat. Soc.* **2000**, *49*, 227–245. [CrossRef]
21. Lin, N.; Emanuel, K.; Oppenheimer, M.; Vanmarcke, E. Physically based assessment of hurricane surge threat under climate change. *Nat. Clim. Chang.* **2012**, *2*, 462–467. [CrossRef]
22. Bloemendaal, N.; de Moel, H.; Muis, S.; Haigh, I.D.; Aerts, J.C.J.H. Estimation of global tropical cyclone wind speed probabilities using the STORM dataset. *Sci. Data* **2020**, *7*, 377. [CrossRef] [PubMed]
23. Nakajo, S.; Mori, N.; Yasuda, T.; Mase, H. Global stochastic tropical cyclone model based on principal component analysis and cluster analysis. *J. Appl. Meteorol. Clim.* **2014**, *53*, 1547–1577. [CrossRef]
24. Lee, C.Y.; Tippett, M.K.; Sobel, A.H.; Camargo, S.J. An environmentally forced tropical cyclone hazard model. *J Adv. Model. Earth Syst.* **2018**, *10*, 223–241. [CrossRef]
25. Ying, M.; Zhang, W.; Yu, H.; Lu, X.; Feng, J.; Fan, Y.; Zhu, Y.; Chen, D. An overview of the China Meteorological Administration tropical cyclone database. *J. Atmos. Ocean. Technol.* **2014**, *31*, 287–301. [CrossRef]
26. Lu, X.Q.; Yu, H.; Ying, M.; Zhao, B.K.; Zhang, S.; Lin, L.M.; Bai, L.N.; Wan, R.J. Western North Pacific tropical cyclone database created by the China Meteorological Administration. *Adv. Atmos. Sci.* **2021**, *38*, 690–699. [CrossRef]
27. Yang, Y.X.; Xia, J.D. Characteristics of Northwest Pacific tropical cyclones. *Nav. Chin.* **2019**, *42*, 114–119.
28. Lv, S.; Sun, Y.; Zhong, Z.; Shen, Y.X. Possible reasons for the migration of tropical cyclone track over the western north pacific: Interdecadal pacific oscillation modulation. *Front. Earth Sci.* **2022**, *10*, 994876. [CrossRef]
29. Yu, Q.; Wang, X.W.; Fang, Y.J.; Ning, Y.Z.; Yuan, P.Q.; Xi, B.R.; Wang, R.Z. Comprehensive investigation on spatiotemporal variations of tropical cyclone activities in the Western North Pacific, 1950–2019. *J. Mar. Sci. Eng.* **2023**, *11*, 946. [CrossRef]
30. Bloemendaal, N.; Haigh, I.D.; de Moel, H. *STORM IBTrACS Present Climate Synthetic Tropical Cyclone Tracks*; 4TU.Centre for Research Data: Delft, The Netherlands, 2019. [CrossRef]
31. Knapp, K.R.; Kruk, M.C.; Levinson, D.H.; Diamond, H.J.; Neumann, C.J. The International Best Track Archive for Climate Stewardship (IBTrACS): Unifying tropical cyclone best track data. *Bull. Am. Meteorol. Soc.* **2010**, *91*, 363–376. [CrossRef]

32. Knapp, K.R.; Diamond, H.J.; Kossin, J.P.; Kruk, M.C.; Schreck, C.J. International Best Track Archive for Climate Stewardship (IBTrACS) Project, Version 4. NOAA National Centers for Environmental Information. 2018. Available online: https://www.ncei.noaa.gov/products/international-best-track-archive (accessed on 25 May 2022).
33. Lu, X.Q.; Lei, X.T.; Yu, H.; Zhao, B.K. An objective TC intensity estimation method based on satellite data. *J. Appl. Meteor. Sci.* **2014**, *25*, 52–58.
34. Lomax, R.G.; Hahs-Vaughn, D.L. *Statistical Concepts-A Second Course*; Routledge: New York, NY, USA, 2013.
35. *GB/T 19201-2006*; Grade of Tropical Cyclones. Standardization Administration of the People's Republic of China: Beijing, China, 2006.
36. Simpson, R.H.; Saffir, H.J.W. The hurricane disaster potential scale. *Weatherwise* **1974**, *27*, 169.
37. Knuth, D.E. *The Art of Computer Programming*; Pearson Education: New York, NY, USA, 1997.
38. Cerveny, R.S.; Newman, L.E. Climatological relationships between tropical cyclones and rainfall. *Mon. Weather. Rev.* **2000**, *128*, 3329–3336. [CrossRef]
39. Phadke, A.C.; Martino, C.D.; Cheung, K.F.; Houston, S.H. Modeling of tropical cyclone winds and waves for emergency management. *Ocean Eng.* **2003**, *30*, 553–578. [CrossRef]
40. Bloemendaal, N.; Muis, S.; Haarsma, R.J.; Verlaan, M.; Apecechea, M.I.; de Moel, H.; Ward, P.J.; Aerts, J.C.J.H. Global modeling of tropical cyclone storm surges using high-resolution forecasts. *Clim. Dyn.* **2019**, *52*, 5031–5044. [CrossRef]

Journal of
Marine Science and Engineering

MDPI

Article

Morphological Changes in Storm Hinnamnor and the Numerical Modeling of Overwash

Bohyeon Hwang [1], Kideok Do [2,*] and Sungyeol Chang [3]

1 Department of Convergence Study on the Ocean Science and Technology, Korea Maritime and Ocean University, Busan 49112, Republic of Korea; zpzpxpxp@gmail.com
2 Department of Ocean Engineering, Korea Maritime and Ocean University, Busan 49112, Republic of Korea
3 Haeyeon Engineering and Consultants Corporation, Gangneung-si 25623, Republic of Korea; sungyeoly@naver.com
* Correspondence: kddo@kmou.ac.kr; Tel.: +82-51-410-5248

Abstract: Constant changes occur in coastal areas over different timescales, requiring observation and modeling. Specifically, modeling morphological changes resulting from short-term events, such as storms, is of great importance in coastal management. Parameter calibration is necessary to achieve more accurate simulations of process-based models that focus on specific locations and event characteristics. In this study, the XBeach depth-averaged model was adopted to simulate subaerial data pre- and post-storms, and overwash phenomena were observed using the data acquired through unmanned aerial vehicles. The parameters used for the model calibration included those proposed in previous studies. However, an emphasis was placed on calibrating the parameters related to sediment transport that were directly associated with overwash and deposition. Specifically, the parameters corresponding to the waveform parameters, wave skewness, and wave asymmetry were either integrated or separated to enable an adequate representation of the deposition resulting from overwash events. The performance and sensitivity of the model to changes in volume were assessed. Overall, the waveform parameters exhibit significant sensitivity to volume changes, forming the basis for calibrating the deposition effects caused by overwashing. These results are expected to assist in the more effective selection and calibration of parameters for simulating sediment deposition due to overwash events.

Keywords: morphological response; UAV (unmanned aerial vehicle); overwash; numerical modeling; XBeach

Citation: Hwang, B.; Do, K.; Chang, S. Morphological Changes in Storm Hinnamnor and the Numerical Modeling of Overwash. *J. Mar. Sci. Eng.* **2024**, *12*, 196. https://doi.org/10.3390/jmse12010196

Academic Editor: Deniz Velioglu Sogut

Received: 15 December 2023
Revised: 15 January 2024
Accepted: 19 January 2024
Published: 22 January 2024

1. Introduction

Changes in coastal areas occur over various timescales and can be attributed to both human activities and natural phenomena. Among these, short-term extreme events, such as storms, can cause significant morphological changes in coastal areas. These events can lead to erosion and even overwash, which can directly affect not only the beach, but also human settlements located beyond revetments. Hence, precise observations and effective numerical modeling must be performed for the management of erosion and the associated morphological changes induced by overwashing along coastlines [1]. Various models can be used to perform such a numerical modeling; however, they often involve different assumptions and empirical formulations [2]. To achieve reasonable results, the parameters provided by these models must be calibrated according to the specific region and target event or phenomenon [3].

In 2022, Storm Hinnamnor significantly affected Songjeong Beach in Busan, South Korea. To assess this impact, a survey was conducted using unmanned aerial vehicles (UAVs), which revealed significant erosion at the front of the beach and deposition due to overwashing at the back. In this study, the XBeach model [2], which is effective for simulating erosion caused by storms on sandy beaches [4–6], was employed to simulate both erosion and overwash-induced deposition. XBeach was originally developed to simulate the collapse of barrier islands on dissipative beaches, and its default parameters have been criticized for overestimating offshore sediment transport [7]. Because of the model's inherent nonlinearity and its reliance on empirical formulations, a proper parameter calibration is essential for obtaining accurate results. Various calibration methods have been proposed in previous studies [4,5,8]. However, the trial-and-error method, which typically relies on the experience and knowledge of model users, is commonly used. For an effective calibration, the roles and sensitivities of the parameters within the model must be understood.

This study aims to simulate the overwash and resultant deposition during a storm period by calibrating the waveform parameters in XBeach. XBeach utilizes the advection–diffusion equation for sediment transport. In this equation, the non-linearity term includes the effects of wave skewness and wave asymmetry. The influence of wave skewness and asymmetry on the sediment advection velocity has been well explained by van Thiel de Vries [9]. In XBeach, the parameters for the wave asymmetry and skewness are defined as facAs and facSk, respectively, and can be represented as facua when these parameters have identical values. Many prior studies have opted for simulations with facua instead of facAs and facSk to reduce the number of parameters requiring calibrations, and such simulations have shown high accuracy for erosion. Facua is often directly linked to asymmetric flow, with Nederhoff [10] demonstrating a high accuracy for erosion (BSS of 0.83) by calibrating facua to a value of 0.25 and explaining that an increase in facua reduces the net sediment transport in the offshore direction. Saber et al. [11] discussed the significant impact of facua on the onshore (offshore) velocity, which is closely linked to sediment transport, stating that the default value of facua (0.1) induced an overestimation of erosion. They suggested a more effective simulation of erosion by correlating it with the average slope angle. In their study of multiple storm events in XBeach simulations, Jin et al. showed that the sensitivity of facua was the highest, significantly influencing the model's accuracy [5]. Therefore, this research aims to compare and analyze the results of separating facua into facAs and facSk, not only in terms of the erosion caused by overwash, but also for the resultant deposition.

In this study, two statistical schemes and a volume acquired through a UAV observation are employed as the basis for evaluating the model's results. While the beach data for pre- and post-storm events were obtained, depth data immediately after the storm were not available; hence, the evaluation was restricted to the beach data.

The research area and UAV survey results are presented in Section 2. Section 3 describes the XBeach model, input data required for the model, and parameters. It also introduces the statistical schemes used for the model accuracy assessment. Section 4 presents the results, and Sections 5 and 6 present the discussion and conclusions, respectively.

2. Field Data Collection

2.1. Study Area

Figure 1 shows the location of Songjeong Beach in the study area. Songjeong Beach is a predominant pocket beach located in Busan, Republic of Korea, characterized by a wave-dominated area (129°11′45′′–129°12′23′′ E, 35°10′24′′–35°10′56′′ N). With a length of approximately 1.2 km, the beach width ranges from 43 to 60 m. The beach primarily consists of sand with a median grain size (D_{50}) of 0.42 mm. In addition, structures composed of boulders were observed on the flank of the T headland. This region has been consistently subjected to erosion, prompting the Ministry of Oceans and Fisheries to categorize it with erosion grades C to D for ongoing management (A = excellent, B = moderate, C = concern, and D = serious). Consequently, annual nutrition projects are currently underway in this area. Figure 1 shows the presence of a well-defined crescentic sandbar prior to a storm event. While the typical tidal range is approximately 1–2 m, a notable elevation in the sea level occurs during a storm surge.

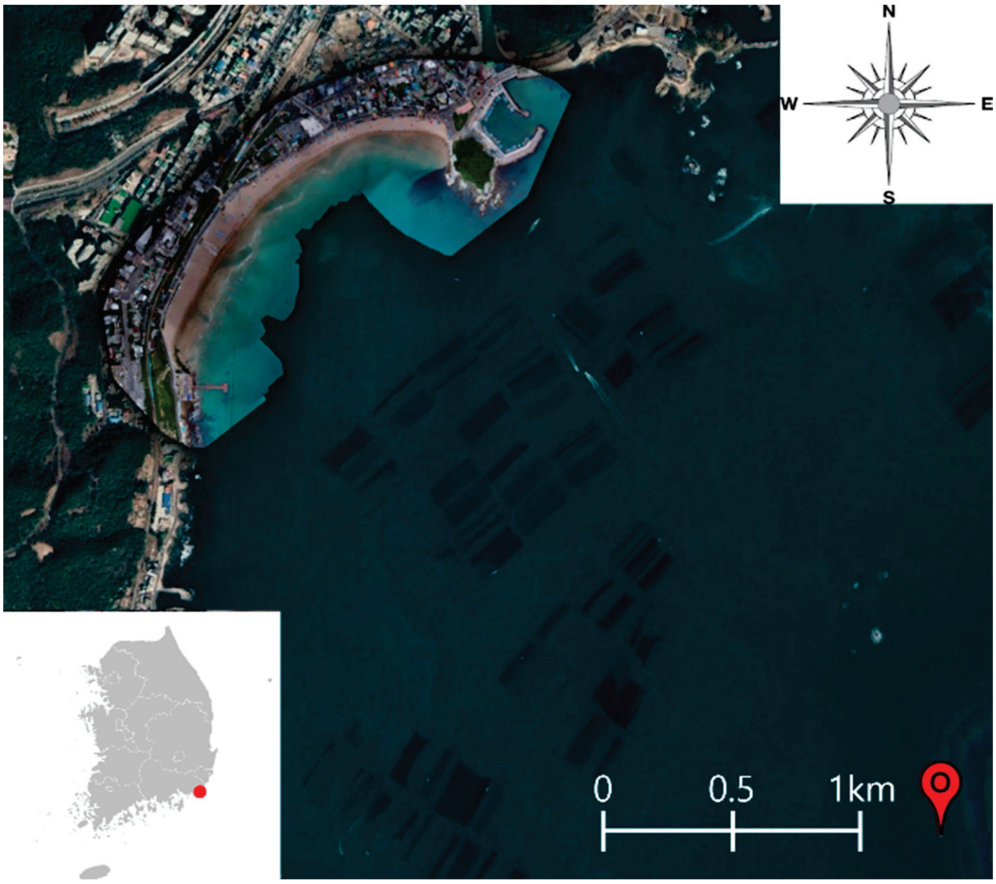

Figure 1. Location of Songjeong beach. Google Earth with orthomosaic image from the UAV, taken on 29 August 2022. The buoy was installed at 'O'.

2.2. Storm Condition

On 28 August 2022, Storm Hinnamnor originated in the northwestern Pacific and exhibited an initial wind speed of 15 m/s as it progressed northward. The central minimum pressure reached 955 hPa and struck Busan, Republic of Korea, on 5 September at 21:00. The wave data were obtained using a buoy deployed by the Korea Hydrographic and Oceanographic Agency (KHOA). Figure 2a shows the significant wave height, wave period, wave direction, and tide level over time during the storm. The maximum recorded significant wave height was 10.5 m, with the wave period ranging from 9 to 10 s. Using this dataset, the wave rose diagram (Figure 2b) shows easterly waves at 90–100° during the storm period. Figure 2c shows the path of Storm Hinnamnor throughout its formation and dissipation phases. The storm had a direct impact on Busan, leading to a low central pressure and subsequent storm surge, resulting in a rise in sea level, causing erosion and overwashing with substantial waves.

2.3. Observation Method

Morphological changes in the beach due to Storm Hinnamnor were captured through observations conducted with a UAV, both pre- and post-storms. Observations were performed on 29 August 2022, prior to the storm strike, and on 7 September 2022, following its impact. A Phantom 4 RTK was utilized for these observations, set to operate at an altitude of 100 m with an overlap and side lap of 80% and a speed of 7.9 m/s. Approximately 720 images were captured. Equipped with real-time kinematic (RTK) technology, the Phantom 4 RTK allows the production of highly accurate data through a real-time correction using the Global Navigation Satellite System (GNSS). Nonetheless, for the accuracy assessment and calibration, 12 ground control points (GCPs) were established; their locations are shown in Figure 3. The integration of approximately 720 photographs and data calibration with the GCPs were performed using the Pix4Dmapper (ver.4.8.4) software. This process enabled the acquisition of high-accuracy values with an accuracy assessment based on the observational data and GCPs presented in Table 1.

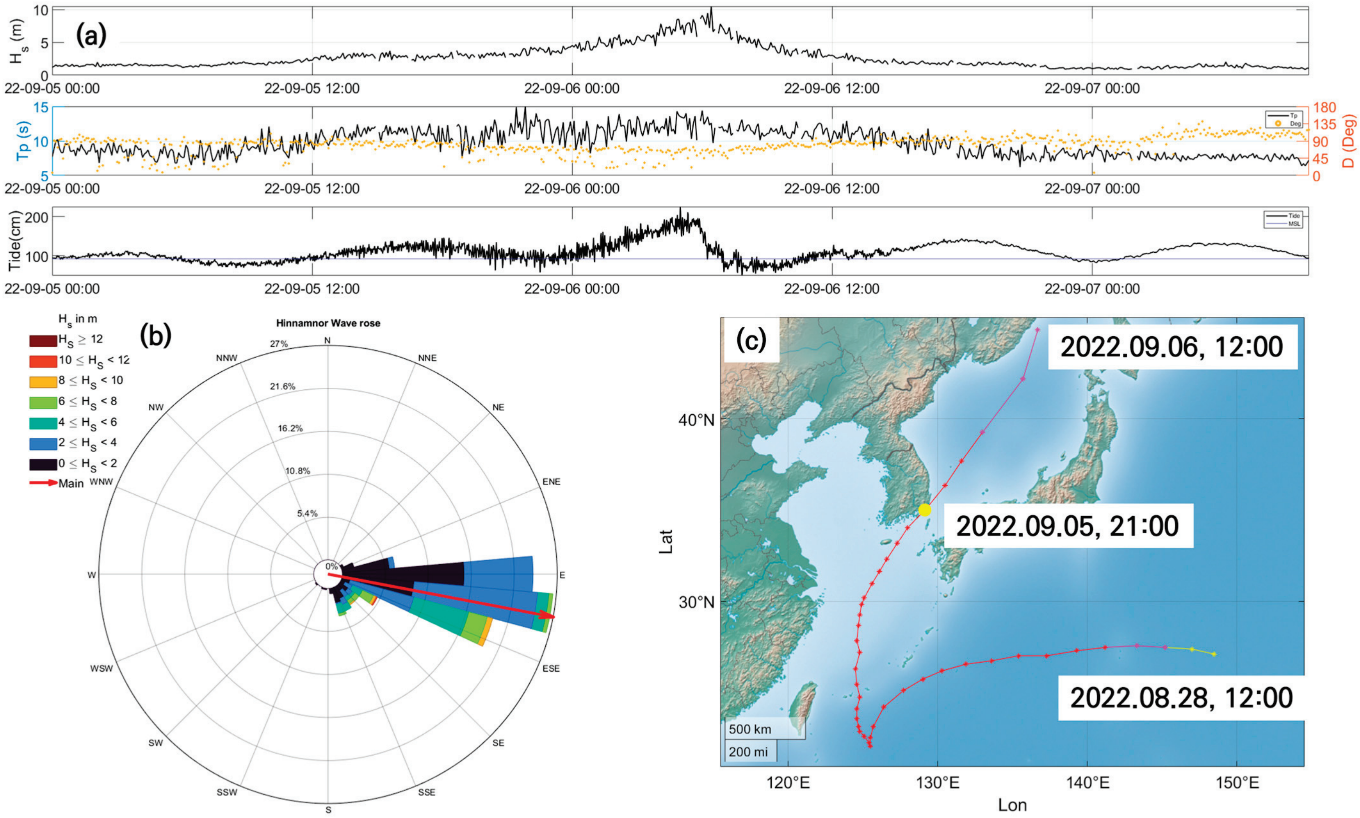

Figure 2. Wave data during the storm period. (**a**) Significant wave height, spectral peak period, wave direction, and tide elevation time series at Songjeong Beach. (**b**) Wave rose diagram. (**c**) Paths of storm Hinnamnor with the study area (yellow dot) and arrival time. The color of the lines indicates the intensity of the storm. In the depicted graph, the yellow line represents TS (Tropical Storm), the pink line denotes STS (Severe Tropical Storm), and the red line signifies TY (Typhoon, Storm).

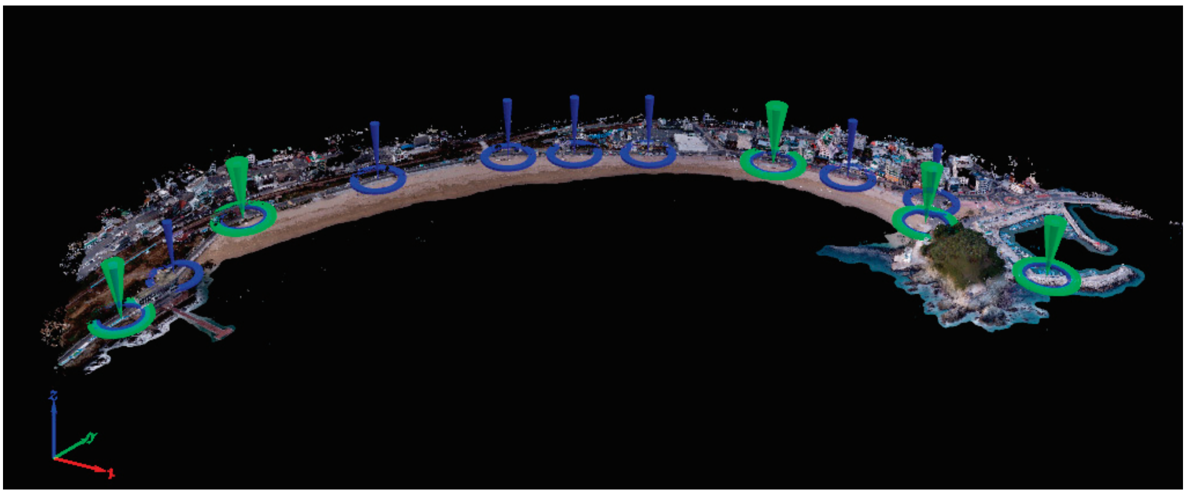

Figure 3. Positions of the ground control points (GCPs) in Songjeong Beach.

Table 1. Standard deviation (Std.Dev) and root mean square error (RMSE) per observation ID (Obs ID).

Obs ID	Std. Dev (X/Y/Z) (m)	RMSE (X/Y/Z) (m)
Pre-storm	0.005/0.006/0.013	0.005/0.005/0.013
Post-storm	0.007/0.001/0.009	0.007/0.011/0.009
Recovery	0.001/0.009/0.010	0.010/0.009/0.010

2.4. Volumetric Changes and Classification of the Beach

UAVs were used to examine the changes in the beach before and after a storm event. Table 2 presents the volumetric analysis and the calculated erosion quantities for Songjeong Beach derived from the UAV survey data. The vertical reference for the volume measurement was based on the elevation calculated using the approximate lowest water level and datum level (App.LLW). Volume comparisons were conducted in common areas where the pre- and post-storm regions overlapped to ensure consistency. This approach was necessary owing to the lack of altitude observations by UAVs in some areas caused by the run-up from storm surges. Prior to the arrival of the storm on 29 August 2022, the observed volume was 69,939.2 m^3. The post-storm assessment on 7 September 2022 indicated an erosion value of 9533 m^3, resulting in a remaining volume of 60,406.2 m^3. Figure 4a depicts the elevation differences post- and pre-storm events based on the UAV data comparison. Erosion is evident along the frontal section of the coastline, with overwash and deposition observed in the rear section near the revetment site. The most extreme erosion event occurred in the northeastern SW region of the beach.

Table 2. Erosion and volume of pre- and post-storm events.

	Pre-Storm	Post-Storm
Obs Date	29 August 2022	7 September 2022
Volume (m^3)	69,939.2	60,406.2
Erosion (m^3)	9533	

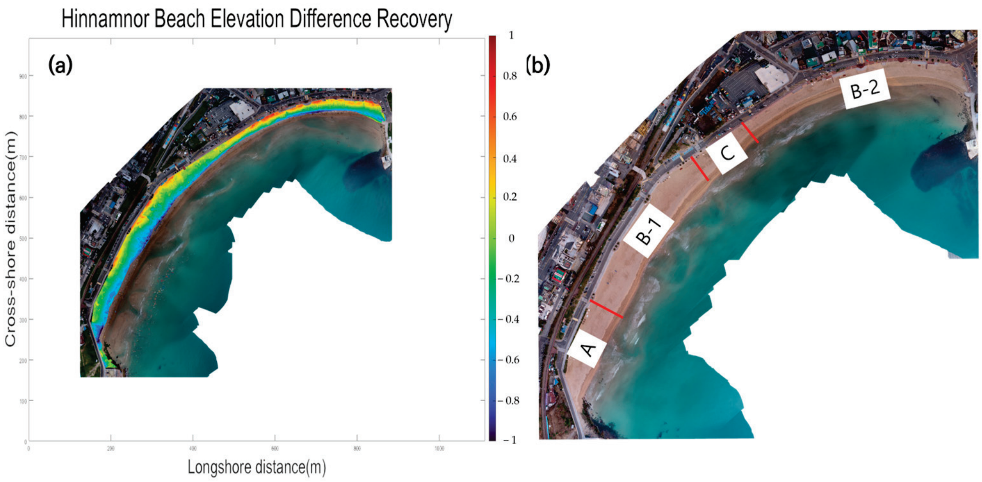

Figure 4. (**a**) Elevation differences after and before the arrival of Storm Hinnamnor. (**b**) Beach divided according to their characteristics.

Based on the elevation differences shown in Figure 4a, the beaches were categorized into three types. Type A refers to areas with significant erosion throughout; type B refers to areas with erosion at the front and deposition in the rear owing to overwash; and type C refers to areas with erosion at the front and minimal changes in the rear. The results when these areas are marked in the study area are shown in Figure 4b. Type A is located in the SW region of the beach, and type B is the predominant type.

3. Method of Numerical Modeling

3.1. Description and Domain with Model Set

XBeach is a two-dimensional, depth-averaged (i.e., 2DH) numerical model that integrates fluid dynamics and morphodynamic processes to simulate wave propagation and morphological changes under short-term storm wave conditions. The storm event in the study area was modeled using XBeach (1.23.5527) and the surfbeat mode (XBSB), specifically designed to simulate hydrodynamics and morphological changes in narrow areas, such as beaches, dunes, and barrier islands, during storm wave events. The XBSB model calculates the hydrodynamics (shortwave, longwave, and roller energy) with wave and water-level inputs as boundary conditions. Subsequently, it simulates the morphodynamics, including sediment transport and the resulting bed-level changes. Figure 5a,b show the orthogonal grid and pre-depth data used for the XBeach modeling. Depth data were provided by an external agency and utilized in this study. The data surveyed on 23 August 2022, before the storm, underwent precise calibrations with an error margin of approximately 1 m. Depth measurements were conducted from 0 to 5 m using a single beam, whereas depths beyond this range were surveyed using a multibeam approach. Owing to the essential nature of data correction, a calibration was performed using DGNSS, a motion sensor, and a gyrocompass. Additionally, tidal and sound speed corrections were implemented to minimize the data errors. The grid resolution was configured to increase the density closer to the nearshore, thereby optimizing the simulation of the morphological changes within the surf and swash zones. Conversely, the grid size was proportionally enlarged seaward. Specifically, the cross-shore grid size ranged from 3 to 20 m, while the longshore grid maintained a consistent resolution of 10 m, resulting in a 201 × 201 grid configuration. The structures, including revetments, were designated as non-erodible layers. The wave boundary conditions were defined using the time-varying JONSWAP spectrum based on the observation data, incorporating the parameters (Hs, Tp, and Dp) outlined in Section 2.2. Temporal variations in the water level were derived from the tide data in Section 2.2, serving as the water level boundary conditions. The modeling period spanned from 29 August to 7 September, following the UAV observational data. For the computational efficiency, significant wave heights of less than 1 m were excluded. The morphological acceleration factor (morfac) was set at 10.

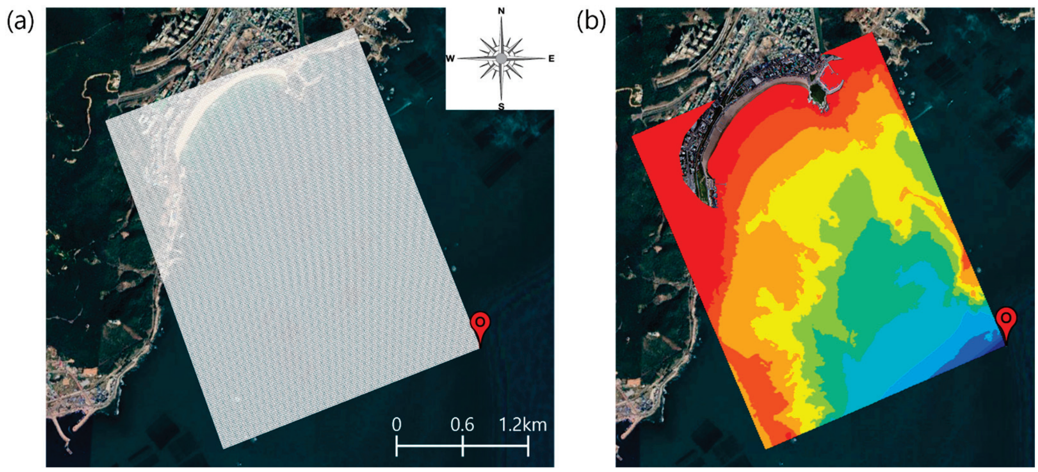

Figure 5. (**a**) Orthogonal grid domain for XBeach modeling with Google Earth image. (**b**) Depth with UAV orthomosaic and Google Earth image. The red dots represent the locations where wave data were acquired.

3.2. Parameter Calibration

The default parameter settings of XBeach were calibrated for North Sea wave conditions off the Dutch coast and were specifically designed to simulate the collapse of barrier islands during storms. Consequently, the offshore sediment transport and morphological changes were overestimated under typical beach conditions. To address this limitation, ongoing discussions focus on various parameter calibration methods [3,4,12,13]. In this study, a trial-and-error approach was employed based on the parameters proposed in previous studies [5] along with additional parameters, with the aim of simulating overwash during storm events.

Various formulations were embedded in the XBeach model, allowing for an effective simulation of the morphological changes specific to the study area. Among these, the discussions on sediment transport equations are extensive. XBeach offers sediment transport formulations from Soulsby–Van Rijn [14], van Thiel de Vries–Van Rijn [9,15,16], and Van Rijn [17]. A primary distinction between the widely used Soulsby and van Thiel de Vries–Van Rijn equations is that Soulsby employs a drag coefficient to determine the equilibrium sediment concentration, which is absent from van Thiel de Vries–Van Rijn. Additionally, the van Thiel de Vries–Van Rijn equation distinguishes between currents and waves in its calculation of critical velocity, whereas Soulsby does not. Although each formulation has its strengths, the effectiveness largely depends on the features of the coastal environment. For instance, De Vet et al. compared the Soulsby–Van Rijn and van Thiel de Vries–Van Rijn formulations, suggesting that the latter provided more credible results [18]. The van Thiel de Vries–Van Rijn equation was noted to represent breaching more effectively and overwashing than the Soulsby equation, which overestimated the erosion rates. Conversely, Craig et al. [19] favored Soulsby in modeling the microtidal, wave-dominated hydrodynamic environment of the Upper Texas Coast (UTC), effectively simulating phenomena, such as collision, overwash, and inundation. Similarly, Orzech et al. [20] showed commendable Brier Skill Score results for Monterey Bay using the XBeach 2DH model. Monterey Bay, located in California, is characterized by its mild alongshore currents, rip channel bathymetry, and tidal range of approximately 1.6 m, features that resonate closely with the Songjeong Beach studied in this research. Consequently, this study aimed to simulate sediment transport by employing the Soulsby equation.

Within the XBeach model, two formulations related to shortwave breaking exist: the Roelvink et al. and Daly formulas. The Roelvink equation was used by default for all the statistical analyses. This equation is based on an empirical formula that incorporates the breaking coefficient (gamma) and the ratio of the wave height to the water depth. However, Daly et al. observed that this equation tended to underestimate the wave energy dissipation when the water depth increases rapidly. In response to this result, Daly introduced the parameter gamma2, which allowed for a more precise determination of wave breaking, even in areas with sharp changes in the water depth. Furthermore, when dealing with depths that have a plane slope instead of steep inclines, the differences in the results generated by the two formulas are negligible. In this study, based on the previous research, specific parameters and their associated formulas were adopted, and the Daly equation was used for the model setup.

Based on this, the gamma and gamma2 parameters were employed, and the waveform parameters related to the wave skewness and asymmetry, which were closely related to sediment transport, were calibrated. XBeach offered the two waveform equations provided by Ruessink et al. [21] and van Thiel [9]. Both computed skewness and asymmetry. The formula of Ruessink et al. suggests the Ursell number parameter, which is based on over 30,000 field observations of orbital skewness and asymmetry collected under non-breaking and breaking conditions. Based on the significant wave height, wave period, and water depth, they reported that the skewness and asymmetry were efficiently represented. Another approach involved the equation proposed by van Thiel et al., which was an extension of the wave-shaped model presented by Rienecker et al. [22]. This model describes the shortwave shape as a weighted sum of eight sine and cosine functions. Skewness and asymmetry were then represented based on the computed near-bed shortwave flow velocity using this model. However, it remains unclear which of the two equations is more accurate [11]. In this study, the default equation provided by van Thiel was used.

Several studies discuss the effects of skewness and asymmetry on sediment transport [11,13,23]. According to van Thiel et al. [9], Stokes waves exhibit higher onshore flow velocities than offshore waves. This implies that the sediment movement is more pronounced during the wave crest than during the wave trough. Consequently, skewness and asymmetry influence the Eulerian velocities through an additional onshore sediment advection velocity, denoted as u_a. Using skewness and asymmetry, u_a can be represented as:

$$u_a = (f_{Sk} S_k - f_{As} A_s) u_{rms} \tag{1}$$

where f_{Sk} is a coefficient related to the phase shift of the intrawave sediment concentration, flow, and skewness. f_{As} is the coefficient pertaining to the phase shift between the flow and the suspended sediment for asymmetry. Assuming that f_{Sk} and f_{As} are equivalent, they can be expressed as f_{ua}, and the equation can be summarized as:

$$u_a = f_{ua}(S_k - \ A_s) u_{rms} \tag{2}$$

In XBeach, facua is denoted as a coefficient associated with the phase shift between intrawave sediment suspensions and orbital flow. In previous studies [5], facua was used. A comparison with the sets of facSk and facAs was conducted in this study. Based on these observations, it was suggested that the profile shapes in the shoaling and breaker zones were significantly influenced by facSk. An increase in fasSk was linked to an increase in wave skewness, which was associated with an increase in offshore sediment fluxes, whereas [24] the cross-shore profiles in the surf and swash zones were believed to be affected by facAs. As facAs increases, the asymmetry in the waves is enhanced, leading to an increase in onshore sediment transport. Based on this, the set parameter values and their ranges have been summarized in Table 3.

Table 3. Parameter descriptions and values.

	Description	Calibration Value or Range
gamma	Breaker parameter in Daly formula	0.52
gamma2	Set stop point of breaking in Daly formula	0.3
facua	Time-averaged flows due to wave skewness and asymmetry (facua = facSk = facAs)	0.09:0.03:0.42
facAs	Time-averaged flows due to wave asymmetry	0.09:0.03:0.36
facSk	Time-averaged flows due to wave skewness	0.09:0.03:0.36
D_{50}	Median grain size of sediment (mm)	0.42
break	Type of wave breaking formula	Roevink_Daly
form	Type of sediment transport formula	Soulsby-vanrijn

Observational UAV data were used to calibrate the parameters. Comparisons between the observational and model values were only performed in overlapping areas, which, owing to the characteristics of the UAV, were confined to the subaerial region [7,19]. Based on this, the simulation skill proposed by Gallagher et al. (1998) [25] could be employed to assess the accuracy of the elevation difference obtained from the UAV and model output. This skill is defined as follows:

$$Skill = 1 - \frac{\sum_{i=1}^{N}\left(dz_{b_{UAV,i}} - dz_{b_{XBeach,i}}\right)^2}{\sum_{i=1}^{N}\left(dz_{b_{UAV,i}}\right)^2} \tag{3}$$

where N is the number of data points (i.e., the number of grids) in the overlapping section between the UAV's pre- and post-data and the output of the model. $dz_{b_{UAV,i}}$ denotes the observed bed-level change in i, whereas $dz_{b_{XBeach,i}}$ is the modeled bed-level change at point i. A skill value of 1 indicated a perfect match between the model predictions and observed data, indicating optimal accuracy. A skill of 0 suggested that the model's accuracy was equivalent to random or base-level predictions, whereas a negative skill indicated that the model's predictions were less accurate and that it performed poorly (Table 4). Furthermore, the determination of the mean error allowed us to distinguish between biases resulting from systematic differences in the model outcomes and random variations. The equations for this are as follows:

$$Bias = \frac{1}{N}\sum_{i=1}^{N}\left(z_{b_{post-storm,Model,i}} - z_{b_{post-storm,UAV,i}}\right) \tag{4}$$

where $z_{b_{post-storm,Model,i}}$ is the post-elevation of the model in cell i and $z_{b_{post-storm,UAV,i}}$ is the post-elevation of the observation data. A positive bias indicated that the model predicted higher elevations than those observed, whereas a negative bias signified that the model predicted lower elevations than those observed (Table 4).

Table 4. Qualification of XBeach's performance.

	Skill	Bias
>0	Good (=1, perfect)	Model predicts higher results than Obs
=0	Nothing	Same
<0	Poor	Model predicts lower results than Obs

4. Results

4.1. Parameter Calibration Results: Sensitivity of Volumetric Information

In this study, as previously mentioned, gamma and gamma2 related to wave breaking were utilized according to the values used in the previous research by Jin et al. [5]. Only the waveform parameters, namely, facua, facAs, and facSk, were employed for calibrations. Additionally, the performance of the model was evaluated based on two statistical schemes and observed volumetric changes in the beach. The sensitivity of each parameter to the volume was first examined. As shown in Table 3, 12 facua cases were selected to simulate beach morphological changes. Figure 6 shows the changes in the volume with increasing facua values. The volume increased almost proportionally with the increase in facua [26], reaffirming the significant impact of wave nonlinearity on sediment movement. However, as depicted in the graph of facua in Figure 6, although the volume increases uniformly with an increase in facua, the skill value, which represents the accuracy, decreases as it approaches the observed volume value of 60,406.2 m^3. This suggests that the increase in facua is unsuitable for simulating the unbalanced phenomena of erosion at the front and deposition at the rear because it leads to an overall increase in volume across the entire beach area.

The calibration was conducted by separating facua into facAs and facSk. A total of 100 cases were selected to model the morphological responses. Figure 7 shows the changes in volume with varying facAs at the same facSk. Overall, an increase in facAs led to an increase in the beach volume when facSk remained constant. This reaffirmed that an increase in the impact of wave asymmetry led to an increase in sediment transport to the land. Similar to facua, the skill value generally showed a sharp decline when it exceeded 0.33. Figure 8 presents a graph depicting the changes in the volume and skill value with varying facSk values for the same facAs. The graph exhibits irregular patterns, which are different from those of facua or facAs. An increase in facSk did not uniformly increase the volume; instead, an increase in facAs generally led to an increase in the overall volume. The increase in facSk was found to enhance sediment movement, but did not determine the direction of movement, indicating potential transport both offshore and onshore.

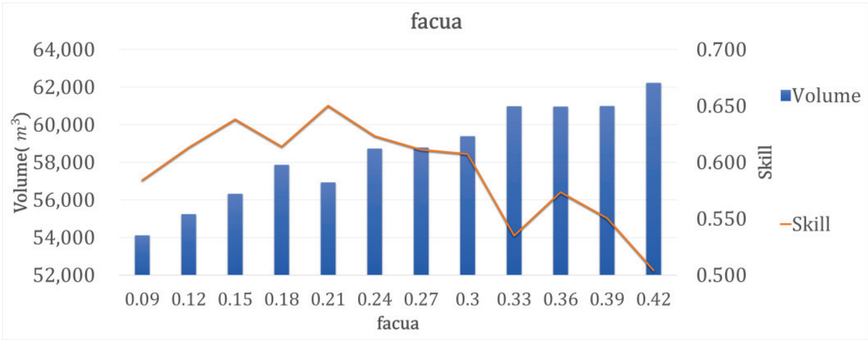

Figure 6. The variations in volume and skill values in response to the changes in facua.

Figure 7. The variations in volume and skill values in response to changes in facAs, with a constant facSk.

Figure 8. Changes in volume and skill values are shown in response to variations in facSk while maintaining a constant facAs.

4.2. Parameter Calibration Result: Skill and Bias

In addition to the volumetric results described in Section 4.1, skill and bias were utilized to assess the accuracy and understand the trends of the skill values for each case. The changes in skill values corresponding to variations in the parameters of facua, facAs, and facSk are shown in Figures 6–8. While generally maintaining high values of approximately 0.5, facua and facAs exhibited a sharp decline in skill values beyond 0.33. This decrease from values above 0.5 indicates the successful simulation of erosion at the front; however, erosion is underestimated when the values exceed 0.33. In contrast, facSk showed irregular patterns for skill values. The calibrated results based on these findings are summarized in Table 5. ID1 represents the case where facua is used, whereas ID2 indicates the case where facua is separated into facAs and facSk. The highest skill value, showing a volume similar to that of the observed data, was achieved by facua at 0.3, with a skill value of 0.555 and a bias of −0.083, suggesting a slight overestimation of erosion. Additionally, skill values and biases were analyzed by segmenting them into different areas. The segmentation was based on morphological changes, categorized as type A for areas with significant overall erosion, type B for deposition due to overwash, and type C for erosion at the front with minimal changes in the rear (Figure 4b). The skill values and biases of each segment are listed in Table 6. ID1, the result of the calibration using facua, showed high values overall, except for area A. Area A, characterized by severe erosion at the rear, was insufficiently simulated. Despite the inadequate simulation of the deposition at the rear, a high skill value of 0.773 was obtained for area B, indicating the result of the simulation of erosion at the front. A depiction of the elevation difference of the beach is shown in Figure 9c. Although the erosion at the front was somewhat overestimated, a high-level simulation of the front erosion was achieved compared with the observed values (Figure 9a). However, the simulation of deposition due to overwashing did not yield sufficiently reasonable results.

Table 5. Calibration parameters of facua (ID1), facAs, and facSk (ID2).

ID	Waveform Parameter			Skill	Bias	Volume
	facua	facAs	facSk			
1	0.3			0.555	−0.083	59,646.9
2		0.27	0.18	0.623	−0.082	59,870.5
Obs						60,406.2

Table 6. Skill and bias values for each section.

ID	Skill_A	Skill_B1	Skill_C	Skill_B2
1	0.261	0.773	0.665	0.663
2	0.278	0.850	0.767	0.676
ID	**Bias_A**	**Bias_B1**	**Bias_C**	**Bias_B2**
1	0.048	−0.026	−0.005	−0.090
2	0.027	−0.019	−0.002	−0.084

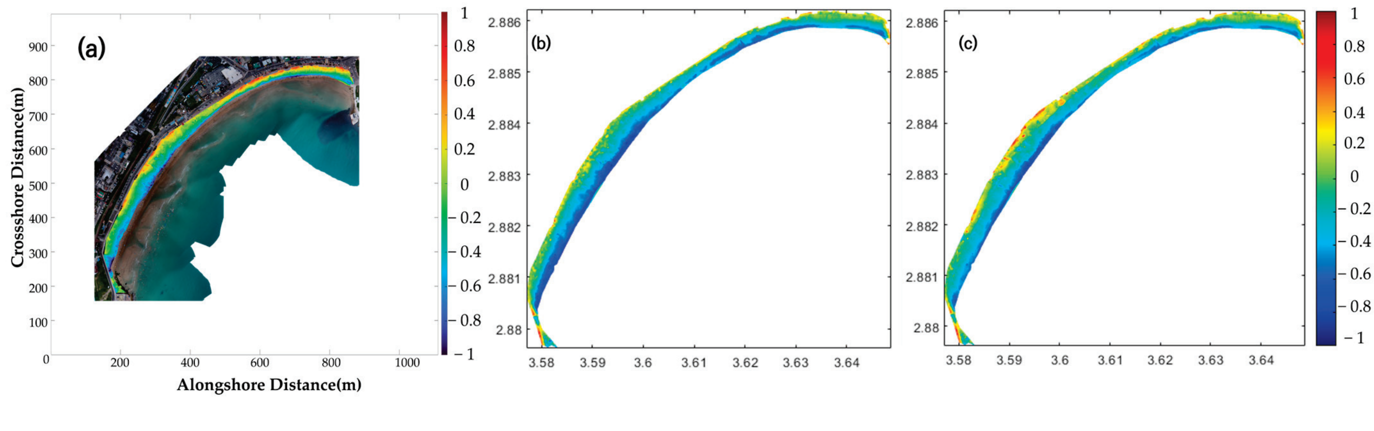

Figure 9. Elevation differences of observed data (**a**), ID2 (**b**), and ID1 (**c**).

By contrast, ID2, which was calibrated separately, yielded more effective results. The calibration values for facAs and facSk were 0.27 and 0.18, respectively, resulting in a volume similar to the observed data with a skill value of 0.623 and a bias of −0.082 (Table 5). These values were higher than those obtained for the facua calibration, indicating greater precision. A detailed analysis conducted by segmenting the different areas is presented in Table 6.

The skill value and bias of ID2 demonstrate that the skill in area B1 increases to 0.850, as shown in Figure 9b. Compared with Figure 9c, this figure reveals that the deposition near the revetment at the rear is more effectively simulated. Skill_A, representing areas with overall erosion, still shows low values, which can be attributed to the focus on effectively simulating deposition due to overwash during the calibration process. This resulted in a somewhat improved skill value from a separate calibration, but it remained lower than that of skill_B1. By separating facua into facAs, which increased sediment transport to the land, and facSk, which facilitated sediment movement, a more detailed calibration was possible. This allowed the simulation of the overwash and its associated deposition. Although an increase in parameters requiring calibrations could impose additional burdens on model users, it appeared necessary to simulate the overwash and resultant deposition effectively.

5. Discussions

Significant erosion and overwash-induced deposition around revetments were observed following the 2022 storm Hinnamnor. Such overwash events, which can directly or indirectly harm humans, underscore the importance of numerically simulating and preventing them. To simulate these morphological responses, numerical simulations based on UAV data collected before and after the typhoons were conducted. The model employed for the simulation was XBeach, a process-based, depth-averaged model specialized for short-term localized morphological changes in beaches. XBeach can simulate various hydrodynamic and morphodynamic processes and embed approximately 250 parameters that require calibrations according to the geomorphological characteristics of the target area and input data, such as wave conditions. This research utilized a parameter set from previous studies with a high BSS in the storm cluster, while calibrating the waveform-related parameters closely tied to sediment transport for a more effective overwash simulation.

The waveform parameters included facSk for skewness, facAs for asymmetry, and facua, which was an integrated representation of these two parameters. Using gamma and gamma2 from previous studies, the calibration of these three waveform parameters was performed to simulate the overwash and resultant deposition. The evaluation of the model employed simulation skill, applicable only when the ground-level data from UAVs or LiDAR were available, and bias was used to estimate the extent of overestimations of erosion and deposition. In addition, the advantages of UAVs in measuring beach volumes were leveraged as a metric for the parameter calibration.

Calibrations using facua, facAs, and facSk demonstrated an efficient simulation of frontal erosion. Both parameters had high values and skill values above 0.5, maintaining reasonable volumes while simulating frontal erosion. However, the facua fell short in simulating the deposition in the rear areas due to overwash. The increase in facua led to an overall increase in onshore sediment transport. However, this also resulted in difficulties in simultaneously simulating erosion at the front and deposition at the rear. Calibrations were performed using the facAs and facSk separation, which successfully represented both frontal erosion and rear deposition. However, the simulations of areas experiencing overall erosion were not successful. Various reasons have been hypothesized for this, with the median grain size (D_{50}) being a likely factor. The study area, Songjeong Beach, is predominantly sandy and contains gravel and rocky formations in its SW region. The simulation used a consistent sand grain size based on D_{50}, which could have contributed to these discrepancies. Another factor considered was the use of waveform-related parameters for the calibrations. The primary objective of this study was to simulate overwash and its deposition; hence, only waveform parameters directly related to sediment transport were calibrated, whereas other parameters were adopted from previous studies. Given the variety of XBeach parameters, further research involving additional calibrations is warranted.

An additional analysis was conducted to investigate the sensitivity of the volume to facua, facSk, and facAs. The facua parameter demonstrated an almost perfectly proportional relationship to the beach volume, indicating that an increase in facua activated onshore sediment transport. Similarly, with a constant facSk, an increase in facAs led to an increase in the beach volume.

6. Conclusions

The following conclusions were drawn:

1. Utilizing the parameters of facua, facSk (skewness), and facAs (asymmetry), which integrated the wave-shape parameters closely related to sediment movement, in addition to the previously proposed parameters, was effective for modeling the phenomenon of overwash. The use of facSk and facAs was particularly effective in simulating overwashing.
2. Although an increase in the number of parameters to be calibrated could pose a burden on the model user, it was necessary to calibrate them separately when aiming for a more accurate simulation of the overwash and subsequent sediment deposition.
3. Generally, an increase in facAs was associated with an overall increase in the beach volume (indicating increased onshore sediment transport), whereas facSk did not show a similar trend.

Author Contributions: Conceptualization, B.H. and K.D.; data curation, B.H. and S.C.; formal analysis, B.H.; funding acquisition, K.D.; investigation, B.H. and K.D.; methodology, B.H. and K.D.; project administration, K.D.; resources, B.H. and S.C.; software, B.H. and K.D.; supervision, K.D.; validation, B.H. and K.D.; visualization, B.H.; writing—original draft, B.H. and K.D.; writing—review and editing, B.H., K.D. and S.C. All authors have read and agreed to the published version of the manuscript.

Funding: This research was funded by the Korea Institute of Marine Science and Technology Promotion, the project titled 'Cyclic Adaptive Coastal Erosion Management Technology Development' (RS-2023-00256687), and the National Research Foundation of Korea (NRF-2022R1I1A3065599).

Institutional Review Board Statement: Not applicable.

Informed Consent Statement: Not applicable.

Data Availability Statement: Data are contained within the article.

Conflicts of Interest: Author Sungyeol Chang was employed by the company Haeyeon Engineering and Consultants Corporation. The remaining authors declare that the research was conducted in the absence of any commercial or financial relationships that could be construed as a potential conflict of interest.

References

1. Karanci, A.; Brodie, K.L.; Spore, N.J.; Jeziorska, J.; Sciaudone, E.J. Unmanned Aerial Vehicle Data Integration for Coastal Modeling. In Proceedings of the Coastal Sediments 2019: Proceedings of the 9th International Conference, Petersburg, FL, USA, 27–31 May 2019.
2. Roelvink, D.; Reniers, A.; van Dongeren, A.; van Thiel de Vries, J.; McCall, R.; Lescinski, J. Modelling storm impacts on beaches, dunes, and barrier islands. *Coast. Eng.* **2009**, *56*, 1133–1152. [CrossRef]
3. Do, K.; Shin, S.; Cox, D.; Yoo, J. Numerical Simulation and Large-scale Physical Modelling of Coastal Sand Dune Erosion. *J. Coast. Res.* **2018**, *1*, 196–200. [CrossRef]
4. Bae, H.; Do, K.; Kim, I.; Chang, S. Proposal of parameter range that offered optimal performance in the coastal morphodynamic model (XBeach) through GLUE. *J. Ocean. Eng. Technol.* **2022**, *36*, 251–269. [CrossRef]
5. Jin, H.; Do, K.; Kim, I.; Chang, S. Sensitivity analysis of event-specific calibration data and its application to modeling of subaerial storm erosion under complex bathymetry. *J. Mar. Sci. Eng.* **2022**, *10*, 1389. [CrossRef]
6. Daly, C.; Roelvink, D.; van Dongeren, A.; van Thiel de Vries, J.; McCall, R. Validation of an advective-deterministic approach to short wave breaking in a surf-beat model. *Coast. Eng.* **2012**, *60*, 69–83. [CrossRef]
7. McCall, R.T.; Van Thiel de Vries, J.S.M.; Plant, N.G.; Van Dongeren, A.R.; Roelvink, J.A.; Thompson, D.M.; Reniers, A.J.H.M. Two-dimensional time dependent hurricane overwash and erosion modeling at Santa Rosa island. *Coast. Eng.* **2010**, *57*, 668–683. [CrossRef]
8. Harley, M.D.; Turner, I.L.; Kinsela, M.A.; Middleton, J.H.; Mumford, P.J.; Splinter, K.D.; Phillips, M.S.; Simmons, J.A.; Hanslow, D.J.; Short, A.D. Extreme coastal erosion enhanced by anomalous extratropical storm wave direction. *Sci. Rep.* **2017**, *7*, 6033. [CrossRef] [PubMed]

9. Van Thiel de Vries, J.S.M. *Dune Erosion during Storm Surges*; IOS Press BV: Amsterdam, The Netherlands, 2009.
10. Nederhoff, C.M. Modeling the Effects of Hard Structures on Dune Erosion and Overwash Hindcasting the Impact of Hurricane Sandy on New Jersey with XBeach. Masters' Thesis, Delft University of Technology, Delft, The Netherlands, 2014.
11. Elsayed, S.M. *Breaching of Coastal Barriers under Extreme Storm Surges and Implications for Groundwater Contamination: Improvement and Extension of the XBeach Model to Account for New Physical Processes*; Technische Universitt Braunschweig: Braunschweig, Germany, 2017.
12. McCall, R. The Longshore Dimension in Dune Overwash Modelling. Masters' Thesis, Delft University of Technology, Delft, The Netherlands, 2008.
13. Gruwez, V.; Verheyen, B.; Wauters, P.; Bolle, A. 2DH Morphodynamic Time-Dependent Hindcast Modelling of a Groyne System in Ghana. In Proceedings of the 11th International Conference on Hydroscience and Engineering Antwerp, Hamburg, Germany, 28 September–2 October 2014.
14. Soulsby, R.L. *Dynamics of Marine Sands*; Tomas Telford Publication: London, UK, 1997; ISBN 072772584X/9780727725844.
15. Van Rijn, L.C. Unified view of sediment transport by currents and waves. I: Initiation of motion, bed roughness, and bed-load transport. *J. Hydraul. Eng.* **2007**, *133*, 649–667. [CrossRef]
16. Van Rijn, L.C. Unified view of sediment transport by currents and waves. II: Suspended transport. *J. Hyrdraul. Eng.* **2007**, *133*, 668–689. [CrossRef]
17. Van Rijn, L.C. *Principles of Sediment Transport in Rivers, Estuaries and Coastal Seas*; Aqua Publications: Amsterdam, The Netherlands, 1993.
18. De Vet, P.L.M.; McCall, R.T.; Den Bien, J.P.; Stive, M.J.F.; Van Ormondt, M. Modelling Dune Erosion, Overwash and Breaching at Fire Island (NY) during Hurricane Sandy. In Proceedings of the Coastal Sediment 2015, San Diego, CA, USA, 11–15 May 2015; pp. 1–10.
19. Harter, C.; Figlus, J. Numerical modeling of the morphodynamic response of a low-lying barrier island beach and foredune system inundated during Hurricane Ike using XBeach and CSHORE. *Coast. Eng.* **2017**, *120*, 64–74. [CrossRef]
20. Orzech, M.D.; Reniers, A.J.H.M.; Thornton, E.B.; MacMahan, J.H. Megacusps on rip channel bathymetry: Observations and modeling. *Coast. Eng.* **2011**, *58*, 890–907. [CrossRef]
21. Ruessink, B.G.; Ramaekers, G.; Van Rijn, L.C. On the Parameterization of the free-stream non-linear wave orbital motion in nearshore morphodynamic models. *Coast. Eng.* **2012**, *65*, 56–63. [CrossRef]
22. Rienecker, M.M.; Fenton, J.D. A Fourier approximation method for steady water waves. *J. Fluid. Mech.* **1981**, *104*, 119–137. [CrossRef]
23. Do, K.; Yoo, J. Morphological response to storms in an embayed beach having limited sediment thickness. *Estuar. Coast. Shelf. Sci.* **2020**, *234*, 106636. [CrossRef]
24. Pender, D.; Karunarathna, H. A statistical-process based approach for modelling beach profile variability. *Coast. Eng.* **2013**, *81*, 19–29. [CrossRef]
25. Gallagher, E.L.; Elgar, S.; Guza, R.T. Observations of sand bar evolution on a natural beach. *J. Geophys. Res. Oceans* **1998**, *103*, 3203–3215. [CrossRef]
26. Grasso, F.; Michallet, H.; Barthélemy, E. Sediment transport associated with morphological beach changes forced by irregular asymmetric, skewed waves. *J. Geophys. Res. Oceans* **2011**, *116*, C03020. [CrossRef]

Journal of
Marine Science and Engineering

MDPI

Article

Non-Equilibrium Scour Evolution around an Emerged Structure Exposed to a Transient Wave

Deniz Velioglu Sogut [1,*], Erdinc Sogut [2], Ali Farhadzadeh [3] and Tian-Jian Hsu [4]

[1] Department of Ocean Engineering and Marine Sciences, College of Engineering and Science, Florida Institute of Technology, Melbourne, FL 32901, USA
[2] Department of Geology and Geophysics, Woods Hole Oceanographic Institution, Falmouth, MA 02543, USA; erdinc.sogut@whoi.edu
[3] Department of Civil Engineering, College of Engineering and Applied Sciences, Stony Brook University, Stony Brook, NY 11794, USA; ali.farhadzadeh@stonybrook.edu
[4] Department of Civil and Environmental Engineering, Center for Applied Coastal Research, University of Delaware, Newark, DE 19716, USA; thsu@udel.edu
* Correspondence: dvelioglusogut@fit.edu

Abstract: The present study evaluates the performance of two numerical approaches in estimating non-equilibrium scour patterns around a non-slender square structure subjected to a transient wave, by comparing numerical findings with experimental data. This study also investigates the impact of the structure's positioning on bed evolution, analyzing configurations where the structure is either attached to the sidewall or positioned at the centerline of the wave flume. The first numerical method treats sediment particles as a distinct continuum phase, directly solving the continuity and momentum equations for both sediment and fluid phases. The second method estimates sediment transport using the quadratic law of bottom shear stress, yielding robust predictions of bed evolution through meticulous calibration and validation. The findings reveal that both methods underestimate vortex-induced near-bed vertical velocities. Deposits formed along vortex trajectories are overestimated by the first method, while the second method satisfactorily predicts the bed evolution beneath these paths. Scour holes caused by wave impingement tend to backfill as the flow intensity diminishes. The second method cannot sufficiently capture this backfilling, whereas the first method adequately reflects the phenomenon. Overall, this study highlights significant variations in the predictive capabilities of both methods in regard to the evolution of non-equilibrium scour at low Keulegan–Carpenter numbers.

Keywords: Keulegan–Carpenter number; solitary wave; non slender; wave–structure interaction; FLOW-3D; SedWaveFoam

Citation: Velioglu Sogut, D.; Sogut, E.; Farhadzadeh, A.; Hsu, T.-J. Non-Equilibrium Scour Evolution around an Emerged Structure Exposed to a Transient Wave. *J. Mar. Sci. Eng.* **2024**, *12*, 946. https://doi.org/10.3390/jmse12060946

Academic Editor: Constantine Michailides

Received: 25 April 2024
Revised: 28 May 2024
Accepted: 1 June 2024
Published: 5 June 2024

1. Introduction

The increase in the magnitude and frequency of storms is a crucial aspect of climate change, where larger ocean waves lead to more frequent and harsher storm surge and flooding events. The most recent examples are Hurricanes Ian and Nicole, which made landfall in Florida on 28 September 2022 and 10 November 2022 as powerful Category 4 and 1 storms, respectively. Ian came ashore as one of the strongest storms ever to strike Florida, leaving behind massive coastal damage and widespread power outages. Nicole was the first storm to make landfall on Florida's east coast since 2005, crossing the same area that had been devastated by Ian six weeks earlier. Its massive size caused widespread heavy rainfall and high winds across the Bahamas, Florida, and the Greater Antilles, leading to power outages, substantial damage to infrastructure and residential buildings, and extensive beach erosion along Florida's east coast. These extreme flooding events underscore the need for more in-depth studies on the failures of beachfront structures in the low-elevation urbanized coastal zones. An important factor that contributes to the failure of beachfront structures during such events is the scouring process [1,2].

Wave- and/or current-induced equilibrium scour around slender cylindrical structures has been extensively studied [3–20] due to its relevance to a wide range of applications such as offshore wind farms in the renewable energy industry and bridges in the transportation sector. Studies on the equilibrium scour of slender square structures under different flow conditions have also been conducted [17,21–23]. However, knowledge on wave-induced non-equilibrium scour processes around non-slender structures remains limited due to lack of conclusive data. Non-equilibrium scour is a constantly evolving scour pattern, as erosion and accretion are not in equilibrium. Various factors contribute to non-equilibrium scour, including changes in flow velocity, sediment size distribution, and turbulence intensity. It is commonly observed during transient flow conditions such as waves, storm-driven floods, or tidal fluctuations. Understanding non-equilibrium scour is essential for the design and maintenance of infrastructure, as it can lead to significant alterations in the bathymetry around structures, posing risks to their stability and safety. Therefore, investigating and predicting non-equilibrium scour processes is crucial for risk mitigation and the integrity of coastal and hydraulic structures. Recent field investigations have shown that wave-induced scour around beachfront structures is highly dependent on the structure's size and placement within an array [24–26]. Although these investigations provide insight into the scouring process during extreme overland flooding events, they do not contribute significantly to the accurate prediction of non-equilibrium scour around beachfront structures.

Sediment transport processes can be numerically described by an equation set that simulates the spatial and temporal evolution of a fluid flow carrying sediment as it interacts with the adjacent mobile bed [27]. Numerical models that simulate sediment transport aim to predict the overall mass flux and sediment concentration at each point in the domain with reasonable accuracy. However, the literature review shows that studies investigating the capability of these models in predicting non-equilibrium scour around non-slender structures are still lacking. This gap in knowledge motivates the current work.

The present study aims to investigate the morphological changes in a sandy bed when a transient wave interacts with an emerged non-slender square structure, using a combination of wave flume experiments and high-fidelity numerical simulations. Additionally, the effect of structure position on bed evolution was examined by considering two different layouts, one where the structure was attached to the sidewall and the other where it was positioned at the centerline. To numerically study the test cases mentioned above, two different approaches were employed.

The first approach utilized SedWaveFoam, a numerical tool that considers the sediment layer as a separate phase in addition to air and water phases and solves Reynolds-averaged Navier–Stokes (RANS) equations. This tool differs from single-phase models that rely on assumptions of bed/suspended load and bed shear stress [28–30] because it directly solves the continuity and momentum equations for sediment, water, and air phases [31]. The second approach employed FLOW-3D, which estimates sediment transport using the quadratic law of bottom shear stress for three-dimensional (3D) turbulent flow and resolves the flow field using the RANS equations. However, the morphodynamics module of FLOW-3D is case specific and requires calibration and validation to obtain robust estimations of bed evolution [32,33].

In this study, a comprehensive comparative analysis was performed to assess the predictive capabilities of the two different approaches as well as some of their shortcomings in estimating the non-equilibrium scour around a non-slender emerged square structure exposed a transient wave. It should be noted that the current version of SedWaveFoam only supports the $k - \varepsilon$ turbulence scheme, whereas FLOW-3D adopts the large eddy simulation (LES) scheme to simulate the turbulent flow characteristics. Here, the authors regard the two approaches as different tools, with discussions centered on a broad framework. The capability of the models was tested for a low Keulegan–Carpenter (KC) number, and discussions were based on the non-equilibrium scour characteristics, suspended sediment concentration, and patterns of sediment deposits in the vicinity of the structure. The present study advances knowledge in the field of coastal and hydraulic engineering, offering guidance for scientific community on selecting the most appropriate modeling approach for similar scenarios. Overall, the effort provides valuable insights that can enhance coastal resilience in the face of dynamic environmental conditions.

This research builds on the authors' previous work [34–36], which focused on the formation and evolution of non-equilibrium scour around square non-slender vertical structures under solitary wave and/or combined flow (wave and current) actions. The authors extend their previous work by providing high-fidelity numerical investigations using a finer mesh and two different layouts to further investigate the underlying physics of the phenomenon.

2. Physical Modeling

The experiments were carried out using the 25 m long $\times$ 1.5 m wide $\times$ 1.5 m deep wave/current flume at Stony Brook University's Coastal and Hydraulic Engineering Research Laboratory (CHERL). The piston-type wet-back wavemaker had an active wave absorption system (AWAS) that minimized the effect of wave reflection. To further dampen the reflected waves, a honeycomb mesh that acted as a passive wave energy absorption system was placed at the end of the wave flume (Figure 1). A sharp-edged wooden block with cross-sectional dimensions 0.5 m $\times$ 0.5 m was placed on a 0.18 m thick sand layer with a median grain diameter of $d_{50} = 0.27$ mm. The wave paddle was programmed to generate a solitary wave as described by [37]

$$\eta(x,t) = H\,\mathrm{sech}^2(k(1-ct)) \tag{1}$$

where η is the water surface elevation, c is the wave celerity, t is time and k is the wave number defined as $\sqrt{3H/4h^3}$. The incident wave height (H) at the paddle was 10 cm, with a period (T) of 3.20 s. The wave propagated over a 0.48 m water depth (h), which was reduced to 0.30 m on the sandy bed. The flume experiments were conducted for two layouts: (1) structure attached to the sidewall (side) and (2) structure positioned at the centerline (center). The KC number used in the experiments is 3.14. While the experiments were not specifically tailored to replicate a precise real-life condition, the structure and flow parameters followed the Froude similitude with a λ = 1:40 length scale [17].

In small-scale flume experiments utilizing relatively large structures, blockage effects may arise, leading to an increase in flow velocity and potentially causing contraction scour. Various researchers have outlined specific geometric ratios necessary to ensure that blockage effects on scour depth are minimal [19,38,39]. The distance of the structure from a wall could impact the findings, leading to accelerated flow and changes in the wake structure. In potential flow theory, the wall effect is considered negligible when a structure is located at a distance from the wall equal to its dimension [40]. Therefore, the blockage ratio is not expected to significantly impact local hydrodynamics in the experiments.

The instantaneous free surface elevation was measured via eight Edinburgh Designs WG8USB resistive wave gauges (WG) with a sampling frequency of 128 Hz. The velocity field was captured by three Nortek Vectrino Acoustic Doppler Velocimeters (ADV) with a sampling rate of 25 Hz. The 3D velocity field was measured at one-third the still water depth $(h/3)$ above the sandy bed. The surface of the sand layer was scanned using an HR-Wallingford HRBP-1070 bed profiler system equipped with a laser probe with an accuracy of ± 0.5 mm. The scanned area measured 2.5 m in length and 1.5 m in width. The limitations in the maneuverability of the probe arm assembly created a ~2 cm wide blind zone around the structure, necessitating manual measurement. The surface of the sandy bed was carefully leveled prior to each test, and the water level was allowed to settle and be free from disturbances before conducting each trial. The number and plan view of the instruments are shown in Figure 1. Further details on the experimental procedure can be found in [36].

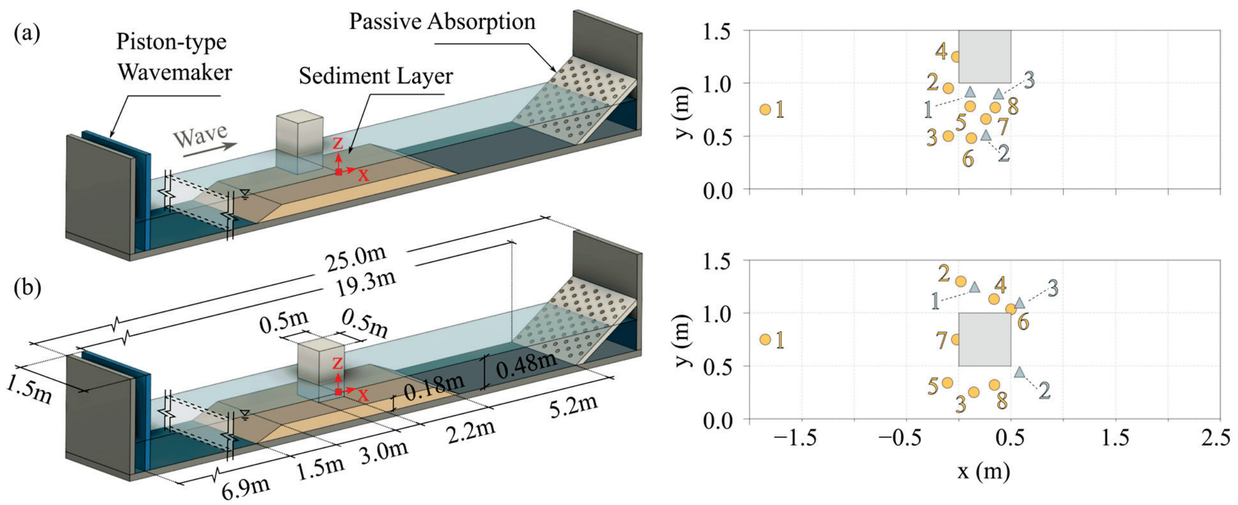

Figure 1. Experimental setup and plan view of WGs and ADVs for (**a**) side and (**b**) center layouts. Yellow circle and gray triangle represent WG and ADV, respectively.

3. Numerical Modeling

As previously mentioned, this study presents a comparative analysis of the scour formation around the structure, utilizing two high-fidelity numerical models to predict sediment motions and transport. One model employs multiphase flow physics, while the other uses conventional bedload/suspended load formulations. Here, a brief description of each model is presented.

3.1. SedWaveFoam

SedWaveFoam, developed within the OpenFOAM environment, is an open-source Eulerian two-phase model for sediment transport [31]. This model combines the SedFoam [41], InterFoam [42], and waves2Foam [43] models. The Reynolds-averaged mass conservation equations for the air (a), water (w), and sediment (s) phases [42,44] are resolved by treating the air and water as two immiscible fluids, collectively referred to as the fluid-phase (f). The sediment is modeled as a miscible phase in the fluid, resulting in a two-phase flow. To resolve the interface of the air and water phases, SedWaveFoam uses an interface tracking scheme [31,42,45]. The mass conservation equations of the fluid and sediment phases are written as follows:

$$\frac{\partial \phi^f}{\partial t} + \frac{\partial \phi^f u_i^f}{\partial x_i} = \left(\frac{\partial \phi^a}{\partial t} + \frac{\partial \phi^a u_i^a}{\partial x_i} \right) + \left(\frac{\partial \phi^w}{\partial t} + \frac{\partial \phi^w u_i^w}{\partial x_i} \right) = 0 \quad (2)$$

$$\frac{\partial \phi^s}{\partial t} + \frac{\partial \phi^s u_i^s}{\partial x_i} = 0 \quad (3)$$

where ϕ^a, ϕ^w, and ϕ^s represent the volumetric concentrations and u^a, u^w, and u^s are the velocities of the air, water, and sediment phases, respectively. The fluid-phase volumetric concentration and velocity are modelled as $\phi^f = \phi^a + \phi^w$ and $u^f = (\phi^a u^a + \phi^w u^w)/\phi^f$, respectively. The global mass conservation satisfies $\phi^a + \phi^w + \phi^s = 1$.

The simplified Reynolds-averaged momentum equations for the two-phase flow are as follows:

$$\frac{\partial \rho^f \phi^f u_i^f}{\partial t} + \frac{\partial \rho^f \phi^f u_i^f u_j^f}{\partial x_j} = -\phi^f \frac{\partial P^f}{\partial x_i} + \rho^f \phi^f g \delta_{i3} - \sigma_t \gamma_s \frac{\partial \phi^a}{\partial x_i} + \frac{\partial \tau_{ij}^f}{\partial x_j} + M_i^{fs} \quad (4)$$

$$\frac{\partial \rho^s \phi^s u_i^s}{\partial t} + \frac{\partial \rho^s \phi^s u_i^s u_j^s}{\partial x_j} = -\phi^s \frac{\partial P^f}{\partial x_i} - \frac{\partial P^s}{\partial x_i} + \rho^s \phi^s g \delta_{i3} - \sigma_t \gamma_s \frac{\partial \phi^s}{\partial x_i} + \frac{\partial \tau_{ij}^s}{\partial x_j} + M_i^{sf} \quad (5)$$

where ρ^s and ρ^f are the densities of sediment and fluid phases, and the density of the fluid phase is modelled as $\rho^f = (\phi^a\rho^a + \phi^w\rho^w)/\phi^f$. Here, the densities are adopted as $\rho^a = 1$ kg/m^3, $\rho^w = 1000$ kg/m^3, and $\rho^s = 2650$ kg/m^3. P^f and P^s stand for the fluid and particle pressures, and the fluid and particle shear stresses are symbolized by the terms τ_{ij}^f and τ_{ij}^s, respectively. g is the gravitational acceleration and δ_{i3} is the Dirac delta function. The term $\sigma_t\gamma_s$ represents the surface tension where σ_t and γ_s are the surface tension coefficient and surface curvature, respectively. The fluid stress, τ_{ij}^f is modeled using a two-equation $\mathrm{k}-\varepsilon$ model [31,45]. The interphase momentum transfer between fluid–sediment (M_i^{fs}) and sediment–fluid (M_i^{sf}) is a function of drag force and turbulent suspension [41,46] and follows Newton's third law ($M_i^{fs} = M_i^{sf}$). The particle pressure, P^s, and particle shear stress, τ_{ij}^s, are modelled as a function of the collisional and frictional components of the intergranular interactions with the former using the kinetic theory of granular flow [47]. The reader is kindly referred to [31,41,45,46] for more detail.

3.2. FLOW-3D

FLOW-3D is a computational fluid dynamics (CFD) software package that utilizes the finite volume method (FVM) to solve the 3D Reynolds-averaged Navier–Stokes equations [48]. The model employs volume-based techniques for simulation, where the equations are formulated with area and volume porosity functions, which are essential for the Fractional Area/Volume Obstacle Representation Method, FAVOR$^{\mathrm{TM}}$ [49,50], while the free surface is defined using a volume of fluid (VOF) function [51]. For incompressible fluids, FLOW-3D utilizes the general mass continuity and momentum equations:

$$\frac{\partial}{\partial x_i}(u_i A_i) = 0 \tag{6}$$

$$\frac{\partial u_i}{\partial t} + \frac{1}{V_F}\left\{u_j A_j \frac{\partial u_i}{\partial x_j}\right\} = -\frac{1}{\rho}\frac{\partial P}{\partial x_i} + G_i + f_i \tag{7}$$

where $i,\ j = 1, 2, 3$ represent the 3D flow field, u_i is the fluid velocity, A_i is the fractional area open to fluid flow, t is time, V_F is the fractional volume open to flow, ρ is the fluid density, P is pressure, G_i is the body acceleration and f_i is the viscous acceleration.

The VOF function, F, satisfies the following:

$$\frac{\partial F}{\partial t} + \frac{1}{V_F}\left[\frac{\partial}{\partial x_i}(F A_i u_i)\right] = F_{DIF} \tag{8}$$

where

$$F_{DIF} = \frac{1}{V_F}\left[\frac{\partial}{\partial x_i}\left(\nu_F A_i \frac{\partial F}{\partial x_i}\right)\right] \tag{9}$$

and the diffusion coefficient is $\nu_F = \sigma_c \mu_f/\rho$. The constant, σ_c, is referred to as turbulent Schmidt number, and μ_f is the dynamic viscosity of fluid.

The turbulence models implemented in FLOW-3D differ slightly from conventional formulations due to the inclusion of the FAVOR$^{\mathrm{TM}}$ method in the equations and a generalized treatment of turbulence production associated with buoyancy forces [48].

Notably, FLOW-3D offers several turbulence model closures, including the two-equation $\mathrm{k}-\omega$, renormalization group (RNG) $\mathrm{k}-\varepsilon$, and large eddy simulation (LES) [48,49]. Moreover, the hydrodynamic solver of FLOW-3D is fully coupled with a sediment transport module that simulates morphological changes resulting from various physical processes, such as bedload transport, entrainment, and deposition. The standard wall function is employed to evaluate bed shear stress in 3D turbulent flows, incorporating bed surface roughness proportional to the median grain size:

$$k_s = c_{\mathrm{rough}} d_{50} \tag{10}$$

where k_s is the Nikuradse roughness of the bed surface, c_{rough} is a user-defined coefficient with default value 2.5, and d_{50} is the median grain size.

In FLOW-3D, the suspended sediment is modeled as a scalar mass concentration that is assumed to be uniform across each computational cell and coupled with the density and viscosity of the fluid cell. To simulate the entrainment of sediment grains, FLOW-3D employs the equation of [52] to calculate the lift velocity of the entrained sediment grains.

$$u_{\mathrm{lift}} = \alpha \mathrm{n}_s d_*^{0.3} \left(\theta - \theta'_{\mathrm{cr}}\right)^{1.5} \sqrt{\frac{\|g\| d_{50}\left(\rho_s - \rho_f\right)}{\rho_f}} \tag{11}$$

where u_{lift} is the entrainment lift velocity of sediment, α is the entrainment parameter with a recommended value of 0.018 [52], n_s is the vector normal to the bed interface, θ and θ_{cr} are the local and critical Shields parameters given by [53], $\|g\|$ is the magnitude of the gravitational acceleration, ρ_s and ρ_f are the sediment and fluid densities, respectively, and d_* is a dimensionless grain diameter given by the following equation:

$$d_* = d_{50}\left[\frac{\rho_f\left(\rho_s - \rho_f\right)\|g\|}{\mu_f^2}\right]^{1/3} \tag{12}$$

The settling velocity of a sediment grain is given as follows [53]:

$$u_{\mathrm{settling}} = \frac{\nu_F}{d_{50}}\left[\left(10.36^2 + 1.049 d_*^3\right)^{0.5} - 10.36\right] \tag{13}$$

The bedload transport in each mesh cell can be calculated by three different formulations: Nielsen [54]

$$\Phi = \beta_{\mathrm{Nie}} \theta^{0.5}\left(\theta - \theta'_{\mathrm{cr}}\right) \tag{14}$$

van Rijn [55]

$$\Phi = \beta_{\mathrm{VR}} d_*^{-0.3}\left(\frac{\theta}{\theta'_{\mathrm{cr}}} - 1\right)^{2.1} \tag{15}$$

Meyer-Peter and Müller [56]

$$\Phi = \beta_{\mathrm{MPM}}\left(\theta - \theta'_{\mathrm{cr}}\right)^{1.5} \tag{16}$$

Here, Φ is the dimensionless bed-load transport rate; β_{Nie}, β_{VR}, and β_{MPM} are coefficients typically taken as 12.0, 0.053, and 8.0, respectively.

The suspended sediment concentration is calculated as follows:

$$\frac{\partial c_s}{\partial t} + \nabla\cdot(u_s c_s) = \nabla\cdot\nabla(D c_s) \tag{17}$$

where c_s is the suspended sediment volume concentration, D is the diffusivity, u_s is the suspended sediment velocity calculated as $u_s = \overline{u} + u_{\mathrm{settling}} c_s$, $\overline{u}$ being the velocity of the fluid–sediment mixture.

3.3. Implementation

To accurately recreate the water surface variations recorded at WG1, the SedWaveFoam model requires a sufficient number of harmonics, defined by their amplitudes, phases, and periods. To generate the input boundary conditions, the incident wave signal recorded at WG1 was transformed using the fast Fourier transform (FFT) algorithm, and its harmonics were used. The rigid boundaries of the numerical wave flume (NWF) were defined as no-slip/wall boundaries. To prevent wave reflection from the landward end, an absorption boundary condition was applied at the outlet, where an inward corrective velocity was generated to absorb the incident wave. The depth of the water, gravitational acceleration, and the free surface height of the border were factors considered in determining this velocity [57,58].

The incident wave time series measured at WG1 was directly applied at the inlet of the FLOW-3D NWF, with the flume bottom, sidewalls, and structure defined as wall/no-slip boundaries. The NWF had a wave absorbing (sponge) layer, where an artificial linear damping force was implemented to dissipate wave motion [48]. The wave-absorbing boundary was enforced by selecting an outflow boundary condition at the outlet.

The index of agreement (IA) metric [59] was employed to measure the accuracy of the simulations. IA accounts for phase disagreements, where IA = 1 and IA = 0 indicate perfect agreement and disagreement, respectively. To that end, the mesh was refined until the calculated IA for the measured versus computed horizontal velocity components, u, remained relatively unchanged (Figure 2). Mesh independence was achieved at a minimum cell size of 2.5 mm for both models. The center layout yielded the same results as the side layout.

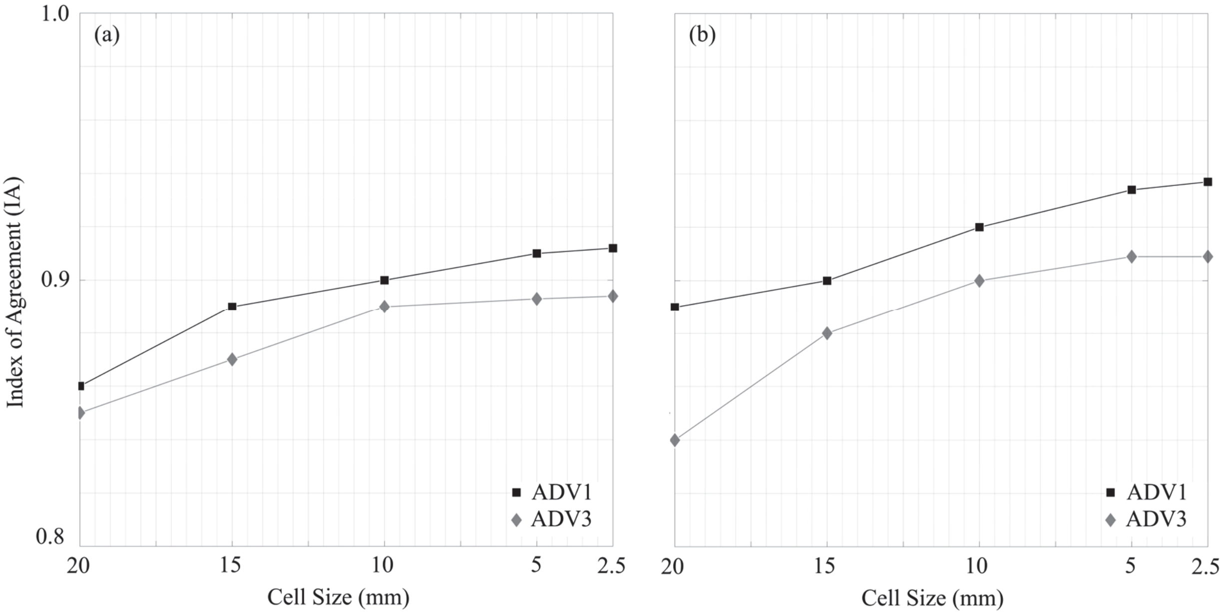

Figure 2. Grid sensitivity analyses based on the horizontal velocity component, u, captured by ADV1 and ADV3 for side layout: (**a**) SedWaveFoam; (**b**) FLOW-3D.

Figure 3 illustrates the final mesh structure utilized in the NWF. The largest cell size on the $x-y$ plane was 25 mm, which was gradually refined to a smaller cell size near the structure. The optimal cell size of 2.5 mm, as determined from grid sensitivity analyses, was employed in the refinement area marked by a dashed rectangle (Figure 3). Moreover, the region spanning from $z = -0.33$ m to $z = -0.30$ m underwent further refinement from 5 mm to 0.5 mm to achieve a more precise prediction of scouring.

To ensure model stability and convergence, the simulations used an adaptive time step with a maximum Courant number of 0.2. The model outputs had a sampling rate of 25 Hz, consistent with that of the ADVs. The total number of grid points in the FLOW-3D NWF for the side layout was ~7.2×10^6 and the clock time for a 15 s simulation was 102 h using 8 cores of a 12th Gen Intel Core i9-12900KF processor. The total number of grid points for the center layout, on the other hand, was ~17.4×10^6, with 130 h clock time. Even though the same variable mesh was adopted in both models in the vicinity of the structure, the SedWaveFoam NWF required longer wave generation and absorption zones for numerical stability. This resulted in an increase in the total number of grid points to ~22.5×10^6 and ~44.2×10^6 for the side and center layouts, respectively. The clock time of the 15 s SedWaveFoam simulation was 300 h for the side layout and 624 h for the center layout on

Blueshark High Performance Computing Cluster at Florida Tech with 10 × 2 × Hexa-Core Intel Xeon X5650 @ 2.67GHz CPUs (120 cores). (Intel, Santa Clara, CA, USA).

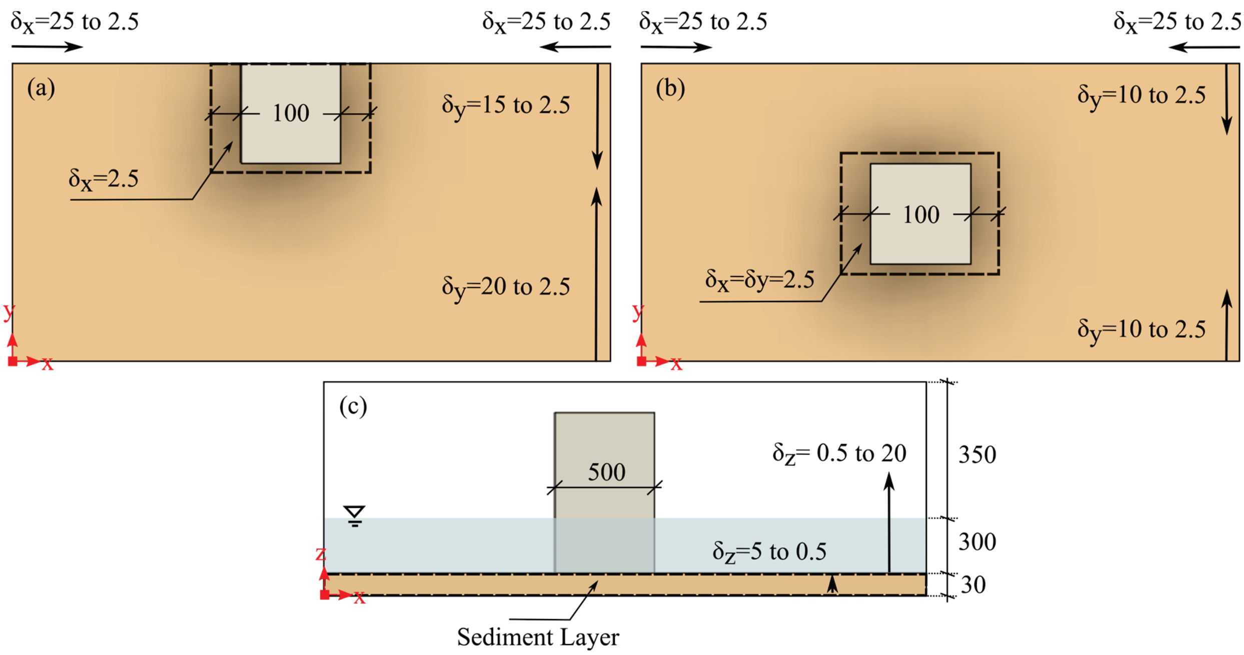

Figure 3. Final mesh of NWF for both models. (**a**) side; (**b**) center layouts on $x - y$ plane; (**c**) both layouts on $x - z$ plane. All units are in mm. Not to scale.

3.4. Validation

The accuracy of the numerical models is evaluated in both time and frequency domains. The wave gauges and ADVs were replicated in the NWF as line probes at the same locations as those in the experiments.

Figure 4a,b illustrates the temporal variations of the free surface elevation (η) at three selected wave gauge positions—WG1, WG2, WG3, and WG4 for the side layout and WG1, WG2, WG3, and WG7 for the center layout. WG1 is the wave gauge closest to the wave maker in both layouts, illustrating the time series profile of the incident wave generated by the wave maker. The height of the solitary wave measured by WG1 is 0.097 m. The gauges WG2 and WG3 measure the surface fluctuations of the channeled flows in both layouts, and WG4 and WG7 are the gauges that are attached to the structure's seaside face for the side and center layouts, respectively. The IA values for η range between 0.9–1.0, indicating a good agreement (Table 1).

The streamwise (u), spanwise (v), and vertical (w) velocity components at the three ADV locations are shown in Figure 4c,d. The raw velocity data were filtered to remove the noise resulting from potential air entrainment and suspended sediment. The noise was filtered based on a correlation $\geq$ 75% and signal-to-noise ratio (SNR) $\geq$ 10–15. Compared to the free surface elevations, the velocity field has lower IA values, especially for spanwise and vertical velocity components (Table 1). These discrepancies are attributed to the residual noise in the measured data. The lowest IAs are related to the vertical velocity component, w, which is considerably small compared to the other two velocity components. Overall, a satisfactory performance was achieved.

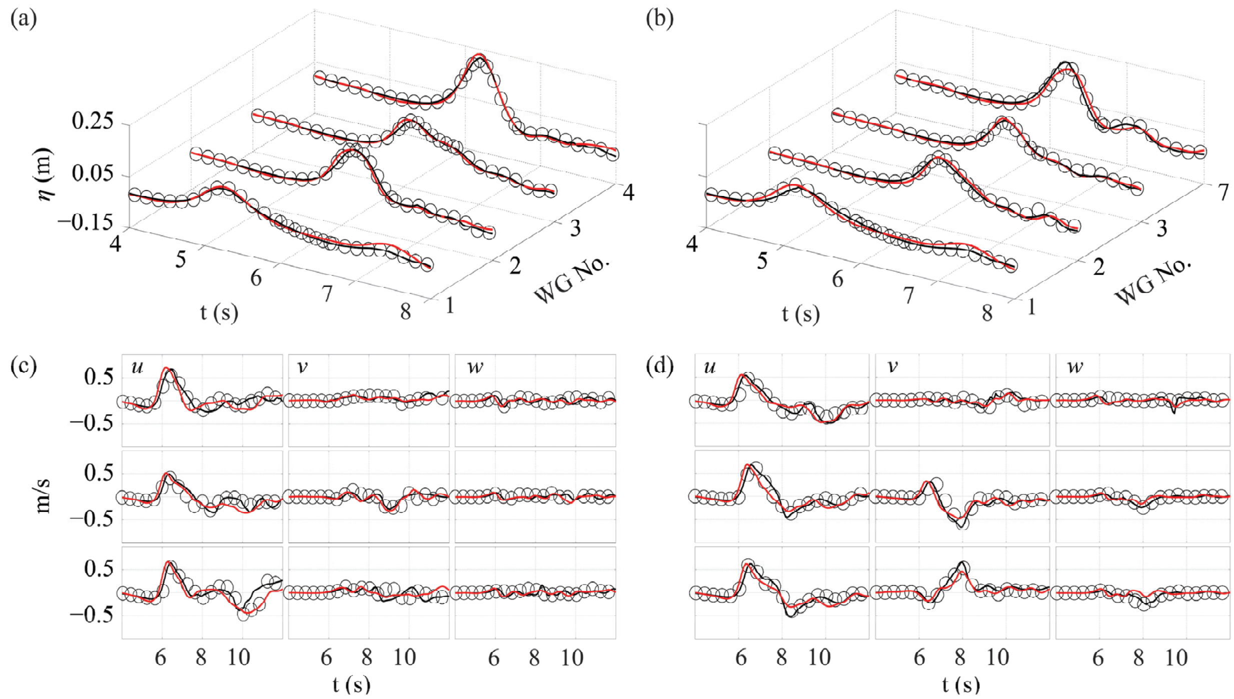

Figure 4. Comparison of measured (gray circles) and computed free surface elevations (η) and velocity components: (**a**–**c**) side; (**b**–**d**) center layout. Red and black solid lines represent SedWaveFoam and FLOW-3D results, respectively.

Table 1. Index of agreement (IA) for free surface elevations and velocity components.

		WG1	**WG2**	**WG3**	**WG4**	**WG5**	**WG6**	**WG7**	**WG8**
SedWaveFoam	Side	0.974	0.980	0.978	0.977	0.966	0.959	0.951	0.944
	Center	0.971	0.975	0.977	0.973	0.964	0.953	0.949	0.944
FLOW-3D	Side	0.998	0.985	0.982	0.969	0.988	0.976	0.982	0.977
	Center	0.989	0.979	0.978	0.965	0.986	0.902	0.978	0.963

		ADV1			**ADV2**			**ADV3**		
		u	v	w	u	v	w	u	v	w
SedWaveFoam	Side	0.912	0.685	0.661	0.925	0.784	0.545	0.894	0.681	0.554
	Center	0.923	0.798	0.653	0.949	0.726	0.671	0.905	0.714	0.608
FLOW-3D	Side	0.937	0.738	0.646	0.934	0.751	0.671	0.909	0.686	0.589
	Center	0.972	0.773	0.642	0.958	0.779	0.701	0.927	0.724	0.614

3.5. Model Calibration

The sediment transport module of FLOW-3D is case specific, which requires careful calibration and validation through several parameters such as the entrainment parameter, α_i; bedload transport model type; and turbulence scheme. The following subsections provide an in-depth calibration analysis using the abovementioned parameters.

3.5.1. Entrainment Parameter

Wake vortices are the main driving mechanism of scouring around structures under wave action, where suspended sediment transport is identified as the major transport mode [11,12,17,35,36,60]. Therefore, accurately replicating the suspended sediment concentration in the FLOW-3D model is crucial. To achieve reliable results, it is imperative to adjust the lifting velocity (Equation (11)), which is a function of the entrainment parameter (α).

Figure 5 shows the comparisons of the measured and predicted bed elevation (S) using three different entrainment parameters ranging from $\alpha = 0.018$ (default) to $\alpha = 0.18$ at a particular time instant ($t = 15$ s) as an example. The predicted bed elevations for both layouts did not align well with the experimental results when the recommended value of the entrainment parameter, $\alpha = 0.018$, was employed. Of the parameters tested, $\alpha = 0.18$ was found to provide the best outcome based on the comparison of the scour and deposition patterns as well as the maximum scour depths for both layouts (Figure 5).

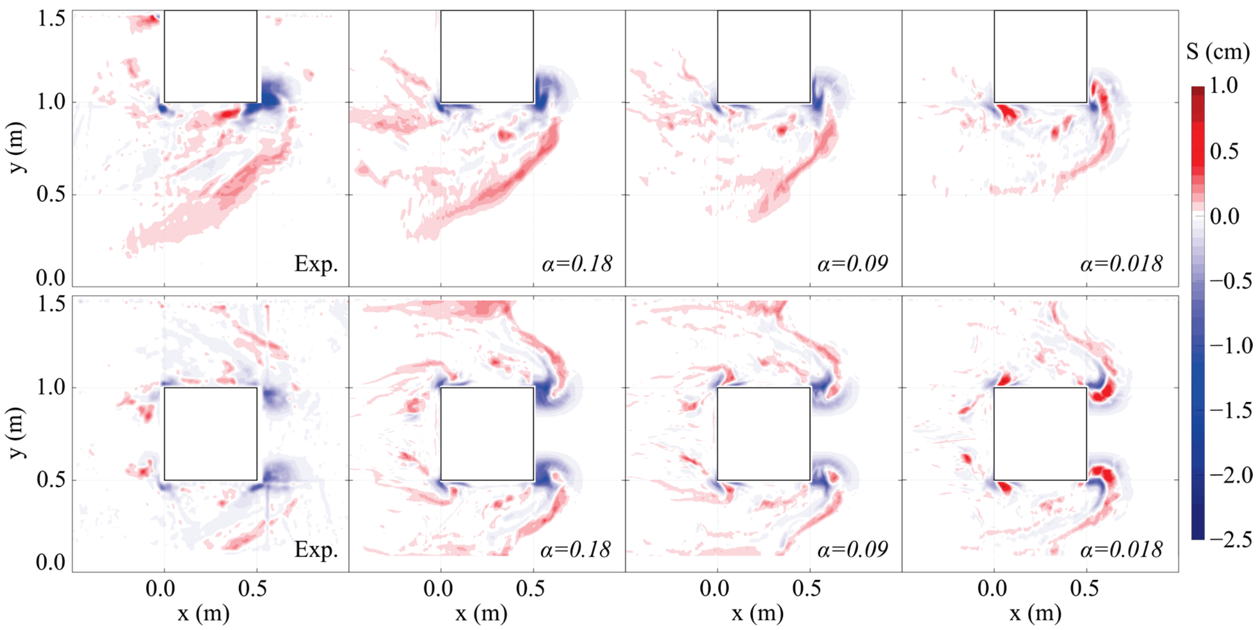

Figure 5. Plan view of sandy bed at $t = 15$ s. Upper panels: side layout. Lower panels: center layout. The figure compares the measured and predicted bed elevations using three different α values.

3.5.2. Bedload Transport Model

FLOW-3D considers a packed bed as an erodible solid object, with its morphological changes governed by the conservation of sediment mass. Bedload transport is described as sediment moving laterally along the channel without being suspended. The model computes bedload transport in each mesh cell using equations from Nielsen [54], van Rijn [55], or Meyer-Peter and Müller [56]. These three equations were compared to determine the most applicable approach for the default roughness coefficient, $c_{rough} = k_s/d_{50} = 2.5$, where $d_{50} = 0.27$ mm (Figure 6). The Nielsen equation produced the best results, with the scour and deposition trends closely matching the experimental data. The predictions were consistent with the center layout.

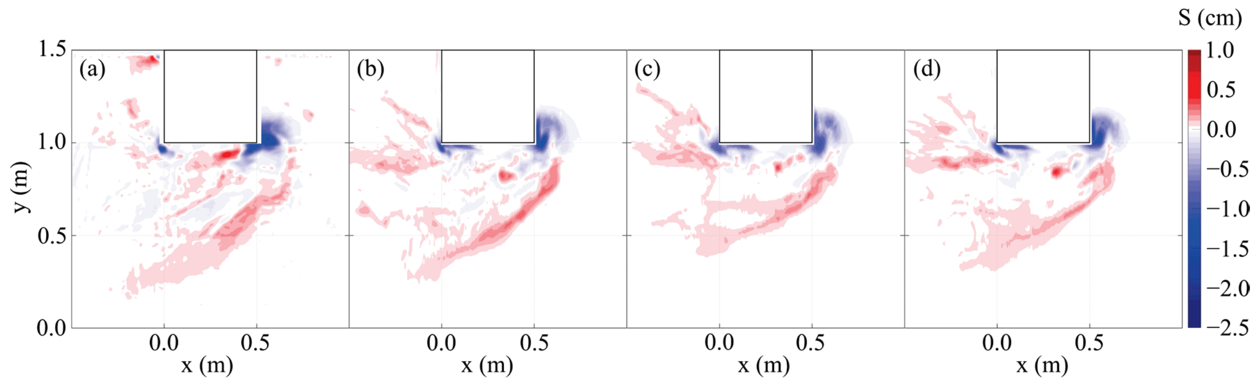

Figure 6. Plan view of sandy bed at $t = 15$ s. (**a**) Measurement; FLOW-3D results obtained using equations of (**b**) Nielsen; (**c**) van Rjin; (**d**) Meyer-Peter–Müller.

3.5.3. Turbulence Scheme

The simulations were carried out using four different turbulence schemes: (i) the two-equation $\mathrm{k}-\omega$ model [61–63]—suitable for modeling free shear flows with streamwise pressure gradients like spreading jets, wakes, and plumes; (ii) the two-equation $\mathrm{k}-\varepsilon$ model [64]—dynamically calculates the turbulent mixing length and thus useful for a wide range of flows [65]; (iii) the renormalized group (RNG) $\mathrm{k}-\varepsilon$ model [66,67]—extends the capabilities of the standard $\mathrm{k}-\varepsilon$ model and provide a better coverage for transitionally turbulent flows; (iv) the LES model—resolves most of the turbulent fluctuations directly, thus requiring much more computational resources compared to the two-equation models. Figure 7 highlights the implication of these four turbulence schemes in terms of scour and depositions in the vicinity of the structure for the side layout.

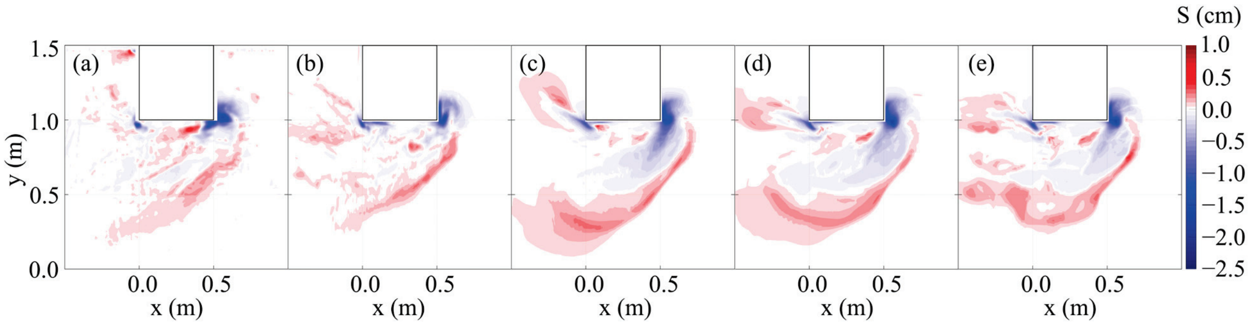

Figure 7. Plan view of sandy bed at $t = 15$ s. (**a**) Measurement; FLOW-3D results for different turbulence schemes: (**b**) LES; (**c**) RNG; (**d**) $\mathrm{k}-\varepsilon$; (**e**) $\mathrm{k}-\omega$.

The LES scheme predicted both seaside and leeside non-equilibrium scour reasonably well, while the RNG, $\mathrm{k}-\varepsilon$, and $\mathrm{k}-\omega$ schemes struggled to effectively predict the depositions around the structure. Instead, these approaches computed large scour footprints on the leeside of the structure that extended along a $\sim 45^{\circ}$ line towards the center of the NWF—a phenomenon that was not observed during the experiments. Similar results were obtained for the center layout, where the LES scheme provided the best result with respect to non-equilibrium scour prediction.

In summary, the calibration analysis indicates that FLOW-3D produced the best bed elevation predictions with $\alpha_i = 0.18$, the Nielsen [54] bed load transport model, and LES as the turbulence scheme.

4. Results and Discussion

A comparative analysis of the SedWaveFoam and FLOW-3D performances is presented in the following.

In Figure 8, we observe the spatial distributions of the instantaneous surface horizontal velocity, $U = \sqrt{u^2 + v^2}$, and the vertical velocity component, w, at two different depths: $h/3$ m above the sandy bed and on the surface of the sandy bed. The most intense vortex motion is observed between $t = 7$ s and $t = 8$ s, shortly after the wave impinges on the structure. The spatial distributions of U and w simulated by both models are quite similar for these time instants. The highest surface horizontal velocities are observed in the area near the vortex cores, which become less intense as the water level rises under the crest of the solitary wave.

Both the surface horizontal and vertical velocities above the bed increase as the wake vortex moves along its spiral trajectory (Figure 8a,c) for both layouts. However, the same trend is not observed on the bed surface, where the magnitude of these velocities does not change significantly with respect to time (Figure 8b,d). These findings suggest that changes in vortex intensity do not necessarily have an impact on sediment suspension above a certain elevation from the bed.

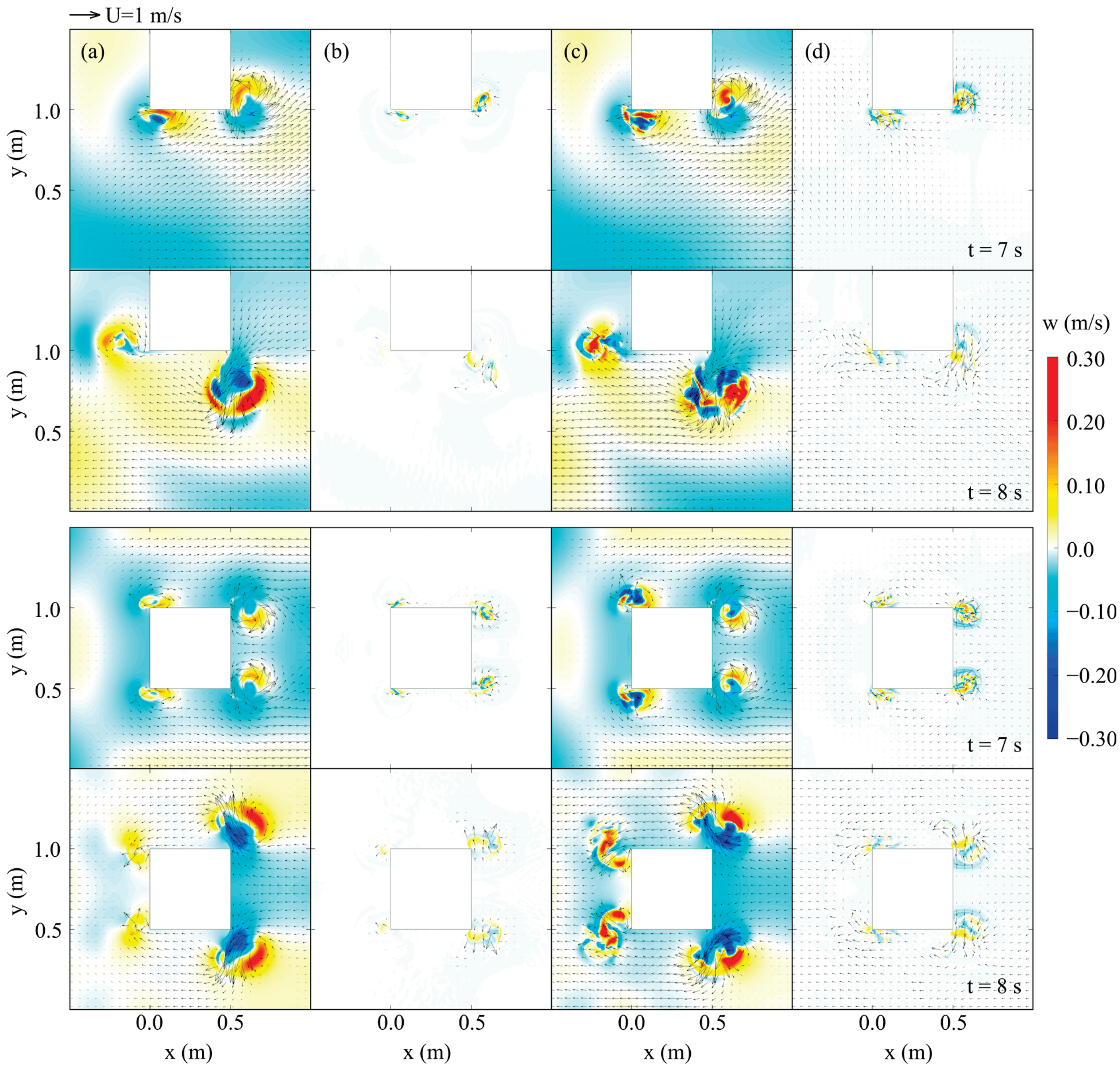

Figure 8. Spatial distributions of U and w at $t = 7$ s and $t = 8$ s, extracted from (**a**,**c**) $h/3$ m above bed; (**b**,**d**) bed surface. (**a**,**b**) and (**c**,**d**) are SedWaveFoam and FLOW-3D results, respectively. Upper two panels: side layout. Lower two panels: center layout.

Figure 9 depicts the spatial distributions of the instantaneous surface horizontal velocity, U, and the out-of-plane vorticity, ω_z, extracted at the two different depths—$h/3$ m above the sandy bed and on the bed surface—at $t = 7$ s and $t = 8$ s. The spatial distribution of ω_z simulated by both models is very similar, where the intensity ranges from -30 Hz to 30 Hz. The clockwise (CW) and counterclockwise (CCW) spinning vorticities at $t = 8$ s—marked with hot and cold colors, respectively—are the vortex doublets (i.e., ω_{za} and $\omega_{za'}$; ω_{zb} and $\omega_{zb'}$). For the center layout, a symmetric pattern of vortex pairs is formed on both seaside and leeside, with the structure's centerline being the line of symmetry. The wake vortices, ω_{zb} and ω_{zc}, are found to be larger and more intense than the out-of-plane vortices, ω_{za} and ω_{zd}, that occur at the seaside of the structure. The CCW rotating out-of-plane vortices follow a spiral trajectory for both layouts. On the other hand, the formation of CW rotating vortices, $\omega_{z'}$, is attributed to the offshore-directed flow. These vortices adopt a path that is close to a 45° line.

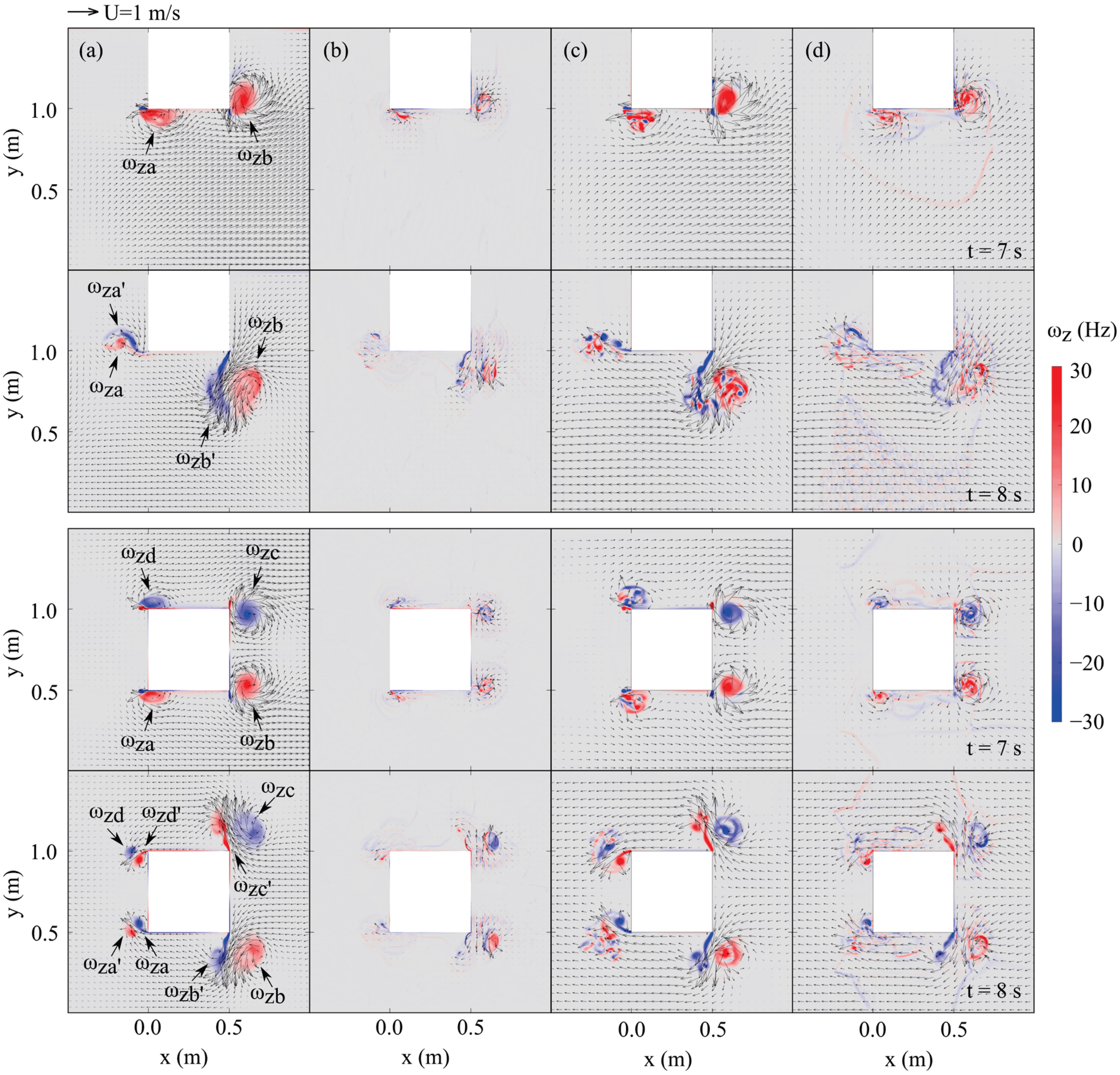

Figure 9. Spatial distributions of U and ω_z at $t = 7$ s and $t = 8$ s, extracted from (**a**,**c**) $h/3$ m above bed; (**b**,**d**) bed surface. (**a**,**b**) and (**c**,**d**) are SedWaveFoam and FLOW-3D results, respectively. Upper two panels: side layout. Lower two panels: center layout.

Figures 10 and 11 present the spatiotemporal variation in bed elevation and sediment volumetric concentration (ϕ^s) in the vicinity of the structure for both layouts. Here, the relative position of the bed within each cell is obtained by taking ϕ^s as 0.5 based on VOF method (Figures 10 and 11—upper panels). The values of ϕ^s range between 0 and 0.6 since the porosity of the sediment (i.e., the fluid fraction) is 0.4 (Figures 10 and 11—lower panels). As SedWaveFoam solves for the three phases, it treats sediment as a single separate phase in addition to air and water phases. Therefore, the instantaneous "spikes" ($S > 0$) in Figures 10a and 11a (upper panels) represent suspended sediment, which is included in the predicted bed elevation. FLOW-3D, on the other hand, employs the quadratic law of bottom shear stress and Equations (14)–(17) to estimate the bed load and suspended sediment concentration and generates separate outputs for bed elevation and sediment transport modes. Consequently, the FLOW-3D output does not reflect any instantaneous "spikes" (Figures 10b and 11b).

Both models predict that soon after the wave impingement on the structure, a significant amount of sediment is suspended near the edges, followed by the formation of scour holes. The highest suspended sediment concentration is confined within the lowest 30% of the water column (i.e., $z = -0.30$ m and $z = -0.22$ m) around the cores of the wake vortices. This can be attributed to the underprediction of the vortex-induced near-bed vertical velocity (w_n) by both models, which is unable to carry the suspended sediment further upward towards the free surface. Furthermore, between $t = 6$ s and $t = 8$ s, the dominant sediment transport mode is the suspended load, which is the determining factor denoting the deposition and/or erosion patterns.

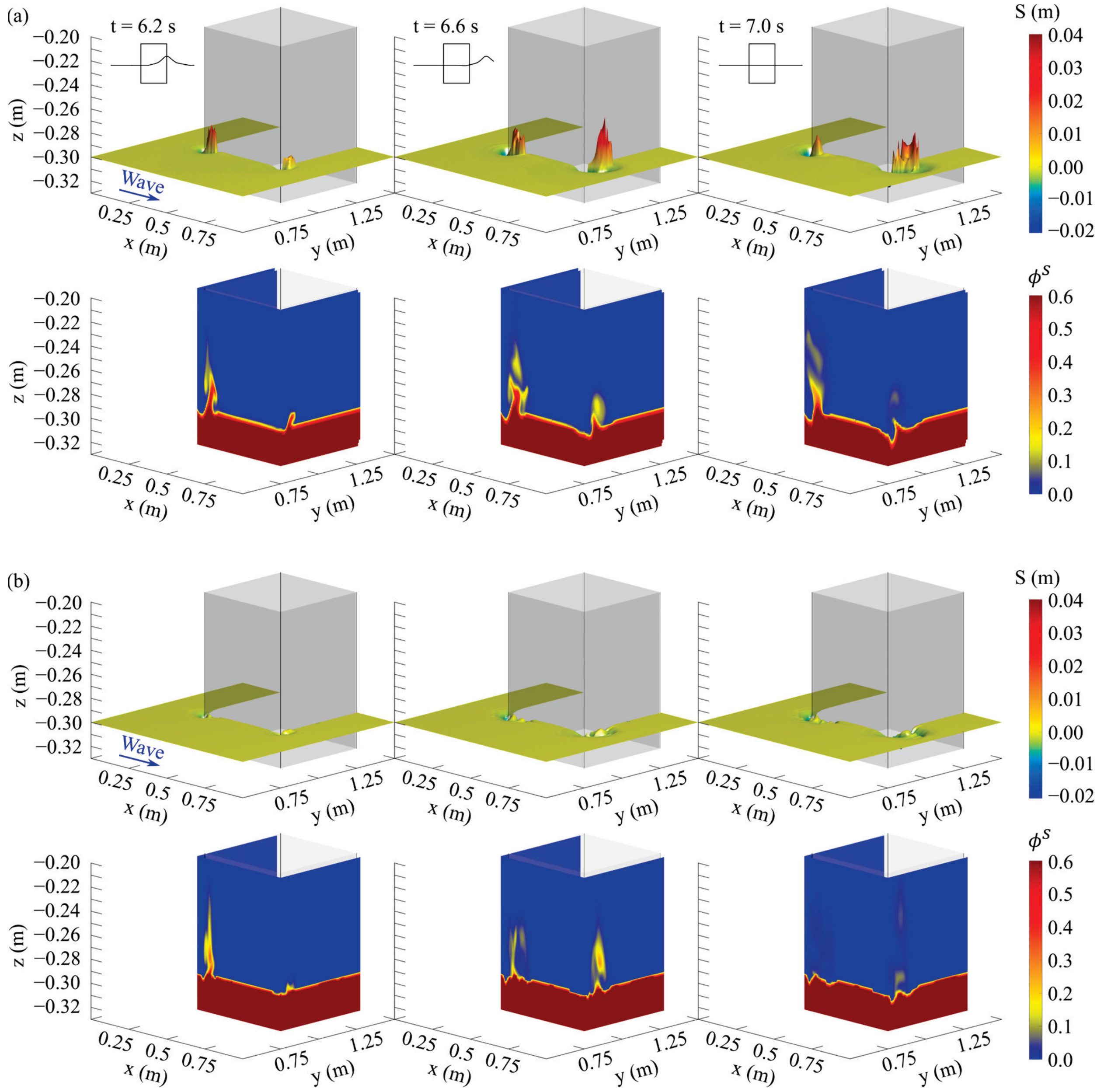

Figure 10. Bed elevation and suspended sediment concentration (ϕ^s) in the vicinity of the structure at various time instants for side layout. (**a**) SedWaveFoam results; (**b**) FLOW-3D results.

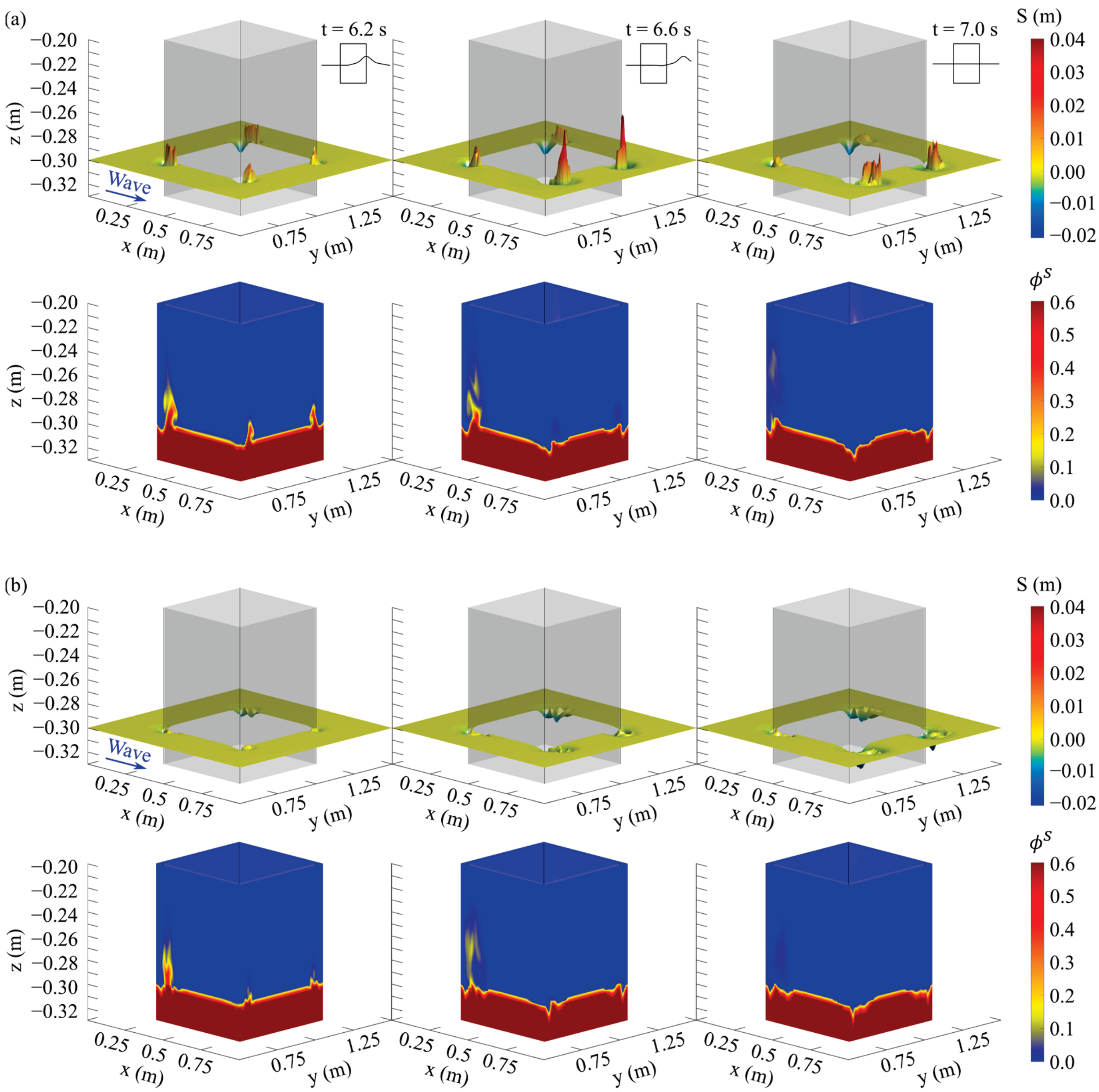

Figure 11. Bed elevation and suspended sediment concentration (ϕ^s) in the vicinity of the structure at various time instants for center layout. (**a**) SedWaveFoam results; (**b**) FLOW-3D results.

The suspended sediment concentration in the vicinity of the structure is relatively lower when the structure is placed in the center of the NWF (Figures 10b and 11b) owing to a less intense near-bed vorticity for the center layout (Figure 9b,d) compared to that of the side layout. Accordingly, the scour holes around the structure's edges are relatively shallower for the center layout, consistently predicted by two models (Figures 10a and 11a). The difference in the scour hole depths between the two layouts is more distinctive in the FLOW-3D predictions, possibly because the suspended sediment concentration is considerably lower than that predicted by SedWaveFoam.

The instantaneous suspended sediment concentrations at the leeside edge of the structure simulated by SedWaveFoam and FLOW-3D follow a similar trend for both layouts. The sediment that is captured by the out-of-plane vortex is carried up to $z = -0.22$ m and $z = -0.24$ m for the side and center layouts, respectively. On the other hand, the instantaneous suspended sediment concentrations at the seaside edge of the structure simulated by SedWaveFoam follow a different trend than that of FLOW-3D. The difference can be attributed to the intensity of the wake vortex simulated by both models. In particular, for the center layout, the suspended sediment concentration simulated by SedWaveFoam is relatively higher, where it is carried up to $z = -0.28$ m.

Figure 12—upper panels depict the trajectories of the primary vortices and the plan view of sandy bed at $t = 15$ s for both layouts. The changes in the sandy bed morphology occur primarily along the vortex trajectories. The sediment mobilized by the near-bed vertical velocity (w_n) is entrapped by out-of-plane and wake vortices. The less intense out-of-plane vortices transport and deposit the sediment in the vicinity of the structure. On the other hand, as the wake vortices drift further seaward, they can no longer sustain their energy and start to dissipate, leaving sediment deposits along their trajectories. When the structure is placed on the side of the wave flume, the path of the out-of-plane vortices simulated by SedWaveFoam is quite similar to that of experiments (i.e., the dotted arrows), while the out-of-plane vortex trajectory simulated by FLOW-3D slightly differs from the measurements. The traces of the sediment deposits captured by the wake vortex and simulated by SedWaveFoam are oriented ~35 degrees (Figure 12a) with respect to the incident wave direction, while the wake vortex simulated by FLOW-3D travels along a nearly 45-degree trajectory (Figure 12b), consistent with the observations marked by the dotted arrows. For the center layout, the trajectory of the out-of-plane vortex pair bends towards the structure's seaside wall (Figure 12e), forming a thin layer of sediment deposit along the trajectory. On the other hand, the wake vortex pair follows a spiral path (Figure 12f), forming scour holes along the leeside edges, and depositing sediment along its trajectory. The vortex pair trajectories simulated by both models are quite similar to the observations. Contrary to the laboratory observations, SedWaveFoam predicts additional sediment deposits along the trajectory of the wake vortices for both layouts (Figure 12c,g). This is most likely due to the poor performance of the $k - \varepsilon$ model, which underpredicts w_n. For the side layout, the predicted scour hole depth is lower than the measured value, whereas the model predicts deeper scour holes around the edges of the structure for the center layout. Both SedWaveFoam and FLOW-3D underestimate the depth of the scour holes at the structure's edges for the side layout, whereas they overpredict the scour holes for the center layout (Figure 12d,h). Overall, it is seen that FLOW-3D performs better than SedWaveFoam at predicting the final bed elevation. This finding is mainly attributed to the LES turbulence scheme used in FLOW-3D, which assists the model in resolving smaller eddies that may still contribute to bed evolution.

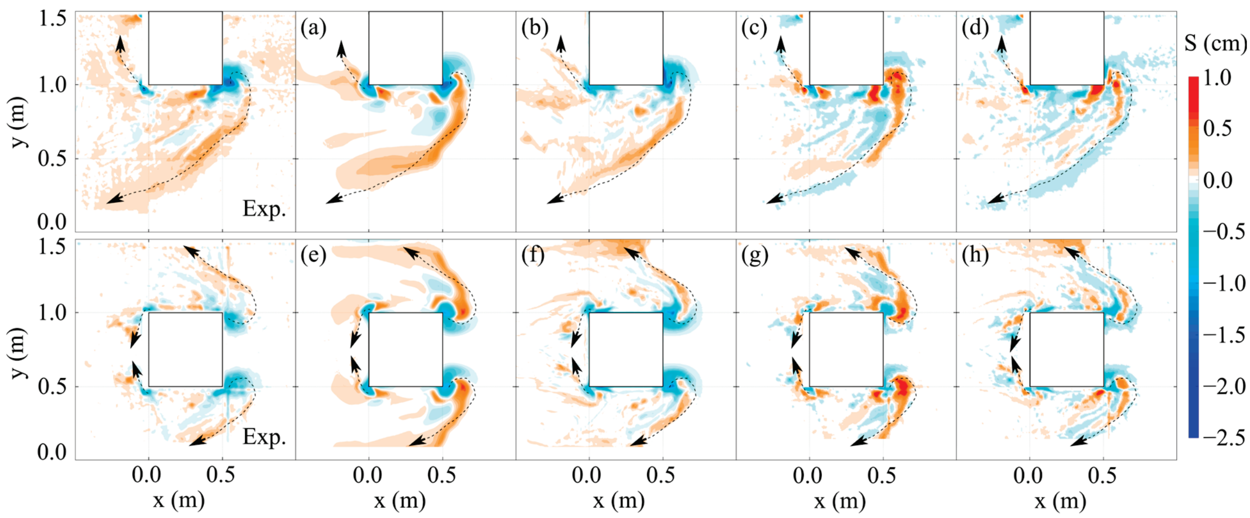

Figure 12. Plan view of sandy bed at $t = 15$ s. Upper panels: side layout. Lower panels: center layout. (**a**,**e**) SedWaveFoam results; (**b**,**f**) FLOW-3D results; (**c**,**g**) difference between SedWaveFoam results and measurement; (**d**,**h**) difference between FLOW-3D results and measurement.

The instantaneous bed elevation along the vortex trajectories at $t = 15$ s, extracted from the measured final bed elevation, for both seaside and leeside of the structure is plotted in Figure 13 for both layouts. The inconsistencies between the predicted and actual bed elevations, Δz, are calculated by subtracting the actual bed elevation from those simulated by the two models. The shaded panels in Figure 13 present Δz, where the dashed red and black lines represent the deviation of the SedWaveFoam and FLOW-3D simulations from the measurements, respectively. The scour induced by both out-of-plane and wake vortices is followed by areas of mild deposition along the vortex trajectories. The vortex effect on the bottom is inferred by comparing the scour depth for both layouts. The near-bed vorticity is relatively higher for the side layout (Figure 9), leading to deeper scour holes both at the leeside and seaside of the structure. SedWaveFoam slightly overestimates deposits along vortex trajectories for both layouts. FLOW-3D, on the other hand, performs better in predicting deposits beneath the vortex paths at the structure's seaside for both layouts; however, the deposits towards the structure's leeside are underestimated for the side layout. Both models fail to accurately predict the vortex-induced scour, which is most noticeable at the structure's seaside for the side layout.

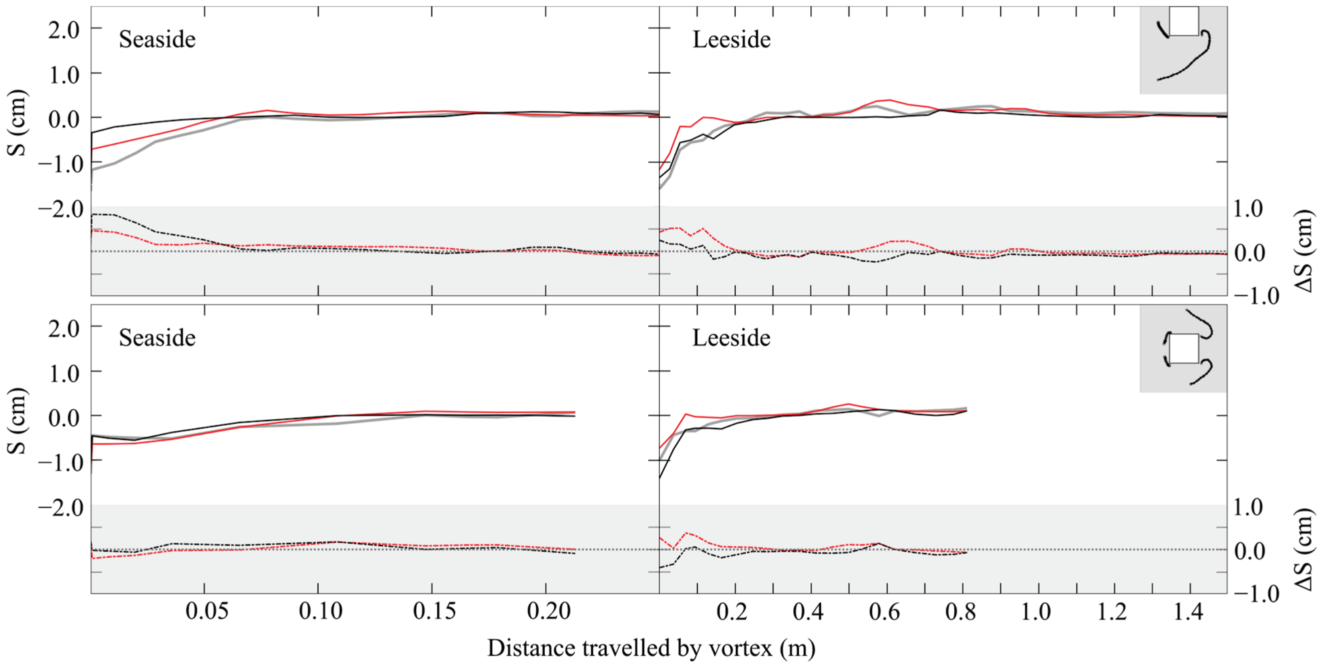

Figure 13. Elevation of sandy bed along vortex trajectories at seaside and leeside of the structure at $t = 15$ s. Upper panels: side layout. Lower panels: center layout. Gray, red, and black lines represent measurement, SedWaveFoam, and FLOW-3D results, respectively.

The temporal evolution of the maximum scour depth on the seaside and leeside of the structure is shown in Figure 14, where the measured maximum scour at $t = 15$ s is denoted by "X". The scour holes generated by the wave impingement are backfilled after the wave passes the structure and the flow climate gets milder. The backfilling is more prominent in SedWaveFoam results, where the initial scour depth is considerably reduced between $t = 7$ s and $t = 8$ s. The scour depth on the seaside is relatively constant until $t = 13$ s before it undergoes a sudden increase. The scour depth then remains constant, implying that stability is reached. On the other hand, the scour hole formed at the leeside of the structure is disrupted at $t = 10.5$ s both for the side and center layout, where an increase in scour depth is followed by abrupt backfilling. This is probably associated with the settling of sand that was previously suspended by the strong wake vortices during wave impingement. FLOW-3D simulations do not reflect the backfilling of the initially formed scour. The scour depth reaches its maximum depth at $t = 8$ s for both layouts and does not show any variation until $t = 15$ s.

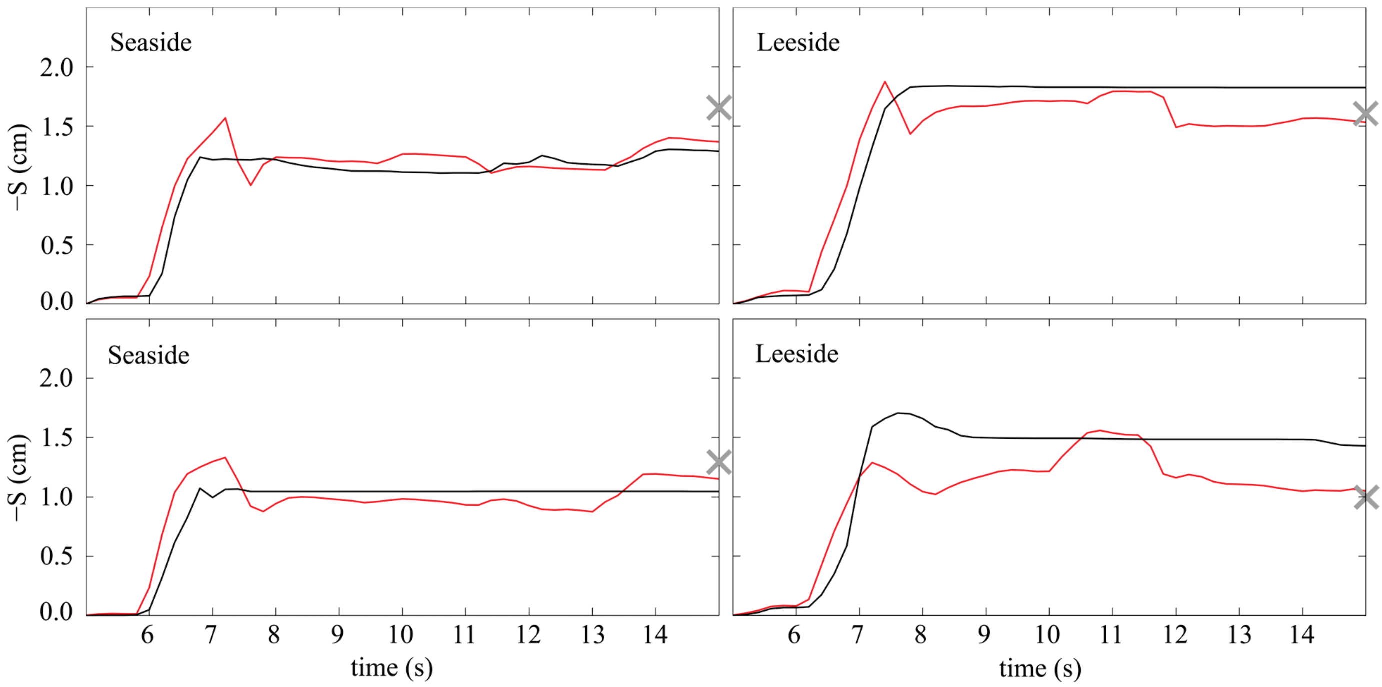

Figure 14. Temporal evolution of maximum scour depth at seaside and leeside of the structure. Upper panels: side layout. Lower panels: center layout. Red and black lines represent SedWaveFoam and FLOW-3D results, respectively. X represents the measured maximum scour depth.

SedWaveFoam manages to capture the backfilling process that is observed during the experiments after the wave impingement and predicts the maximum scour depth with reasonable accuracy. FLOW-3D, on the other hand, performs poorly and fails to accurately predict the maximum scour depth at $t = 15$ s. Overall, SedWaveFoam performs better in capturing the temporal evolution of the maximum scour depth for both layouts.

The cross-sectional view of sandy bed along two lines, i.e., line A–A, and D–D, at $t = 15$ s is given in Figure 15. The cross-sections are taken 3 cm away from the structure for both layouts. SedWaveFoam underestimates the seaside and leeside scour depths for the side layout and predicts depositions in the vicinity of the structure, which are not observed in the experiments for both layouts. The disparity seen between the measurement and SedWaveFoam results is most likely due to $k - \varepsilon$ model, which inherently underestimates the intensity of the vortex in the case of adverse pressure caused by flow blockage [61,68–70]. These vortices are unlikely to carry the trapped sediment away from the structure, resulting in the depositions depicted in Figure 15. Compared to SedWaveFoam, FLOW-3D demonstrates a better performance in predicting the cross-sectional bed evolution. For both layouts, the model predicts no depositions near the structure, while the scour depth is slightly underpredicted for the side layout. Both models overestimate the scour depth for the center layout. This is attributed to the predicted near-bed vorticities, which are relatively higher compared to the experiments.

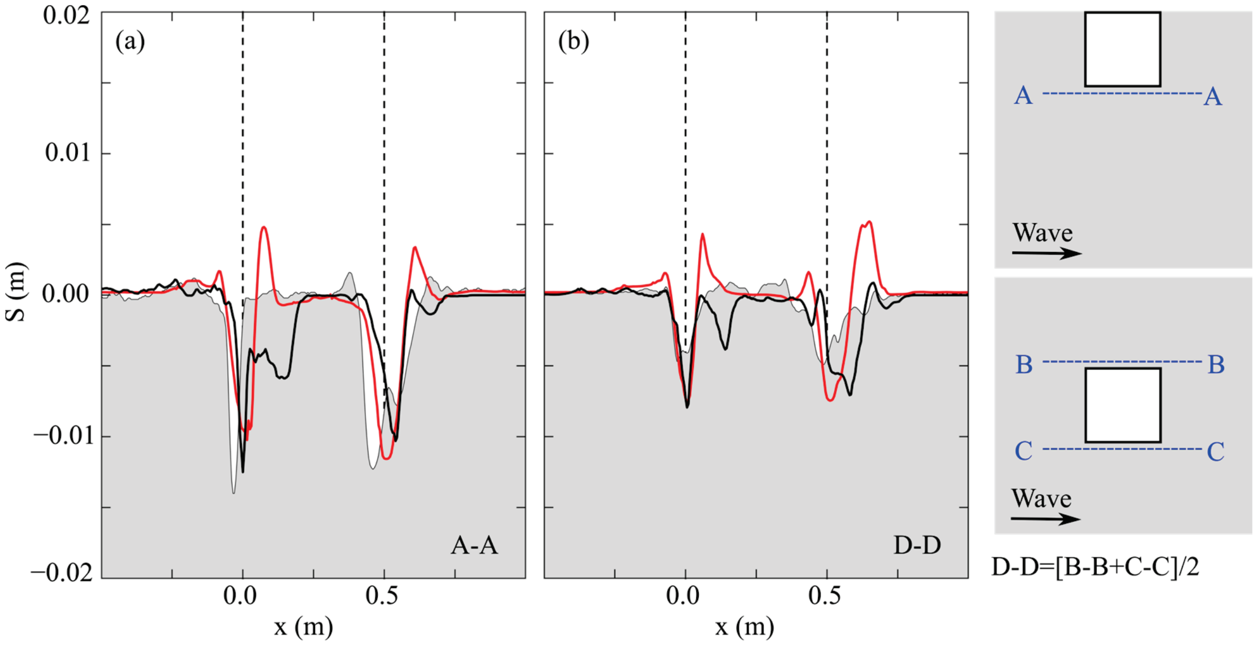

Figure 15. Cross-sectional view of sandy bed along line A–A and D–D at $t = 15$ s: (**a**) side layout; (**b**) center layout. Gray, red, and black solid lines represent measurement, SedWaveFoam, and FLOW-3D results, respectively. Gray dashed line represents the structure.

5. Conclusions

The present study presents a thorough analysis of the accuracy of two different approaches in estimating the non-equilibrium scour around a non-slender structure exposed to a transient wave as well as a detailed description of the scouring and deposition processes based on laboratory observations and numerical simulations. The first numerical method treats the sediment layer as a separate phase and directly solves continuity and momentum equations for the sediment, water, and air phases by implementing the $k - \varepsilon$ turbulence scheme. The second numerical approach estimates sediment transport using conventional bedload and suspended load methods where the quadratic law of bottom shear stress for 3D turbulent flow is assumed and the LES scheme is utilized.

The most intense vortex motion is seen immediately after the wave impinges on the structure. The area around the vortex cores has the highest surface horizontal velocities, which decrease in intensity as water depth increases. For both layouts, the surface horizontal and vertical velocities increase as the wake vortex moves along its spiral trajectory. The same pattern is not seen near the sandy bed, where the magnitude of these velocities does not vary dramatically over time. The wake vortices are larger and more intense than the out-of-plane vortices that form at the structure's seaside. The predicted suspended sediment concentration is mostly confined between $z = -0.30$ m and $z = -0.22$ m, which is attributed to the underestimation of vortex-induced near-bed vertical velocities by both SedWaveFoam and FLOW-3D. It is found that the suspended sediment concentration in the vicinity of the structure is relatively lower when the structure is placed in the center of the NWF. This is expected given that the near-bed vorticity magnitudes of the vortex pairs in the center layout are smaller than those in the side layout. As a result, the scour around the structure's edges is deeper when the structure is placed on the side of the NWF. SedWaveFoam overestimates the deposits along vortex trajectories for both layouts, whereas FLOW-3D satisfactorily predicts scour and depositions beneath vortex paths. When the wave passes the structure and the flow climate becomes milder, the scour holes caused by the wave impingement are backfilled. SedWaveFoam can estimate the maximum scour depth and capture this backfilling. FLOW-3D results, on the other hand, do not reflect the backfilling that is seen during the experiments and the model fails to accurately predict the maximum scour depth. SedWaveFoam results indicate noticeable depositions along the cross-sections taken 3 cm away from the structure. These depositions are not observed in the experiments for both layouts. Both SedWaveFoam and FLOW-3D underpredict the scour depth for the side layout and overestimate the scour depth for the center layout.

No clear-cut case can be made for the advantages of utilizing any of the two different approaches based on the available evidence because the capabilities of SedWaveFoam and FLOW-3D in predicting the non-equilibrium scour for a low KC number vary greatly. Each model has its pros and cons, which were covered in detail in the preceding sections, and the results discussed here do not support the use of one model over another. However, the unwanted depositions in the vicinity of the structure and along vortex trajectories simulated by SedWaveFoam suggest that incorporating LES into SedWaveFoam could be a viable approach for future model improvement. On the other hand, the two equation turbulence schemes embedded in FLOW-3D fail to procure reliable results regarding the evolution of the sandy bed and the LES scheme is strongly encouraged to reach more accurate results. Unlike SedWaveFoam, FLOW-3D requires careful calibration of the entrainment parameter for each test case to properly estimate the suspended sediment concentration and backfilling, which shows that the model is case specific and should be used with caution.

The results of this study are only applicable to the flow conditions, structure size, and placements considered. For definitive conclusions addressing the scour around non-slender square structures under transient wave conditions, a more thorough investigation including a wider variety of flow conditions, structure dimensions, and layouts is required.

Author Contributions: Conceptualization, D.V.S., E.S. and A.F.; Methodology, D.V.S. and E.S.; Software, D.V.S. and T.-J.H.; Investigation, D.V.S.; Resources, D.V.S. and A.F.; Data curation, D.V.S. and E.S.; Writing—original draft, D.V.S.; Writing—review & editing, E.S., A.F. and T.-J.H.; Visualization, D.V.S. and E.S. All authors have read and agreed to the published version of the manuscript.

Funding: This material is based upon work supported by the National Science Foundation under grant no. CNS 09-23050. The authors acknowledge funding from the National Sciences Foundation through grants CMMI-2050798 and CMMI-2050854.

Institutional Review Board Statement: Not applicable.

Informed Consent Statement: Not applicable.

Data Availability Statement: Data are contained within the article.

Acknowledgments: FLOW-3D HYDRO software was made available through the FLOW-3D Academic Program.

Conflicts of Interest: The authors declare no conflict of interest.

References

1. Larsen, B.E.; Fuhrman, D.R.; Baykal, C.; Sumer, B.M. Tsunami-induced scour around monopile foundations. *Coast. Eng.* **2017**, *129*, 36–49. [CrossRef]
2. Williams, I.A.; Fuhrman, D.R. Numerical simulation of tsunami-scale wave boundary layers. *Coast. Eng.* **2016**, *110*, 17–31. [CrossRef]
3. Breusers, H.N.C.; Nicollet, G.; Shen, H. Local scour around cylindrical piers. *J. Hydraul. Res.* **1977**, *15*, 211–252. [CrossRef]
4. Carreiras, J.; Larroudé, P.; Seabra-Santos, F.; Mory, M. Wave scour around piles. In Proceedings of the 27th International Conference on Coastal Engineering 2000, Sydney, Australia, 16–21 July 2000; pp. 1860–1870.
5. Carreiras, J.; Carmo, J.D.; Seabra-Santos, F. Settlement of vertical piles exposed to waves. *Coast. Eng.* **2003**, *47*, 355–365. [CrossRef]
6. Dey, S.; Sumer, B.M.; Fredsøe, J. Control of scour at vertical circular piles under waves and current. *J. Hydraul. Eng.* **2006**, *132*, 270–279. [CrossRef]
7. Dey, S.; Helkjær, A.; Sumer, B.M.; Fredsøe, J. Scour at vertical piles in sand-clay mixtures under waves. *J. Waterw. Port Coast. Ocean Eng.* **2011**, *137*, 324–331. [CrossRef]
8. Kobayashi, T. 3-D Analysis of flow around a vertical cylinder on a scoured bed. In Proceedings of the 23rd International Conference on Coastal Engineering, Venice, Italy, 4–9 October 1992; pp. 3482–3495.
9. Kobayashi, T.; Oda, K. Experimental study on developing process of local scour around a vertical cylinder. In Proceedings of the 24th International Conference on Coastal Engineering, Kobe, Japan, 23 October 1994; pp. 1284–1297. [CrossRef]

10. Raaijmakers, T.; Rudolph, D. Time-dependent scour development under combined current and waves conditions-laboratory experiments with online monitoring technique. In Proceedings of the 4th International Conference on Scour and Erosion, ICSE, Tokyo, Japan, 5–7 November 2008; pp. 152–161.
11. Sumer, B.M.; Christiansen, N.; Fredsoe, J. Time scale of scour around a vertical pile. In Proceedings of the ISOPE International Ocean and Polar Engineering Conference, San Francisco, CA, USA, 14–19 June 1992; p. ISOPE-I-92-259.
12. Sumer, B.M.; Fredsøe, J.; Christiansen, N. Scour around vertical pile in waves. *J. Waterw. Port Coast. Ocean Eng.* **1992**, *118*, 15–31. [CrossRef]
13. Sumer, B.M.; Christiansen, N.; Fredsøe, J. Influence of cross section on wave scour around piles. *J. Waterw. Port Coast. Ocean Eng.* **1993**, *119*, 477–495. [CrossRef]
14. Sumer, B.M.; Fredsøe, J.; Christiansen, N.; Hansen, S.B. Bed shear stress and scour around coastal structures. In Proceedings of the 24th International Conference on Coastal Engineering, Kobe, Japan, 23 October 1994; pp. 1595–1609.
15. Sumer, B.M.; Fredsøe, J. Scour around pile in combined waves and current. *J. Hydraul. Eng.* **2001**, *127*, 403–411. [CrossRef]
16. Sumer, B.M.; Fredsøe, J. Time scale of scour around a large vertical cylinder in waves. In Proceedings of the ISOPE International Ocean and Polar Engineering Conference, Kitakyushu, Japan, 26–31 May 2002; p. ISOPE-I-02-143.
17. Sumer, B.M.; Fredsøe, J. The mechanics of scour in the marine environment. In *Advanced Series on Ocean Engineering*; Word Scientific: Singapore, 2002.
18. Sumer, B.M. Mathematical modelling of scour: A review. *J. Hydraul. Res.* **2007**, *45*, 723–735. [CrossRef]
19. Whitehouse, R. *Scour at Marine Structures: A Manual for Practical Applications*; Thomas Telford: London, UK, 1998.
20. Zanke, U.C.; Hsu, T.-W.; Roland, A.; Link, O.; Diab, R. Equilibrium scour depths around piles in noncohesive sediments under currents and waves. *Coast. Eng.* **2011**, *58*, 986–991. [CrossRef]
21. Rance, P.J. *The Potential for Scour around Large Objects, One-Day Seminar of Scour Prevention Techniques around Offshore Structures*; Society for Underwater Technology: London, UK, 1980; p. 41.
22. Nakamura, T.; Kuramitsu, Y.; Mizutani, N. Tsunami scour around a square structure. *Coast. Eng. J.* **2008**, *50*, 209–246. [CrossRef]
23. McGovern, D.; Todd, D.; Rossetto, T.; Whitehouse, R.; Monaghan, J.; Gomes, E. Experimental observations of tsunami induced scour at onshore structures. *Coast. Eng.* **2019**, *152*, 103505. [CrossRef]
24. Kato, F.; Sato, S.; Yeh, H. Large-scale experiment on dynamic response of sand bed around a cylinder due to tsunami. In Proceedings of the 27th International Conference on Coastal Engineering 2000, Sydney, Australia, 16–21 July 2000; pp. 1848–1859.
25. Mehrzad, S.; Nistor, I.; Rennie, C.D. Experimental modeling of supercritical flows induced erosion around structures. In Proceedings of the 6th International Conference Application of Physical Modeling in Coastal and Port Engineering and Science, Ottawa, ON, Canada, 10–13 May 2016; pp. 1–13.
26. Briganti, R.; Musumeci, R.E.; van der Meer, J.; Romano, A.; Stancanelli, L.M.; Kudella, M.; Akbar, R.; Mukhdiar, R.; Altomare, C.; Suzuki, T.; et al. Wave overtopping at near-vertical seawalls: Influence of foreshore evolution during storms. *Ocean Eng.* **2022**, *261*, 112024. [CrossRef]
27. Slingerland, R.L. Numerical models and simulation of sediment transport and deposition. In *Sedimentology: Encyclopedia of Earth Science*; Springer: Berlin/Heidelberg, Germany, 1978.
28. Henderson, S.M.; Allen, J.S.; Newberger, P.A. Nearshore sandbar migration predicted by an eddy-diffusive boundary layer model. *J. Geophys. Res. Ocean.* **2004**, *109*, C06024. [CrossRef]
29. Kranenburg, W.M.; Ribberink, J.S.; Uittenbogaard, R.E.; Hulscher, S.J.M.H. Net currents in the wave bottom boundary layer: On waveshape streaming and progressive wave streaming. *J. Geophys. Res. Earth Surf.* **2012**, *117*, F03005. [CrossRef]
30. Kranenburg, W.M.; Ribberink, J.S.; Schretlen, J.J.L.M.; Uittenbogaard, R.E. Sand transport beneath waves: The role of progressive wave streaming and other free surface effects. *J. Geophys. Res. Earth Surf.* **2013**, *118*, 122–139. [CrossRef]
31. Kim, Y.; Cheng, Z.; Hsu, T.; Chauchat, J. A Numerical study of sheet flow under monochromatic nonbreaking waves using a free surface resolving eulerian two-phase flow model. *J. Geophys. Res. Ocean.* **2018**, *123*, 4693–4719. [CrossRef]
32. Fox, B.; Feurich, R. CFD analysis of local scour at bridge piers. In Proceedings of the Federal Interagency Sedimentation and Hydrologic Modeling SEDHYD Conference, Reno, NV, USA, 24–28 June 2019; pp. 24–28.
33. Le Quere, P.A.; Nistor, I.; Mohammadian, A. Numerical modeling of tsunami-induced scouring around a square column: Performance assessment of FLOW-3D and Delft3D. *J. Coast. Res.* **2020**, *36*, 1278–1291. [CrossRef]
34. Sogut, E.; Farhadzadeh, A. Scouring and loading of idealized beachfront building during overland flooding. *Coast. Eng. Proc.* **2020**, *28*, 7. [CrossRef]
35. Sogut, E.; Hsu, T.-J.; Farhadzadeh, A. Experimental and numerical investigations of solitary wave-induced non-equilibrium scour around structure of square cross-section on sandy berm. *Coast. Eng.* **2022**, *173*, 104091. [CrossRef]
36. Sogut, E.; Sogut, D.V.; Farhadzadeh, A. Experimental study of bed evolution around a non-slender square structure under combined solitary wave and steady current actions. *Ocean Eng.* **2022**, *266*, 112792. [CrossRef]
37. Munk, W.H. The solitary wave theory and its application to surf problems. *Ann. N. Y. Acad. Sci.* **1949**, *51*, 376–424. [CrossRef]
38. Chiew, Y.M.; Melville, B.W. Local scour around bridge piers. *J. Hydraul. Res.* **1987**, *25*, 15–26. [CrossRef]
39. Ballio, F.; Teruzzi, A.; Radice, A. Constriction effects in clear-water scour at abutments. *J. Hydraul. Eng.* **2009**, *135*, 140–145. [CrossRef]
40. Sumer, B.M. *Hydrodynamics around Cylindrical Structures*; World Scientific: Singapore, 2006; Volume 26.

41. Chauchat, J.; Cheng, Z.; Nagel, T.; Bonamy, C.; Hsu, T.-J. SedFoam-2.0: A 3-D two-phase flow numerical model for sediment transport. *Geosci. Model Dev.* **2017**, *10*, 4367–4392. [CrossRef]
42. Berberović, E.; van Hinsberg, N.P.; Jakirlić, S.; Roisman, I.V.; Tropea, C. Drop impact onto a liquid layer of finite thickness: Dynamics of the cavity evolution. *Phys. Rev. E* **2009**, *79*, 036306. [CrossRef]
43. Jacobsen, N.G.; Fuhrman, D.R.; Fredsøe, J. A wave generation toolbox for the open-source CFD library: OpenFoam®. *Int. J. Numer. Methods Fluids* **2012**, *70*, 1073–1088. [CrossRef]
44. A Drew, D. Mathematical Modeling of Two-Phase Flow. *Annu. Rev. Fluid Mech.* **1983**, *15*, 261–291. [CrossRef]
45. Kim, Y.; Mieras, R.S.; Cheng, Z.; Anderson, D.; Hsu, T.-J.; Puleo, J.A.; Cox, D. A numerical study of sheet flow driven by velocity and acceleration skewed near-breaking waves on a sandbar using SedWaveFoam. *Coast. Eng.* **2019**, *152*, 103526. [CrossRef]
46. Cheng, Z.; Hsu, T.-J.; Calantoni, J. SedFoam: A multi-dimensional Eulerian two-phase model for sediment transport and its application to momentary bed failure. *Coast. Eng.* **2017**, *119*, 32–50. [CrossRef]
47. Hsu, T.-J.; Hanes, D.M. Effects of wave shape on sheet flow sediment transport. *J. Geophys. Res. Ocean.* **2004**, *109*, C05025. [CrossRef]
48. Flow Science. *FLOW-3D Version 12.0 User Manual*; Flow Science, Inc.: Santa Fe, NM, USA, 2019. Available online: https://www.flow3d.com (accessed on 12 March 2023).
49. Velioglu, D. Advanced Two- and Three-Dimensional Tsunami Models: Benchmarking and Validation. Ph.D. Dissertation, Middle East Technical University, Ankara, Turkey, 2017.
50. Hirt, C.W. A porosity technique for the definition of obstacles in rectangular cell meshes. In Proceedings of the 4th International Conference Ship Hydrodynamics, Washington, DC, USA, 24–27 September 1985.
51. Hirt, C.W.; Nichols, B.D. Volume of fluid (VOF) method for the dynamics of free boundaries. *J. Comput. Phys.* **1981**, *39*, 201–225. [CrossRef]
52. Mastbergen, D.R.; Van Den Berg, J.H. Breaching in fine sands and the generation of sustained turbidity currents in submarine canyons. *Sedimentology* **2003**, *50*, 625–637. [CrossRef]
53. Soulsby, R.L. Dynamics of marine sands: A manual for practical applications. *Oceanogr. Lit. Rev.* **1997**, *9*, 947.
54. Nielsen, P. *Coastal Bottom Boundary Layers and Sediment Transport*; World Scientific: Singapore, 1992; Volume 4.
55. Van Rijn, L.C. Sediment transport, part I: Bed load transport. *J. Hydraul. Eng.* **1984**, *110*, 1431–1456. [CrossRef]
56. Meyer-Peter, E.; Müller, R. Formulas for bed-load transport. In Proceedings of the IAHSR 2nd Meeting, Stockholm, Appendix 2, Stockholm, Sweden, 7 June 1948.
57. Higuera, P.; Lara, J.L.; Losada, I.J. Realistic wave generation and active wave absorption for Navier–Stokes models: Application to OpenFOAM®. *Coast. Eng.* **2013**, *71*, 102–118. [CrossRef]
58. Higuera, P.; Losada, I.J.; Lara, J.L. Three-dimensional numerical wave generation with moving boundaries. *Coast. Eng.* **2015**, *101*, 35–47. [CrossRef]
59. Willmott, C.J.; Ackleson, S.G.; Davis, R.E.; Feddema, J.J.; Klink, K.M.; Legates, D.R.; O'Donnell, J.; Rowe, C.M. Statistics for the evaluation and comparison of models. *J. Geophys. Res. Ocean.* **1985**, *90*, 8995–9005. [CrossRef]
60. Sogut, E. Wave and Current Interactions with Sharp-Edged Beachfront Structures on Rigid and Erodible Berms. Ph.D. Dissertation, State University of New York, Stony Brook, NY, USA, 2021.
61. Wilcox, D.C. Multiscale model for turbulent flows. *AIAA J.* **1988**, *26*, 1311–1320. [CrossRef]
62. Wilcox, D.C. *Turbulence Modeling for CFD*; DCW Industries: La Canada, CA, USA, 1998; Volume 2, pp. 103–217.
63. Wilcox, D.C. Formulation of the k-w turbulence model revisited. *AIAA J.* **2008**, *46*, 2823–2838. [CrossRef]
64. Harlow, F.H.; Nakayama, P.I. Turbulence transport equations. *Phys. Fluids* **1967**, *10*, 2323–2332. [CrossRef]
65. Rodi, W. *Turbulence Models and Their Application in Hydraulics*; CRC Press: London, UK, 2000.
66. Yakhot, V.; Orszag, S.A. Renormalization group analysis of turbulence. I. Basic theory. *J. Sci. Comput.* **1986**, *1*, 3–51. [CrossRef]
67. Yakhot, V.; Smith, L.M. The renormalization group, the ε-expansion and derivation of turbulence models. *J. Sci. Comput.* **1992**, *7*, 35–61. [CrossRef]
68. Menter, F.R. Elements of inductrial heat tranfer predictions. In Proceedings of the 16th Brazilian Congress of Mechanical Engineering (COBEM), Uberlandia, Brazil, 26–30 November 2001.
69. Menter, F.R.; Kuntz, M.; Langtry, R. Ten years of industrial experience with the SST turbulence model. *Turbul. Heat Mass Transf.* **2003**, *4*, 625–632.
70. Pope, S.B. Turbulent flows. *Meas. Sci. Technol.* **2001**, *12*, 2020–2021. [CrossRef]

Journal of
Marine Science and Engineering

MDPI

Article

Evaluating Vegetation Effects on Wave Attenuation and Dune Erosion during Hurricane

Mengdi Ma [1,2], Wenrui Huang [2,3,*], Sungmoon Jung [2], Christopher Oslon [3], Kai Yin [1] and Sudong Xu [1]

[1] Department of Port, Waterway and Coastal Engineering, School of Transportation, Southeast University, Nanjing 211189, China; mma4@fsu.edu (M.M.)
[2] Department of Civil and Environmental Engineering, FAMU-FSU College of Engineering, Florida State University, Tallahassee, FL 32310, USA
[3] Department of Civil and Environmental Engineering, FAMU-FSU College of Engineering, Florida A&M University, Tallahassee, FL 32310, USA
* Correspondence: whuang@eng.famu.fsu.edu

Abstract: This study employs the XBeach surfbeat model (XBSB) to explore the effects of vegetation on wave attenuation and dune erosion in a case study of Mexico Beach during Hurricane Michael. The XBSB model was validated against laboratory experiments of wave-induced dune erosion and wave attenuation by vegetation. In the case study of vegetation on dunes in Mexico Beach during Hurricane Michael, different vegetation drag coefficients were evaluated to investigate the effects of vegetation on wave attenuation and dune erosion. LiDAR data of dune profiles before and after Hurricane Michael were used for model validation. The findings reveal that vegetation on dunes significantly affects wave attenuation and dune erosion. Under vegetated conditions, as the vegetation drag coefficient value increases, wave attenuation also increases, leading to a reduction of dune erosion. An increase in vegetation density enhances wave attenuation in the vegetated area, including reductions in significant wave height and flow velocity. However, the rate of change in attenuation decreases as the vegetation density increases. Through simulations under regular wave condition on Mexico Beach, an optimal vegetation density was identified as 800 units/m^2. Beyond this density, additional vegetation does not substantially improve wave attenuation. Furthermore, the position of the dune crest elevation is related to the location where the alongshore flow velocity begins to decrease. The findings highlight the essential role of coastal vegetation in enhancing coastal resilience against hurricanes.

Keywords: XBeach model; vegetation drag coefficient; vegetation density; dune erosion; wave attenuation

Citation: Ma, M.; Huang, W.; Jung, S.; Oslon, C.; Yin, K.; Xu, S. Evaluating Vegetation Effects on Wave Attenuation and Dune Erosion during Hurricane. *J. Mar. Sci. Eng.* **2024**, *12*, 1326. https://doi.org/10.3390/jmse12081326

Academic Editor: Deniz Velioglu Sogut

Received: 27 June 2024
Revised: 31 July 2024
Accepted: 2 August 2024
Published: 6 August 2024

1. Introduction

Extreme weather events like hurricanes could cause significant erosion to coastal sand dunes in a short period time by inducing high water levels accompanied with high waves and strong currents [1–3]. Previous study of Shaw Alex et al. [4] has demonstrated that dune failure significantly increased flooding during storms, highlighting the crucial role of dune protection in coastal defense. D'Alessandro and Tomasicchio [5] conducted large-scale physical model tests to investigate the effects of wave period and water depth on the resilience of the exposed dune under irregular wave attacks. Aquatic vegetation contributes to protect dune systems and coastal protection by damping the incoming water [6–11]. The findings of Unguendoli et al. [12] indicated that seagrass was able to reduce beach erosion volumes up to 55% as well as produced an average attenuation of 32% of the storm peak. Jacob et al.'s study [13] also agreed that seagrass expansion could be a useful addition to engineered coastal protection measures. Consequently, with the impact of aquatic vegetation on wave attenuation receiving increasing attention in recent years, the strategy of using vegetation to protect coastal dunes and reduce erosion has been applied to many studies [14–16].

To investigate the mechanisms of wave energy reduction due to aquatic vegetation, various studies have been developed. Numerous laboratory experiments examine wave attenuation by vegetation [17–19]. For example, a large-scale experimental study was employed to study wave damping over artificial Posidonia oceanic meadow [20]. Besides, some studies combined laboratory experiments and numerical models to explore the interactions between wave and vegetation providing significant insights into the effects of vegetation on wave energy dissipation. Chalmoukis [21] used a porous medium model to simulate a three-dimensional, two-phase flow past coastal vegetation fields. The model, validated against experimental data, assessed the impact of equivalent porosity and cross-shore length on wave behavior over a sloped beach. Holzenthal et al. [22] studied the influence of flexible, buoyant submerged aquatic vegetation on localized velocity fields, circulation pathways, and overall tidal behavior by coupling a dynamic friction model with a depth-integrated circulation-wave model.

Additionally, some studies have used Manning's roughness coefficients to represent vegetation in wave attenuation investigations [23–25]. For instance, Lapetina et al. [26] indicated that 2D storm surge models typically use an enhanced Manning's coefficient to represent the effects of coastal vegetation on flow. Medeiros [27] suggested values of 0.138 for Manning's n and 2.34 m for initial water level based on field investigations in mangrove-covered regions of southwest Florida. However, Baron-Hyppolite et al. [28] pointed out that simplistically treating vegetation as enhanced bottom roughness underestimated the complexity of wave-vegetation interactions, thereby underestimating wave energy dissipation (error > 30%) while those cases with explicit representation of vegetation showed good consistency with field data (error < 20%). Besides, Abdoali et al. [29] indicated that the Manning's n cannot accurately represent all key physical phenomena of vegetation in water, prompting the use of numerical models that consider vegetation characteristics to estimate dissipation more accurately, such as the SWAN model [30] and XBeach model [31]. The vegetation dissipation formulas applied in these models are functions combined with local hydrodynamic conditions and can directly reflect measurable vegetation characteristics. For example, Musumeci et al. [32] used a coupled SWAN model and XBeach model to simulate the impact of vegetation on coastal erosion and flooding risks.

The complexity of natural systems, combined with the extreme magnitudes of storm conditions—such as surges, wave heights, and wind speeds—presents substantial challenges. Meanwhile, this complexity results in a lack of comprehensive data needed for accurate validation [33]. Moreover, existing physical model experiments struggle to replicate the extreme hydrodynamic conditions of severe storms and the realistic growth patterns of vegetation [16]. These limitations hinder the accurate assessment of vegetation's role in coastal defense [34]. Garzon et al. [35] investigated the ability of Spartina alterniflora saltmarshes to attenuate wave energy during storm surge conditions in the Chesapeake Bay. However, the research gaps remain in understanding the mechanisms by which vegetation affects wave attenuation and dune protection under extreme hydrodynamic conditions. To address the research gaps, our study aims to employ a one-dimensional XBeach model based on dune profile data collected pre- and post-hurricane to study the interactions between wave, dune, and vegetation. This method will enable us to investigate the protective functions of vegetation on dunes and its efficacy in wave attenuation during storm surge conditions. A detailed introduction to the XBeach model will also be provided in Section 2. The vegetation drag coefficient (C_D) is a critical parameter in the XBeach model for calculating vegetation-induced wave dissipation. In Section 2, this paper will thoroughly review the literature on determining C_D, aiming to identify the most suitable values for our study using the XBeach model.

The remainder of this paper is organized as follows: XBeach surfbeat model descriptions and a review of vegetation drag coefficient are presented in Section 2; Section 3 introduces the model validation of two laboratory experiments; Section 4 presents the

XBeach surfbeat model application in real study case; and Sections 5 and 6 present the discussion and conclusions, respectively. In this study, to aid readers in understanding the abbreviations used in the main text, a table listing each abbreviation used in this manuscript along with its full form is provided in Appendix A.

2. Model Descriptions and C_D Values Review

2.1. XBeach Surfbeat Model Descriptions

The XBeach surfbeat model (XBSB) is a two-dimensional, advanced numerical model that was developed for simulating nearshore hydrodynamics and morphodynamics under varying wave conditions [31]. The model employs shallow water equations, which assume a linear variation of pressure with depth and focus on depth-averaged hydrodynamics. This approach allows the XBSB model to efficiently simulate long-wave processes, including storm surges, tides, and tsunami inundation. While the model's assumptions facilitate computational efficiency, they may limit its ability to capture detailed processes in regions with rapid changes in water depth. Nevertheless, the XBSB model is widely recognized for its ability to predict dune erosion, overwash, and coastal barrier breaches, offering valuable insights for coastal management and protection strategies [36–38]. For example, Sánchez-Artús et al. [39] used XBeach model to evaluate the performance of dunes as coastal protection measures for the barrier beach under three different storm events.

For modeling the interaction between vegetation and wave dissipation, XBeach utilizes the method proposed by Mendez and Losada [40], which was later adjusted by Suzuki et al. [41]to account for the effects of vertical heterogeneity introduced by vegetation. The dissipation of short waves caused by vegetation can be solved as a function of local wave height and several vegetation parameters. Vegetation can be represented by vertical elements of different properties, allowing for the simulation of damping effects of vegetation with characteristics like mangroves, which have densely packed roots but sparse stem areas. The total dissipation term can then be calculated as the sum of dissipation amounts for each vegetation layer as shown in Equation (1).

$$D_v = \sum_{i=1}^{n_v} D_{v,i} \tag{1}$$

where $D_{v,i}$ is the dissipation amount in the vegetation layer i; n_v is the number of vegetation layers.

The dissipation amount for each layer is calculated by the following equations:

$$D_{v,i} = A_v \times \frac{\rho C_{D,i} b_{v,i} N_{v,i}}{2\sqrt{\pi}} \left(\frac{kg}{2\sigma}\right)^3 H_{rms}{}^3 \tag{2}$$

$$A_v = \frac{\left(sinh^3 k\alpha_i h - sinh^3 k\alpha_{i-1} h\right) + 3(sinhk\alpha_i h - sinhk\alpha_{i-1} h)}{3kcosh^3 kh} \tag{3}$$

$$\alpha_i = h_v / h \tag{4}$$

For the specific vegetation layer i, $C_{D,i}$ is the drag coefficient, $b_{v,i}$ is the diameter of the vegetation stems, $N_{v,i}$ is the vegetation density, H_{rms} is the root-mean-square wave height, and α_i is the relative vegetation height in vegetation layer i.

In this paper, we only studied a single vegetation layer, assuming that the vegetation is vertically uniform. Therefore, when i = 1, the formula for the wave energy dissipation under the above vegetation field is as Equation (5).

$$D_v = \frac{sinh^3 kh_v + 3sinhkh_v}{3kcosh^3 kh} \times \frac{\rho C_D b_v N_v}{2\sqrt{\pi}} \left(\frac{kg}{2\sigma}\right)^3 H_{rms}{}^3 \tag{5}$$

2.2. A Review of C_D Determination

The interaction between waves and coastal vegetation is a dynamic and multifaceted process that significantly influences coastal defense by modifying wave characteristics. Central to understanding this interaction is the vegetation drag coefficient (C_D), an empirical parameter critical for calculating the wave energy dissipation and the drag resistance presented by the vegetation [42–44].

Estimating C_D has long been a focus in coastal engineering, with methodologies grounded in field observations, laboratory experiments, and numerical modeling. A notable study in the Yangtze Estuary in 2019 revealed that Phragmites australis outperformed Scirpus mariqueter in wave attenuation due to its greater biomass and structural strength, suggesting a mixed-species strategy could bolster coastal protection [45]. Zhang et al. [46] developed a new C_D calculation formula through field observations. Ding et al. [47] established a new formulation for the C_D based on biomechanical properties and field data from Terrebonne Bay, LA. Preliminary validation with laboratory experiments on synthetic vegetation confirmed the model's improved accuracy in predicting hydrodynamic changes in marshes, highlighting its utility in assessing vegetation's protective effects against waves and surges. Physical experiments were conducted [48] on idealized flexible vegetation in salt marshes to investigate the relationship between C_D and other parameters such as the degree of submergence, stem density, and wave height. As for most existing numerical models for wave attenuation, such as SWAN [30], XBeach [31], and SWASH [49], they are typically combined with physical experiments to explore the estimation of C_D value. In this paper, we will choose the XBeach model, which can explicitly represent vegetation characteristics, as the numerical model tool.

The C_D is usually an empirical parameter used to calculate wave energy dissipation. The drag force exerted by the rigid vegetation on the currents differs significantly from that exerted by flexible vegetation due to differences in their deformation characteristics. For rigid vegetation, since its shape and position do not change with the current, the drag coefficient C_D used to calculate the drag force is constant. Studies by Kothyari et al. [50] and Liu et al. [51] both examined the drag coefficient for rigid vegetation in open channel flow, with Liu's research even investigating the calculation of C_D under subcritical conditions in open channels. Other scholars, such as Hu et al. [52], Van Rooijen et al. [53], and Etminan et al. [54] have also developed formulations for C_D of rigid vegetation. Additionally, some scholars have begun using artificial neural networks to estimate C_D of rigid vegetation [55,56].

In contrast, for flexible vegetation, the deformation under the action of water flow will affect the resistance characteristics. The formation of the shear layer at the top of submerged flexible vegetation is a crucial characteristic of the flow [57,58]. Current physical experiments on the C_D for flexible vegetation [59,60] have shown that the magnitude of C_D is related to the Reynolds number (Re) [61] and the Keulegan–Carpenter number (KC) [40]. Typically, the Re parameter helps characterize the flow regime around the vegetation, distinguishing between laminar and turbulent flows and their respective impacts on wave interactions. The KC number is used to describe oscillatory flow conditions, reflecting the balance between inertia and drag forces acting on vegetation. These parameters are instrumental in predicting the C_D, providing a deeper understanding of the vegetative wave damping performance across different species and environmental conditions. Physical experiments found that C_D decreases with the increase of the Re and the KC number [59,60]. Houser et al. [57] found that the relationship between the drag coefficient and the Re depends on the flexibility and morphology of the vegetation. The greater the flexibility, the more the drag coefficient is reduced. Their research also discovered that flexible vegetation has a smaller drag coefficient compared to rigid vegetation. In the studies conducted by José Francisco Sánchez-González et al. [62], a fitting relationship between C_D and KC was obtained through best fit analysis of physical experiment data. Subsequently, Yin, Xu et al. [63,64] used this fitting relationship between C_D and KC to establish semi-empirical formulas for the C_D of flexible vegetation that can be applied to the XBeach model.

Chen et al. [65] evaluated the effectiveness of two methods for determining C_D, which are crucial for assessing wave damping in vegetated coastal areas, and introduced a new C_D-KC relation for combined wave-current flows. The findings highlighted the superior performance of the direct measurement approach over the conventional calibration method in predicting wave dissipation, proposing a unified C_D-KC relation that could enhance the modeling of wave-vegetation interactions. Additionally, Wang et al. [66] provided a semi-empirical formula to estimate the C_D for flexible vegetation. In addition to classifying vegetation as flexible or rigid, some scholars also study the impact of submersion on C_D. Some formulations specifically address either submerged vegetation [67,68] or emerged vegetation [69,70], while others encompass both [71,72]. Table 1 reviews C_D relations in vegetation-wave interaction and their deriving methods. The research on empirical formulas for C_D mentioned above mostly remains at the physical experimental stage and has not been applied to real engineering problems. Through this review, we determined that the findings of Garzon et al. [35] are the most suitable for application in our model because they used field observations under storm conditions to obtain the relationship of C_D with the modified Re and KC.

Table 1. A review of C_D relations in vegetation-wave interaction and their deriving methods associated with Re or KC.

Reference	Vegetation	Wave	Method	Re or KC Range	Formula
Hu et al. (2014) [52]	Rigid	R	Directed measurement	(300, 4700)	$C_D = 1.04 + \left(\frac{730}{Re}\right)^{1.37}$
ROOIJEN et al. (2015) [73]	Rigid	I	Calibration	/	/
Mendez et al. (1999) [74]	Rigid	R	Calibration	(200, 15,500)	$C_D = 0.08 + \left(\frac{2200}{Re}\right)^{2.2}$
Chen et al. (2018) [65]	Rigid	R	Calibration	(4, 120)	$C_D = 1.17 + 12.89KC^{-1.25}$
Wu et al. (2016) [75]	Rigid	I	Calibration	/	/
Wang et al. (2020) [76]	Rigid	S	Directed measurement	(532, 8048)	$C_D = 0.08 + \left(\frac{6436}{Re}\right)^{0.8957}$
Kelty et al. (2022) [77]	Rigid	I	Calibration	(4900, 190,000)	$C_D = 0.6 + \left(\frac{30{,}000}{Re}\right)$
Veelen et al. (2021) [78]	quasi-flexible	R	Calibration	(570,1500)	$C_D = 1.04 + \left(\frac{730}{Re}\right)^{1.37}$
Kobayashi et al. (1993) [61]	flexible	/	Calibration	(2200, 18,000)	$C_D = 0.08 + \left(\frac{2200}{Re}\right)^{2.4}$
Maza et al. (2013) [79]	flexible	R	Calibration	(2000, 7000)	$C_D = 1.61 + \left(\frac{4600}{Re}\right)^{1.9}$
Anderson and Smith (2014) [34]	flexible	I	Calibration	(533, 2296)	$C_D = 0.76 + \left(\frac{744.2}{Re}\right)^{1.27}$
Losada et al. (2016) [80]	flexible	R	Calibration	(4000, 160,000)	$C_D = 0.08 + \left(\frac{50{,}000}{Re*}\right)^{2.2}$
		I	Calibration	(20,000, 60,000)	$C_D = 0.08 + \left(\frac{22{,}000}{Re*}\right)^{2.2}$
Yin et al. (2022) [63]	flexible	R	Calibration	(0, 500)	$C_D = \left(\frac{150.5}{KC}\right)^{0.5952}$
Yin et al. (2023) [81]	flexible	R	Calibration	(28, 108)	$C_D = 0.929 + \left(\frac{41.434}{KC}\right)^{5.663}$
Liu et al. (2023) [68]	flexible	R	Calibration	(75, 230)	$C_D = \left(\frac{25.4}{KC}\right)^{0.6}$
Garzon et al. (2019) [35]	flexible	/	Calibration	(100, 6000)	$C_D = 0.411 + \left(\frac{514}{Re*}\right)^{0.5}$
Reis et al. (2024) [82]	flexible	R	Directed measurement	(22, 60)	$C_D = 1.09 + \left(\frac{22}{KC}\right)^{5.56}$

Notes: R is regular wave; I is irregular wave; S is solitary wave. The C_D formulation by Garzon et al. (2019) [35] was applied in this study. Re is Reynolds number and KC is the Keulegan–Carpenter number. In the 5th column, Ranges of KC number are marked with underline while ranges of Re are shown without underline. *Re* * means modified *Re*.

3. Model Validation by Comparing to Laboratory Experiments

In this paper, we investigate the possibility of applying the C_D values of empirical formulation to real-world scenarios by replicating and validating two classic physical flume experiments. The primary objective is to demonstrate the model's capability to predict interactions between vegetation, waves, and dunes under extreme storm conditions. The first experiment focused on the model's ability to accurately capture the evolution of dunes. The second experiment was chosen to validate XBSB's ability to accurately predict the effect of vegetation on wave attenuation under regular wave conditions.

3.1. Case 1: Laboratory Experiment for Wave-Induced Sand Dune Erosion

In this case study, we conducted a comprehensive evaluation of XBeach surfbeat model, focusing on the erosion of sand dunes under storm surge conditions. Our approach replicated and validated the experimental setup detailed in Berard's study [83], matching physical model parameters, including sediment characteristics and wave conditions.

We set the wave parameters to reflect the conditions in the reference study, with a significant wave height (Hs) of 0.16 m and a mean absolute wave period (Tm01) of 2.3 s. The model incorporated two still water levels, 0.40 m for the Low-water test (LW) and 0.47 m for the High-water test (HW), simulating different tidal conditions. This dual setup allowed us to simulate two scenarios: LWSB (Low-water) and HWSB (High-water), providing insights into dune erosion under varying hydrodynamic stresses. LWSB and HWSB simulated results in the collision regime and inundation regime, respectively. We refined some parameters in our simulations. The parameters are listed in Table 2 including the comparisons with the referred paper. The one-dimensional model's mesh, covering a 25 m cross-section, was configured for computational efficiency. From 3.8 m to 4.3 m, a 0.1 m grid was used; from 4.3 m to 20.4 m, a 0.5 m grid; and from 20.4 m to 25 m, a finer 0.025 m grid (Shown in Figure 1). All simulations share these parameter values, signifying a standardized approach.

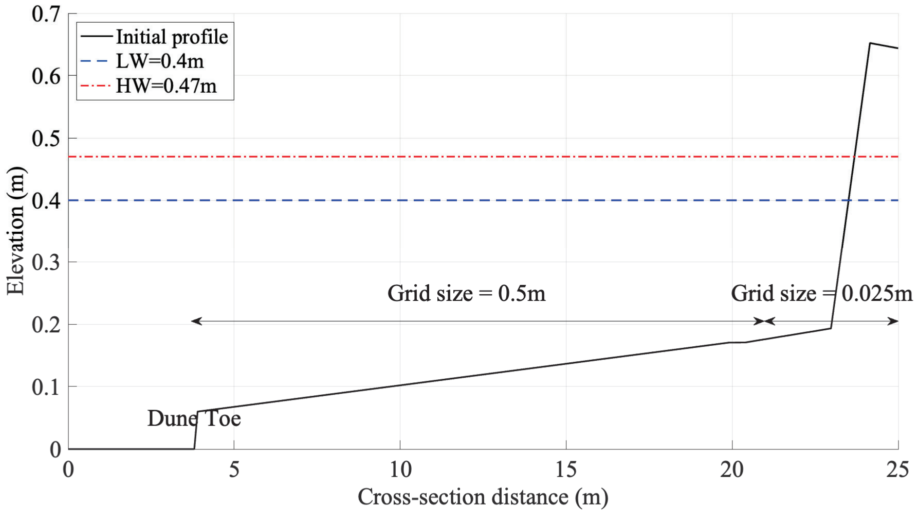

Figure 1. Numerical model domain indicating the initial bathymetry, still water levels for the LW and HW tests, and variable horizontal grid size.

In the hydrodynamic validation, the dune face was designated as a non-erodible layer. Figure 2 illustrates the cross-shore profiles of still water level (SWL) and observed significant wave height under low water (LW) and high water (HW) conditions, capturing the collision and overwash regimes, respectively. In Figure 2, LWSB and HWSB are simulated results by red dash lines. The sum of square residuals (SSR) is used to quantify the model performance, as shown in Figure 2c,d. The significant wave height (Hs) predictions from the XBSB model closely match the observed data, indicating the model's superior capability to simulate the complexities of wave interaction with a static dune structure.

$$SSR = \sum \left(H_{s,lab} - H_{s,mod}\right)^2 \tag{6}$$

Building on the hydrodynamic validation, we assessed the morphological responses of the dune profile under various water levels. The morphological evolution of the dune profile was analyzed using simulations for low (LW) and high water (HW) tests, replicating dune responses over 510 min for LW and 270 min for HW. The model performance was evaluated using the Brier Skill Score (BSS) [84], which was applied as a quantitative measure of the model's accuracy in simulating the morphological evolution of the dune profile. A BSS of 1 indicates high accuracy, while a BSS ≤ 0 indicates poor predictive capability. Scores below 0.3 are considered bad, 0.3–0.6 are fair, 0.6–0.8 are good, and above 0.8 are excellent. The BSS is calculated using Equation (7).

$$BSS = 1 - \frac{\sum\left(\left|zb_{post} - zb_{mod}\right|\right)^2}{\sum\left(\left|zb_{post} - zb_{pre}\right|\right)^2} \tag{7}$$

where zb_{post} indicates the observed bed elevation post-hurricane, zb_{mod} is the bed elevation results obtained from XBeach models, and zb_{pre} represents the initial bed elevation pre-hurricane.

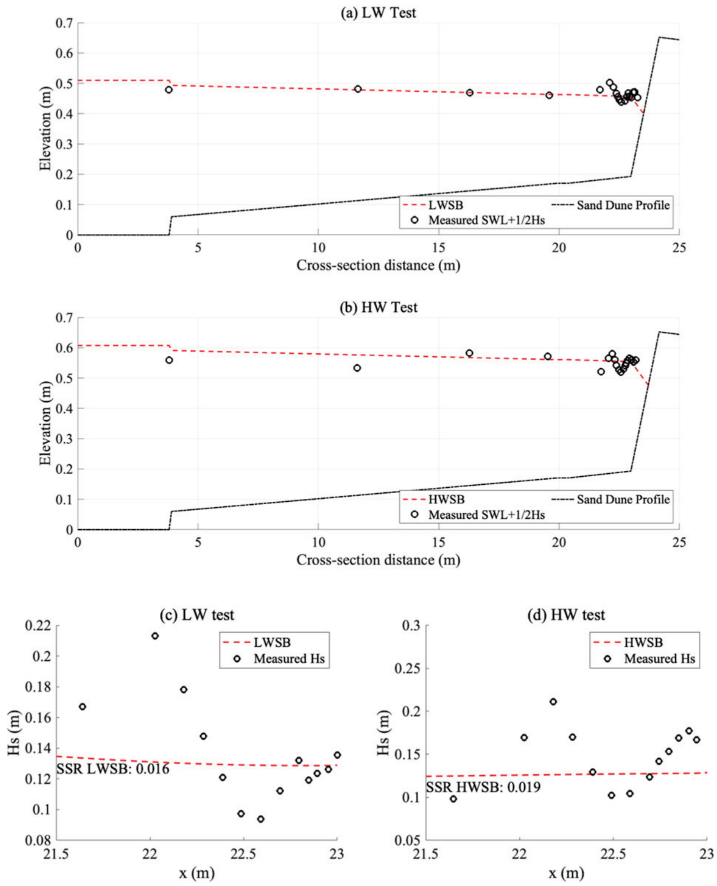

Figure 2. Validation of XBSB Models under varying water level conditions. (**a**) Modeled water surface level (red dash line) of the LW test; (**b**) Modeled water surface level (red dash line) of the HW test; (**c**) Modeled Hs (red dash line) near the dune of the LW test; (**d**) Modeled Hs (red dash line) near the dune of the HW test. LW is low-water test; HW is high-water test.

Table 2. Extended input parameters for dune morphology simulation.

Parameter	Meaning	Value	Berard's Study Value
wetslp	Critical wet slope for underwater avalanching	0.15	0.3
responseangle	Angle of repose affecting dune steepness	25 degree	30 degree
hswitch	Switch depth from wet to dry avalanche	0.005 m	0.005 m
form	Sediment transport formulation	vanthiel_vanrijn	vanthiel_vanrijn or soulsby_vanrijn
eps	Threshold water depth for cell inundation	0.09	0.09 or 0.02

The comparative analysis of dune profile evolution during LW test scenarios (Figure 3a,b) reveals the capabilities of the XBSB model low-water level (LW test). Initially, at 4 min, the XBSB model shows significant precision with BSS values of 0.888. This accuracy persists until 270 min with a BSS of 0.863, indicating the model's effectiveness in simulating early-stage erosive dynamics. However, by 510 min, the BSS diminishes to 0.767, suggesting decreased accuracy over time due to potential overpredictions of erosive processes. Analyzing the dune profile evolution during high-water level (HW) tests for the XBSB model, as shown in Figure 3c,d, highlights its performance in the overtopping regime. The model demonstrates high accuracy in the initial stages, with BSS values of 0.924 at 8 min. This indicates a strong ability to simulate dune erosion. However, accuracy declines at the 270-min mark, with a BSS of 0.875, suggesting the model initially overestimates erosion rates and underestimates dune face retreat over time. This analysis shows the XBSB model's strong initial accuracy in simulating erosive processes under various water levels, with high BSS values.

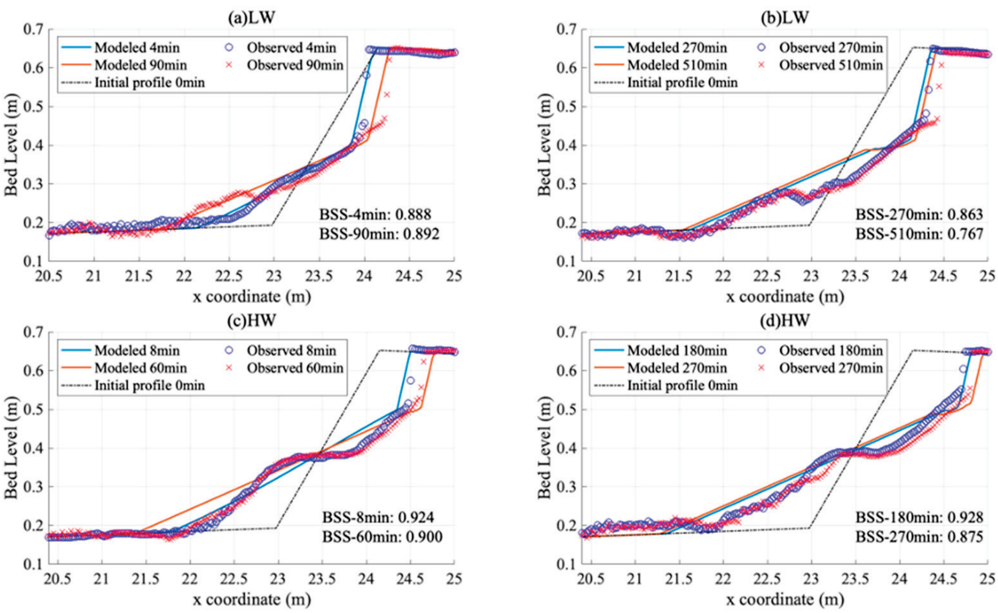

Figure 3. Temporal evolution of dune profile predictions using the XBSB Model: (**a**,**b**) during LW Test (SWL = 0.4 m), (**c**,**d**) during HW Test (SWL = 0.47 m).

3.2. Case 2: Laboratory Experiment for Regular Wave Attenuation over Vegetation

This section utilized the one-dimensional XBSB model to simulate and reproduce physical model experiments of the attenuation of regular waves under the influence of vegetation conducted by Yin et al. [63]. The numerical model setup was consistent with the physical setup of the laboratory experiment, and the configuration and calibration of model coefficients replicated the water level conditions along the physical flume. The XBeach model adjusted the length of the physical flume, selecting only the key flume before and after the vegetated area as the experimental cross-sections.

The entire experimental section was six meters long with a flat and fixed bottom. The first two meters of the area had no vegetation and was mainly used for stabilizing and calibrating wave conditions. This was followed by a 3.16 m vegetated area. The final 0.84 m also had no vegetation. The vegetation had a stem height of 0.25 m, a diameter of 0.0043 m, and a density of 1012 units/m^2. These vegetation parameters were consistent with the laboratory experiment. The drag coefficient C_D was adjusted based on the results of the simulated wave heights. In the first scenario, the initial significant wave height was 0.08 m with a wave period of 1.4 s and the initial water level was 0.35 m. In the second scenario, the initial significant wave height remained the same at 0.08 m with a wave period also at 1.4 s, but the initial water level was increased to 0.4 m. The third scenario introduced changes in significant wave height, wave period, and initial water level. The grid spacing varied from 0.1 m to 0.03 m, with a total of 153 grid points. In the model, the vegetation zone spanned from 2 m to 5.16 m, consisting of 112 grid points, with vegetation present on 56 of those points. The total runtime of the model was 3000 s, and data were output every 0.35 s or 0.4 s. The sketch of the XBeach model and vegetation field is shown in Figure 4.

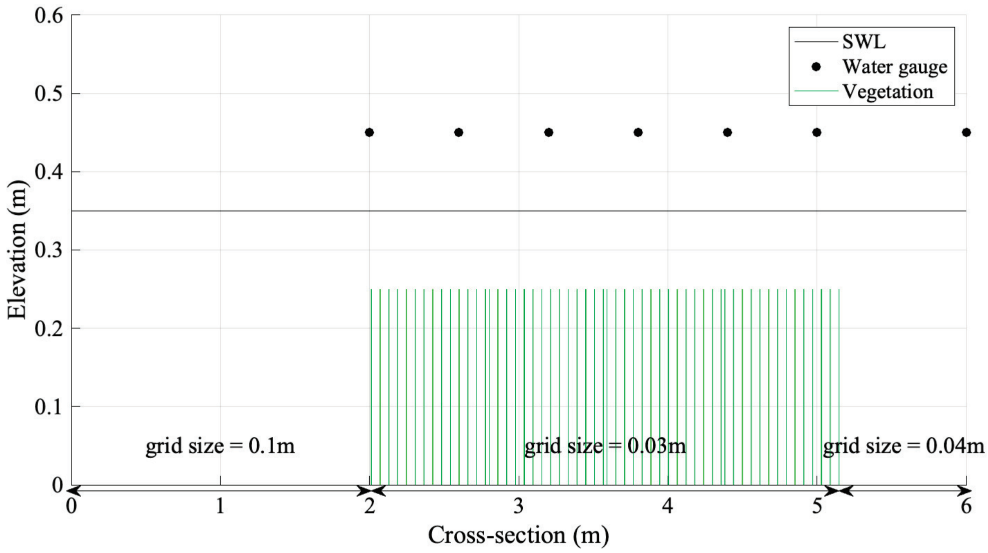

Figure 4. XBeach model setup and vegetation field.

The modeled significant wave heights were in good agreement with the observed data in Figure 5, demonstrating that the XBSB model replicated the conditions of the physical flume well. Observations from Figure 5 clearly show that vegetation has a notable attenuation effect on waves across all three scenarios. In the first scenario, the wave height decreased by 0.013 m, in the second scenario it decreased by 0.011 m, and in the third scenario, the reduction was more significant, amounting to 0.022 m. Comparing scenarios 1 and 2, it is evident that an increase in water level leads to a decrease in the alongshore fluctuation of measured wave heights, with the percentage of wave height attenuation dropping from 16.8% to 14.1%. The third scenario shows the most significant wave height attenuation, reaching 18.5%. Meanwhile, given the low RMSE values (Table 3) and the close match between the observed and modeled data points, especially within the region where vegetation is present (the green window), the conclusion is that the C_D calibrated by the XBSB model can accurately reflect the wave attenuation characteristics of the vegetation in the flume, making it suitable for simulating the propagation process of waves in vegetated areas.

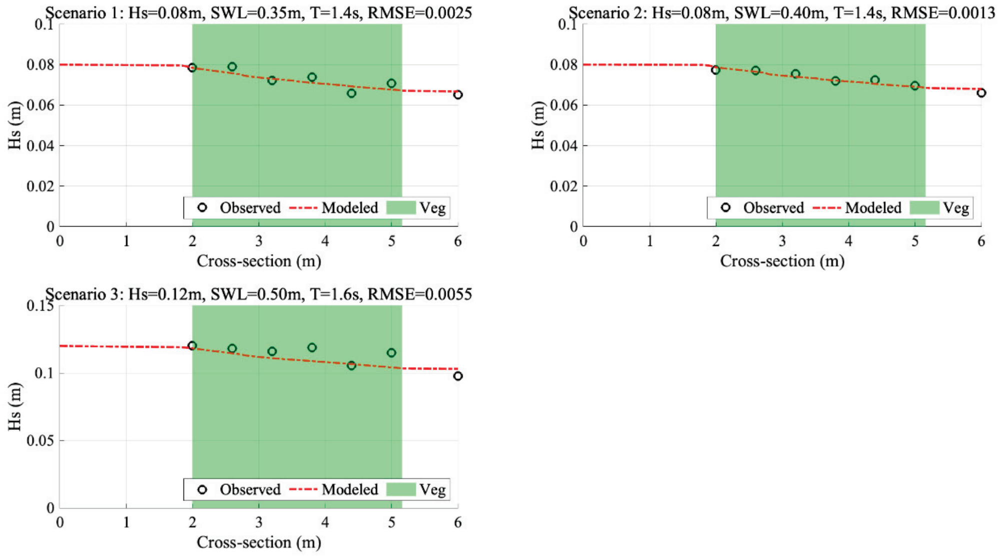

Figure 5. Different scenarios of observed and modeled wave attenuation by homogeneous flexible vegetation. The green window denotes the vegetation field.

Table 3. Boundary conditions and RMSEs for different scenarios.

Case No.	Hs (m)	SWL (m)	T (s)	C_D	RMSE (m)
1	0.08	0.35	1.4	0.8	0.0025
2	0.08	0.4	1.4	0.8	0.0013
3	0.12	0.5	1.6	1.47	0.0055

4. XBeach Modeling of Vegetation Effects on Wave Attenuation and Dune Erosion in Mexico Beach, FL

Building upon the foundation laid out in Sections 2 and 3, we evaluated the capability of the XBSB model to simulate and forecast the interactions between waves, sand dunes, and vegetation. The good model performance in these sections provides a basis for the following application. In this section, we have applied the XBSB model to a one-dimensional dune setup located at Mexico Beach, Florida, USA (Figure 6), aiming to examine the wave attenuation and dune erosion under extreme storm conditions with different vegetation cover.

Figure 6. Aerial view (from NOAA LiDAR Database website [85]) and the location of the dune profile on Mexico Beach, Florida, USA.

4.1. Model Setup

The bed elevation of dune profile data was sourced from NOAA LiDAR Database website [85], which offers pre- and post-hurricane LiDAR data. This dataset enables detailed analysis of geomorphic changes in response to Hurricane Michael. In our previous study, we have already validated a two-dimensional XBSB model on Mexico Beach, demonstrating strong performance [86]. Therefore, we used the best-performing parameters from that study in the present model and applied the same boundary conditions, including significant wave height and storm surge data (Figure 7). Unlike the previous large-scale study, which represented vegetation as bottom friction using Manning's coefficient, this one-dimensional model features detailed vegetation parameters and higher grid resolution in vegetated areas. This approach provides a more accurate simulation of wave-vegetation interactions and wave behavior near dunes. Detailed model settings are provided below.

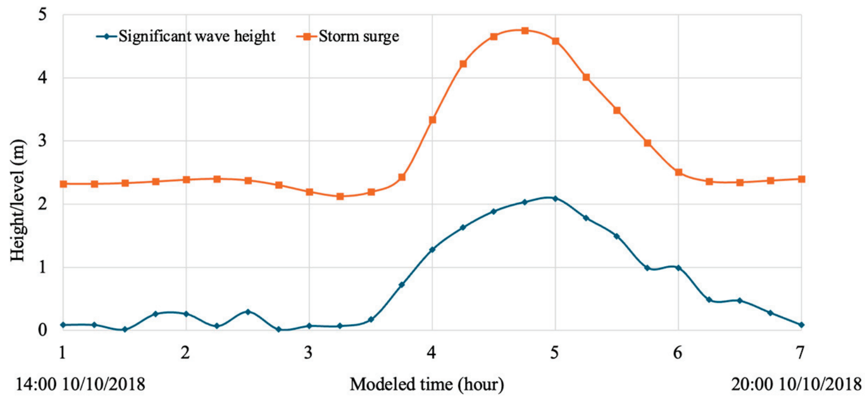

Figure 7. Boundary conditions of the one-dimensional XBSB model.

As depicted in Figure 8, the one-dimensional XBeach model has a span of approximately 310 m. The grid size varied across the model domain. From x = 0 to x = 156 m, the spatial resolution was set at 5 m. In the dune area, which extended from x = 156 m to x = 260 m, a finer spatial resolution of 0.5 m was employed to capture the intricate interactions. Beyond x = 260 m, the resolution was reverted to 5 m. Based on the field investigation and Google map, a 10-m vegetation section was set up on the dune crest, referred to as Veg area in Figure 7. The vegetation density (N) was estimated at 200 units/m^2 as well as a vegetation height (ah) of 0.7 m, with a stem diameter (bv) of 0.005 m based on natural conditions inferred from field surveys shown in Figure 9. Table 4 shows the vegetation parameters for the three model cases. The first case was without vegetation and was used as a comparison for the vegetation cases. In the second case, a drag coefficient of 1.47 was used, while in the last case, a C_D of 0.8 was applied. Furthermore, a house structure was integrated into the model behind the dune. The structure stood 10 m in height and extended 20 m along the x-axis. The area under the house was designated as a non-erodible layer, suggesting no morphodynamical evolution here. Through these settings, the model aims to offer critical insights into the role of vegetation in enhancing dune stability during severe weather conditions.

Table 4. The vegetation parameters for the different model cases.

Case No.	Parameter			
	C_D	N (Units/m^2)	bv (m)	ah (m)
1	/	/	/	/
2	0.8	200	0.005	0.7
3	1.47	200	0.005	0.7

Note: Case 1 represents no-vegetation condition Model setup.

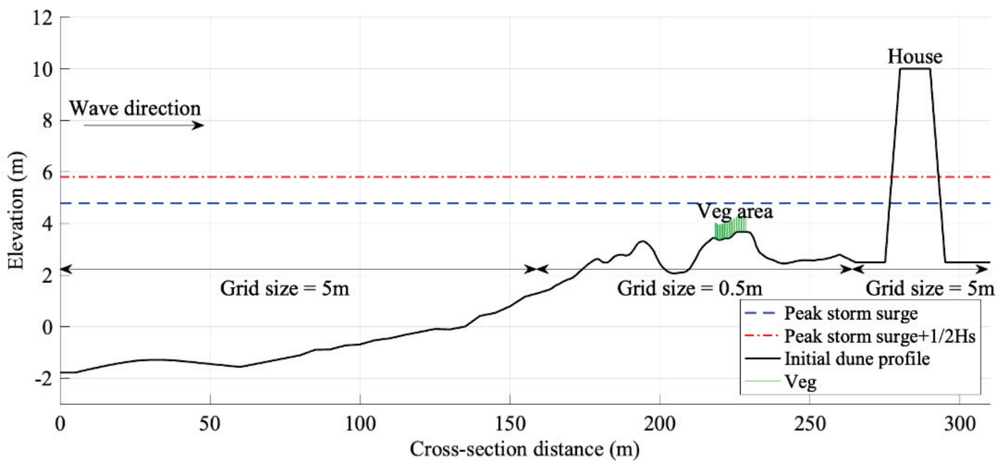

Figure 8. Onedimensional XBeach model setup illustrating vegetation cover conditions and house location at Mexico Beach. Peak storm surge is the largest storm surge level during Hurricane Michael.

Figure 9. Vegetation on sand dunes on Mexico Beach, FL before Hurricane Michael https://www.onlyinyourstate.com/florida/fl-forgotten-coast-small-beach-town/ (accessed on 5 July 2018).

4.2. Model Simulations under Wave Condition of Hurricane Michael

We used the empirical formulations of C_D conducted by Garzon et al. [35] and Yin et al. [63] to calibrate the XBSB model. The full C_D formulas are listed in Table 1. The resulting values were 1.47 and 0.8. Besides, based on Section 4.1, we compared the modeled dune elevations with the observed post-hurricane LiDAR data in Figure 10. Figure 10 illustrates the evolution of dune profiles under varying drag coefficients during Hurricane Michael. The figure presented five distinct profiles: the observed initial pre-hurricane profile, the observed post-hurricane profile, a modeled profile without vegetation, and two modeled profiles with vegetation of different C_D values. The observed post-hurricane profile showed marked changes, indicating significant morphological activity caused by the hurricane. To validate the performance of the model, we calculated the Brier Skill Scores (BSS) for three cases. Among them, the case with vegetation and a drag coefficient of 1.47 yielded a BSS of 0.742, which is greater than 0.6. According to the BSS classification in Section 3.1, this indicates that the model performance is good. In contrast, the case with a C_D of 0.8 resulted in a BSS of 0.518, indicating fair model performance. This also indicates that, in this specific field application, Garzon's formula for the drag coefficient was more suitable than Yin's formula. Therefore, we used the model with a C_D of 1.47 for the sensitivity analysis in Section 4.3. Additionally, the modeled profile without vegetation demonstrates the most pronounced departure from the observed initial conditions. This profile exhibited the highest average deviation with an RMSE of 0.392 m and experienced the most substantial erosion at a depth of 1.105 m. This highlights the erosion vulnerability of dune beds in the absence of vegetation and underscores the stabilizing role that vegetation plays in dune ecosystems.

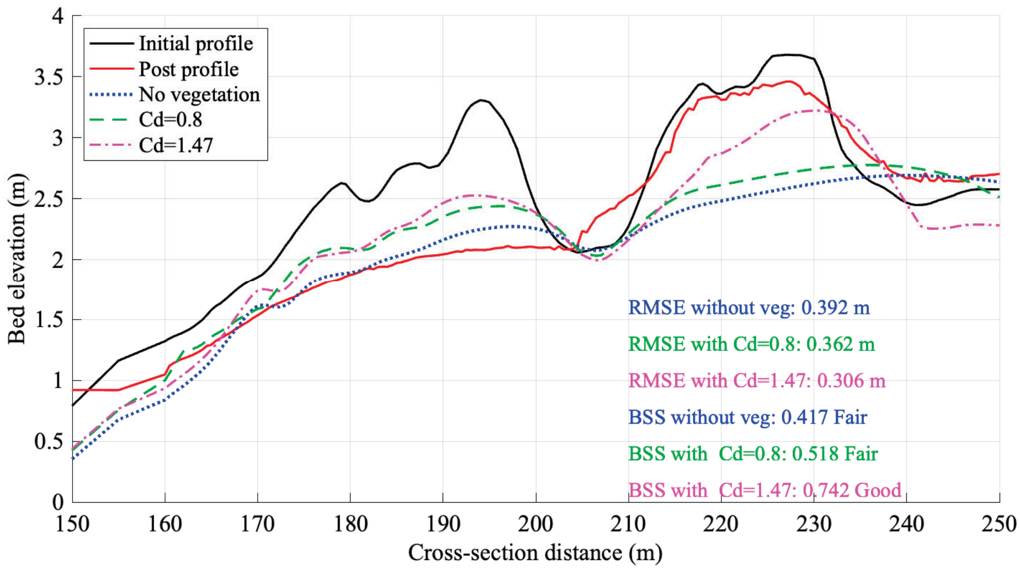

Figure 10. Dune profile evolutions with different C_D during Hurricane Michael, the vegetation area shown in Figure 9.

We compared the significant wave heights (Hs) along the profile at the peak storm surge level in Figure 11. Between 120 m and 160 m, Hs fluctuates around 1.7 m for all three conditions. However, beyond 160 m, particularly within the vegetated area from 218 m to 228 m, Hs significantly decreases. The no vegetation scenario consistently showed higher Hs, with a wave height reduction of 0.11 m, indicating less wave attenuation. In contrast, the C_D = 0.8 scenario showed a moderate decrease in Hs, with a reduction of 0.15 m, while the C_D = 1.47 scenario exhibited the most substantial wave height reduction of 0.46 m. This demonstrates that higher drag coefficients result in more wave attenuation.

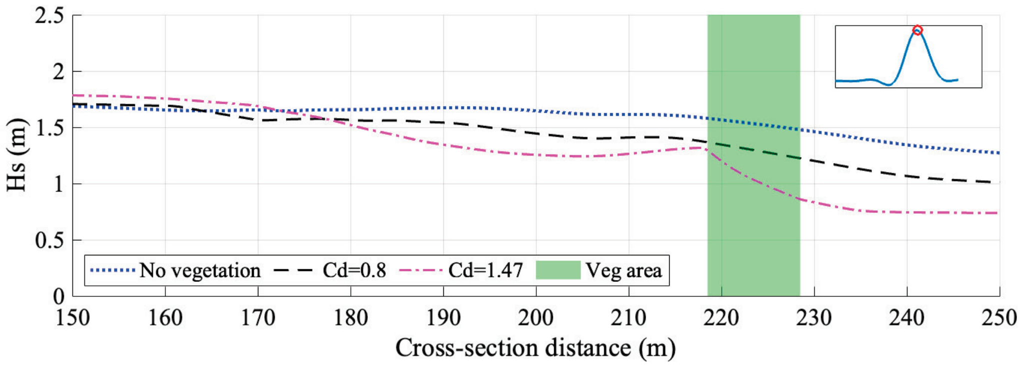

Figure 11. Significant wave height variation along cross-section with different vegetation drag coefficients C_D at peak storm surge level (red circle), showing vegetation effects on wave attenuation.

4.3. Sensitivity Analysis of Vegetation Effects under Regular Wave Condition

In this section, we conducted a sensitivity analysis on the impact of vegetation density on dune erosion and wave attenuation under regular wave conditions. Based on the predicted results from the XBSB models in Section 4.2, we examined various vegetation cover scenarios. The various vegetation densities of study cases are listed in Table 5. The input tide boundary condition was the peak storm surge of 4.76 m. The input wave condition was a significant wave height of 1.98 m during Hurricane Michael, as shown in Figure 7. The model ran for 3 h, simulating the evolution of the dune, the changes in flow velocities, and the changes in significant wave heights under different vegetation densities. The baseline parameters for the XBSB model remain consistent with those in Section 4.2, featuring a vegetation height of 0.7 m and a stem diameter of 0.005 m. This comprehensive suite of cases allows for an in-depth analysis of the interaction between vegetation and wave dynamics, highlighting the potential of vegetation in mitigating coastal erosion and enhancing dune protection under storm surge conditions.

Table 5. Different vegetation cover scenarios with various densities.

Case No.	Density N (Units/m^2)
case 4	No vegetation
case 5	200
case 6	500
case 7	800
case 8	1200

Figure 12 illustrates the simulation results of the XBSB model for cases 4 to 8 with various vegetation densities. Figure 12a shows that as vegetation density increased, the attenuation of significant wave height within the vegetated zones became more pronounced. The x-coordinate at which this attenuation stabilized moves closer to the initial range of the vegetated area as density increases. The moving of the stabilization point reflects the increased efficiency of denser vegetation in absorbing and dissipating wave energy. Specific attenuation values are provided in Table 6. Generally, higher vegetation densities resulted in a greater value of wave attenuation, with the maximum wave height reduction observed at N = 800 units/m^2. However, beyond a density of 800 units/m^2, the impact of density on wave reduction tended to decrease. This stabilization may be due to the drag effect of vegetation reaching a "saturation point", where further increases in vegetation density had minimal additional impact on wave reduction. This indicated an optimal vegetation density threshold, beyond which extra vegetation could not significantly enhance wave energy dissipation. Figure 12b shows the variation in mean flow velocity along the cross-section during the model run. When the flow reached the vegetated area, all cases with different vegetation densities experienced an immediate drop in velocity, followed by slight fluctuations within the vegetated zone. Subsequently, the flow velocity increased again due to the decline in bed elevation behind the vegetation area. Figure 12c revealed the bed elevation along the cross-section under different vegetation densities. Without vegetation cover, the dune was almost entirely removed. With vegetation present, significant protection of the dune was observed. At a vegetation density of N = 200 units/m^2, the dune crest moved noticeably landward. As the density continued to increase, the dune crest position shifted forward again. This shift was related to the x-coordinate position where the flow velocity begins to drop, as shown in Figure 12b. Additionally, unlike the significant differences in wave height attenuation across various vegetation densities, the reduction in dune crest elevation does not show significant differences under different vegetation densities.

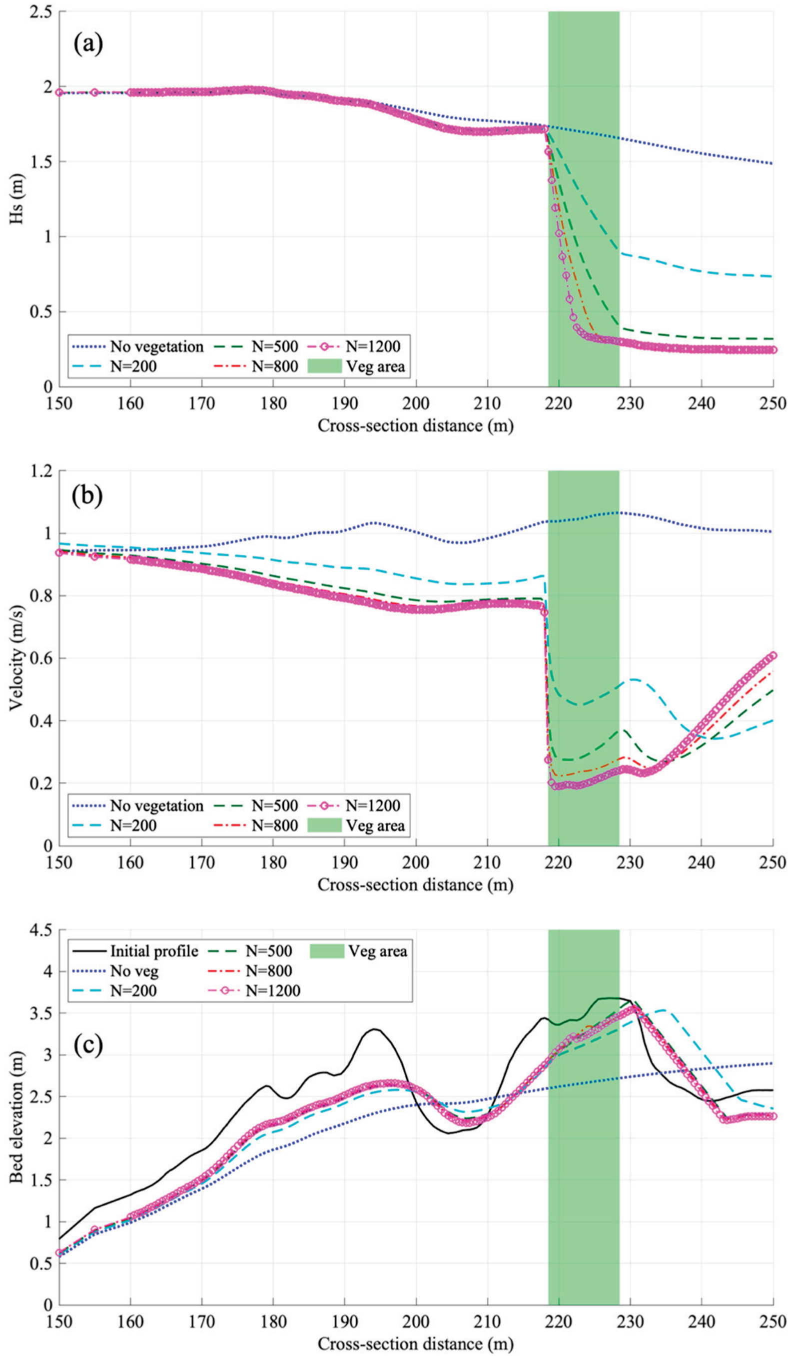

Figure 12. Impact of vegetation density on (**a**) average significant wave height, (**b**) average flow velocity, and (**c**) final bed elevation.

Table 6. Impact of density of vegetation on significant wave height reduction.

Distance	Significant Wave Height (m)				
	No veg	N = 200 (Units/m^2)	N = 500 (Units/m^2)	N = 800 (Units/m^2)	N = 1200 (Units/m^2)
x = 218 (m)	1.74	1.72	1.72	1.72	1.72
x = 228 (m)	1.66	0.90	0.40	0.28	0.30
Reduction (m)	0.08	0.82	1.32	1.44	1.42
Rate (%)	0	47.73	76.92	83.88	82.67
Δ Rate (%)	0	47.73	29.19	6.96	−1.21

5. Discussion

In this paper, we applied the XBeach model to evaluate the effects of vegetation on wave attenuation and dune erosion. Because lab experimental data for vegetation on dune is not available, we used the experiment data from the work of Berard et al. [83] and Yin's laboratory experiments [63] to validate the performance of the XBSB model in predicting and simulating the effects of vegetation on dune erosion and wave attenuation. The field application of XBeach to Mexico Beach under Hurricane Michael as described in Section 4.1 fills the current research gap on wave actions on sand dunes with vegetation. The data set of storm surges, waves, vegetation, beach, and dune profiles before and after Hurricane Michael from LiDAR surveys provided a good model validation for vegetation on dunes under hurricane wave conditions, as shown in Figures 8–10. LiDAR data of dune profiles before and after Hurricane Michael were used for model validation (Figure 10).

As can be seen in Figures 10 and 11, compared with the observed post-hurricane dune elevation, vegetation on dunes reduced dune erosion and enhanced coastal resilience. This conclusion aligns with the findings of some recent studies [87,88] that demonstrated that vegetation significantly reduces wave heights, thus lowering flooding and erosion risks and providing multiple ecosystem benefits. However, because the XBSB is based on some modeling simplifications, the actual applications of vegetating the sand dune warrants further exploration. One notable simplification in the XBSB model is the representation of vegetation as uniformly distributed, slender, cylindrical structures. In reality, the vegetation does not grow uniformly across the dune surface and has leaves that contribute to the complexity of their density distribution. For example, Suzuki et al. [89] pointed out that drag force induced by horizontal vegetation stems/roots and porosity are often neglected in numerical models. A more accurate method might be to set up horizontal vegetation fields with various densities in future studies.

Another important point to consider is that in real extreme hydrodynamic scenarios, storm surges and huge waves can uproot or flatten thin plants or cause vegetation to be dislodged from the dunes due to erosion. This reduction in vegetation cover can diminish the ability to attenuate wave energy and stabilize the sand substrate, thus exacerbating erosion. However, these factors are not accounted for in the XBSB simulations. A report on Indonesia [90] recommended the planting of shade vegetation and fruit trees in the costal front zone to reduce the impact of coastal erosion. These strategies suggested that trees can provide a green barrier due to their deeper root systems and more significant biomass, which may enhance dune stability and wave energy dissipation. Future research should investigate the effects of different types of vegetation, including shrubs and trees, under extreme hydrodynamic forces.

Based on the findings in Section 4.3, vegetation density plays a crucial role in wave attenuation and erosion resistance. However, the relationship is not linear. There is a critical density, beyond which additional vegetation does not significantly reduce wave energy or dune erosion, indicating that there is an optimal density for maximizing protective benefits. In practical engineering, when considering the planting of vegetation on dunes, it is essential to determine and implement this optimal density. This finding resonates with the findings of Chen et al. [88], which emphasizes that optimizing the location and size of vegetation is crucial to increasing efficiency. This study only presents one single case in Mexico Beach during Hurricane Michael. Therefore, the optimal density simulated could vary under different environmental conditions, vegetation types, and storm scenarios. Therefore, further study is necessary to establish a range of optimal densities across various contexts. For example, studies should examine regional variations in optimal vegetation density. Factors such as local climate, dune morphology, and typical vegetation type can influence the effectiveness of vegetation in mitigating erosion and attenuating waves.

6. Conclusions

This study applied the XBeach surfbeat model to evaluate the effects of vegetation on wave attenuation and dune erosion. Validation against laboratory experiments demonstrated the model's reliability. The case study of vegetation on dunes during Hurricane Michael shows the importance of vegetation for dune morphology during hurricanes. Vegetation stabilizes dunes and reduces erosion, with vegetated dunes showing significantly less erosion. In general, an increase in vegetation density enhances wave attenuation and reduces erosion rates. A saturation point has been identified where additional density does not significantly increase wave attenuation. The implications of this study for coastal resilience planning are significant. XBeach surfbeat model that predicts and enhances the protective functions of coastal vegetation on sand dunes is valuable for coastal resilience planning. This study expanded the application range of laboratory vegetation drag force parameters to the field application to account for the interactions among waves, dunes, and vegetation under actual hurricane conditions.

Author Contributions: Conceptualization, M.M., W.H. and S.J.; methodology and validation M.M.; formal analysis and investigation, M.M.; resources and data curation, M.M., K.Y. and S.X.; writing—original draft preparation, M.M.; writing—review and editing, M.M., W.H., S.J. and C.O.; visualization M.M.; supervision, W.H. and S.J. All authors have read and agreed to the published version of the manuscript.

Funding: This research received no external funding.

Data Availability Statement: Upon request.

Conflicts of Interest: The authors declare no conflicts of interest.

Appendix A

Table A1. List of Abbreviations Used in the Manuscript.

Abbreviation	Full Form
XBSB	XBeach surfbeat model
LiDAR	Light Detection and Ranging
C_D	Vegetation drag coefficient
Re	Reynolds number
KC	Keulegan–Carpenter number
LW	Low-water test
HW	High-water test
LWSB	Simulated results of Low-water test
HWSB	Simulated results of High-water test
SWL	Still water level
BSS	Brier Skill Score
SSR	Sum of square residuals
Hs	Significant wave height
RMSE	Root means square error

References

1. Leonardi, N.; Carnacina, I.; Donatelli, C.; Ganju, N.K.; Plater, A.J.; Schuerch, M.; Temmerman, S. Dynamic interactions between coastal storms and salt marshes: A review. *Geomorphology* **2018**, *301*, 92–107. [CrossRef]
2. Husemann, P.; Romão, F.; Lima, M.; Costas, S.; Coelho, C. Review of the Quantification of Aeolian Sediment Transport in Coastal Areas. *J. Mar. Sci. Eng.* **2024**, *12*, 755. [CrossRef]
3. Saengsupavanich, C. Elevated water level from wind along the Gulf of Thailand. *Thalass. Int. J. Mar. Sci.* **2017**, *33*, 179–185. [CrossRef]
4. Shaw, A.; Hashemi, M.R.; Spaulding, M.; Oakley, B.; Baxter, C. Effect of coastal erosion on storm surge: A case study in the southern coast of Rhode Island. *J. Mar. Sci. Eng.* **2016**, *4*, 85. [CrossRef]
5. D'Alessandro, F.; Tomasicchio, G.R. Wave–dune interaction and beach resilience in large-scale physical model tests. *Coast. Eng.* **2016**, *116*, 15–25. [CrossRef]
6. Neumeier, U.; Ciavola, P. Flow resistance and associated sedimentary processes in a Spartina maritima salt-marsh. *J. Coast. Res.* **2004**, *20*, 435–447. [CrossRef]
7. Nepf, H.M. Flow and transport in regions with aquatic vegetation. *Annu. Rev. Fluid Mech.* **2012**, *44*, 123–142. [CrossRef]

8. Maximiliano-Cordova, C.; Silva, R.; Mendoza, E.; Chávez, V.; Martínez, M.L.; Feagin, R.A. Morphological Performance of Vegetated and Non-Vegetated Coastal Dunes with Rocky and Geotextile Tube Cores under Storm Conditions. *J. Mar. Sci. Eng.* **2023**, *11*, 2061. [CrossRef]
9. Mendoza, E.; Odériz, I.; Martínez, M.L.; Silva, R. Measurements and modelling of small scale processes of vegetation preventing dune erosion. *J. Coast. Res.* **2017**, *77*, 19–27. [CrossRef]
10. Türker, U.; Yagci, O.; Kabdasli, M.S. Impact of nearshore vegetation on coastal dune erosion: Assessment through laboratory experiments. *Environ. Earth Sci.* **2019**, *78*, 1–14. [CrossRef]
11. Anderson, M.E.; Smith, J.M.; McKay, S.K. *Wave Dissipation by Vegetation*; TU Delft: Delft, The Netherlands, 2011.
12. Unguendoli, S.; Biolchi, L.G.; Aguzzi, M.; Pillai, U.P.A.; Alessandri, J.; Valentini, A. A modeling application of integrated nature based solutions (NBS) for coastal erosion and flooding mitigation in the Emilia-Romagna coastline (Northeast Italy). *Sci. Total Environ.* **2023**, *867*, 161357. [CrossRef] [PubMed]
13. Jacob, B.; Dolch, T.; Wurpts, A.; Staneva, J. Evaluation of seagrass as a nature-based solution for coastal protection in the German Wadden Sea. *Ocean Dyn.* **2023**, *73*, 699–727. [CrossRef]
14. Coops, H.; Geilen, N.; Verheij, H.J.; Boeters, R.; van der Velde, G. Interactions between waves, bank erosion and emergent vegetation: An experimental study in a wave tank. *Aquat. Bot.* **1996**, *53*, 187–198. [CrossRef]
15. Borsje, B.W.; van Wesenbeeck, B.K.; Dekker, F.; Paalvast, P.; Bouma, T.J.; van Katwijk, M.M.; de Vries, M.B. How ecological engineering can serve in coastal protection. *Ecol. Eng.* **2011**, *37*, 113–122. [CrossRef]
16. Figlus, J.; Sigren, J.M.; Power, M.J.; Armitage, A.R. Physical model experiment investigating interactions between different dune vegetation and morphology changes under wave impact. In Proceedings of the Coastal Dynamics, Helsingør, Denmark, 12–16 June 2017; pp. 470–480.
17. Ozeren, Y.; Wren, D.; Wu, W. Experimental investigation of wave attenuation through model and live vegetation. *J. Waterw. Port Coast. Ocean Eng.* **2014**, *140*, 04014019. [CrossRef]
18. Blackmar, P.J.; Cox, D.T.; Wu, W.-C. Laboratory observations and numerical simulations of wave height attenuation in heterogeneous vegetation. *J. Waterw. Port Coast. Ocean Eng.* **2014**, *140*, 56–65. [CrossRef]
19. John, B.M.; Shirlal, K.G.; Rao, S. Laboratory investigations of wave attenuation by simulated vegetation of varying densities. *ISH J. Hydraul. Eng.* **2019**, *25*, 203–213. [CrossRef]
20. Koftis, T.; Prinos, P.; Stratigaki, V. Wave damping over artificial Posidonia oceanica meadow: A large-scale experimental study. *Coast. Eng.* **2013**, *73*, 71–83. [CrossRef]
21. Chalmoukis, I.A.; Leftheriotis, G.A.; Dimas, A.A. Large-Eddy Simulation of Wave Attenuation and Breaking on a Beach with Coastal Vegetation Modelled as Porous Medium. *J. Mar. Sci. Eng.* **2023**, *11*, 519. [CrossRef]
22. Holzenthal, E.R.; Hill, D.F.; Wengrove, M.E. Multi-Scale Influence of Flexible Submerged Aquatic Vegetation (SAV) on Estuarine Hydrodynamics. *J. Mar. Sci. Eng.* **2022**, *10*, 554. [CrossRef]
23. Dietrich, J.; Westerink, J.; Kennedy, A.; Smith, J.; Jensen, R.; Zijlema, M.; Holthuijsen, L.; Dawson, C.; Luettich, R.; Powell, M. Hurricane Gustav (2008) waves and storm surge: Hindcast, synoptic analysis, and validation in Southern Louisiana. *Mon. Weather Rev.* **2011**, *139*, 2488–2522. [CrossRef]
24. Bender, C.; Smith, J.M.; Kennedy, A.; Jensen, R. STWAVE simulation of Hurricane Ike: Model results and comparison to data. *Coast. Eng.* **2013**, *73*, 58–70. [CrossRef]
25. Bryant, M.A.; Jensen, R.E. Application of the nearshore wave model STWAVE to the North Atlantic coast comprehensive study. *J. Waterw. Port Coast. Ocean Eng.* **2017**, *143*, 04017026. [CrossRef]
26. Lapetina, A.; Sheng, Y.P. Three-dimensional modeling of storm surge and inundation including the effects of coastal vegetation. *Estuaries Coasts* **2014**, *37*, 1028–1040. [CrossRef]
27. Medeiros, S.C. Hydraulic Bottom Friction and Aerodynamic Roughness Coefficients for Mangroves in Southwest Florida, USA. *J. Mar. Sci. Eng.* **2023**, *11*, 2053. [CrossRef]
28. Baron-Hyppolite, C.; Lashley, C.H.; Garzon, J.; Miesse, T.; Ferreira, C.; Bricker, J.D. Comparison of implicit and explicit vegetation representations in SWAN hindcasting wave dissipation by coastal wetlands in Chesapeake Bay. *Geosciences* **2018**, *9*, 8. [CrossRef]
29. Abdolali, A.; Hesser, T.J.; Anderson Bryant, M.; Roland, A.; Khalid, A.; Smith, J.; Ferreira, C.; Mehra, A.; Sikiric, M.D. Wave attenuation by vegetation: Model implementation and validation study. *Front. Built Environ.* **2022**, *8*, 891612. [CrossRef]
30. Booij, N.; Holthuijsen, L.; Ris, R. The "SWAN" wave model for shallow water. In *Coastal Engineering 1996*; ASCE Library: Reston, VA, USA, 1996; pp. 668–676.
31. Roelvink, D.; Reniers, A.; Van Dongeren, A.; Van Thiel de Vries, J.; Lescinski, J.; McCall, R. XBeach model description and manual. *Unesco-IHE Inst. Water Educ. Deltares Delft Univ. Tecnhol. Rep. June* **2010**, *21*, 2010.
32. Musumeci, R.E.; Marino, M.; Cavallaro, L.; Foti, E. Does Coastal Wetland Restoration Work as a Climate Change Adaptation Strategy? The Case of the South-East of Sicily Coast. *Coast. Eng. Proc.* **2022**, *37*, 66. [CrossRef]
33. Sigren, J.M.; Figlus, J.; Highfield, W.; Feagin, R.A.; Armitage, A.R. The effects of coastal dune volume and vegetation on storm-induced property damage: Analysis from Hurricane Ike. *J. Coast. Res.* **2018**, *34*, 164–173. [CrossRef]
34. Anderson, M.E.; Smith, J. Wave attenuation by flexible, idealized salt marsh vegetation. *Coast. Eng.* **2014**, *83*, 82–92. [CrossRef]
35. Garzon, J.L.; Maza, M.; Ferreira, C.; Lara, J.; Losada, I. Wave attenuation by Spartina saltmarshes in the Chesapeake Bay under storm surge conditions. *J. Geophys. Res. Ocean.* **2019**, *124*, 5220–5243. [CrossRef]

36. Jin, H.; Do, K.; Kim, I.; Chang, S. Sensitivity analysis of event-specific calibration data and its application to modeling of subaerial storm erosion under complex bathymetry. *J. Mar. Sci. Eng.* **2022**, *10*, 1389. [CrossRef]
37. Hwang, B.; Do, K.; Chang, S. Morphological Changes in Storm Hinnamnor and the Numerical Modeling of Overwash. *J. Mar. Sci. Eng.* **2024**, *12*, 196. [CrossRef]
38. Costa, G.P.; Marino, M.; Cáceres, I.; Musumeci, R.E. Effectiveness of Dune Reconstruction and Beach Nourishment to Mitigate Coastal Erosion of the Ebro Delta (Spain). *J. Mar. Sci. Eng.* **2023**, *11*, 1908. [CrossRef]
39. Sánchez-Artús, X.; Subbiah, B.; Gracia, V.; Espino, M.; Grifoll, M.; Espanya, A.; Sánchez-Arcilla, A. Evaluating barrier beach protection with numerical modelling. A practical case. *Coast. Eng.* **2024**, *191*, 104522. [CrossRef]
40. Mendez, F.J.; Losada, I.J. An empirical model to estimate the propagation of random breaking and nonbreaking waves over vegetation fields. *Coast. Eng.* **2004**, *51*, 103–118. [CrossRef]
41. Suzuki, T.; Zijlema, M.; Burger, B.; Meijer, M.C.; Narayan, S. Wave dissipation by vegetation with layer schematization in SWAN. *Coast. Eng.* **2012**, *59*, 64–71. [CrossRef]
42. Henry, P.-Y.; Myrhaug, D.; Aberle, J. Drag forces on aquatic plants in nonlinear random waves plus current. *Estuar. Coast. Shelf Sci.* **2015**, *165*, 10–24. [CrossRef]
43. Zhang, Z.; Huang, B.; Tan, C.; Cheng, X. A study on the drag coefficient in wave attenuation by vegetation. *Hydrol. Earth Syst. Sci.* **2021**, *25*, 4825–4834. [CrossRef]
44. Wang, Y.; Yin, Z.; Liu, Y. Experimental investigation of wave attenuation and bulk drag coefficient in mangrove forest with complex root morphology. *Appl. Ocean Res.* **2022**, *118*, 102974. [CrossRef]
45. Zhang, W.; Ge, Z.-M.; Li, S.-H.; Tan, L.-S.; Zhou, K.; Li, Y.-L.; Xie, L.-N.; Dai, Z.-J. The role of seasonal vegetation properties in determining the wave attenuation capacity of coastal marshes: Implications for building natural defenses. *Ecol. Eng.* **2022**, *175*, 106494. [CrossRef]
46. Zhang, X.; Lin, P.; Gong, Z.; Li, B.; Chen, X. Wave attenuation by Spartina alterniflora under macro-tidal and storm surge conditions. *Wetlands* **2020**, *40*, 2151–2162. [CrossRef]
47. Ding, Y.; Rosati, J.D.; Johnson, B.D.; Chen, Q.J.; Zhu, L. *Implementation of Flexible Vegetation into CSHORE for Modeling Wave Attenuation*; ERDC-Library: Vicksburg, MS, USA, 2022. [CrossRef]
48. Wang, H.; Yin, Z.; Luan, Y.; Wang, Y.; Liu, D. Hydrodynamic characteristics of idealized flexible vegetation under regular waves: Experimental investigations and analysis. *J. Coast. Res.* **2022**, *38*, 673–680. [CrossRef]
49. Zijlema, M.; Stelling, G.; Smit, P. SWASH: An operational public domain code for simulating wave fields and rapidly varied flows in coastal waters. *Coast. Eng.* **2011**, *58*, 992–1012. [CrossRef]
50. Kothyari, U.C.; Hayashi, K.; Hashimoto, H. Drag coefficient of unsubmerged rigid vegetation stems in open channel flows. *J. Hydraul. Res.* **2009**, *47*, 691–699. [CrossRef]
51. Liu, X.-g.; Zeng, Y.-h. Drag coefficient for rigid vegetation in subcritical open channel. *Procedia Eng.* **2016**, *154*, 1124–1131. [CrossRef]
52. Hu, Z.; Suzuki, T.; Zitman, T.; Uittewaal, W.; Stive, M. Laboratory study on wave dissipation by vegetation in combined current–wave flow. *Coast. Eng.* **2014**, *88*, 131–142. [CrossRef]
53. Van Rooijen, A.; McCall, R.; Van Thiel de Vries, J.; Van Dongeren, A.; Reniers, A.; Roelvink, J. Modeling the effect of wave-vegetation interaction on wave setup. *J. Geophys. Res. Ocean.* **2016**, *121*, 4341–4359. [CrossRef]
54. Etminan, V.; Lowe, R.J.; Ghisalberti, M. A new model for predicting the drag exerted by vegetation canopies. *Water Resour. Res.* **2017**, *53*, 3179–3196. [CrossRef]
55. Wang, Y.; Liu, Y.; Yin, Z.; Jiang, X.; Yang, G. Numerical simulation of wave propagation through rigid vegetation and a predictive model of drag coefficient using an artificial neural network. *Ocean Eng.* **2023**, *281*, 114792. [CrossRef]
56. Ahmed, A.; Valyrakis, M.; Ghumman, A.R.; Farooq, R.; Pasha, G.A.; Janjua, S.; Raza, A. Experimental and Artificial Neural Network (ANN) modeling of instream vegetation hydrodynamic resistance. *Hydrology* **2023**, *10*, 73. [CrossRef]
57. Houser, C.; Trimble, S.; Morales, B. Influence of blade flexibility on the drag coefficient of aquatic vegetation. *Estuaries Coasts* **2015**, *38*, 569–577. [CrossRef]
58. Luhar, M.; Infantes, E.; Nepf, H. Seagrass blade motion under waves and its impact on wave decay. *J. Geophys. Res. Ocean.* **2017**, *122*, 3736–3752. [CrossRef]
59. Augustin, L.N.; Irish, J.L.; Lynett, P. Laboratory and numerical studies of wave damping by emergent and near-emergent wetland vegetation. *Coast. Eng.* **2009**, *56*, 332–340. [CrossRef]
60. Riffe, K.C.; Henderson, S.M.; Mullarney, J.C. Wave dissipation by flexible vegetation. *Geophys. Res. Lett.* **2011**, *38*, L18607. [CrossRef]
61. Kobayashi, N.; Raichle, A.W.; Asano, T. Wave attenuation by vegetation. *J. Waterw. Port Coast. Ocean Eng.* **1993**, *119*, 30–48. [CrossRef]
62. Sánchez-González, J.F.; Sánchez-Rojas, V.; Memos, C.D. Wave attenuation due to Posidonia oceanica meadows. *J. Hydraul. Res.* **2011**, *49*, 503–514. [CrossRef]
63. Yin, K.; Xu, S.; Gong, S.; Chen, J.; Wang, Y.; Li, M. Modeling wave attenuation by submerged flexible vegetation with XBeach phase-averaged model. *Ocean Eng.* **2022**, *257*, 111646. [CrossRef]
64. Yin, K.; Xu, S.; Huang, W.; Liu, S.; Li, M. Numerical investigation of wave attenuation by coupled flexible vegetation dynamic model and XBeach wave model. *Ocean Eng.* **2021**, *235*, 109357. [CrossRef]

65. Chen, H.; Ni, Y.; Li, Y.; Liu, F.; Ou, S.; Su, M.; Peng, Y.; Hu, Z.; Uijttewaal, W.; Suzuki, T. Deriving vegetation drag coefficients in combined wave-current flows by calibration and direct measurement methods. *Adv. Water Resour.* **2018**, *122*, 217–227. [CrossRef]
66. Wang, Y.; Yin, Z.; Liu, Y. Predicting the bulk drag coefficient of flexible vegetation in wave flows based on a genetic programming algorithm. *Ocean Eng.* **2021**, *223*, 108694. [CrossRef]
67. Tang, H.; Tian, Z.; Yan, J.; Yuan, S. Determining drag coefficients and their application in modelling of turbulent flow with submerged vegetation. *Adv. Water Resour.* **2014**, *69*, 134–145. [CrossRef]
68. Liu, S.; Xu, S.; Yin, K. Optimization of the drag coefficient in wave attenuation by submerged rigid and flexible vegetation based on experimental and numerical studies. *Ocean Eng.* **2023**, *285*, 115382. [CrossRef]
69. Wang, W.-J.; Huai, W.-X.; Thompson, S.; Peng, W.-Q.; Katul, G.G. Drag coefficient estimation using flume experiments in shallow non-uniform water flow within emergent vegetation during rainfall. *Ecol. Indic.* **2018**, *92*, 367–378. [CrossRef]
70. D'Ippolito, A.; Lauria, A.; Alfonsi, G.; Calomino, F. Investigation of flow resistance exerted by rigid emergent vegetation in open channel. *Acta Geophys.* **2019**, *67*, 971–986. [CrossRef]
71. Yang, T.-Y.; Chan, I.-C. Drag Force Modeling of Surface Wave Dissipation by a Vegetation Field. *Water* **2020**, *12*, 2513. [CrossRef]
72. Sohrabi, S.; Afzalimehr, H.; Singh, V.P. Estimation of drag coefficient of emergent and submerged vegetation patches with various densities and arrangements in open channel flow. *ISH J. Hydraul. Eng.* **2023**, *29*, 297–307. [CrossRef]
73. Van Rooijen, A.; Van Thiel de Vries, J.; McCall, R.; Van Dongeren, A.; Roelvink, J.; Reniers, A. Modeling of wave attenuation by vegetation with XBeach. In Proceedings of the E-Proceedings 36th IAHR World Congress, The Hague, The Netherland, 28 June–3 July 2015; pp. 1–7.
74. Méndez, F.J.; Losada, I.J.; Losada, M.A. Hydrodynamics induced by wind waves in a vegetation field. *J. Geophys. Res. Ocean.* **1999**, *104*, 18383–18396. [CrossRef]
75. Wu, W.-C.; Ma, G.; Cox, D.T. Modeling wave attenuation induced by the vertical density variations of vegetation. *Coast. Eng.* **2016**, *112*, 17–27. [CrossRef]
76. Wang, Y.; Yin, Z.; Liu, Y. Numerical investigation of solitary wave attenuation and resistance induced by rigid vegetation based on a 3-D RANS model. *Adv. Water Resour.* **2020**, *146*, 103755. [CrossRef]
77. Kelty, K.; Tomiczek, T.; Cox, D.T.; Lomonaco, P.; Mitchell, W. Prototype-scale physical model of wave attenuation through a mangrove forest of moderate cross-shore thickness: Lidar-based characterization and Reynolds scaling for engineering with nature. *Front. Mar. Sci.* **2022**, *8*, 780946. [CrossRef]
78. van Veelen, T.J.; Karunarathna, H.; Reeve, D.E. Modelling wave attenuation by quasi-flexible coastal vegetation. *Coast. Eng.* **2021**, *164*, 103820. [CrossRef]
79. Maza, M.; Lara, J.L.; Losada, I.J. A coupled model of submerged vegetation under oscillatory flow using Navier–Stokes equations. *Coast. Eng.* **2013**, *80*, 16–34. [CrossRef]
80. Losada, I.J.; Maza, M.; Lara, J.L. A new formulation for vegetation-induced damping under combined waves and currents. *Coast. Eng.* **2016**, *107*, 1–13. [CrossRef]
81. Yin, K.; Lin, M.; Xu, S.; Hao, J.; Mao, L.; Li, M. Numerical investigation of submerged flexible vegetation dynamics and wave attenuation under combined waves and following currents. *Ocean Eng.* **2023**, *278*, 114437. [CrossRef]
82. Reis, R.A.; Fortes, C.J.; Rodrigues, J.A.; Hu, Z.; Suzuki, T. Experimental study on drag coefficient of flexible vegetation under non-breaking waves. *Ocean Eng.* **2024**, *296*, 117002. [CrossRef]
83. Berard, N.A.; Mulligan, R.P.; da Silva, A.M.F.; Dibajnia, M. Evaluation of XBeach performance for the erosion of a laboratory sand dune. *Coast. Eng.* **2017**, *125*, 70–80. [CrossRef]
84. van Rijn, L.C.; Walstra, D.J.; Grasmeijer, B.; Sutherland, J.; Pan, S.; Sierra, J. The predictability of cross-shore bed evolution of sandy beaches at the time scale of storms and seasons using process-based profile models. *Coast. Eng.* **2003**, *47*, 295–327. [CrossRef]
85. NOAA. Digital Coast: Data Access Viewer. Available online: https://coast.noaa.gov/dataviewer/#/lidar/search/-9507789.843104137,3495380.7300894624,-9506600.926338501,3496285.0420898707 (accessed on 10 January 2024).
86. Ma, M.; Huang, W.; Jung, S.; Xu, S.; Vijayan, L. Modeling hurricane wave propagation and attenuation after overtopping sand dunes during storm surge. *Ocean Eng.* **2024**, *292*, 116590. [CrossRef]
87. Sierra, J.P.; Gracia, V.; Castell, X.; García-León, M.; Mösso, C.; Lin-Ye, J. Potential of transplanted seagrass meadows on wave attenuation in a fetch-limited environment. *J. Mar. Sci. Eng.* **2023**, *11*, 1186. [CrossRef]
88. Chen, W.; Staneva, J.; Jacob, B.; Sánchez-Artús, X.; Wurpts, A. What-if nature-based storm buffers on mitigating coastal erosion. *Sci. Total Environ.* **2024**, *928*, 172247. [CrossRef] [PubMed]
89. Suzuki, T.; Hu, Z.; Kumada, K.; Phan, L.K.; Zijlema, M. Non-hydrostatic modeling of drag, inertia and porous effects in wave propagation over dense vegetation fields. *Coast. Eng.* **2019**, *149*, 49–64. [CrossRef]
90. Setyawan, W.B. Adaptation strategy to coastal erosion by rural communities: Lessons learned from Ujunggebang village, Indramayu, West Java, Indonesia. *Marit. Technol. Res.* **2022**, *4*, 252846. [CrossRef]

Journal of
Marine Science and Engineering

Article

Spatiotemporal Climatology of Georgia Tropical Cyclones and Associated Rainfall

Reilly Corkran *, Jill Trepanier and Vincent Brown

Department of Geography and Anthropology, Louisiana State University, 227 Howe-Russell Geoscience Complex, Baton Rouge, LA 70803, USA
* Correspondence: rcorkr1@lsu.edu

Abstract: Tropical cyclones (TCs), often characterized by high wind speeds and heavy rainfall, cause widespread devastation, affecting millions of people and leading to economic losses worldwide. TC-specific research in Georgia is scarce, likely due to the minimal geographical extent of its coast and the infrequency of direct landfalls. Research on Georgia TCs does not account for storms that make landfall in other southeastern states (e.g., Florida) and continue north, northeast, or northwest into Georgia. This study used the North Atlantic Basin hurricane database (HURDAT2) to quantify the spatiotemporal patterns of direct and indirect landfalling of Georgia tropical cyclones (>16 ms^{-1}) from 1851 to 2021. TC-induced rainfall was also quantified using rainfall data (nClimGrid-Daily and nClimGrid) from 1951 to 2021 to estimate the proportion of Georgia's total annual and monthly rainfall attributed to TCs. A multi-methodological approach, incorporating statistics and mapping, is employed to assess the trends of Georgia's tropical cyclones and the associated rainfall. The study analyzed 113 TCs and found that, on average, less than one TC annually ($\bar{x}$ = 0.66) traverses the state. September averaged the highest percentage (25%) of TC-induced rainfall, followed by October (14%), and August (13%). This pattern aligns with the TC season, with the highest frequency of TCs occurring in September (n = 35), followed by August (n = 25), and October (n = 18). We found that 10% of tropical storms make landfall on the coastline, while the remaining 91% enter Georgia by making landfall in Florida (92%), Louisiana (7%), or South Carolina (1%) first. A threat of TCs during the peak of the season emphasizes the importance of heightened awareness, increased planning practices, and resource allocation during these periods to protect Georgia's history and natural beauty, and its residents.

Keywords: tropical cyclones; Georgia; precipitation

Citation: Corkran, R.; Trepanier, J.; Brown, V. Spatiotemporal Climatology of Georgia Tropical Cyclones and Associated Rainfall. *J. Mar. Sci. Eng.* **2024**, *12*, 1693. https://doi.org/10.3390/jmse12101693

Academic Editor: Deniz Velioglu Sogut

Received: 30 July 2024
Revised: 11 September 2024
Accepted: 12 September 2024
Published: 24 September 2024

1. Introduction

1.1. Tropical Cyclone Damage in Georgia

The United States coastline stretches 5955 km (3700 miles) along the Gulf of Mexico (GOM) and the Atlantic Seaboard [1]. Within this extensive coastline, the state of Georgia accounts for 160 km (100 miles). Coastal locations throughout the GOM and North Atlantic frequently experience tropical cyclones (TCs), or low-pressure systems with strong rotating winds [2].

Georgia has experienced 107 individual billion-dollar disaster events since 1980, the most of any state in the Southeast U.S. [3]. Twenty-four of these disasters were attributed to TCs [3] experienced by Georgia and the surrounding states. These TCs were the costliest disasters in the region, with an estimated loss of USD 10–20 billion. The most recent TC was Hurricane Idalia in August 2023. Hurricane Idalia is estimated to have resulted in USD 3.5 billion in damages due to strong winds, flooding, heavy rainfall, storm surge, and downed trees [3]. Less than 24 h before landfall, Hurricane Idalia rapidly intensified, leaving residents scrambling to evacuate [4]. Rapid intensification is defined as a one-minute maximum sustained surface wind speed that increases by ≥30 knots over

24 h [5]. Hurricane Idalia was predicted to travel through Savannah, Georgia, but ultimately moved in a more northward direction. Many residents in the northern regions who were not planning on evacuating experienced heavy rainfall, flooding, and intense winds [6]. Valdosta, Georgia, experienced extensive infrastructure damage due to the lack of TC-resistant infrastructure [6].

Hurricane Irma in September 2017 caused USD 54 million in damage from falling trees, debris, strong winds, power outages, extensive flooding, and storm surge [7]. Two fatalities were reported in northern Georgia due to falling trees, with many other reports involving major injuries [7]. Rainfall across the state ranged from 30.48 mm (1.2 in) in northern Georgia to 341.9 mm (13.46 in) in the coastal area around Brunswick. Due to drier-than-normal conditions preceding the storm, the state experienced extensive flooding in multiple regions [7]. Over 900,000 residents lost power across the state, which took days to restore due to the damage around the region [8].

Hurricanes are TCs that exhibit 1-minute sustained winds of $\geq$33 ms^{-1}. Over half ($\sim$60%) of all hurricanes that affect Georgia travel from the south or southeast [9]. In this paper, a Georgia hurricane is defined as a hurricane that enters the state's boundary at hurricane-strength wind intensity, regardless of whether it makes direct landfall. TCs infrequently make direct landfall in Georgia due to the short coastline. Over 161 years, only 14 hurricanes moved directly across Georgia's coastline without previously making landfall somewhere else along the U.S. coastline [10]. More frequently, TCs affect Georgia after making initial landfall in other states, such as Florida. A subset of storms will enter Georgia at hurricane intensity and quickly downgrade into tropical storms. These tropical storms can still cause immense damage for residents, as seen in Hurricanes Idalia, Irma, and Michael, which all became tropical storms shortly after entering Georgia. Indirect TCs entering the state at hurricane intensity through Florida should be considered part of Georgia's historical hurricane occurrences.

1.2. Hurricane Michael in Georgia

Hurricane Michael (2018) was a Category 5 ($\geq$69 ms^{-1}) hurricane on the Saffir–Simpson Wind Scale while in the GOM, and it made landfall just southeast of Panama City, Florida, as a Category 5 storm. The system formed in the Caribbean Sea on 2 October 2018, and by 7 October, it formed into a tropical depression off the coast of Cozumel, Mexico [11]. The system rapidly intensified before traveling off the west coast of Cuba, where maximum sustained winds reached 43.7 ms^{-1} (85 kt; 95 mph) [11]. At landfall, Hurricane Michael exhibited maximum sustained wind speeds of 71.9 ms^{-1} (140 kt; 161 mph) [11]. The event accelerated northeastward into Georgia as a Category 3 hurricane. Michael weakened into a tropical storm as it passed southeast of Macon, Georgia ($\sim$265 km north of the Florida border), and continued through Augusta, Georgia, and into the Carolinas. The remnant low of Michael traveled into the Atlantic, where it dissipated off the northern coast of Portugal on 15 October [11].

Donaldsonville, Georgia, reported a maximum wind gust of 44 ms^{-1} (85 kt; 100 mph). Hurricane Michael produced three tornadoes: Two rated as EF-0 (105–137 km/h) were recorded in Fulton and Crawford County, and one EF-1 (138–177 km/h) tornado occurred in Peach County with minor damages reported [11]. One fatality was reported due to a falling tree during the storm. Southwestern and Central Georgia reported wind damage in the agriculture/forestry sector, with Donaldsonville reporting damage to 99% of the homes and agriculture in the region. Dougherty County, Georgia, reported approximately 3000 residential structures damaged and 49 destroyed. NOAA's National Centers for Environmental Information (NCEI) estimated USD 25 billion in damages from Hurricane Michael in the U.S. in 2018, with USD 4.7 billion occurring in Georgia from property, agricultural, and forestry losses [11].

As seen with Hurricane Michael, Irma, and Idalia, heavy rainfall is a common hazard associated with TCs. Intense, sustained rainfall can overwhelm rivers, streams, and drainage systems, leading to flash floods and the inundation of communities [12].

Rainfall and associated flood waters can lead to the failure of infrastructure, such as buildings, bridges, and roads [13–15] and/or cause erosion to undermine foundations and structures [14]. TC rainfall can destroy crops by causing flooding or providing excessive moisture for certain plants [16]. Soil erosion and agricultural schedules are important to obtain a yield with certain crops, and changes to these can affect the food supply chain [16].

The aftermath of TCs often results in prolonged and unexpected impacts that extend far beyond the immediate damage. For instance, Hurricane Michael's passage through Georgia led to the downing of a vast number of trees that altered the landscape [17]. The accumulated fallen timber, which eventually dried, became fuel for a severe wildfire season the following year. The 2017 wildfire season included the devastating West Mims Fire, ignited by a lightning strike in the Okefenokee National Wildlife Refuge [18]. This fire caused mandatory evacuations in southern Georgia due to its severity [18]. Spanning approximately 140,000 acres, the fire affected not just Georgia but also reached Florida [18]. It threatened residents, firefighters, homes, Georgia's landscape, and other species. The initial devastation caused by a TC is often the beginning, with subsequent effects impacting ecosystems and communities.

These examples illustrate that a hurricane does not need to make direct landfall on the coast of Georgia to inflict considerable damage throughout the state. Research must encompass the effects of TCs on entire states, not just on specific regions. Georgia is included in many southeastern regional studies on TCs that focus on states that experience more direct landfalls. While regional-scale research is valuable, a statewide approach is equally important.

1.3. Research Problem and Purpose

Few studies specifically focus on TCs in Georgia at a state level, likely due to the coast's minimal geographical extent and the relative infrequency of direct landfalls. This dearth of research affects the public's understanding of TCs in Georgia, which leaves residents without necessary planning information. TC research in the state focuses specifically on coastal Georgia [10,19,20]. Concentrating on a specific region deprives the remainder of the state of essential information needed to prepare for a severe event.

A comprehensive evaluation of the spatiotemporal characteristics of Georgia's TCs is imperative to accurately assess and prepare for potential TCs in specific sub-regions in the state. The analytical approach enables the state to identify and prioritize regions requiring targeted assistance, resources, or disaster recovery initiatives before, during, and after the hurricane season [3]. Regions historically prone to TCs often equip their infrastructure to withstand the multifaceted impacts of such storms, including storm surges, high-velocity wind gusts, and intense rainfall [21]. However, the current lack of TC-related research within Georgia presents a substantial challenge. Without detailed knowledge of areas susceptible to TCs, there is a heightened risk of existing infrastructure that may not adequately fortify against the destructive nature of these extreme weather events [22]. While Georgia may not frequently experience TCs, closely monitoring and preparing for TCs remains critical [10]. Though less intense than hurricanes, tropical storms can still inflict considerable damage due to their potential association with heavy rainfall and strong winds [23]. Consequently, a thorough understanding of these weather events is essential for effective state-level planning and response strategies [19]. Additionally, the characteristics of TCs may change in the future [24], and it is imperative to inform communities of their historical risk and how that may change.

This research focuses on Georgia's spatiotemporal characteristics (e.g., frequency, intensity, and location) of direct and indirect TCs exceeding 16 ms^{-1}. There is an additional emphasis on TC rainfall, showing the proportion of annual and monthly rainfall from TCs. Descriptive statistics are used to provide the spatiotemporal characteristics of Georgia TCs, including seasonality, intensity, frequency, and distribution. The research used ArcGIS Pro to aggregate monthly and annual precipitation and calculate the amount of TC rainfall in the state.

2. Materials and Methods

2.1. HURDAT2

TC data from the North Atlantic Basin hurricane database (HURDAT2) consist of data on TCs occurring in the North Atlantic Basin since 1851 [25]. HURDAT2 includes location and wind speed information at six-hourly increments for each known track in the basin. Beginning in 1961, synoptic observations at landfall were added outside the six-hour increments. Elsner and Jagger [2] provided an interpolation method that produces hourly values along the known track using the six-hourly and synoptic data. The hourly interpolated data are generated through spline interpolation [2]. This method ensures the retention of values at the designated six-hour intervals, employing a piecewise polynomial to obtain the values between the six-hour increments [2]. The geographic positions of the TCs are interpolated by using spherical geometry on the splines [2]. The data subset encompasses a comprehensive time frame from 1851 to 2021. Despite the acknowledged constraints inherent in earlier records, including the extensive historical data is vital. This approach facilitates a thorough examination of potential trends in TCs in Georgia.

HURDAT2 has limited reporting before the pre-flight (before 1944) and pre-satellite (before 1966) era [25]. This results in underestimations of storm frequency due to earlier data relying on human observations, leading to higher rates of classification or missed storms due to the lack of human presence at sea during storm occurrences [25]. TC intensities may be under-analyzed or categorized as lower than the actual event [25]. This study focuses on TCs that have crossed the Georgia border, so many concerns over the earlier records (e.g., missed open ocean storms) are less relevant here. Confidence in the estimations increases when a storm has made landfall, as land observations become more straightforward compared to open ocean observations [25].

This study only focused on TCs with sustained 1-minute wind speeds exceeding 16 ms^{-1} within Georgia. The data were a subset to exclude storms that occurred only as extratropical cyclones, subtropical depressions, subtropical storms, tropical waves, or disturbances. Due to this, TC rainfall in this study is underrepresented. In the context of this study, the term 'indirect' is used to describe TCs that did not make landfall on Georgia's coastline but entered through another location. In contrast, the term 'direct' defines storms that made landfall on Georgia's coastline. We used the R Program for Statistical Computing for statistics and graphics [26]. ArcGIS Pro was used for data analysis and data mapping [27].

2.2. nClimGrid-Daily

Daily precipitation data for this study were attained from the NCEI's nClimGrid-Daily, which consists of daily high-resolution of 0.04178° (nominally 5 km) precipitation, among other variables, from 1951 to near present [28]. The dataset includes information from the cooperative Observer Program (COOP), the Automated Surface Observing System (ASOS), and the Remote Automatic Weather Stations (RAWSs) [28]. RAWSs are only used for temperature and are, thus, not used here. The thin-plate smoothing splines method was used for a wide range of topographical and climatic features and still shows the complexity of the terrain and coastal proximity [28]. This approach collectively minimizes the likelihood of interpolation errors, making it suitable for daily temperature and precipitation at various spatial scales [29,30].

One limitation of the nClimGrid-Daily is the variation in daily observation times of stations incorporated into grid estimation. Such variations can lead to discrepancies in recorded precipitation values [31]. To minimize this impact, the dataset included daily measurements taken at midnight, 0500, 0600, 0700, 0800, and 0900 local time. These times were chosen because they are the most common for reporting [28]. Morning observations were combined with midnight observations from the previous day to align the data further. This method enhances the consistency between the two 24 h observation periods ending at these times [28].

The varying observation time of nClimGrid-Daily creates a challenge when identifying the exact dates when the TCs caused precipitation in Georgia. TCs enter Georgia at varying hours throughout any given day. To align with the nClimGrid-Daily rainfall observation times, this study reevaluated the days when TCs entered the state. If a TC entered Georgia at or after 1000 EST, rainfall data from the next day were used. If the TC entered Georgia before 1000 EST, the reported HURDAT2 date was used. This was to account for rainfall that may have been combined with the previous day's data due to most reports coming in between 0000 and 0900.

2.3. Analytical Approach

Descriptive statistics summarize the entire database of TCs in Georgia, revealing the main characteristics. This includes determining average frequency, analyzing monthly occurrences, and identifying the weakest and strongest wind intensities recorded in the state. This study used descriptive statistics to calculate the average intensity of TCs and assess the years with the highest and lowest TC activity. This method illustrates the range and patterns of TCs in Georgia, laying a foundation for future assessments of the potential impacts on the region.

This study used a 500 km buffer (250 km buffer on each side of the track's center point) around the interpolated HURDAT2 tracks to isolate the TC rainfall from any influences from other meteorological systems [32]. Any buffers intersecting with the Georgia state border were used in the rainfall portion of this study [33].

From 1951 to 2021, the total rainfall that occurred on the days of each TC was aggregated annually. The start date for each storm was the first day that the storm buffer intersected Georgia, and the end date was the last day of the intersection. Statistical summaries for months and years are provided. Some storms have rainfall spanning over two months. For example, Hurricane Ernesto in 2006 entered Georgia on 31 August and departed the state on 1 September. Both days were included for aggregation, and each monthly summary was considered separately.

The rainfall data were clipped to the Georgia state boundary. The rainfall from each TC was then summed to find the total rainfall in Georgia from these events. The TC rainfall was next divided by the annual rainfall from 1951 to 2021. The daily rainfall grids were used to calculate each TC's rainfall and then compared to the annual rainfall grids (e.g., from all sources of precipitation). The annual grids were calculated by summing the monthly gridded rainfall. The monthly gridded rainfall data were extracted from the sister dataset—nClimGrid-Daily. The nClimGrid-Daily dataset was standardized with nClimGrid-Monthly to ensure consistency across various products and applications [28].

The procedure applies to both annual and monthly rainfall averages. First, the annual TC gridded rainfall total was determined by summing the precipitation from each TC and clipping it to Georgia's state boundary. To determine TCs' contribution to the state's precipitation, the sum was divided by the total rainfall from 1951 to 2021. Precipitation data were averaged by month. TCs affecting Georgia across two months were divided to ensure accurate attribution to the correct month. For accurate monthly rainfall estimates, the total precipitation and TCs affecting Georgia were both divided by 71 years to account for months with no precipitation in the dataset. Finally, TC monthly averages were divided by the total monthly rainfall.

3. Results

3.1. Descriptive Statistics

This study analyzed 113 tropical storms and hurricanes occurring within the boundary of Georgia from 1851 to 2021 (Table 1). The classification of storm type was based on the intensity of the TCs when the storm entered the state's boundaries either on the coast or through another state, reflecting the varied intensities experienced throughout the state.

Table 1. Tropical cyclones in Georgia from 1851 to 2021 separated by landfall intensity and direct/indirect landfall. Percentage of total TCs relates to Georgia's total.

Event Type	Total Count	Hurricanes	Tropical Storms	Percentages of Total TCs
Direct Landfall	10	4	9	9%
Indirect Landfall	103	19	83	91%
Total Impact	113	24	89	100%

Figure 1 depicts the 10 direct landfalling TCs in Georgia categorized by storm type. Figure 1b shows the 103 indirect landfalling TCs in Georgia categorized by storm type. These indirect TCs form within the Atlantic Basin, Caribbean Sea, and Gulf of Mexico, and the tracks make initial landfall in Florida (92%), Louisiana (7%), or South Carolina (1%).

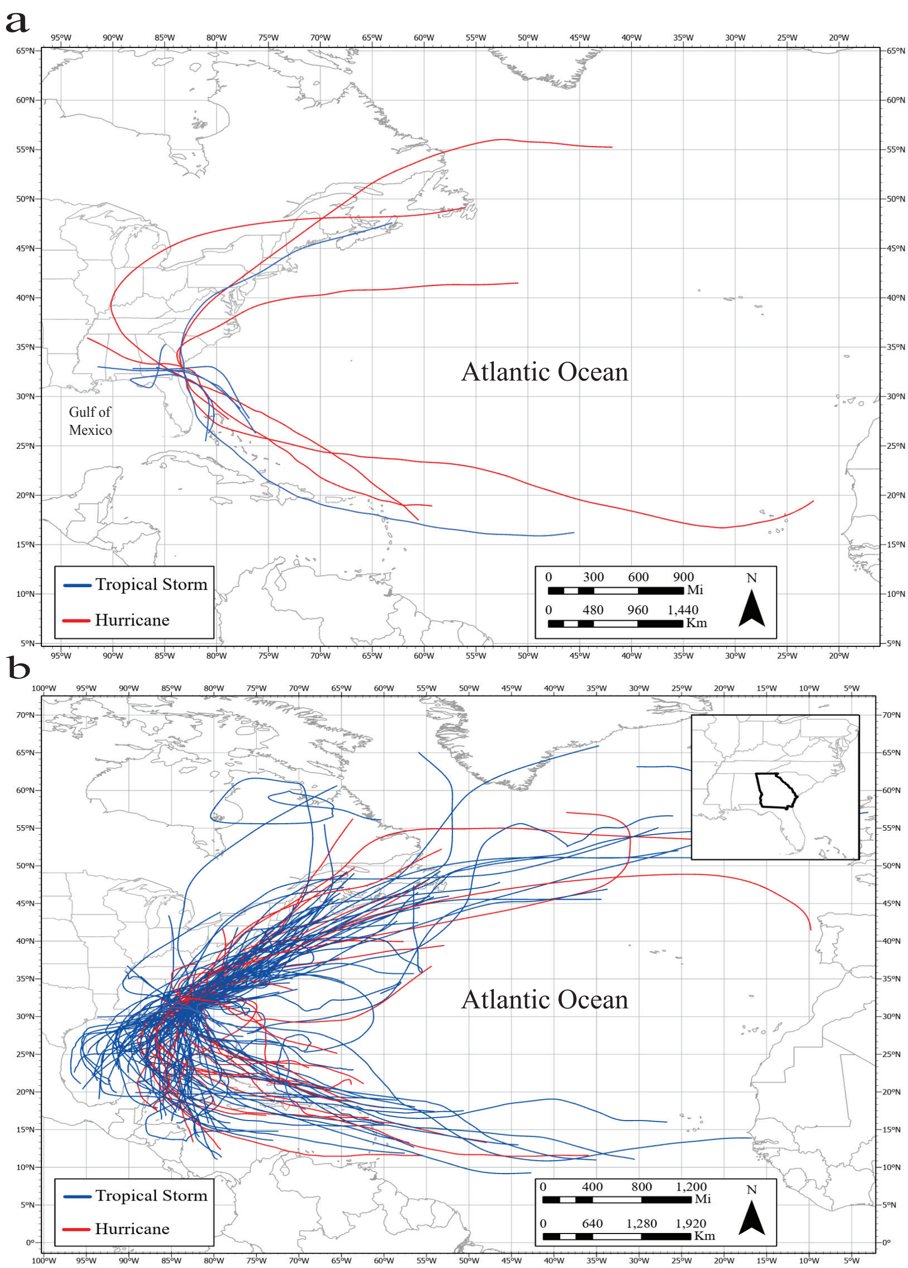

Figure 1. (**a**) Track map of direct landfalling tropical cyclones on the coastline of Georgia from 1851 to 2021; (**b**) track map of indirect landfalling tropical cyclones in the state of Georgia from 1851 to 2021.

Figures 2 and 3 are heat maps highlighting the specific locations where TCs have entered and exited the state. The first entrance of each TC track into the state is considered. One track from an unnamed TC in 1947 entered the state multiple times due to the track's curvature but only the initial entrance is considered. Two TCs only had one track segment enter the state before leaving the state. These two storms (Unnamed 1874 and Eta 2020) are included in both the entrance and exit maps. Each TC's point of entry or exit is marked with a black dot. Each point has a buffer with a 40.3 km (25 mi) radius to determine the overlap among points, indicating areas where multiple buffers intersect. On the maps, red areas indicate regions with the highest density of entry points, while green represents the areas with little TC activity within a 40.3 km radius. Regions without color signify the sparsest areas, where TCs have not directly entered or exited. However, this does not imply that these areas have been completely unaffected by TCs. The densest entry area is along the southern border, where most tracks made landfall in Florida from the GOM and then continued into Georgia, followed by the sparsest area along the western border.

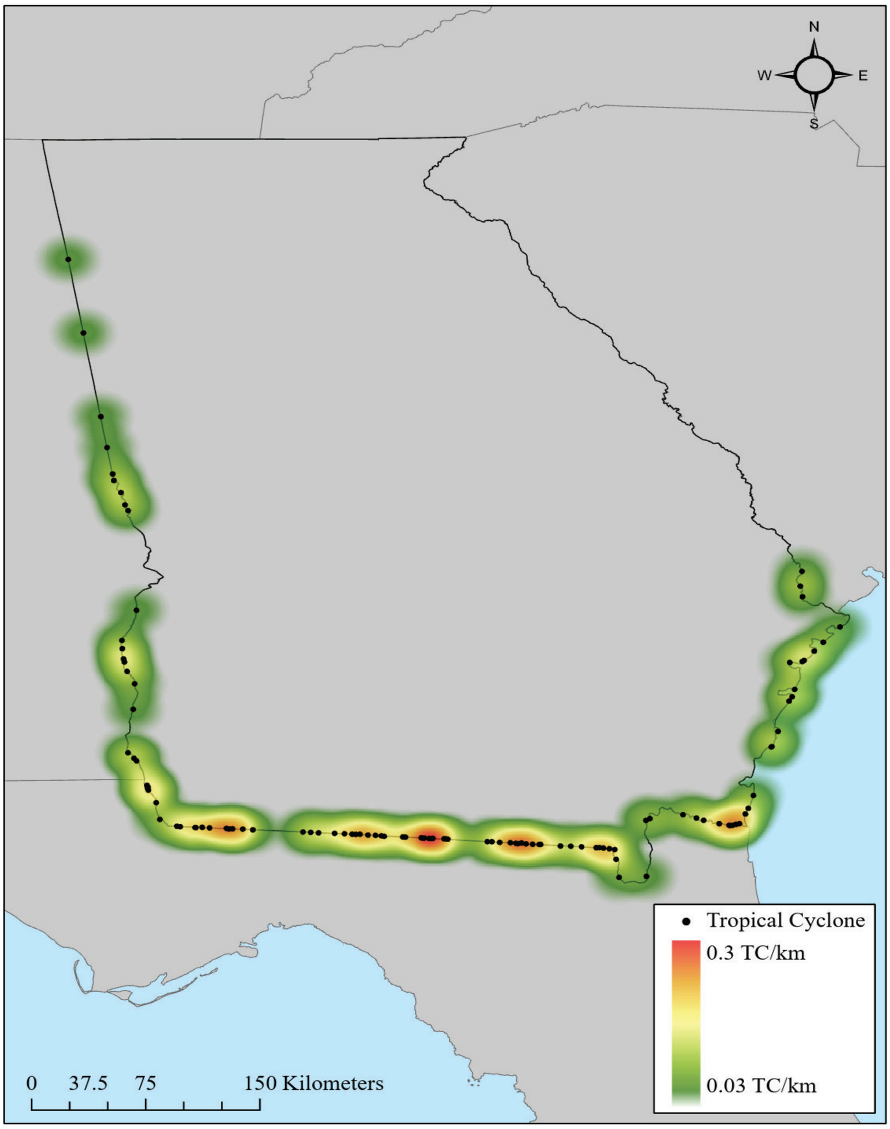

Figure 2. Heat map of first tropical cyclone entry points into Georgia, 1851–2021.

Figure 3 is a heat map for the exit points of TCs in Georgia from 1851 to 2021. There are nine TCs not considered in this map as they became tropical depressions $\leq 16\ \mathrm{ms}^{-1}$ within the state's borders. These storms were all unnamed systems (1871, 1873, 1875, 1887, 1916, 1917, 1933, and 1966) except for Florence in 1953. Most storms exited on the eastern edge of the state, with the densest area along the southeastern border. This is because most TCs entered from the south and traveled eastward; however, some TCs continued north into Tennessee or North Carolina. TCs that made direct landfall on the coastal area tended to move westward exiting along the state's western border.

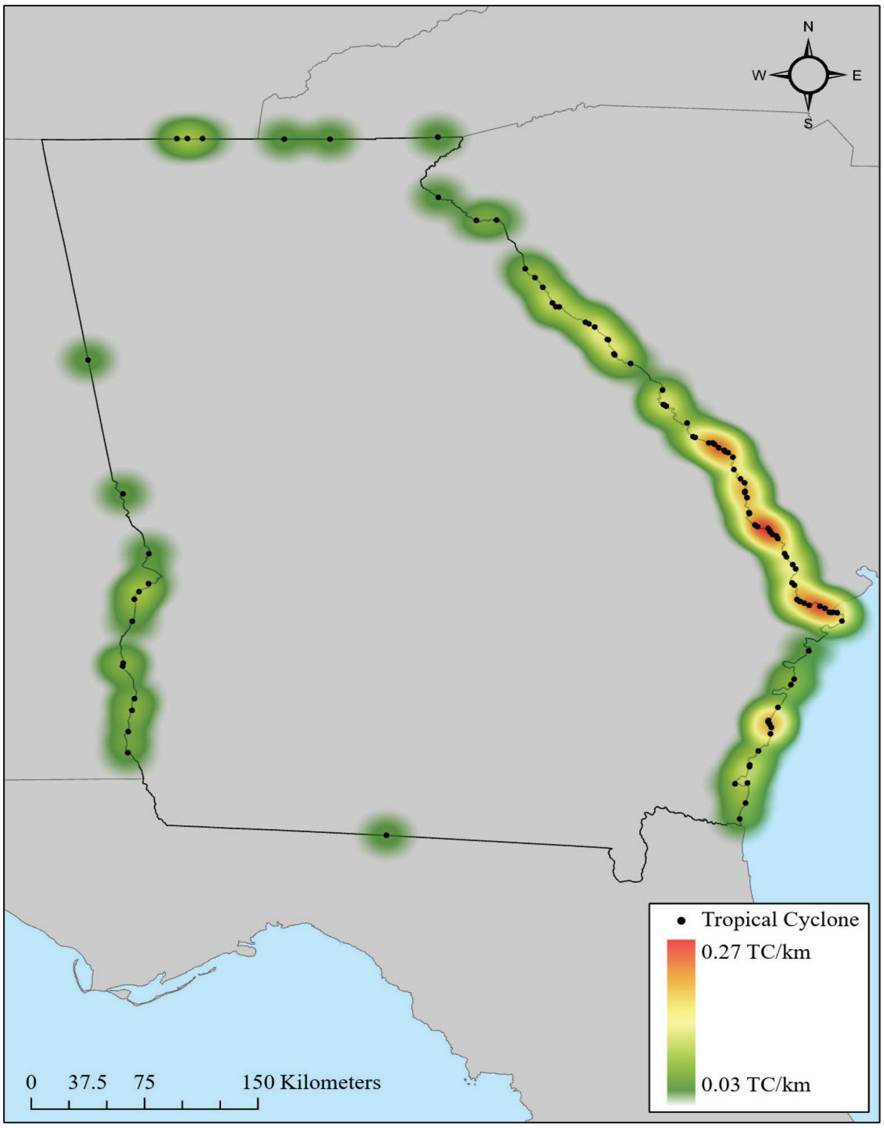

Figure 3. Heat map of tropical cyclone exit points along the Georgia border, 1851–2021.

Table 2 shows the distribution of annual Georgia TC counts categorized by the Saffir–Simpson Hurricane Wind Scale (NOAA 2020). Category 4 and Category 5 hurricanes have not occurred in the state's known history. Hurricane Michael in 2018 and the Unnamed 1898 hurricane both maintained Category 3 hurricane status as the tracks entered Georgia but decayed as the storms traveled further inland. The Unnamed 1898 hurricane made landfall on 2 October from the Atlantic Ocean on the southern coastline of Georgia with an estimated wind speed of 57 ms^{-1}. The Unnamed 1898 hurricane decayed and downgraded into a tropical storm around 201.1 km (125 mi) in Georgia. Hurricane Michael entered the southwestern corner of Georgia from the GOM with a wind speed of 53 ms^{-1}. Hurricane Michael decayed and downgraded into a tropical storm around 144.8 km (90 mi) from the state's border.

Table 2. Category distribution of tropical cyclones in Georgia, 1851–2021.

Tropical Cyclone (16–32 ms^{-1})	Category 1 (33–42 ms^{-1})	Category 2 (43–49 ms^{-1})	Category 3 (50–58 ms^{-1})	Category 4 (59–70 ms^{-1})	Category 5 ($\geq$70 ms^{-1})
89	15	7	2	0	0

Figure 4 illustrates the time series of annual Georgia TCs over the 171-year period. When considering all TCs, the average rate is 0.66 TC/yr, with a σ^2 of 0.65. When considering only tropical storms, the rates are 0.52 TS/yr (σ^2 = 0.56) and hurricanes and 0.14 hur/yr (σ^2 = 0.145). Most of the hurricanes (27%, n = 21) occurred in the first one hundred years of the dataset. Only three hurricanes occurred after 1950.

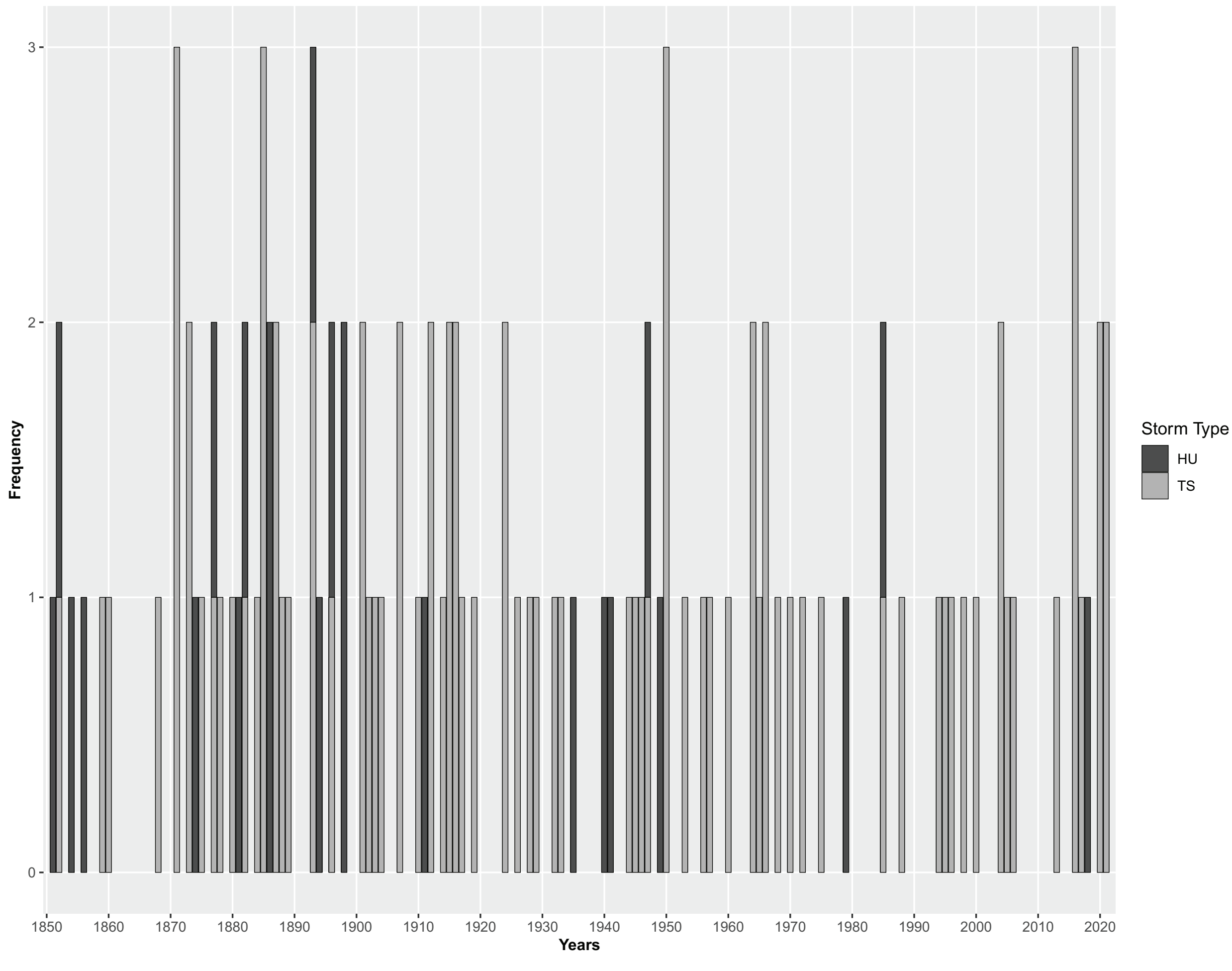

Figure 4. Georgia's annual tropical cyclone occurrence (1851–2021) categorized by intensity.

3.2. Tropical Cyclone Seasonality

TC seasonality in Georgia is shown in Figure 5. The most active months of the hurricane season were August, September, and October [34]. September was the most active month for TCs in Georgia (n = 40; 35%), followed by October (n = 27; 24%). August was the most active hurricane month (n = 8; 7%). May had two recorded tropical storms outside of the official hurricane season. This is not uncommon, and further analysis of the storms is included below. June experienced a high number of TCs (n = 15; 13%).

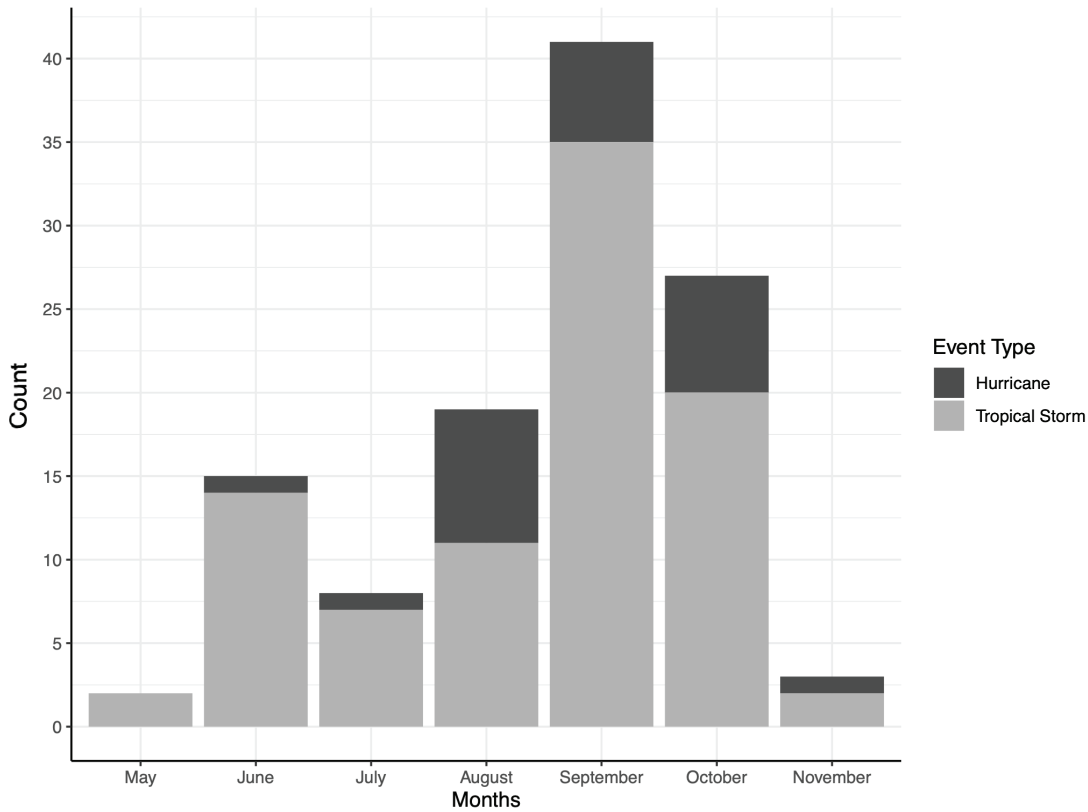

Figure 5. The seasonality of tropical cyclones within the Georgia state boundary separated by intensity.

3.3. Wind Intensity

Figure 6 illustrates the maximum wind speeds (ms^{-1}) of TCs in Georgia. Most TCs decayed upon entering the state's boundaries. However, five TCs increased wind speed as they moved further into the state. Two TCs reached their peak wind speeds approximately 50 miles north of the southern border of Georgia, with the intensity of a tropical storm and tropical depression. Another two storms originating from the GOM passed through Florida and into Georgia, achieving their maximum wind speeds as tropical storms at the Georgia–South Carolina border. These storms traveled nearly 225 km (140 mi) northeast from their entry point into Georgia while increasing in intensity. Additionally, Hurricane Dora (1964) made landfall in Florida from the Atlantic, moved west, and then turned northeast through western Georgia, covering about 410 km (260 mi) of the state before its highest wind speed was recorded as it crossed into South Carolina. The maximum wind speed was 54.6 ms^{-1} by an unnamed Category 3 hurricane in 1898. The mean wind speed was 27.2 ms^{-1} with a σ^2 of 75.8.

3.4. Annual Average Rainfall

The study analyzed 119 storms occurring between 1951 and 2021 based on the available rainfall data. Figure 7 shows the TC tracks when rainfall data were available. A 500 km buffer was added around each track to determine the area where rainfall might have occurred from the TC. When the buffer intersected Georgia, the TC and associated rainfall were included. TCs were, again, categorized into tropical storms and hurricanes based on the highest maximum sustained wind recorded within the buffer area. There were 42 (35%) hurricanes and 77 (65%) tropical storms. Across the 119 TCs, there were 295 days of observed precipitation within the state's border, equivalent to roughly 1% of all days during the period of study (1951–2021).

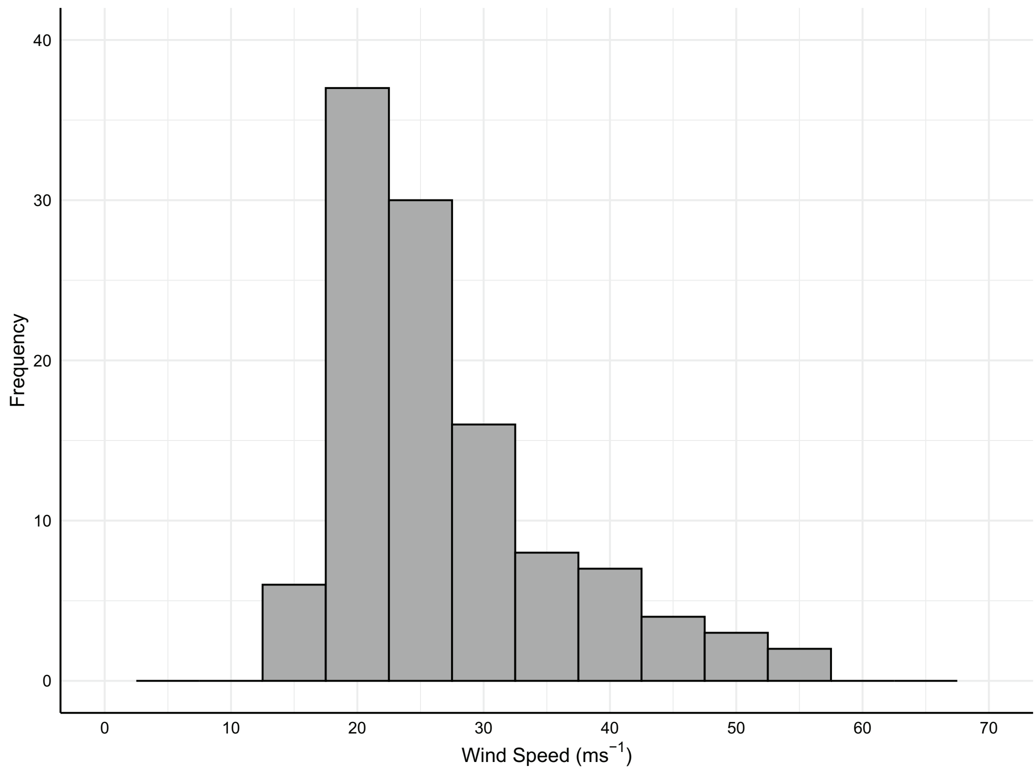

Figure 6. Distribution of tropical cyclone maximum intensity within the state of Georgia from 1851 to 2021.

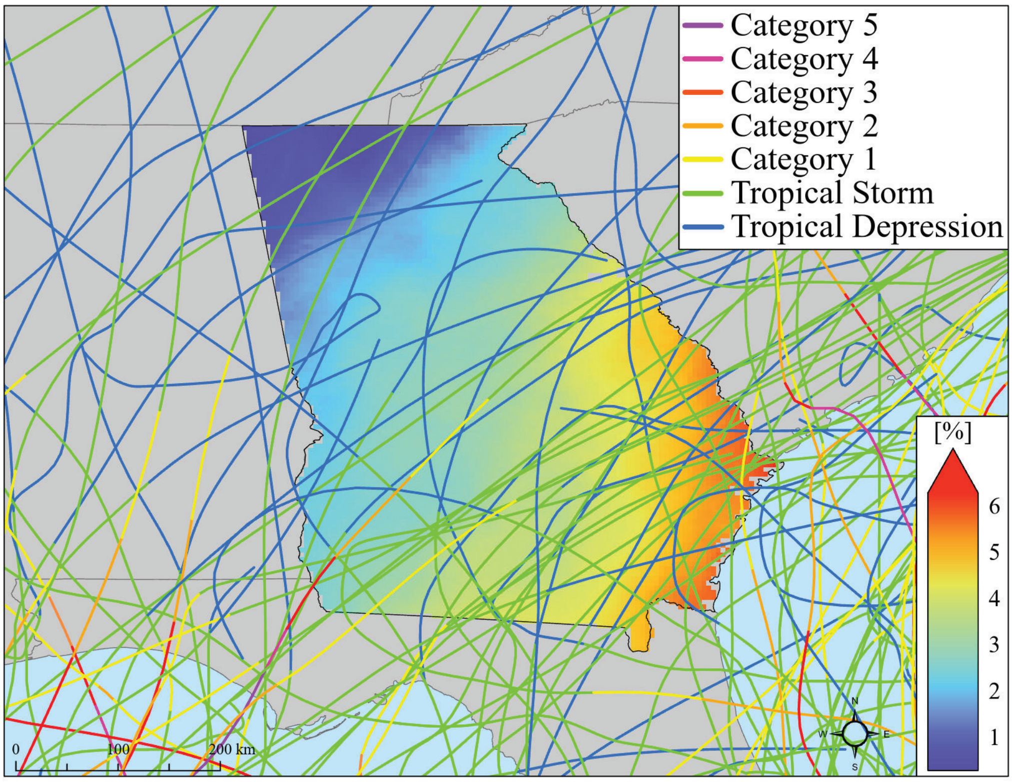

Figure 7. Tropical cyclone tracks used to find the annual TC precipitation in Georgia from 1951 to 2021.

Georgia is divided into five distinct regions, including the Appalachian Plateau, the Ridge and Valley region, the Blue Ridge Mountains, the Piedmont region, and the Coastal Plain (Figure 8). The Coastal Plain can be divided into the upper and lower regions. When discussing the rainfall in this study, the regions will be referenced to provide spatial context regarding where rainfall occurs within the state.

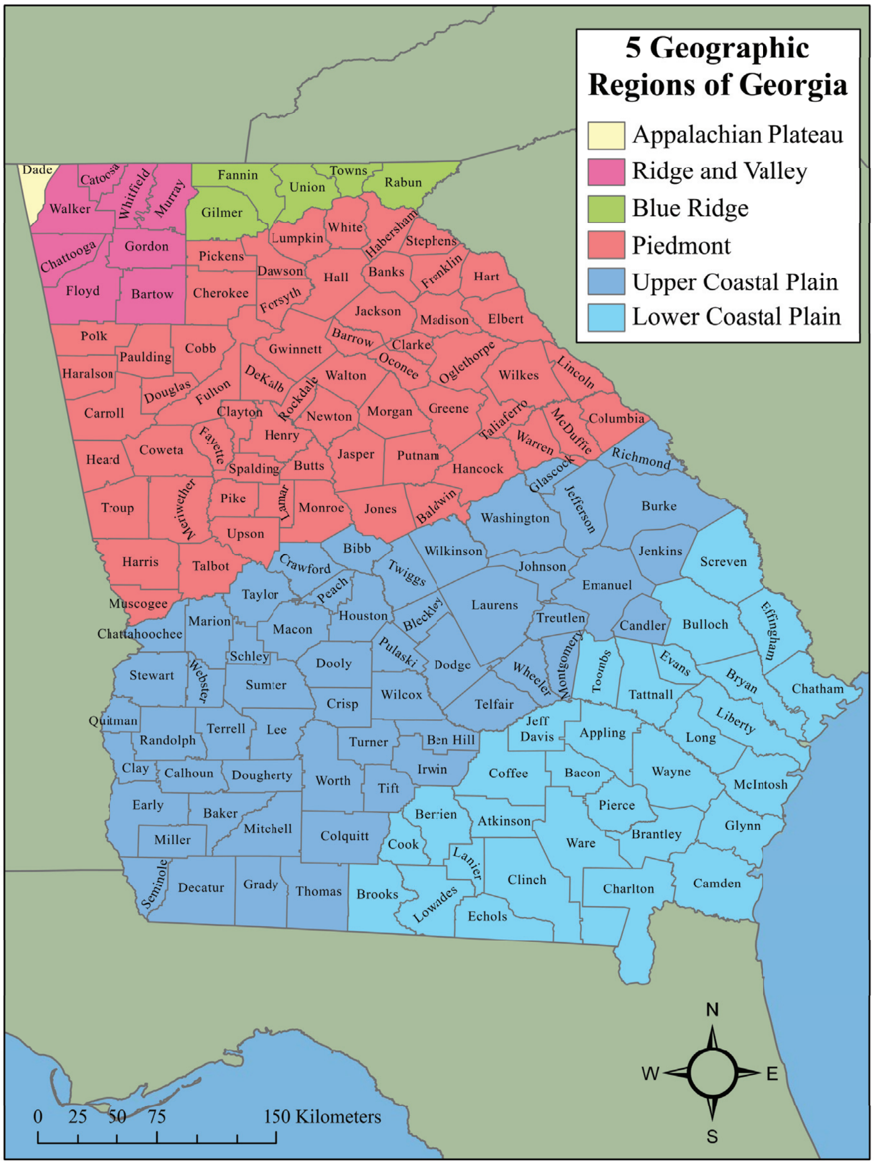

Figure 8. The five geographic regions of Georgia with county delineation and the Coastal Plain divided into the upper and lower regions.

Figure 9 shows the rainfall attributed to TCs across the state by percent of total Georgia annual rainfall. Along the coastline, approximately 5–6% of annual rainfall is attributed to TCs. This value gradually diminishes moving toward the northwest. The Piedmont and Upper Coastal Plain regions receive an average of 2–4% of annual rainfall from TCs. The northwestern portion of the state receives $\leq$ 1% annual rainfall from TCs.

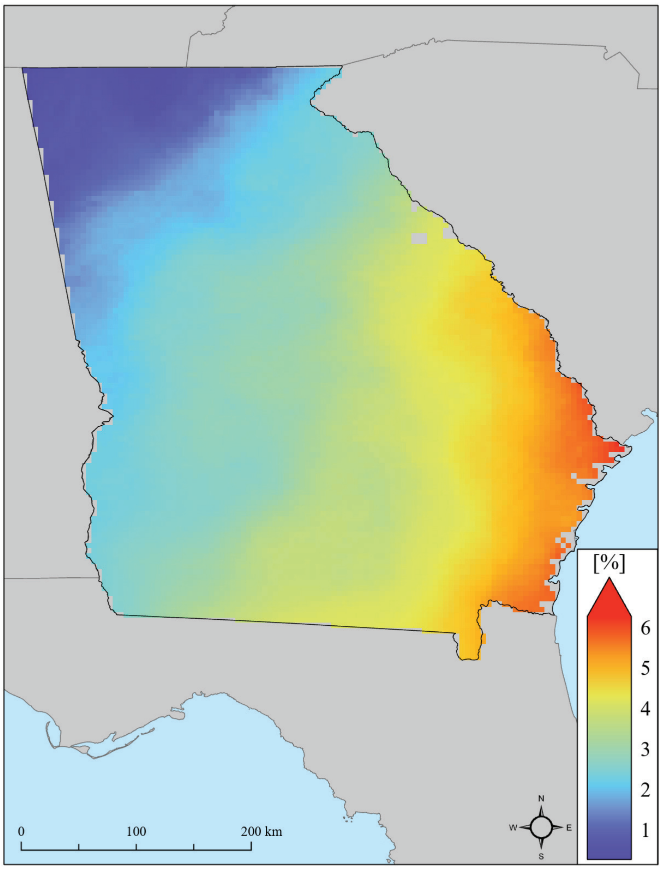

Figure 9. Annual TC precipitation percentage in Georgia from 1951 to 2021.

3.5. Monthly Tropical Cyclone Precipitation and Tracks

Understanding the distribution of TC rainfall across months of the TC season and the proportion of annual rainfall is important for planning purposes. May is not considered a part of the North Atlantic TC season, but of the 119 TCs in this portion of the study, 7 TCs occurred in May (Figure 10a). Five of these pre-season May TCs (all tropical storm strength) have occurred since 2012. May has a high precipitation concentration from TCs in the Lower Coastal Plain, 3–5% (Figure 11a). The rest of the state has an average of 0–2% annual precipitation from TCs.

In total, 19 TCs have occurred in June since 1951 (Figure 10b). Of these, 3 were hurricanes, and 16 were tropical storms. Most of the June tracks form in the GOM. The western Caribbean is known for retaining its warmth well into the later part of the hurricane season. However, Figure 10b suggests that this region starts to warm up earlier in the season than previously thought, potentially indicating a longer period of elevated temperatures [35]. Most of the TCs travel into Georgia from the GOM, traveling northeast into the Atlantic.

In June, the highest precipitation concentration is along the southeastern border with 4% of its annual precipitation from TCs (Figure 11b). The Lower Coastal Plain receives 3% of average annual precipitation from TCs. The Upper Coastal Plain and Piedmont region receive 2%, with the remainder of the state receiving 0–2%.

July observed 13 TCs with 5 hurricanes and 8 tropical storms, as shown in Figure 10c. Three TCs formed in the Southern Atlantic, six in the GOM, and four east of Georgia's border in the Atlantic.

July has a high precipitation concentration from TCs in the western Piedmont region, around 4% (Figure 11c). This is surprising as most of the tracks travel near the state's southeastern region (Figure 10c). This could be because the tracks closest to this region did not produce much rainfall. The southeast and northern regions receive an average of 0–4% of their annual rainfall from TCs.

Figure 10d depicts the tracks that occurred in August. Three tracks in Figure 10d are also shown in September's (Figure 10e) track map because the storms spanned the two months. There were 25 TCs that occurred in August, with 6 hurricanes and 19 tropical storms. Twenty of the August TCs formed in the Atlantic, with seven forming near the coast of Florida and/or South Carolina.

August has a high concentration of TC rainfall along the eastern border of Georgia (Figure 11d). This is likely due to the number of storms traveling through Georgia and South Carolina. The southwestern portion of the state has a range of 2–3% on average TC precipitation per year. The northeastern region has the highest annual average concentration of rainfall, with an average range of 4–5%.

There were 35 TCs in September (Figure 10e). September experienced the highest number of hurricanes, with a total of 19. In addition, there were 16 tropical storms in September. There is one TC that is also represented in October's (Figure 10f) track map because it spanned the two months. Most of the storms formed in the Atlantic, with only six TCs forming in the GOM.

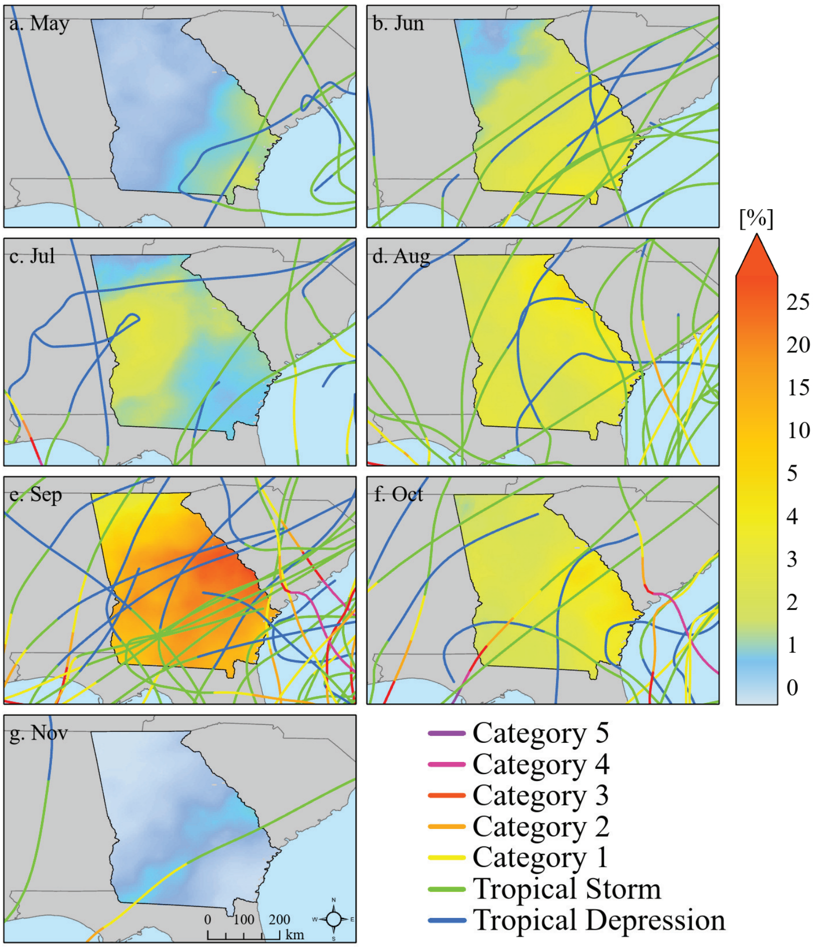

Figure 10. TC Tracks that occurred from May to November in Georgia from 1951 to 2021; monthly average rainfall data attributed to tropical cyclones from May to November.

Figure 11e shows that September had the highest average rainfall compared to all other months. The highest concentration of precipitation is attributed to TCs along the eastern border moving inland within the Coastal Plain and Piedmont regions. This could be due to the high-traffic area of TCs that traveled specifically in that area (Figure 10e). Most of the state receives an average of at least 3% of its annual rainfall from TCs in September. The only exception is along the eastern border, which receives 20–25%, and this is the highest concentration of rainfall averages for this region compared to the other months.

Figure 10f shows that October had 18 TCs with 8 hurricanes and 10 tropical storms. One TC formed in the middle of the Atlantic Ocean while the rest formed in the GOM, Caribbean Sea, or the southern portion of the Atlantic Ocean. Figure 11f shows that the highest concentration of 10% of rainfall in October occurs along the eastern border within the eastern border of the Coastal Plain. The rest of the state sees varying concentrations of around 1–4% of its rainfall from TCs.

Figure 10g shows that November only had two TCs with one hurricane and one tropical storm. Hurricane Kate (1985) traveled through Georgia from the GOM, and it formed in the Atlantic Ocean. Tropical storm Juan (1985) formed in the GOM and traveled within the buffer, so it never moved over any part of Georgia. The majority of the rainfall this month is attributed to Hurricane Kate.

Figure 11g shows that the highest concentration of precipitation was due to Hurricane Kate. The rainfall was highest as the hurricane entered the southwest region and exited along the middle of the eastern border. This precipitation was mainly concentrated in the Upper Coastal Plain. The southern coastline and the northern portion of the state received no rainfall from TCs during this month.

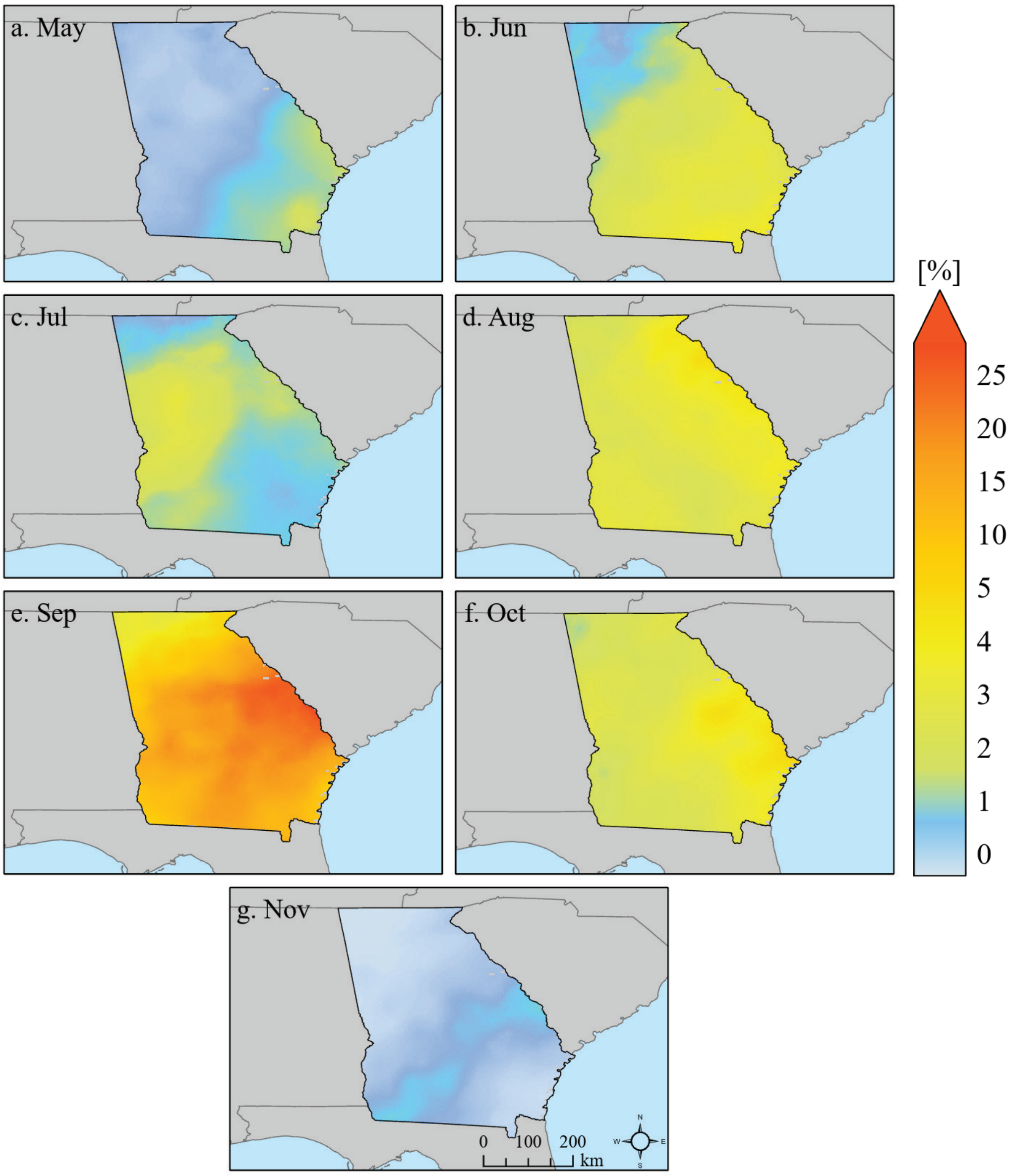

Figure 11. Average TC precipitation percentage for May–November in Georgia from 1951 to 2021.

4. Discussion

This research focused on the spatial characteristics of tropical cyclone (TC) frequency, intensity, and rainfall in Georgia, USA. The study found that 113 TCs entered the state of Georgia from 1851 to 2021. Previously, the authors of [10] found 14 hurricanes that made direct landfall on Georgia's coast from 1851 to 2014. Of the 113 TCs in this study, 24 were categorized as hurricanes, and 89 were categorized as tropical storms as they entered the state's borders. Consistent with the established patterns of activity, Georgia's TC season was most active during the months of August, September, and October [34]. September had the highest TC frequency (n = 40; 35%), October had the second highest TC frequency (n = 27; 23%), and August had the highest frequency of hurricanes (n = 8; 7%). A surprising early batch of May (n = 2; 2%) and June TCs (n = 15; 13%) was seen within the data. The early occurrence of TCs in June and May may be attributed to the position of the Bermuda High, which increases the likelihood of landfall in the Gulf of Mexico earlier in the TC season [36]. The maximum wind speed observed was 54.6 ms^{-1} by an unnamed hurricane in 1898. The minimum wind speed observed was 16.3 ms^{-1} by an unnamed storm in 1904. The mean wind speed for indirect and direct landfalls in GA observed across the dataset was 27.2 ms^{-1}. A study found that Georgia's coastline experiences TCs with an average of lower wind speeds compared to the coastline of South Carolina [37].

Another study revealed that all category hurricanes in Georgia have decreased over time [10]. Many studies primarily concentrate on the assessment of lifetime maximum intensity over the open ocean, rather than the intensity when a TC reaches land and moves inland, which complicates making direct comparisons [37]. Bettinger et al. (2009) and others found that TCs making landfall on the Gulf of Mexico coast decrease in intensity more quickly than similar storms making landfall on Georgia's coastline [37]. These findings challenge prevailing assumptions about the impact of changing climate conditions on hurricane behavior in the North Atlantic Basin. In the Georgia TC dataset, most hurricanes (87%) occurred in the first 100 years of the data. This is likely causing the decreasing trend in intensity. Another probable factor contributing to the decrease in TC intensity is the transformation of Georgia's landscape. The region's transformation has been shaped by a confluence of factors, including natural processes, natural disasters, demographic changes, and economic developments. Georgia has continually increased in urbanization, which can disrupt the essential conditions required for a TC to maintain or increase in intensity. Severe storms still existed in the later years, including Hurricane Michael in 2018. Further statistical analysis should be conducted to focus on the modern (flight/satellite era to the present) tropical cyclones in Georgia [25]. This will assist in seeing what the trends and characteristics of modern TCs are. Georgia TCs occur most often in September, which aligns with the most active month for TCs throughout the basin [34]. This has implications for disaster preparedness and resource allocation, emphasizing the importance of heightened vigilance and readiness during September. On average, Georgia experiences 0.66 TCs (0.52 tropical storms and 0.14 hurricanes) per year. While it is not expected to be an annual occurrence, the threat of TCs remains within Georgia and is heightened in the middle of the season.

TC-induced rainfall was observed at high percentages across the Coastal Plain and the Piedmont region when compared to annual rainfall totals. Other studies have conducted similar TC rainfall research on the east coast [32,38,39]. The differences between this study and the previous studies include the time span, study area, and rainfall dataset. The studies found similar results for Georgia while having a lower resolution [32,38,39]. Similar to this study, there is little variability in the Appalachian Plateau and the Ridge and Valley regions of Georgia. This study had a higher resolution and found that 1–5% of TC-induced rainfall occurred on average along the coastline. The 3% or lower TC-induced rainfall was seen in the northwestern portion of the state. Figures 9 and 11, showing the Piedmont region, as well as Upper, and Lower Coastal Plains, indicate more variability in the amount of rainfall compared to Nogeuria and Keim's study [32,38,39].

May and November had the lowest TC-induced rainfall amounts, with 3% and 1%, respectively. Only two TCs were recorded in November. The most TC-induced rainfall occurred in September and October, with 25% and 14%, respectively.

The impact of TCs on regions in Georgia can vary based on whether the landfall was direct or indirect. Nonetheless, both scenarios entail considerable risks of flash floods and intense winds. This study also acknowledges indirect TC-related impacts not previously or extensively mentioned, such as tornadoes and wildfires. Furthermore, a severe hurricane is not limited by whether a TC makes direct or indirect landfall in a region.

5. Conclusions

The spatial and temporal patterns of TC-induced rainfall further emphasize the varied impacts these storms have across different regions of Georgia. The coastline and the Piedmont regions experienced a higher percentage of TC-induced precipitation. This variability in impact allows for an approach to disaster preparedness and response that is tailored to the specific vulnerabilities of each region.

Rainfall during September occurs across the entire state, regardless of the region. The emphasis on September as a peak month for TCs underscores the need for targeted preparedness efforts during this period. The provided annual averages contribute to a comprehensive characterization of Georgia's tropical weather patterns, providing valuable insights for future research and policy considerations. This research aims to represent the people who are underrepresented in the literature and in planning practices to create a safer environment and to spread information to better protect the public. Hurricane Idalia and Hurricane Michael prove that hurricanes make their way into Georgia and have a major impact on the region, yet the public focuses on hurricanes' impact in Florida, South Carolina, and North Carolina. Hurricanes and tropical storms continue to impact Georgia, and this research serves as an updated climatology to help protect Georgia's history, natural beauty, and the people within.

Author Contributions: Conceptualization, R.C. and J.T.; methodology, R.C., J.T., and V.B.; software, R.C., J.T., and V.B.; validation, R.C., J.T., and V.B.; formal analysis, R.C.; investigation, R.C.; resources, J.T. and V.B.; data curation, R.C.; writing—original draft preparation, R.C.; writing—review and editing, R.C., J.T., and V.B.; visualization, R.C.; supervision, J.T.; project administration, J.T.; funding acquisition, Not applicable. All authors have read and agreed to the published version of the manuscript.

Funding: This research received no external funding.

Institutional Review Board Statement: Not applicable.

Data Availability Statement: Any specific requests for data can be handled by the Corresponding Author. "HURDAT2" at https://www.nhc.noaa.gov/data/ (accessed on 16 March 2024).

Conflicts of Interest: The authors declare no conflicts of interest. The funders had no role in the design of the study; in the collection, analyses, or interpretation of data; in the writing of the manuscript; or in the decision to publish the results.

References

1. Oceanic, N.; Administration, A. *The Coastline of the United States*; Pamphlet; Government Printing Office: Washington, DC, USA, 1975.
2. Elsner, J.B.; Jagger, T.H. *Hurricane Climatology: A Modern Statistical Guide Using R*; Oxford University Press: Oxford, UK , 2013.
3. National Centers for Environmental Information. *U.S. Billion-Dollar Weather and Climate Disasters*; National Centers for Environmental Information: Silver Spring, MD, USA, 2024.
4. Cangialosi, J.P.; Alaka, L. HURRICANE IDALIA . In *Tropical Cyclone Report AL102023*; National Hurricane Center: Miami, FL, USA, 2024.
5. Kaplan, J.; Rozoff, C.M.; DeMaria, M.; Sampson, C.R.; Kossin, J.P.; Velden, C.S.; Cione, J.J.; Dunion, J.P.; Knaff, J.A.; Zhang, J.A.; et al. Evaluating Environmental Impacts on Tropical Cyclone Rapid Intensification Predictability Utilizing Statistical Models. *Weather Forecast.* **2015**, *30*, 1374–1396. [CrossRef]

6. Hunter, K. Hurricane Idalia Got Much Stronger Overnight and Shifted West. South Georgians Weren't Ready. *Ledger-Enquirer* 2023 .
7. NOAA. *Irma Causes Widespread Damage in Georgia. Peachtree City, Georgia*; National Weather Service: Fort Worth, TX, USA, 2017.
8. Chappell, B. Power Outages Persist for Millions in Florida, Georgia and Carolinas after Irma. *NPR* **2017**, *13*.
9. Blake, E.; Landsea, C.; Gibney, E. The deadliest, costliest, and most intense United States tropical cyclones from 1851 to 2010 (and other frequently requested hurricane facts). In *Noaa Technical Memorandum Nws Nhc-6*; National Oceanic and Atmospheric Administration: Charleston, SC, USA, 2011.
10. Bossak, B.; Keihany, S.; Welford, M.; Gibney, E. Coastal Georgia Is Not Immune: Hurricane History, 1851–2012. *Southeast. Geogr.* **2014**, *54*, 323–333. [CrossRef]
11. Beven, J.; Berg, R.; Hagan, A. HURRICANE MICHAEL. In *Tropical Cyclone Report AL142018*; National Hurricane Center: Miami, FL, USA, 2019.
12. Rogers, R.; Marks, F.D.; Marchok, T. Tropical Cyclone Rainfall. *Encycl. Hydrol. Sci.* **2009**, *3*, 1–24.
13. Terry, J.P. *Tropical Cyclones: Climatology and Impacts in the South Pacific*; Springer: New York, NY, USA, 2007.
14. Koetse, M.J.; Rietveld, P. The impact of climate change and weather on transport: An overview of empirical findings. *Transp. Res. Part D Transp. Environ.* **2009**, *14*, 205–221. [CrossRef]
15. Cozannet, G.L.; Modaressi, H.; Pedreros, R.; Garcin, M.; Krien, Y.; Desramaut, N. *Encyclopedia of Natural Hazards*; Chapter Storm Surge; Springer: Dordrecht, The Netherlands, 2016.
16. Loayza, N.V.; Olaberría, E.; Rigolini, J.; Christiaensen, L. Natural Disasters and Growth: Going Beyond the Averages. *World Dev.* **2012**, *40*, 1317–1336. [CrossRef]
17. Henderson, J.D.; Abt, R.C.; Abt, K.L.; Baker, J.; Sheffield, R. Impacts of hurricanes on forest markets and economic welfare: The case of hurricane Michael. *For. Policy Econ.* **2022**, *140*, 102735. [CrossRef]
18. Darnell, T. Wildfire on Florida/Georgia Border Worsens, Evacuations Ordered. *USA Today*, 9 May 2017.
19. Cederholm, A.M. A Hurricane Risk Assessment for Chatham County, Georgia. Master's Thesis, Auburn University, Auburn, AL, USA, 2014.
20. Lard, A. GIS–Based Land Use Hurricane Storm Surge Analysis: A Case Study for Chatham County, Georgia. Master's Thesis, Savannah State University, Auburn, AL, USA, 2015.
21. Frankson, R.; Kunkel, K.E.; Stevens, L.E.; Sweet, W.; Murphey, B.; Rayne, S. STATE CLIMATE SUMMARIES 2022. In *NOAA Technical Report NESDIS 150-GA*; National Oceanic and Atmospheric Administration: Boulder, CO, USA, 2022.
22. Wang, C.; Zhang, H.; Feng, K.; Li, Q. Assessing hurricane damage costs in the presence of vulnerability model uncertainty. *Nat. Hazards* **2017**, *85*, 1621–1635. [CrossRef]
23. Rappaport, E.N. Loss of Life in the United States Associated with Recent Atlantic Tropical Cyclones. *Bull. Am. Meteorol. Soc.* **2000**, *81*, 2065–2074. [CrossRef]
24. Knutson, T.; Camargo, S.J.; Chan, J.C.L.; Emanuel, K.; Ho, C.H.; Kossin, J.; Mohapatra, M.; Satoh, M.; Sugi, M.; Walsh, K.; et al. Tropical Cyclones and Climate Change Assessment: Part II: Projected Response to Anthropogenic Warming. *Bull. Am. Meteorol. Soc.* **2020**, *101*, E303–E322. [CrossRef]
25. Landsea, C.W.; Franklin, J.L. Atlantic Hurricane Database Uncertainty and Presentation of a New Database Format. *Mon. Weather Rev.* **2013**, *141*, 3576–3592. [CrossRef]
26. RCoreTeam. *R: A Language and Environment for Statistical Computing;* R Foundation for Statistical Computing: Vienna, Austria, 2023.
27. Esri. *ArcGIS Pro Desktop*, Version 3.0.3; Esri: Hong Kong, China, 2022.
28. Durre, I.; Arguez, A.; Schreck, C.J., III; Squires, M.F.; Vose, R.S. Daily High-Resolution Temperature and Precipitation Fields for the Contiguous United States from 1951 to Present. *J. Atmos. Ocean. Technol.* **2022**, *39*, 1837–1855. [CrossRef]
29. Haylock, M.R.; Hofstra, N.; Tank, A.M.G.K.; Klok, E.J.; Jones, P.D.; New, M. A European daily high-resolution gridded data set of surface temperature and precipitation for 1950–2006. *J. Geophys. Res.* **2008**, *113*. [CrossRef]
30. Hutchinson, M.F.; McKenney, D.W.; Lawrence, K.; Pedlarand, J.H.; Hopkinson, R.F.; Milewska, E.; Papadopol, P. Development and Testing of Canada-Wide Interpolated Spatial Models of Daily Minimum—Maximum Temperature and Precipitation for 1961–2003. *J. Appl. Meteorol. Climatol.* **2009**, *48*, 725–741. [CrossRef]
31. Janis, M.J. Observation-Time-Dependent Biases and Departures for Daily Minimum and Maximum Air Temperatures. *J. Appl. Meteorol. Climatol.* **2002**, *41*, 588–603. [CrossRef]
32. Ricardo Nogueria, B.K. Contributions of Atlantic tropical cyclones to monthly and seasonal rainfall in the eastern United States 1960–2007. *Theor. Appl. Climatol.* **2011**, *103*, 213. [CrossRef]
33. Bureau, U.S.C. *2022 TIGER/Line Shapefiles (Machine Readable Data Files)*; U.S. Department of Commerce: Washington, DC, USA, 2023.
34. Klotzbach, P.J.; Gray, W.M. Forecasting September Atlantic Basin Tropical Cyclone Activity. *Weather Forecast.* **2003**, *18*, 1109–1128. [CrossRef]
35. Clinton Beckford, K.R. *Globalization, Agriculture and Food in the Caribbean*, 1st ed.; Palgrave Macmillan: London, UK, 2016.
36. Scowcroft, G.; Ginis, I.; Knowlton, C.; Yablonsky, R.; Morin, H.; McIntire, D. *Hurricanes: Science and Society*; University of Rhode Island: Kingston, RI, USA, 2011.

37. Bettinger, P.; Merry, K.; Hepinstall, J. Average Tropical Cyclone Intensity Along the Georgia, Alabama, Mississippi, and North Florida Coasts. *Southeast. Geogr.* **2009**, *49*, 49–66. [CrossRef]
38. Knight, D.B.; Davis, R.E. Climatology of Tropical Cyclone Rainfall in the Southeastern United States. *Phys. Geogr.* **2007**, *28*, 126–147. [CrossRef]
39. Knight, D.; Davis, R. Contribution of tropical cyclones to extreme rainfall events in the southeastern United States. *J. Geophys. Res.* **2009**, *114*. [CrossRef]

Journal of
Marine Science and Engineering

Article

Coastal Protection for Tsunamis

Angela Santos [1,*] and Nelson Mileu [2]

[1] Centre of Geographical Studies, Associate Laboratory TERRA, Institute of Geography and Spatial Planning of the University of Lisbon, Rua Branca Edmée Marques, 1600-276 Lisboa, Portugal
[2] Centre of Geographical Studies, Institute of Geography and Spatial Planning of the University of Lisbon, Rua Branca Edmée Marques, 1600-276 Lisboa, Portugal; nmileu@edu.ulisboa.pt
* Correspondence: angela.santos@edu.ulisboa.pt

Abstract: Previous research showed that a tsunami similar to the 1755 event would inundate Caxias' low-ground areas in Oeiras municipality, Portugal. However, the streets of downtown Caxias were not well reproduced, which is a limitation of the area's mitigation strategies and evacuation plan. For these reasons, new Lidar data were used for the first time in Portugal. The new local topography data allowed the construction of a more accurate DEM, which was used in the tsunami numerical model to update and improve the inundation results. As a complement, a field survey was conducted in several locations to assess coastal features and protection. The numerical model results show that low-ground areas up to 6 m in height were inundated by the tsunami, including the residential area, the road, and the railway. To stop the tsunami waves from inundating these areas, it is proposed that the construction of more sea walls up to 7 m in height and a third bridge over the Barcarena Stream, only for pedestrians, ranging from 5 to 7 m in height, which will serve as a gate for the incoming tsunami waves. These coastal protections should be part of the strategy to mitigate coastal overtopping (winter storm surges and tsunamis) not only in Caxias but also in other coastal zones.

Keywords: coastal protection; tsunami; field survey; tsunami numerical model; Portugal

Citation: Santos, A.; Mileu, N. Coastal Protection for Tsunamis. *J. Mar. Sci. Eng.* **2024**, *12*, 2349. https://doi.org/10.3390/jmse12122349

Academic Editor: Deniz Velioglu Sogut

Received: 14 September 2024
Revised: 7 December 2024
Accepted: 17 December 2024
Published: 21 December 2024

1. Introduction

Worldwide, coastal areas are quite vulnerable to extreme events such as winter storm surges, hurricanes, typhoons, and tsunamis or meteo-tsunamis. Some of these past disasters inundated the low-ground areas, causing severe damage and fatalities, as presented by, for example, refs. [1,2]. These situations are even more aggravated due to coastal erosion [3] and the sea level rise. Simultaneously, the populations are more attracted to the coastal areas due to urban occupation, tourism or leisure purposes, industry, and services, which increase the population's exposure to these natural disasters [2].

As a consequence, many published papers assess shoreline changes and their impacts on coastal structures in the worldwide coastal evolution. To cope with this problem, the Journal of Marine Science and Engineering (MDPI) has published more than 200 papers related to coastal protection from 2023 till August 2024 and about 100 papers related to tsunamis in the period 2021–2024, too many to conduct a citation of all of them. Still, in this study, several worldwide case studies are presented. For example, ref. [4] presented the installation of buffer blocks on the coastline of Germany. On the other hand, natural Mangrove belt forests are important not only for the ecosystem but also for coastal protection [5]. However, these natural resources have been disappearing over the decades in Vietnam, and artificial breakwaters have been constructed, which have shown to be highly effective in reducing wave height impact. Still, structural failures can occur when a tsunami overtops a breakwater [6]. Following the 2004 Indian Ocean Tsunami, the role of mangroves also proved to be very effective in the reduction in the tsunami impact at Banda Aceh, Indonesia [7,8]. On the other hand, other natural features such as vegetation and sand dunes are also very effective in wave attenuation, as discussed in a beach in Florida, EUA [9].

In Portugal, the complexity of the coastal zone was shown [10] to be due mainly to four typologies (cluster analysis): natural systems in disequilibrium, with predominantly environmental impacts; anthropogenic areas, with high population density, predominantly natural coastal protection, or no protection; natural systems in equilibrium, with few impacts; and predominantly artificial areas, with coastal protection intervention and multiple impacts. On the other hand, numerical modeling was used to calculate the wave overtopping phenomenon on a Portuguese alongshore coastal defense structure [11]. Furthermore, ref. [12] showed the assessment of susceptibility to maritime flooding on the Northern coast of Portugal is based mainly on two variables: the wave climate and the morphological state of the beaches. Moreover, ref. [13] analyzed tide gauge data from Portuguese stations from 1980 to 2016 that shows about a 0.1 m increase in the mean sea level. The authors conducted a probabilistic analysis to estimate the sea level rise till 2100 and concluded the average rising of the mean sea level is about 0.7 m for a return period of 50 years.

In addition, there are specific guidelines for the Oeiras municipality, Portugal (see location in Figure 1a,b). The Municipal Plan of Adaptation to Climate Change in Oeiras [14] claims that "on all the beaches of the municipality, it is projected that the rise from the mean sea level implies a significant reduction in that capacity, which could derail its beach exploration", with examples being Caxias Beach. In addition, the Energy and Climate Action Plan of Oeiras (PAECO 2030+) [15], in the Strategic Axis of Water System and Estuarine Edge, the specific measures are to promote the riverfront adaptation to the average water level rise and flood enlargement and to promote the protection of buildings at risk of coastal flood or coastal overtopping and existing coastal defense and port structures and beach protection and maintenance.

Previous research [16] has shown the 1755 tsunami arrived at Caxias (Figure 1) 33 min after the earthquake, at the beaches inundating the low-ground areas of the Caxias downtown (Figure 1c), as well as the Caxias Public Park and Royal Estate of Caxias. In the tsunami inundation zone, there are about 40 buildings: about 25 that are residential, about 10 that are military, two restaurants (#C) located at the São Bruno beach, the sewage facility treatment (building #A), one service (building #B), and the São Bruno Fortress (#D). These results are important to understand the overall tsunami impact and evacuation conditions, as discussed by these authors [16]. However, the Digital Elevation Model (DEM) used in the tsunami numerical model had 9 m of cell size resolution, which is not enough to reproduce the detailed local features of Caxias, such as the streets of the residential area of Caxias downtown and the parks and gardens layout. In general, the topography data in Portugal are still of low resolution, and to solve this problem, new topography data were collected by using LIDAR technology. To the authors' knowledge, this is the first time that this type of technology has been used in Portugal in the context of tsunami numerical modeling, which is why this study is considered to be innovative. The use of new data allows the reproduction of the DEM of the study area more accurately.

Therefore, the study area taken in this paper is Caxias (Figure 1), which incorporates the Caxias and São Bruno beaches, is localized in Oeiras municipality, and is integrated into the Lisbon Metropolitan Area, Portugal. Its geographical coordinates are 38°41′55″ N, 9°16′45″ W, and 38°41′54″ N, 9°16′27″ W. These beaches flank the Barcarena Stream, which is about 25 m wide, and are bordered to the north by the Cascais railway line, built in 1890, and the National Road 6 (Marginal Avenue), inaugurated in 1940 [17]. Two important architectural heritage properties stand out near the beaches: the Caxias Royal Estate and the São Bruno Fortress, which was also inundated by the tsunami (building #C). Built in the 17th century, the Caxias Royal Estate stands out for its unique architectural design, environment, living style, and landscape qualities, which constitute a singular cultural heritage [18], while the São Bruno Bruno is one of the military defense constructions at the entrance to the Tagus River. Moreover, the location of the Caxias Train Station (red building in Figure 1c) and several parking lots near the Caxias and São Bruno beaches make the area even more attractive to residents and tourists.

Moreover, the pandemic situation due to COVID-19 was a unique opportunity to register in real-time the present population on both beaches. At the time, the recommendation considering the social distance of 1.5 m [19] for the maximum beach capacity was 1700 people in Caxias Beach. In São Bruno Beach, the maximum capacity was 969 people [20], obtained from a simple rate formula (maximum beach capacity = beach area/8.5 m^2). Thus, the Oeiras City Hall installed turnstile control data at the beach accesses (#1 to #5, in Figure 1c) to ensure the health and safety of beach users. The population data at the beaches consisted of 24 h records during the summer months of June to September 2021 [20]. The data are still very relevant since there are no available data on the number of present populations at both beaches before and after 2021. The data showed the maximum number of people registered in Caxias Beach on 22 August 2021 between 15 h (622 people) and 18 h (734 people). In São Bruno Beach, the maximum number of people was registered on 4 July 2021 between 11 h (133 people) and 16 h (241 people).

As pointed out by a previous study [16], a basic tsunami scenario is already contemplated in the Municipal Emergency Plan [21] that needs to be reviewed and updated. On the other hand, the Caxias and São Bruno beaches have five accesses: beach access #1 and #5 are stairs, while beach access #2 is a tunnel, and beach accesses #3 and #4 are ramps. Although there is high ground nearby, the configuration of these exits may cause some confusion to beach users if an emergency evacuation is necessary, and for that reason, the local tsunami hazard on each beach was classified as high [16]. Nevertheless, the new topography data allow an upgrade of the tsunami numerical model setting from five computational regions [16] to six regions (this study), with a 9 m cell size to a 3 m cell size, respectively. In computational region 6, the local features of Caxias are accurately reproduced, including streets and ramps to access the beaches.

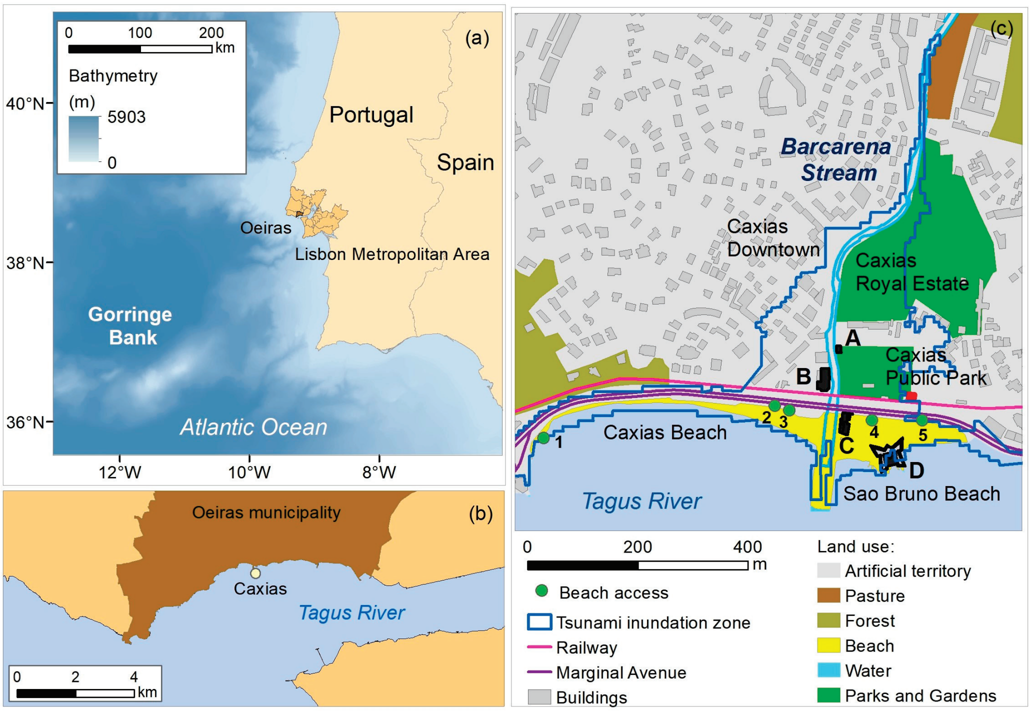

Figure 1. Geographical Framework of the study area, with the administrative limits [22]: (**a**) location of Oeiras municipality; (**b**) location of the Caxias area in Oeiras municipality; (**c**) details of the railway, road, buildings [23], and land use (adapted from [24]) in the Caxias area. The tsunami inundation zone was calculated by previous research [16] with a cell size resolution of 9 m. Highlighted buildings: A—sewage treatment facility; B—service; C—restaurant; D—São Bruno Fortress; Red building—Caxias train station.

Thus, the objectives of this research are as follows: (1) to conduct a follow-up of a previous publication [16] by using new topographic data obtained from Lidar Technology to update the tsunami numerical model results of the 1755 event at Caxias and São Bruno Beaches, in the vicinity of Barcarena Stream, in Oeiras municipality, Portugal. (2) Propose several coastal protection measures in order to increase the safety of coastal communities to extreme coastal events in the study area. Moreover, these methods can be applied to other coastal regions in the world, particularly in low-ground areas.

2. Materials and Methods

This study is a follow-up of previous research [16], and the methodology is the same. The tsunami numerical modeling was carried out using the TUNAMI-N2 code of Tohoku University, which considers the non-linear shallow water equations discretized with a staggered leap-frog finite difference scheme [25]. This method has been used to study many tsunamis, such as the 2004 Indian Ocean Tsunami [26], the 2011 Tohoku Tsunami [27], the 2016 Fukushima Tsunami [28], and the 2024 Ishikawa Prefecture tsunami in Japan [29].

The equations were applied to the nesting of six computational regions, where each region has a progressively smaller area and finer grid cell size (from 729 m in Region 1 to 3 m in Region 6), being included in the previous computational region, as presented in Figure 2. The computational regions 1 to 5 are the same as those used in a previous publication [16], on which several bathymetry charts and topography maps with different scales are based.

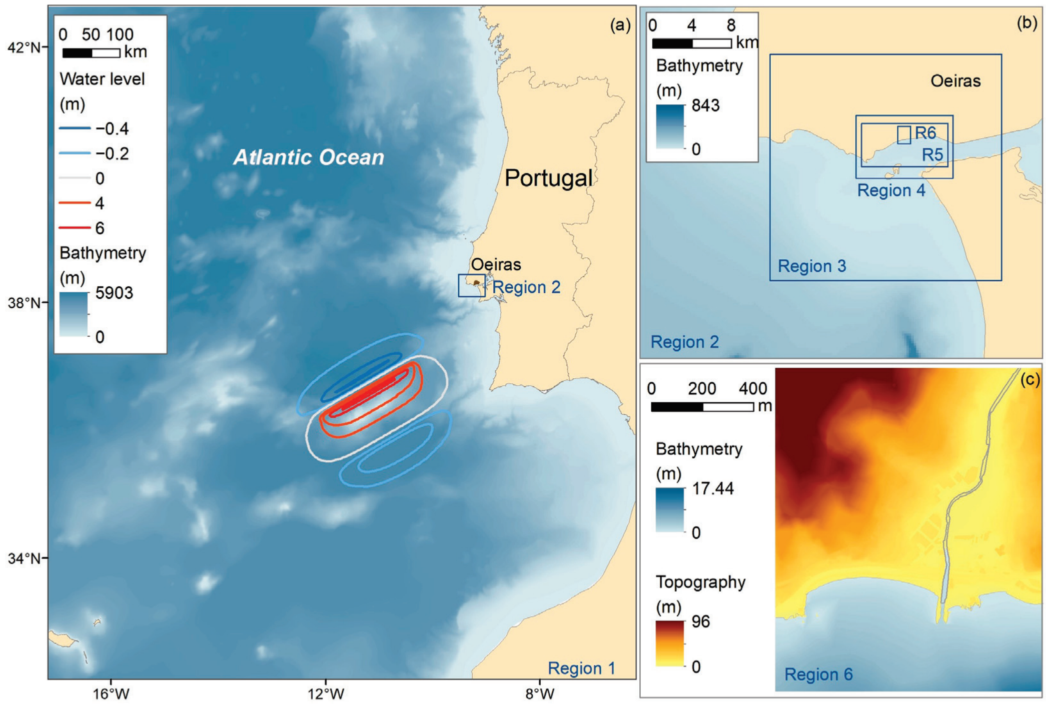

Figure 2. Conditions of the numerical model setting in the Caxias coastal area of Oeiras municipality: (**a**) Region 1 and initial sea surface displacement of the 1755 tsunami; (**b**) Region 2 and the placement of Regions 3 to 6; (**c**) Details of computational Region 6.

In addition, computational region 6 is new in this study. New topographic data allowed a more detailed and realistic construction of the digital elevation model with a 3 m cell size to reproduce the local features such as streets, sidewalks, and the stream layout. The data collection was based on a laser scan of the study area carried out using a RIEGL VUX laser scanner installed on a helicopter. This mission was carried out on 11 May 2020 at an average altitude of about 61 m (200 feet) and an average speed of about 74 km/h (40 knots). The main technical characteristics of the survey were a nominal point density of a minimum of 16 points per m², a nominal pulse spacing of <0.25 m, and multiple discrete returns (minimum potential of 4 per pulse). The absolute vertical accuracy for the LiDAR survey and derived digital elevation model was computed for non-vegetated areas with an RMSEz of <0.10 m at more than a 95% confidence level.

Also, as in the previous research [16], the tsunami source model considered in this study is the 1755 tsunami, which is located on the Gorringe Bank (Figure 1a). The initial sea surface displacement was calculated by using the Okada formulas [30] in Region 1, which led to a maximum uplift of about +6.0 m and a subsidence of −0.4 m (Figure 2a). This source model was proposed and validated for the 1755 tsunami at the regional and local scales [31–37].

As a complement to the tsunami numerical model, a field survey (Figure 3) was conducted on several occasions. Field surveys are important to assess coastal conditions, including collecting evidence during and after coastal disasters like winter storm surges and tsunamis [38]. In Portugal (Figure 3a), the surveys were conducted on several spots of Caxias (this study) on different occasions from May 2022 to June 2024.

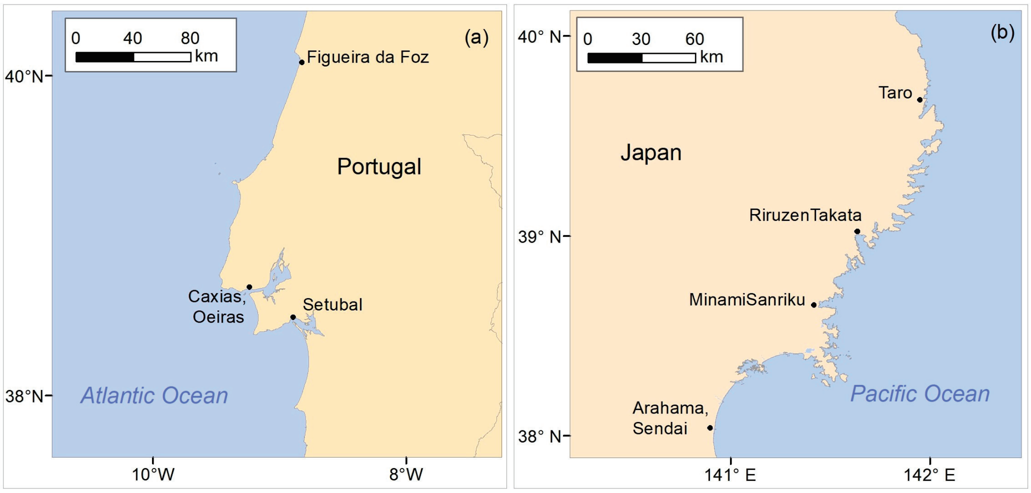

Figure 3. Location of places where the several field surveys were conducted on several occasions: (**a**) Portugal; (**b**) Japan.

In addition, previous field surveys conducted in 2013 on two other locations of the Portuguese coastline (Figure 3a) help to discuss and interpret the results obtained in this study to support natural coastal protection. The surveys were conducted in Cova Beach, Figueira da Foz, located at 40°07′24″ N, 8°51′48″ W, and Urban Health Park, Setubal, located at 38°31′05″ N, 8°54′11″ W. These places show examples of natural protection of the coastline.

On the other hand, the experience obtained with the field survey in Japan in 2012, after the 2011 Tohoku Tsunami (Figure 3b), allows a more comprehensive knowledge in the discussion of the several types of coastal protection proposed in this study. In Japan, the technical visit was conducted in Taro, located at 39°44′08″ N, 141°58′19″ E; RikuzenTakata, located at 39°00′13″ N, 141°37′33″ E; MinamiSanriku, located at 38°40′29″ N, 141°26′51″ E; and Arahama, Sendai, located at 38°13′15″ N, 140°59′00″ E. These places show examples of natural protection of the coastline and the impact of the construction of seawalls and tsunami gates.

3. Results

The tsunami numerical model on computational region 6 produced several output results, such as the water level variation snapshots, inundation depth, maximum water level, and water level time series, as presented in Figures 4 and 5. In addition, the field survey results are presented in Figure 6, showing a view of the several spots of the study area to help conduct a comprehensive analysis of the tsunami impact.

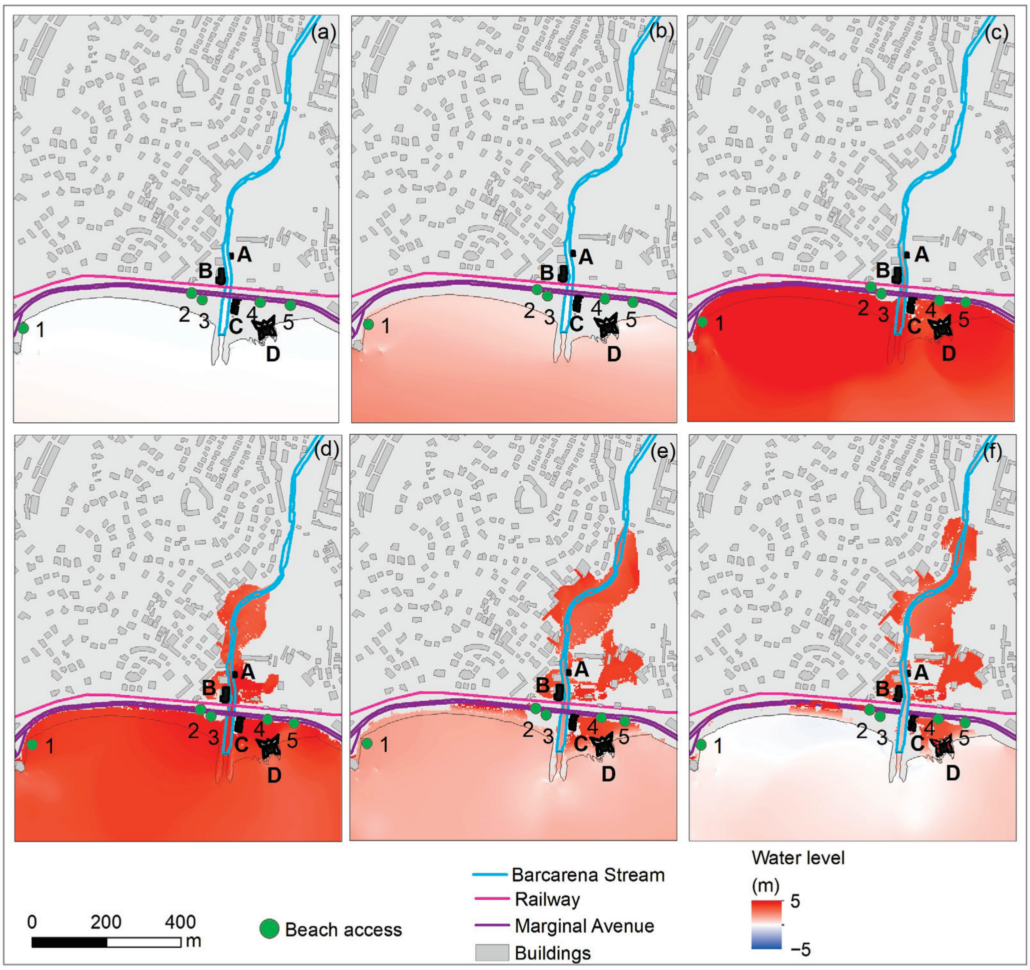

Figure 4. Tsunami numerical model results for the elapsed time after the earthquake of water level snapshots showing the arrival of the first tsunami wave: (**a**) 31 min; (**b**) 32 min; (**c**) 33 min; (**d**) 34 min; (**e**) 35 min; (**f**) 36 min. Highlighted buildings: A—Sewage treatment facility; B—Service; C—Restaurant; D—São Bruno Fortress.

The water level snapshots results show the first tsunami wave arrived offshore the Caxias and São Bruno beaches 31 min after the earthquake (Figure 4a), taking two more minutes to completely inundate the Caxias beach, the section of the Marginal Avenue (about 460 m length), and the São Bruno beach as well as its sidewalk (Figure 4c). The field survey shows that Marginal Avenue has four traffic lanes (Figure 6a), with a total width of about 15 m. On the other hand, the railway, which was not hit by the tsunami, has two lanes with also a total width of about 15 m.

The first wave travels upstream the Barcarena Stream, overtopping its margins, which are made of brick and concrete walls with different heights (Figure 6b,c), inundating the low ground of the Caxias downtown, the Caxias Public Park, and the Royal Estate of Caxias, from 34 min (Figure 4d) after the earthquake, and continues to spread for at least 2 more minutes (Figure 4e,f). The field survey shows there are sections of the Barcarena Stream that are only protected by a fence, while other parts have vegetation or sea walls (Figure 6b,c).

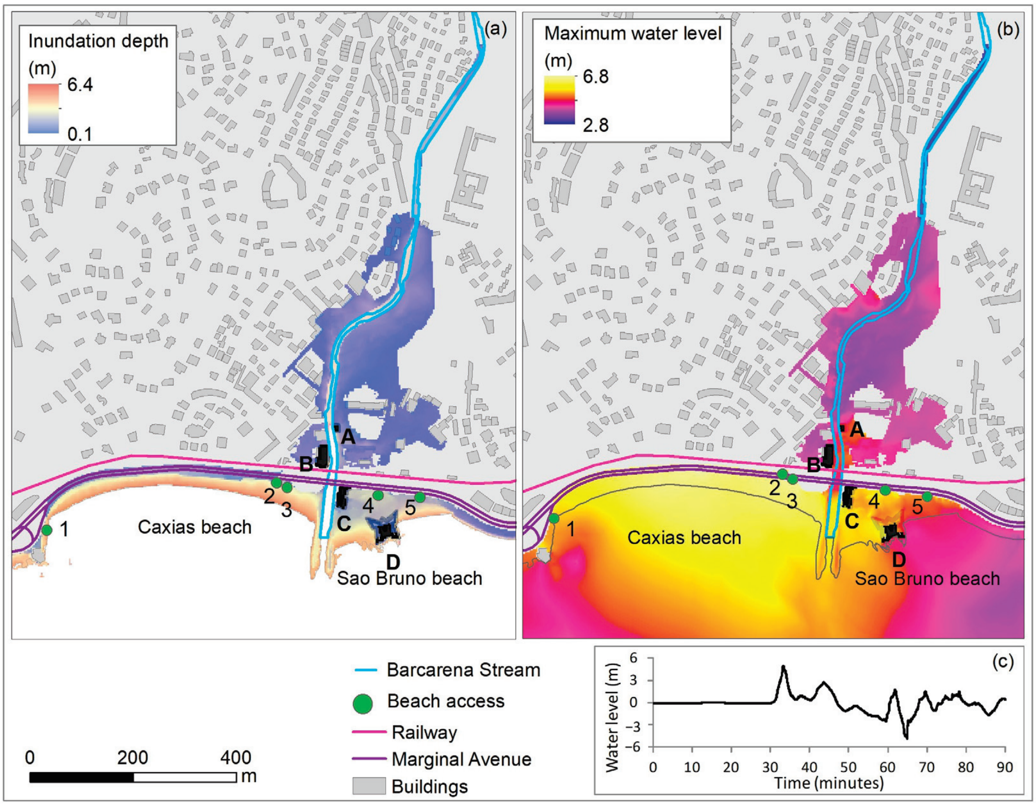

Figure 5. Tsunami numerical model results on computational region 6: (**a**) Inundation depth; (**b**) maximum water level; (**c**) Water level time series in Caxias. Highlighted constructions: A—Sewage treatment facility; B—Service; C—Restaurant; D—São Bruno Fortress.

The inundation depth results (Figure 5a) provide the water level above the ground (local topography data) for each computational pixel with a cell size of 3 m. The results show that Caxias Beach is completely inundated, and the highest value is 6.4 m, and the lowest is 1.7 m. The tsunami also inundates the stretch of Marginal Avenue with values up to 1.3 m high. Therefore, the road is not a safe place for people to evacuate. The values at São Bruno beach vary between 1.8 m and 5.6 m, and the sidewalk and the low ground area are completely inundated up to 2.4 m high.

The field survey shows a view of the São Bruno beach and sidewalk (Figure 6d); as the tsunami reaches the seawall of Marginal Avenue, it may cause some scouring and damage on hit. Although the tsunami does not reach the road, which is located above 6 m height, there are only two beach accesses (#4 and #5) that may not be large enough for beach users to safely evacuate the beach.

However, the results on the computational region 6 with a pixel cell size of 3 m (this study) show the railway was not hit by the tsunami because it is located on higher ground (from 6.5 m height). In the previous study [16], where the tsunami numerical results on computational Region 5 were carried out with a pixel cell size of 9 m, the tsunami hit the railway and overtopped it, inundating the Caxias downtown and the Caxias Public Park (Figure 1). Two computational factors influenced these results: the new Lidar data allowed a more accurate Digital Elevation Model (DEM), and the setting of the numerical model (Figure 2) allowed the reproduction of the coastal features of the study area.

Moreover, the tsunami traveled upstream the Barcarena Stream for 1120 m, inundating the low ground margins for a section of about 560 m, conducting to an inundation depth at the Caxias downtown up to 3.1 m high, up to 2.6 m at the Caxias Public Park, and up to 0.9 m in the Royal Estate of Caxias.

On the other hand, the maximum water level results (Figure 5b) provide the water level above the mean sea level for each computational pixel with a cell size of 3 m, including on-land and offshore outputs. The results show that at Caxias Beach, the highest value is 6.5 m, and the lowest is 5.4 m. The tsunami also inundates the section of Marginal Avenue with 5.8 m to 6.8 m height but does not overtop the bridges over the Barcarena Stream (Figure 6a) because they are located at about 6 m height and the maximum water level reaches up to 4.9 m height. In the stretch of the inundated areas of the Caxias downtown and Caxias Royal Estate (about 550 m long), the maximum water level at the Barcarena Stream reaches 4.9 m, decreasing gradually upstream to a height of 3.2 m. In the last stretch of about 370 m, where there is no inundation, the water remains restricted within the stream margins and reaches 2.8 m in height. The maximum water level at the Caxias downtown varies between 3.9 m and 4.8 m in height, 4.0 m to 5.0 m in height at the Caxias Public Park, and 3.2 m to 4.5 m in height in the Royal Estate of Caxias. Offshore the São Bruno beach, the water level varies between 3.8 m and 5.6 m, and offshore the Caxias beach, 4.4 m and 6.4 m.

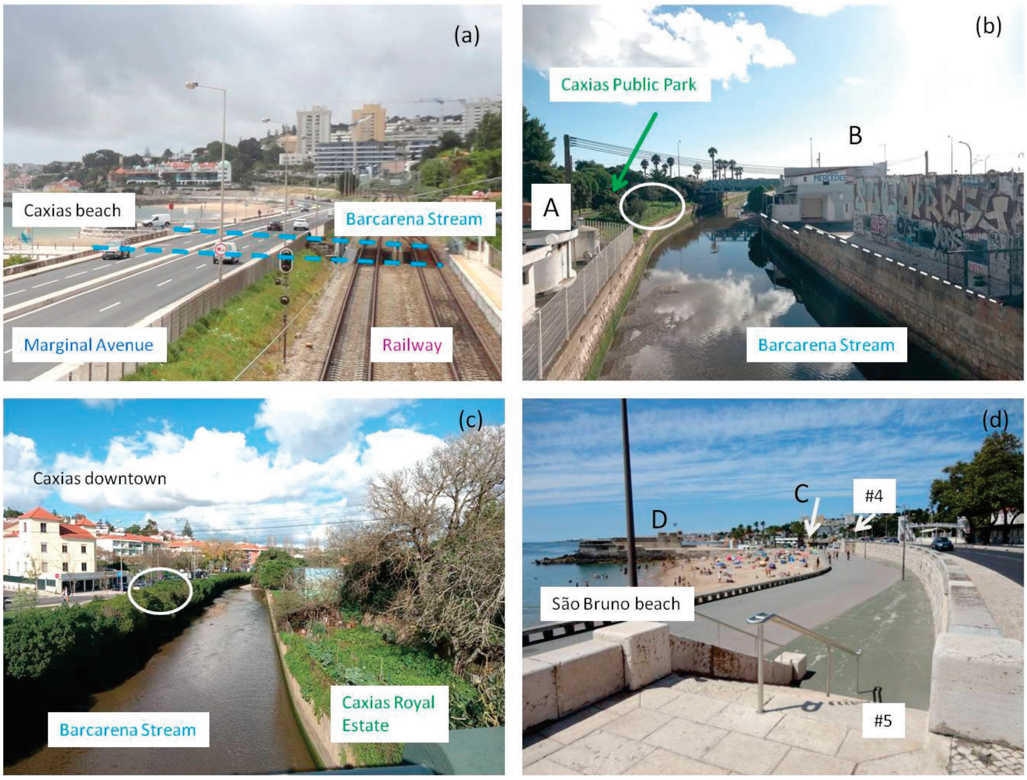

Figure 6. Field surveys were conducted in different spots of the study area. See Figure 1 for locations: (**a**) Caxias beach and a view of Marginal Avenue and railway on 30 April 2024; (**b**) a view of Barcarena Stream in the vicinity of the Caxias Public Park on 2 December 2023. The dashed lines highlight the brick wall at different heights. Building A: Sewage treatment facility; Building B: service. The white circle shows an area with only a fence for protection; (**c**) View of the Barcarena stream in the vicinity of the Caxias downtown and Royal Estate of Caxias. The white circle shows an area with vegetation belt protection about 2 m high; (**d**) São Bruno beach on 28 August 2024. Building C—restaurant; building D—São Bruno Fortress; beach access #4 is a ramp; beach access #5 is a stair.

Finally, the water level time series (Figure 5c) shows the first wave arrives at the coastline of Caxias 31 min (picked at the +0.1 m height) after the earthquake, and the peak of the first wave is 4.98 m at 33 min. The second wave reaches 2.69 m at 44 min, followed by other minor waves with maximum water levels between 1.5 and 1.7 m, with sea level variations for 90 min.

4. Discussion

Natural landscapes, such as mangrove forests in Asia [5,7,8] or sand dunes [9,39], protect the coastal areas without human intervention. The field survey conducted in Figueira da Foz, Portugal (Figure 7a) shows that sand dunes offer natural protection against extreme coastal events. Nevertheless, constant erosion requires monitoring and, in some places, the construction of spurs and other artificial constructions. However, unlike Figueira da Foz, the Caxias coastal area is not naturally protected by sand dunes. Therefore, other solutions must be planned to allow coastal protection.

Figure 7. Field survey in Portugal showing natural coastal protection: (**a**) Cova beach, Figueira da Foz. The sand dunes reach up to 10–14 m in height. Photo taken on 2 June 2013; (**b**) Urban Health Park (Jardim da Saude), Setubal with pine trees and elevated ground. Photo taken on 20 June 2013.

The results presented in Section 3 show the tsunami in the section of Caxias Beach inundates Marginal Avenue. Not only is this a very hazardous situation for the vehicles that circulate on the road, but the air cavity pressure and cavity water depth behaviors when a tsunami overtops a breakwater [6] can cause damage to the seawall, including the scouring of the foundations. This situation was observed during the 2011 Tohoku Tsunami in Taro, during which parts of the breakwater were ripped off (Figure 8a). Similar damage due to scoring was also observed in several infrastructures after the 2015 Illapel Tsunami in Chile [40].

In addition, the winter storm surges also raise some concern for the protection of coastal areas, especially during high tides. An example is the Monica Depression that hit Portugal's mainland from 7 to 10 March 2024 [41]. The field survey conducted at Caxias Beach during and after this storm (Figure 9) shows the waves inundated the beach, and the water almost reached the sea wall of Marginal Avenue.

To solve this situation, it is proposed to expand the seawall of Marginal Avenue, that is, to continue with the silting of the beach, which has been carried out since the 1940s. The new area to be constructed must have a height of at least 7 m and be at least 10 m wide. In addition, the new area must include some "green belt" with the plantation of several species of bushes and trees.

The "green belt" provides shade, but it has also proved to be an effective barrier to water pressure [42]. The field survey conducted on several coastal areas shows this type of coastal protection has been successfully carried out in Setubal, Portugal (Figure 7b), and in Sendai and Rikuzentakata, Japan (Figure 8b,c).

Similarly, the results presented in Section 3 show that the São Bruno beach is inundated by the tsunami hitting the sidewalk. Although the water does not reach Marginal Avenue, it may cause damage and score to the seawall. To solve this problem, it is proposed to increase the height of the sidewalk at São Bruno beach (Figure 6d) as a ramp with a low slope angle from the current 4 m to 7 m. The restaurant (building #D), which is located at about 4 m, should also be replaced with a higher topography level of 7 m in height.

Figure 8. Field survey conducted in Japan on 18–19 February 2012: (**a**) Remains of the breakwater and one building in Taro; (**b**) Part of the pine tree forest belt at Arahama, Sendai. (**c**) Only one tree stands from the pine tree forest belt, "The Miracle Pine Tree," Rikuzentakata; (**d**) Tsunami gate at the River Hachiman, Minami-Sanriku.

In addition, the evidence left by the sand and the debris deposited inside the tunnel of Caxias beach (Figure 9c) due to the Depression Monica shows the maximum inundation reached about 3.8 m in height. On the other hand, the probabilistic estimation for the mean sea level rise to a return period of 50 years is 0.7 m [13]. For these reasons, the new maritime sidewalk to be constructed at Caxias Beachshould be constructed at least 4.5 m high and about 10 m wide.

Moreover, there is evidence that the area of Caxias Beach has been decreasing due to the yearly sand erosion combined with the lack of maintenance of the beach. Thus, it is important that the sand is replaced to reach 3.5 m in height and to increase the width of the beach from the current 50 m to 85 m. As a consequence, there will be a shift in the coastline.

Nevertheless, it is important to point out that placing a breakwater or buffer block offshore of the Caxias and São Bruno beaches would decrease the depth of tsunami inundation, as discussed, for example, by [4]. However, this option is not possible to install for coastal protection in the study area because an offshore breakwater is not esthetically appealing for both residents and tourists, as well as may constitute a hazard to navigation on the Tagus River.

In addition, the quality of the water at Caxias and São Bruno beaches is not very good. Portugal has the Blue Flag Award [43]: each year, the Blue Flag is granted to the beaches that follow several criteria, including water quality. In 2024, Caxias and São Bruno beaches did not receive the Blue Flag. The water is regularly analyzed by chemical and biological contents of the water [44], showing both beaches are acceptable for public use. Although the water quality analysis and local circulation are outside of the scope of this paper, to improve the water quality at the beaches, it is recommended to relocate the sewage treatment facility (Building #A) or to impose more strict methods to filter the water that is dumped into the Barcarena Stream. Thus, adding offshore breakwaters of buffer blocks may cause the possibility of reducing or even cutting altogether the water regeneration in the high-low-tide currents since it may promote low water circulation and high residence time inside the trapped area by the breakwater, which in turn would cause a significant decrease in the water quality.

Figure 9. Field surveys were conducted in different spots of the study area. See Figure 1 for locations: (**a**) Beach Access #1 during the Depression Monica on 10 March 2024; (**b**) Beach Access #1 on 17 December 2023; (**c**) Sand deposited inside the tunnel (Beach Access #2) due to the Depression Monica on 13 March 2024; (**d**) Tunnel was cleaned (Beach Access #2) on 30 April 2024.

The results presented in Section 3 show the tsunami overtops the margins of the Barcarena Stream. The field survey shows there is already some effort to protect the low-ground area with sea walls and vegetation (Figure 5b,c). Thus, it is proposed that the continuation of the construction of the levees and increasing their heights range from 4.8 m to 7.2 m at the tsunami inundation zone. Moreover, the field survey in MinamiSanrilu (Figure 8d) shows that a tsunami gate could be an effective structure to decrease the tsunami impact upstream of the Barcarena Stream. On the other hand, the field survey conducted in MinamiSanriru also shows that some sections of the gates failed to be low because of damage due to the earthquake. In addition, the cost–benefit makes this option not realistic to be applied in Portugal. Instead, it is proposed that the construction of a new bridge only for pedestrians (Figure 10) be done. The bridge would allow the passage between the Caxias and São Bruno beaches as a continuous maritime sidewalk. The damage on bridges related to tsunamis overtopping the upper decks has been analyzed [45,46]; thus, to avoid this situation, the new proposed bridge in the river mouth of the Barcarena Stream should be at 7 m height.

Figure 10. Proposal to build a new bridge over the Barcarena Stream. This third bridge is only for pedestrians and bicycles and should have a height ranging from 5 to 7 m since, at present, Marginal Avenue is at about 6 m height, and the lower part of the bridge is at 5 m height. In addition, the new bridge should have a design to deflect the incoming sea waves.

Thus, the proposed Digital Elevation Model (DEM) was added to the topography of computational region 6 (Figure 2c), and the tsunami numerical model was carried out again. Moreover, the new beach accesses must be done exclusively by ramps (#R1 to R6, in Figures 11 and 12), similar to the existing beach accesses #3 and #4 (Figure 1). Figures 11 and 12 show the results of the new simulation, with the proposed DEM that would allow further coastal protection. The first tsunami wave inundates the Caxias beach, its new sidewalk, and the São Bruno beach. It travels upstream of the Barcarena Stream but does not overtop its margins (Figure 11), and at 36 minutes is at about 500 m inland (Figure 11b).

The inundation depth results (Figure 12a) show that Caxias Beach is completely inundated, with the lowest value of 1.8 m and the highest value of 6.1 m, and the values at São Bruno Beach vary between 1.8 m and 5.3 m, which are very similar to the results obtained with the current DEM (Figure 6a). However, it does not inundate the new seawall at Caxias beach with 7 m height, and therefore, Marginal Avenue is not hit, nor is the new sidewalk and restaurant (Building #C) at São Bruno beach.

The maximum water level results (Figure 12b) show that at Caxias Beach, the lowest is 5.2 m, and the highest is 6.1 m. The tsunami does not overtop the bridges over the Barcarena Stream (Figures 5a and 10) because they are located at about 6 m height, and the maximum water level ranges between 5.6 m and 5.8 m height. Still, the water may reach the lower part of the bridges, which are about 5 m high, and for this reason, the new proposed pedestrian bridge should serve as a tsunami gate to protect the existing bridges of Marginal Avenue and the railway (Figure 5a). Still, a careful analysis must be carried out before the construction of the new bridge due to the interaction between decks of twin-box bridges [45]. The tsunami travels upstream of the Barcarena Stream, and the water remains within its margins, with the maximum water level ranging between 2.1 m and 5.8 m. Finally, the water level time series (Figure 12c) shows the tsunami has the same behavior offshore, with no variation from Figure 6c.

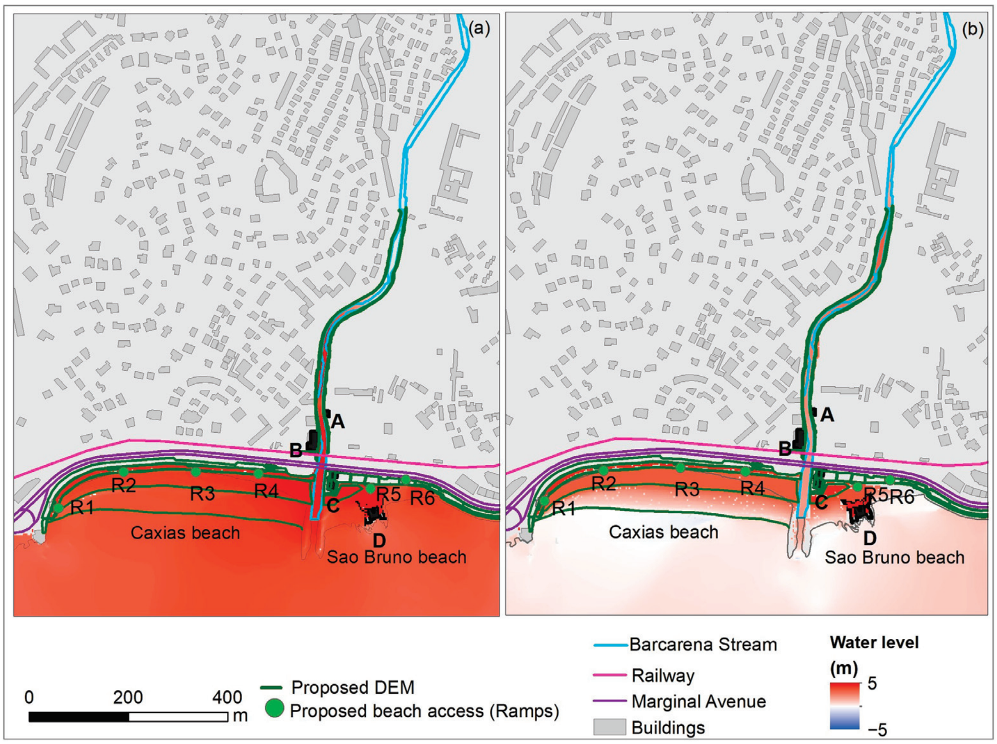

Figure 11. Tsunami numerical model results for the elapsed time after the earthquake of water level snapshots showing the arrival of the first tsunami wave, with the proposed DEM (Digital Elevation Model) represented by the green line: (**a**) 34 min, (**b**) 36 min; Highlighted buildings: A—Sewage treatment facility; B—Service; C—Restaurant; D—São Bruno Fortress.

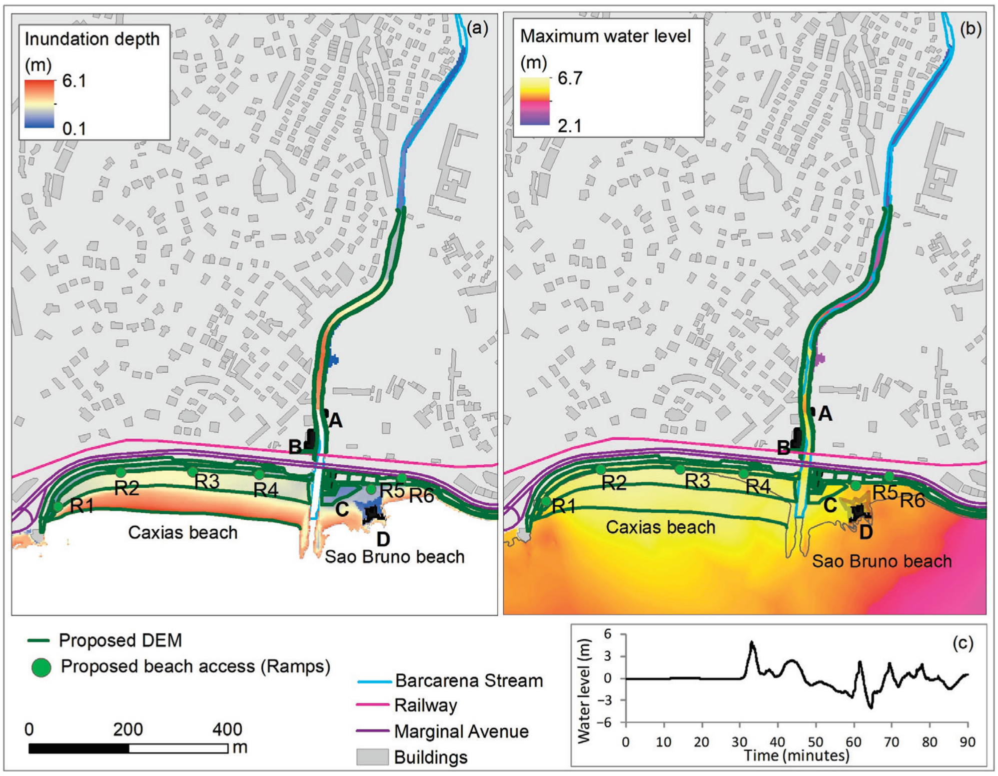

Figure 12. Tsunami numerical model results on computational region 6, with the proposed DEM (digital elevation model) represented by the green line: (**a**) Inundation depth; (**b**) maximum water

level; (**c**) Water level time series in Caxias. Highlighted buildings: A—Sewage treatment facility; B—Service; C—Restaurant; D—São Bruno Fortress.

5. Conclusions

The new Lidar technology has shown to be a very important tool for collecting detailed topography at the local scale. The new topographic data allowed the construction of a more accurate Digital Elevation Model (DEM) of the study area with a cell size pixel of 3 m, which reproduced the local features such as streets.

The tsunami numerical model results show that a tsunami similar to the 1755 event arrived at Caxias 33 min after the earthquake, inundating the Caxias beach and Marginal Avenue; the downtown of Caxias was also inundated, including residential buildings, 34 min after the earthquake.

On the other hand, although tsunamis are rare events, in recent years, winter storm surges have become more frequent and severe, which, combined with the sea level rise, are a concern for low-ground areas. An example was the Depression Monica, which hit Caxias in March 2024. The water reached a maximum height of 3.8 m and inundated the Caxias beach and the tunnel (beach access #2).

For these reasons, it is proposed to continue the silting process of Caxias Beach by the construction of a new seawall with a height of 7 m, and the new sidewalk at the beach should be at least 4.5 m in height. At São Bruno Beach, it is proposed to increase the height of the present sidewalk from the current 4 m height to a 7 m height, with a gentle slope. The restaurant on this beach (building #C) should also be moved to a height of 7 m. The levees of the margins of the Barcarena Stream should have a height ranging between 4.8 m and 7.2 m. Moreover, it is proposed that the construction of a third bridge for pedestrians will serve as a gate for incoming sea waves. The numerical simulation considering the proposed DEM with new seawalls shows the tsunami inundates only the low-ground areas of the Caxias and São Bruno beaches, and all the seawalls are not overtopped.

These coastal protections should be part of the strategy to mitigate coastal overtopping (winter storm surges and tsunamis) not only in Caxias but also in other coastal zones. The proposed coastal protections will allow redundant protection to the beach users since it will allow a quick evacuation to safe, higher ground but also reduce the impact on buildings as well as on the road, railway, and the other two bridges.

Author Contributions: Conceptualization, A.S. and N.M.; methodology, A.S. and N.M.; calculations and field survey, A.S.; writing—original draft preparation, A.S. and N.M.; writing—review and editing, A.S. and N.M.; visualization, A.S. All authors have read and agreed to the published version of the manuscript.

Funding: This research was supported by Portuguese national funds through the Fundação para a Ciência e a Tecnologia (FCT, I.P.) under the funding "UIDB/GEO/00295/2020" and "UIDP/GEO/00295/2020".

Institutional Review Board Statement: Not applicable.

Informed Consent Statement: Not applicable.

Data Availability Statement: The data that support the findings of this study are available on request from the corresponding authors.

Conflicts of Interest: The authors declare no conflicts of interest.

References

1. Barui, I.; Bhaktaa, S.; Ghosha, K.; Shawb, R. Assessment of household vulnerability to embankment breaching in the coastal area of the Indian Sundarban. *Int. J. Disaster Risk Reduct.* **2024**, *110*, 104632. [CrossRef]
2. Cisternas, P.C.; Cifuentes, L.A.; Bronfman, N.C.; Repetto, P.B.; Castaneda, J.V. Household preparedness for multi-natural hazards in coastal communities. *Int. J. Disaster Risk Reduct.* **2024**, *109*, 104584. [CrossRef]

3. Gasc-Barbier, M.; Mateos, R.M.; Iasio, C.; Chanal, A.; Villatte, A.; Bernardie, S.; Reyes-Carmonab, C.; Sarro, R.; Martínez-Corbella, M.; Luque, J.A.; et al. Crisis exercise in the framework of coastal geohazards: Experience in the Balearic islands (Spain). *Int. J. Disaster Risk Reduct.* **2024**, *102*, 104270. [CrossRef]
4. Nageswaran, P.; Oetjen, J.; Harish, S.; Sriram, V.; Sundar, V.; Schüttrumpf, H. Buffer Blocks as Wave Energy Dissipators: Flow Depth Reduction. *J. Mar. Sci. Eng.* **2024**, *12*, 1145. [CrossRef]
5. Ty, T.V.; Duy, D.V.; Phat, L.T.; Minh, H.V.T.; Thanh, N.T.; Uyen, N.T.N.; Downes, N.K. Coastal Erosion Dynamics and Protective Measures in the Vietnamese Mekong Delta. *J. Mar. Sci. Eng.* **2024**, *12*, 1094. [CrossRef]
6. Kim, T.; Malherbe, J.N.; Shimpalee, S.; Bricker, J.D. Sub-Nappe Air Cavity Pressure and Cavity Water Depth during Caisson Breakwater Overtopping by a Tsunami. *J. Mar. Sci. Eng.* **2024**, *12*, 1135. [CrossRef]
7. Yanagisawa, H.; Koshimura, K.; Miyagi, T.; Oie, T.; Imamura, F. The Potential Role of Mitigating Effects of Mangrove Forest against the 2004 Indian Ocean Tsunami in Banda Aceh. *Proc. Coast. Eng. JSCE* **2007**, *54*, 246–250. (In Japanese) [CrossRef]
8. Yanagisawa, H.; Koshimura, S.; Miyagi, T.; Imamura, F. Tsunami damage reduction performance of a mangrove forest in Banda Aceh, Indonesia inferred from field data and a numerical model. *J. Geophys. Res. Oceans* **2010**, *115*, C06032. [CrossRef]
9. Ma, M.; Huang, W.; Jung, S.; Oslon, C.; Yin, K.; Xu, S. Evaluating Vegetation Effects on Wave Attenuation and Dune Erosion during Hurricane. *J. Mar. Sci. Eng.* **2024**, *12*, 1326. [CrossRef]
10. Barros, J.L.; Santos, P.P.; Tavares, A.O.; Freire, P.; Fortunato, A.B.; Rilo, A.; Oliveira, F.S.B.F. The complexity of the coastal zone: Definition of typologies in Portugal as a contribution to coastal disaster risk reduction and management. *Int. J. Disaster Risk Reduct.* **2023**, *86*, 103556. [CrossRef]
11. Oliveira, J.N.C.; Oliveira, F.S.B.F.; Neves, M.G.; Clavero, M.; Trigo-Teixeira, A.A. Modeling Wave Overtopping on a Seawall with XBeach, IH2VOF, and Mase Formulas. *Water* **2020**, *12*, 2526. [CrossRef]
12. Santos, D.; Abreu, T.; Bernardes, C.; Baptista, P. Coastal flood susceptibility assessment along the Northern coast of Portugal. *Int. J. Disaster Risk Reduct.* **2024**, *108*, 104556. [CrossRef]
13. Antunes, C.; Rocha, C.; Catita, C. Coastal Flood Assessment due to Sea Level Rise and Extreme Storm Events: A Case Study of the Atlantic Coast of Portugal's Mainland. *Geosciences* **2019**, *9*, 239. [CrossRef]
14. Dias, L.F.; Santos, F.D. Oeiras Municipal Climate Change Adaptation Plan. 2019; 27p. Available online: https://oeirasinterativa.oeiras.pt/dadosabertos/dataset/pmaaco-sumario-executivo (accessed on 12 September 2024). (In Portuguese).
15. Nunes, E.; Henriques, R.P.; Martins, A.S.; Silva, I.; Lima, P. Oeiras Energy and Climate Action Plan (PAECO 2030+). 2023; 37p. Available online: https://www.oeiras.pt/-/plano-de-acao-energia-e-clima-de-oeiras-paeco-2030 (accessed on 12 September 2024). (In Portuguese).
16. Santos, A.; Fernandes, J.; Mileu, N. Tsunami Hazard Assessment at Oeiras Municipality, Portugal. *J. Mar. Sci. Eng.* **2022**, *10*, 1120. [CrossRef]
17. Henriques, J. The construction of the Marginal Road–1940—When progress meets tradition. Pedra&Cal–Revista da Conservação do Património Arquitectónico e da Reabilitação do edificado, No 19, 2003; pp. 32–33. Available online: http://www.gecorpa.pt/Upload/Revistas/Rev19_Revista_Completa.pdf (accessed on 12 September 2024). (In Portuguese).
18. Marques, R. Caxias Royal Estate as an Architectural and Landscape Heritage Site in the Municipality of Oeiras. A Case Study. Master Thesis, Faculdade de Ciências Sociais e Humanas, New University of Lisbon, Lisbon, Portugal, 2020; 57p. Available online: https://run.unl.pt/bitstream/10362/111668/1/Documento%20Final%20Disserta%C3%A7%C3%A3o%20-%20vers%C3%A3o%20corrigida%20e%20melhorada%20ap%C3%B3s%20defesa%20p%C3%BAblica.pdf (accessed on 12 September 2024). (In Portuguese).
19. Agência Portuguesa do Ambiente. Despacho No: 05/VPRES/2021, de 08 de maio de 2021, ANEXO II. 2021. Available online: https://apambiente.pt/sites/default/files/_A_APA/Comunicacao/Epoca_balnear/Anexo_II_DespachoVP_CapacidadeOcupacaoPraias_2021.pdf (accessed on 12 September 2024). (In Portuguese).
20. Fernandes, J. Evacuation Strategies in Case of Tsunami on the Beaches of the Municipality of Oeiras. Master Thesis, Lisbon University, Lisboa, Portugal, 2023; 143p. Available online: https://repositorio.ulisboa.pt/handle/10451/64355 (accessed on 12 September 2024). (In Portuguese).
21. Municipality of Oeiras. Emergency Municipal Plan of Civil Protection, 2018; pp. 1–59. Available online: http://planos.prociv.pt/Documents/132131286457737300.pdf (accessed on 12 September 2022). (In Portuguese).
22. DGT–General Direction of the Territory. Official Administrative Chart of Portugal. 2023. Available online: https://www.dgterritorio.gov.pt/cartografia/cartografia-tematica/caop (accessed on 12 September 2024). (In Portuguese)
23. OpenStreetMap Contributors. OpenStreetMap Foundation. Available as Open Data Under the Open Data Commons Open Database License (ODbL). 2024. Available online: https://www.openstreetmap.org (accessed on 12 September 2024).
24. COS—Chart of the Land Use. 2018. Available online: https://www.dgterritorio.gov.pt/Carta-de-Uso-e-Ocupacao-do-Solo-para-2018/ (accessed on 12 September 2024). (In Portuguese)
25. Imamura, F. Review of tsunami simulation with a finite difference method. In *Long-Wave Runup Models*; World Scientific: Singapore, 1995; pp. 25–42.
26. Koshimura, S.; Oie, T.; Yanagisawa, H.; Imamura, F. Developing fragility functions for tsunami damage estimation using numerical model and post-tsunami data from Banda Aceh, Indonesia. *Coast. Eng. J.* **2009**, *51*, 243–273. [CrossRef]
27. Mas, E.; Suppasri, A.; Imamura, F.; Koshimura, S. Agent-based simulation of the 2011 great east Japan earthquake/tsunami evacuation: An integrated model of tsunami inundation and evacuation. *J. Nat. Disaster Sci.* **2012**, *34*, 41–57.28. [CrossRef]

28. Cheng, A.; Suppasri, A.; Heidarzadeh, M.; Adriano, B.; Ting Chua, C.; Imamura, F. Tsunami wave characteristics in Sendai Bay, Japan, following the 2016 Mw 6.9 Fukushima earthquake. *Ocean Eng.* **2023**, *287*, 115676. [CrossRef]
29. Pakoksung, K.; Suppasri, A.; Imamura, F. Preliminary modeling and analysis of the Tsunami generated by the 2024 Noto Peninsula earthquake on 1 January: Wave characteristics in the Sea of Japan. *Ocean Eng.* **2024**, *307*, 118172. [CrossRef]
30. Okada, Y. Surface deformation due to shear and tensile faults in a half space. *Bull. Seismol. Soc. Am.* **1985**, *75*, 1135–1154. [CrossRef]
31. Johnston, A. Seismic moment assessment of earthquakes in stable continental regions—III. New Madrid 1811–1812, Charleston 1886 and Lisbon 1755. *Geophys. J. Int.* **1996**, *126*, 314–344. [CrossRef]
32. Vilanova, S.; Nunes, C.; Fonseca, J. Lisbon 1755: A case of triggered onshore rupture? *Bull. Seismol. Soc. Am.* **2003**, *93*, 2056–2068. [CrossRef]
33. Grandin, R.; Borges, J.F.; Bezzeghoud, M.; Caldeira, B.; Carrilho, F. Simulations of strong ground motion in SW Iberia for the 1969 February 28 (Ms = 8.0) and the 1755 November 1 (M ~ 8.5) earthquakes—II. Strong ground motion simulations. *Geophys. J. Int.* **2007**, *171*, 807–822. [CrossRef]
34. Santos, A.; Koshimura, S.; Imamura, F. The 1755 Lisbon Tsunami: Tsunami source determination and its validation. *J. Disaster Res.* **2009**, *4*, 41–52. Available online: https://www.fujipress.jp/jdr/dr/dsstr000400010041/ (accessed on 12 September 2024). [CrossRef]
35. Santos, A.; Koshimura, S. The 1755 Lisbon Tsunami at Vila do Bispo Municipality, Portugal. *J. Disaster Res.* **2015**, *10*, 1067–1080. Available online: https://www.fujipress.jp/jdr/dr/dsstr001000061067 (accessed on 12 September 2024). [CrossRef]
36. Santos, A.; Correia, M.; Loureiro, C.; Fernandes, P.; Marques da Costa, N. The historical reconstruction of the 1755 earthquake and tsunami in downtown Lisbon, Portugal. *J. Mar. Sci. Eng.* **2019**, *7*, 208. [CrossRef]
37. Santos, A.; Rijo, D. New data of the 1755 earthquake and tsunami in Lisbon, Portugal. *Geosciences* **2022**, *12*, 286. [CrossRef]
38. Heidarzadeh, M.; Ishibe, T.; Gusman, A.; Miyazaki, H. Field surveys of tsunami runup and damage following the January 2024 Mw 7.5 Noto (Japan sea) tsunamigenic earthquake. *Ocean Eng.* **2024**, *307*, 118140. [CrossRef]
39. Maximiliano-Cordova, C.; Silva, R.; Mendoza, E.; Chávez, V.; Martínez, M.L.; Feagin, R.A. Morphological Performance of Vegetated and Non-Vegetated Coastal Dunes with Rocky and Geotextile Tube Cores under Storm Conditions. *J. Mar. Sci. Eng.* **2023**, *11*, 2061. [CrossRef]
40. Rodwell, J.; Williams, J.H.; Paulik, R. Empirical Fragility Assessment of Three-Waters and Railway Infrastructure Damaged by the 2015 Illapel Tsunami, Chile. *J. Mar. Sci. Eng.* **2023**, *11*, 1991. [CrossRef]
41. IPMA—Instituo Portugues do Mar e da Atmosfera. Boletim Climático Portugal Continental, Março 2024, 20p, ISSN 2183-1076. Available online: https://www.ipma.pt/resources.www/docs/im.publicacoes/edicoes.online/20240412/cmzpfbYAMoFvSGMxYtxE/cli_20240301_20240331_pcl_mm_co_pt.pdf (accessed on 12 September 2024). (In Portuguese).
42. Chau, T.V.; Jung, S.; Kim, M.; Na, W.-B. Analysis of the Bending Height of Flexible Marine Vegetation. *J. Mar. Sci. Eng.* **2024**, *12*, 1054. [CrossRef]
43. Blue Flag. 2024. List of Award-Winning Locations by Region. Available online: https://bandeiraazul.abaae.pt/galardoados/galardoados-2024/ (accessed on 12 September 2024). (In Portuguese).
44. SNIRH—National System of Information of Hydrological Services. 2024. Bathing Waters 2024 (Water Quality Analysis). Available online: https://snirh.apambiente.pt/snirh/_dadossintese/zbalnear/janela/par_graficos.php?code_cee=PTCQ9L&ano=2024 (accessed on 12 September 2024). (In Portuguese).
45. Yan, Q.; Li, X.; Jia, B.; Yu, X.; Luo, Y. Numerical Investigation of Tsunami Wave Force Acting on Twin Box-Girder Bridges. *J. Mar. Sci. Eng.* **2024**, *12*, 1171. [CrossRef]
46. Zheng, Y.; Kosa, K.; Sasaki, T. Tsunami damage analysis for bridges in Shizugawa area. *J. Struct. Eng.* **2013**, *59A*, 439–449. [CrossRef]

Journal of
Marine Science and Engineering

MDPI

Article

Tracing the 2018 Sulawesi Earthquake and Tsunami's Impact on Palu, Indonesia: A Remote Sensing Analysis

Youshuang Hu [1], Aggeliki Barberopoulou [2,*] and Magaly Koch [3]

1 Department of Geography, Sustainability, Community, and Urban Studies, University of Connecticut, Storrs, CT 06269, USA; youshuang.hu@uconn.edu
2 Prometheus Space Technologies 2, Kifissias Av. & D. Gounari 95, 15124 Marousi, Greece
3 Department of Earth & Environment, Boston University, Boston, MA 02215, USA; mkoch@bu.edu
* Correspondence: aggeliki@eo-prometheus.space

Abstract: The 2018 Sulawesi Earthquake and Tsunami serves as a backdrop for this work, which employs simple and straightforward remote sensing techniques to determine the extent of the destruction and indirectly evaluate the region's vulnerability to such catastrophic events. Documenting damage from tsunamis is only meaningful shortly after the disaster has occurred because governmental agencies clean up debris and start the recovery process within a few hours after the destruction has occurred, deeming impact estimates unreliable. Sentinel-2 and Maxar WorldView-3 satellite images were used to calculate well-known environmental indices to delineate the tsunami-affected areas in Palu, Indonesia. The use of NDVI, NDSI, and NDWI indices has allowed for a quantifiable measure of the changes in vegetation, soil moisture, and water bodies, providing a clear demarcation of the tsunami's impact on land cover. The final tsunami inundation map indicates that the areas most affected by the tsunami are found in the urban center, low-lying regions, and along the coast. This work charts the aftermath of one of Indonesia's recent tsunamis but may also lay the groundwork for an easy, handy, and low-cost approach to quickly identify tsunami-affected zones. While previous studies have used high-resolution remote sensing methods such as LiDAR or SAR, our study emphasizes accessibility and simplicity, making it more feasible for resource-constrained regions or rapid disaster response. The scientific novelty lies in the integration of widely used environmental indices (dNDVI, dNDWI, and dNDSI) with threshold-based Decision Tree classification to delineate tsunami-affected areas. Unlike many studies that rely on advanced or proprietary tools, we demonstrate that comparable results can be achieved with cost-effective open-source data and straightforward methodologies. Additionally, we address the challenge of differentiating tsunami impacts from other phenomena (et, liquefaction) through index-based thresholds and propose a framework that is adaptable to other vulnerable coastal regions.

Keywords: remote sensing; natural hazards; environmental indices; land cover change; vulnerability assessment; Indonesia; tsunami

Academic Editor: Deniz Velioglu Sogut

Received: 2 December 2024
Revised: 11 January 2025
Accepted: 15 January 2025
Published: 19 January 2025

Citation: Hu, Y.; Barberopoulou, A.; Koch, M. Tracing the 2018 Sulawesi Earthquake and Tsunami's Impact on Palu, Indonesia: A Remote Sensing Analysis. *J. Mar. Sci. Eng.* **2025**, *13*, 178. https://doi.org/10.3390/jmse13010178

1. Introduction

Tsunamis are a result of the sudden displacement of the water column, triggered by events such as earthquakes, volcanic eruptions, submarine landslides, or atmospheric disturbances (e.g., [1–7]). Tsunamis can be highly destructive through inundation, erosion, strong currents in ports and harbors, and scouring caused by strong forces generated during the receding of waters, leading to loss of life and property damage (e.g., [8–16]). On many occasions, tsunamis caused more damage than the earthquakes that triggered them (e.g., Chile 1960, Alaska 1964, Tohoku 2011, Banda Aceh, 2004).

Indonesia is vulnerable to earthquakes, tsunamis, and volcanic eruptions due to its geographic location at the junction of three tectonic plates (the Indo-Australian Plate, the Eurasian Plate, and the Pacific Plate) [17–19]. Because of this tectonic setting, the presence of numerous underwater volcanoes combined with a densely populated coastal zone means that a large part of the country's population is exposed to a number of coastal hazards including tsunamis as we have observed in the recent past (e.g., the 2004 Banda Aceh tsunami; [17–21]). According to the global tsunami database, a total of 77 tsunamis have been documented in Indonesia since 1608 [22]. These tsunamis have claimed the lives of more than 368,000 people in the country [22]. Among these, the catastrophic 2004 Indian Ocean tsunami alone killed 167,540 people in Indonesia and more than 220,000 people in 14 countries in Asia and Africa (Table 1) [23].

Table 1. Summary of significant life losses (>100) in Indonesia from recent tsunamis [22].

Name	Date (mm/dd/yr)	Source	Location	Earthquake Magnitude	Maximum Water Height (m)	Total Deaths
2004 Indian Ocean Tsunami	12/24/2004	Earthquake	Sumatra	9.1	50.9	227,899
2005 Nisa-Simeulue Tsunami	03/28/2005	Earthquake	Indonesia	8.6	4.2	1313
2006 Pangandaran Tsunami	07/17/2006	Earthquake	South of Java	7.7	20.9	802
2010 Mentawai Tsunami	10/25/2010	Earthquake	Sumatra	7.8	16.9	431
2018 Sulawesi Tsunami	09/20/2018	Earthquake and Volcano	Sulawesi	7.5	10.73	4340
2018 Sunda strait Tsunami	12/22/2018	Volcano and Landslide	Krakatau	*	85	437

* The 2018 Sunda Strait tsunami was not directly caused by an earthquake, so it does not have a seismic magnitude.

More recently, an M7.5 earthquake struck Central Sulawesi island, Indonesia, on 28 September 2018 at 6:03 p.m. local time (10:03 UTC). The earthquake caused severe damage to buildings and infrastructure and was responsible for more than three thousand deaths and many more people injured. The impact of this event is attributed to ground shaking, major liquefaction, landslides, and a tsunami. This was a large strike-slip faulting event at a shallow depth that generated a tsunami that caused damage through flooding, debris, ground erosion, and scouring [24–27].

Remote sensing, the technique of obtaining information about objects from a distance, has become a crucial tool in disaster management. Regarding tsunamis, satellite imagery has primarily been used for post-event damage assessment or as a source of byproducts (e.g., DEMs, friction maps) that serve as inputs to numerical models. Pioneering studies, like those following the 2004 Indian Ocean tsunami, utilized satellite imagery to map affected coastlines and assess the extent of inundation (e.g., [28–33]). These early applications relied mainly on optical imagery.

Recent technological advancements have broadened the scope of remote sensing in tsunami science. High-resolution satellite imagery, LiDAR (Light Detection and Ranging), and radar technologies have enabled more detailed and accurate assessments of tsunami inundation and impact. For instance, Chiroiu et al. [30] demonstrated the use of high-resolution satellite data for rapid damage assessment in coastal zones. Studies like those by Tang et al. [29] explored the use of satellite altimetry data to detect sea-level anomalies indicative of tsunamis. Similarly, SAR (Synthetic Aperture Radar) data, due to their ability to penetrate cloud cover and capture surface roughness, have been explored in detecting tsunami wavefronts and forecasting their impact [31]. Most of these studies have focused on the use of satellite imagery to estimate post-tsunami damage such as the extent of inundation and structural damage and evaluate the impact on natural resources (e.g., [32–38]). For example, Gokon et al. [39] highlighted the usefulness of remote sensing in understanding the extent of damage to aid effective recovery and rehabilitation efforts.

It has previously been verified that it is possible to identify tsunami-inundated areas by observing changes in spectral indices. Specifically, Yamazaki et al. [33] carried out a field survey in southern Thailand to examine areas severely affected by the Banda Aceh 2004 Boxing Day tsunami using GPS cameras and a handheld spectrometer. Three conditions of vegetation were measured: healthy (replanted), seriously affected (yellow), and dead. There were clear differences in the reflectance curves among these three conditions, with healthy plants showing a rapid increase in reflectance between the visible red (R) and near-infrared (NIR) bands. This characteristic was reduced in the unhealthy plants and was absent in the dead plants [33]. These notable changes in vegetation reflectance, offer an effective way to evaluate the impact of tsunamis on coastal vegetation.

Remote sensing techniques have also been employed to study the environmental impacts of tsunamis, such as changes in land cover, coastal erosion, and sedimentation. Research by Yamazaki et al. [33] using multispectral imagery provided insights into the long-term ecological effects of tsunamis on coastal environments. The integration of remote sensing data with Geographic Information System (GIS) platforms and modeling techniques may offer significant advancements to traditional tsunami hazard studies. This integration allows for more comprehensive spatial analysis and modeling of tsunami risks and impacts (e.g., [39]). Studies by Taubenböck et al. [40] illustrate how combining satellite data with GIS models can enhance tsunami hazard mapping and risk assessment.

Despite significant progress, challenges remain in remote sensing applications in tsunami science. These include limitations in spatial and temporal resolution, data availability, and the need for rapid data processing during emergency situations. Future research is likely to focus on integrating real-time data processing, improving the accuracy of early warning systems, and enhancing the resolution of satellite data [41]. Remote sensing can become an indispensable tool in tsunami analysis, offering valuable data for early warning, impact assessment, and recovery planning. As technology advances, its role in understanding and mitigating tsunami risks is likely to grow, providing more precise and timely information to safeguard vulnerable coastal communities.

Studies have shown that the financial impact of natural disasters is significant and rising (e.g., [42–46]). Additionally, investments in disaster risk mitigation may be economically beneficial; research suggests that every dollar spent on mitigation can save a substantial amount in post-disaster rebuilding efforts [42–47]. The costs associated with natural disaster management in Palu, which include research, disaster preparedness, and other aspects, have been substantial. In the aftermath of the 2018 earthquake and tsunami, the region faced significant challenges. While specific financial figures for research and disaster preparedness activities in Palu are not readily available, the overall impact of losses was estimated to be IDR 2.89 trillion (1 billion IDR approximately equals USD 64,000), with damage costs amounting to IDR 15.58 trillion due to the disaster [48].

This study aims to use easy, handy, and low-cost Remote Sensing techniques to quickly identify tsunami-affected zones in Palu. This is to enhance future disaster readiness by accurately mapping and assessing the extent of areas affected by the 2018 Sulawesi Earthquake and Tsunami in Palu. This should be a low-cost methodology using satellite imagery from open sources that can be simple and quick with the potential to be implemented in an early warning system or post-disaster for disaster management.

2. Data and Methods

2.1. Study Area

This study was conducted in the city of Palu, located in Central Sulawesi Province, Indonesia (Figure 1). Palu, the capital and largest city of the province spans an area of 395 km^2, situated between 0°39′ S to 0°56′ S latitude and 119°45′ E to 120°1′ E longitude (Palu, 2022). According to the 2020 Indonesian census (2021), the city has a population of 373,218, making it the third-most populous city on the island after Makassar and Manado. Palu is situated on the Palu-Koro Fault and is frequently struck by earthquakes, such as the 2018 Sulawesi earthquake [17,24,25]. The local landscape includes a narrow valley surrounded by steep mountains, with the Palu River running through the city and coastal lowlands prone to flooding and tsunamis [25]. Settlement patterns are concentrated along riverbanks, coastal zones, and valley floors, where rapid urbanization and informal housing have increased the population's exposure to natural hazards [25]. According to Indonesia's National Disaster Management Agency, the earthquake-triggered secondary natural disasters, including soil liquefaction, landslides, and tsunamis, significantly affected Palu. For example, the 2018 earthquake caused one of the largest soil liquefaction-induced mass landslides in the world (e.g., [24–27]).

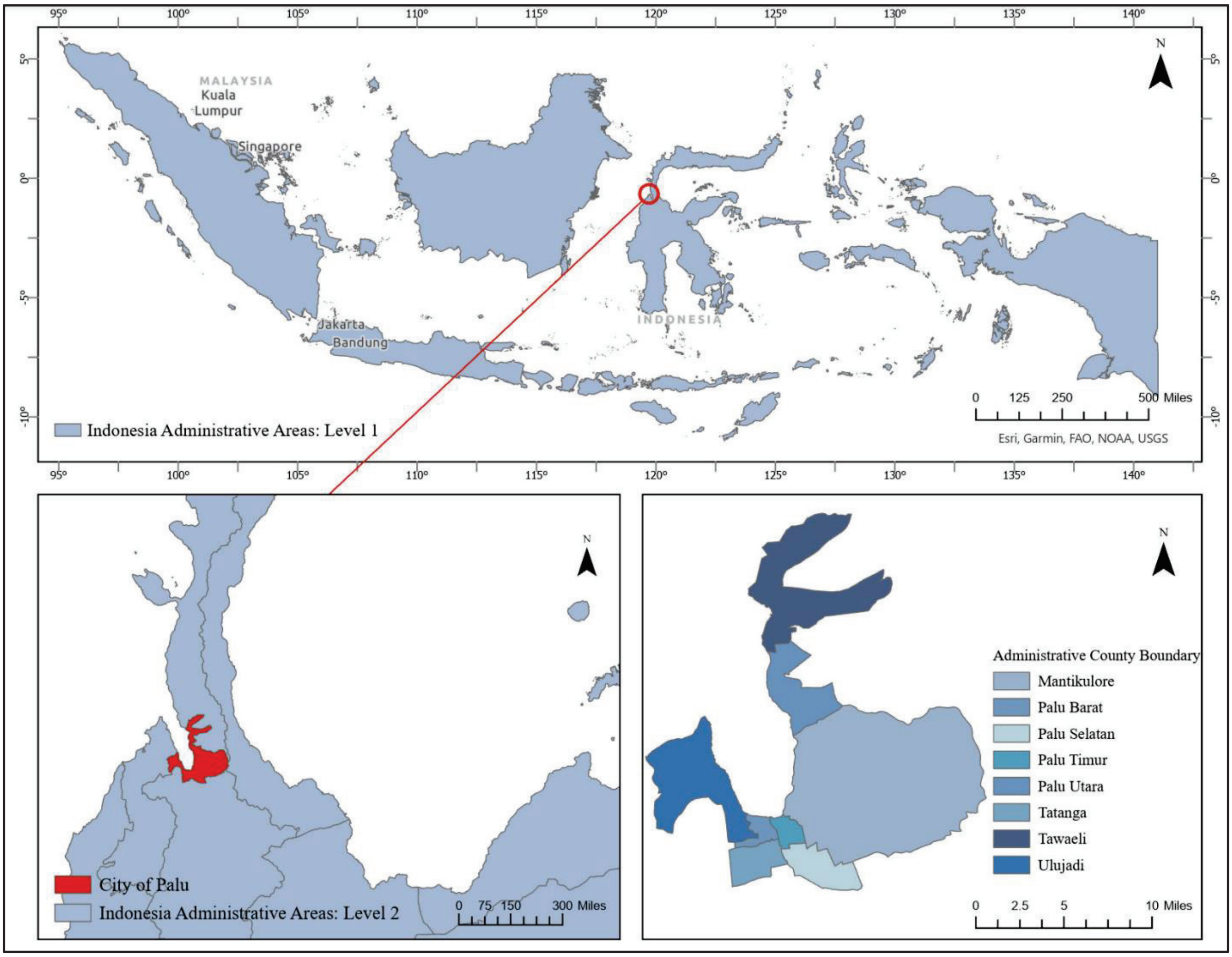

Figure 1. (**Top**) Relative location of Sulawesi Island and Palu City (red circle) in Indonesia. (**Lower left**) Study Area: Palu City (red). (**Lower right**) Palu City Administrative Division.

2.2. Data

Our primary data source is Sentinel-2 imagery, provided by the European Space Agency (ESA). The Sentinel-2 mission comprises two identical satellites, Sentinel-2A and Sentinel-2B, launched in 2015 and 2017, respectively. These satellites are equipped with a high-resolution multispectral imaging instrument capable of capturing Earth's surface at a spatial resolution of up to 10 m. The instrument collects data across 13 spectral bands, spanning from visible light to near infrared. This range supports a variety of applications, including land use and land cover mapping, vegetation monitoring, and disaster response. For this study, Sentinel-2 images from 27 September 2018 (pre-tsunami and 2 October 2018 (post-tsunami) were analyzed to assess the impact of the tsunami, as shown in Table 2.

Table 2. Sentinel-2 imagery description table.

	Satellite and Mission ID	Product Level	Spatial Resolution	Band Number	Production Baseline	Orbit Number	Acquisition Sensing Time
Pre-tsunami	Sentinel-2 S2B	Level-1C	10 m	Band 2 Band 3 Band 4 Band 8	N0206	R103	09/27/2018
	Sentinel-2 S2B	Level-1C	20 m	Band 5 Band 6 Band 7 Band 8A Band 11 Band 12	N0206	R103	09/27/2018
	Sentinel-2 S2B	Level-1C	60 m	Band 1 Band 9 Band 10	N0206	R103	09/27/2018
Post-tsunami	Sentinel-2 S2A	Level-1C	1 0m	Band 2 Band 3 Band 4 Band 8	N0206	R103	10/02/2018
	Sentinel-2 S2A	Level-1C	20 m	Band 5 Band 6 Band 7 Band 8A Band 11 Band 12	N0206	R103	10/02/2018
	Sentinel-2 S2A	Level-1C	60 m	Band 1 Band 9 Band 10	N0206	R103	10/02/2018

An additional remote sensing dataset used is Maxar WorldView-3 imagery (Table 3). Maxar Technologies, a leading space technology and intelligence company, operates a suite of commercial imaging satellites capable of capturing high-resolution images of Earth for diverse applications, including environmental monitoring, urban planning, and disaster management. Through its Open Data Program, Maxar provides free satellite imagery for disaster response, making high-quality geospatial data available to support organizations during major crisis events. This program has been activated for various disasters, including earthquakes and hurricanes, offering essential data to aid in response, management, and relief efforts.

Table 3. Maxar WorldView imagery description table.

	Satellite	Band Number	Spatial Resolution	Acquisition Sensing Time
Pre-tsunami	WorldView-3	1 Panchromatic band (450–800 nm)	0.31 m	08/17/2018
	WorldView-3	8 Visible Near Infrared (VNIR) bands	1.24 m at nadir	08/17/2018
	WorldView-3	8 Shortwave Infrared (SWIR) bands	3.70 m at nadir	08/17/2018
	WorldView-3	12 CAVIS (Clouds, Aerosols, Vapors, Ice, and Snow) bands	30 m at nadir	08/17/2018
Post-tsunami	WorldView-3	1 Panchromatic band (450–800 nm)	0.31m	10/02/2018
	WorldView-3	8 Visible Near Infrared (VNIR) bands	1.24 m at nadir	10/02/2018
	WorldView-3	8 Shortwave Infrared (SWIR) bands	3.70 m at nadir	10/02/2018
	WorldView-3	12 CAVIS (Clouds, Aerosols, Vapors, Ice, and Snow) bands	30 m at nadir	10/02/2018

2.3. Remote Sensing Workflow

The techniques presented here are meant to capture the imprint of the 2018 tsunami in the post-disaster landscape. The analysis captures all these through a combination of common tools such as indices, color composites, classification, and threshold analysis. For example, the Normalized Difference Vegetation Index (NDVI) is commonly used to estimate vegetation density, but in a post-tsunami environment, NDVI should be able to determine the extent of vegetation erosion and increased soil moisture. The hypothesis is that the density of vegetation in the study area will decrease following the tsunami, as indicated by a decline in NDVI values, while water and soil indices are expected to increase. NDVI is supplemented by the Normalized Difference Water Index (NDWI) and the Normalized Difference Soil Index (NDSI) as indicators of water presence and soil changes, therefore acting as a proxy of the tsunami impact on the ground.

The workflow outlined in Figure 2 describes the main steps in the process of using remote sensing data to identify tsunami-impacted areas. The key steps include:

1. **Acquisition of Sentinel-2 imagery** for pre- and post-tsunami periods;
2. **Data preprocessing**, which involves atmospheric correction, radiometric calibration, and resampling to convert raw Digital Number (DN) values into reflectance values;
3. **Index calculations** for NDVI, NDSI, and NDWI from reflectance data to distinguish various land and water features;
4. **Visual analysis** with Maxar Satellite Imagery to identify affected and unaffected regions by the tsunami;
5. **Comparative analysis of indices** before and after the tsunami to detect changes in vegetation, soil, and water;
6. **Threshold determination** using cumulative frequency distribution to classify impacted areas based on index variations;
7. **Output generation**, producing a map that clearly marks tsunami-affected areas, serving as a valuable tool for disaster response and assessment.

2.4. Index Formulas

This study utilizes three commonly used vegetation indices: NDVI, NDWI, and NDSI. The Normalized Difference Vegetation Index (NDVI) quantifies vegetation by measuring the contrast between near-infrared light, which vegetation reflects strongly, and red light, which it absorbs. This method is useful for assessing both the amount and health of plant growth, as higher NDVI values indicate denser vegetation. Additionally, NDVI effectively suppresses open-water features [49]. NDVI is calculated as follows:

$$NDVI = Index(NIR, RED) = \frac{(NIR - RED)}{(NIR + RED)} \tag{1}$$

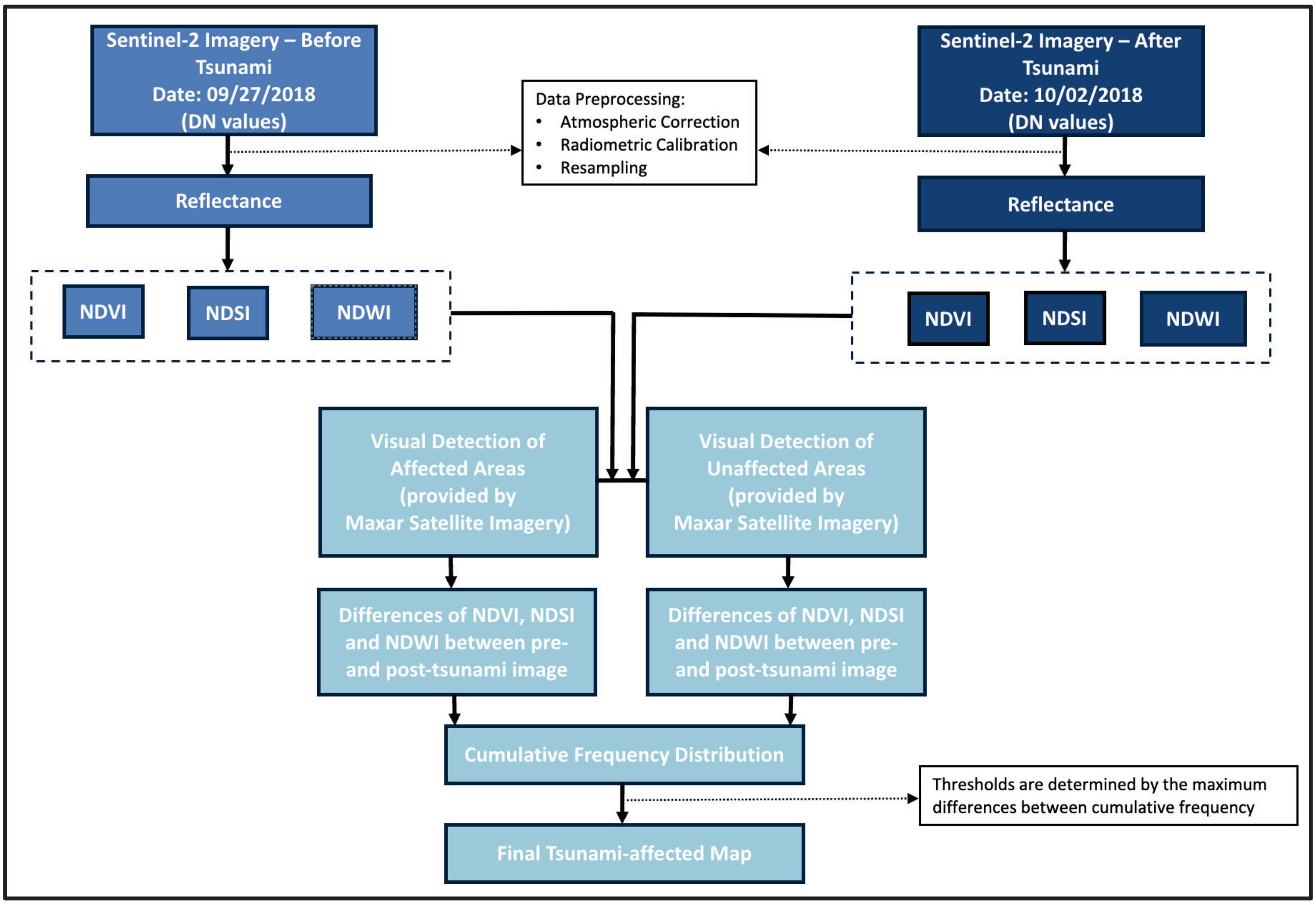

Figure 2. Remote Sensing Workflow. To derive the final tsunami-affected areas, a Decision Tree classification method was employed, integrating the dNDVI, dNDSI, and dNDWI values obtained from pre- and post-event indices.

For Sentinel-2, the vegetation index is calculated as

$$NDVI = Index(B8, B4) = \frac{(B8 - B4)}{(B8 + B4)} \tag{2}$$

where *Red* and *NIR* are the reflectance of red and near-infrared bands, respectively. The NDVI formula takes these differences into account and generates a value ranging from −1 to +1, where higher values indicate healthier and more abundant vegetation. If the NDVI equation were inverted and the green band were employed, the results would likewise be inverted, with vegetation being suppressed and open-water features enhanced [49].

The equation for Normalized Difference Water Index (NDWI) is calculated as follows:

$$NDWI = Index\ (GREEN,\ NIR) = \frac{(GREEN - NIR)}{(GREEN + NIR)} \tag{3}$$

For Sentinel-2, the water index is calculated as

$$NDWI = Index\ (B3,\ B8) = \frac{(B3 - B8)}{(B3 + B8)} \tag{4}$$

where Green and NIR refer to the reflectance values of the green and near-infrared bands, respectively. The result of this equation highlights water features with positive values, while soil and terrestrial vegetation are represented by zero or negative values. The equation for the Normalized Difference Soil Index (NDSI) [50] is as follows:

$$NDSI = Index\ (RED,\ BLUE) = \frac{(RED - BLUE)}{(RED + BLUE)} \tag{5}$$

For Sentinel-2, the soil index is calculated as

$$NDSI = Index\ (B4, B2) = \frac{(B4 - B2)}{(B4 + B2)} \tag{6}$$

In addition to the well-known indices above, other common remote sensing tools were employed to identify tsunami-impacted areas and the inundation extent such as true color composites and false color composites. False color composites use non-visible bands of the electromagnetic spectrum and map them to visible colors to highlight features that are not easily discerned in true-color imagery.

3. Results

3.1. Color Composites

A false color composite using satellite images taken after the Palu tsunami event on 2 October 2018 is used here. Specifically, Short-Wave Infrared (SWIR), Visible Near Infrared (VNIR), and Red bands were assigned to the RGB (Red, Green, Blue) color channels, respectively. The strength of the false color composites is that land cover types such as vegetation or water can appear in various colors depending on the band combination used. The goal is to enhance visualization of the different land cover types for analysis or processing. In the FCC used here, urban areas or bare ground appear in shades of purple, pink, grey, or brown while water appears in dark blue (Figure 3).

3.2. Computation of Indices

Three different vegetation indices have been used for our analysis that are further discussed next.

3.2.1. Normalized Difference Vegetation Index

NDVI values for pre- and post-tsunami imagery were calculated (Figure 4) and reclassified based on the NDVI classification criteria developed by Al-Doski et al. [51]. NDVI is used as a measure of vegetation health, with higher values indicating denser healthier vegetation. Image values were classified into three categories (Figure 4) that represent values from -1 to 0 (water, snow, and clouds), values from 0 to 0.2 (barren land, built-up areas, and rock), and vegetation from 0.2 to 1. The comparison shows little change in the water, snow, and cloud class, while there is an apparent increase in barren land along the coastline especially WNW-facing coastlines, suggesting vegetation loss and soil exposure due to the tsunami. This significant alteration within a five-day interval suggests the impact of a coastal hazard (tsunami) on the land surface.

Figure 3. False color composite after the tsunami (2018/02/10 (SWIR, VNIR, and RED as RGB bands).

Basic statistics calculated from the pre- and after-NDVI values (Table 4) also support the NDVI maps (Figure 4). Before the tsunami, the imagery showed NDVI values ranging from a minimum of −0.32 to a maximum of 0.95, with an average of 0.37. After the tsunami, both the maximum and mean NDVI values declined: the minimum NDVI fell to −0.42, the maximum to 0.88, and the mean to 0.34. These changes indicate an overall reduction in vegetation health immediately following the tsunami.

Table 4. NDVI value calculation for pre- and post-tsunami imagery.

	Min	Max	Mean	StdDev
NDVI: Pre-tsunami Imagery (2018/09/27)	−0.32	0.95	**0.37**	0.20
NDVI: Post-tsunami Imagery (2018/10/02)	−0.42	0.88	**0.34**	0.19

3.2.2. Normalized Difference Water Index

The Normalized Difference Water Index (NDWI) maps (Figure 5) illustrate the area of interest before (left) and after (right) the Palu tsunami. This index is a valuable tool for identifying water features, with values ranging from −1 to 1. Typically, non-water areas are represented within the range of −1 to 0, while water bodies correspond to values from 0 to 1. The pre-tsunami map, dated 27 September 2018, captures water bodies prior to the tsunami. Any changes (i.e., increase) to water bodies post-tsunami in the 2 October 2018 map should be attributed to the inundation associated with the tsunami. Together, these maps provide compelling visual evidence of the alterations in water extent following the disaster.

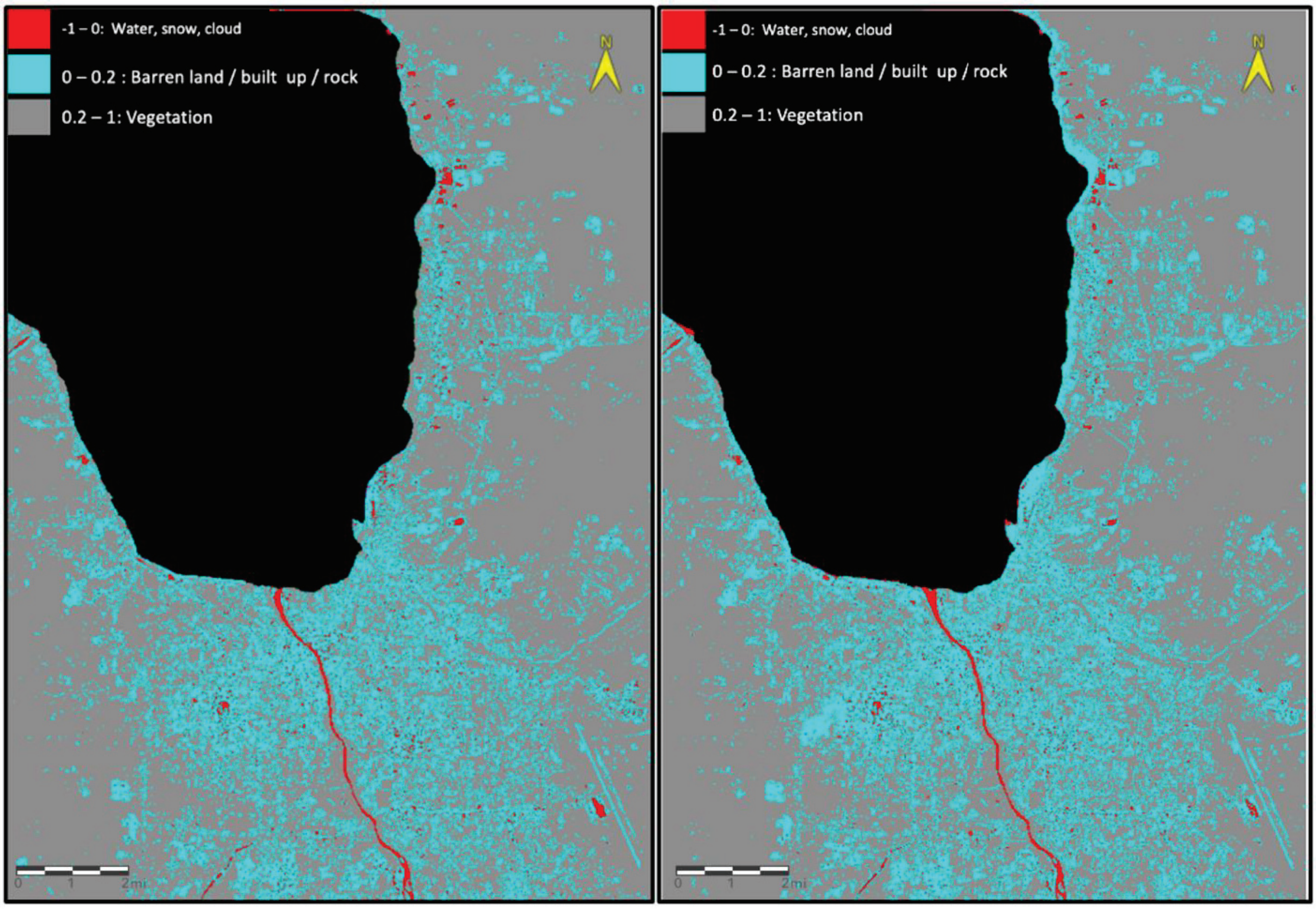

Figure 4. Reclassified NDVI for pre-tsunami (2018/09/27) (**left**) and post-tsunami imagery (2018/10/02) based on the NDVI classification criteria developed by Al-Doski et al. [51] (**right**).

Table 5 presents basic statistics summarizing the NDWI values recorded before and after the Palu tsunami. The mean NDWI value post-tsunami is slightly higher than the pre-tsunami value, suggesting a minor increase in water content; however, the difference is minimal. For a more comprehensive understanding of these changes, Figure 5 offers a visual representation of the distribution and extent of water features, effectively highlighting any changes to land cover due to the tsunami.

Table 5. NDWI value calculation for pre- and post-tsunami imagery.

	Min	Max	Mean	StdDev
NDWI: Pre-tsunami Imagery (2018/09/27)	−0.95	0.50	**−0.38**	0.17
NDWI: Post-tsunami Imagery (2018/10/02)	−0.10	0.54	**−0.37**	0.16

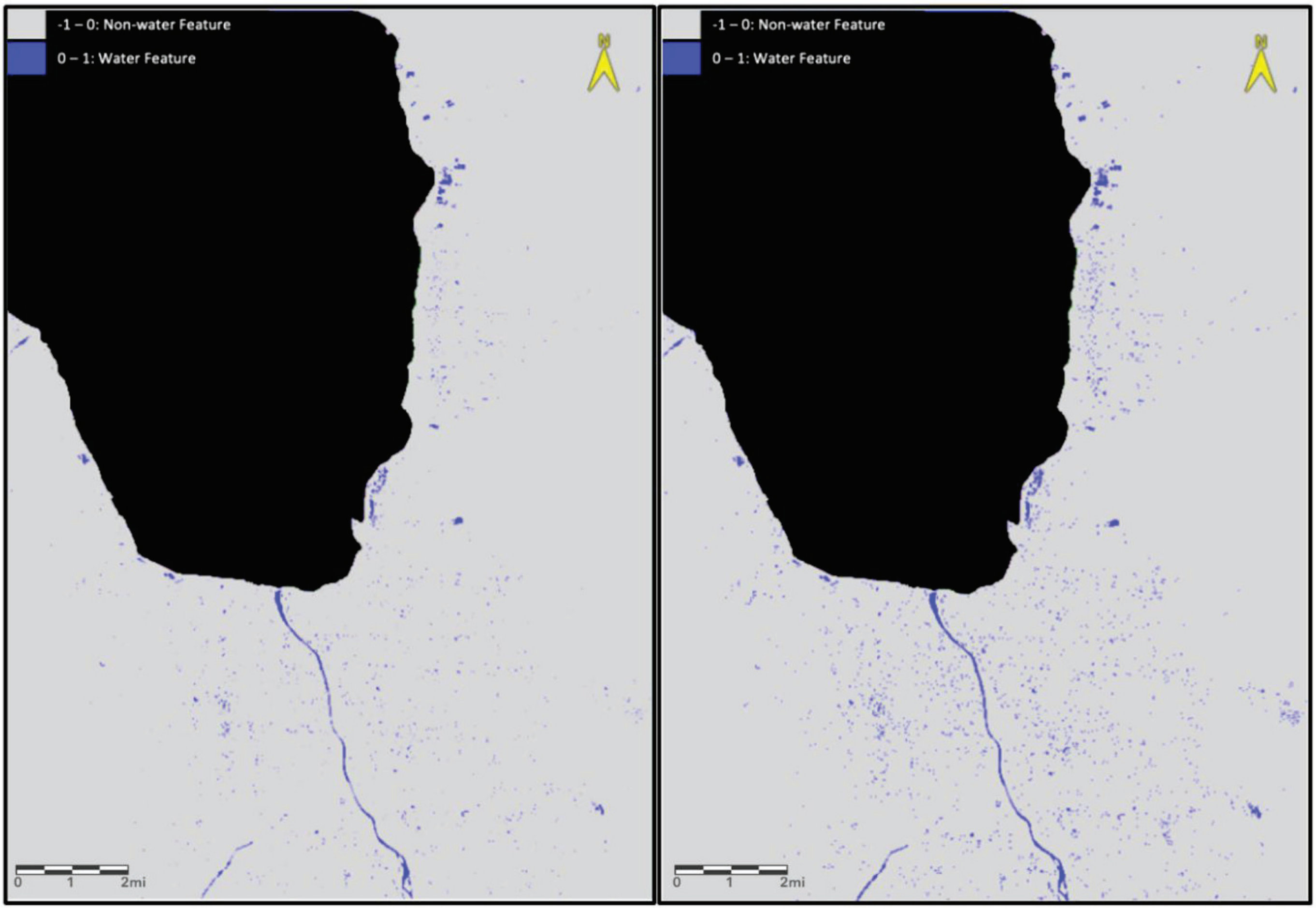

Figure 5. Reclassified NDWI for pre-tsunami (2018/09/27) (**left**) and post-tsunami imagery (2018/10/02) (**right**).

3.2.3. Normalized Difference Soil Index

Complementing the previous 2 indices, NDSI may help in identifying and interpreting changes on the ground surface due to the tsunami. As shown in Figure 6, the NDSI shows soil surface changes, and in this instance, a clear increase in soil features (yellow) is visible in the post-tsunami image (Figure 6 right). Such a change following the tsunami may be due to the removal of vegetation or other cover, revealing more of the soil surface underneath or the deposition of sediments on top of other land cover types.

Table 6 provides a summary of statistical data for NDSI from imagery captured before and after the Palu tsunami. The NDSI is used to differentiate between soil and non-soil surface features. The post-tsunami imagery shows an increase in both the maximum NDSI value and the mean NDSI value, indicating a greater presence or exposure of soil features after the event. This can be attributed to the disturbance caused by the tsunami, which may have cleared away vegetation or other surface materials, exposing the soil underneath, or the deposition of sediments manifesting as soil. NDSI shows the largest changes due to the tsunami than any other index used here. The standard deviation in the post-tsunami data is slightly lower than in the pre-tsunami data, suggesting less variability in soil exposure after the tsunami.

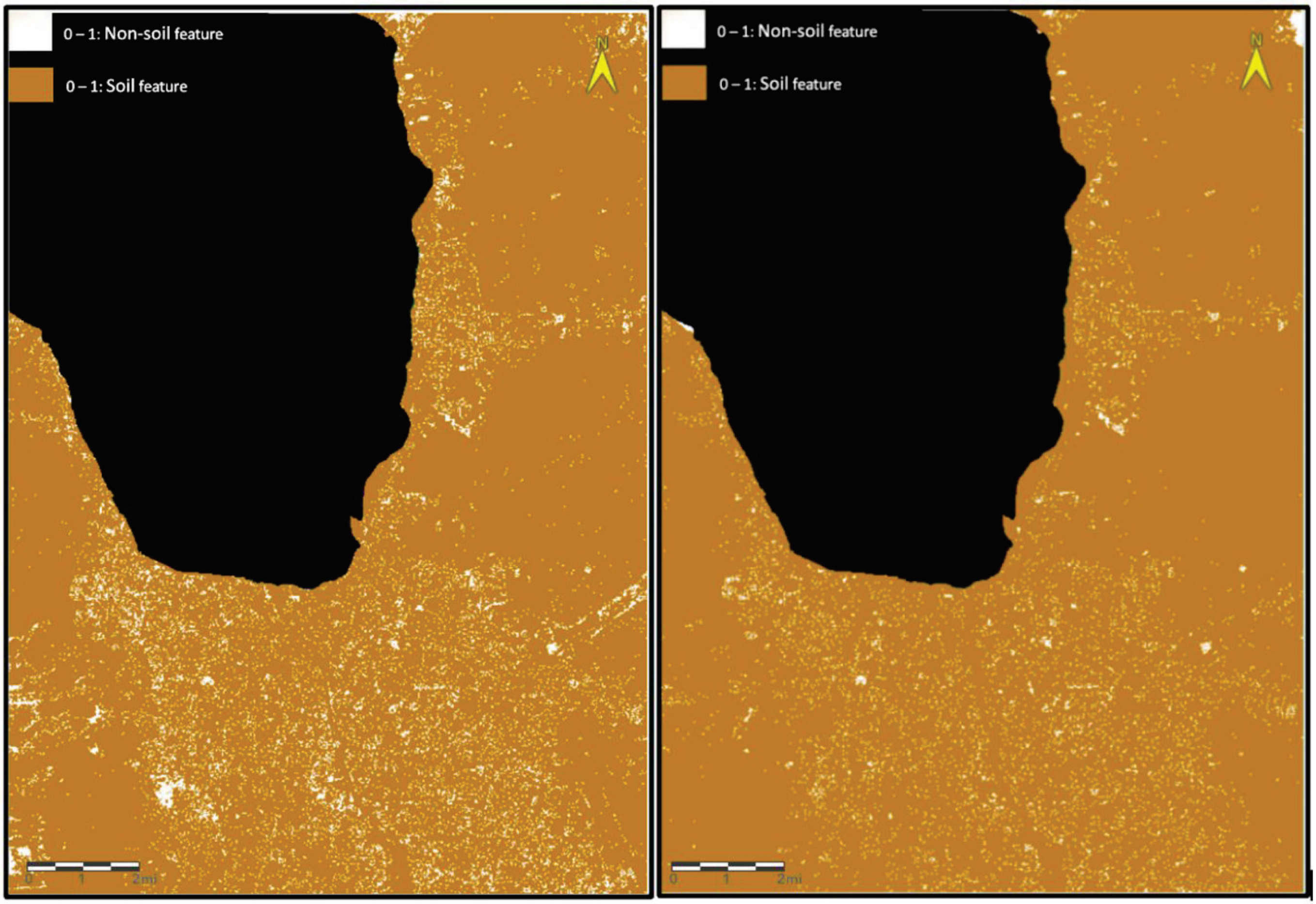

Figure 6. Reclassified NDSI for pre-tsunami (2018/09/27) (**left**) and post-tsunami imagery (2018/10/02) (**right**).

Table 6. NDSI value summary for pre- and post-tsunami imagery.

	Min	Max	Mean	StdDev
NDSI: Pre-tsunami Imagery (2018/09/27)	−0.66	0.66	**0.11**	0.08
NDSI: Post-tsunami Imagery (2018/10/02)	−0.57	0.10	**0.14**	0.08

3.3. Threshold Analysis

To obtain more precise threshold values, we concentrated on a smaller research area located in the northeast part of Palu, which was highly affected by the tsunami and had a clear boundary between the impacted and unaffected areas. By narrowing down the study area, we can conduct a more rigorous analysis to gain a better understanding of the disaster's extent and related characteristics. This approach allows us to provide more precise data for threshold analysis and mapping of the tsunami-affected regions, thereby increasing the accuracy of the results.

The NDVI, NDSI, and NDWI were calculated based on the formulas presented in Section 2.4. Typically, higher NDVI values indicate greater vegetation coverage, while higher NDSI and NDWI values indicate more soil moisture and water bodies, respectively. The most prominent changes in NDVI, NDSI, and NDWI values in tsunami-affected areas are shown in Figure 7. As seen in Figure 7, NDVI decreases (darker shade), and NDSI and NDWI increase (lighter shade) in the tsunami-affected areas. These observations are based on the effects of the tsunami, which caused vegetation to wash away or become dead/weakened, exposed the soil, and increased soil moisture. Differences in the indices between areas affected and unaffected by the tsunami are readily apparent, and these disparities can serve as reliable indicators of tsunami inundation.

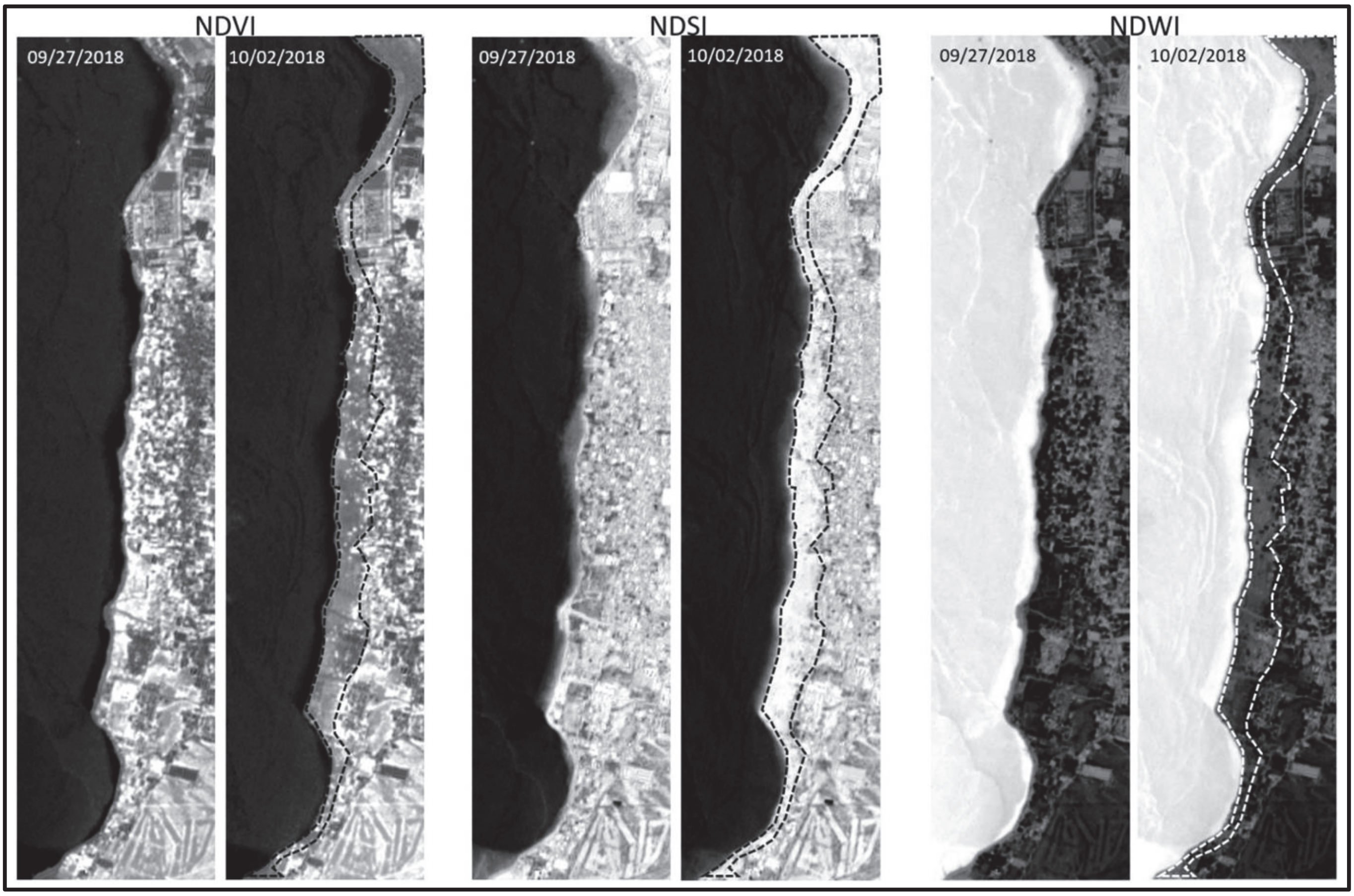

Figure 7. Computed NDVI, NDSI, and NDWI for pre-tsunami (2018/09/27) and post-tsunami (2018/10/02) for a small area of Palu. Dashed line delineates the area affected by the tsunami in the post-disaster images.

Research indicates two methodologies for setting threshold values to assess tsunami impact: using solely post-tsunami imagery or comparing both pre- and post-tsunami images [50]. The first approach is viable when pre-event images are unavailable. However, juxtaposing images from before and after an event typically yields a more accurate assessment [49,50]. This study employed the comparative method for spatial analysis of the tsunami's effects and to establish reliable threshold values.

The image taken on 27 September 2018, serves as a pre-tsunami depiction, while the one captured on 2 October 2018, serves as a post-tsunami representation (Figure 7). To further analyze the data, the distribution of index differences between affected and unaffected areas was also calculated. The resulting cumulative frequency distribution of the difference for NDVI, NDSI, and NDWI in both affected and unaffected areas is displayed in Figure 8. By identifying the maximum difference between their cumulative frequency distributions, it is feasible to establish a threshold value that can effectively distinguish the two classes (unaffected vs affected). By utilizing this approach, the calculated thresholds for NDVI, NDSI, and NDWI were found to be -0.2, 0, and 0.04, respectively. In summary, based on pre-tsunami and post-tsunami images, pixels with an NDVI (-0.2) value below the calculated threshold, and NDSI (0) and NDWI values (0.04) exceeding the determined thresholds, are classified as tsunami-affected areas.

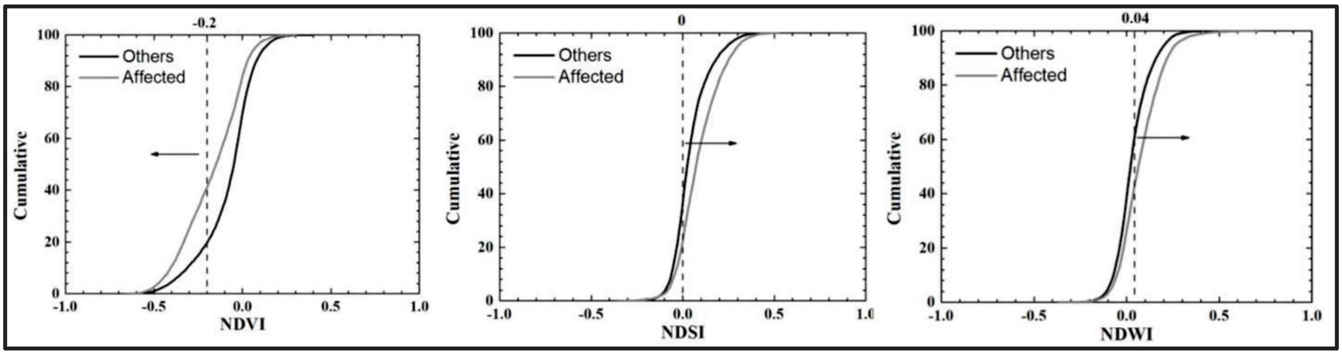

Figure 8. Cumulative frequency distribution of the differences between NDVI, NDSI, and NDWI.

Using the thresholds for the three indices (NDVI, NDSI, and NDWI), we applied these values to our research area, as illustrated in Figure 9. More specifically, as described above, pixels with an NDVI value below the calculated threshold (<−0.2) and NDSI and NDWI values exceeding the determined thresholds (>0 and >0.04) are classified as tsunami-affected areas. Illustrated in Figure 10, the entire city was impacted by the tsunami, with the tsunami-affected areas primarily concentrated along the coastal regions of Palu. Furthermore, it is important to note that Balaroa City, located in the southwest part of Palu, was also affected by soil liquefaction after the earthquake and subsequently buried (Figure 9).

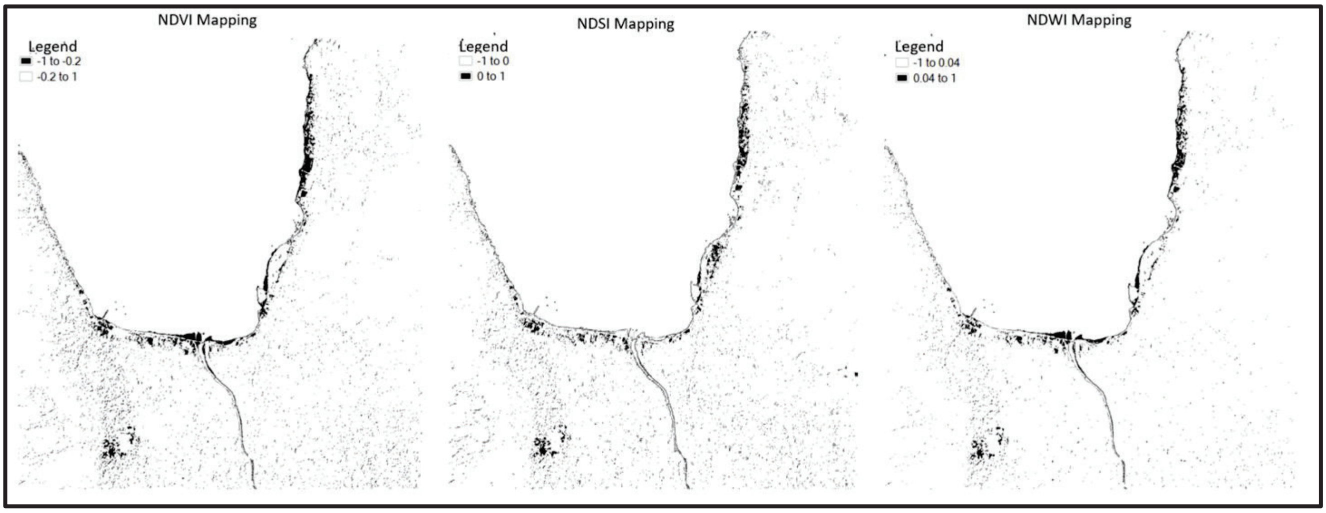

Figure 9. Mapping NDVI, NDSI, and NDWI based on the threshold values. Dark pixels indicate areas impacted by the tsunami.

To derive the final tsunami-affected areas, a Decision Tree classification method was employed, integrating the dNDVI, dNDSI, and dNDWI values obtained from pre- and post-event indices. The Decision Tree is a rule-based classification approach that uses a hierarchical structure to assign each pixel to a specific class (e.g., tsunami-affected or unaffected) based on a set of conditions. In this study, thresholds for the indices were established using cumulative frequency distribution analysis. Pixels with values below the NDVI threshold (−0.2) and above the NDSI (0) and NDWI (0.04) thresholds were classified as tsunami-affected areas.

Figure 10. Final tsunami inundation map using a Decision Tree classification method, integrating the dNDVI, dNDSI, and dNDWI values obtained from pre- and post-event indices.

This method allowed the systematic combination of the three indices to discern changes in water, soil, and vegetation caused by the tsunami. By leveraging these indices in a hierarchical decision-making framework, the Decision Tree enhanced classification accuracy, particularly in complex environments where a single index might be insufficient. Figure 10 illustrates the "cumulative" classification result, with tsunami-impacted regions marked in red predominantly concentrated along the coastal areas. However, it is evident from Figure 10 that the method also captured impacts beyond tsunami inundation, such as liquefaction, landslides, and other secondary effects triggered by the earthquake. This limitation highlights the need for additional techniques or data to refine the classification further.

4. Discussion and Conclusions

This work focused on the application of freely available and low-cost remote sensing techniques, specifically leveraging Sentinel-2 and Maxar imagery, to quickly and effectively identify tsunami-affected areas. The remote sensing techniques employed in this study were designed to capture the impacts of tsunamis on the post-disaster landscape shortly after the event and before cleanup efforts by governmental agencies could alter the ground conditions. While previous studies have used high-resolution remote sensing methods such as LiDAR or SAR, our study emphasized accessibility and simplicity, making it more feasible for resource-constrained regions or rapid disaster response.

The results have successfully demonstrated the application of straightforward remote sensing techniques in mapping tsunami-affected areas in Palu, Indonesia, highlighting the capabilities of Sentinel-2 imagery in disaster assessment. The use of dNDVI, dNDSI, and dNDWI indices has allowed for a quantifiable measure of the changes in vegetation, soil moisture, and water bodies, providing a clear demarcation of the tsunami's impact. This approach offers an understanding of disaster impacts, informing better preparedness and response strategies with easy-to-implement tools that are widely used.

The scientific novelty lies in the integration of widely used environmental indices (dNDVI, dNDWI, and dNDSI) with threshold-based Decision Tree classification to delineate tsunami-affected areas. Unlike many studies that rely on advanced or proprietary tools, we demonstrated that comparable results can be achieved with cost-effective open-source data and straightforward methodologies. Additionally, we addressed the challenge of differentiating tsunami impacts from other phenomena (e.g., liquefaction) through index-based thresholds and proposed a framework that is adaptable to other vulnerable coastal regions.

The final tsunami inundation map indicates that areas most affected by the tsunami are located in the urban center, low-lying regions, and along the coast. The tsunami inundation map appears to capture more than tsunami-affected areas such as liquefaction. Other methods (e.g., GIS) such as the Analytic Hierarchy Process (AHP) method, although somewhat subjective, can provide validation against the tsunami inundation map, confirming the importance of topography, slope, and land use as critical factors in tsunami inundation [52–54] but also in helping to differentiate between tsunamis and other areas impacted by different phenomena (liquefaction). This synthesis of various data types can provide a more nuanced understanding of vulnerability and impact.

The effective use of remote sensing in this study underscores their potential in disaster management. Policies should support the investment in and utilization of these technologies for better disaster preparedness, risk assessment, and recovery planning. The study's findings can be used in urban planning that integrates resilience against natural disasters. Tools such as those used here can be implemented by international agencies that deal with disaster assessment and management such as Copernicus Emergency Management Services (https://emergency.copernicus.eu/) or local agencies for better planning and preparedness. The implementation characteristics depend on the needs of the agency.

While this study has provided significant insights, several limitations must be acknowledged. Firstly, the spatial resolution of remote sensing data, while sufficient for broad assessments, may not capture the finer details necessary for micro-scale planning. This limitation points to the need for higher-resolution data or supplementary ground truthing for more detailed analysis. Secondly, the remote sensing data for this study, with only a five-day interval between pre- and post-tsunami images, presents a unique dataset. Such timely data acquisition is not always feasible, as obtaining simultaneous pre- and post-event images is often not possible in many scenarios.

The impact captured in satellite images may not be easily differentiated from other secondary effects such as liquefaction, which coincided the Palu tsunami. One of the challenges of delineating the tsunami impact is the differentiation of the tsunami signature to other secondary or seasonal effects. In our case, we were able to overcome the contamination of results by seasonal vegetation changes and pre-existing environmental conditions because the remote sensing images used in this study were acquired within a time span of no more than five days before and after the tsunami, eliminating concerns about seasonal changes. Further improving tools used here in this direction would be highly beneficial. Additionally, the study's focus on Palu may limit the generalizability of findings to other regions with different geographical and socio-economic contexts. Future research could address these constraints by incorporating a broader range of case studies and employing more sophisticated remote sensing technologies as they become available.

Author Contributions: Conceptualization Y.H., A.B. and M.K.; methodology, Y.H. and M.K.; software, Y.H.; validation, Y.H.; formal analysis, Y.H.; investigation, Y.H., A.B. and M.K.; resources, Y.H., A.B. and M.K.; data curation, Y.H. writing—original draft preparation, Y.H. and A.B.; writing—review and editing, Y.H., A.B. and M.K.; visualization, Y.H.; supervision, A.B. and M.K.; project administration, A.B. and M.K. All authors have read and agreed to the published version of the manuscript.

Funding: This research received no external funding.

Institutional Review Board Statement: The current analysis did not constitute human subject research and was exempt from further IRB review.

Informed Consent Statement: Not applicable.

Data Availability Statement: All the data used in this study are available online.

Acknowledgments: The work was completed while at Tufts University.

Conflicts of Interest: Author Aggeliki Barberopoulou was employed by the company Prometheus Space Technologies 2. The remaining authors declare that the research was conducted in the absence of any commercial or financial relationships that could be construed as a potential conflict of interest.

References

1. Koshimura, S.; Moya, L.; Mas, E.; Bai, Y. Tsunami Damage Detection with Remote Sensing: A Review. *Geosciences* **2020**, *10*, 177. [CrossRef]
2. Shuto, N.; Fujima, K. A Short History of Tsunami Research and Countermeasures in Japan. *Proc. Jpn. Acad. Ser. B Phys. Biol. Sci.* **2009**, *85*, 267–275. [CrossRef]
3. Kanamori, H. Mechanism of Tsunami Earthquakes. *Phys. Earth Planet. Inter.* **1972**, *6*, 346–359. [CrossRef]
4. Abe, K. Tsunami and Mechanism of Great Earthquakes. *Phys. Earth Planet. Inter.* **1973**, *7*, 193–203. [CrossRef]
5. Röbke, B.R.; Vött, A. The Tsunami Phenomenon. *Prog. Oceanogr.* **2017**, *159*, 296–312. [CrossRef]
6. Harbitz, C.B.; Løvholt, F.; Pedersen, G.; Masson, D.G. Mechanisms of Tsunami Generation by Submarine Landslides: A Short Review. *Nor. J. Geol.* **2006**, *86*, 255–264.
7. Papadopoulos, G.A.; Gràcia, E.; Urgeles, R.; Sallares, V.; De Martini, P.M.; Pantosti, D.; González, M.; Yalciner, A.C.; Mascle, J.; Sakellariou, D.; et al. Historical and Pre-Historical Tsunamis in the Mediterranean and Its Connected Seas: Geological Signatures, Generation Mechanisms and Coastal Impacts. *Mar. Geol.* **2014**, *354*, 81–109. [CrossRef]
8. Jaumé, S.C.; Sykes, L.R. Evolving Towards a Critical Point: A Review of Accelerating Seismic Moment/Energy Release Prior to Large and Great Earthquakes. In *Seismicity Patterns, Their Statistical Significance and Physical Meaning*; Wyss, M., Shimazaki, K., Ito, A., Eds.; Birkhäuser: Basel, Switzerland, 1999; pp. 279–305.
9. van Rijsingen, E.; Lallemand, S.; Peyret, M.; Arcay, D.; Heuret, A.; Funiciello, F.; Corbi, F. How Subduction Interface Roughness Influences the Occurrence of Large Interplate Earthquakes. *Geochem. Geophys. Geosyst.* **2018**, *19*, 2342–2370. [CrossRef]
10. Han, S.-C.; Sauber, J.; Luthcke, S. Regional Gravity Decrease After the 2010 Maule (Chile) Earthquake Indicates Large-Scale Mass Redistribution. *Geophys. Res. Lett.* **2010**, *37*, L23307. [CrossRef]
11. Baba, T.; Cummins, P.R. Contiguous Rupture Areas of Two Nankai Trough Earthquakes Revealed by High-Resolution Tsunami Waveform Inversion. *Geophys. Res. Lett.* **2005**, *32*, L08305. [CrossRef]
12. Thiel, C.C., Jr.; Zsutty, T.C. Earthquake Characteristics and Damage Statistics. *Earthq. Spectra* **1987**, *3*, 747–792. [CrossRef]
13. Wesnousky, S.G. Displacement and Geometrical Characteristics of Earthquake Surface Ruptures: Issues and Implications for Seismic-Hazard Analysis and the Process of Earthquake Rupture. *Bull. Seismol. Soc. Am.* **2008**, *98*, 1609–1632. [CrossRef]
14. Oth, A. On the Characteristics of Earthquake Stress Release Variations in Japan. *Earth Planet. Sci. Lett.* **2013**, *377–378*, 132–141. [CrossRef]
15. Van Dorn, W.G. Some Tsunami Characteristics Deducible from Tide Records. *J. Phys. Oceanogr.* **1984**, *14*, 353–363. [CrossRef]
16. Løvholt, F.; Pedersen, G.; Harbitz, C.B.; Glimsdal, S.; Kim, J. On the Characteristics of Landslide Tsunamis. *Philos. Trans. R. Soc. A Math. Phys. Eng. Sci.* **2015**, *373*, 20140376. [CrossRef]
17. Reid, J.A.; Mooney, W.D. Tsunami Occurrence 1900–2020: A Global Review, with Examples from Indonesia. *Pure Appl. Geophys.* **2023**, *180*, 1549–1571. [CrossRef]

18. Muhari, A.; Diposaptono, S.; Imamura, F. Toward an Integrated Tsunami Disaster Mitigation: Lessons Learned from Previous Tsunami Events in Indonesia. *J. Nat. Disaster Sci.* **2007**, *29*, 13–19. [CrossRef]
19. Esteban, M.; Tsimopoulou, V.; Mikami, T.; Yun, N.Y.; Suppasri, A.; Shibayama, T. Recent Tsunamis Events and Preparedness: Development of Tsunami Awareness in Indonesia, Chile and Japan. *Int. J. Disaster Risk Reduct.* **2013**, *5*, 84–97. [CrossRef]
20. Mutaqin, B.W.; Lavigne, F.; Hadmoko, D.S.; Ngalawani, M.N. Volcanic eruption-induced tsunami in Indonesia: A review. *IOP Conf. Ser. Earth Environ. Sci.* **2019**, *256*, 012023. [CrossRef]
21. Supriatna, J. *Konservasi Biodiversitas: Teori dan Praktik di Indonesia*; Yayasan Pustaka Obor Indonesia: Jakarta, Indonesia, 2018.
22. National Geophysical Data Center/World Data Service. NCEI/WDS Global Historical Tsunami Database. NOAA National Centers for Environmental Information. Available online: https://data.noaa.gov/metaview/page?xml=NOAA/NESDIS/NGDC/MGG/Hazards/iso/xml/G02151.xml&view=getDataView (accessed on 16 January 2024). [CrossRef]
23. Intergovernmental Oceanographic Commission (IOC) of UNESCO. Tsunami Programme—Pacific. Available online: https://tsunami.ioc.unesco.org/en/pacific (accessed on 16 January 2024).
24. Valkaniotis, S.; Ganas, A.; Tsironi, V.; Barberopoulou, A. *A Preliminary Report on the M7.5 Palu Earthquake Co-Seismic Ruptures and Landslides Using Image Correlation Techniques on Optical Satellite Data*; Zenodo: Genève, Switzerland, 2018. [CrossRef]
25. Paulik, R.; Gusman, A.; Williams, J.H.; Pratama, G.M.; Lin, S.-L.; Prawirabhakti, A.; Sulendra, K.; Zachari, M.Y.; Fortuna, Z.E.D.; Layuk, N.B.P.; et al. Tsunami hazard and built environment damage observations from Palu City after the September 28, 2018 Sulawesi earthquake and tsunami. *Pure Appl. Geophys.* **2019**, *176*, 3305–3321. [CrossRef]
26. Rahardjo, P.P. Study on the phenomena of liquefaction-induced massive landslides in 28 September 2018 Palu-Donggala earthquake. In *Understanding and Reducing Landslide Disaster Risk: Volume 5 Catastrophic Landslides and Frontiers of Landslide Science*, 5th ed.; Elsevier: London, UK, 2021; pp. 25–48.
27. Omira, R.; Dogan, G.G.; Hidayat, R.; Husrin, S.; Prasetya, G.; Annunziato, A.; Proietti, C.; Probst, P.; Paparo, M.A.; Wronna, M.; et al. The September 28th, 2018, tsunami in Palu-Sulawesi, Indonesia: A post-event field survey. *Pure Appl. Geophys.* **2019**, *176*, 1379–1395. [CrossRef]
28. Ramírez-Herrera, M.T.; Navarrete-Pacheco, J.A. Satellite data for a rapid assessment of tsunami inundation areas after the 2011 Tohoku tsunami. *Pure Appl. Geophys.* **2013**, *170*, 1067–1080. [CrossRef]
29. Tang, L.; Titov, V.; Chamberlin, C. Assessment of potential tsunami impact for Southern California, USA using satellite altimetry data. *Nat. Hazards* **2016**, *82*, 359–370.
30. Chiroiu, L.; André, C.; Rekacewicz, P. High-resolution satellite imagery in coastal disaster management: Assessing the 2004 Tsunami impact. *Disaster Prevention and Management* **2018**, *27*, 578–590.
31. Liu, P.L.; Lynett, P.; Fernando, H. Observation of the 2011 Tohoku tsunami using satellite SAR data. *Remote Sens. Environ.* **2015**, *159*, 202–215.
32. Sepúlveda, I.; Tozer, B.; Haase, J.S.; Liu, P.L.F.; Grigoriu, M. Modeling uncertainties of bathymetry predicted with satellite altimetry data and application to tsunami hazard assessments. *J. Geophys. Res. Solid Earth* **2020**, *125*, e2020JB019735. [CrossRef]
33. Yamazaki, F.; Matsuoka, M.; Warnitchai, P.; Polngam, S.; Ghosh, S. Tsunami reconnaissance survey in Thailand using satellite images and GPS. *Asian J. Geoinform.* **2005**, *5*, 53–61.
34. Paris, R.; Lavigne, F.; Wassmer, P.; Sartohadi, J. Coastal sedimentation associated with the December 26, 2004 tsunami in Lhok Nga, west Banda Aceh (Sumatra, Indonesia). *Mar. Geol.* **2007**, *238*, 93–106. [CrossRef]
35. Lavigne, F.; Paris, R.; Grancher, D.; Wassmer, P.; Brunstein, D.; Vautier, F.; Flohic, F.; De Coster, B.; Gunawan, T.; Gomez, C.; et al. Reconstruction of tsunami inland propagation on December 26, 2004, in Banda Aceh, Indonesia, through field investigations. *Pure Appl. Geophys.* **2009**, *166*, 259–281. [CrossRef]
36. Borrero, J.C. Field survey of northern Sumatra and Banda Aceh, Indonesia after the tsunami and earthquake of 26 December 2004. *Seismol. Res. Lett.* **2005**, *76*, 312–320. [CrossRef]
37. Koshimura, S.; Gokon, H.; Fukuoka, T.; Hayashi, S. Remote sensing and GIS-based approach to identify the impact of the 2011 Tohoku Earthquake tsunami disaster. *J. Jpn. Assoc. Earthq. Eng.* **2012**, *12*, 50–62.
38. Sambah, A.B.; Miura, F. Spatial data analysis and remote sensing for observing tsunami-inundated areas. *Int. J. Remote Sens.* **2016**, *37*, 2047–2065. [CrossRef]
39. Gokon, H.; Koshimura, S.; Matsuoka, M. Remote sensing-based assessment of tsunami vulnerability and risk in coastal areas. *Int. J. Disaster Risk Reduct.* **2017**, *22*, 487–501.
40. Taubenböck, H.; Post, J.; Kiefl, R.; Roth, A.; Ismail, F.; Strunz, G.; Dech, S. Risk and vulnerability assessment to tsunami hazard using very high resolution satellite data—The case study of Padang, Indonesia. *Nat. Hazards Earth Syst. Sci.* **2008**, *8*, 409–420. [CrossRef]
41. Li, X. Real-Time High-Rate GNSS Techniques for Earthquake Monitoring and Early Warning. *Remote Sens.* **2015**, *7*, 12346–12364.
42. National Oceanic and Atmospheric Administration. 2021 U.S. Billion-Dollar Weather and Climate Disasters: A Historical Perspective. *Climate.gov*. 2021. Available online: https://www.climate.gov/news-features/blogs/beyond-data/2021-us-billion-dollar-weather-and-climate-disasters-historical (accessed on 22 December 2024).

43. Kreimer, A. Social and Economic Impacts of Natural Disasters. *Int. Geol. Rev.* **2001**, *43*, 401–405. [CrossRef]
44. Keerthiratne, S.; Tol, R.S. Impact of Natural Disasters on Financial Development. *Econ. Disasters Clim. Chang.* **2017**, *1*, 33–54. [CrossRef]
45. Chang, C.P.; Zhang, L.W. Do Natural Disasters Increase Financial Risks? An Empirical Analysis. *Bull. Monet. Econ. Bank.* **2020**, *23*, 61–86.
46. Bhola, V.; Hertelendy, A.; Hart, A.; Adnan, S.B.; Ciottone, G. Escalating costs of billion-dollar disasters in the US: Climate change necessitates disaster risk reduction. *J. Clim. Chang. Health* **2023**, *10*, 100201. [CrossRef]
47. Samad, M.A.; Ali, M.N.; Khairil, M. Indonesian Disaster Governance: Public Policy and Social Economic Impact. *Elem. Educ. Online* **2021**, *20*, 73–88.
48. Damarjati, D. Management Earthquake and Tsunami Disaster in Palu, Indonesia. *IJSSHR* **2022**, *5*. 284-288. Available online: https://ijsshr.in/v5i1/38.php (accessed on 22 December 2024).
49. McFeeters, S.K. The use of the Normalized Difference Water Index (NDWI) in the delineation of open water features. *Int. J. Remote Sens.* **1996**, *17*, 1425–1432. [CrossRef]
50. Kouchi, K.I.; Yamazaki, F. Characteristics of tsunami-affected areas in moderate resolution satellite images. *IEEE Trans. Geosci. Remote Sens.* **2007**, *45*, 1650–1657. [CrossRef]
51. Al-Doski, J.; Mansor, S.B.; Shafri, H.Z.M. NDVI differencing and post-classification to detect vegetation changes in Halabja City, Iraq. *IOSR J. Appl. Geol. Geophys.* **2013**, *1*, 1–10. [CrossRef]
52. Banai, R. Fuzziness in geographic information systems: Contributions from the analytic hierarchy process. *Int. J. Geogr. Inf. Syst.* **1993**, *7*, 315–329. [CrossRef]
53. Dyer, J.S. Remarks on the analytic hierarchy process. *Manag. Sci.* **1990**, *36*, 249–258. [CrossRef]
54. Saaty, T.L. Decision making with the analytic hierarchy process. *Int. J. Serv. Sci.* **2008**, *1*, 83–98. [CrossRef]

Journal of
Marine Science and Engineering

MDPI

Article

Structural Failure Modes of Single-Story Timber Houses Under Tsunami Loads Using ASCE 7'S Energy Grade Line Analysis

Darko Otey [1], Juan Carlos Vielma [1,*] and Patricio Winckler [2,3,4,*]

1 Escuela de Ingeniería Civil, Pontificia Universidad Católica de Valparaíso, Brasil Ave. 2950, Valparaíso 2340025, Chile; darko.otey.m@mail.pucv.cl
2 Escuela de Ingeniería Oceánica, Universidad de Valparaíso, Valparaíso 2362844, Chile
3 National Research Center for Integrated Natural Disaster Management (CIGIDEN), Vicuña Mackenna 4860, Santiago de Chile 7820436, Chile
4 Centro de Observación Marino para Estudios de Riesgos del Ambiente Costero (COSTAR), Valparaíso 2362844, Chile
* Correspondence: juan.vielma@pucv.cl (J.C.V.); patricio.winckler@uv.cl (P.W.)

Abstract: The structural response of single-story timber houses subjected to the 27 February 2010 Chile tsunami is studied in San Juan Bautista, an island town located nearly 600 km westward from the earthquake's rupture source, in the Pacific Ocean. The ASCE 7-22 energy grade line analysis (EGLA) is used to calculate flow depths and velocities as functions of the topography and recorded runup. To understand the structural response along the topography, reactions and displacements are computed at six positions every 50 m from the coastline. Houses are modeled using the Robot software, considering dead and live loads cases under the Load and Resistance Factor Design (LRFD) philosophy. The results show that houses located near the coastline experience severe displacements and collapse due to a combination of hydrodynamic forces, drag and buoyancy, which significantly reduces the efficiency of the foundations' anchorage. Structures far from the coastline are less exposed to reduced velocities, resulting in decreased displacements, structural demand and a tendency to float. Finally, the methodology is validated by applying a nonlinear analysis of the structures subjected to tsunami loads at the different positions considered in this study. Despite their seismic resistance, lightweight timber houses are shown to not be suitable for areas prone to tsunamis. Tsunami-resilient design should therefore consider heavier and more rigid materials in flooding areas and the relocation of lightweight structures in safe zones.

Keywords: tsunami; energy grade line analysis; ASCE 7-22; nonlinear analysis; 27 February 2010 Chile earthquake

Academic Editor: Deniz Velioglu Sogut

Received: 6 February 2025
Revised: 24 February 2025
Accepted: 25 February 2025
Published: 28 February 2025

Citation: Otey, D.; Vielma, J.C.; Winckler, P. Structural Failure Modes of Single-Story Timber Houses Under Tsunami Loads Using ASCE 7'S Energy Grade Line Analysis. *J. Mar. Sci. Eng.* **2025**, *13*, 484. https://doi.org/10.3390/jmse13030484

1. Introduction

Tsunamis have posed persistent threats throughout human history, causing devastating material and human losses. While tsunamis can be triggered by several phenomena, their most significant source are large megathrust earthquakes such as those in the Indian Ocean (2004), Chile (2010) and Japan (2011). The increasing exposure of coastal settlements to these events highlights the need to study their effects on infrastructure [1,2] to ensure structural integrity and facilitate evacuation. Various design codes have been developed to design tsunami resilient structures, with a particular emphasis on reinforced concrete and structural steel buildings [3–5]. However, the behavior of smaller, lightweight residential buildings near potential tsunami inundation zones has been overlooked.

1.1. Impacts of Tsunamis on Buildings

Tsunami impacts on coastal structures have been well-documented following the large megathrust earthquakes that occurred in the 20th century. For example, Ghobarah et al. [6] conducted a detailed analysis of the impact of the 2004 Indian Ocean tsunami on buildings, bridges and infrastructure in Thailand and Indonesia. Similarly, Fritz et al. [7], Robertson et al. [8] and Zareian et al. [9] documented the extensive damage to residential and industrial facilities following the 2010 Maule earthquake and tsunami, emphasizing the need for robust design and construction practices to mitigate future risks. In addition, Jayaratne et al. [10] identified key failure mechanisms and proposed a validated model for predicting scour depth in coastal structures impacted by the 2011 Tohoku tsunami in Japan, while Koshimura et al. [11] focused on tsunami impact on structures for the same event.

Several studies have addressed the response of structures affected by tsunamis, focusing on different aspects of the phenomena; some have highlighted the role of the environment (e.g., topography and location) on the impact on buildings [12,13] while others have noted that the urban configuration may either channel the flow, thus increasing speeds, or reduce the impact in presence of robust structures on the front line [14]. It has been noted that typical timber and masonry housing structures experience significant damage under moderate flows, with high chances of collapse for depths above 2 m [12,13], while reinforced concrete and steel structures are more resilient [13,15]. Overall, the structural damage depends largely on the material, the suitability of the design [15] and the year of construction [16]. As preventive measures against structural failure, a series of recommendations focused on reinforced concrete structures have been offered [15].

Experimental studies have significantly advanced the understanding of tsunami forces and their impact on structures. For example, Kihara et al. [17,18] conducted large-scale experiments on concrete vertical walls, identifying critical response characteristics under tsunami wave pressures and debris impacts. Similarly, Naito et al. [19,20] explored the effects of shipping containers on coastal structures, highlighting the need for site-specific assessments of debris impact potential. The importance of these findings is further emphasized by Robertson et al. [8], who provided valuable insights into the hydrodynamic loading required to cause structural failures during tsunamis.

1.2. Methods Used to Compute the Structural Response of Buildings

Recent advancements in tsunami-resilient design standards have significantly contributed to enhancing the structural reliability of coastal infrastructure. Existing methodologies for structural analysis in the context of tsunamis range from complex numerical models to physical models. Linton et al. [21], for example, assessed the hydrodynamic conditions and structural response of several full-scale light-frame wood walls subjected to tsunamis using the Large Wave Flume of the NEES Tsunami Facility at Oregon State University. Alternatively, Krautwald et al. [22] challenged the common assumption that buildings remain rigid during hydrodynamic loading by testing the deformation of an idealized light-frame timber structure at the Large Wave Flume of the Coastal Research Center in Hannover.

Fragility curves, which describe the probability of structural failure using empirical data, have been widely used. For instance, Suppasri et al. [23] developed fragility curves based on data from 250,000 buildings affected by the 2011 Japan tsunami. However, while fragility curves provide valuable insights, they are often generalized and empirical. On the other hand, the nonlinear static pushover analysis offers a more precise method for analyzing specific structures but requires significant computational resources, making it impractical for widespread application. Examples include the publications by Baiguera et al. [24] and Aegerter et al. [25], which performed pushover analysis on structures using

OpenSees [26] and ETABS [27] software, respectively. Another alternative for structural analysis is the energy grade line analysis (EGLA) method of the ASCE 7-22 [28], which provides a simplified yet useful tool for designing structures to withstand tsunami loads.

Among the methodologies used to assess the structural response to tsunamis, the energy grade line analysis (EGLA) has been incorporated into the ASCE 7-22 standard as a practical approach for estimating flood depths and flow velocities based on runup data and topography. Its simplicity and applicability in exploratory studies have made it an attractive tool for evaluating hydrodynamic loads on coastal structures. However, as a method based on simplified assumptions about tsunami flow, EGLA does not explicitly capture transient effects, local turbulence, or three-dimensional interactions between the flow and the built environment. Therefore, its application should be considered within a preliminary estimation framework and supplemented with other tools whenever possible.

1.3. The ASCE 7′s EGLA

This research analyzes the behavior of a single-family timber structure subjected to loads generated by a tsunami, characterized by the ASCE 7-22 [28] method called energy grade line, which relates the hydraulic energy line with the data of a previously recorded tsunami, such as runups and the topography of the study site, with their respective horizontal flood distances; all of this is to interpret the heights and velocities that occur throughout the analysis area [29,30]. The introduction of the ASCE 7-16 standard marked a major step forward in establishing guidelines for designing structures to withstand tsunami loads [31]. Carden et al. [32] demonstrated the application of the EGLA and ASCE 7-16 provisions in mitigating structural failures during the 2011 Tohoku tsunami, highlighting the method's reliability and the conservative nature of the load estimates. Along this line, Chock et al. [33] conducted a comprehensive structural reliability analysis for tsunami hydrodynamic loads, utilizing Monte Carlo simulations to validate the probabilistic limit state reliabilities for various structural components, further affirming the robustness of ASCE 7-16 provisions. Chock [34] provided a detailed explanation of the technical basis and methodology underlying the tsunami-resilient design requirements in the ASCE 7-16 standard, emphasizing the integration of probabilistic hazard analysis, tsunami physics and fluid mechanics into a unified design framework. The EGLA, as outlined in the updated ASCE 7-22, offers a simplified yet effective tool for designing tsunami-resistant structures. Carden et al. [32] showed its effectiveness in mitigating structural failures during the 2011 Tohoku tsunami while Tada et al. [35] analyzed over 500 inundation measurements in Sendai, enhancing its accuracy for predicting tsunami-induced inundation heights.

In this study, we analyze the structural response of a timber single-story house using ASCE 7-22's EGLA in the insular town of San Juan Bautista, Robinson Crusoe Island, Juan Fernández Archipelago (Figure 1). The results obtained with EGLA are further validated with nonlinear structural analyses of the structure under equivalent tsunami loads.

While the EGLA method provides a reasonable estimation of tsunami hydrodynamic parameters, its application should be considered an approximation tool in structural design. ASCE 7-22 states that this method is suitable for initial estimations and exploratory studies but does not replace more detailed approaches based on numerical modeling. In this study, EGLA is used as a practical approach to obtain a preliminary estimation of hydrodynamic loads and to evaluate the structural response of timber houses in San Juan Bautista, analyzing its applicability in the context of lightweight buildings exposed to tsunamis; however, its results should be interpreted with caution and adjusted when possible.

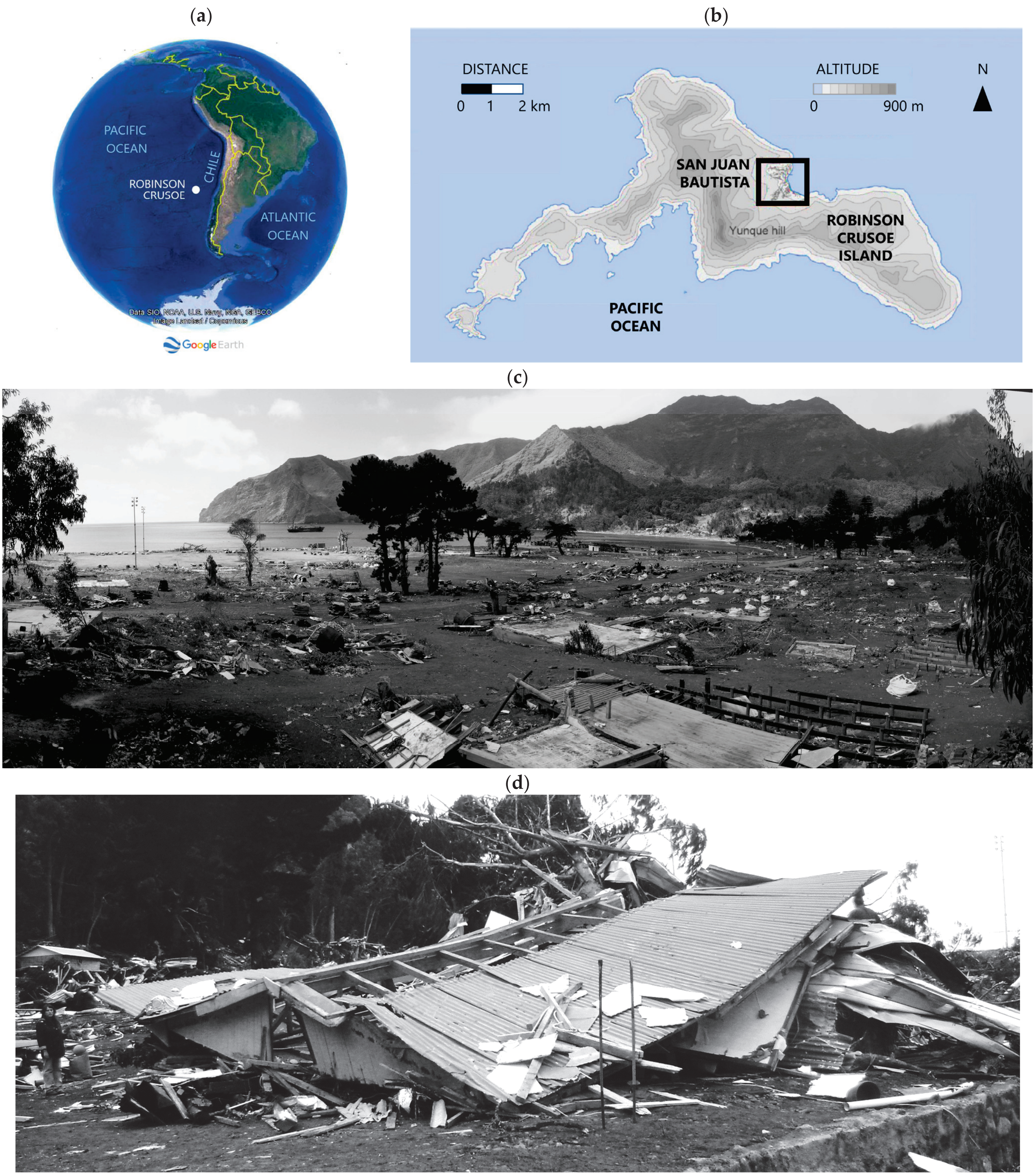

Figure 1. Location of (**a**) Robinson Crusoe Island and (**b**) the town of San Juan Bautista. The different failure modes caused by 27 February 2010 tsunami in San Juan Bautista are shown in (**c**,**d**). At the shore, houses were washed away by strong currents (**c**) whereas near the flooding line, houses floated due to buoyant forces (**b**). (**c**) is reproduced from Breuer et al. [36].

2. The 27 February 2010 Tsunami in San Juan Bautista

On 27 February 2010, a Mw = 8.8 earthquake occurred off the coast of Chile, generating a destructive tsunami along the continental coast, Easter Island and the small town of San Juan Bautista on Robinson Crusoe Island. Located 680 off the coast of Chile, San Juan Bautista was impacted by the first tsunami 49 min after the main shock as a slow-moving flood followed by a violent wave caused the total destruction of 160 houses and 18 casualties [7,37]. The loss of the buildings accounted for 40.1% housing and a great portion of basic services [36]. The aftermath was recorded in documentaries by UV [38]. According to Breuer et al. [36], this tsunami is part of a long-lasting list of 56 events affecting the island since 1591, some of which were destructive (1730, 1751, 1835, 1868, 1877, 1946, 1960).

Immediately following the earthquake, a series of post-tsunami surveys were launched to characterize the impact on the town. Two sites within Robinson Crusoe were surveyed by Fritz et al. [7] (Figure 8a) but the profile in San Juan Bautista (Figure 8b) coincided with the most affected area. The lower part of the town was severely affected by the tsunami, leaving 16 casualties, 160 ruined houses and most of the public facilities destroyed [36]. As Breuer et al. [36] observed during a survey conducted one month following the tsunami, weak structural joints connecting the houses to their foundations could explain why the structures floated, since this created buoyancy on the higher ground (Figure 1a), while near the coast, scour and high impact loads due to the high speeds also contributed to the overall damage (Figure 1b). These hypothetical failure modes, however, have not undergone a rigorous structural analysis, which could inform future design guidelines.

There are two reasons implied by Breuer et al. [36] that explain the huge structural damage in San Juan Bautista: (a) building materials are scarce and maintenance costs high as they sometimes rely on offshore supply and (b) the limited usable space due to the volcanic structure of the island has promoted the construction of single-story family houses in tsunami-exposed areas. Additionally, the existing Communal Regulating Plan enforced by the time of the 2010 tsunami authorized the construction of housing, commercial buildings and public facilities in exposed areas, without prescribing structural types (e.g., frames, walls, cables) and materials (e.g., masonry, reinforced concrete, wood, steel). Consequently, the prevailing structural typology prior to the 2010 tsunamis consisted of single-story timber houses with weak anchoring systems (aimed to transfer dead and live loads to the ground) and a low ratio between window-to-wall areas, which made them highly impermeable to the tsunami. It should be noted that all 160 buildings in the flooded area were fully damaged, regardless of whether they were affected by strong currents or water depths. However, the failure modes slightly differed with the distance to the shore. According to Breuer et al. [36], weak structural joints connecting the houses to their foundations explain why some houses floated due to buoyancy on the higher ground where the flow was relatively slow (Figure 8a), which is a structural failure documented earlier in past events [39,40]. Our analysis is conducted on a topographic profile along La Pólvora Street, where a maximum penetration and runup within the town were recorded by Fritz et al. [7].

3. Methodology

Following ASCE 7-22, Chapter 6, in this study, it is assumed that structures are subjected to hydrostatic and hydrodynamic forces, waterborne debris accumulation and impact loads. Due to the in situ evidence later discussed, the scour or geotechnical damage of the soil are disregarded. Seismic ground motion effects on structures are disregarded, as the triggering earthquake occurred in the Chile–Perú subduction zone, nearly 600 km east from Robinson Crusoe Island, and islanders did not feel the shaking. Our focus is on single-story timber houses, disregarding critical facilities which were completely destroyed during the 27 February 2010 tsunami [37].

3.1. EGLA of Maximum Inundation Depths and Flow Velocity

The analysis is conducted on a topographic profile along La Pólvora Street (Figure 2), where a runup of 18.3 m was recorded at an inundation distance of 295 m and two records of flow depths were recorded by Fritz et al. [7]. The maximum inundation depths and flow velocity along the ground elevation profile up to the runup are determined using the EGLA (Figure 3). The ground elevation along the transect is represented as a series of linear sloped segments each with a Manning's coefficient consistent with the equivalent terrain macroroughness friction of that terrain segment. The EGLA is performed incrementally across the topographic transect in a stepwise procedure from the runup (where the hydraulic head is zero and the water elevation is equal to the runup) to the mean water shoreline using Equation (1)

$$E_i = E_{i-1} + (\varphi_i + s_i)\Delta x_i \tag{1}$$

where E_i is the hydraulic head at point i, given by

$$E_i = h_i + u_i^2/2g = h_i\left(1 + Fr_i^2/2\right). \tag{2}$$

Here, h_i is the inundation depth, u_i the maximum flow velocity, φ_i the average ground slope between i and $i-1$, $Fr_i = u_i/\sqrt{gh_i}$ the Froude number, Δx_i the increment of horizontal distance between the consecutive points of coordinate x_i measured inland from the still water level (SWL as in Figure 3) and s_i the friction slope of the energy grade line between consecutive points, calculated as follows:

$$s_i = u_i^2 n^2 / h_i^{4/3} \tag{3}$$

where $n = 0.025$ is the Manning's coefficient, defined for open land or field according to ASCE 7-22. This value neglects the frictional effects of the houses and built environment that existed before and was washed away by the tsunamis. Velocity is determined as a function of inundation depth, in accordance with the prescribed value of the Froude number calculated according to Equation (4).

$$Fr = \alpha\sqrt{1 - x/X_R} \tag{4}$$

where $\alpha = 1.0$ and X_R is the design inundation distance inland from Medium High Water (MHW) shoreline. No bore correction is conducted as the nearshore bathymetry is too steep to generate a bore. Table 1 shows the parameters used in the EGLA. The resulting flow depth and velocities are then corrected to fit the flow depths obtained by Fritz et al. [7].

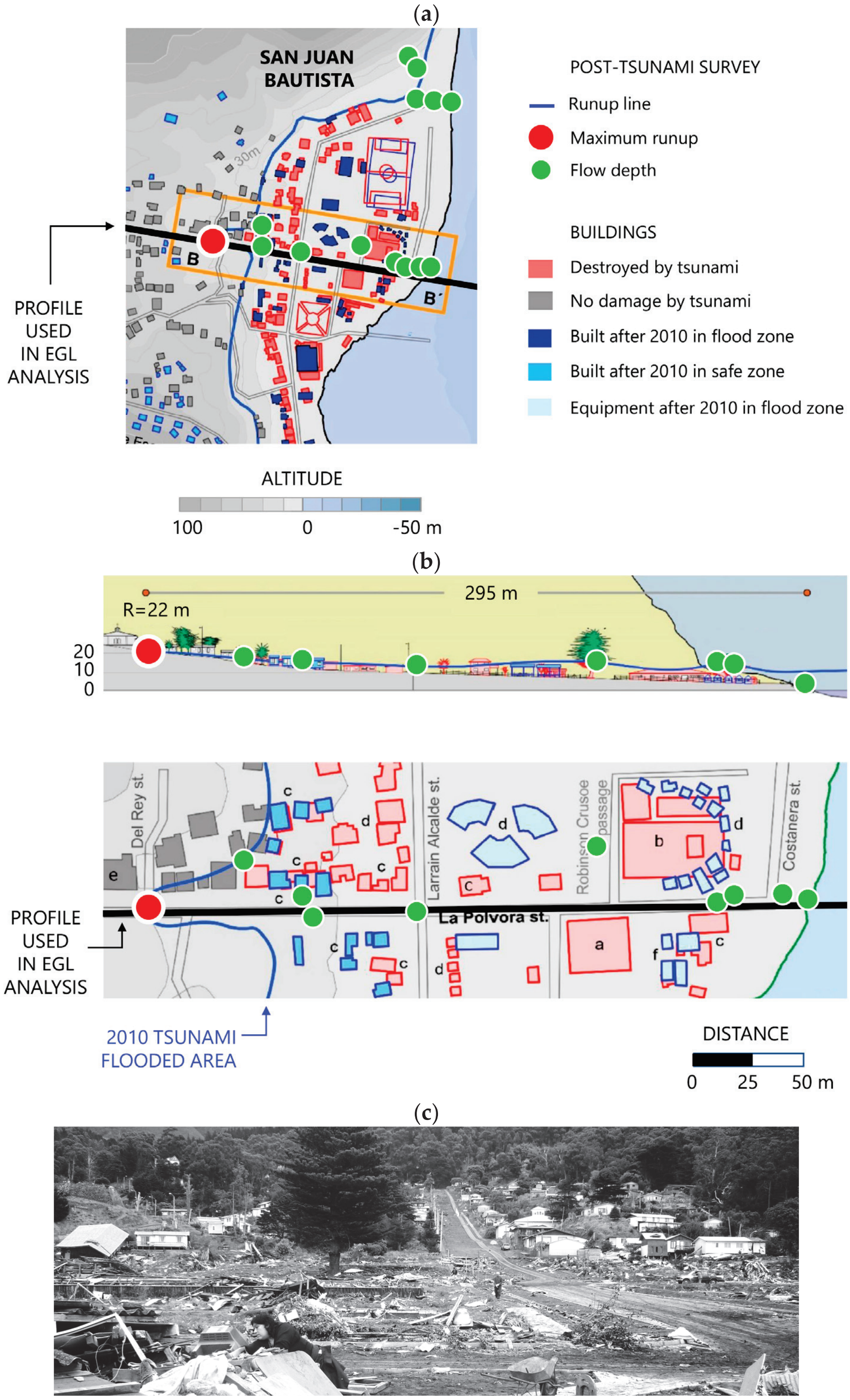

Figure 2. (**a**) Topographic profile used in the EGLA, with flow depths recorded by Fritz et al. [7], maximum runup by Winckler et al. [41] and buildings identified before and after the 2010 tsunami by Breuer et al. [36]. (**b**) Elevation and plan view of the area neighboring La Pólvora Street including gymnasium [a], school [b], houses [c], touristic and commercial infrastructure [d], church [e] and warehouses for fishing activities [f]. (**c**) La Pólvora Street, as observed from its lower section.

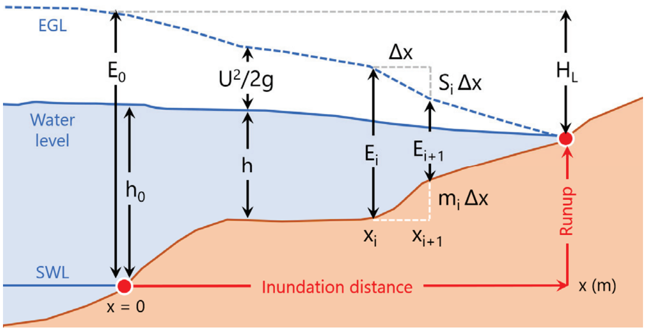

Figure 3. Illustration of the EGLA across an inundated transect, where the incident tsunami flow is from left to right. EGL: energy grade line. SWL: still water level. Adapted from ASCE 7-22.

Table 1. Parameters used in the EGLA.

Parameter	Symbol	Dimension	Value
Overall building width	B	m	6.6
Manning's roughness coefficient	n	-	0.025
Height of wall	h_w	m	2.4
Width subject to force	b	m	6.6
Minimum fluid specific weight density	γ_s	kN/m3	11
Minimum fluid mass density	ρ_s	g/cm3	1.1
Importance factor	I_{tsu}	-	1
Drag coefficient	Cd	-	1.25
Proportion of closure coefficient	C_{cx}	-	4.42
Story height of story x	h_{sx}	m	4.35
Time interval	Δt	s	1

3.2. Tsunami Hydrodynamic Loads

The methodology includes the estimation of flow depths and depth-averaged horizontal flow speeds using the ASCE 7-22′s EGLA, from which computed hydrostatic, drag and impact forces are used in the structural analysis of a timber single-story house. The application is based on the combination of a proprietary Matlab (R2022a) script for the computation of hydrodynamic loads and the use of the software Robot Structural Analysis Professional 2024 (referred as Robot hereafter) [42] to compute the structural response on several locations within a topographic profile of La Pólvora Street, where a maximum penetration of 295 m and a runup of 18.3 were reported by Fritz et al. [7].

Figure 4 shows the flow depth obtained from the EGLA and different house positions where the structural analysis is conducted, as well as the dominant hydrostatic and hydrodynamic loads during and after the impact of a tsunami. The buoyancy force, the unbalanced lateral hydrostatic force, the drag force and the impact of wood logs are evaluated following ASCE 7-22, FEMA P-646 [43] and NCh3363 2015 [44].

3.2.1. Buoyancy Force

The buoyancy force (F_b) is evaluated in accordance with Equation (5):

$$F_b = \gamma_s \, V_W \tag{5}$$

where γ_s is the minimum fluid weight density for design hydrostatic loads and V_W is the displaced water volume. For modeling purposes, this force is applied as a pressure, since this facilitates the modeling of the claddings. The buoyancy of the vertical walls is discarded as these have an almost negligible volume and thus a small buoyancy compared to the other acting forces.

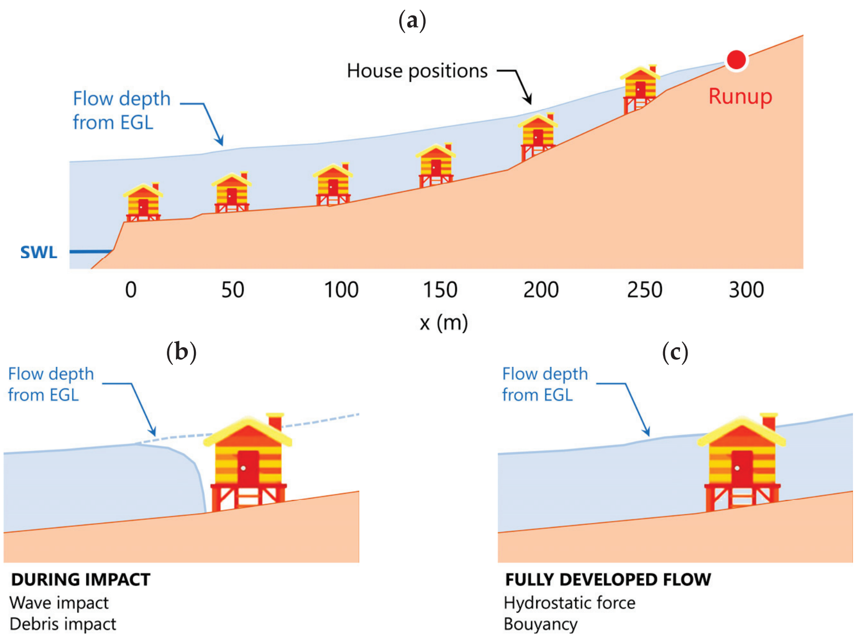

Figure 4. (**a**) Flow depth obtained from the EGLA and different house positions (0, 50, 100, 150, 200 and 250 m) where the structural analysis is conducted. (**b**,**c**) show the dominant hydrostatic and hydrodynamic loads during the impact of a tsunami and when the flow is fully developed around the house, respectively.

3.2.2. Unbalanced Lateral Hydrostatic Force

The unbalanced hydrostatic lateral force (F_h), when the flow does not overtop the wall, is determined using Equation (6):

$$F_h = 1/2\,\gamma_s b h^2 \tag{6}$$

where b is the width of the building subject to force and h the tsunami inundation depth above the grade plane at the structure. Where the flow overtops the wall, the lateral hydrostatic force on the wall is determined using Equation (7):

$$F_b = 0.6\gamma_s(2h - h_w)\; bh_w \tag{7}$$

where h_w is the height of wall. The forces in Equations (2) and (3) were applied as the equivalent distributed forces of triangular and trapezoidal shapes on walls.

3.2.3. Drag Force

The drag force is computed with Equation (8):

$$F_{dx} = 0.5\rho_s I_{tsu} C_d C_{cx} b h_{sx} u^2 \tag{8}$$

where ρ_s is the minimum fluid mass density for hydrodynamic design, I_{tsu} the importance factor for tsunami forces to account for additional uncertainty in estimated parameters, C_d the drag coefficient based on quasi-steady forces, C_{cx} the proportion of closure coefficient, b the width of the building subject to force and u the tsunami flow velocity.

3.2.4. Impact of Wood Logs

The nominal maximum instantaneous debris impact force was preliminarily computed using ASCE 7-22 (Equations (6.11-2) and (6.11-3)) but the resulting value (130 tonf) was considered excessive (Appendix A). Alternatively, we calculate the impact force (F_{IF}) by floating objects from NCh3363 2015 [44], which assumes a debris of 500 kg impacting on a time interval ($\Delta t = 1$ s for timber structures) at the speed of the tsunami u.

$$F_{IF} = 500(u/\Delta t) \tag{9}$$

This force is applied to the front wall at the level reached by the tsunami inundation depth when it is lower than the height of the structure $(h > h_w)$ and at its centroid when the depth exceeds the structure. Impact forces are applied when the tsunami impacts the structure (Figure 4b) and once the flow has reached a relatively uniform and stationary pattern around the house (Figure 4c).

3.2.5. Load Cases

Load cases are based on the LRFD philosophy from ASCE 7-22, which is integrated into Robot. A seismic nature is assigned to tsunami load so that its amplification factor corresponds to an accidental combination.

3.3. Structural Modeling of a Timber Single-Story House

A 60 m^2 timber single-story house with a gable roof is modeled using Robot. To compute the hydrodynamic loads, we conservatively disregard the openings (e.g., doors and windows). The timber structure is modeled using Grade C16 Pinus radiata [45], a material locally used according to the Chilean code NCh1198 [46]. The timber structure's configuration includes 7.5 cm $\times$ 7.5 cm elements for corner supports, 5 cm $\times$ 5 cm elements spaced every 50 cm for walls and roofing, 5 cm $\times$ 7.5 cm elements for roof beams, 15 cm $\times$ 2.5 cm bars for trusses and 15 cm $\times$ 10 cm elements for floor beams. The 20 cm $\times$ 20 cm concrete pedestals spaced 1.5 m and braced to the floor beams are considered as the top of the foundation (Figure 5). Structural failure modes include failures due to bending, shear, buckling, torsion and fatigue. Emphasis is placed on the structural failure under combined loads in an Ultimate Limit State (ULS).

Dead, live and roof live loads are considered constant and valued according to the Chilean code NCh1537 [47]. The dead load is considered for the entire structure, except for the house's floor, where a distributed surface dead load of 0.1 kPa is assumed for a 1-inch-thick floor made of white pine wood elements of 420 kgf/m^3 [45] with enclosures. Uniformly distributed live loads of 2 kPa are considered for floors and roofs, with this load applied to general use areas and bedrooms. A 0.3 kPa uniformly distributed live load for the roof (3.3 m long, 1.94 m high and a slope of 58%) is determined based on the slope and tributary area of each structural frame. Tsunami loads (hydrostatic, hydrodynamic and debris impact) are assumed to act perpendicular to timber single-story houses positioned every 50 m along La Pólvora Street (e.g., $x = 0$, 50, 100, 150, 200 and 250 m, being $x = 0$ m the coastline and 250 m near the runup). Table 2 summarizes the flow depths immediately before (seaward), in the centroid of and immediately after (landward) each house's location.

3.4. Load Combinatios

Load cases and weighting factors prescribed in ASCE 7-22 are used herein (Table 3). The following combinations are used:

$$1.4D \tag{10}$$

$$1.2D + 1.6L + (0.5L_r \text{ or } 0.3S \text{ or } 0.5R) \tag{11}$$

$$1.2D + (1.6L_r \text{ or } 1.0S \text{ or } 1.6R) + (L \text{ or } 0.5W) \tag{12}$$

where D is the dead load, L the live load, L_r the roof live load, S the snow load, R the rain load and W the wind load. The combinations considering the interaction of tsunami loads with gravity loads are as follows:

$$0.9D + F_{TSU} + H_{TSU} \tag{13}$$

$$1.2D + F_{TSU} + 0.5L + 0.2S + H_{TSU} \tag{14}$$

where F_{TSU} is the direct tsunami load, H_{TSU} the load induced by earth pressure under submerged conditions, L the live load and S the snow load. We disregard snow, rain and wind loads due to the location of the study. Load cases are considered during the impact of the tsunami (I), as in Figure 4b, and when the flow has completely flooded the surrounding area of the house (F), as in Figure 4c. The pressures obtained on the different faces of the structure are shown schematically in Figure 6.

Table 2. Flow depths and loads acting on a timber single-story house positioned every 50 m along La Pólvora Street. h_s, h_c and h_l are the flow depths immediately seaward, in the centroid and immediately inland of each house, respectively. P_b is the buoyancy pressure, P_h the lateral hydrostatic pressure, P_d the drag pressure and F_{if} the impact force from floating objects.

x m	h_s m	h_c m	h_l m	P_b kPa	P_h kPa	P_d kPa	F_{if} kN
250	2.48	2.15	1.81	27.31	13.66	2.27	1.01
200	4.55	4.36	4.16	47.85	31.40	8.34	1.93
150	5.54	5.48	5.41	47.85	44.37	15.20	2.61
100	6.05	6.02	6.00	47.85	51.10	22.14	3.14
50	5.99	6.00	6.00	47.85	50.38	27.42	3.50
0	6.62	6.37	6.12	47.85	58.64	36.35	4.03

Table 3. Load cases corresponding to the ultimate limit state (ULS). In this table, D represents the dead load, L the live load, F_d the drag force, F_{if} the impact force from floating objects, F_b the buoyant force and F_h the lateral hydrostatic force. The value corresponds to the amplification in the load cases. The sign is positive for a force acting landwards and negative seaward. Parentheses (I) and (F) correspond to load cases during the impact of the tsunami and when the flow has completely flooded the surrounding area of the house, respectively.

Load Case	D	L	F_d	F_{if}	F_b	F_h
C1	1.4	-	-	-	-	-
C2	1.2	1.6	-	-	-	-
C3	1.2	-	-	-	-	-
C4	1.2	0.5	-	-	-	-
C5	0.9	-	-	-	-	-
C6 (I)	1.2	0.5	1	1	-	-
C7 (I)	1.2	-	1	1	-	-
C8 (I)	1.2	0.5	−1	−1	-	-
C9 (I)	1.2	-	−1	−1	-	-
C10 (I)	0.9	-	1	1	-	-
C11 (I)	0.9	-	−1	−1	-	-
C6 (F)	1.2	0.5	-	-	1	1
C7 (F)	1.2	-	-	-	1	1
C8 (F)	1.2	0.5	-	-	−1	−1
C9 (F)	1.2	-	-	-	−1	−1
C10 (F)	0.9	-	-	-	1	1
C11 (F)	0.9	-	-	-	−1	−1

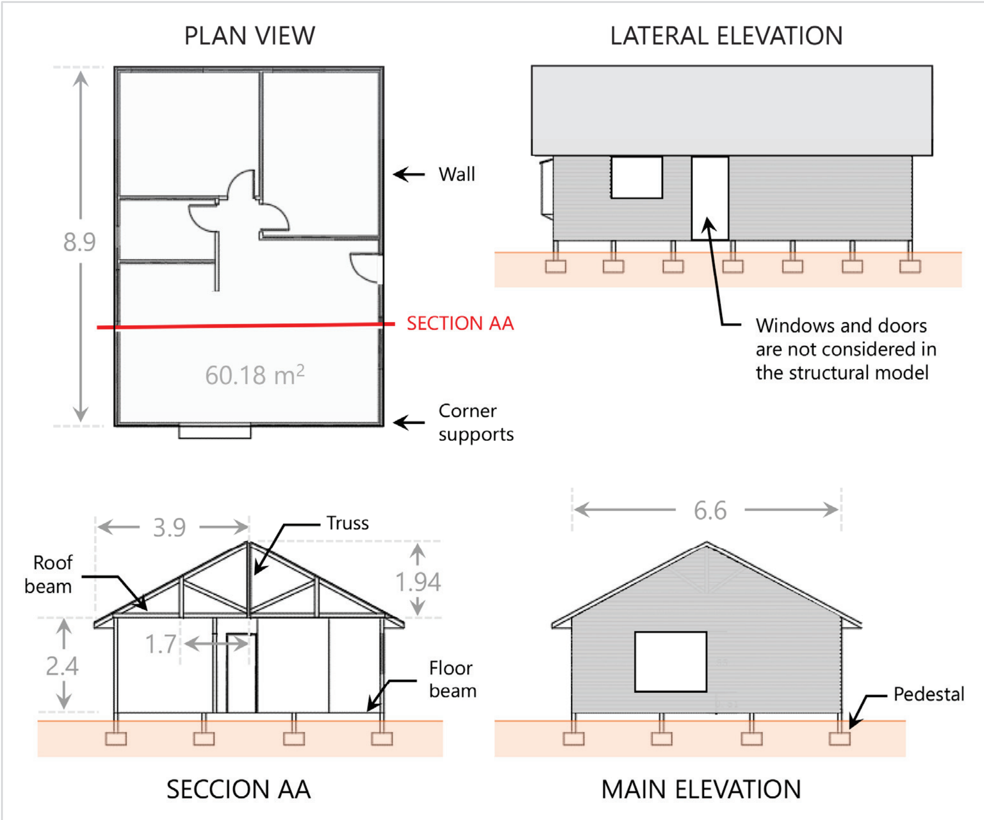

Figure 5. Drawings of the timber single-story house used in the analysis. Relevant dimensions are shown. Windows and doors are not considered in the structural model.

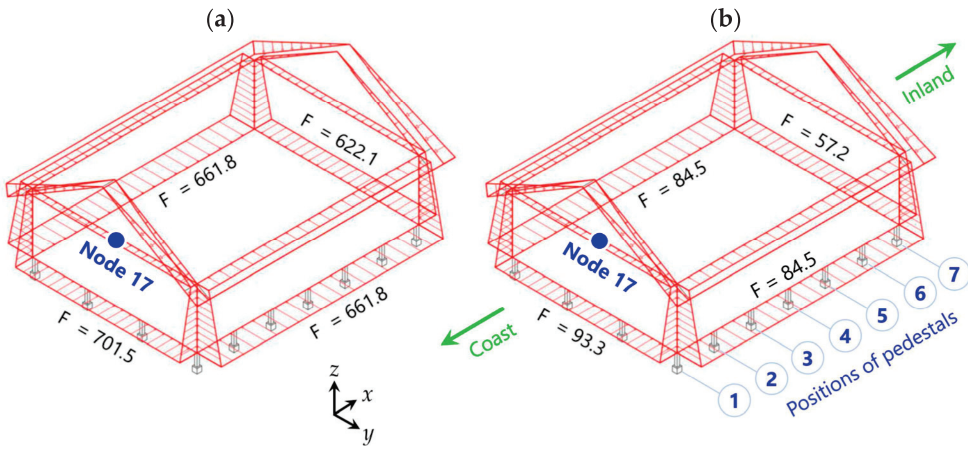

Figure 6. Hydrostatic force in kN/m in (**a**) position $x = 0$ m and (**b**) position $x = 250$ m. Structural node 17 is the one with maximum displacement along the x-axis at $x = 0$ m in load case C10 (I).

3.5. Nonlinear Analysis

The results obtained with EGLA are further validated with nonlinear structural analyses of the structure under equivalent tsunami loads. For this, the structure is modeled considering two sources of nonlinearity: (1) the constitutive nonlinearity, linked to the response of the constituent materials of the structure and (2), the geometric nonlinearity, which affects very flexible structures [48]. As described above, the structure is composed of reinforced concrete members for the pedestals that support the timber superstructure and transmit the loads to the foundations. Concrete and reinforcing steel are modeled using Mander et al.'s [49] and Menegotto and Pinto's [50] models, respectively. Timber elements are modeled using the elastic-plastic model with a small hardening fraction (0.5%) [51]. The details of these models are shown in Tables 4–6.

Table 4. Constitutive model parameters for timber elements of Pinus Radiata.

Parameter	Dimensions	Value
Compression strength	MPa	4.26
Strength lower bound	MPa	3.7
Bending strength	MPa	8.6
Modulus of elasticity	MPa	8829
Specific weight	kN/m^3	4.9

Table 5. Constitutive model parameters by Mander et al. for concrete grade G25.

Parameter	Dimensions	Value
Compression strength	MPa	33
Strength lower bound	MPa	25
Tension strength	MPa	2.6
Modulus of elasticity	MPa	26,999
Specific weight	kN/m^3	24

Table 6. Constitutive model parameters by Menegotto and Pinto for steel grade A630–420H. A1, A2, A3 and A4 correspond to transition curve shape calibrating coefficients.

Parameter	Dimensions	Value
Modulus of elasticity E	MPa	200,000
Yield strength F_y	MPa	490
Strain hardening parameter	-	0.005
Transition curve initial shape parameter	-	20
Coefficient A1	-	18.5
Coefficient A2	-	0.15
Coefficient A3	-	0
Coefficient A4	-	1
Fracture/buckling strain	-	1
Specific weight	kN/m^3	78

The gravity loads applied to the nonlinear model are the same as those described above for the linear model (Section 3.3). Loads produced by the tsunami are applied sequentially, considering their variation with respect to the flood height. The tsunami pressure acts on the façade (main elevation in Figure 5). Figure 7 shows an isometric view of the nonlinear model, with the gravity and tsunami loads applied at the nodes of the façade. The nonlinear analysis is carried out, having, as the main variable, the flood height indicated for each position with respect to at $x = 0$ m (Table 2). The procedure contained in ASCE 7-22 is applied to determine the loads on the façade; the SeismoStruct V-24 [52] software is used to perform the analysis.

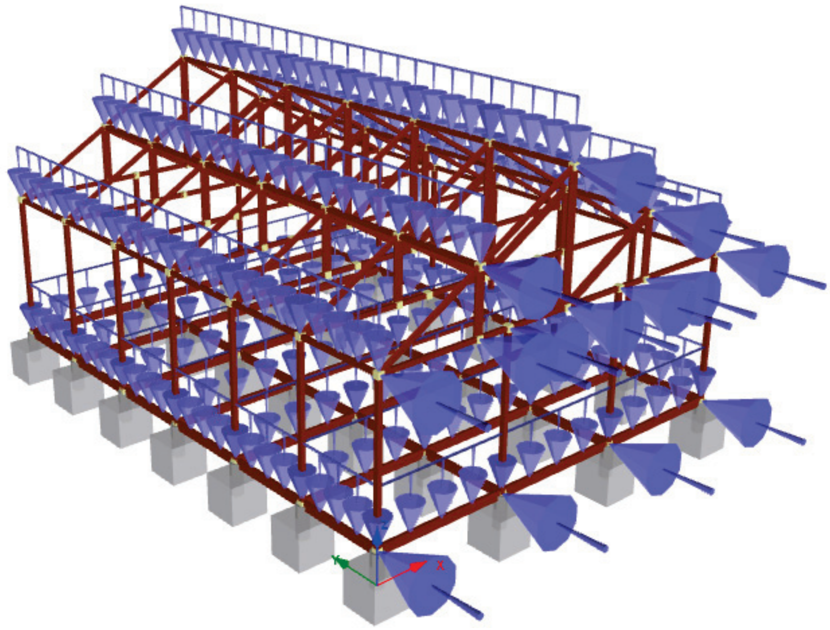

Figure 7. Isometric view of the nonlinear structural model, with gravity loads and tsunami loads.

It should be noted that the nonlinear analysis model is based on the fiber approach, in which the cross-sections of structural members are discretized into fibers adapted to the section geometry. In the case of reinforced concrete structural members, the fibers consist of cover concrete, core concrete and composite fibers made of core concrete and reinforcing steel. For the timber components, homogeneous fibers of this material are considered.

The analysis framework established in ASCE 7-22 follows an incremental approach, where the loads are progressively applied in a series of finite steps. In each step, a load increment is applied to the nodes of the façade, as illustrated in Figure 7. These load increments correspond to the hydrostatic height, which is updated at each step of the analysis. As the loads increase, the internal stresses within the fibers of the structural members also rise. When these stresses exceed the strength limits specified in Tables 4–6, plasticization begins, leading to the progressive damage of the components.

For each load increment, the displacements at the center of gravity of the roof and the base shear in the direction of the incoming wave are computed. By plotting the base shear force against the roof displacement, a capacity curve is obtained, from which critical points of structural response are analyzed. The nonlinear analysis only considers the application of the aforementioned loads, excluding other forces such as impact and buoyancy.

To evaluate the progression of tsunami-induced damage to the structure, two performance criteria are defined based on the strain limits of radiata pine timber [53]. The first strain threshold corresponds to the point where the material ceases to exhibit approximately linear behavior, while the second threshold marks the peak stress point, beyond which the material begins to lose its load-bearing capacity. Determining the displacements at which these limit values are reached allows for the monitoring of the evolution of damage in the different structural members.

4. Results

4.1. EGLA of Maximum Inundation Depths and Flow Velocities

Figure 8a shows the EGL in a gray dashed line at different house positions where the structural analysis is conducted, as well as the flow depths and runup recorded by Fritz et al. [7]. As the reported flow depths are smaller than the EGL, the latter is reduced by a factor of 0.5 to fit the data. The EGL and corrected flow depths differ by as much as 6.2 m at

$x = 100$ m, which could be attributed to several causes, as later discussed. Figure 8b shows the flow depth and velocity as obtained from the Corrected EGL.

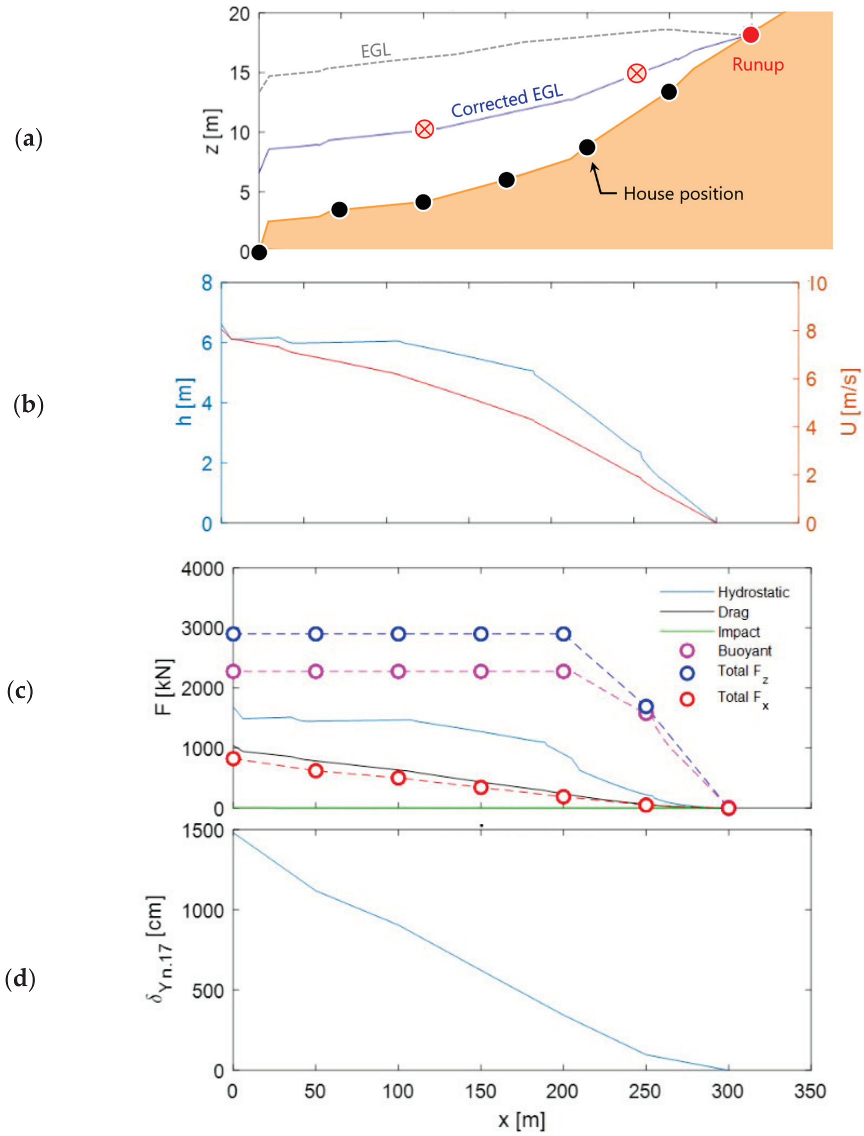

Figure 8. (**a**) EGL and corrected EGL for flow depths (crossed circles) and runup recorded by Fritz et al. [7] at different house positions ($x = 0$, 50, 100, 150, 200 and 250 m) where the structural analysis is conducted. (**b**) Flow depth and velocity inferred from the EGLA. (**c**) Forces generated by the tsunami and reactions of the structure in the x-axis and z-axis and (**d**) displacement of node 17 that deforms the most in the analysis performed.

4.2. Relative Displacements

The structural damage was determined based on the criterion of relative displacements caused by the tsunami. As inferred from the structural analysis of all house positions, the structural node of maximum displacement along the x-axis corresponds to node 17 (Figure 6) at $x = 0$ m in load case C10 (I). Then, the maximum displacement at $x = 0$ m is compared with the other house positions, resulting in Figure 8d. We found that relative displacements exceeding tens of meters would occur under linear elastic behavior, leading to structural collapse due to the fragility of the material and the connections of the timber structures.

4.3. Supports Reactions

Figure 8c shows a significant reduction in the shear force in the flow direction between $x = 0$ m and 250 m. The high values of the shear force for the position $x = 0$ explain the collapse experienced in houses close to the coastline, as observed in Figure 1d. This decrease can explain the dominant failure mode of the buildings closest to the coastline, which were probably separated from their supports as a result of the shear (e.g., Figure 1d). As for the moment, there is not such a drastic reduction when comparing the house positions, thus their influence in house position located at $x = 0$ m may mean that the failure mode far from the coastline is caused more by the overturning of the structure.

The forces and moments at each of the supports of the structure for the C12 load case (the combination with largest resultant in x-axis) at the two loading instants are presented in Figures 9 and 10 for the positions 0 m and 250 m, respectively. The reactions correspond to the combined and factored loads as indicated above. Tables 7 and 8 shows the resulting load cases for a house position located at $x = 0$ m and $x = 250$ m, respectively. The reactions shown in Figure 8a are obtained from Tables 7 and 8. Figure 8c summarizes the results of the forces caused by the tsunami in the x- and z-axes, for all house positions.

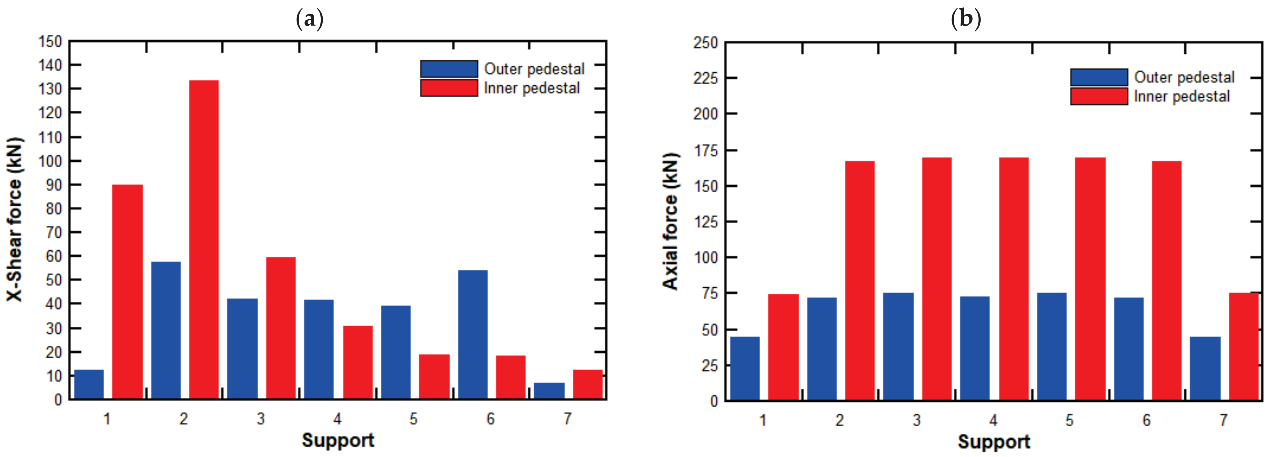

Figure 9. Reactions in the supports for the loading corresponding to a house position at $x = 0$ m from the coastline (**a**) in the x-axis and (**b**) z-axis. The numbers from 1 to 7 represent the positions of the pedestals shown in Figure 6.

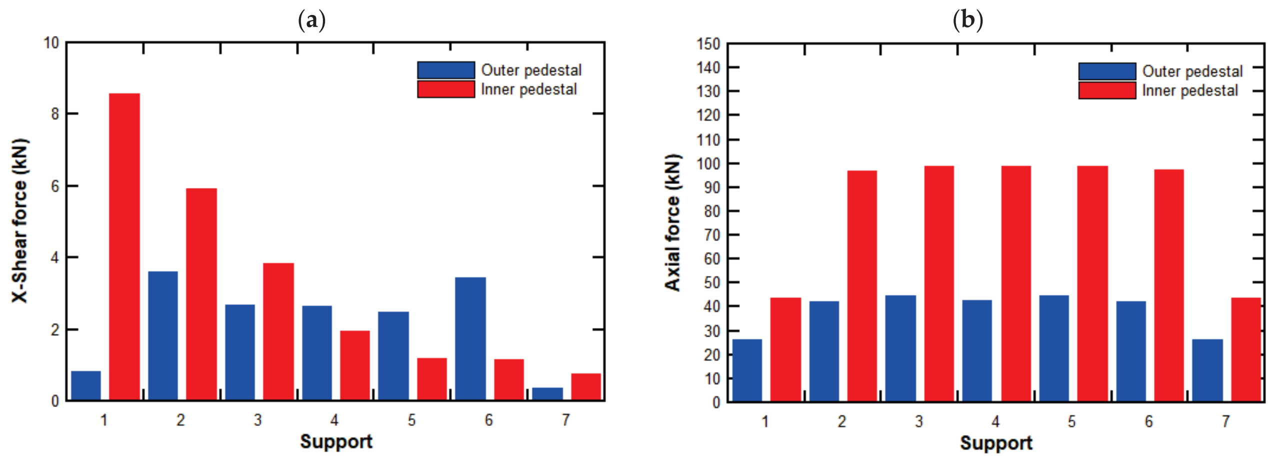

Figure 10. Reactions in the supports for the loading corresponding to a house position at $x = 250$ m from the coastline (**a**) in the x-axis and (**b**) z-axis. The numbers from 1 to 7 represent the positions of the pedestals shown in Figure 6.

Table 7. Resulting load cases for a house position located at $x = 0$ m from the shoreline. F_x, F_y and F_z are the resulting forces in the *x*-, *y*- and *z*-axes, respectively, while M_x, M_y and M_z are the resulting moments in the *x*-, *y*- and *z*-axes, respectively. Parentheses (I) and (F) correspond to load cases during the impact of the tsunami and when the flow has completely flooded the surrounding area of the house, respectively.

Load Case	F_x kN	F_y kN	F_z kN	M_x kNm	M_y kNm	M_z kNm
C1	0	0	18.2	0	0	0
C2	0	0	241.5	0	0.01	0
C3	0	0	15.6	0	0	0
C4	0	0	86.2	0	0	0
C5	0	0	11.7	0	0	0
C6 (I)	−825.5	0	86.2	0	540.2	0
C7 (I)	−825.5	0	15.6	0	540.2	0
C8 (I)	825.5	0	86.2	0	−540.2	0
C9 (I)	825.5	0	15.6	0	−540.2	0
C10 (I)	−825.5	0	11.7	0	540.2	0
C11 (I)	825.5	0	11.7	0	−540.2	0
C6 (F)	0	0	−2727.6	0	0	0
C7 (F)	0	0	−2798.2	0	−0.01	0
C8 (F)	0	0	2900.1	0	0.01	0
C9 (F)	0	0	2829.5	0	0.01	0
C10 (F)	0	0	−2802.2	0	−0.01	0
C11 (F)	0	0	2825.6	0	0.01	0

Table 8. Resulting load cases for a house position located at $x = 250$ m from the shoreline. F_x, F_y and F_z are the resulting forces in the *x*-, *y*- and *z*-axes, respectively, while M_x, M_y and M_z are the resulting moments in the *x*-, *y*- and *z*-axes, respectively. Parentheses (I) and (F) correspond to load cases during the impact of the tsunami and when the flow has completely flooded the surrounding area of the house, respectively.

Load Case	F_x kN	F_y kN	F_z kN	M_x kNm	M_y kNm	M_z kNm
C1	0	0	18.23	0	0	0
C2	0	0	241.53	0	0.01	0
C3	0	0	15.63	0	0	0
C4	0	0	86.22	0	0	0
C5	0	0	11.72	0	0	0
C6 (I)	−52.32	0	86.22	0	34.42	0
C7 (I)	−52.32	0	15.63	0	34.41	0
C8 (I)	52.32	0	86.22	0	−34.41	0
C9 (I)	52.32	0	15.63	0	−34.41	0
C10 (I)	−52.32	0	11.72	0	34.41	0
C11 (I)	52.32	0	11.72	0	−34.41	0
C6 (F)	0	0	−1520	0	0	0
C7 (F)	312.36	0	−1590.6	0	0	0
C8 (F)	−312.36	0	52.32	0	0.01	0
C9 (F)	0	0	1621.86	0	0.01	0
C10 (F)	0	0	−1594.51	0	0	0
C11 (F)	0	0	1617.95	0	0.01	0

The nonlinear analysis applied to the structure has allowed the obtainment of the capacity curves for each of the positions considered in the study. These curves are shown in Figure 11. Note that for the positions between 0 m and 200 m, the capacity curves are similar, since the tsunami loads are produced by flood heights that generate loads that cause the structure to collapse. On the contrary, for the position 250 m from the coast, the flood height has been significantly reduced, producing an effect of reducing the loads on the façade that practically maintains the elastic behaviour of the structural elements.

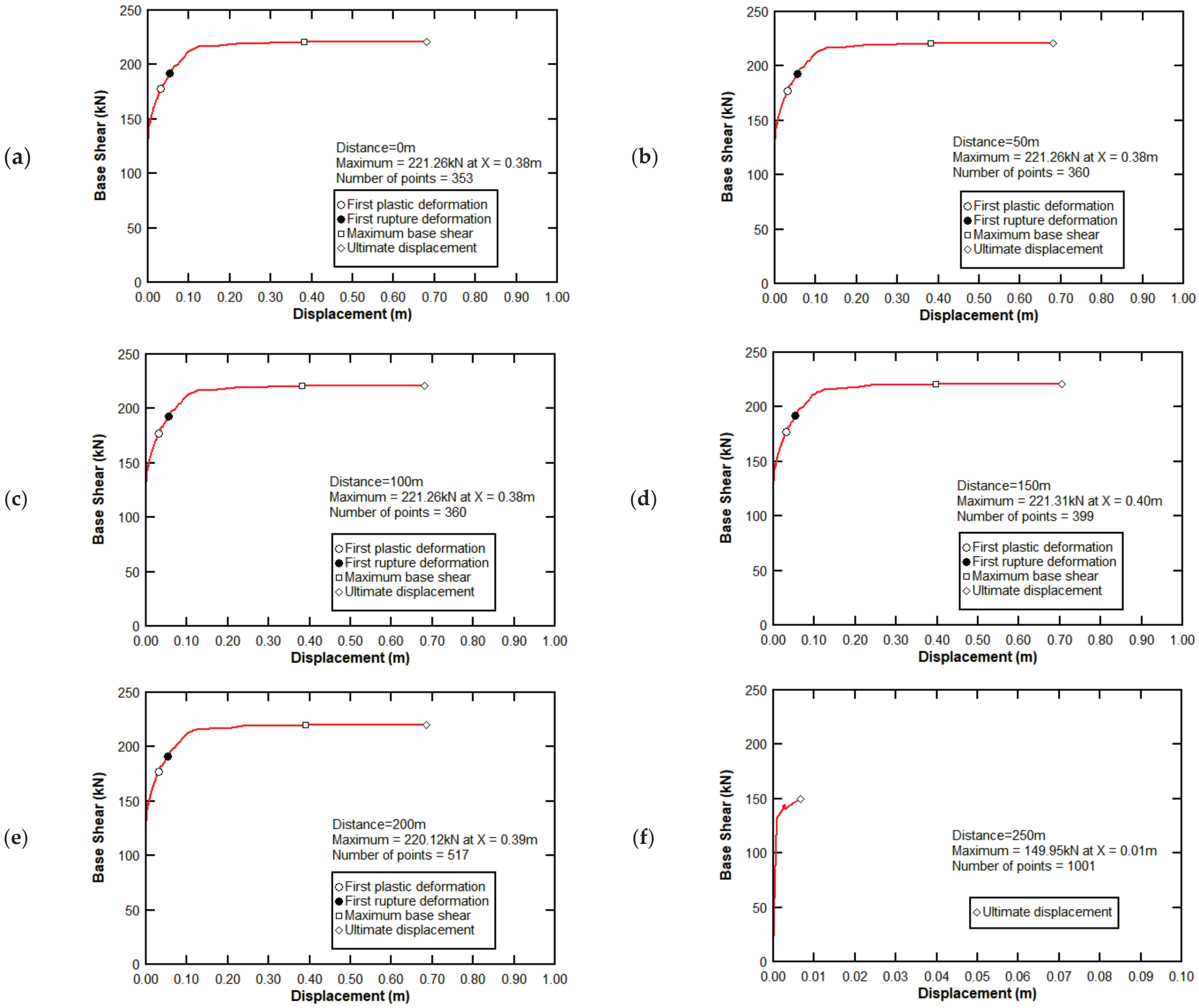

Figure 11. Capacity curves obtained from the nonlinear analysis for the positions from the shoreline of (**a**) $x = 0$ m, (**b**) 50 m, (**c**) 100 m, (**d**) 150 m, (**e**) 200 m and (**f**) 250 m.

The curves in Figure 11 show points at which the first member reaches plastic deformation and points at which the first failure deformation is reached in one of the members. As soon as damage begins to occur, the curves flatten progressively until reaching the point at which the greatest shear force is reached at the base, whose values are shown in Figure 11. Note that for the positions between $x = 0$ m and 200 m, the point of maximum shear force has practically the same value. From that point onwards, there is a sustained reduction in the lateral force resistance capacity, reaching the point corresponding to the ultimate displacement.

Figure 12 shows the damage at the point of maximum shear force, including points where both plastic deformations (ochre circles) and breaking deformations in the timber elements (pink circles) have occurred. The figure shows the damage for the position $x = 200$ m; however, it shows similar damage to other positions ($x = 0$ m to 150 m). The model located at $x = 250$ m does not show damage and is thus omitted herein. The noticeable damage in Figure 12a shows that the well-known floor mechanism is formed, where a kinematically unstable structure having all the ends of columns with ball joints cannot sustain greater lateral forces, causing it to collapse. Similarly, Figure 12b shows that tsunami loads cause serious damage to the structural members of the façade at the analysis point for which the maximum shear force is reached, being an indication that these members have collapsed. Finally, note that the reinforced concrete pedestals and the floor frame beams do not show damage, coinciding with the damage observed in houses located near the runup line, as shown in Figure 1c and noticed by Breuer et al. [36].

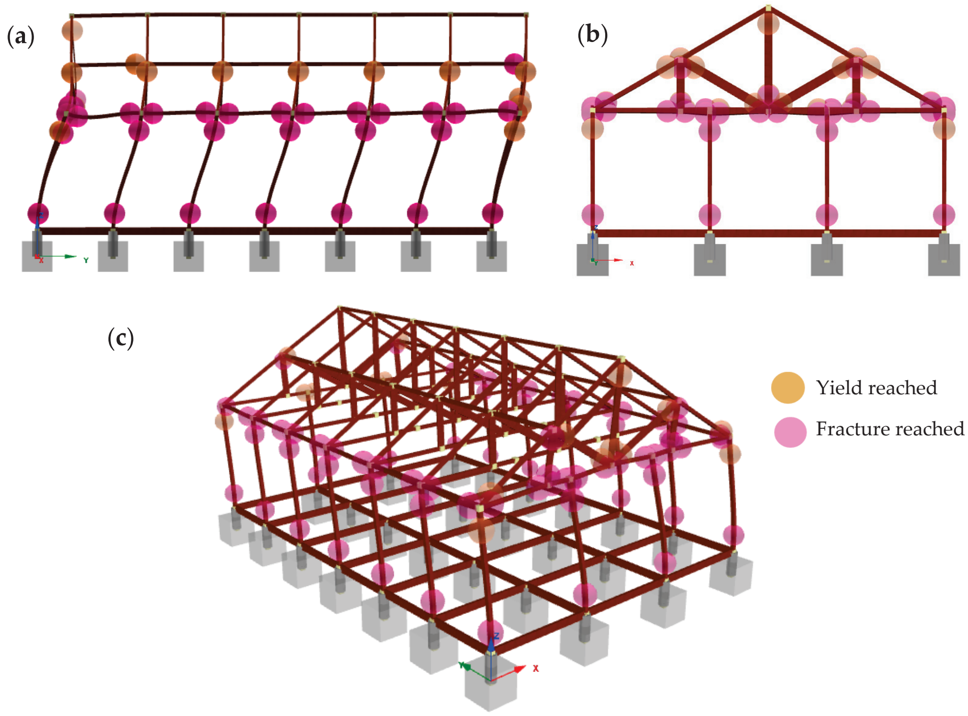

Figure 12. Deformed and damaged structure at the point of maximum shear force reached. (**a**) Right side elevation view, (**b**) front elevation view and (**c**) isometric view.

5. Discussion

5.1. Hydrodynamic Loads Using the EGLA

The application of the EGLA provides an easy way to estimate flow depths and velocities throughout La Pólvora's topographic profile, given that in situ records are available. However, as shown in Figure 8a, its straightforward application provides a significant overestimation of flow depths, which in turn results in an overestimation of the hydrodynamic forces.

One of the challenges in applying EGLA is the propagation of uncertainties in the estimation of hydrodynamic loads. As shown in Figure 8a, the uncorrected EGL curve overestimates flood depths compared to the field data recorded by Fritz et al. [7]. To mitigate this discrepancy, a correction factor was applied to the EGL curve, ensuring better agreement with the observed values. However, it is important to note that in scenarios where field data are not available to make adjustments, EGLA may introduce variations in the determination of structural loads. Consequently, the loads obtained herein should be considered conservative estimates, useful for assessing trends in structural response but not necessarily representative of the actual loads experienced during a tsunami.

This difference could be attributed to the highly transient and nonuniform flow which is neglected in the EGLA (e.g., stationary flow, neglected vertical accelerations, friction parametrization based on Manning's formula for uniform stationary flow) or the reliability of the in situ records of flow depths, which are assumed to be reliable herein. For the analyzed case, the use of an ad hoc reduction coefficient to the EGL is a simplified but reasonable alternative given that in situ data are available. However, in applications where only modeled runups are available (e.g., flooding charts), sensitivity analyses and/or calibration processes should be conducted to constrain the uncertainty of the method.

No attempts to compute inundation depths and flow velocities from a time history inundation analysis are conducted herein, as the tide gauge in the pier of San Juan Bautista was destroyed during the tsunami [41]. Therefore, maximum inundation depths and velocities are assumed to be in phase, thus providing a conservative estimation of tsunami loads. Additionally, the flow is assumed to be parallel to La Pólvora's topographic profile and to all houses' positions considered herein, thus neglecting the transverse effects (along the y-axis) on the structural response of each structure. An improvement from EGLA could be achieved by means of more sophisticated methods which could recover the transient nature of the flow, the phase lag of flow depths and velocities, the horizontal pattern of the flow (e.g., Shallow Water Equations or Boussinesq type of equations) and, eventually, the three-dimensional nature of the flow triggered by the steep nearshore bathymetry characterizing the neighboring San Juan Bautista (e.g., Reynolds-Averaged Navier–Stokes equations, Large Eddy Simulations).

While more advanced methods—such as numerical modeling based on Shallow Water Equations (SWE) or Reynolds Averaged Navier–Stokes (RANS) equations—would allow for a more accurate representation of the temporal and spatial evolution of tsunami flow, our study does not aim to provide a comprehensive validation of hydrodynamic parameters other than water levels captured in situ. Instead, our approach focuses on the structural response of timber houses under hydrodynamic loads estimated using a practical method. Future research could complement this analysis with more detailed studies incorporating advanced numerical modeling to assess the degree of uncertainty associated with the use of EGLA in this type of application.

5.2. Structural Analysis Using the EGLA

According to ASCE 7-22, Chapter 6, buildings in tsunami-exposed areas are subjected to hydrostatic and hydrodynamic forces, waterborne debris accumulation and impact loads, subsidence and scour. In this study, we disregard scour or the geotechnical damage of the soil, as there was no ubiquitous evidence of such phenomena during the field surveys by Fritz et al. [7] and Breuer et al. [36]. Additionally, being far from the rupture, there is no evidence of subsidence following the 27 February 2010 earthquake in the town of San Juan Bautista.

As for the structural analysis, Figures 8a and 9a show that the support reactions in the x-axis at the coastline ($x = 0$ m) is 16 times larger than those in the farthest position ($x = 250$ m). In contrast, along the z-axis, the ratio is 1.8 for the same positions. The total forces in the y-axis are zero in all cases, as the flow depth is assumed to be equal on both sides of the structure, causing the lateral hydrostatic forces to cancel each other out.

Figures 8a and 9a also show that the shear forces in the x-axis decrease as the house location is further from the coastline. This is because the drag and impact forces of floating objects scale with the square of the flow velocity, the latter of which decreases as the flow depth does. In the z-axis, forces remain constant up to $x = 200$ m as the structure is completely submerged (i.e., the displaced volume is equal to the house's volume), then decrease considerably at $x = 250$ m, as the house becomes partially flooded.

Upon examining the resulting structural deformations, the maximum inter-story drift of 4.94 is observed at node 17 in the x-axis for the structure's position at the coastline ($x = 0$ m) under the most unfavorable load case. This value significantly exceeds the maximum inter-story drift considered in the design of timber frame structures [54,55], suggesting that the structures experience complete collapse due to the tsunami. Such a large inter-story drift is obtained by considering the linear elastic behavior of structural elements, which, due to their flexibility, tend to deform under combined loading actions. Additionally, displacements are significant across all positions of the structure, indicating that the house reaches collapse as it can no longer support its own weight due to the overturning moments produced by the shifting centers of gravity of the structural components.

5.3. Failure Due to Buoyancy

Our results do not provide sufficient details to conclude whether houses float or fail due to tsunami impact, but provide spatial estimates of force magnitudes prompting the latter (i.e., buoyancy) or former (i.e., hydrodynamic and impact forces) failure modes. The few houses that presumably floated (Figure 1c) were constrained to the last few meters before the runup, which were not fully captured with the spatial spacing of 50 m considered for each house position. This could be further improved by increasing the spatial resolution of the analysis for this particular case, by conducting sensitivity analyses for simplified flow conditions and structures or more sophisticated methods. Additionally, from the three post-tsunami field surveys conducted by the Ocean Engineering team at Universidad de Valparaíso [41], structural damage was only assessed on 28 March 2010, nearly one month after the tsunami, and after reconstruction works had concluded. By this time, clear evidence of structural damage was scarce and likely modified.

Fortunately, structural failure due to buoyancy has been investigated by several researchers. Yeh et al. [56], for example, found that buoyancy reduces the net force on the structural body, thereby diminishing the recovery forces needed to resist sliding and overturning failures. They concluded that the failure patterns of buildings following the 2011 Tohoku earthquake and tsunami were diverse: some buildings inland failed during the runup while others failed during the drawdown, being pushed towards the sea. This suggests that forces of the external flow alone may not govern the failure mode, but the stability of buildings previously weakened by buoyancy force may have played a role in their failure. Conversely, del Zoppo et al. [57] showed that buoyancy can lead to failure in combination with other effects associated with tsunamis.

Buoyancy can be a critical factor when coastal buildings feature fragile vertical enclosures, such as walls, doors and windows. Indeed, Yeh et al. [58,59] showed that precarious constructions with vertical enclosures survived the tsunami following the Tohoku earthquake, allowing us to deduce that buoyancy played a decisive role in San Juan Bautista, as single-story houses exhibited similar features of fragile vertical enclosures. This digression is, however, tentative in San Juan Bautista, as the majority of timber houses were fully destroyed, their parts scattered and then mixed with the flow, thus making the identification of failure modes hard.

5.4. Contribution to the Resilience of Coastal Communities

The resilience of specific urban or rural communities to tsunamis is very sensitive to the location and distance of buildings with respect to the coast [60]. This is especially true for timber structures, which despite their ductile performance, are highly vulnerable to the action of tsunamis [60,61]. To reduce the impact of tsunamis, a "location criterion" where timber houses are located above the flooding line should therefore be combined with the design of mitigation works, the use of other structural typologies or reinforcements at the most stressed points of structures [61]. However, localized damage in exposed houses due to the impact of floating objects [62] is highly expected, regardless of the typology or materials used. To plan effective interventions, the planning process should also be based on resilience metrics [63] and the use of fragility curves and/or surfaces, such as those developed in earthquake-resistant design [60,64]. Last but not least, the resilience of communities should be improved by matching urban planning with the implementation of early warning systems to evacuate the population to safe shelters, designed in accordance with regulatory provisions [65].

6. Conclusions

This study assesses the structural response of single-story timber houses subjected to tsunami-induced loads using the EGLA method in different positions along a topographic profile in San Juan Bautista. We aimed to understand the failure modes of these lightweight structures and to determine whether the distance from the coast can be considered a factor in improving the safety of such constructions against future events.

As for the estimation of hydrodynamic loads, the EGLA provides a simple approach whenever in situ records are available. However, more sophisticated hydrodynamic models (e.g., SWE or RANS) could improve accuracy by capturing transient flow behaviors and three-dimensional effects which are not considered in EGLA.

Structural (linear) analyses reveal that, near the coastline, timber houses experience excessively large displacements and structural collapse as a result of a combination of buoyancy, impact, hydrodynamic and drag forces. The presence of buoyant forces (~290 ton-f) exacerbates structural instability in houses near the shore, reducing the foundations' anchorage efficiency and contributing to structural flotation. On the contrary, the farther from the coastline, the lower the depths and flow velocities, which leads to a decrease in drag forces and results in decreased displacements and reduced structural demand.

The nonlinear analysis confirms the results obtained from the linear analysis, since the structure collapses in all positions in the first 200 m from the coastline, while presenting a very low demand near the maximum runup, for which the structure remains elastic, without any of its members showing damage. Consequently, the methodology based on EGLA provides consistent results of the behavior of structures subjected to large tsunami forces, without requiring very sophisticated and laborious analyses such as those involving the nonlinearity characteristics of the structures.

Given the limitations of nonlinear analysis, the analysis applied to the structure located at $x = 250$ m only considers the lateral forces caused by the tsunami acting on the façade. However, it is expected that the buoyancy forces will cause the collapse of the structure, since they reach a value close to 1600 kN.

Despite their seismic resistance, lightweight timber structures are not suitable for areas prone to tsunamis. The use of heavier and more rigid materials, such as reinforced concrete, is recommended to withstand hydrodynamic and buoyant forces effectively. An interesting exercise would be to implement nonlinear analysis in steel, reinforced concrete and masonry structures responding to tsunami loads, aiming to provide guidelines for the design of structures of different materials, e.g., [66–69]. Future research should also evaluate the performance of different configurations (e.g., two or more story houses, elevated houses, the use of composite materials) to establish comprehensive design guidelines for tsunami-prone areas. Overall, the study highlights the need for stricter building codes in coastal regions, the use of tsunami-resilient design materials and the relocation of lightweight structures further inland to mitigate risk.

While EGLA provides practical estimates of tsunami-induced loads on coastal structures, its application in structural design should be approached with caution. ASCE 7-22 acknowledges that EGLA is a useful method for exploratory studies and preliminary estimations; however, its use as the sole tool for designing tsunami-resilient structures should be supplemented with more rigorous approaches whenever feasible. In particular, combining EGLA with detailed structural analyses or advanced hydrodynamic modeling could offer a more accurate assessment of structural performance under extreme loads.

Additionally, land-use planning and the selection of appropriate construction materials remain key factors in mitigating damage in tsunami-prone areas.

Future research should explore the performance of different building materials under tsunami-induced loads, particularly reinforced concrete, steel and hybrid structural systems. Conducting nonlinear analyses on these materials could provide a comparative assessment of their resistance to hydrodynamic forces and their failure mechanisms, contributing to the development of more robust design guidelines. Additionally, optimizing disaster-resistant designs through computational techniques, such as performance-based design approaches or topology optimization, could help to enhance structural resilience in tsunami-prone areas. These studies could also incorporate experimental validations to further refine numerical modeling techniques and improve the accuracy of failure predictions for different structural typologies.

Author Contributions: Conceptualization, P.W. and D.O.M.; methodology, P.W.; software, D.O.M., P.W. and J.C.V.; validation, P.W. and J.C.V.; formal analysis, D.O.M., P.W. and J.C.V.; investigation, D.O.M.; resources, P.W. and J.C.V.; data curation, P.W. and J.C.V.; writing—original draft preparation, D.O.M.; writing—review and editing, P.W. and J.C.V.; visualization, P.W.; supervision, P.W. and J.C.V. All authors have read and agreed to the published version of the manuscript.

Funding: This research received no external funding.

Institutional Review Board Statement: Not applicable.

Informed Consent Statement: Not applicable.

Data Availability Statement: The research data are available in the authors' files and may be provided to interested parties upon direct request by email.

Acknowledgments: The authors wish to express their gratitude to the Pontificia Universidad Católica de Valparaíso and the Universidad de Valparaíso, in whose facilities this research was carried out.

Conflicts of Interest: The authors declare no conflicts of interest.

Appendix A. Impact of Wood Logs Using ASCE 7-22

The nominal maximum instantaneous debris impact force (F_{ni}) is determined in accordance with Equation (A1)

$$F_{ni} = u_{max}\sqrt{k\ m_d} \tag{A1}$$

where u_{max} is the maximum flow velocity at depths sufficient to float the debris, k the effective stiffness of the impacting debris or the lateral stiffness of the impacted structural element(s) deformed by the impact, whichever is less and m_d the mass of the debris. The instantaneous debris impact force (F_i) is determined with Equation (A2)

$$F_i = I_{tsu} C_o F_{ni} \tag{A2}$$

where C_o is the orientation coefficient ($C_o = 0.65$ for logs and poles). Logs are assumed to strike longitudinally for the calculation of debris stiffness in the equation. The stiffness of logs is calculated as $k = EA/L$, in which E is the longitudinal modulus of elasticity of the log, A its cross-sectional area and L its length. A Pinus radiata wood log, 2.5 m long and 75 cm in diameter with a density of 420 kg/m^3 and an elastic modulus of 7900 MPa, is considered. Along with Eucalyptus, Pinus radiata is the most abundant species in the lower part of San Juan Bautista. With these assumptions, the impact force resulted in $F_i = 130$ tonf, which was considered excessive.

Table A1. Parameters used to compute impact of wood logs using ASCE 7-22.

Parameter	Symbol	Dimension	Value
Effective stiffness of the impacting logs	k	kN/m	1.39×10^6
Maximum velocity at depths of debris	u_{max}	m/s	8.05
Mass of debris object	m_d	kg	500
Orientation coefficient	C_o	-	0.65

References

1. Stolle, J.; Takabatake, T.; Nistor, I.; Mikami, T.; Nishizaki, S.; Hamano, G.; Ishii, H.; Shibayama, T.; Goseberg, N.; Petriu, E. Experimental investigation of debris damming loads under transient supercritical flow conditions. *Coast. Eng.* **2018**, *139*, 16–31. [CrossRef]
2. Aguiniga, F.; Jaiswal, M.; Sai, J.; Cox, D.; Gupta, R.; Lindt, J. Experimental study of tsunami forces on structures. In *Coastal Hazards*; American Society of Civil Engineers: Reston, VA, USA, 2013; pp. 111–118. [CrossRef]
3. Bremm, G.; Goseberg, N.; Schlurmann, T.; Nistor, I. Long Wave Flow Interaction with a Single Square Structure on a Sloping Beach. *J. Mar. Sci. Eng.* **2015**, *3*, 821–844. [CrossRef]
4. Goseberg, N.; Schlurmann, T. Non-stationary Flow around Buildings during Run-up of Tsunami Waves on a Plain Beach. *Coast. Eng. Proc.* **2014**, *1*, 21. [CrossRef]
5. Goseberg, N.; Wurpts, A.; Schlurmann, T. Laboratory-Scale Generation of Tsunami and Long Waves. *Coast. Eng.* **2013**, *79*, 57–74. [CrossRef]
6. Ghobarah, A.; Saatcioglu, M.; Nistor, I. The Impact of the 26 December 2004 Earthquake and Tsunami on Structures and Infrastructure. *Eng. Struct.* **2006**, *28*, 312–326. [CrossRef]
7. Fritz, H.; Petroff, C.; Catalán, P.; Cienfuegos, R.; Winckler, P.; Kalligeris, N.; Weiss, R.; Barrientos, S.; Meneses, G.; Valderas-Bermejo, C.; et al. Field Survey of the 27 February 2010 Chile Tsunami. *Pure Appl. Geophys.* **2011**, *168*, 1989–2010. [CrossRef]
8. Robertson, I.; Chock, G.; Morla, J. Structural Analysis of Selected Failures Caused by the 27 February 2010 Chile Tsunami. *Earthq. Spectra* **2012**, *28*, 215–243. [CrossRef]
9. Zareian, F.; Aguirre, C.; Beltran, J.; Cruz, E.; Herrera, R.; Leon, R.; Millan, A.; Verdugo, A. Reconnaissance Report of Chilean Industrial Facilities Affected by the 2010 Chile Offshore Bío-Bío Earthquake. *Earthq. Spectra* **2012**, *28*, 513–532. [CrossRef]
10. Jayaratne, M.; Premaratne, B.; Adewale, A.; Mikami, T.; Matsuba, S.; Shibayama, T.; Esteban, M.; Nistor, I. Failure Mechanisms and Local Scour at Coastal Structures Induced by Tsunami. *Coast. Eng. J.* **2016**, *58*, 1640017-1–1640017-38. [CrossRef]
11. Koshimura, S.; Hayashi, S.; Gokon, H. The Impact of the 2011 Tohoku Earthquake Tsunami Disaster and Implications to the Reconstruction. *Soils Found.* **2014**, *54*, 560–572. [CrossRef]
12. Amakuni, K.; Terazono, N.; Yamamoto, T.; Enomoto, T. Basic Analysis on Building Damages by Tsunami Due to the 2011 Great East Japan Earthquake Disaster Using GIS. In Proceedings of the 15th World Conference on Earthquake Engineering, Lisbon, Portugal, 24–28 September 2012.
13. Charvet, I.; Suppasri, A.; Imamura, F. Empirical Fragility Analysis of Building Damage Caused by the 2011 Great East Japan Tsunami in Ishinomaki City Using Ordinal Regression, and Influence of Key Geographical Features. *Stoch. Environ. Res. Risk Assess.* **2014**, *28*, 1853–1867. [CrossRef]
14. Chock, G.; Robertson, I.N. Tsunami Design Criteria and Load Cases of the ASCE 7-16 Chapter 6, Tsunami Loads and Effects. In Proceedings of the 16th World Conference on Earthquake Engineering, 16WCEE, Santiago de Chile, Chile, 9–13 January 2017.
15. Robertson, I.N.; Thomas, S.A. Prototype Building Tsunami Design Examples. In Proceedings of the 16th World Conference on Earthquake Engineering, 16WCEE, Santiago de Chile, Chile, 9–13 January 2017.
16. Charvet, I.; Macabuag, J.; Rossetto, T. Estimating Tsunami-Induced Building Damage through Fragility Functions: Critical Review and Research Needs. *Front. Built Environ.* **2017**, *3*, 36. [CrossRef]
17. Kihara, N.; Kaida, H.; Shibayama, A.; Miyagawa, Y. Responses of Concrete Vertical Walls to Tsunami Wave Pressures and Debris Impact. *Coast. Eng. Proc.* **2018**, *1*, 38. [CrossRef]
18. Kihara, N.; Niida, Y.; Takabatake, D.; Kaida, H.; Shibayama, A.; Miyagawa, Y. Large-Scale Experiments on Tsunami-Induced Pressure on a Vertical Tide Wall. *Coast. Eng.* **2015**, *99*, 46–63. [CrossRef]
19. Naito, C.J.; Riggs, H.R.; Wei, Y.; Cercone, C. Shipping-Container Impact Assessment for Tsunamis. *J. Waterw. Port Coast. Ocean Eng.* **2016**, *142*, 05016003. [CrossRef]
20. Naito, C.J.; Cercone, C.; Riggs, H.R.; Cox, D. Procedure for Site Assessment of the Potential for Tsunami Debris Impact. *J. Waterw. Port Coast. Ocean Eng.* **2014**, *140*, 223–232. [CrossRef]
21. Linton, D.; Gupta, R.; Cox, D.; van de Lindt, J.; Oshnack, M.E.; Clauson, M. Evaluation of Tsunami Loads on Wood-Frame Walls at Full Scale. *J. Struct. Eng.* **2013**, *139*, 1318–1325. [CrossRef]

22. Krautwald, C.; von Häfen, H.; Niebuhr, P.; Vögele, K.; Stolle, J.; Schimmels, S.; Schürenkamp, D.; Sieder, M.; Goseberg, N. Collapse Processes and Associated Loading of Square Light-Frame Timber Structures Due to Bore-Type Waves. *Coast. Eng.* **2022**, *177*, 104178. [CrossRef]
23. Suppasri, A.; Mas, E.; Charvet, I.; Gunasekera, R.; Imai, K.; Fukutani, Y.; Abe, Y.; Imamura, F. Building Damage Characteristics Based on Surveyed Data and Fragility Curves of the 2011 Great East Japan Tsunami. *Nat. Hazards* **2013**, *66*, 319–341. [CrossRef]
24. Baiguera, M.; Rossetto, T.; Robertson, I.N.; Petrone, C. Towards a Tsunami Nonlinear Static Analysis Procedure for the ASCE 7 Standard. In Proceedings of the 2nd International Conference on Natural Hazards & Infrastructure 2019, Chania, Greece, 23–26 June 2019.
25. Aegerter, D.W.; Robertson, I.N. Push-over Tsunami Analysis Using ETABS. In Proceedings of the Current Perspectives and New Directions in Mechanics, Modelling and Design of Structural Systems, Proceedings of the 8th International Conference on Structural Engineering, Mechanics and Computation 2022, Cape Town, South Africa, 5–7 September 2022; CRC Press/Balkema: Boca Raton, FL, USA, 2023; pp. 221–227.
26. McKenna, F.; Fenves, G.L.; Scott, M.H.; Jeremic, B. Open system for earthquake engineering simulation (OpenSees). In *Computer Program*; University of California: Berkeley, CA, USA, 2000. Available online: https://opensees.berkeley.edu/ (accessed on 15 June 2024).
27. CSI (Computers and Structures, Inc.). *ETABS Integrated Building Design Software, Version 2018*; CSI: Walnut Creek, CA, USA, 2018. Available online: https://www.csiamerica.com/products/etabs (accessed on 1 December 2024).
28. American Society of Civil Engineers. *Minimum Design Loads and Associated Criteria for Buildings and Other Structures*; ASCE7-22: Reston, VA, USA, 2022; ISBN 9780784415788.
29. Kriebel, D.L.; Lynett, P.J.; Cox, D.T.; Petroff, C.; Robertson, I.N.; Chock, G.Y.K. Energy method for approximating overland tsunami flows. *J. Waterw. Port Coast. Ocean Eng.* **2017**, *143*, 1–19. [CrossRef]
30. Wiebe, D.M. Tsunami Inundation: Estimating Damage and Predicting Flow. Properties. Master's Thesis, Oregon State University, Corvallis, OR, USA, 2013.
31. American Society of Civil Engineers. *Minimum Design Loads for Buildings and Other Structures*; ASCE 7-16: Reston, VA, USA, 2017.
32. Carden, L.; Chock, G.; Yu, G.; Robertson, I. The New ASCE Tsunami Design Standard Applied to Mitigate Tohoku Tsunami Building Structural Failure Mechanisms. In *Handbook of Coastal Disaster Mitigation for Engineers and Planners*; Shibayama, T., Esteban, M., Takagi, H., Eds.; Elsevier: Amsterdam, The Netherlands, 2015; pp. 461–490. [CrossRef]
33. Chock, G.; Yu, G.; Thio, H.; Lynett, P. Target Structural Reliability Analysis for Tsunami Hydrodynamic Loads of the ASCE 7 Standard. *J. Struct. Eng.* **2016**, *142*, 04016092. [CrossRef]
34. Chock, G. Design for Tsunami Loads and Effects in the ASCE 7-16 Standard. *J. Struct. Eng.* **2016**, *142*, 04016093. [CrossRef]
35. Tada, T.; Miyata, Y.; Bathurst, R. Energy Grade Line Analysis of Tsunami Run-up on the Sendai Plain after the 2011 Tohoku Earthquake. *Coast. Eng.* **2018**, *140*, 306–315. [CrossRef]
36. Breuer, W.A.; Igualt, F.; Contreras-López, M.; Winckler, P.; Zambra, C. Tsunami Impact and Resilience Cycle in an Insular Town: The Case of Robinson Crusoe Island, Chile. *Ocean Coast. Manag.* **2021**, *209*, 105714. [CrossRef]
37. Contreras, M.; Winckler, P. Pérdidas de vidas, viviendas, infraestructura y embarcaciones por el Tsunami del 27 de Febrero de 2010 en la costa central de Chile. *Obras Proy.* **2013**, *14*, 6–19. [CrossRef]
38. UV. El Sonido de Robinson. Escuela de Ingeniería Civil Oceánica, Universidad de Valparaíso and Mosca Films. 2010. Available online: https://www.youtube.com/watch?v=pWtCDsXpWcE (accessed on 1 November 2023).
39. Chock, G.; Carden, L.; Robertson, I.; Olsen, M.; Yu, G. Tohoku tsunami-induced building failure analysis with implications for US tsunami and seismic design codes. *Earthq. Spectra* **2013**, *29* (Suppl. S1), 99–126. [CrossRef]
40. Chock, G.; Robertson, I.; Kriebel, D.; Francis, M.; Nistor, I. *Tohoku, Japan, Earthquake and Tsunami of 2011: Performance of Structures under Tsunami Loads*; Book Set: Tohoku Earthquake; American Society of Civil Engineers: Reston, VA, USA, 2013.
41. Winckler, P.; Reyes, M.; Sepúlveda, I.; Molina, M. El Tsunami del 27-02-2010 en Isla Robinson Crusoe, Archipiélago Juan Fernández. Preparado Para la Ilustre Municipalidad de Juan Fernández. Technical Report. 2010. Available online: http://ingenieriaoceanica3.uv.cl/sitio/index.php/documentos-ico/84-el-tsunami-del-27-02-2010-en-isla-robinsoncrusoe-archipielago-juan-fernandez (accessed on 1 November 2023).
42. Autodesk. *Robot Structural Analysis Professional*; Version 2024; Autodesk, Inc.: San Rafael, CA, USA, 2024. Available online: https://www.autodesk.com/products/robot-structural-analysis/overview (accessed on 1 July 2023).
43. FEMA (Federal Emergency Management Agency). *Guidelines for Design of Structures for Vertical Evacuation from Tsunamis*, 3rd ed.; US Department of Homeland Security, Federal Emergency Management Agency: Washington, DC, USA, 2019.
44. INN (Instituto Nacional de Normalización). *NCh 3363 of. 2015. Diseño Estructural-Edificaciones en Áreas de Riesgo de Inundación Por Tsunami o Seiche*; INN: Santiago, Chile, 2015.
45. CMPC Maderas SpA, Pino Radiata. Available online: www.cmpcmaderas.com (accessed on 5 February 2024).
46. INN (Instituto Nacional de Normalización). *NCh 1198 of. 2014. Madera-Construcción en Madera-Cálculo*; INN: Santiago, Chile, 2014.

47. INN (Instituto Nacional de Normalización). *NCh 1537 of. 2009. Diseño Estructural-Cargas Permanentes y Cargas de Uso*; INN: Santiago, Chile, 2009.
48. Vielma-Quintero, J.C.; Carvallo, J.; Vielma, J.C. Comparative assessment of performance-based design methodologies applied to a R.C. shear-wall building. *Buildings* **2023**, *13*, 1492. [CrossRef]
49. Mander, J.B.; Priestley, M.J.N.; Park, R. Theoretical Stress-Strain Model for Confined Concrete. *J. Struct. Eng.* **1988**, *114*, 1804–1826. [CrossRef]
50. Menegotto, M.; Pinto, P.E. Method of analysis for cyclically loaded R.C. plane frames including changes in geometry and nonelastic behavior of elements under combined normal force and bending. In *Symposium on the Resistance and Ultimate Deformability of Structures Acted on by Well Defined Repeated Loads, International Association for Bridge and Structural Engineering*; IABSE: Zurich, Switzerland, 1973; pp. 15–22.
51. Perez, A. Comparison of Compression Tests on Structural Wood Using UNE and ASTM Standards. Master Thesis, University of Valladolid, Valladolid, Spain, 2014. (In Spanish)
52. Seismosoft Ltd. *SeismoStruct 2024 User Manual—A Computer Program for Static and Dynamic Nonlinear Analysis of Framed Structures*; Seismosoft Ltd.: Pavia, Italy, 2021. Available online: https://seismosoft.com/ (accessed on 11 December 2024).
53. Ariete, N. Characterization of Pinus radiata D. Don wood subjected to a thermal modification process using an immersion environment. Bachelor Thesis, Austral University of Chile, Valdivia, Chile, 2010. (In Spanish)
54. van de Lindt, J.W.; Pei, S.; Pang, W.; Rosowsky, D.V. IDA Comparison of IBC-Designed and DDD-Designed Six-Story Light-Frame Wood Buildings. *J. Perform. Constr. Facil.* **2011**, *25*, 138–142. [CrossRef]
55. Namba, T.; Nakagawa, T.; Isoda, H.; Kado, Y.; Odani, R.; Takino, A. Seismic Response Comparison of Full-Scale Moment-Resisting Timber Frame and Joint Test Result. *J. Struct. Eng.* **2023**, *149*, 04023079. [CrossRef]
56. Yeh, H.; Barbosa, A.; Ko, H.; Cawley, J. Tsunami loadings on structures: Review and analysis. *Int. Conf. Coastal. Eng.* **2014**, *1*, 4. [CrossRef]
57. del Zoppo, M.; Rossetto, T.; Ludovico, M.d.; Prota, A. Effect of buoyancy loads on the tsunami fragility of reinforced concrete frames including consideration of blow-out slabs. *Res. Sq.* **2022**, *preprint*. [CrossRef]
58. Yeh, H.; Sato, S.; Tajima, Y. The 11 March 2011 East Japan Earthquake and Tsunami: Tsunami Effects on Coastal Infrastructure and Buildings. Pure Appl. *Geophys.* **2013**, *170*, 1019–1031. [CrossRef]
59. Manawasekara, C.; Mizutani, N.; Nakamura, T.; Aoki, S. Failure of concrete structure under tsunami loading. *J. JSCE* **2014**, *2*, 214–223. [CrossRef] [PubMed]
60. Harati, M.; Van De Lindt, J.W. Community-Level Resilience Analysis Using Earthquake-Tsunami Fragility Surfaces. *Resilient Cities Struct.* **2024**, *3*, 101–115. [CrossRef]
61. Villagra, P.; Herrmann, M.G.; Quintana, C.; Sepúlveda, R.D. Community Resilience to Tsunamis along the Southeastern Pacific: A Multivariate Approach Incorporating Physical, Environmental, and Social Indicators. *Nat. Hazards* **2017**, *88*, 1087–1111. [CrossRef]
62. Frucht, E.; Salamon, A.; Rozelle, J.; Levi, T.; Calvo, R.; Avirav, V.; Burns, J.N.; Zuzak, C.; Gal, E.; Trapper, P.; et al. Tsunami Loss Assessment Based on Hazus Approach–The Bat Galim, Israel, Case Study. *Eng. Geol.* **2021**, *289*, 106175. [CrossRef]
63. Mebarki, A.; Jerez, S.; Prodhomme, G.; Reimeringer, M. Natural Hazards, Vulnerability and Structural Resilience: Tsunamis and Industrial Tanks. *Geomat. Nat. Hazards Risk* **2016**, *7*, 5–17. [CrossRef]
64. Attary, N.; Unnikrishnan, V.U.; Van De Lindt, J.W.; Cox, D.T.; Barbosa, A.R. Performance-Based Tsunami Engineering Methodology for Risk Assessment of Structures. *Eng. Struct.* **2017**, *141*, 676–686. [CrossRef]
65. León, J.; March, A. Urban Morphology as a Tool for Supporting Tsunami Rapid Resilience: A Case Study of Talcahuano, Chile. *Habitat Int.* **2014**, *43*, 250–262. [CrossRef]
66. Petrone, C.; Rossetto, T.; Goda, K. Fragility assessment of a RC structure under tsunami actions via nonlinear static and dynamic analyses. *Eng. Struct.* **2017**, *136*, 36–53. [CrossRef]
67. Petrone, C.; Rossetto, T.; Baiguera, M.; Bustamante, C.; Ioannou, I. Fragility functions for a reinforced concrete structure subjected to earthquake and tsunami in sequence. *Eng. Struct.* **2020**, *205*, 110120. [CrossRef]
68. Tagle, S.J.; Jünemann, R.; Vásquez, J.; de la Llera, J.C.; Baiguera, M. Performance of a reinforced concrete wall building subjected to sequential earthquake and tsunami loading. *Eng. Struct.* **2021**, *238*, 111995. [CrossRef]
69. Karafagka, S.; Fotopoulou, S.; Pitilakis, K. Analytical tsunami fragility curves for seaport RC buildings and steel light frame warehouses. *Soil Dyn. Earthq. Eng.* **2018**, *112*, 118–137. [CrossRef]

MDPI AG
Grosspeteranlage 5
4052 Basel
Switzerland
Tel.: +41 61 683 77 34

Journal of Marine Science and Engineering Editorial Office
E-mail: jmse@mdpi.com
www.mdpi.com/journal/jmse

Academic Open
Access Publishing

mdpi.com

ISBN 978-3-7258-4134-9